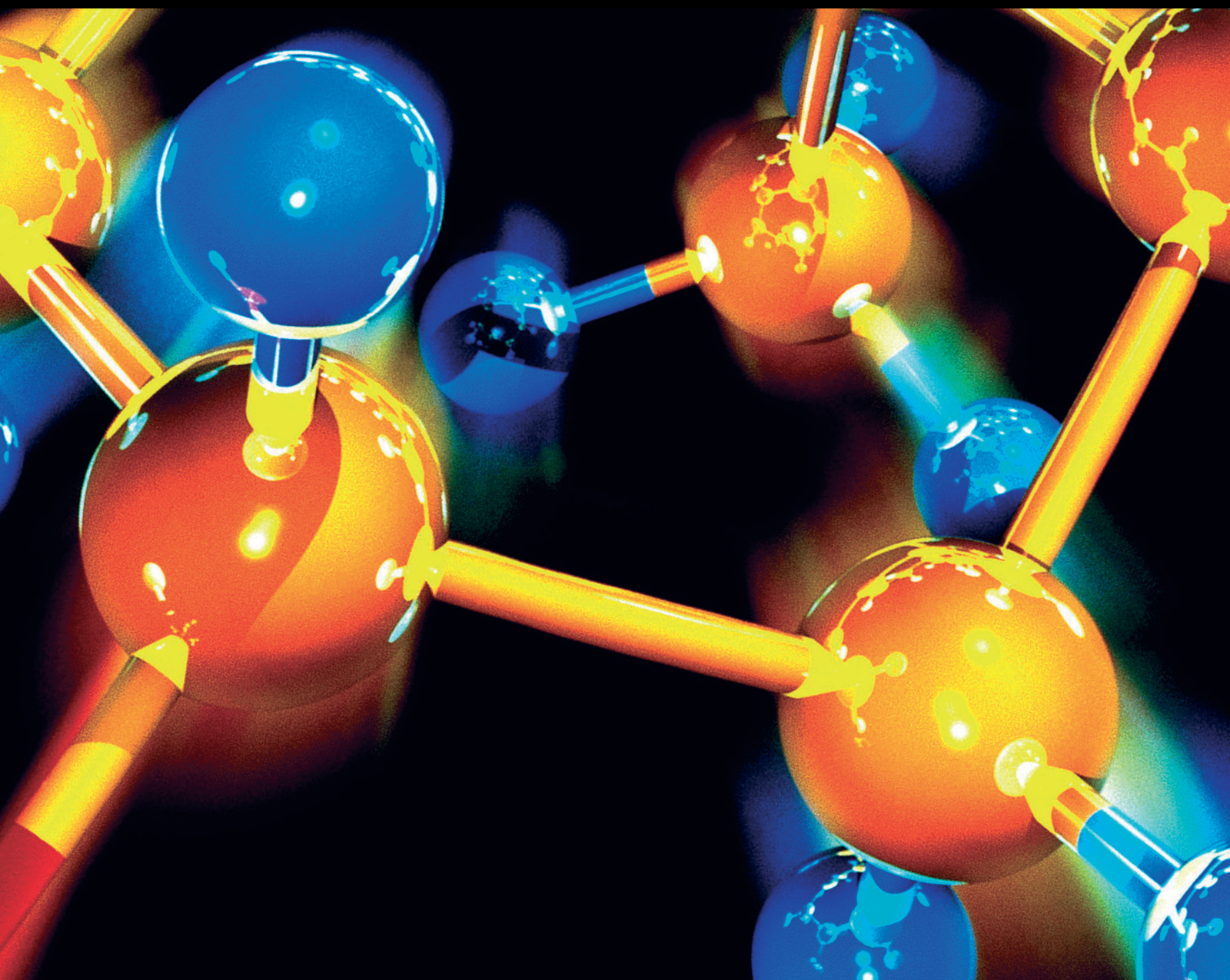# Futuristic Materials for Electrochemical Energy Storage and Conversion Systems

Lead Guest Editor: Ajay Rakkesh Rajendran
Guest Editors: K. K. Aruna and Javier Rodríguez Varela

Futuristic Materials for Electrochemical Energy Storage and Conversion Systems

Futuristic Materials for Electrochemical Energy Storage and Conversion Systems

Lead Guest Editor: Ajay Rakkesh Rajendran
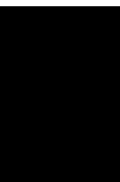Guest Editors: K. K. Aruna and Javier Rodríguez Varela

Fatih Deniz (iD), Turkey
Claudio Di Iaconi, Italy
Irene Dini (iD), Italy
Daniele Dondi, Italy
Yingchao Dong (iD), China
Dennis Douroumis (iD), United Kingdom
John Drexler, USA
Qizhen Du, China
Yuanyuan Duan (iD), China
Philippe Dugourd, France
Frederic Dumur (iD), France
Grégory Durand (iD), France
Mehmet E. Duru, Turkey
Takayuki Ebata (iD), Japan
Arturo Espinosa Ferao (iD), Spain
Valdemar Esteves (iD), Portugal
Cristina Femoni (iD), Italy
Gang Feng, China
Dieter Fenske, Germany
Jorge F. Fernandez-Sanchez (iD), Spain
Alberto Figoli (iD), Italy
Elena Forte, Italy
Sylvain Franger (iD), France
Emiliano Fratini (iD), Italy
Franco Frau (iD), Italy
Bartolo Gabriele (iD), Italy
Guillaume Galliero (iD), France
Andrea Gambaro (iD), Italy
Vijay Kumar Garlapati, India
James W. Gauld (iD), Canada
Barbara Gawdzik (iD), Poland
Pier Luigi Gentili (iD), Italy
Beatrice Giannetta (iD), Italy
Dimosthenis L. Giokas (iD), Greece
Alejandro Giorgetti (iD), Italy
Alexandre Giuliani (iD), France
Elena Gomez (iD), Spain
Yves Grohens, France
Katharina Grupp, Germany
Luis F. Guido (iD), Portugal
Maolin Guo, USA
Wenshan Guo (iD), Australia
Leena Gupta (iD), India
Muhammad J. Habib, USA
Jae Ryang Hahn, Republic of Korea

Christopher G. Hamaker (iD), USA
Ashanul Haque (iD), Saudi Arabia
Yusuke Hara, Japan
Naoki Haraguchi, Japan
Serkos A. Haroutounian (iD), Greece
Rudi Hendra (iD), Indonesia
Javier Hernandez-Borges (iD), Spain
Miguel Herrero, Spain
Mark Hoffmann (iD), USA
Hanmin Huang, China
Doina Humelnicu (iD), Romania
Charlotte Hurel, France
Nenad Ignjatović (iD), Serbia
Ales Imramovsky (iD), Czech Republic
Muhammad Jahangir, Pakistan
Philippe Jeandet (iD), France
Sipak Joyasawal, USA
Sławomir M. Kaczmarek, Poland
Ewa Kaczorek, Poland
Mostafa Khajeh, Iran
Srećko I. Kirin (iD), Croatia
Anton Kokalj (iD), Slovenia
Sevgi Kolaylı (iD), Turkey
Takeshi Kondo (iD), Japan
Christos Kordulis, Greece
Ioannis D. Kostas (iD), Greece
Yiannis Kourkoutas (iD), Greece
Henryk Kozlowski, Poland
Yoshihiro Kudo (iD), Japan
Avvaru Praveen Kumar (iD), Ethiopia
Dhanaji Lade, USA
Isabel Lara (iD), Spain
Jolanta N. Latosinska (iD), Poland
João Paulo Leal (iD), Portugal
Woojin Lee, Kazakhstan
Yuan-Pern Lee (iD), Taiwan
Matthias Lein (iD), New Zealand
Huabing Li, China
Jinan Li (iD), USA
Kokhwa Lim (iD), Singapore
Teik-Cheng Lim (iD), Singapore
Jianqiang Liu (iD), China
Xi Liu (iD), China
Xinyong Liu (iD), China
Zhong-Wen Liu (iD), China

Vikram Sarpe, USA
Adrian Saura-Sanmartin, Spain
Stéphanie Sayen, France
Ewa Schab-Balcerzak, Poland
Hartwig Schulz, Germany
Gulaim A. Seisenbaeva, Sweden
Serkan Selli, Turkey
Murat Senturk, Turkey
Beatrice Severino, Italy
Sunil Shah Shah, USA
Ashutosh Sharma, USA
Hideaki Shirota, Japan
Cláudia G. Silva, Portugal
Ajaya Kumar Singh, India
Vijay Siripuram, USA
Ponnurengam Malliappan Sivakumar, Japan
Tomás Sobrino, Spain
Raquel G. Soengas, Spain
Yujiang Song, China
Olivier Soppera, France
Radhey Srivastava, USA
Vivek Srivastava, India
Theocharis C. Stamatatos, Greece
Athanassios Stavrakoudis, Greece
Darren Sun, Singapore
Arun Suneja, USA
Kamal Swami, USA
B.E. Kumara Swamy, India
Elad Tako, USA
Shoufeng Tang, China
Zhenwei Tang, China
Vijai Kumar Reddy Tangadanchu, USA
Franco Tassi, Italy
Alexander Tatarinov, Russia
Lorena Tavano, Italy
Tullia Tedeschi, Italy
Vinod Kumar Tiwari, India
Augusto C. Tome, Portugal
Fernanda Tonelli, Brazil
Naoki Toyooka, Japan
Andrea Trabocchi, Italy
Philippe Trens, France
Ekaterina Tsipis, Russia
Esteban P. Urriolabeitia, Spain

Toyonobu Usuki, Japan
Giuseppe Valacchi, Italy
Ganga Reddy Velma, USA
Marco Viccaro, Italy
Jaime Villaverde, Spain
Marc Visseaux, France
Balaga Viswanadham, India
Alessandro Volonterio, Italy
Zoran Vujcic, Serbia
Chun-Hua Wang, China
Leiming Wang, China
Carmen Wängler, Germany
Wieslaw Wiczkowski, Poland
Bryan M. Wong, USA
Frank Wuest, Canada
Yang Xu, USA
Dharmendra Kumar Yadav, Republic of Korea
Maria C. Yebra-Biurrun, Spain
Dr Nagesh G Yernale, India
Tomokazu Yoshimura, Japan
Maryam Yousaf, China
Sedat Yurdakal, Turkey
Shin-ichi Yusa, Japan
Claudio Zaccone, Italy
Ronen Zangi, Spain
John CG Zhao, USA
Zhen Zhao, China
Antonio Zizzi, Italy
Mire Zloh, United Kingdom
Grigoris Zoidis, Greece
Deniz ŞAHİN, Turkey

Contents

Retracted: Chemical Regulation Effect of Water Use Efficiency of Maize Intercropping
Journal of Chemistry
Retraction (1 page), Article ID 9860645, Volume 2023 (2023)

Retracted: Numerical Simulation of Hot Stamping Forming of AZ Series Magnesium Alloys and Optimization of Die Process
Journal of Chemistry
Retraction (1 page), Article ID 9860563, Volume 2023 (2023)

Retracted: Art Decoration Design of Electrochemical Silicon Oxide Ceramic Sculpture Based on 3D Printing Technology
Journal of Chemistry
Retraction (1 page), Article ID 9852901, Volume 2023 (2023)

Retracted: Electrochemical Preparation of Recycled Self-Compacting Concrete Composite Beams and Their Application in Prefabricated Buildings
Journal of Chemistry
Retraction (1 page), Article ID 9847676, Volume 2023 (2023)

Retracted: Experimental Study on Compressive Strength of Ultrahigh Performance Concrete Prefabricated Wall Structure
Journal of Chemistry
Retraction (1 page), Article ID 9845657, Volume 2023 (2023)

Retracted: Study on the Color Genesis of South Red Agate and the Geological Characteristics of the Siliceous Gravel Layer
Journal of Chemistry
Retraction (1 page), Article ID 9843284, Volume 2023 (2023)

Retracted: Application of Chemical Technology of Water-Based Acrylic Dipping Paint in Art Painting Creation
Journal of Chemistry
Retraction (1 page), Article ID 9837350, Volume 2023 (2023)

Retracted: Art Design of Ceramic Sculpture Based on 3D Printing Technology and Electrochemistry
Journal of Chemistry
Retraction (1 page), Article ID 9835682, Volume 2023 (2023)

Retracted: Application of ZnO Semiconductor Nanomaterial Ink in Packaging and Printing Design
Journal of Chemistry
Retraction (1 page), Article ID 9835180, Volume 2023 (2023)

Retracted: Application of CAD/CAM Technology in Electrochemical Relief Design and Processing of Ceramic Art
Journal of Chemistry
Retraction (1 page), Article ID 9834687, Volume 2023 (2023)

Contents

Contents

Contents

Retraction

Retracted: Simulation of the Electro-Superconducting System Based on the H Equation

Journal of Chemistry

This article has been retracted by Hindawi following an investigation undertaken by the publisher [1]. This investigation has uncovered evidence of one or more of the following indicators of systematic manipulation of the publication process:

(1) Discrepancies in scope

(2) Discrepancies in the description of the research reported

(3) Discrepancies between the availability of data and the research described

(4) Inappropriate citations

(5) Incoherent, meaningless and/or irrelevant content included in the article

(6) Manipulated or compromised peer review

The presence of these indicators undermines our confidence in the integrity of the article's content and we cannot, therefore, vouch for its reliability. Please note that this notice is intended solely to alert readers that the content of this article is unreliable. We have not investigated whether authors were aware of or involved in the systematic manipulation of the publication process.

Wiley and Hindawi regrets that the usual quality checks did not identify these issues before publication and have since put additional measures in place to safeguard research integrity.

We wish to credit our own Research Integrity and Research Publishing teams and anonymous and named external researchers and research integrity experts for contributing to this investigation.

The corresponding author, as the representative of all authors, has been given the opportunity to register their agreement or disagreement to this retraction. We have kept a record of any response received.

References

[1] J. Zhang, "Simulation of the Electro-Superconducting System Based on the H Equation," *Journal of Chemistry*, vol. 2022, Article ID 6831771, 7 pages, 2022.

Retraction

Retracted: Modeling of Vapor-Liquid Equilibrium for Electrolyte Solutions Based on COSMO-RS Interaction

Journal of Chemistry

This article has been retracted by Hindawi following an investigation undertaken by the publisher [1]. This investigation has uncovered evidence of one or more of the following indicators of systematic manipulation of the publication process:

(1) Discrepancies in scope

(2) Discrepancies in the description of the research reported

(3) Discrepancies between the availability of data and the research described

(4) Inappropriate citations

(5) Incoherent, meaningless and/or irrelevant content included in the article

(6) Manipulated or compromised peer review

The presence of these indicators undermines our confidence in the integrity of the article's content and we cannot, therefore, vouch for its reliability. Please note that this notice is intended solely to alert readers that the content of this article is unreliable. We have not investigated whether authors were aware of or involved in the systematic manipulation of the publication process.

Wiley and Hindawi regrets that the usual quality checks did not identify these issues before publication and have since put additional measures in place to safeguard research integrity.

We wish to credit our own Research Integrity and Research Publishing teams and anonymous and named external researchers and research integrity experts for contributing to this investigation.

The corresponding author, as the representative of all authors, has been given the opportunity to register their agreement or disagreement to this retraction. We have kept a record of any response received.

References

[1] W. Liu, C. Zhao, Y. Zhou, and X. Xu, "Modeling of Vapor-Liquid Equilibrium for Electrolyte Solutions Based on COSMO-RS Interaction," *Journal of Chemistry*, vol. 2022, Article ID 9070055, 13 pages, 2022.

Retraction

Retracted: Enhanced Performance of Sn@Pt Core-Shell Nanocatalysts Supported on Two Different Carbon Structures for the Hydrogen Oxidation Reaction in Acid Media

Journal of Chemistry

This article has been retracted by Hindawi following an investigation undertaken by the publisher [1]. This investigation has uncovered evidence of one or more of the following indicators of systematic manipulation of the publication process:

(1) Discrepancies in scope

(2) Discrepancies in the description of the research reported

(3) Discrepancies between the availability of data and the research described

(4) Inappropriate citations

(5) Incoherent, meaningless and/or irrelevant content included in the article

(6) Manipulated or compromised peer review

The presence of these indicators undermines our confidence in the integrity of the article's content and we cannot, therefore, vouch for its reliability. Please note that this notice is intended solely to alert readers that the content of this article is unreliable. We have not investigated whether authors were aware of or involved in the systematic manipulation of the publication process.

Wiley and Hindawi regrets that the usual quality checks did not identify these issues before publication and have since put additional measures in place to safeguard research integrity.

We wish to credit our own Research Integrity and Research Publishing teams and anonymous and named external researchers and research integrity experts for contributing to this investigation.

The corresponding author, as the representative of all authors, has been given the opportunity to register their agreement or disagreement to this retraction. We have kept a record of any response received.

References

[1] F. J. Rodríguez-Varela, G. Hernández-Vázquez, S. Dessources et al., "Enhanced Performance of Sn@Pt Core-Shell Nanocatalysts Supported on Two Different Carbon Structures for the Hydrogen Oxidation Reaction in Acid Media," *Journal of Chemistry*, vol. 2022, Article ID 2982594, 12 pages, 2022.

Retraction

Retracted: Combination of Fruit and Vegetable Storage and Fresh-Keeping with Postharvest Heat Treatment

Journal of Chemistry

This article has been retracted by Hindawi following an investigation undertaken by the publisher [1]. This investigation has uncovered evidence of one or more of the following indicators of systematic manipulation of the publication process:

(1) Discrepancies in scope

(2) Discrepancies in the description of the research reported

(3) Discrepancies between the availability of data and the research described

(4) Inappropriate citations

(5) Incoherent, meaningless and/or irrelevant content included in the article

(6) Manipulated or compromised peer review

The presence of these indicators undermines our confidence in the integrity of the article's content and we cannot, therefore, vouch for its reliability. Please note that this notice is intended solely to alert readers that the content of this article is unreliable. We have not investigated whether authors were aware of or involved in the systematic manipulation of the publication process.

Wiley and Hindawi regrets that the usual quality checks did not identify these issues before publication and have since put additional measures in place to safeguard research integrity.

We wish to credit our own Research Integrity and Research Publishing teams and anonymous and named external researchers and research integrity experts for contributing to this investigation.

The corresponding author, as the representative of all authors, has been given the opportunity to register their agreement or disagreement to this retraction. We have kept a record of any response received.

References

[1] Y. Zhao and R. Zheng, "Combination of Fruit and Vegetable Storage and Fresh-Keeping with Postharvest Heat Treatment," *Journal of Chemistry*, vol. 2022, Article ID 8681499, 12 pages, 2022.

Retraction

Retracted: Mechanical Performance Analysis of Steel Beam-Column Joints in Fabricated Multirise Steel Structures after Fire

Journal of Chemistry

This article has been retracted by Hindawi, as publisher, following an investigation undertaken by the publisher [1]. This investigation has uncovered evidence of systematic manipulation of the publication and peer-review process. We cannot, therefore, vouch for the reliability or integrity of this article.

Please note that this notice is intended solely to alert readers that the peer-review process of this article has been compromised.

Wiley and Hindawi regret that the usual quality checks did not identify these issues before publication and have since put additional measures in place to safeguard research integrity.

We wish to credit our Research Integrity and Research Publishing teams and anonymous and named external researchers and research integrity experts for contributing to this investigation.

The corresponding author, as the representative of all authors, has been given the opportunity to register their agreement or disagreement to this retraction. We have kept a record of any response received.

References

[1] F. Liu, X. Wang, B. Cai, X. Li, and L. Yang, "Mechanical Performance Analysis of Steel Beam-Column Joints in Fabricated Multirise Steel Structures after Fire," *Journal of Chemistry*, vol. 2022, Article ID 7425801, 8 pages, 2022.

Retraction

Retracted: Application of Nanofluid Electrochemistry in Heat Dissipation of Permanent Magnet Synchronous Motors

Journal of Chemistry

This article has been retracted by Hindawi following an investigation undertaken by the publisher [1]. This investigation has uncovered evidence of one or more of the following indicators of systematic manipulation of the publication process:

(1) Discrepancies in scope

(2) Discrepancies in the description of the research reported

(3) Discrepancies between the availability of data and the research described

(4) Inappropriate citations

(5) Incoherent, meaningless and/or irrelevant content included in the article

(6) Peer-review manipulation

The presence of these indicators undermines our confidence in the integrity of the article's content and we cannot, therefore, vouch for its reliability. Please note that this notice is intended solely to alert readers that the content of this article is unreliable. We have not investigated whether authors were aware of or involved in the systematic manipulation of the publication process.

Wiley and Hindawi regrets that the usual quality checks did not identify these issues before publication and have since put additional measures in place to safeguard research integrity.

We wish to credit our own Research Integrity and Research Publishing teams and anonymous and named external researchers and research integrity experts for contributing to this investigation.

The corresponding author, as the representative of all authors, has been given the opportunity to register their agreement or disagreement to this retraction. We have kept a record of any response received.

References

[1] X. Lin and G. Xie, "Application of Nanofluid Electrochemistry in Heat Dissipation of Permanent Magnet Synchronous Motors," *Journal of Chemistry*, vol. 2022, Article ID 3681749, 7 pages, 2022.

Retraction

Retracted: Application of Visual Communication Combined with Electrochemistry in Ceramic Carving Product Design

Journal of Chemistry

This article has been retracted by Hindawi following an investigation undertaken by the publisher [1]. This investigation has uncovered evidence of one or more of the following indicators of systematic manipulation of the publication process:

(1) Discrepancies in scope

(2) Discrepancies in the description of the research reported

(3) Discrepancies between the availability of data and the research described

(4) Inappropriate citations

(5) Incoherent, meaningless and/or irrelevant content included in the article

(6) Peer-review manipulation

The presence of these indicators undermines our confidence in the integrity of the article's content and we cannot, therefore, vouch for its reliability. Please note that this notice is intended solely to alert readers that the content of this article is unreliable. We have not investigated whether authors were aware of or involved in the systematic manipulation of the publication process.

Wiley and Hindawi regrets that the usual quality checks did not identify these issues before publication and have since put additional measures in place to safeguard research integrity.

We wish to credit our own Research Integrity and Research Publishing teams and anonymous and named external researchers and research integrity experts for contributing to this investigation.

The corresponding author, as the representative of all authors, has been given the opportunity to register their agreement or disagreement to this retraction. We have kept a record of any response received.

References

[1] J. Geng, "Application of Visual Communication Combined with Electrochemistry in Ceramic Carving Product Design," *Journal of Chemistry*, vol. 2022, Article ID 5768966, 7 pages, 2022.

Retraction

Retracted: Influence of Electrochemical Anticorrosion Technology on Concrete Structure and Performance

Journal of Chemistry

This article has been retracted by Hindawi following an investigation undertaken by the publisher [1]. This investigation has uncovered evidence of one or more of the following indicators of systematic manipulation of the publication process:

(1) Discrepancies in scope

(2) Discrepancies in the description of the research reported

(3) Discrepancies between the availability of data and the research described

(4) Inappropriate citations

(5) Incoherent, meaningless and/or irrelevant content included in the article

(6) Peer-review manipulation

The presence of these indicators undermines our confidence in the integrity of the article's content and we cannot, therefore, vouch for its reliability. Please note that this notice is intended solely to alert readers that the content of this article is unreliable. We have not investigated whether authors were aware of or involved in the systematic manipulation of the publication process.

Wiley and Hindawi regrets that the usual quality checks did not identify these issues before publication and have since put additional measures in place to safeguard research integrity.

We wish to credit our own Research Integrity and Research Publishing teams and anonymous and named external researchers and research integrity experts for contributing to this investigation.

The corresponding author, as the representative of all authors, has been given the opportunity to register their agreement or disagreement to this retraction. We have kept a record of any response received.

References

[1] Q. Yang, "Influence of Electrochemical Anticorrosion Technology on Concrete Structure and Performance," *Journal of Chemistry*, vol. 2022, Article ID 5702379, 7 pages, 2022.

Retraction

Retracted: Electrochemical Seismic Design and Artificial Intelligence System Modeling of High-Rise Steel Structure Buildings

Journal of Chemistry

This article has been retracted by Hindawi following an investigation undertaken by the publisher [1]. This investigation has uncovered evidence of one or more of the following indicators of systematic manipulation of the publication process:

(1) Discrepancies in scope

(2) Discrepancies in the description of the research reported

(3) Discrepancies between the availability of data and the research described

(4) Inappropriate citations

(5) Incoherent, meaningless and/or irrelevant content included in the article

(6) Peer-review manipulation

The presence of these indicators undermines our confidence in the integrity of the article's content and we cannot, therefore, vouch for its reliability. Please note that this notice is intended solely to alert readers that the content of this article is unreliable. We have not investigated whether authors were aware of or involved in the systematic manipulation of the publication process.

Wiley and Hindawi regrets that the usual quality checks did not identify these issues before publication and have since put additional measures in place to safeguard research integrity.

We wish to credit our own Research Integrity and Research Publishing teams and anonymous and named external researchers and research integrity experts for contributing to this investigation.

The corresponding author, as the representative of all authors, has been given the opportunity to register their agreement or disagreement to this retraction. We have kept a record of any response received.

References

[1] W. Xia, "Electrochemical Seismic Design and Artificial Intelligence System Modeling of High-Rise Steel Structure Buildings," *Journal of Chemistry*, vol. 2022, Article ID 8693110, 8 pages, 2022.

Retraction

Retracted: Surface Damage Coupling Mechanism of Plain Weave Art Ceramic Matrix Composites

Journal of Chemistry

This article has been retracted by Hindawi following an investigation undertaken by the publisher [1]. This investigation has uncovered evidence of one or more of the following indicators of systematic manipulation of the publication process:

(1) Discrepancies in scope

(2) Discrepancies in the description of the research reported

(3) Discrepancies between the availability of data and the research described

(4) Inappropriate citations

(5) Incoherent, meaningless and/or irrelevant content included in the article

(6) Peer-review manipulation

The presence of these indicators undermines our confidence in the integrity of the article's content and we cannot, therefore, vouch for its reliability. Please note that this notice is intended solely to alert readers that the content of this article is unreliable. We have not investigated whether authors were aware of or involved in the systematic manipulation of the publication process.

Wiley and Hindawi regrets that the usual quality checks did not identify these issues before publication and have since put additional measures in place to safeguard research integrity.

We wish to credit our own Research Integrity and Research Publishing teams and anonymous and named external researchers and research integrity experts for contributing to this investigation.

The corresponding author, as the representative of all authors, has been given the opportunity to register their agreement or disagreement to this retraction. We have kept a record of any response received.

References

[1] G. Li, "Surface Damage Coupling Mechanism of Plain Weave Art Ceramic Matrix Composites," *Journal of Chemistry*, vol. 2022, Article ID 3519967, 7 pages, 2022.

Retraction

Retracted: Chemical Regulation Effect of Water Use Efficiency of Maize Intercropping

Journal of Chemistry

This article has been retracted by Hindawi following an investigation undertaken by the publisher [1]. This investigation has uncovered evidence of one or more of the following indicators of systematic manipulation of the publication process:

(1) Discrepancies in scope

(2) Discrepancies in the description of the research reported

(3) Discrepancies between the availability of data and the research described

(4) Inappropriate citations

(5) Incoherent, meaningless and/or irrelevant content included in the article

(6) Peer-review manipulation

The presence of these indicators undermines our confidence in the integrity of the article's content and we cannot, therefore, vouch for its reliability. Please note that this notice is intended solely to alert readers that the content of this article is unreliable. We have not investigated whether authors were aware of or involved in the systematic manipulation of the publication process.

Wiley and Hindawi regrets that the usual quality checks did not identify these issues before publication and have since put additional measures in place to safeguard research integrity.

We wish to credit our own Research Integrity and Research Publishing teams and anonymous and named external researchers and research integrity experts for contributing to this investigation.

The corresponding author, as the representative of all authors, has been given the opportunity to register their agreement or disagreement to this retraction. We have kept a record of any response received.

References

[1] H. Chen and L. Huang, "Chemical Regulation Effect of Water Use Efficiency of Maize Intercropping," *Journal of Chemistry*, vol. 2022, Article ID 2914749, 8 pages, 2022.

Hindawi

Retraction

Retracted: Numerical Simulation of Hot Stamping Forming of AZ Series Magnesium Alloys and Optimization of Die Process

Journal of Chemistry

This article has been retracted by Hindawi following an investigation undertaken by the publisher [1]. This investigation has uncovered evidence of one or more of the following indicators of systematic manipulation of the publication process:

(1) Discrepancies in scope

(2) Discrepancies in the description of the research reported

(3) Discrepancies between the availability of data and the research described

(4) Inappropriate citations

(5) Incoherent, meaningless and/or irrelevant content included in the article

(6) Peer-review manipulation

The presence of these indicators undermines our confidence in the integrity of the article's content and we cannot, therefore, vouch for its reliability. Please note that this notice is intended solely to alert readers that the content of this article is unreliable. We have not investigated whether authors were aware of or involved in the systematic manipulation of the publication process.

Wiley and Hindawi regrets that the usual quality checks did not identify these issues before publication and have since put additional measures in place to safeguard research integrity.

We wish to credit our own Research Integrity and Research Publishing teams and anonymous and named external researchers and research integrity experts for contributing to this investigation.

The corresponding author, as the representative of all authors, has been given the opportunity to register their agreement or disagreement to this retraction. We have kept a record of any response received.

References

[1] F. Qian, "Numerical Simulation of Hot Stamping Forming of AZ Series Magnesium Alloys and Optimization of Die Process," *Journal of Chemistry*, vol. 2022, Article ID 6484242, 7 pages, 2022.

Retraction

Retracted: Art Decoration Design of Electrochemical Silicon Oxide Ceramic Sculpture Based on 3D Printing Technology

Journal of Chemistry

This article has been retracted by Hindawi following an investigation undertaken by the publisher [1]. This investigation has uncovered evidence of one or more of the following indicators of systematic manipulation of the publication process:

(1) Discrepancies in scope

(2) Discrepancies in the description of the research reported

(3) Discrepancies between the availability of data and the research described

(4) Inappropriate citations

(5) Incoherent, meaningless and/or irrelevant content included in the article

(6) Peer-review manipulation

The presence of these indicators undermines our confidence in the integrity of the article's content and we cannot, therefore, vouch for its reliability. Please note that this notice is intended solely to alert readers that the content of this article is unreliable. We have not investigated whether authors were aware of or involved in the systematic manipulation of the publication process.

Wiley and Hindawi regrets that the usual quality checks did not identify these issues before publication and have since put additional measures in place to safeguard research integrity.

We wish to credit our own Research Integrity and Research Publishing teams and anonymous and named external researchers and research integrity experts for contributing to this investigation.

The corresponding author, as the representative of all authors, has been given the opportunity to register their agreement or disagreement to this retraction. We have kept a record of any response received.

References

[1] J. Guo, "Art Decoration Design of Electrochemical Silicon Oxide Ceramic Sculpture Based on 3D Printing Technology," *Journal of Chemistry*, vol. 2022, Article ID 9728402, 9 pages, 2022.

Retraction

Retracted: Electrochemical Preparation of Recycled Self-Compacting Concrete Composite Beams and Their Application in Prefabricated Buildings

Journal of Chemistry

This article has been retracted by Hindawi following an investigation undertaken by the publisher [1]. This investigation has uncovered evidence of one or more of the following indicators of systematic manipulation of the publication process:

(1) Discrepancies in scope

(2) Discrepancies in the description of the research reported

(3) Discrepancies between the availability of data and the research described

(4) Inappropriate citations

(5) Incoherent, meaningless and/or irrelevant content included in the article

(6) Peer-review manipulation

The presence of these indicators undermines our confidence in the integrity of the article's content and we cannot, therefore, vouch for its reliability. Please note that this notice is intended solely to alert readers that the content of this article is unreliable. We have not investigated whether authors were aware of or involved in the systematic manipulation of the publication process.

Wiley and Hindawi regrets that the usual quality checks did not identify these issues before publication and have since put additional measures in place to safeguard research integrity.

We wish to credit our own Research Integrity and Research Publishing teams and anonymous and named external researchers and research integrity experts for contributing to this investigation.

The corresponding author, as the representative of all authors, has been given the opportunity to register their agreement or disagreement to this retraction. We have kept a record of any response received.

References

[1] Y. Yuan and Y. Zhu, "Electrochemical Preparation of Recycled Self-Compacting Concrete Composite Beams and Their Application in Prefabricated Buildings," *Journal of Chemistry*, vol. 2022, Article ID 4748456, 8 pages, 2022.

Hindawi

Retraction

Retracted: Experimental Study on Compressive Strength of Ultrahigh Performance Concrete Prefabricated Wall Structure

Journal of Chemistry

This article has been retracted by Hindawi following an investigation undertaken by the publisher [1]. This investigation has uncovered evidence of one or more of the following indicators of systematic manipulation of the publication process:

(1) Discrepancies in scope

(2) Discrepancies in the description of the research reported

(3) Discrepancies between the availability of data and the research described

(4) Inappropriate citations

(5) Incoherent, meaningless and/or irrelevant content included in the article

(6) Peer-review manipulation

The presence of these indicators undermines our confidence in the integrity of the article's content and we cannot, therefore, vouch for its reliability. Please note that this notice is intended solely to alert readers that the content of this article is unreliable. We have not investigated whether authors were aware of or involved in the systematic manipulation of the publication process.

Wiley and Hindawi regrets that the usual quality checks did not identify these issues before publication and have since put additional measures in place to safeguard research integrity.

We wish to credit our own Research Integrity and Research Publishing teams and anonymous and named external researchers and research integrity experts for contributing to this investigation.

The corresponding author, as the representative of all authors, has been given the opportunity to register their agreement or disagreement to this retraction. We have kept a record of any response received.

References

[1] J. Cao, Y. Dai, L. Hu, Y. luo, F. Long, and S. Ding, "Experimental Study on Compressive Strength of Ultrahigh Performance Concrete Prefabricated Wall Structure," *Journal of Chemistry*, vol. 2022, Article ID 3380144, 7 pages, 2022.

Retraction

Retracted: Study on the Color Genesis of South Red Agate and the Geological Characteristics of the Siliceous Gravel Layer

Journal of Chemistry

This article has been retracted by Hindawi following an investigation undertaken by the publisher [1]. This investigation has uncovered evidence of one or more of the following indicators of systematic manipulation of the publication process:

(1) Discrepancies in scope

(2) Discrepancies in the description of the research reported

(3) Discrepancies between the availability of data and the research described

(4) Inappropriate citations

(5) Incoherent, meaningless and/or irrelevant content included in the article

(6) Peer-review manipulation

The presence of these indicators undermines our confidence in the integrity of the article's content and we cannot, therefore, vouch for its reliability. Please note that this notice is intended solely to alert readers that the content of this article is unreliable. We have not investigated whether authors were aware of or involved in the systematic manipulation of the publication process.

Wiley and Hindawi regrets that the usual quality checks did not identify these issues before publication and have since put additional measures in place to safeguard research integrity.

We wish to credit our own Research Integrity and Research Publishing teams and anonymous and named external researchers and research integrity experts for contributing to this investigation.

The corresponding author, as the representative of all authors, has been given the opportunity to register their agreement or disagreement to this retraction. We have kept a record of any response received.

References

[1] K. Li and Y. Yuan, "Study on the Color Genesis of South Red Agate and the Geological Characteristics of the Siliceous Gravel Layer," *Journal of Chemistry*, vol. 2022, Article ID 9157753, 7 pages, 2022.

Retraction

Retracted: Application of Chemical Technology of Water-Based Acrylic Dipping Paint in Art Painting Creation

Journal of Chemistry

This article has been retracted by Hindawi following an investigation undertaken by the publisher [1]. This investigation has uncovered evidence of one or more of the following indicators of systematic manipulation of the publication process:

(1) Discrepancies in scope

(2) Discrepancies in the description of the research reported

(3) Discrepancies between the availability of data and the research described

(4) Inappropriate citations

(5) Incoherent, meaningless and/or irrelevant content included in the article

(6) Peer-review manipulation

The presence of these indicators undermines our confidence in the integrity of the article's content and we cannot, therefore, vouch for its reliability. Please note that this notice is intended solely to alert readers that the content of this article is unreliable. We have not investigated whether authors were aware of or involved in the systematic manipulation of the publication process.

Wiley and Hindawi regrets that the usual quality checks did not identify these issues before publication and have since put additional measures in place to safeguard research integrity.

We wish to credit our own Research Integrity and Research Publishing teams and anonymous and named external researchers and research integrity experts for contributing to this investigation.

The corresponding author, as the representative of all authors, has been given the opportunity to register their agreement or disagreement to this retraction. We have kept a record of any response received.

References

[1] X. Kong and X. Meng, "Application of Chemical Technology of Water-Based Acrylic Dipping Paint in Art Painting Creation," *Journal of Chemistry*, vol. 2022, Article ID 7715011, 7 pages, 2022.

Retraction

Retracted: Art Design of Ceramic Sculpture Based on 3D Printing Technology and Electrochemistry

Journal of Chemistry

This article has been retracted by Hindawi following an investigation undertaken by the publisher [1]. This investigation has uncovered evidence of one or more of the following indicators of systematic manipulation of the publication process:

(1) Discrepancies in scope

(2) Discrepancies in the description of the research reported

(3) Discrepancies between the availability of data and the research described

(4) Inappropriate citations

(5) Incoherent, meaningless and/or irrelevant content included in the article

(6) Peer-review manipulation

The presence of these indicators undermines our confidence in the integrity of the article's content and we cannot, therefore, vouch for its reliability. Please note that this notice is intended solely to alert readers that the content of this article is unreliable. We have not investigated whether authors were aware of or involved in the systematic manipulation of the publication process.

Wiley and Hindawi regrets that the usual quality checks did not identify these issues before publication and have since put additional measures in place to safeguard research integrity.

We wish to credit our own Research Integrity and Research Publishing teams and anonymous and named external researchers and research integrity experts for contributing to this investigation.

The corresponding author, as the representative of all authors, has been given the opportunity to register their agreement or disagreement to this retraction. We have kept a record of any response received.

References

[1] J. Zhu and W. Liu, "Art Design of Ceramic Sculpture Based on 3D Printing Technology and Electrochemistry," *Journal of Chemistry*, vol. 2022, Article ID 3190499, 9 pages, 2022.

Retraction

Retracted: Application of ZnO Semiconductor Nanomaterial Ink in Packaging and Printing Design

Journal of Chemistry

This article has been retracted by Hindawi following an investigation undertaken by the publisher [1]. This investigation has uncovered evidence of one or more of the following indicators of systematic manipulation of the publication process:

(1) Discrepancies in scope

(2) Discrepancies in the description of the research reported

(3) Discrepancies between the availability of data and the research described

(4) Inappropriate citations

(5) Incoherent, meaningless and/or irrelevant content included in the article

(6) Peer-review manipulation

The presence of these indicators undermines our confidence in the integrity of the article's content and we cannot, therefore, vouch for its reliability. Please note that this notice is intended solely to alert readers that the content of this article is unreliable. We have not investigated whether authors were aware of or involved in the systematic manipulation of the publication process.

Wiley and Hindawi regrets that the usual quality checks did not identify these issues before publication and have since put additional measures in place to safeguard research integrity.

We wish to credit our own Research Integrity and Research Publishing teams and anonymous and named external researchers and research integrity experts for contributing to this investigation.

The corresponding author, as the representative of all authors, has been given the opportunity to register their agreement or disagreement to this retraction. We have kept a record of any response received.

References

[1] C. Guo, "Application of ZnO Semiconductor Nanomaterial Ink in Packaging and Printing Design," *Journal of Chemistry*, vol. 2022, Article ID 6166533, 7 pages, 2022.

Retraction

Retracted: Application of CAD/CAM Technology in Electrochemical Relief Design and Processing of Ceramic Art

Journal of Chemistry

This article has been retracted by Hindawi following an investigation undertaken by the publisher [1]. This investigation has uncovered evidence of one or more of the following indicators of systematic manipulation of the publication process:

(1) Discrepancies in scope

(2) Discrepancies in the description of the research reported

(3) Discrepancies between the availability of data and the research described

(4) Inappropriate citations

(5) Incoherent, meaningless and/or irrelevant content included in the article

(6) Peer-review manipulation

The presence of these indicators undermines our confidence in the integrity of the article's content and we cannot, therefore, vouch for its reliability. Please note that this notice is intended solely to alert readers that the content of this article is unreliable. We have not investigated whether authors were aware of or involved in the systematic manipulation of the publication process.

Wiley and Hindawi regrets that the usual quality checks did not identify these issues before publication and have since put additional measures in place to safeguard research integrity.

We wish to credit our own Research Integrity and Research Publishing teams and anonymous and named external researchers and research integrity experts for contributing to this investigation.

The corresponding author, as the representative of all authors, has been given the opportunity to register their agreement or disagreement to this retraction. We have kept a record of any response received.

References

[1] H. Li, "Application of CAD/CAM Technology in Electrochemical Relief Design and Processing of Ceramic Art," *Journal of Chemistry*, vol. 2022, Article ID 8190143, 6 pages, 2022.

Retraction

Retracted: Monitoring of Nitrogen Transport Data in Pear Leaves Based on Infrared Spectroscopy

Journal of Chemistry

This article has been retracted by Hindawi following an investigation undertaken by the publisher [1]. This investigation has uncovered evidence of one or more of the following indicators of systematic manipulation of the publication process:

(1) Discrepancies in scope

(2) Discrepancies in the description of the research reported

(3) Discrepancies between the availability of data and the research described

(4) Inappropriate citations

(5) Incoherent, meaningless and/or irrelevant content included in the article

(6) Peer-review manipulation

The presence of these indicators undermines our confidence in the integrity of the article's content and we cannot, therefore, vouch for its reliability. Please note that this notice is intended solely to alert readers that the content of this article is unreliable. We have not investigated whether authors were aware of or involved in the systematic manipulation of the publication process.

Wiley and Hindawi regrets that the usual quality checks did not identify these issues before publication and have since put additional measures in place to safeguard research integrity.

We wish to credit our own Research Integrity and Research Publishing teams and anonymous and named external researchers and research integrity experts for contributing to this investigation.

The corresponding author, as the representative of all authors, has been given the opportunity to register their agreement or disagreement to this retraction. We have kept a record of any response received.

References

[1] Z. Fan, D. Wang, and N. Zhang, "Monitoring of Nitrogen Transport Data in Pear Leaves Based on Infrared Spectroscopy," *Journal of Chemistry*, vol. 2022, Article ID 1547582, 9 pages, 2022.

Hindawi

Retraction

Retracted: Chemical Characteristics of Coil Heavy Metal Elements and Ecological Security Risks Caused by Fertilization

Journal of Chemistry

This article has been retracted by Hindawi following an investigation undertaken by the publisher [1]. This investigation has uncovered evidence of one or more of the following indicators of systematic manipulation of the publication process:

(1) Discrepancies in scope

(2) Discrepancies in the description of the research reported

(3) Discrepancies between the availability of data and the research described

(4) Inappropriate citations

(5) Incoherent, meaningless and/or irrelevant content included in the article

(6) Peer-review manipulation

The presence of these indicators undermines our confidence in the integrity of the article's content and we cannot, therefore, vouch for its reliability. Please note that this notice is intended solely to alert readers that the content of this article is unreliable. We have not investigated whether authors were aware of or involved in the systematic manipulation of the publication process.

Wiley and Hindawi regrets that the usual quality checks did not identify these issues before publication and have since put additional measures in place to safeguard research integrity.

We wish to credit our own Research Integrity and Research Publishing teams and anonymous and named external researchers and research integrity experts for contributing to this investigation.

The corresponding author, as the representative of all authors, has been given the opportunity to register their agreement or disagreement to this retraction. We have kept a record of any response received.

References

[1] Y. Ma, Q. Hao, and A. Zhong, "Chemical Characteristics of Coil Heavy Metal Elements and Ecological Security Risks Caused by Fertilization," *Journal of Chemistry*, vol. 2022, Article ID 4211602, 7 pages, 2022.

Hindawi

Retraction

Retracted: Electrochemical-Based Extraction, Separation, and Purification of Coumarin Compounds from *Trifolium chinensis*

Journal of Chemistry

This article has been retracted by Hindawi following an investigation undertaken by the publisher [1]. This investigation has uncovered evidence of one or more of the following indicators of systematic manipulation of the publication process:

(1) Discrepancies in scope

(2) Discrepancies in the description of the research reported

(3) Discrepancies between the availability of data and the research described

(4) Inappropriate citations

(5) Incoherent, meaningless and/or irrelevant content included in the article

(6) Peer-review manipulation

The presence of these indicators undermines our confidence in the integrity of the article's content and we cannot, therefore, vouch for its reliability. Please note that this notice is intended solely to alert readers that the content of this article is unreliable. We have not investigated whether authors were aware of or involved in the systematic manipulation of the publication process.

Wiley and Hindawi regrets that the usual quality checks did not identify these issues before publication and have since put additional measures in place to safeguard research integrity.

We wish to credit our own Research Integrity and Research Publishing teams and anonymous and named external researchers and research integrity experts for contributing to this investigation.

The corresponding author, as the representative of all authors, has been given the opportunity to register their agreement or disagreement to this retraction. We have kept a record of any response received.

References

[1] Y. Zhu, W. Wang, R. Ruan, and J. Chen, "Electrochemical-Based Extraction, Separation, and Purification of Coumarin Compounds from *Trifolium chinensis*," *Journal of Chemistry*, vol. 2022, Article ID 6466271, 6 pages, 2022.

Retraction

Retracted: Electrochemical Application of Structured Color Nanotextile Materials in Garment Design

Journal of Chemistry

This article has been retracted by Hindawi following an investigation undertaken by the publisher [1]. This investigation has uncovered evidence of one or more of the following indicators of systematic manipulation of the publication process:

(1) Discrepancies in scope

(2) Discrepancies in the description of the research reported

(3) Discrepancies between the availability of data and the research described

(4) Inappropriate citations

(5) Incoherent, meaningless and/or irrelevant content included in the article

(6) Peer-review manipulation

The presence of these indicators undermines our confidence in the integrity of the article's content and we cannot, therefore, vouch for its reliability. Please note that this notice is intended solely to alert readers that the content of this article is unreliable. We have not investigated whether authors were aware of or involved in the systematic manipulation of the publication process.

Wiley and Hindawi regrets that the usual quality checks did not identify these issues before publication and have since put additional measures in place to safeguard research integrity.

We wish to credit our own Research Integrity and Research Publishing teams and anonymous and named external researchers and research integrity experts for contributing to this investigation.

The corresponding author, as the representative of all authors, has been given the opportunity to register their agreement or disagreement to this retraction. We have kept a record of any response received.

References

[1] Z. Zhang, "Electrochemical Application of Structured Color Nanotextile Materials in Garment Design," *Journal of Chemistry*, vol. 2022, Article ID 2044265, 7 pages, 2022.

Retraction

Retracted: Durability Test and Mechanical Properties of CFRP Bolt under Accelerated Corrosion Conditions

Journal of Chemistry

This article has been retracted by Hindawi following an investigation undertaken by the publisher [1]. This investigation has uncovered evidence of one or more of the following indicators of systematic manipulation of the publication process:

(1) Discrepancies in scope

(2) Discrepancies in the description of the research reported

(3) Discrepancies between the availability of data and the research described

(4) Inappropriate citations

(5) Incoherent, meaningless and/or irrelevant content included in the article

(6) Peer-review manipulation

The presence of these indicators undermines our confidence in the integrity of the article's content and we cannot, therefore, vouch for its reliability. Please note that this notice is intended solely to alert readers that the content of this article is unreliable. We have not investigated whether authors were aware of or involved in the systematic manipulation of the publication process.

Wiley and Hindawi regrets that the usual quality checks did not identify these issues before publication and have since put additional measures in place to safeguard research integrity.

We wish to credit our own Research Integrity and Research Publishing teams and anonymous and named external researchers and research integrity experts for contributing to this investigation.

The corresponding author, as the representative of all authors, has been given the opportunity to register their agreement or disagreement to this retraction. We have kept a record of any response received.

References

[1] Q. Li, X. Li, and L. Guo, "Durability Test and Mechanical Properties of CFRP Bolt under Accelerated Corrosion Conditions," *Journal of Chemistry*, vol. 2022, Article ID 2094640, 7 pages, 2022.

Retraction

Retracted: Study on Early Warning of Karst Collapse Based on the BP Neural Network

Journal of Chemistry

This article has been retracted by Hindawi following an investigation undertaken by the publisher [1]. This investigation has uncovered evidence of one or more of the following indicators of systematic manipulation of the publication process:

(1) Discrepancies in scope

(2) Discrepancies in the description of the research reported

(3) Discrepancies between the availability of data and the research described

(4) Inappropriate citations

(5) Incoherent, meaningless and/or irrelevant content included in the article

(6) Peer-review manipulation

The presence of these indicators undermines our confidence in the integrity of the article's content and we cannot, therefore, vouch for its reliability. Please note that this notice is intended solely to alert readers that the content of this article is unreliable. We have not investigated whether authors were aware of or involved in the systematic manipulation of the publication process.

Wiley and Hindawi regrets that the usual quality checks did not identify these issues before publication and have since put additional measures in place to safeguard research integrity.

We wish to credit our own Research Integrity and Research Publishing teams and anonymous and named external researchers and research integrity experts for contributing to this investigation.

The corresponding author, as the representative of all authors, has been given the opportunity to register their agreement or disagreement to this retraction. We have kept a record of any response received.

References

[1] D. Chen, "Study on Early Warning of Karst Collapse Based on the BP Neural Network," *Journal of Chemistry*, vol. 2022, Article ID 1799772, 7 pages, 2022.

Retraction

Retracted: Quantitative Detection of Amino Acids and Carnitine in Human Blood and Quality Control of Peptide Drugs

Journal of Chemistry

This article has been retracted by Hindawi following an investigation undertaken by the publisher [1]. This investigation has uncovered evidence of one or more of the following indicators of systematic manipulation of the publication process:

(1) Discrepancies in scope

(2) Discrepancies in the description of the research reported

(3) Discrepancies between the availability of data and the research described

(4) Inappropriate citations

(5) Incoherent, meaningless and/or irrelevant content included in the article

(6) Peer-review manipulation

The presence of these indicators undermines our confidence in the integrity of the article's content and we cannot, therefore, vouch for its reliability. Please note that this notice is intended solely to alert readers that the content of this article is unreliable. We have not investigated whether authors were aware of or involved in the systematic manipulation of the publication process.

In addition, our investigation has also shown that one or more of the following human-subject reporting requirements has not been met in this article: ethical approval by an Institutional Review Board (IRB) committee or equivalent, patient/participant consent to participate, and/or agreement to publish patient/participant details (where relevant).

Wiley and Hindawi regrets that the usual quality checks did not identify these issues before publication and have since put additional measures in place to safeguard research integrity.

We wish to credit our own Research Integrity and Research Publishing teams and anonymous and named external researchers and research integrity experts for contributing to this investigation.

The corresponding author, as the representative of all authors, has been given the opportunity to register their agreement or disagreement to this retraction. We have kept a record of any response received.

References

[1] Y. Ma, Y. Zhu, Z. Lu et al., "Quantitative Detection of Amino Acids and Carnitine in Human Blood and Quality Control of Peptide Drugs," *Journal of Chemistry*, vol. 2022, Article ID 1652592, 6 pages, 2022.

Retraction

Retracted: Application of Lightweight Thermal Insulation Building Materials for Green Building Design

Journal of Chemistry

This article has been retracted by Hindawi following an investigation undertaken by the publisher [1]. This investigation has uncovered evidence of one or more of the following indicators of systematic manipulation of the publication process:

(1) Discrepancies in scope

(2) Discrepancies in the description of the research reported

(3) Discrepancies between the availability of data and the research described

(4) Inappropriate citations

(5) Incoherent, meaningless and/or irrelevant content included in the article

(6) Peer-review manipulation

The presence of these indicators undermines our confidence in the integrity of the article's content and we cannot, therefore, vouch for its reliability. Please note that this notice is intended solely to alert readers that the content of this article is unreliable. We have not investigated whether authors were aware of or involved in the systematic manipulation of the publication process.

Wiley and Hindawi regrets that the usual quality checks did not identify these issues before publication and have since put additional measures in place to safeguard research integrity.

We wish to credit our own Research Integrity and Research Publishing teams and anonymous and named external researchers and research integrity experts for contributing to this investigation.

The corresponding author, as the representative of all authors, has been given the opportunity to register their agreement or disagreement to this retraction. We have kept a record of any response received.

References

[1] L. Liu and Y. Zhai, "Application of Lightweight Thermal Insulation Building Materials for Green Building Design," *Journal of Chemistry*, vol. 2022, Article ID 7044427, 7 pages, 2022.

Hindawi

Retraction

Retracted: Research Progress of Polycyclic Aromatic Hydrocarbons Pretreatment Methods and Application of Computer Simulation Technology for Prediction and Degradation of Electrochemical Concentration Detection

Journal of Chemistry

This article has been retracted by Hindawi following an investigation undertaken by the publisher [1]. This investigation has uncovered evidence of one or more of the following indicators of systematic manipulation of the publication process:

(1) Discrepancies in scope

(2) Discrepancies in the description of the research reported

(3) Discrepancies between the availability of data and the research described

(4) Inappropriate citations

(5) Incoherent, meaningless and/or irrelevant content included in the article

(6) Peer-review manipulation

The presence of these indicators undermines our confidence in the integrity of the article's content and we cannot, therefore, vouch for its reliability. Please note that this notice is intended solely to alert readers that the content of this article is unreliable. We have not investigated whether authors were aware of or involved in the systematic manipulation of the publication process.

Wiley and Hindawi regrets that the usual quality checks did not identify these issues before publication and have since put additional measures in place to safeguard research integrity.

We wish to credit our own Research Integrity and Research Publishing teams and anonymous and named external researchers and research integrity experts for contributing to this investigation.

The corresponding author, as the representative of all authors, has been given the opportunity to register their agreement or disagreement to this retraction. We have kept a record of any response received.

References

[1] H. Chang and Y. Lu, "Research Progress of Polycyclic Aromatic Hydrocarbons Pretreatment Methods and Application of Computer Simulation Technology for Prediction and Degradation of Electrochemical Concentration Detection," *Journal of Chemistry*, vol. 2022, Article ID 6288072, 16 pages, 2022.

Retraction

Retracted: Application of Computer-Aided Precious Metal Materials in Electrochemistry of Ceramic Jewelry Design

Journal of Chemistry

This article has been retracted by Hindawi following an investigation undertaken by the publisher [1]. This investigation has uncovered evidence of one or more of the following indicators of systematic manipulation of the publication process:

(1) Discrepancies in scope

(2) Discrepancies in the description of the research reported

(3) Discrepancies between the availability of data and the research described

(4) Inappropriate citations

(5) Incoherent, meaningless and/or irrelevant content included in the article

(6) Peer-review manipulation

The presence of these indicators undermines our confidence in the integrity of the article's content and we cannot, therefore, vouch for its reliability. Please note that this notice is intended solely to alert readers that the content of this article is unreliable. We have not investigated whether authors were aware of or involved in the systematic manipulation of the publication process.

Wiley and Hindawi regrets that the usual quality checks did not identify these issues before publication and have since put additional measures in place to safeguard research integrity.

We wish to credit our own Research Integrity and Research Publishing teams and anonymous and named external researchers and research integrity experts for contributing to this investigation.

The corresponding author, as the representative of all authors, has been given the opportunity to register their agreement or disagreement to this retraction. We have kept a record of any response received.

References

[1] J. Li, "Application of Computer-Aided Precious Metal Materials in Electrochemistry of Ceramic Jewelry Design," *Journal of Chemistry*, vol. 2022, Article ID 6990393, 8 pages, 2022.

Retraction

Retracted: Monitoring of Nitrogen Transport in Pear Trees Based on Ground Hyperspectral Remote Sensing and Digital Image Information

Journal of Chemistry

This article has been retracted by Hindawi following an investigation undertaken by the publisher [1]. This investigation has uncovered evidence of one or more of the following indicators of systematic manipulation of the publication process:

(1) Discrepancies in scope

(2) Discrepancies in the description of the research reported

(3) Discrepancies between the availability of data and the research described

(4) Inappropriate citations

(5) Incoherent, meaningless and/or irrelevant content included in the article

(6) Peer-review manipulation

The presence of these indicators undermines our confidence in the integrity of the article's content and we cannot, therefore, vouch for its reliability. Please note that this notice is intended solely to alert readers that the content of this article is unreliable. We have not investigated whether authors were aware of or involved in the systematic manipulation of the publication process.

Wiley and Hindawi regrets that the usual quality checks did not identify these issues before publication and have since put additional measures in place to safeguard research integrity.

We wish to credit our own Research Integrity and Research Publishing teams and anonymous and named external researchers and research integrity experts for contributing to this investigation.

The corresponding author, as the representative of all authors, has been given the opportunity to register their agreement or disagreement to this retraction. We have kept a record of any response received.

References

[1] Z. Fan, D. Wang, N. Zhang, and B. Zhou, "Monitoring of Nitrogen Transport in Pear Trees Based on Ground Hyperspectral Remote Sensing and Digital Image Information," *Journal of Chemistry*, vol. 2022, Article ID 7590846, 7 pages, 2022.

Retraction

Retracted: Numerical Simulation of Fine Blanking Die Wear and Die Performance Analysis

Journal of Chemistry

This article has been retracted by Hindawi following an investigation undertaken by the publisher [1]. This investigation has uncovered evidence of one or more of the following indicators of systematic manipulation of the publication process:

(1) Discrepancies in scope

(2) Discrepancies in the description of the research reported

(3) Discrepancies between the availability of data and the research described

(4) Inappropriate citations

(5) Incoherent, meaningless and/or irrelevant content included in the article

(6) Peer-review manipulation

The presence of these indicators undermines our confidence in the integrity of the article's content and we cannot, therefore, vouch for its reliability. Please note that this notice is intended solely to alert readers that the content of this article is unreliable. We have not investigated whether authors were aware of or involved in the systematic manipulation of the publication process.

Wiley and Hindawi regrets that the usual quality checks did not identify these issues before publication and have since put additional measures in place to safeguard research integrity.

We wish to credit our own Research Integrity and Research Publishing teams and anonymous and named external researchers and research integrity experts for contributing to this investigation.

The corresponding author, as the representative of all authors, has been given the opportunity to register their agreement or disagreement to this retraction. We have kept a record of any response received.

References

[1] Y. Li, Y. Zhao, and Y. Hao, "Numerical Simulation of Fine Blanking Die Wear and Die Performance Analysis," *Journal of Chemistry*, vol. 2022, Article ID 9893356, 7 pages, 2022.

Hindawi

Retraction

Retracted: The Adsorption of VOCs by Honeycomb Ceramics Loaded with Molecular Sieves

Journal of Chemistry

This article has been retracted by Hindawi following an investigation undertaken by the publisher [1]. This investigation has uncovered evidence of one or more of the following indicators of systematic manipulation of the publication process:

(1) Discrepancies in scope

(2) Discrepancies in the description of the research reported

(3) Discrepancies between the availability of data and the research described

(4) Inappropriate citations

(5) Incoherent, meaningless and/or irrelevant content included in the article

(6) Peer-review manipulation

The presence of these indicators undermines our confidence in the integrity of the article's content and we cannot, therefore, vouch for its reliability. Please note that this notice is intended solely to alert readers that the content of this article is unreliable. We have not investigated whether authors were aware of or involved in the systematic manipulation of the publication process.

Wiley and Hindawi regrets that the usual quality checks did not identify these issues before publication and have since put additional measures in place to safeguard research integrity.

We wish to credit our own Research Integrity and Research Publishing teams and anonymous and named external researchers and research integrity experts for contributing to this investigation.

The corresponding author, as the representative of all authors, has been given the opportunity to register their agreement or disagreement to this retraction. We have kept a record of any response received.

References

[1] P. Zhang, "The Adsorption of VOCs by Honeycomb Ceramics Loaded with Molecular Sieves," *Journal of Chemistry*, vol. 2022, Article ID 7207403, 7 pages, 2022.

Retraction

Retracted: Electrochemical Mechanical Properties of Beam-Column Joints of Building Steel Structures under Impact Loads

Journal of Chemistry

This article has been retracted by Hindawi following an investigation undertaken by the publisher [1]. This investigation has uncovered evidence of one or more of the following indicators of systematic manipulation of the publication process:

(1) Discrepancies in scope

(2) Discrepancies in the description of the research reported

(3) Discrepancies between the availability of data and the research described

(4) Inappropriate citations

(5) Incoherent, meaningless and/or irrelevant content included in the article

(6) Peer-review manipulation

The presence of these indicators undermines our confidence in the integrity of the article's content and we cannot, therefore, vouch for its reliability. Please note that this notice is intended solely to alert readers that the content of this article is unreliable. We have not investigated whether authors were aware of or involved in the systematic manipulation of the publication process.

Wiley and Hindawi regrets that the usual quality checks did not identify these issues before publication and have since put additional measures in place to safeguard research integrity.

We wish to credit our own Research Integrity and Research Publishing teams and anonymous and named external researchers and research integrity experts for contributing to this investigation.

The corresponding author, as the representative of all authors, has been given the opportunity to register their agreement or disagreement to this retraction. We have kept a record of any response received.

References

[1] L. Qian, "Electrochemical Mechanical Properties of Beam-Column Joints of Building Steel Structures under Impact Loads," *Journal of Chemistry*, vol. 2022, Article ID 4942187, 9 pages, 2022.

Hindawi

Retraction

Retracted: Application of Foam Glass-Ceramic Composite Thermal Insulation Material in Traditional Buildings

Journal of Chemistry

This article has been retracted by Hindawi following an investigation undertaken by the publisher [1]. This investigation has uncovered evidence of one or more of the following indicators of systematic manipulation of the publication process:

(1) Discrepancies in scope

(2) Discrepancies in the description of the research reported

(3) Discrepancies between the availability of data and the research described

(4) Inappropriate citations

(5) Incoherent, meaningless and/or irrelevant content included in the article

(6) Peer-review manipulation

The presence of these indicators undermines our confidence in the integrity of the article's content and we cannot, therefore, vouch for its reliability. Please note that this notice is intended solely to alert readers that the content of this article is unreliable. We have not investigated whether authors were aware of or involved in the systematic manipulation of the publication process.

Wiley and Hindawi regrets that the usual quality checks did not identify these issues before publication and have since put additional measures in place to safeguard research integrity.

We wish to credit our own Research Integrity and Research Publishing teams and anonymous and named external researchers and research integrity experts for contributing to this investigation.

The corresponding author, as the representative of all authors, has been given the opportunity to register their agreement or disagreement to this retraction. We have kept a record of any response received.

References

[1] Q. Yu, "Application of Foam Glass-Ceramic Composite Thermal Insulation Material in Traditional Buildings," *Journal of Chemistry*, vol. 2022, Article ID 9662805, 9 pages, 2022.

Hindawi

Retraction

Retracted: Combination of Fruit and Vegetable Storage and Fresh-Keeping with Postharvest Heat Treatment

Journal of Chemistry

This article has been retracted by Hindawi following an investigation undertaken by the publisher [1]. This investigation has uncovered evidence of one or more of the following indicators of systematic manipulation of the publication process:

(1) Discrepancies in scope

(2) Discrepancies in the description of the research reported

(3) Discrepancies between the availability of data and the research described

(4) Inappropriate citations

(5) Incoherent, meaningless and/or irrelevant content included in the article

(6) Manipulated or compromised peer review

The presence of these indicators undermines our confidence in the integrity of the article's content and we cannot, therefore, vouch for its reliability. Please note that this notice is intended solely to alert readers that the content of this article is unreliable. We have not investigated whether authors were aware of or involved in the systematic manipulation of the publication process.

Wiley and Hindawi regrets that the usual quality checks did not identify these issues before publication and have since put additional measures in place to safeguard research integrity.

We wish to credit our own Research Integrity and Research Publishing teams and anonymous and named external researchers and research integrity experts for contributing to this investigation.

The corresponding author, as the representative of all authors, has been given the opportunity to register their agreement or disagreement to this retraction. We have kept a record of any response received.

References

[1] Y. Zhao and R. Zheng, "Combination of Fruit and Vegetable Storage and Fresh-Keeping with Postharvest Heat Treatment," *Journal of Chemistry*, vol. 2022, Article ID 8681499, 12 pages, 2022.

Hindawi

Research Article

Combination of Fruit and Vegetable Storage and Fresh-Keeping with Postharvest Heat Treatment

Yunfeng Zhao [1] **and Ruisheng Zheng** [2]

[1]*Analysis and Testing Center, Yancheng Institute of Technology, Yancheng 224051, Jiangsu, China*
[2]*College of Oceanology and Food Science, Quanzhou Normal University, Quanzhou 362002, Fujian, China*

Correspondence should be addressed to Yunfeng Zhao; zhaoyunfeng1188@126.com

Hot water treatment can effectively improve the storage quality and shelf life of harvested vegetables. The essence of this method is the heat transfer process in which heat is transferred from the high-temperature treatment medium to the low-temperature fruit and vegetable tissues. However, most of the current research projects only focus on the effect of heat treatment on the biological aspects of fruits and vegetables. From the perspective of fruit and vegetable storage and preservation, there are few internal mechanisms that heat treatment affects biological preservation, and most of the research projects only focus on continuous heat treatment. This article aims to study the combination of storage and preservation of fruits and vegetables with postharvest processing technology. To this end, this article proposes the combined use of heat treatment technology through the analysis and improvement of data acquisition problems in the heat treatment process to make the data obtained more reliable and, at the same time, design experiments to explore the improved heat treatment technology. The experimental results in this paper show that the improved storage and preservation of fruits and vegetables combined with postharvest heat treatment technology improves the preservation of fruits and vegetables by 37%. In addition, the overall taste of fruits and vegetables during the preservation process has not been greatly lost, only reduced by 7%, which can be well applied to actual fruit and vegetable processing.

1. Introduction

Fruit and vegetable agricultural products are rich in nutritional value and low in fat content. They are more and more favored by consumers, and their consumption is increasing year by year. Green fruits and vegetables are perishable. Due to the aggravation of environmental and industrial pollution, the public pays more and more attention to the fresh-keeping quality of fruits and vegetables. However, the fruit and vegetable preservation industry in China started late, the green awareness is weak, and the postharvest processing technology and methods are backward, resulting in a huge waste of resources and economic losses in harvesting vegetables. According to incomplete market statistics, domestic fruit and vegetable rot per year exceeds 80 million tons, plus labor and equipment costs, causing huge economic losses of more than 75 billion yuan

in the fruit and vegetable field each year, and the total social industry share is as high as 30% and above.

As a country with a large population, China will have huge market potential in the fruit and vegetable industry for a long period of time in the future. However, in recent years, due to the repeated occurrence of food safety accidents and the over-standard, illegal, and abuse of chemical preservatives, the public has many doubts about the safety and effectiveness of chemical preservatives. Therefore, reducing the hidden safety hazards in the field of fruit and vegetable preservation and enhancing the research of fruit and vegetable preservation and storage technology are urgent to improve the development of China's agriculture and enhance the utilization and safety of food.

As early as the last decade, the heat treatment technology of fruits and vegetables was discovered and put into research in the 20th century. Its safety and effectiveness have made

general public approval. For this reason, more and more people have begun to invest in this research. Vigneault et al. believe that although specific physical treatment methods, such as heating and ultraviolet radiation, have been developed to increase the phytochemical composition of horticultural products, there is little information about the engineering aspects of these treatment methods. They reviewed the engineering aspects related to phytochemical enhancement of physical processing to determine the process parameters required to obtain reproducible results, the basic information required for process scale-up, and the key parameters required to ensure proper monitoring and control for commercial applications [1]. Marti-Herrero et al. evaluated the feasibility of treating fruit and vegetable waste from the municipal market in a full-scale anaerobic digester with the lowest implementation and operating costs, that is, no pretreatment, clean water consumption, and active heating or mixing are required. For this reason, under actual operation and weather conditions in Bolivia for a year, a $13.9 \, m^3$ digester was monitored, which forced solids to be submerged, obtained heat through solar radiation, and recirculated sewage [2]. Huang et al. conducted the single factor test based on the Box–Behnken response surface optimization test. The optimal ratio of the compound vegetable and fruit modifier is 11.10% for tomato, 6.53% for ginger, 6.70% for kiwi, and 10.15% for papaya juice, and the sensory score for beef is 95.10 [3]. Namrata et al. believe that the plant hormone ethylene has many beneficial and harmful effects on the postharvest quality and storage life of fruits and vegetables. Given the current global challenge of reducing postharvest loss and waste of fruits and vegetables, the importance of ethylene management in the supply chain is of paramount importance. For this reason, they have applied various methods in the supply chain over the years. However, under real-time storage and transportation conditions, effective management of ethylene is still a challenging task [4]. In his article, Maxkamov focused on the world population's increasing demand for agricultural products year by year, as well as the unequal use of modern technology in solving these problems and agricultural production and exports [5]. Li et al. reported that *Yarrowia lipolytica* was engineered to produce SA from the hydrolysate of fruit and vegetable waste (FVW). They optimized the hydrolysis conditions and then proved the feasibility of using the hydrolysate to produce SA through *Yarrowia lipolytica* PSA02004. Using $100 \, gL^{-1}$ of FVW hydrolysate containing glucose and 4% corn steep liquor (CSL) as fermentation medium, the SA titer and yield of $43.1 \, gL^{-1}$ and $0.46 \, gg^{-1}$, respectively, were obtained through free cell batch fermentation [6]. George et al. used the Page model to analyze the response surface and determine the key factors affecting drying. The response surface analysis shows that temperature, speed, and initial moisture content are the key drying factors. In order to achieve the drying prediction, a quadratic formula with two variables and a chart relating the drying time to temperature and speed are given, based on a drying moisture content of 10% [7]. Chander and Kannadhasan eliminated the threat by processing and recycling FVW into animal and poultry feed. They outlined the

potential of FVW as animal and poultry feed. In addition, they also described the way forward and strategies to cope with restrictions and challenges, with special mention of FVW, emphasized social marketing of waste disposal, and emphasized the collaborative participation of stakeholders involved in the fruit and vegetable value chain [8]. The above-mentioned documents are very detailed in the description of related food insurance and heat treatment technology and also have detailed explanations on the use of related technologies; but none of them combined the two for research and analysis, and there are not many studies on the effects of treatment.

The innovation of this article is to use the heat treatment technology of fruits and vegetables as the technical support, combined with the improvement of the related fruits and vegetables storage and preservation theory, analyze its specific data acquisition methods, improve its data acquisition methods, ensure the accuracy of data acquisition, and ensure the accurate implementation and precise control of heat treatment technology.

2. Heat Treatment and Preservation Methods of Fruits and Vegetables

2.1. Fruit and Vegetable Heat Treatment Unit. Fruit and vegetable heat treatment equipment is the basis for research on heat-treatment-related technologies. At present, there are few research projects on heat treatment equipment at home and abroad, and electric heating methods are mostly used to directly prepare treated water, which has low energy efficiency. In order to improve the energy efficiency of the equipment, this chapter builds fruit and vegetable heat treatment equipment based on the heat pump principle to produce the required hot water. The operation of heat treatment equipment for fruits and vegetables can be divided into the heating stage of the treatment medium and the heat treatment stage of fruits and vegetables [9]. During the heating phase of the treatment medium, the system runs in the reverse cycle to continuously transfer heat to the medium in the fruit and vegetable treatment tank through the plate heat exchanger, and the temperature of the treatment medium continues to rise with the running time. When the temperature of the processing medium reaches the set value, it will enter the fruit and vegetable heat treatment stage [10]. The load of the unit during the heat treatment stage of fruits and vegetables mainly comes from the heat dissipation of the maintenance structure and the heat absorption of fruits and vegetables. Therefore, in the heat treatment stage of fruits and vegetables, the total load of the unit is constantly changing, and the heat generated by the fixed frequency operation of the compressor does not match the load of the unit [11]. Fruits and vegetables are highly sensitive to the temperature of the processing medium, and fluctuations in the temperature of the medium affect the effect of heat treatment, and even heat damage may occur [12]. In order to better improve the temperature control accuracy of the heat treatment medium of fruits and vegetables, this chapter is based on the traditional PID control method in the heat treatment stage of fruits and vegetables, adding the idea of
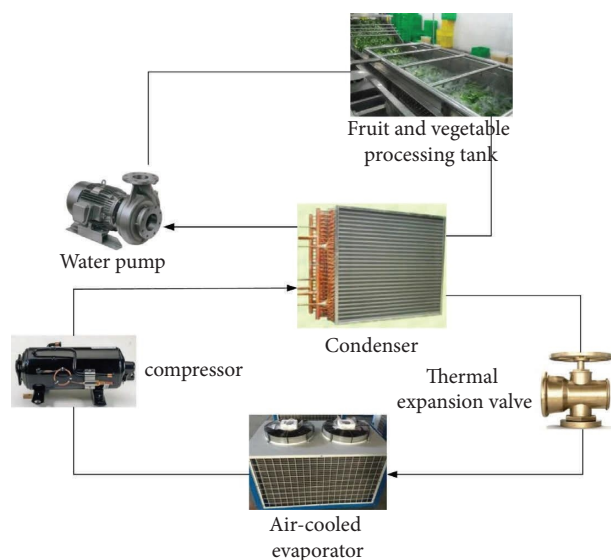
Figure 1: Schematic diagram of the heat treatment system for fruits and vegetables.

feedforward control to improve the control performance of the system. And the automation control program was written based on Siemens PLCS7-200 as the core. The article studies the operating characteristics of fixed frequency (30, 40, 50 Hz) in the medium heating stage, and the parameter law of the medium temperature in the processing tank, the temperature of the fruit and vegetable tissue, and the energy consumption under the PID frequency conversion or the PID frequency conversion control with feedforward during the fruit and vegetable heat treatment phase provide guarantee for further research on heat treatment of fruits and vegetables [13].

The unit mainly includes two subsystems, which are a heat pump system, composed of a compressor, a fin heat exchanger, a throttling device, and a plate heat exchanger, and the fruit and vegetable heat treatment system, composed of a plate heat exchanger, fruit and vegetable processing tank, filter, water pump, etc. [14]. Figure 1 shows the principle diagram of hot water produced by fruit and vegetable processing equipment.

In the fruit and vegetable heat treatment system, the heat treatment medium first exchanges heat with the heat pump working fluid through the condenser, and then it enters the treatment tank under the action of the circulating water pump to heat the fruits and vegetables [15]. Appropriate heat treatment does not affect weight loss, but heat treatment with too high processing temperature will accelerate the weight loss of fruits and vegetables during storage. The higher the temperature and the longer the time, the faster the weight loss of fruits and vegetables.

The harvested vegetables undergo various physiological activities at all times during the storage process. With reference to previous research conclusions, the constructed physical model was divided into several layers to correspond to different organizational structures. To simplify the model, the following assumptions were made: the difference in thermophysical properties only exists between the layers, and the thermophysical properties of the same layer are the same. Fruits and vegetables were simplified into cylindrical shape, and the tissue temperature was uniform before processing. The heat treatment process is relatively short, and the evaporation of surface water can be ignored. During the heat treatment of fruits and vegetables, the surface convective heat transfer coefficient was equal everywhere, ignoring the respiration heat of fruits and vegetables [16].

In the heat treatment process, distilled water is used as the treatment medium, the surface of fruits and vegetables and the treatment medium undergo convective heat exchange, which in turn generates heat exchange, and heat conduction occurs in the internal tissue. Based on the assumptions and simplifications, the internal, central, and external tissues of fruits and vegetables are, respectively, corresponding to the three layers of the physical model: the inner, middle, and outer layers, and each layer has no heat transfer resistance and is closely connected, as shown in Figure 2.

As an important pest quarantine method, heat treatment is to kill the individual insects in the fruit after a period of time under specific temperature conditions. After heat treatment of fruits and vegetables, it can control postharvest diseases caused by more than 20 kinds of bacteria, such as *Colletotrichum, Penicillium*, *Pythium*, Sclerotinia, *Polytrichum, Rhizopus, Alternaria, Chromobia, Phoma, Mucor, Phytophthora*, and *Erwinia*. The effect of heat treatment on the growth and development of insects is mainly manifested in the production of heat shock proteins in their bodies. Within the critical temperature range, the metabolism and respiration of insects increase as the body temperature of insects increases, and the nervous system and endocrine system of insects become disordered with the increase of body temperature. Heat treatment achieves the purpose of improving postharvest quality, enhancing stress resistance, and preventing postharvest diseases by affecting physiological and biochemical changes.

2.2. Determination of the Correlation Coefficient of Fruits and Vegetables.

In this paper, a thermal probe test system is used to determine the thermal conductivity of the fruit. The thermal probe method is based on the transient hot wire method model. Its basic principle is to insert a sufficiently thin metal needle (radius r_0, length L, and $L \gg r_0$) into a homogeneous and uniform temperature sample. That is, "heating source," applying a constant magnitude of current or power to the metal needle will cause the metal needle to heat up and the temperature will rise, and the metal needle will transfer the heat to the surrounding medium to be measured in a thermally conductive manner, so that the temperature of the medium will rise. The relationship of temperature change with time will vary with the medium to be measured, so it contains the thermal conductivity information of the medium to be measured. According to its "temperature-time" change relationship, the thermal conductivity of the tested sample can be determined.
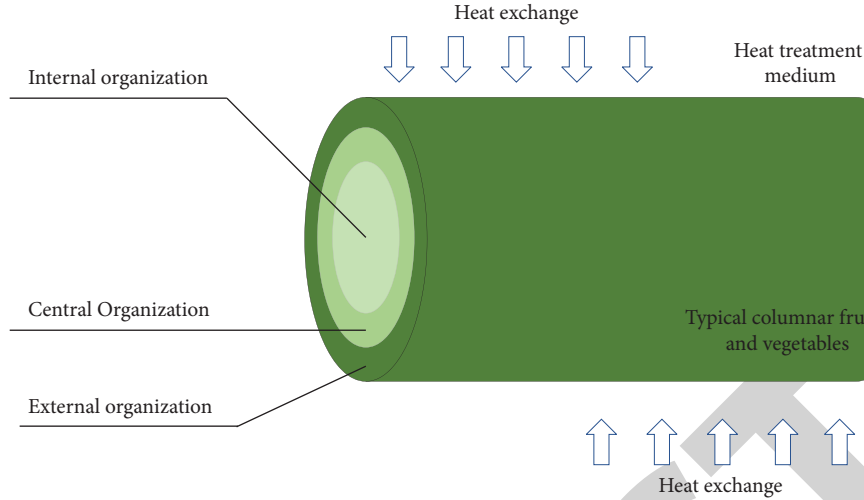
Figure 2: Multilayer physical model of columnar fruits and vegetables.

2.2.1. Determination of Thermal Conductivity of Fruits and Vegetables.

Figure 3 is a schematic diagram of the thermal probe. A slender copper resistance enameled wire is encapsulated in a stainless steel sleeve. The thermal probe is inserted into the object to be tested, and a constant voltage is applied to both ends of the copper wire. The copper wire conducts equal power heat conduction to the surrounding sample to be tested through the insulating layer and the stainless steel sleeve. Assuming that the thermal probe is an infinitely long heat source body, there is no contact thermal resistance on any two contact surfaces of the above model, and the thickness of the electrical insulation layer can be ignored compared with the thickness of the stainless steel casing. Then, the above heat conduction process can be considered as a one-dimensional heat conduction problem in an infinite, isotropic medium. In the cylindrical coordinate system, the governing formula of the nonsteady-state thermal conduction differential formula is as follows.

For copper wire,

$$\frac{1}{r}\frac{\partial}{\partial r}\left(r\frac{\partial t_w}{\partial r}\right) + \frac{q}{\pi r_w^2 \lambda_w} = \frac{1}{\alpha_w \partial \tau}, \quad 0 \le r \le r_w, \tau > 0. \tag{1}$$

For casing,

$$\frac{1}{r}\frac{\partial}{\partial r}\left(r\frac{\partial t_p}{\partial r}\right) = \frac{1}{\alpha_p}\frac{\partial t_p}{\partial \tau}, \quad r_w \le r \le r_p, \tau > 0. \tag{2}$$

For the medium to be tested,

$$\frac{1}{r}\frac{\partial}{\partial r}\left(r\frac{\partial t_m}{\partial}\right) = \frac{1}{\alpha_m}\frac{\partial t_m}{\partial \tau}, \quad r \ge r_p, \tau > 0. \tag{3}$$

Boundary conditions:

$$t_w(r_w, \tau) = t_p(r_w, \tau). \tag{4}$$

Between the hot wire and the metal sleeve,

$$\lambda_w \left(\frac{\partial t_w}{\partial r}\right)_{r_w} = \lambda_p \left(\frac{\partial t_p}{\partial r}\right)_{r_p}. \tag{5}$$
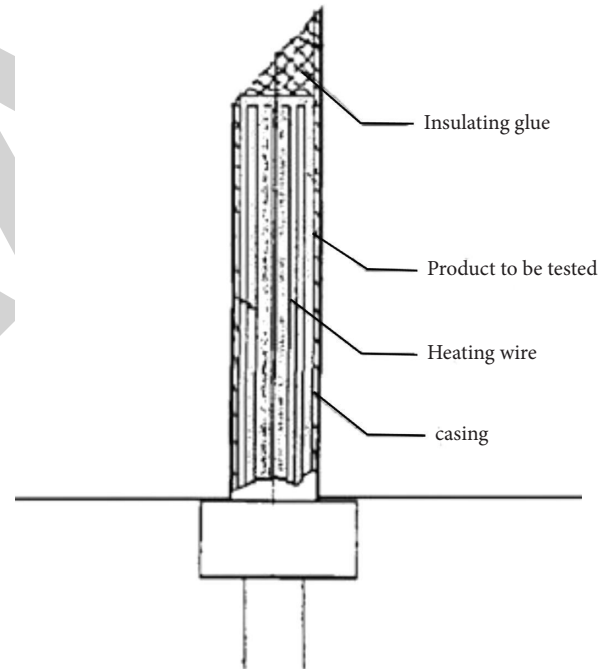
Figure 3: Schematic diagram of thermal probe.

Between the metal casing and the medium to be tested,

$$t_p(r_p, \tau) = t_m(r_p, \tau). \tag{6}$$

At the central axis of the hot wire,

$$\lambda_p \left(\frac{\partial t_p}{\partial r}\right)_{r_p} = \lambda_m \left(\frac{\partial t_m}{\partial r}\right)_{r_m}. \tag{7}$$

$t_w(0, \tau)$ is bounded.
Initial conditions:
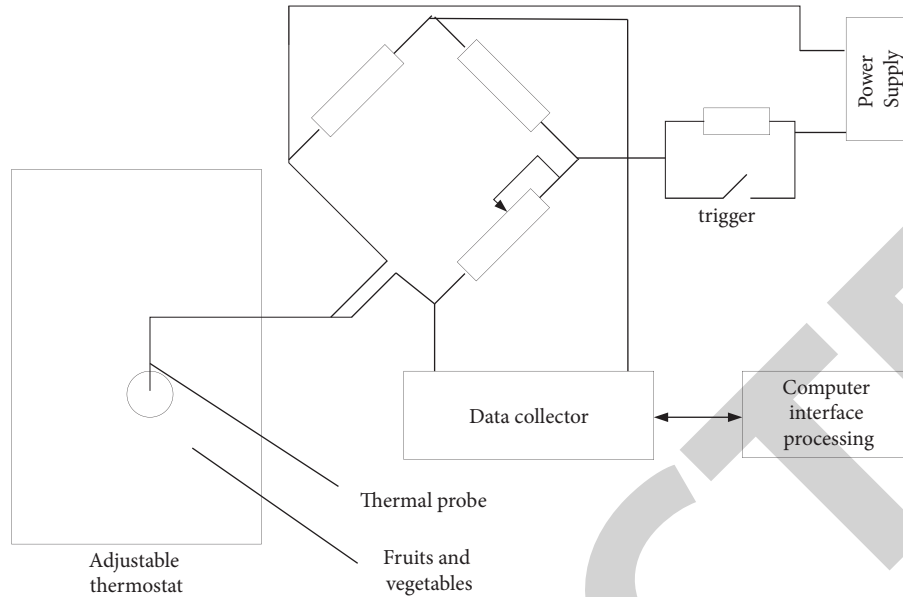
FIGURE 4: Test system diagram.

$$t_w(r, 0) = t_p(r, 0) = t_m(r, 0). \tag{8}$$

In the formula, t is the the difference between the temperature of the hot wire and the initial temperature, °C; λ is the thermal conductivity, W/(m·°C); α is the thermal diffusion coefficient, m^2/s; τ is the heating time, s; r is the radial coordinate, m; and q is the the heating power of the heating wire per unit length, W/m. The subscripts w, p, m, respectively, represent the hot wire, the metal sleeve, and the medium to be tested.

Laplace transformation was used to obtain the exact solution of the differential control formulas. When $a_m t/r_p^2$ is large enough, the thermal conductivity of the medium to be measured can be expressed as follows:

$$\lambda_m = \frac{(q/4\pi)}{(d\overline{t_w}/d\ln t)}. \tag{9}$$

The above formula is the basic formula for measuring the thermal conductivity of an object by the probe method. In theory, as long as the average temperature of the thermal probe and the logarithmic change of time are obtained, the thermal conductivity of the object can be calculated by using formula (9).

The thermal probe and Wheatstone bridge are combined to form a thermal probe test system. The principle of the thermal probe measuring the thermal conductivity of the object is shown in Figure 4. The basic principle is the bridge balance. According to the characteristic that there is a linear relationship between copper resistance and temperature, in the measurement, a constant power is applied to the thermal probe to make the copper wire inside the probe heat up. The temperatures of the copper wire, the stainless steel casing, and the sample to be tested change, which causes the resistance value of the copper wire to change accordingly. In turn, the deviation voltage in the initial balance circuit changes with time, and the output voltage difference signal is processed by the computer to obtain the linear change relationship of the voltage difference with the natural logarithm of time. The thermal conductivity of the tested sample can be obtained. Because it is very difficult to directly measure temperature accurately, this system adopts an indirect measurement method, which converts the temperature difference signal into an easy-to-measure current and voltage amplified signal.

According to formula (9) and electrothermal theory, the thermal conductivity of the sample to be tested can be obtained:

$$\lambda_m = -\frac{\left(V^3 \alpha_0 R_0/R_s^2 64\pi L\right)}{(d(\Delta V)/d(\ln \tau))}, \tag{10}$$

which is

$$\lambda_m = -\frac{\left(V^3/R_s^2\right)C}{(d(\Delta V)/d(\ln \tau))}. \tag{11}$$

In the formula, $C = (\alpha_0 R_0/64\pi L)$ is the the instrument constant of the probe, $\Omega/(m \cdot K \cdot s)$; this parameter is only related to the material and length of the probe itself and has nothing to do with the heating power of the test system and the test temperature; ΔV is the the output voltage difference of the circuit, V; τ is the heating time, s; λ_m is the the thermal conductivity of the sample to be tested, W/m · K; V is the voltage of regulated power supply, V; and R_s is the the initial resistance of the probe, Ω

2.2.2. Determination of the Density of Fruits and Vegetables. The density of fruits and vegetables is defined using formula (12):

$$\rho = \frac{m}{V}. \tag{12}$$

TABLE 1: Fruit thermal properties.

Numbering	Name	λ	ρ	C
1	Orange	0.511	911	4.31
2	Snake fruit	0.418	876	3.51
3	Sweet orange	0.461	839	4.86
4	Apple	0.389	917	3.97
5	Apple pear	0.517	1091	4.56

2.2.3. Determination of Fruit Specific Heat Capacity.

In this study, the heat flow DSC method was used to measure the specific heat capacity of fruit samples. DSC is a thermal analysis instrument that uses the measured energy difference to study the specific heat capacity of the sample and other thermodynamic properties through temperature scanning under the control of a linear temperature program. It is widely used in the measurement of thermophysical properties of solid and liquid substances such as plastics, food, medicine, metals, and composite materials. According to different design principles and structural differences, DSC can be divided into three categories (power compensation type, amplitude modulation type, and heat flow type), of which heat flow is the most used.

The basic principle of heat flow DSC is as follows.

According to the definition of specific heat capacity,

$$c = \frac{dH}{dT} \cdot \frac{1}{M}. \tag{13}$$

Transform the above formula to get

$$\frac{dH}{d\tau} = c \cdot m \cdot \frac{dT}{d\tau}. \tag{14}$$

In the formula, $dH/d\tau$ is the enthalpy conversion rate; c is the specific heat capacity, J/(kg·°C); m is the quality, kg; and $dT/d\tau$ is the temperature change rate.

In order to reduce the error, the indirect method is usually used to determine the specific heat capacity. The indirect method is to scan the temperature of the sample and the standard substance under the same conditions and calculate according to the ordinates of the DSC curve. The commonly used standard material is sapphire, its specific heat capacity is known, and the specific heat capacity does not change in the measured temperature range.

The enthalpy change rate of sapphire is

$$\frac{dH}{d\tau_s} = y_s = c_s \cdot m_s \cdot \frac{dT}{d\tau}. \tag{15}$$

The rate of change of enthalpy of the sample to be tested:

$$\frac{dH}{d\tau} = y = c \cdot m \cdot \frac{dT}{d\tau}. \tag{16}$$

Dividing the two formulas,

$$c = c_s \cdot \frac{m_s \cdot y}{m \cdot y_s}. \tag{17}$$

2.2.4. Determination of Fruit Thermal Diffusivity.

Taking apples and other fruits that need to be heat-treated in the actual production process, their thermal conductivity,

density, and specific heat capacity were measured according to the above steps. Three samples of each fruit were taken, and the average value was taken as the measurement result. The thermal diffusivity definition formula $\alpha = \lambda/pc$ was used to determine its value. The results are shown in Table 1.

It can be seen from Table 1 that the thermal diffusivity of the fruits is not much different, distributed around 4×10^{-8} m^2/s, which is very small compared with metal materials.

2.2.5. Determination of the Convective Heat Transfer Coefficient on Fruit Surface.

Under the guidance of the basic theory of heat transfer, this article uses similarity theory and dimensional analysis to determine the surface convective heat transfer coefficient values in different states of fruit heat treatment. The similarity principle refers to a way to determine the physical quantities of the prototype through experiments by using a model that is similar to the components of the prototype.

The main characteristic numbers that describe the forced convection heat transfer phenomenon of fruit heat treatment are Nusselt number (Nu), Reynolds number (Re), and Prandtl number (Pr):

$$\begin{aligned} Nu_m &= \frac{hd}{\lambda_m}, \\ Re_m &= \frac{ud}{\alpha_m}, \\ Pr_m &= \frac{\nu_m}{\alpha_m}. \end{aligned} \tag{18}$$

According to the dimensional analysis method, the following relations exist among the three:

$$Nu_m = f(Re_m, Pr_m). \tag{19}$$

Because the test is in the hot air treatment environment of the fruit, when the air is forced to sweep the surface of the object, its $Pr_m \approx 0.7$, which is a constant, so the above formula is generally organized into the following index form:

$$Nu_m = CRe_m^n. \tag{20}$$

Among them, according to Newton's cooling formula,

$$h = \frac{\Phi_c}{(t_w - t_f)A}. \tag{21}$$

In this study, an electric heating wire with adjustable power was used to provide the heat source for fruit heat treatment, and a fan was used to change the air flow rate to provide different heat exchange effects. Under the heat exchange balance, all the heat generated by the electric heating wire is transferred to the fruit, and the fruit exchanges heat with the outside air in two ways: convection heat exchange and radiation heat exchange:
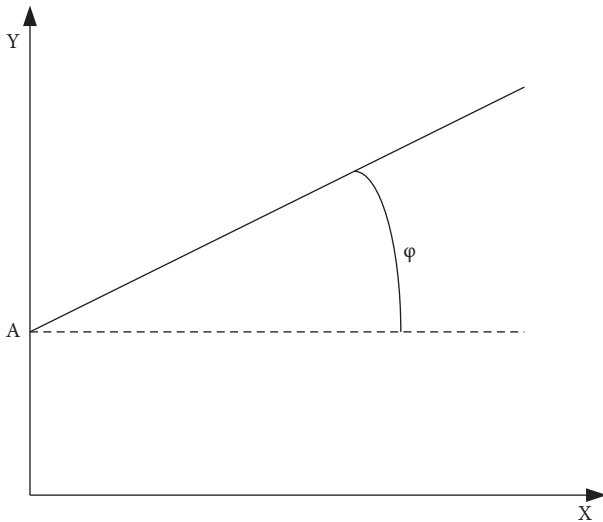
Figure 5: Parameter relationship diagram.

$$\Phi_c = \Phi - \Phi_R,$$

$$\Phi = UI, \tag{22}$$

$$\Phi_R = \varepsilon \cdot C_0 \left[\left(\frac{T_w}{100} \right)^4 - \left(\frac{T_f}{100} \right)^4 \right] \cdot A.$$

It can be seen that, in the heat treatment of the fruit, different values are obtained under different basic parameters. The value under each working condition is expressed in logarithmic coordinates, as shown in Figure 5.

In Figure 5, Y is used to represent $\lg Nu_m$, and X is used to represent $\lg Re_m$; then the linear formula of Figure 5 can be expressed as follows:

$$Y = A + \tan \phi X, \tag{23}$$

which is

$$\lg Nu_m = \lg C + n \lg Re_m. \tag{24}$$

C and n can be obtained from $\lg C = A, n = \tan \phi$.

2.3. Storage and Fresh-Keeping Technology of Harvested Vegetables.

After being harvested, fruits and vegetables are separated from the original growth environment and mother plants. Although they have lost their water and nutrient supply sources, their life activities have not stopped because of this. There are still a series of physiological activities (mainly respiration and evaporation) in circulation and storage. Due to the lack of communication with hormones and nutrient signals in other organs, these processes gradually proceed in the direction of decomposition. They use various organic substances and water stored in themselves, thus making themselves undergo a series of changes (appearance, coloring degree, own weight, tissue hardness, taste characteristics, aromatic smell, etc.) in all aspects.

In the storage environment of fruits and vegetables, even if there is a concentration of one-thousandth of ethylene, it is
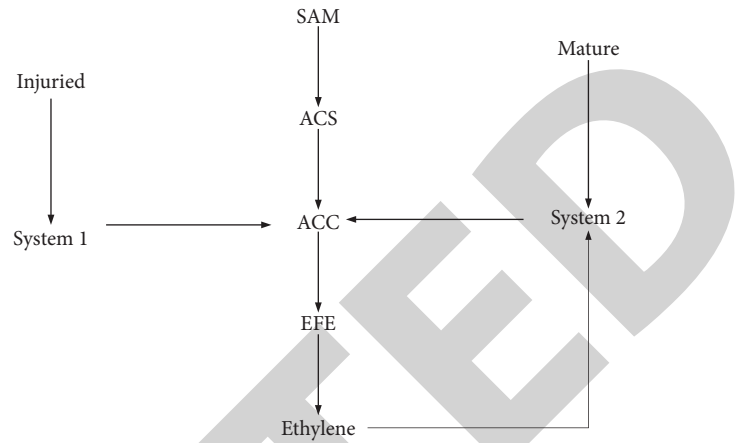
Figure 6: Ethylene biosynthesis and its key steps.

enough to induce the ripening of fruits and vegetables. Therefore, applying ethylene remover within 1–5 days after harvesting fruits and vegetables can inhibit respiration and prevent postripening and aging.

The mechanism of the effect of ethylene ripening is that ethylene initiates the maturation of climacteric fruits, and when climacteric fruits mature, the respiration rises to form a peak. At the same time, a large amount of ethylene can also be seen. Nonclimacteric fruits have no respiratory jump, and the rate of ethylene production during the whole ripening process is very low, and the change is not obvious. This paper proposes two regulating systems for ethylene production in respiratory jump fruits. System I is responsible for the low-concentration basic ethylene production in fruits and vegetables before the jump, and System II is responsible for the large amount of ethylene self-catalyzed production during the ripening process during the jump. System I ethylene is caused by unknown reasons, and the concentration is very low, which can only play a role in controlling and regulating water aging. System I ethylene can start System II ethylene production, which greatly increases the ethylene concentration in the fruit and produces a respiratory jump. The ethylene production rate of nonclimacteric fruits is relatively low, and the changes are stable. During the whole ripening process, only System I ethylene produces ethylene, and System II lacks ethylene production. Figure 6 shows its specific synthesis steps.

The production rate of ethylene in the transition-type fruits and vegetables is very low before the transition, and the corresponding ACC synthase activity, ACC oxidase activity, and ACC content are also very low. Ethylene inhibits the activity of ACC synthase before the respiratory jump, thereby inhibiting the production of ethylene; this is the self-inhibition of ethylene. Ethylene can inhibit ACC synthase before the transition, but it can promote ACC oxidase.

3. Optimization Experiment of Heat Treatment Process for Fruits and Vegetables

3.1. Response Surface Experiment.

The traditional heat treatment process of fruits and vegetables mainly involves two parameters: medium temperature and treatment time.

FIGURE 7: Heat treatment test cucumbers.

TABLE 2: CCD experimental scheme design table (Fire Phoenix).

Std order	Run order	Coded value		Actual value	
		$x1$	$x2$	$X1/°C$	$X2/°C$
12	1	0	0	42	32
9	5	0	0	42	32
10	3	0	0	42	32

TABLE 3: CCD experimental program design table (Dutch cucumber).

Std order	Run order	Coded value		Actual value	
		$x1$	$x2$	$X1/°C$	$X2/°C$
12	1	0	0	40	30
9	2	0	0	40	30
10	3	0	0	40	30

Studies have shown that the optimal heat treatment temperature and treatment time for fruits and vegetables of different types, maturities, and sizes are different. In this chapter, Fire Phoenix and Dutch cucumber with different sizes are selected as test materials. In order to obtain the best heat treatment technology for the two cucumbers and minimize the workload of the experiment, it is necessary to design experiments through optimization methods. Because of the two main influencing factors of heat treatment, this chapter adopts the response surface method to realize the optimization design in the optimization of the heat treatment process of fruits and vegetables.

3.1.1. Test Materials. Both the Fire Phoenix and Dutch cucumbers were purchased from the local fruit and vegetable base; cucumbers of uniform size, uniform maturity, no pests and diseases, and no mechanical damage were picked and shipped back to the laboratory immediately, as shown in Figure 7.

The cucumbers were washed with room temperature water (20°C) for 1 min and then randomly divided into 13 groups. The indexes of each group in the fresh state before treatment in turn were tested, and then heat treatment was carried out with different time-temperature combinations on the two kinds of cucumbers according to Tables 2 and 3.

After the treatment, the groups were numbered, and then an industrial fan was used to dry the moisture on the surface of the cucumber, and the corresponding indicators were tested after being stored at room temperature for 7 days, including weight loss rate, hardness, color difference, and decay index.

The two cucumber tests were divided into 13 groups, including 5 groups of center point tests, 4 groups of factor tests, and 4 groups of pivot point tests. Among them, the postharvest treatment temperature, treatment time, and axis point values (coded value, actual value) are shown in Tables 2 and 3, respectively.

According to the test methods of each response index, the data results of the fresh state of the Fire Phoenix cucumber and the weight loss rate, hardness, color difference, and decay index after the end of storage were obtained. The details are shown in Table 4.

Table 5 shows the results of the analysis of variance of the response surface regression model of the test index weight loss rate. The results show that the correlation coefficient R-squared of the weight loss rate is 0.981, and the correction coefficient adjusted R-squared is equal to 0.967.

4. Induction of Disease Resistance of Melon Fruit by Heat Treatment

4.1. Screening of the Best Heat Treatment Temperature and Time. There are differences in the diameter of the lesions of the fruits with different heat treatments after injury inoculation for 7 days (as shown in Figure 8). Among them, the diameter of the lesions was the largest when treated at 57°C for 3 minutes, and the diameter of the lesions treated at 53°C for 3 minutes was the smallest. There was little difference between the other treatments; on the 7th day of storage, the diseased spot diameter of the treated fruit was significantly lower than that of the control, which was only 80.6% of the control during the same period. Therefore, heat treatment at 53°C for 3 minutes was the best treatment condition.

4.2. The Effect of Heat Treatment on Fruit Phenylpropane Metabolism. Heat treatment can induce the increase of fruit C4H activity, and it is always higher than that of the control. During the storage period, the C4H activity of the fruit showed a trend of increasing first and then decreasing. It reached the maximum on the 12th day, but there was no

TABLE 4: Quality test results of each test group after storage.

| Run order | Actual value | | Weight loss rate | Corresponding value | | Decay index |
	X1/°C	X2/min		Hardness	Chromatic aberration	
1	42	32	15	5	3.63	0
2	42	32	15.15	4.86	3.45	0.04
3	42	32	15.12	4.82	3.75	0
4	42	7.74	17.40	4.58	2.63	0.04
5	31	32.6	17.18	4.36	3.41	0

TABLE 5: Analysis of variance results of the regression model.

Source of variance	Sum of square	Degree of freedom	Mean square	F value	P value
A-Temp	18.17	1	18.17	84.28	<0.0001
B-Time	1.48	1	1.48	7.11	0.0328
AB	5.23	1	5.23	24.36	0.0014
A2	36.48	1	36.48	176.25	<0.0001
B2	17.69	1	17.69	87.14	<0.0001
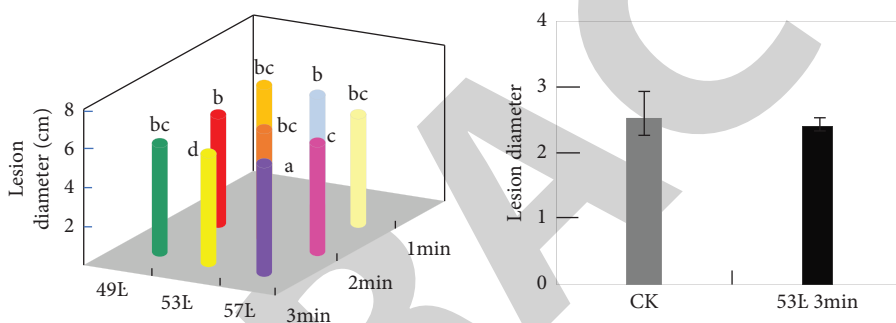
FIGURE 8: The effect of different heat treatment conditions on the diameter of the lesion 7 days after inoculation of fruit injury. Different letters in the figure represent significant differences ($P < 0.05$), and the vertical line in the figure represents standard error ($\pm$SE).
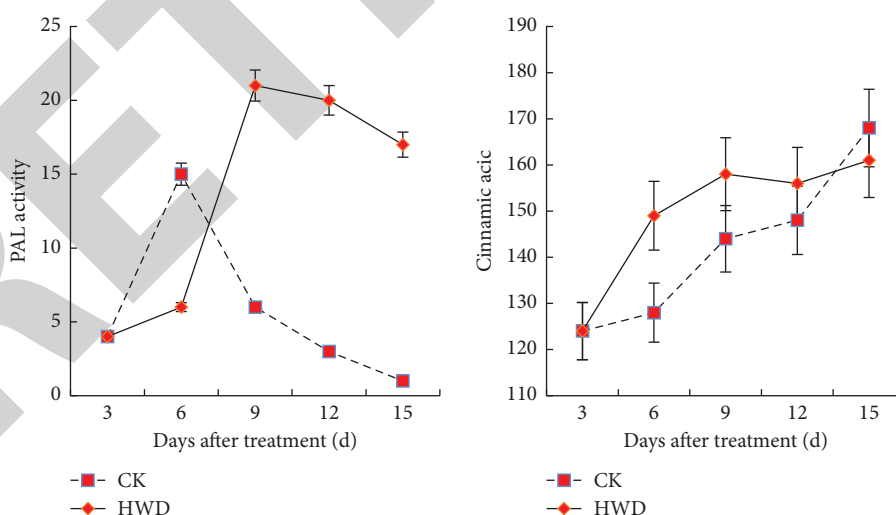
FIGURE 9: The effect of heat treatment on the activity of PAL, C4H, and the content of cinnamic acid and coumaric acid in fruits. The vertical line in the figure represents the standard error ($\pm$SE).

significant difference between the two. On the 3rd day of storage, the C4H activity of the treated fruits was 29.2 times higher than that of the control, and the difference between the two reached the maximum.

Heat treatment can increase the coumaric acid content of fruits. During the storage period, the coumaric acid content of the fruit increased first and then decreased, and both reached the maximum after 9 days of treatment. At this time,
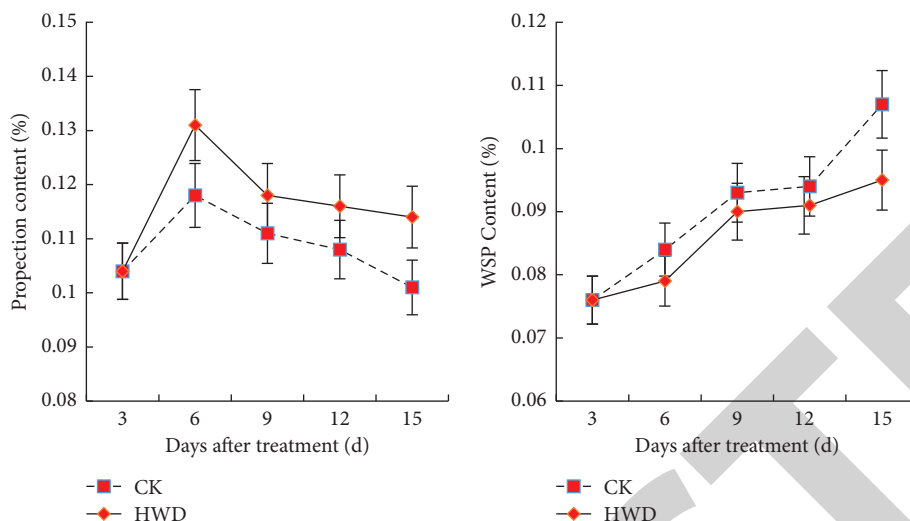
Figure 10: The effect of heat treatment on the content of fruit protopectin, water-soluble pectin, cellulose, and glycoprotein rich in light proline. The vertical line in the figure represents the standard error (±SE).

the coumaric acid content of the treated fruit was 11.7% higher than that of the control; at the end of storage, the difference between the two reached the maximum, and the coumaric acid content of the treated fruit was 25.1% higher than that of the control in the same period. The specific situation is shown in Figure 9.

4.3. The Effect of Heat Treatment on Fruit Cell Wall Components, Related Enzyme Activities, and Epidermal Tissue Structure.

As shown in Figure 10, heat treatment can delay the degradation of fruit pectin. During the storage period, the original pectin content of the fruits increased first and then decreased. On the 3rd day after treatment, the content of protopectin reached the maximum value. At this time, the pectin content of the treated fruit was 11.3% higher than that of the control, and the difference between the two was most obvious; the original pectin content of the treatment at the end of storage was 10.8% higher than the control.

With the extension of the storage period, the content of water-soluble pectin showed an upward trend, and the treatment can delay this trend. On the 6th day of storage, the water-soluble pectin content of both reached the highest, and the water-soluble pectin of the treatment was 10.9% lower than the control in the same period, and the changes in both were very small afterwards.

Heat treatment can delay the degradation of fruit cellulose. The cellulose content of the control fruits reached the maximum on the 3rd day, and the treated fruit reached the maximum on the 9th day. At this time, the difference between the two was most obvious, and the cellulose content of the treated fruit was 36.1% higher than that of the control.

Heat treatment can obviously induce the accumulation of HRGP in fruits. In the early stage of storage, the HRGP content of the treated fruits was lower than that of the control. From the 6th day, the HRGP content of the treated fruits was significantly higher than that of the control. On the 12th and 15th days, the difference between the two

reached the maximum, and the HRGP content of the treatment was 13.6% and 14.5% higher than that of the control in the same period.

4.4. Storage Insurance Quality.

Heat treatment can reduce the SSC content of fruits. During storage, the SSC content of the fruit showed a trend of increasing first and then decreasing. The SSC content of the treated fruit reached the highest on the 6th day, and that of the control reached the highest on the 3rd day. In the later period of storage, the SSC content of the treated fruit was higher than that of the control. On the 6th and 15th days, the SSC content of the treated fruit was 4.5% and 4.2% higher than that of the control in the same period, and the difference between the two was most obvious.

Heat treatment can reduce the TA content of fruits. During storage, the TA content of fruits showed a downward trend, and the TA content of the treated fruit was always higher than that of the control. On the 6th and 15th day of storage, they were 24% and 14.3%, respectively, higher than that of the control in the same period. The specific situation is shown in Figure 11.

Heat treatment can improve the organoleptic quality of the fruit. On the 15th day of storage, the skin and pulp of the heat-treated fruit are milky white, the aroma is coordinated, and the fruit is slightly soft; the control fruit was obviously ripening, the skin and flesh were creamy yellow, and the melon fragrance was prominent. In addition, the skin of the fruit is shrunken, the water loss is serious, the flesh is obviously softened, and the sensory quality is reduced. This shows that heat treatment can delay the ripening of the fruit and maintain the organoleptic quality of the fruit.

Based on the above analysis, we can conclude that, after understanding the heat treatment process of fruits and vegetables and improving the storage of fruits and vegetables, the actual application effect has been greatly improved. The preservation rate of fruits and vegetables has increased
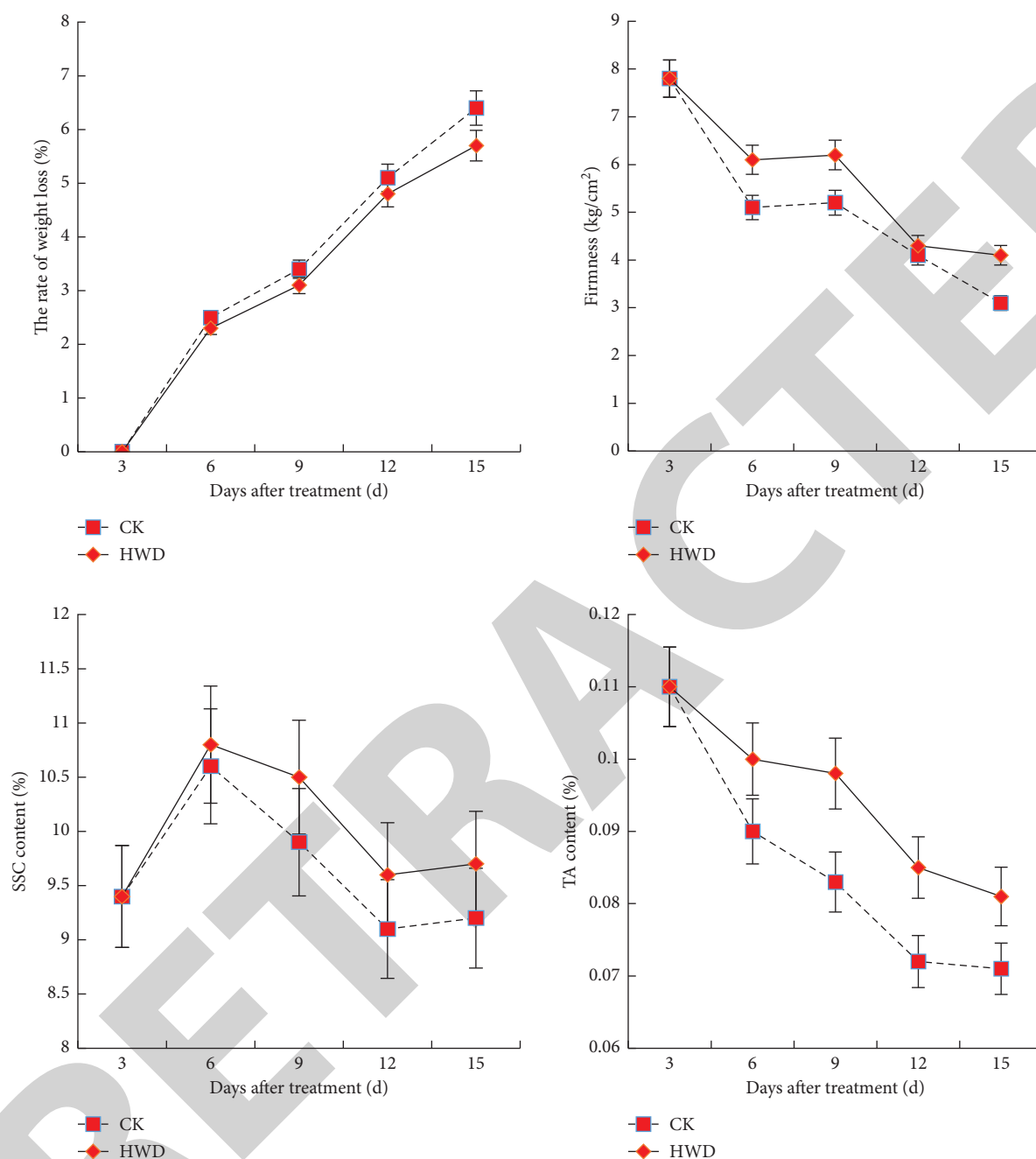
FIGURE 11: The effect of heat treatment on fruit weight loss rate, hardness, soluble solids, and titratable acid content. The vertical line in the figure represents the standard error ($\pm$SE).

by 37%, and the loss of taste during the preservation of fruits and vegetables has been reduced by 7%. For the fresh fruit and vegetable market, this level of improvement is very huge, which can greatly reduce the waste in the transportation process.

5. Conclusions

This article mainly studies the combination of the storage and preservation of fruits and vegetables with the post-harvest heat treatment technology. First of all, this article has conducted a certain understanding of the storage and preservation process of fruits and vegetables and technically decomposed the related heat treatment technology. It conducts a separate analysis of the data collection issues involved in the heat treatment process to ensure the accuracy of data collection. Then, it designs related experiments to explore the optimal performance of the heat treatment of fruits and vegetables and finally combines the analysis part to conduct a comprehensive analysis and exploration of the research objectives of this article and to explore the effect of its improvement.

Retraction

Retracted: Modeling of Vapor-Liquid Equilibrium for Electrolyte Solutions Based on COSMO-RS Interaction

Journal of Chemistry

This article has been retracted by Hindawi following an investigation undertaken by the publisher [1]. This investigation has uncovered evidence of one or more of the following indicators of systematic manipulation of the publication process:

(1) Discrepancies in scope

(2) Discrepancies in the description of the research reported

(3) Discrepancies between the availability of data and the research described

(4) Inappropriate citations

(5) Incoherent, meaningless and/or irrelevant content included in the article

(6) Manipulated or compromised peer review

The presence of these indicators undermines our confidence in the integrity of the article's content and we cannot, therefore, vouch for its reliability. Please note that this notice is intended solely to alert readers that the content of this article is unreliable. We have not investigated whether authors were aware of or involved in the systematic manipulation of the publication process.

Wiley and Hindawi regrets that the usual quality checks did not identify these issues before publication and have since put additional measures in place to safeguard research integrity.

We wish to credit our own Research Integrity and Research Publishing teams and anonymous and named external researchers and research integrity experts for contributing to this investigation.

The corresponding author, as the representative of all authors, has been given the opportunity to register their agreement or disagreement to this retraction. We have kept a record of any response received.

References

[1] W. Liu, C. Zhao, Y. Zhou, and X. Xu, "Modeling of Vapor-Liquid Equilibrium for Electrolyte Solutions Based on COSMO-RS Interaction," *Journal of Chemistry*, vol. 2022, Article ID 9070055, 13 pages, 2022.

Hindawi

Research Article

Modeling of Vapor-Liquid Equilibrium for Electrolyte Solutions Based on COSMO-RS Interaction

Weiping Liu,[1] Chun Zhao,[2,3] Yu Zhou,[1] and Xianzhen Xu [1,3]

[1]*College of Chemistry and Chemical Engineering, Instrumental Analysis Center of Qingdao University, Shandong Sino-Japanese Center for Collaborative Research of Carbon Nanomaterials, Collaborative Innovation Center for Marine Biomass Fiber Materials and Textiles, Laboratory of Fiber Materials and Modern Textile, Qingdao University, Qingdao 266071, Shandong, China*

[2]*Qingdao Hengxing University of Science and Technology, Qingdao 266100, China*

[3]*Qingdao Boting Hydrogen Age Ocean Technology R&D Center, Qingdao Boting Technology Co., Ltd, Qingdao 266100, Shandong, China*

Correspondence should be addressed to Xianzhen Xu; xuxianzhen@qdu.edu.cn

The modeling of phase equilibrium for electrolyte solutions plays an important role in chemical thermodynamics. Modeling and calculation of the vapor-liquid equilibrium (VLE) for an electrolyte solution are studied in this paper. The influence mechanism for the microscopic interaction on the macroscopic VLE is further studied by COSMOtherm. Then, a developed model is proposed. The interaction parameters in the model are linked to the COSMO interaction energy (H_int). The interaction equations are remodeled using 1stopt software, and components are used to replace the "interaction parameters" used in a previous model. The developed model can be used to successfully predict VLE data for electrolyte solutions based on the α and h_i parameters.

1. Introduction

Simulation calculations of the phase equilibrium for electrolyte solutions play an important role in industrial and natural processes. Thermodynamic models are widely used in vapor-liquid equilibrium (VLE), solid-liquid equilibrium (SLE), and liquid-liquid equilibrium calculations. The most used thermodynamic model is the activity coefficient model. Therefore, the study of the activity coefficient model is traditional research, but it is more significant.

Since the proposal of Debye–Hückel's law [1] for a strong electrolyte solution, a number of models have been developed, including physical, chemical, and local composition models [2]. In the physical model, physical interactions have been used to describe the deviation from Debye–Hückel's law, for example, the Pitzer model [3] and the modified Pitzer model [4, 5]. In the chemical model, chemical reactions have been used to describe the properties of electrolyte solutions: the Robinson and Stokes model [6] and the Lu–Maurer model [7]. The local composition models combine the short-range interactions (Wilson [8], NRTL [9], and UNIQUAC [10]) with the long-range interactions (Debye–Hückel's law or modified Debye–Hückel's law [1]. Some examples are the ElecNRTL model [11, 12], the OLI MSE model [13], and Thomsen's model [14]. In addition, many models have been developed and evolved on the basis of the above models, such as the LIQUAC model [15], Xu's model [16], the PSC model [17], the PC-SALT model [18], and so on. As the coefficient models have evolved, there has been great progress in the scope of application and calculation accuracy. Iwai et al. conducted research on simultaneous correlation of liquid-liquid equilibria of ternary systems and phase equilibria of constituent binary systems using an improved new activity coefficient model [19]. Noumir et al. conducted research on isobaric vapor-liquid equilibrium data modeling of ternary systems containing

ionic liquids [20]. However, there are increased limitations in the interpretation of interactions, which represent the bottleneck problem for thermodynamic model research.

In the study of thermodynamic models for electrolyte solutions, many scholars have realized the importance of microinteractions for thermodynamic research. Pitzer [3] recognized the correlation between the interaction between ions and ionic strength and established a more widely used activity coefficient model. Chen [11, 12] considered the contribution of ion electrostatic interactions and improved the local composition model. In addition, many activity coefficient models [21–23] have been established on the basis of the interaction hypothesis. Some scholars have studied the activity coefficient and interaction in thermodynamics using COSMO [24–26]. However, due to the limitation of the experimental conditions at the time, many microscopic interaction concepts are only used for the construction of electrolyte solution models, lacking quantification of the interaction and the structure-activity relationship with the phase balance properties. These are also the main research directions of this paper.

2. The Extended NRTL Model

In this part, the modified NRTL model proposed by Xu et al. [27, 28] was used. The model was applied to calculate the VLE data for mixed electrolyte solutions over wide ranges of temperature and molarity. Based on previous works [27, 28], the impact mechanism of microscopic interactions on macroscopic VLE was further investigated. The thermodynamic activity coefficient model is described as follows:

$$\% \frac{n_t G^e_{NRTL}}{RT} = m_x m_w \left(\frac{\tau_{w,x} G_{w,x}}{m_x + m_w G_{w,x}} + \frac{\tau_{x,w} G_{x,w}}{m_w + m_x G_{x,w}} \right), \quad (1)$$

$$G_{w,x} = \exp(-\alpha \tau_{w,x}), \quad (2)$$

$$G_{x,w} = \exp(-\alpha \tau_{x,w}), \quad (3)$$

where G^e_{NRTL} is the excess Gibbs energy equation of NRTL, n_t is the total molar, m_x is the total molality of solute, and α is the randomness parameter.

$$m_w = \frac{1000}{Ms} - \sum_{i=1}^{n} (h_i m_i), \quad (4)$$

where h_i is the hydration parameter and $Ms = 18.0152$.

$$\tau_{w,x} = \frac{\sum_{i=1}^{n} (\tau_{w,i} m_i)}{\sum_{i=1}^{n} (m_i)}, \quad (5)$$

$$\tau_{x,w} = \frac{\sum_{i=1}^{n} (\tau_{i,w} m_i)}{\sum_{i=1}^{n} (m_i)}, \quad (6)$$

$$\tau_{w,i} = \frac{\tau_{w,i}^{(0)} + \tau_{w,i}^{(1)}}{T}, \quad (7)$$

$$\tau_{i,w} = \frac{\tau_{i,w}^{(0)} + \tau_{i,w}^{(1)}}{T}, \quad (8)$$

where $\tau_{w,x}$ and $\tau_{x,w}$ are water-solute action terms and solute-water action terms. $\tau_{w,i}$ and $\tau_{i,w}$ are the temperature parameters.

In the COSMO calculation process, equations (5) to (8) are very unsatisfactory for the description of the interaction. The new interaction equation is expressed as follows:

$$\tau_{w,x} = \sum_{i=1}^{n} \left(\tau_{w,i}^a \exp(\tau_{w,i}^b m_i) + \tau_{w,i}^c \exp(\tau_{w,i}^d m_i) \right), \quad (9)$$

$$\tau_{x,w} = \sum_{i=1}^{n} \left(\tau_{i,w}^a \exp(\tau_{i,w}^b m_i) + \tau_{i,w}^c \exp(\tau_{i,w}^d m_i) \right), \quad (10)$$

$$\tau_{w,i}^x = \frac{\tau_{w,i}^{(x-0)} + \tau_{w,i}^{(x-1)}}{T + \tau_{w,i}^{(x-2)} \ln(T)}, \quad (11)$$

$$\tau_{i,w}^x = \frac{\tau_{i,w}^{(x-0)} + \tau_{i,w}^{(x-1)}}{T + \tau_{i,w}^{(x-2)} \ln(T)}, \quad (12)$$

where $\tau_{w,x}$ and $\tau_{x,w}$ are water-solute action terms and solute-water action terms. $\tau_{w,i}^a$, $\tau_{w,i}^b$, $\tau_{w,i}^c$, $\tau_{w,i}^d$, $\tau_{i,w}^a$, $\tau_{i,w}^b$, $\tau_{i,w}^c$, and $\tau_{i,w}^d$ are the parameters at the same temperature and $\tau_{w,i}^{(0)}$, $\tau_{w,i}^{(1)}$, $\tau_{w,i}^{(2)}$, $\tau_{i,w}^{(0)}$, $\tau_{i,w}^{(1)}$, and $\tau_{i,w}^{(2)}$ are the temperature parameters.

The final activity coefficient equation for VLE can be written as follows:

$$\ln a_w = \left(\frac{\sum_{i=1}^{n} (\tau_{w,i} m_i) G_{w,x}}{\sum_{i=1}^{n} (m_i) + m_w G_{w,x}} + \frac{\sum_{i=1}^{n} (\tau_{i,w} m_i) G_{x,w}}{m_w + \sum_{i=1}^{n} (m_i) G_{x,w}} \right)$$
$$+ m_w \left(\frac{-\sum_{i=1}^{n} (\tau_{w,i} m_i) G_{w,x}^2}{\left(\sum_{i=1}^{n} (m_i) + m_w G_{w,x} \right)^2} - \frac{\sum_{i=1}^{n} (\tau_{i,w} m_i) G_{x,w}}{\left(m_w + \sum_{i=1}^{n} (m_i) G_{w,x} \right)^2} \right) \quad (13)$$
$$+ \ln \left(\frac{(1000/Ms)}{(1000/Ms) + \sum_{i=1}^{n} (m_i)} \right).$$

In the original model, five parameters need to be correlated, and the interaction term has no physical meaning. In the new equation, two parameters (h and α) were fitted to the literature data. At the same time, the interaction parameters were given a physical meaning by the COSMO interaction. Therefore, the new model was called the NXC model.

2.1. Calculation and Treatment of Interactions. In this part, COSMOtherm 2021 and 1stOpt 9.0 as the main calculation tools were chosen. 1stOpt 9.0 was used to model the interaction data. COSMOtherm 2021 was chosen to calculate the intermolecular interactions in solutions. The model described above is strictly a semiempirical model. The hydration hypotheses and the model have been proposed in previous works. However, the law of microinteraction description is not clear, and the calculation result is not of physical significance. Therefore, the

(a)   (b)   (c)
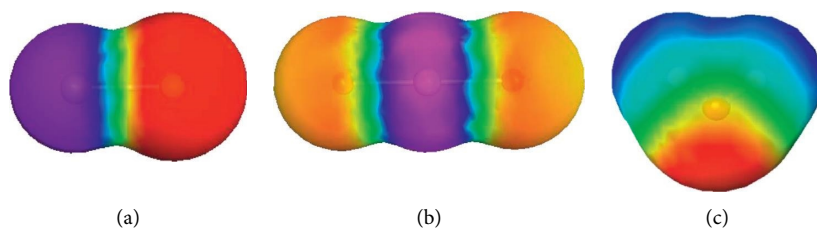
FIGURE 1: The sigma surface of NaCl, CaCl2, and H2O in COSMOtherm.
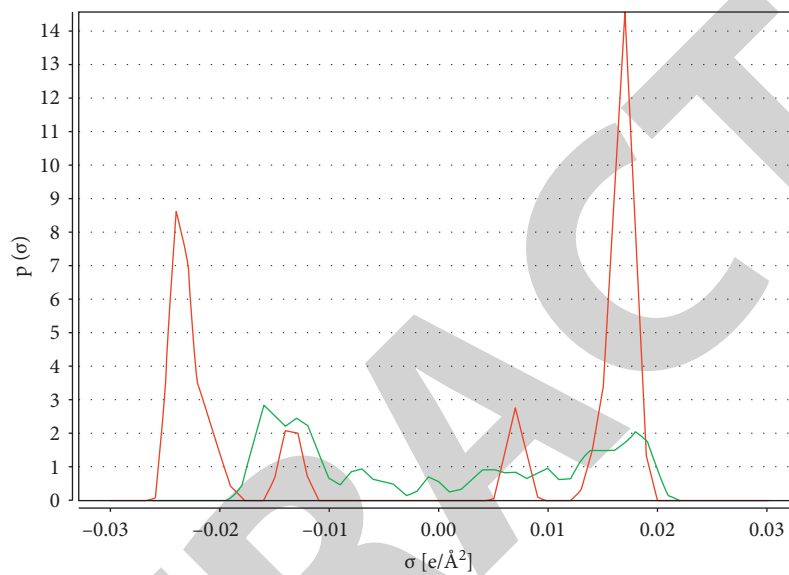
FIGURE 2: The sigma profile and sigma potentials of the NaCl–H$_2$O system (—NaCl and —H$_2$O).
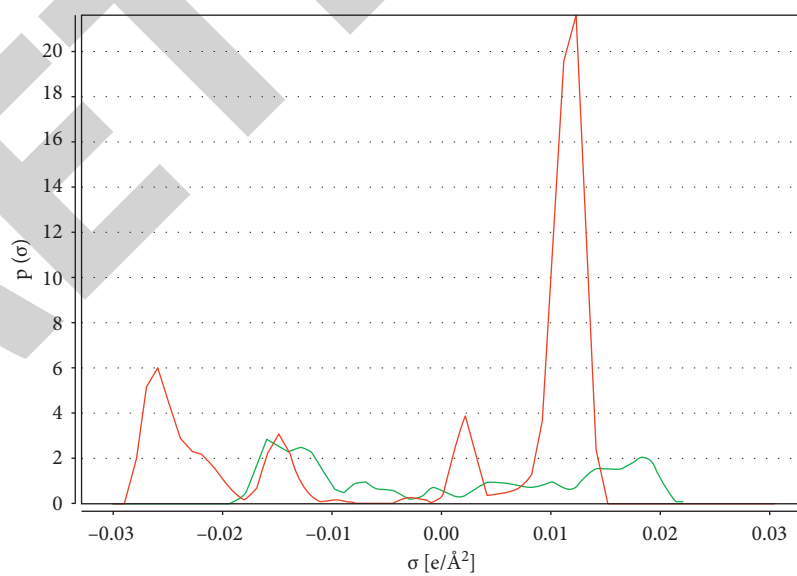
FIGURE 3: The sigma profile and sigma potentials of the CaCl2–H2O system (—NaCl and —H$_2$O).

TABLE 1: Interaction parameters 1.

	BaBr$_2$	CaBr$_2$	CaCl$_2$	CsBr	CsCl
p1_1w	−1.5769E + 02	−1.3593E + 02	1.0610E + 02	−4.0859E + 02	−3.0218E + 02
p1_2w	4.2414E + 03	6.2605E + 03	1.1310E + 00	2.0634E + 04	2.1218E + 04
p1_3w	2.2515E + 01	2.0118E + 01	−1.4046E + 01	5.9403E + 01	4.0615E + 01
p2_1w	1.8751E + 01	1.2875E + 02	−6.2080E − 01	−1.7045E + 00	7.2222E + 01
p2_2w	−8.9121E + 02	−6.8412E + 03	−9.6625E + 01	1.3260E + 02	−4.0655E + 03
p2_3w	−2.7893E + 00	−1.8735E + 01	1.2351E − 01	2.4239E − 01	−1.0373E + 01
p3_1w	1.2176E + 02	−6.6453E + 01	−2.6208E + 01	−2.5105E + 02	−1.2997E + 03
p3_2w	−2.0657E + 03	2.2229E + 03	−3.8316E + 00	4.8514E + 03	4.8162E + 04
p3_3w	−2.0462E + 01	9.3560E + 00	−4.5660E − 01	3.7830E + 01	1.9558E + 02
p4_1w	6.0187E + 01	4.4694E + 00	4.5781E − 02	−7.6258E + 00	6.6019E − 01
p4_2w	−6.8364E + 02	−2.0677E + 02	−5.0076E + 01	3.7699E + 02	−5.7081E + 01
p4_3w	−1.0406E + 01	−6.7164E − 01	−1.6902E − 03	1.1046E + 00	−9.0556E − 02
p1_w1	−5.3010E + 01	−8.9423E + 00	−4.2979E + 02	−1.8027E + 02	−6.1446E + 01
p1_w2	−9.4962E + 01	4.9759E + 02	−8.0065E + 00	6.5646E + 03	3.2598E + 03
p1_w3	8.7205E + 00	1.2512E + 00	6.4195E + 01	2.6804E + 01	8.8857E + 00
p2_w1	−4.6108E + 00	−1.3330E + 01	3.5584E + 00	7.7152E − 01	−4.2985E + 01
p2_w2	−4.3741E + 00	3.8167E + 02	2.4795E + 01	−3.1324E + 01	1.1849E + 03
p2_w3	7.9556E − 01	1.9959E + 00	−7.0131E − 01	−1.1968E − 01	6.7134E + 00
p3_w1	1.0934E + 01	−1.8255E + 02	−4.7059E + 02	−1.7505E + 04	−2.0388E + 02
p3_w2	2.0100E + 02	6.6902E + 03	−8.6895E + 00	1.3965E + 05	7.4887E + 03
p3_w3	−2.3611E + 00	2.7161E + 01	7.7010E + 01	2.9901E + 03	3.0391E + 01
p4_w1	8.0151E + 00	1.0575E + 00	−3.4347E + 01	2.0544E + 04	−2.2007E − 02
p4_w2	−1.6102E + 01	−3.2906E + 01	3.3104E + 01	4.3595E + 01	−9.6404E − 01
p4_w3	−1.3860E + 00	−1.6919E − 01	5.6556E + 00	−3.6060E + 03	2.0855E − 03

TABLE 2: Interaction parameters 2.

	CsI	K$_2$SO$_4$	KBr	KCl	KI
p1_1w	−1.5076E + 02	−1.1322E + 03	−5.2890E + 01	−5.4333E + 02	−1.8317E + 02
p1_2w	2.6520E + 03	4.2812E + 04	3.0350E − 01	1.9740E + 04	9.1426E + 03
p1_3w	2.3379E + 01	1.6695E + 02	7.8620E + 00	8.0107E + 01	2.6456E + 01
p2_1w	−5.8621E + 00	2.6070E + 00	1.1180E − 01	7.6838E − 01	3.4299E + 00
p2_2w	2.4097E + 02	−9.6319E + 01	1.0920E + 01	−3.7842E + 01	−3.4393E + 02
p2_3w	8.9043E − 01	−4.0825E − 01	−4.7342E − 02	−1.1964E − 01	−4.6963E − 01
p3_1w	−2.6669E + 02	1.9933E + 04	−4.3606E + 02	1.9205E + 01	−2.6757E + 02
p3_2w	1.2681E + 04	−4.5828E + 05	1.8225E + 04	−6.4698E + 02	8.5408E + 03
p3_3w	3.7810E + 01	−3.1560E + 03	6.4023E + 01	−3.0149E + 00	3.9541E + 01
p4_1w	7.0415E + 00	1.0497E + 02	−2.4939E + 00	8.7763E − 01	−3.7790E − 02
p4_2w	−3.8769E + 02	−1.1148E + 05	1.0771E + 02	1.1484E + 03	−1.6918E + 01
p4_3w	−1.0392E + 00	2.6699E + 01	3.7404E − 01	−8.2115E − 01	1.2370E − 02
p1_w1	−1.8355E + 02	−1.5942E + 02	−1.7125E + 02	−4.9179E + 03	1.0020E + 00
p1_w2	6.7704E + 03	3.6753E + 03	5.7061E + 03	2.6542E + 05	−4.3740E + 01
p1_w3	2.7265E + 01	2.6165E + 01	2.5726E + 01	7.1036E + 02	−2.0736E − 01
p2_w1	8.0511E − 01	−6.8439E + 00	−3.8125E − 01	1.8534E + 01	1.1224E + 00
p2_w2	−2.6358E + 01	−8.5162E + 01	1.6559E + 01	−3.2290E + 03	5.0608E + 01
p2_w3	−1.2932E − 01	1.2096E + 00	5.4912E − 02	−3.6983E + 00	−2.5325E − 01
p3_w1	0.0000E + 00	−3.6007E + 01	−1.7478E + 01	−1.8633E + 02	−1.8676E + 02
p3_w2	−4.8000E + 01	3.7047E + 03	1.3177E + 03	6.8740E + 03	6.9394E + 03
p3_w3	2.1553E + 01	2.8252E + 00	2.2947E + 00	2.7683E + 01	2.7784E + 01
p4_w1	−3.7960E + 02	−3.4604E + 01	−1.0760E + 00	4.7385E − 01	−1.9094E − 01
p4_w2	3.7578E + 06	1.5639E + 03	6.7959E + 01	−1.6643E + 01	1.4145E + 01
p4_w3	−3.5545E + 08	5.1440E + 00	1.2830E − 01	−7.4893E − 02	2.3459E − 02

interaction term is remodeled based on COSMO calculation data. Therefore, the original model parameters were given the physical meaning of COSMO by calculation and modeling.

2.2. *The Interaction in the COSMO Calculation.* COSMOtherm 2021 (in short COSMO) is a program that computes thermophysical data for liquids. COSMO is based on the COSMO-RS theory of interacting molecular surface

TABLE 3: Interaction parameters 3.

	LiCl	MgCl$_2$	MgSO$_4$	Na$_2$SO$_4$	NaBr
p1_1w	$-1.9624E+02$	$0.0000E+00$	$4.6803E+01$	$1.5595E+04$	$4.7096E+01$
p1_2w	$8.3829E+03$	$7.0357E+02$	$-5.9990E+04$	$-7.1950E+05$	$-2.8374E+03$
p1_3w	$2.9133E+01$	$0.0000E+00$	$5.0704E+01$	$-2.3341E+03$	$-7.0009E+00$
p2_1w	$5.6303E+00$	$-5.4794E+02$	$4.6994E+00$	$-1.9675E+02$	$-1.2808E+01$
p2_2w	$-3.1557E+02$	$-3.4876E-02$	$-2.7374E+02$	$9.3019E+03$	$5.0172E+02$
p2_3w	$-8.6033E-01$	$-6.2864E+01$	$-6.8479E-01$	$2.6397E+01$	$1.8845E+00$
p3_1w	$-2.4250E+02$	$3.1365E+00$	$-6.1472E+02$	$-7.3472E+02$	$-4.8166E+02$
p3_2w	$9.0184E+03$	$1.4238E+01$	$8.2062E+04$	$2.8328E+04$	$1.9590E+04$
p3_3w	$3.5512E+01$	$9.9977E+03$	$3.4574E+01$	$1.0841E+02$	$7.0887E+01$
p4_1w	$1.7942E+00$	$-1.6331E-04$	$5.7804E+00$	$2.0889E+00$	$-1.3560E+00$
p4_2w	$-8.3372E+01$	$-5.5570E+01$	$-3.3880E+02$	$-8.3239E+01$	$5.7880E+01$
p4_3w	$-2.7306E-01$	$-1.5810E+02$	$-8.4090E-01$	$-3.2257E-01$	$1.9850E-01$
p1_w1	$-1.6909E+02$	$-3.4915E+01$	$-1.8918E+02$	$-1.9473E+02$	$-1.2532E+02$
p1_w2	$6.1039E+03$	$-8.0377E+01$	$7.0911E+03$	$8.2187E+03$	$4.0464E+03$
p1_w3	$2.5139E+01$	$-1.5844E+01$	$2.8073E+01$	$2.8559E+01$	$1.8727E+01$
p2_w1	$8.4758E-01$	$-2.3443E+00$	$2.8420E+00$	$-1.9109E+00$	$1.3881E+00$
p2_w2	$-3.6891E+01$	$1.2393E+02$	$-1.1058E+02$	$1.1746E+02$	$-6.3787E+01$
p2_w3	$-1.2922E-01$	$2.8080E-01$	$-4.4140E-01$	$2.6448E-01$	$-2.0735E-01$
p3_w1	$-2.2090E+01$	$2.4764E+01$	$-7.5304E+01$	$4.2513E+00$	$-5.8272E+01$
p3_w2	$1.1497E+03$	$4.2759E+01$	$-6.1590E+00$	$-1.0872E+03$	$2.7566E+03$
p3_w3	$3.1878E+00$	$1.5251E+01$	$-2.2653E+01$	$-2.9049E-01$	$8.5269E+00$
p4_w1	$-1.8311E+01$	$3.1783E+01$	$2.5633E+01$	$-9.4684E-01$	$9.1862E-01$
p4_w2	$1.5655E+03$	$-1.8591E+02$	$-2.0188E+03$	$-4.3411E+01$	$1.6165E+01$
p4_w3	$2.2754E+00$	$-5.4919E+00$	$-6.6956E+00$	$1.9837E-01$	$-1.9654E-01$

TABLE 4: Interaction parameters 4.

	NaCl	NaI	RbCl	SrCl$_2$	ZnCl$_2$
p1_1w	$-1.1661E+02$	$-4.0262E+02$	$-1.4861E+02$	$-1.4894E+02$	$6.6039E+03$
p1_2w	$4.9274E+01$	$1.7533E+04$	$7.9653E+03$	$2.9476E+03$	$-2.0810E+05$
p1_3w	$1.7656E+01$	$5.8586E+01$	$2.1317E+01$	$2.2622E+01$	$-5.4124E+02$
p2_1w	$2.0329E+00$	$-7.0058E-01$	$-2.0617E+00$	$4.9975E+00$	$-3.4050E+02$
p2_2w	$-1.0981E+02$	$3.4959E+01$	$5.5783E+01$	$-2.5181E+02$	$5.8513E+03$
p2_3w	$-2.9922E-01$	$9.5589E-02$	$3.4073E-01$	$-7.3430E-01$	$3.6359E+01$
p3_1w	$-3.1042E+02$	$3.0597E+01$	$-6.0264E+02$	$-1.7136E+02$	$-7.3847E+01$
p3_2w	$1.5486E+04$	$-2.5349E+03$	$2.1380E+04$	$8.2118E+03$	$2.9548E+03$
p3_3w	$4.5170E+01$	$-4.1664E+00$	$8.9281E+01$	$2.4363E+01$	$1.0794E+01$
p4_1w	$1.2298E+02$	$-3.3004E+01$	$-6.8398E-01$	$1.6381E+01$	$4.6732E+00$
p4_2w	$-6.0785E+03$	$1.5906E+03$	$5.3327E+01$	$-9.4137E+02$	$-2.2010E+02$
p4_3w	$-1.8096E+01$	$4.7729E+00$	$8.1138E-02$	$-2.3786E+00$	$-7.0826E-01$
p1_w1	$-1.3776E+02$	$6.4223E+01$	$-5.8723E+01$	$2.6023E+00$	$-7.8527E+01$
p1_w2	$4.4852E+03$	$-3.9484E+03$	$3.2642E+03$	$9.2837E+00$	$3.0765E+03$
p1_w3	$2.0579E+01$	$-9.3726E+00$	$8.4339E+00$	$-4.7917E-01$	$1.1595E+01$
p2_w1	$1.8386E+00$	$1.8314E-01$	$5.6485E-01$	$-8.3981E+00$	$6.3595E+00$
p2_w2	$-8.8162E+01$	$-1.5504E-03$	$-2.6417E+01$	$-3.6593E+00$	$-1.8121E+02$
p2_w3	$-2.7270E-01$	$-4.4962E-02$	$-6.2320E-02$	$1.3420E+00$	$-1.0067E+00$
p3_w1	$-9.6971E+01$	$-2.5433E+02$	$-1.2644E+02$	$-1.9611E+02$	$-9.3813E+01$
p3_w2	$4.7896E+03$	$1.1051E+04$	$3.5827E+03$	$7.2753E+03$	$3.1889E+03$
p3_w3	$1.4194E+01$	$3.7594E+01$	$1.9064E+01$	$2.9190E+01$	$1.4000E+01$
p4_w1	$-2.7864E+01$	$-3.8597E+00$	$-3.4679E-01$	$-2.2429E-01$	$2.9848E+00$
p4_w2	$1.1229E+03$	$1.9773E+02$	$3.6769E+01$	$1.8740E+01$	$-1.9860E+02$
p4_w3	$4.1234E+00$	$5.6372E-01$	$3.9342E-02$	$2.4635E-02$	$-4.1453E-01$

charges [29, 30]. For the calculation of intermolecular interactions, the COSMO-chemical potential-mixture module was used. Before the calculation, compound details need to be entered. There are two main ways to input the components: one is to select the compounds directly in the database, and the other is to establish the new compounds in

TABLE 5: Correlation of VLE data.

System	T/K	Data points	This work		Reference and experiment
			dY/kPa[a]	dP/%[b]	
BaBr$_2$	298.15 to 343.15	63	0.058	0.81	[31, 32]
CaBr$_2$	298.15 to 343.15	63	0.053	1.13	[31, 32]
CaCl$_2$	273.15 to 415.15	236	0.457	1.19	[9, 16, 31, 32]
CsBr	298.15 to 343.15	51	0.064	0.71	[31, 32]
CsCl	298.15 to 343.15	63	0.457	1.19	[31, 32]
CsI	298.15 to 343.15	42	0.032	0.54	[31, 32]
K$_2$SO$_4$	298.15 to 373.65	104	1.067	2.72	[9, 32]
KBr	298.15 to 343.15	51	0.251	3.28	[31, 32]
KCl	273.15 to 343.15	66	0.194	2.50	[9, 16, 31, 32]
KI	298.15 to 343.15	60	0.188	2.24	[31, 32]
LiCl	298.15 to 394.4	47	0.011	0.42	[32, 33]
MgCl$_2$	298.15 to 377.85	120	0.490	1.86	[9, 31, 32]
MgSO$_4$	273.15 to 376.45	120	0.810	1.85	[9, 31, 32]
Na$_2$SO$_4$	273.15 to 298.15	30	0.009	0.46	[9, 32]
NaBr	298.15 to 343.15	47	0.011	0.21	[31, 32]
NaCl	298.15 to 373.15	89	0.097	0.92	[31, 32]
NaI	298.15 to 343.15	58	0.420	3.92	[31, 32]
RbCl	298.15 to 343.15	51	0.293	3.12	[31, 32]
SrCl$_2$	298.15 to 343.15	59	0.230	3.13	[31, 32]
ZnCl$_2$	298.15 to 379.8	23	0.008	0.031	[32, 33]
Average			0.26	1.611	

[a]$dY = (1/N) \sum |P\exp - P\mathrm{cal}|$, where N is the number of data points. [b]$dP = (1/N) \sum |P\exp - P\mathrm{cal}|/P\exp \times 100\%$, where N is the number of data points. $P_{\exp}$ represents the experimental pressure and P_{cal} represents the calculated pressure.

TABLE 6: The parameters α and hi.

	BaBr2	CaBr2	CaCl2	CsBr	CsCl
A	7.9752$E-02$	2.8767$E-01$	1.6389$E-01$	6.7821$E-15$	4.5910$E-01$
h_i	4.6147$E+00$	5.6968$E+00$	2.3336$E+00$	$-8.4186E-01$	$-3.8792E-01$
	CsI	K2SO4	KBr	KCl	KI
A	1.1545$E-14$	5.9029$E-01$	2.6438$E-02$	9.8801$E-03$	2.4789$E-02$
h_i	$-4.6851E-01$	$-1.7788E+01$	$-5.0900E+00$	$-4.9304E+00$	$-2.5134E+00$
	LiCl	MgCl2	MgSO4	Na2SO4	NaBr
A	8.1229$E-02$	2.4432$E-03$	3.2566$E-01$	4.4404$E-01$	3.4094$E-02$
h_i	1.6472$E+00$	6.2690$E+00$	9.8217$E+00$	$-2.4529E+00$	1.4730$E-01$
	NaCl	NaI	RbCl	SrCl2	ZnCl2
A	$-5.8248E-01$	$-4.9761E-01$	$-1.3570E-03$	8.2369$E-02$	7.1066$E-01$
h_i	3.6925$E+00$	5.3929$E+00$	$-2.4792E+00$	3.5726$E+00$	6.2096$E+00$

COSMO-TmoleX. Because the ion pairs and hydration assumptions are involved in the new model, COSMO-TmoleX is selected.

The calculation process is as follows:

(1) The necessary step needs to create a new ion pair "molecular" in TmoleX and optimize the structural formula, such as the sigma surface of NaCl, CaCl2, and H2O shown in Figure 1.

(2) According to the optimization results, a preliminary study on the new ion pair "molecular" is conducted. Sigma profile/potentials are important interaction reference indicators, such as Figures 2 and 3.

(3) The next step is as follows: open chemical potential-mixture in COSMOtherm 2021.

(4) When determining the compound, it is necessary to input the temperature and liquid phase composition and add a calculation table.

(5) Run the job to get the data.

2.3. The Results of COSMO Calculation. When the calculation is completed, the calculation results are analyzed. From the COSMO calculation results, it can be seen that some related data can be obtained, such as the chemical potential of the compound in the mixture, the total mean interaction energy in the mix (H_int), the misfit interaction energy in the mix (H_MF), the H-bond interaction energy in the mix (H_HB), and the vdW interaction energy in the mix (H_vdW).
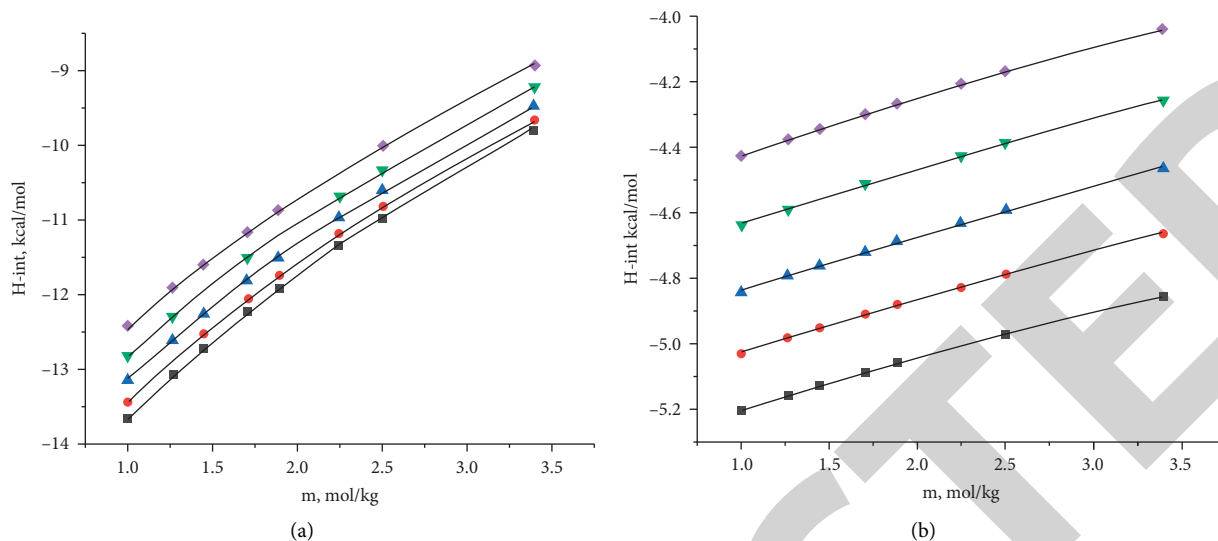
FIGURE 4: Correlation of the interaction data for the BaBr2+H2O system. (a) The interaction of BaBr2 and (b) the interaction of H2O. Symbols (■, T = 303.15 K; ●, T = 313.15 K; ▲, T = 323.15 K; ▼, T = 333.15 K; and ◆, T = 343.15 K :); COSMO data; lines: correlation.
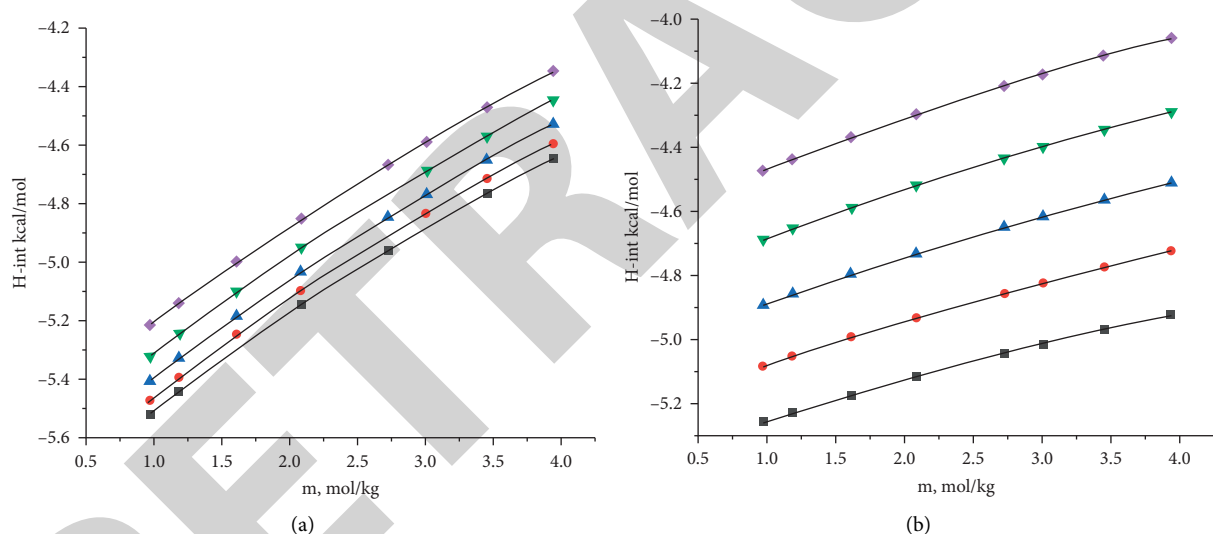
FIGURE 5: Correlation of the interaction data for the CaBr2+H2O system. (a) The interaction of CaBr2 and (b) the interaction of H2O. Symbols (■, T = 303.15 K; ●, T = 313.15 K; ▲, T = 323.15 K; ▼, T = 333.15 K; and ◆, T = 343.15 K :); COSMO data; lines: correlation.

In the model section, equations (5) ~ (8) are the main interaction terms. They described the total interaction. So, the total mean interaction energy (H_int) in COSMOtherm is used as the main research object.

2.4. Modeling of the H_int Interaction by 1stOpt. When the H_int interaction calculation was completed, we modeled the data and established the equations. Then, the established equations were added to the NXC model. During the modeling process, Quick Fit in 1stopt 9.0 was used to model the H_int interaction equations. For this fitting, out of 100,000 equations, the best model was searched. The optimal equation forms are given as follows:

$$\tau_x = \sum_{i=1}^{n} \left(\tau_i^a \exp\left(\tau_i^b m_i \right) + \tau_i^c \exp\left(\tau_i^d m_i \right) \right), \tag{14}$$

$$\tau_i^x = \frac{\tau_i^{(0)} + \tau_i^{(1)}}{T + \tau_i^{(2)} \ln(T)}. \tag{15}$$

After the formulas were determined, the next important step was to fit the parameters for the above equations. These parameters are of physical significance in COSMO, and the interaction terms in the model also have a physical meaning. The parameter fitting was also performed by using 1stopt 9.0. The interaction parameters are listed in Tables 1~4.

(a)

(b)
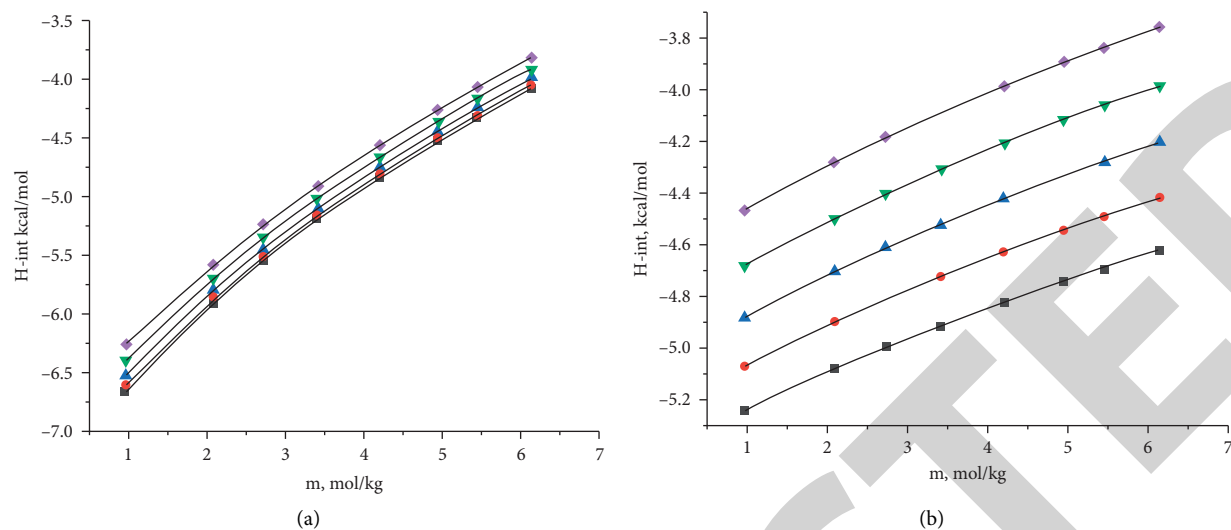
FIGURE 6: Correlation of the interaction data for the CaCl2+H2O system. (a) The interaction of CaCl2 and (b) the interaction of H2O. Symbols (■, T = 303.15 K; ●, T = 313.15 K; ▲, T = 323.15 K; ▼, T = 333.15 K; and ◆, T = 343.15 K :); COSMO data; lines: correlation.

(a)

(b)
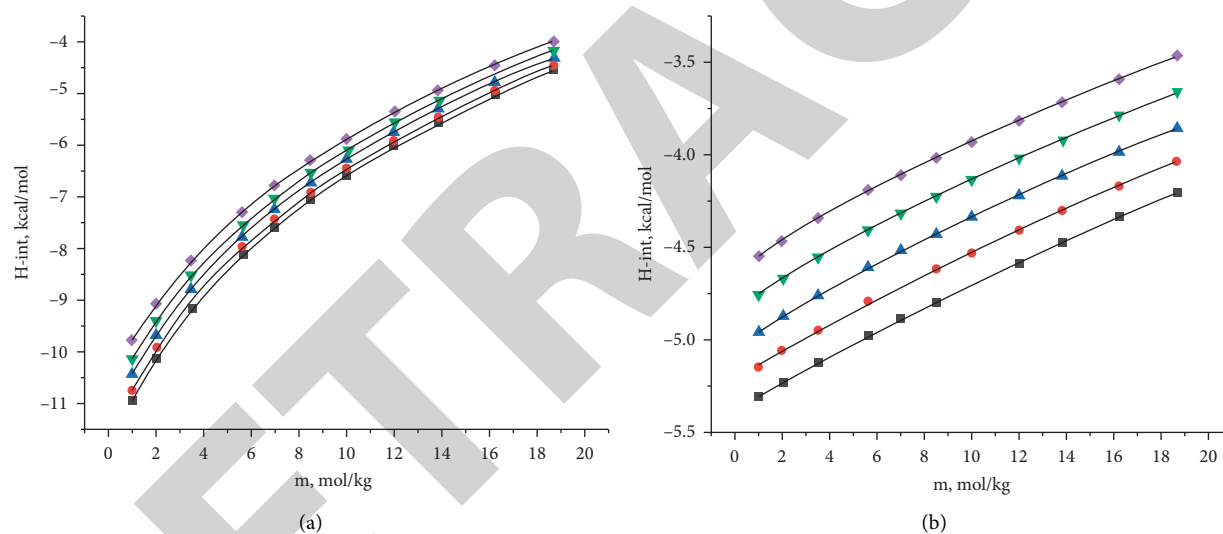
FIGURE 7: Correlation of the interaction data for the LiCl + H_2O system. (a) The interaction of LiCl and (b) the interaction of H_2O. Symbols (■, T = 303.15 K; ●, T = 313.15 K; ▲, T = 323.15 K; ▼, T = 333.15 K, and ◆, T = 343.15 K :); COSMO data; lines: correlation.

TABLE 7: Correlation of H int data.

System	T/K	Salt-water interaction		Water-salt interaction	
		dY/kcal.mol⁻¹ᵃ	dP/%ᵇ	dY/kcal.mol⁻¹ᵃ	dP/%ᵇ
BaBr$_2$	298.15 to 343.15	0.0105	0.0944	0.0024	0.0504
CaBr$_2$	298.15 to 343.15	0.0001	0.0183	0.0003	0.0077
CaCl$_2$	298.15 to 343.15	0.0013	0.0258	0.0004	0.0092
CsBr	298.15 to 343.15	0.0044	0.0261	0.0018	0.0385
CsCl	298.15 to 343.15	0.0144	0.0796	0.0015	0.0319
CsI	298.15 to 343.15	0.0005	0.0037	0.0007	0.6001
K$_2$SO$_4$	298.15 to 343.15	0.0072	0.0216	0.0009	0.0186
KBr	298.15 to 343.15	0.0031	0.0217	0.0015	0.0321
KCl	298.15 to 343.15	0.0073	0.0427	0.0021	0.0425
KI	298.15 to 343.15	0.0053	0.0423	0.0007	0.0172
LiCl	298.15 to 343.15	0.0067	0.1118	0.0029	0.0682
MgCl$_2$	298.15 to 343.15	0.0254	0.8672	0.0029	0.0693

TABLE 7: Continued.

System	T/K	Salt-water interaction		Water-salt interaction	
		dY/kcal.mol^{-1}[a]	dP/%[b]	dY/kcal.mol^{-1}[a]	dP/%[b]
MgSO$_4$	298.15 to 343.15	0.0408	2.7068	0.0021	0.0517
Na$_2$SO$_4$	298.15 to 343.15	0.0124	0.0688	0.0009	0.0187
NaBr	298.15 to 343.15	0.0034	0.0319	0.0024	0.0531
NaCl	298.15 to 343.15	0.0081	0.0614	0.0015	0.0335
NaI	298.15 to 343.15	0.0032	0.0369	0.0031	0.0699
RbCl	298.15 to 343.15	0.0183	0.0995	0.0031	0.0645
SrCl$_2$	298.15 to 343.15	0.0176	0.1568	0.0007	0.0147
ZnCl$_2$	298.15 to 343.15	0.0098	0.6254	0.0037	0.0812
Average		0.010	0.257	0.0018	0.0689

[a]$dY = (1/N) \sum |P_{exp} - P_{cal}|$, where N is the number of data points. [b]$dP = (1/N) \sum |P_{exp} - P_{cal}|/P_{exp} \times 100\%$, where N is the number of data points. P_{exp} represents the experimental pressure and P_{cal} represents the calculated pressure.
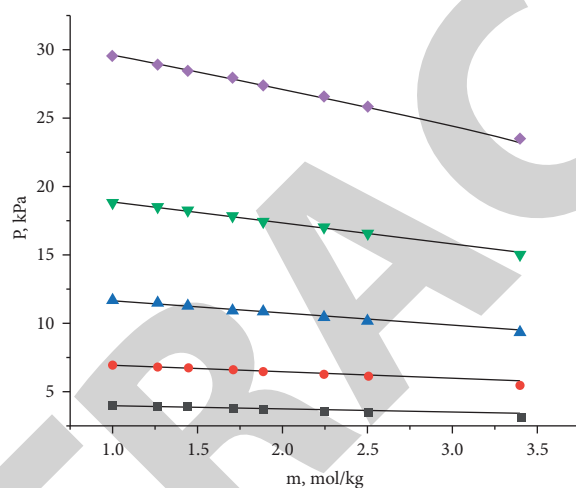
FIGURE 8: Calculation of the VLE for the BaBr2+H2O system. Symbols (■, T = 303.15 K; ●, T = 313.15 K; ▲, T = 323.15 K; ▼, T = 333.15 K; and ◆, T = 343.15 K :); VLE data; lines: calculation.
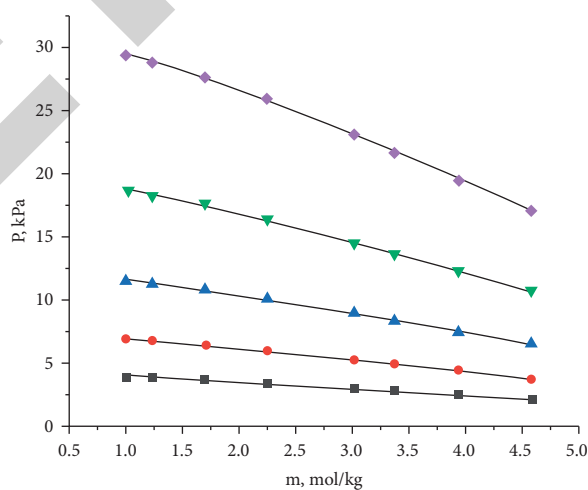
FIGURE 9: Calculation of the VLE for the CaBr2+H2O system. Symbols (■, T = 303.15 K; ●, T = 313.15 K; ▲, T = 323.15 K; ▼, T = 333.15 K; and ◆, T = 343.15 K :); VLE data; lines: calculation.
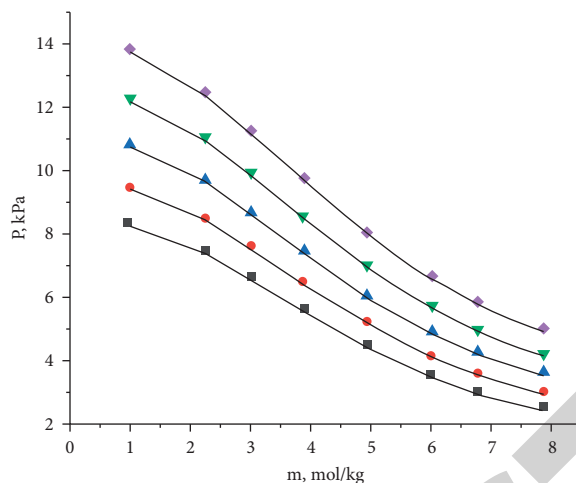
Figure 10: Calculation of the VLE for the CaCl2+H2O system. Symbols (■, T = 303.15 K; ●, T = 313.15 K; ▲, T = 323.15 K; ▼, T = 333.15 K; and ◆, T = 343.15 K :);VLE data; lines: calculation.
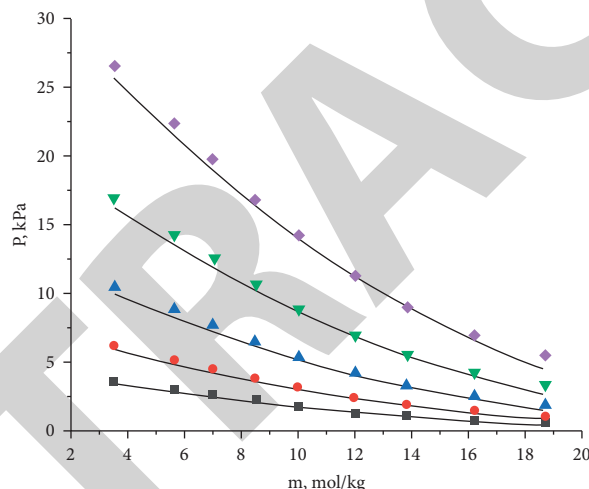
Figure 11: Calculation of the interaction data for the LiCl + H2O system. Symbols (■, T = 303.15 K; ●, T = 313.15 K; ▲, T = 323.15 K; ▼, T = 333.15 K, and ◆, T = 343.15 K :); VLE data; lines: calculation.

Through the above derivation and processing, final model equations (9) ~ (14) were determined. Parameters $\tau_{w,i}^{(x-0)}$, $\tau_{w,i}^{(x-1)}$, $\tau_{w,i}^{(x-2)}$, $\tau_{i,w}^{(x-0)}$, $\tau_{i,w}^{(x-1)}$, and $\tau_{i,w}^{(x-2)}$ were fitted on the basis of the COSMO data. Therefore, it only needs to fit the parameters α and h_i on the basis of the VLE data.

2.5. *Determination of the Parameters α and h_i.* The determination of the model parameters is a critical step in this paper. The interaction parameters were determined based on the COSMO data. Parameters α and h_i are further correlated by using phase equilibrium data. The data used for correlation are VLE data, and the references are listed in Table 5. The parameters α and h_i are listed in Table 6.

3. Results and Discussion

3.1. *The Results of Interaction and Parameters.* In data processing, it can be found that H_int energy is related to concentration, temperature, etc. From Figures 4~7, it can be seen that the energy increases with temperature and concentration.

Equations (13) and (14) were used to correlate the H_int interaction. The calculation results are listed in Table 7. For all systems in this paper, the results show that $dY \le 0.0408$ kcal/mol and the average of $dY = 0.0058$ kcal/mol and $dP \le 2.71\%$ and the average of $dP = 0.162\%$. So, the equations can be better used to describe the change of H_int energy.

$$dY = \left(\frac{1}{N}\right) \sum \left|P_{exp} - P_{cal}\right|, \tag{16}$$

$$dP = \frac{(1/N) \sum \left|P_{exp} - P_{cal}\right|}{P_{exp} \times 100\%}. \tag{17}$$

3.2. *Prediction of the VLE Data in Electrolyte Solutions.* The modified model and parameters described above were used to calculate the VLE data for twenty electrolyte

TABLE 8: Calculations for VLE data.

System	T/Kact	This work		Previous work	
		dY/kPa[a]	dP/%[b]	dY/kPa[a]	dP/%[b]
BaBr$_2$	298.15 to 343.15	0.058	0.81	0.079	0.78
CaBr$_2$	298.15 to 343.15	0.053	1.13	0.049	1.1
CaCl$_2$	273.15 to 415.15	0.457	1.19	0.081	1.82
CsBr	298.15 to 343.15	0.064	0.71	0.097	1.01
CsCl	298.15 to 343.15	0.457	1.19	0.091	0.97
CsI	298.15 to 343.15	0.032	0.54	0.039	0.42
K$_2$SO$_4$	298.15 to 373.65	1.067	2.72	0.051	1.15
KBr	298.15 to 343.15	0.251	3.28	0.077	0.87
KCl	273.15 to 343.15	0.194	2.50	0.044	0.67
KI	298.15 to 343.15	0.188	2.24	0.097	0.95
LiCl	298.15 to 394.4	0.011	0.42	0.018	1.25
MgCl$_2$	298.15 to 377.85	0.490	1.86	0.07	1
MgSO$_4$	273.15 to 376.45	0.810	1.85	0.076	0.85
Na$_2$SO$_4$	273.15 to 298.15	0.009	0.46	0.012	0.53
NaBr	298.15 to 343.15	0.011	0.21	0.048	0.75
NaCl	298.15 to 373.15	0.097	0.92	0.04	0.65
NaI	298.15 to 343.15	0.420	3.92	0.09	0.929
RbCl	298.15 to 343.15	0.293	3.12	0.061	0.69
SrCl$_2$	298.15 to 343.15	0.230	3.13	0.068	0.71
ZnCl$_2$	298.15 to 379.8	0.008	0.031	0.03	1
Average		0.26	1.61	0.061	0.905

[a]$dY = (1/N) \sum |P_{exp} - P_{cal}|$, where N is the number of data points. [b]$dP = (1/N) \sum |P_{exp} - P_{cal}|/P_{exp} \times 100\%$, where N is the number of data points.

solutions at vapor pressures ranging between 6 kPa and 101.325 kPa. The results of the calculation are presented in Table 5, and dY and dP are listed in Table x.

For all systems in this paper, the results show that d$Y \leq 1.067$ kPa and the average of d$Y = 0.26$ kPa and d$P \leq 3.92\%$ and the average of d$P = 3.92\%$. The calculation results for the VLE data are shown in Figure 8–11 for BaBr$_2$, CaBr$_2$, CaCl$_2$, and LiCl systems, respectively.

3.3. Comparison with the Results Obtained from the Previous Model. Some systems were selected to compare the results obtained in this paper and previous calculations. The results of the comparisons are shown in Table 8. From the results, it can be concluded that the maximum dY of the developed model is 1.067 kPa and that the maximum dP is 3.92%. Similarly, the average dY is 0.26 kPa, and the average dP is 1.61%. In general, the results of the model calculations in this paper are not as good as those reported previously, but the parameters are given better physical meaning, and the number of parameters used is lower.

4. Conclusions

Modeling and calculation of VLE for an electrolyte solution are studied in this paper. Based on previous works, a developed NRTL model is proposed. The influence mechanism for the microscopic interaction on macroscopic VLE is further studied by COSMOtherm. It can be obtained from the calculation result of COSMOtherm that the temperature and concentration of electrolyte solutions are higher, and the interaction energy (H_int) is larger. The interaction parameters in the model are

successfully linked to the COSMO interaction energy (H_int) and given a new physical meaning. The model can be used to successfully predict the VLE data for electrolyte solutions at vapor pressures ranging between 6 kPa and 101.325 kPa. It is suitable for most electrolyte solutions. Although the calculation results are slightly inferior to those of previous works, there is an important significance for the establishment of the model framework in this work.

Data Availability

The data used to support the findings of this study are included within the article.

Conflicts of Interest

The authors declare that they have no conflicts of interest.

Acknowledgments

References

[1] M. Costa Reis, "Ion activity models: the Debye-Hückel equation and its extensions," *ChemTexts*, vol. 7, no. 2, p. 9, 2021.

[2] J. M. Prausnitz, R. N. Lichtenthaler, and E. Azevedo, "Molecular thermodynamics of fluid-phase equilibria," *Thermodynamics*, 1999.

[3] K. S. Pitzer, "Thermodynamics of electrolytes. I. Theoretical basis and general equations," *Journal of Physical Chemistry*, vol. 77, no. 2, pp. 268–277, 1973.

[4] A. C. Galvão, Y. P. Jiménez, F. J. Justel, W. S. Robazza, and F. S. Donatti, "Salting-out precipitation of NaCl, KCl and NH4Cl in mixtures of water and methanol described by the modified Pitzer model," *The Journal of Chemical Thermodynamics*, vol. 150, Article ID 106202, 2020.

[5] J. D. Toner, D. C. Catling, and B. Light, "A revised Pitzer model for low-temperature soluble salt assemblages at the Phoenix site, Mars," *Geochimica et Cosmochimica Acta*, vol. 166, pp. 327–343, 2015.

[6] R. H. Stokes and R. A. Robinson, "Solvation equilibria in very concentrated electrolyte solutions," *Journal of Solution Chemistry*, vol. 2, no. 2-3, pp. 173–191, 1973.

[7] X. H. Lu and G. Maurer, "Model for describing activity coefficients in mixed electrolyte aqueous solutions," *AIChE Journal*, vol. 39, no. 9, pp. 1527–1538, 1993.

[8] G. M. Wilson, "Vapor-liquid equilibrium XI. A new expression for the excess free energy of mixing," *Journal of the American Chemical Society*, vol. 86, no. 2, pp. 127–130, 1964.

[9] H. Renon and J. M. Prausnitz, "Local compositions in thermodynamic excess functions for liquid mixtures," *AIChE Journal*, vol. 14, no. 1, pp. 135–144, 1968.

[10] D. S. Abrams and J. M. Prausnitz, "Statistical thermodynamics of liquid mixtures: a new expression for the excess Gibbs energy of partly or completely miscible systems," *AIChE Journal*, vol. 21, no. 1, pp. 116–128, 1975.

[11] C. C. Chen, H. I. Britt, J. F. Boston, and L. B. Evans, "Local composition model for excess Gibbs energy of electrolyte systems. Part I: single solvent, single completely dissociated electrolyte systems," *AIChE Journal*, vol. 28, no. 4, pp. 588–596, 1982.

[12] C. C. Chen and L. B. Evans, "A local composition model for the excess Gibbs energy of aqueous electrolyte systems," *AIChE Journal*, vol. 32, no. 3, pp. 444–454, 1986.

[13] P. Wang, A. Anderko, and R. D. Young, "A speciation-based model for mixed-solvent electrolyte systems," *Fluid Phase Equilibria*, vol. 203, no. 1-2, pp. 141–176, 2002.

[14] K. Thomsen and P. Rasmussen, "Modeling of vapor-liquid-solid equilibrium in gas-aqueous electrolyte systems," *Chemical Engineering Science*, vol. 54, no. 12, pp. 1787–1802, 1999.

[15] J. Gmehling, J. D. Li, and M. Schiller, "A modified unifac model .2. Present parameter matrix and results for different thermodynamic properties," *Industrial & Engineering Chemistry Research*, vol. 32, no. 1, pp. 178–193, 1993.

[16] X. Xu, Y. Hu, X. Wang, and L. Wu, "Experimental and modeling of vapor–liquid equilibria for mixed electrolyte solution systems," *Journal of Chemical & Engineering Data*, vol. 61, no. 7, pp. 2311–2320, 2016.

[17] D. Li, D. Zeng, H. Han, L. Guo, X. Yin, and Y. Yao, "Phase diagrams and thermochemical modeling of salt lake brine systems. I. LiCl+H$_2$O system," *Calphad*, vol. 51, pp. 1–12, 2015.

[18] J. Gross and G. Sadowski, "Application of perturbation theory to a hard-chain reference fluid: an equation of state for square-well chains," *Fluid Phase Equilibria*, vol. 168, no. 2, pp. 183–199, 2000.

[19] Y. Iwai and K. Matsubara, "Simultaneous correlation of liquid-liquid equilibria for ternary systems and phase equilibria for constituent binary systems by modified new activity coefficient model," *Fluid Phase Equilibria*, vol. 556, Article ID 113411, 2022.

[20] A. Noumir and B. Saad, "Modeling of isobaric vapor–liquid equilibrium data for ionic liquid-containing ternary systems," *Russian Journal of Physical Chemistry*, vol. 96, no. 1, pp. 27–35, 2022.

[21] S. Chen, M. Wang, J. Hu, Y. Guo, and T. Deng, "Phase equilibria in the aqueous ternary systems (NaCl + NaBO$_2$ + H$_2$O) and (Na$_2$SO$_4$ + NaBO$_2$ + H$_2$O) at 298.15 K and 0.1 MPa," *Journal of Chemical & Engineering Data*, vol. 63, no. 12, pp. 4662–4668, 2018.

[22] L. Meng, M. S. Gruszkiewicz, T. Deng, Y. Guo, and D. Li, "Isopiestic measurements of thermodynamic properties for the aqueous system LiBr–CaBr$_2$–H$_2$O at 373.15 K," *The Journal of Chemical Thermodynamics*, vol. 129, pp. 83–91, 2019.

[23] J. Zhou, Y. Zeng, G. P. Demopoulos, C. Li, and Z. Li, "Solubility of NaHCO$_3$ and NH$_4$HCO$_3$ in the relevant media and prediction of high-pressure phase equilibria for the NH$_3$–CO$_2$–NaCl–H$_2$O system," *Journal of Chemical & Engineering Data*, vol. 62, no. 12, pp. 4401–4410, 2017.

[24] C. K. Chang, W. L. Chen, D. T. Wu, and S. T. Lin, "Improved directional hydrogen bonding interactions for the prediction of activity coefficients with COSMO-SAC," *Industrial & Engineering Chemistry Research*, vol. 57, no. 32, pp. 11229–11238, 2018.

[25] T. Gerlach, T. Ingram, G. Sieder, and I. Smirnova, "Modeling the solubility of CO2 in aqueous methyl diethanolamine solutions with an electrolyte model based on COSMO-RS," *Fluid Phase Equilibria*, vol. 461, pp. 39–50, 2018.

[26] M. Królikowska, M. Skonieczny, K. Paduszyński, and M. Zawadzki, "Vapor pressure and physicochemical properties of {LiBr + IL-based additive + water} mixtures: experimental data and COSMO-RS predictions," *Journal of Solution Chemistry*, vol. 50, no. 4, pp. 473–502, 2021.

[27] X. Xu, Y. Zhou, Z. Wang, and X. Wang, "Experiment and modeling of vapor–liquid equilibria for H$_2$O+CH$_3$OH+KCl and H$_2$O+CH$_3$OH+NaBr systems," *Calphad*, vol. 63, pp. 134–141, 2018.

[28] X. Xu, N. Zhang, Y. Zhou, Y. Wang, and Z. Wang, "The effects of NaI, KBr, and KI salts on the vapor-liquid equilibrium of the H$_2$O+CH$_3$OH system," *Frontiers of Chemistry*, vol. 8, 2020.

[29] F. Eckert and A. Klamt, "Fast solvent screening via quantum chemistry: COSMO-RS approach," *AIChE Journal*, vol. 48, no. 2, pp. 369–385, 2002.

[30] A. Klamt and F. Eckert, "COSMO-RS: a novel and efficient method for the a priori prediction of thermophysical data of liquids," *Fluid Phase Equilibria*, vol. 172, no. 1, pp. 43–72, 2000.

[31] K. R. Patil, A. D. Tripathi, G. Pathak, and S. S. Katti, "Thermodynamic properties of aqueous electrolyte solutions. 2. Vapor pressure of aqueous solutions of sodium bromide, sodium iodide, potassium chloride, potassium bromide, potassium iodide, rubidium chloride, cesium chloride, cesium bromide, cesium iodide, magnesium chloride, calcium chloride, calcium bromide, calcium iodide, strontium chloride, strontium bromide, strontium iodide, barium chloride,

Retraction

Retracted: Application of ZnO Semiconductor Nanomaterial Ink in Packaging and Printing Design

Journal of Chemistry

This article has been retracted by Hindawi following an investigation undertaken by the publisher [1]. This investigation has uncovered evidence of one or more of the following indicators of systematic manipulation of the publication process:

(1) Discrepancies in scope

(2) Discrepancies in the description of the research reported

(3) Discrepancies between the availability of data and the research described

(4) Inappropriate citations

(5) Incoherent, meaningless and/or irrelevant content included in the article

(6) Peer-review manipulation

The presence of these indicators undermines our confidence in the integrity of the article's content and we cannot, therefore, vouch for its reliability. Please note that this notice is intended solely to alert readers that the content of this article is unreliable. We have not investigated whether authors were aware of or involved in the systematic manipulation of the publication process.

Wiley and Hindawi regrets that the usual quality checks did not identify these issues before publication and have since put additional measures in place to safeguard research integrity.

We wish to credit our own Research Integrity and Research Publishing teams and anonymous and named external researchers and research integrity experts for contributing to this investigation.

The corresponding author, as the representative of all authors, has been given the opportunity to register their agreement or disagreement to this retraction. We have kept a record of any response received.

References

[1] C. Guo, "Application of ZnO Semiconductor Nanomaterial Ink in Packaging and Printing Design," *Journal of Chemistry*, vol. 2022, Article ID 6166533, 7 pages, 2022.

Hindawi

Research Article

Application of ZnO Semiconductor Nanomaterial Ink in Packaging and Printing Design

Changjian Guo ⓘ

Xiamen Institute of Technology, Xiamen, Fujian 361021, China

Correspondence should be addressed to Changjian Guo; 1420720147@xs.hnit.edu.cn

In order to obtain a flat and clear packaging printing pattern, the author proposes a printing method based on ZnO semiconductor nanomaterial ink. The method uses zinc acetate dihydrate as raw material, ethylenediamine as a complexing agent, absolute ethanol as a solvent, and ethyl cellulose as an auxiliary agent to prepare particle-free ZnO functional ink. The ink was spin-coated on a glass substrate, cured at different temperatures on a heating plate for 30 min, and passed through an X-ray diffractometer, a field emission scanning electron microscope, an infrared spectrometer, a synchronous thermal analyzer, an ultraviolet-visible spectrophotometer, and a transmission electron microscopy were used to characterize the synthesized inks and the resulting films. Experiments show that the decomposition temperature of particle-free ZnO conductive ink is much lower than that of zinc acetate precursor; the film cured at 300°C for 30 min has a smooth surface, uniform particle size, good crystallinity, and transmittance of up to 80%. After inkjet printing on the PI flexible substrate, after curing at 300°C for 30 min, the pattern surface is smooth and clear, and the outline is clear. *Conclusion.* The printing method is based on ZnO semiconductor nanomaterial ink. It has good application prospects in packaging and printing design.

1. Introduction

Nanotechnology is a developing technology that emerged in the 1990s. It is a new technology for studying the laws and characteristics of electrons, atoms, and molecules in the space of 0.10–100 nanometers (i.e., one billionth of a meter). Because nanotechnology will eventually enable human beings to manipulate individual atoms and molecules according to their own wishes, so as to achieve effective control of the microscopic world, it is considered to be a hot subject that has an extremely important impact on the generation and development of a series of high-tech in the 21st century. It is listed as one of the key technologies of the 21st century by countries all over the world, and a lot of manpower and material resources are invested in its research and development [1]. By the second half of the 1970s, there were advocates for the development of nanotechnology, but most mainstream scientists at the time were still skeptical. From the mid-1970s to the late 1980s, many scientists successively prepared nano-sized materials in the laboratory

and found that these materials had many wonderful properties. At present, nanotechnology mainly includes many fields, such as nanobiology, nanomechanics, nano-electronics, nanomaterials, atomic and molecular manipulation, and nanomanufacturing. As far as nanomaterials are concerned, due to several major characteristics of nanomaterials, such as small size effect, surface effect, quantum size effect, and macroscopic quantum tunneling effect, some new changes have appeared in the characteristics of sound, light, electromagnetism, and thermodynamics. Therefore, nanomaterials are widely used in various fields, such as the application of nanomaterials in the fields of structural parts, electronic devices, the discipline and field of chemistry, biomedicine and health, textiles, aerospace, sports, agriculture, and other fields [2]. With in-depth research on the preparation, characterization, performance testing, and processing of nanomaterials, its application fields have gradually expanded. From the darling of high technology in the past, it has gradually entered the lives of ordinary people and penetrated into people's clothing, food, housing, and

transportation. It can be said that nanometer technology and nanomaterials have greatly changed human production and lifestyle. Semiconductor photocatalytic materials have outstanding advantages such as high catalytic activity, low cost, low requirements for catalytic conditions, and less repollution and have great application value in the fields of environmental purification and new energy [3]. Among the widely studied semiconductor photocatalytic materials, ZnO has the characteristics of high photosensitivity, a strong driving force for redox reactions, and low cost. It has become one of the core photocatalytic materials in contemporary semiconductor photocatalytic technology. ZnO is a common direct wide bandgap II–VI semiconductor material, with nontoxic, low cost, readily available raw materials, wide bandgap, high exciton binding energy (60 meV), strong radiation resistance, good mechanical, electrical coupling, and other adcantages. ZnO has good film-forming properties, and common thin-film preparation techniques can be used to prepare ZnO thin films. However, the traditional ZnO functional film preparation method has problems such as a long production cycle, complicated operation, and large waste of raw materials, and it is difficult to meet the development requirements of miniaturization and precision of electronic products [4].

The author used zinc acetate dihydrate as the zinc source of the zinc-based ink, ethylenediamine as the complexing agent, ethanol as the solvent, and ethyl cellulose as the auxiliary agent in the ink and synthesized a particle-free ZnO ink with stable performance. In this way, the superiority of ZnO semiconductor nanomaterial ink in packaging and printing applications is verified.

2. Literature Review

Research on the preparation of ZnO nanomaterials: Onuki et al. proposed the coprecipitation method. A suitable precipitating agent is added to the electrolyte solution in which various components coexist, and a chemical reaction occurs to generate a homogeneous precipitation material, and high-purity nano-powder materials can be obtained by drying or calcining. The coprecipitation method is more convenient to synthesize zirconium oxide, with low requirements for equipment and synthesis conditions, low cost, and short synthesis time [5]. Xu et al. proposed the effects of Zn2+ concentration, calcination temperature, and other conditions on the particle size of ZnO nanocrystals during the preparation process and analyzed the mechanism. Experimental results show that the smaller the reaction concentration, the smaller the crystal grain size can be obtained; under the same other reaction conditions, the grain size of the prepared nano-ZnO particles increases gradually with the increase of the calcination temperature [6]. Das et al. proposed metal-organic chemical vapor deposition. The physical vapor deposition method uses high-temperature heat sources such as arc, high frequency, laser, or plasma to heat oxides to vaporize them and then aggregate them into nanoparticles. Among them, the vacuum evaporation method (i.e., heating under vacuum conditions) is the most commonly used. The chemical vapor deposition

method utilizes volatile metal compounds or elemental metal vapors to generate the desired compounds through chemical reactions, mainly including vapor-phase oxidation and vapor-phase pyrolysis [7]. Bairy et al. proposed the hydrothermal method. The main device used in the hydrothermal method is to create a high temperature and high pressure environment in the reactor, which is very different from the outside world. The crystallization products with good properties can be synthesized by using the temperature difference between the inside and outside of the reactor. Crystals with good crystallinity and small particle size can be directly obtained by the hydrothermal method. The preparation process is also relatively simple, and calcination treatment is not required. The crystalline morphology of ZnO grains is very sensitive to the properties of the medium. The grains grown in pure water solution are long and columnar; in a certain alkalinity solution, the grains are tapered; the alkalinity continued to increase, and the grains became biconical. Temperature also has a certain effect on the crystal size [8]. Li et al. proposed fog thermal decomposition. Using the large pressure difference and temperature difference inside and outside the reaction vessel, the metal salt solution can be hydrolyzed to generate a product with uniform components. Compared with other technologies, spray thermal decomposition technology does not require a high vacuum, which greatly simplifies the process and reduces production costs [9]. Ruan et al. proposed the sol-gel method. Zinc oxide quantum dots and thin films are usually synthesized using the sol-gel method. This method is mainly composed of the following three steps: dispersing the precursor in solution, hydrolyzing into the sol, and finally preparing nanostructured materials by drying or even sintering. Using this method, quantum dots were prepared, the size of the product oxide front was successfully regulated, and the size-dependent shift of the absorption and emission spectra of quantum dots was observed [10].

On the basis of the current research, the authors proposed using zinc acetate dihydrate as the zinc source of the zinc-based ink, ethylenediamine as the complexing agent, ethanol as the solvent, and ethyl cellulose as the auxiliary agent in the ink, and they synthesized the properties of a stable particle-free ZnO ink, and the experimental data show that ZnO has a good application prospect in packaging and printing (Figure 1).

3. Research Methods

3.1. Structure of ZnO Semiconductors. ZnO is an amphoteric white oxide (commonly known as zinc white), and the wurtzite structure of ZnO is stable, so it is more common. ZnO with a wurtzite structure has centrosymmetric but no axial symmetry and dangling bonds appear on the crystal surface due to the fracture. The characteristics of the surface section of ZnO crystals have a slight influence on the overall properties of the crystals, which increase with the decrease of their size and even completely change the original properties of the crystals themselves. Therefore, by controlling the structure of zinc oxide, such as size, morphology or surface crystal plane orientation, surface composition, and surface
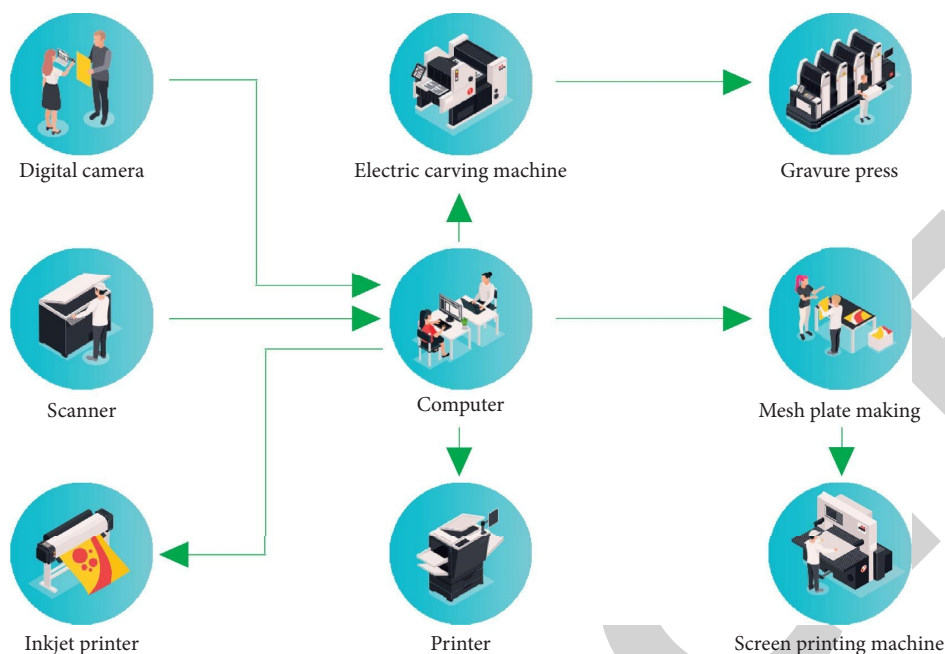
FIGURE 1: Packaging and printing design.

charge, the properties of zinc oxide can be greatly adjusted or changed, thereby obtaining the required luminescence and fluorescence enhancement for applications [11], ferromagnetism, catalytic properties, etc. Among them, micron-sized ZnO has attracted much attention due to its unique properties in the fields of luminescence, photocatalysis, and sensors as shown in Table 1.

3.2. Preparation of Nano-ZnO Arrays. The properties of ZnO strongly depend on its own structure, including grain size, crystal morphology, grain growth orientation, grain aspect ratio, grain density, etc. Meanwhile, the surface properties of ZnO nanoparticles and the packing morphology of the particles also play important roles in many applications. Therefore, it is very meaningful to prepare nano-ZnO arrays with controllable crystal morphology, controllable grain growth orientation, and uniform size. Nano-ZnO arrays have special properties that a single nanomaterial does not possess, so they have broad application prospects, such as sensors, actuators, varistors, catalysts, etc. [12]. There are many ways to prepare nanomaterials, such as the various methods introduced in the previous section; although many nanomaterials with various structures and properties have been synthesized by these methods, there are still some problems, such as the difficulty of particle size and shape, control, disordered arrangement of particles and harsh preparation conditions. Therefore, it is difficult in the field of nanomaterials research to explore a method that can easily prepare particles with controllable size and shape, as well as particle arrangement and order. At present, there are two main methods for preparing well-arranged nanostructure arrays, namely, template synthesis and seeded growth. The template method is more and more mature in research at home

and abroad. The seed crystal growth method is a new process method developed in recent years [13].

3.2.1. Template Method (Template Synthesis). The template method is to introduce monomers, polymer solutions, or melts into the nanopores of the template and obtain structural regularity by chemical or physical methods (electrochemical polymerization, chemical polymerization, polymer solution, and polymer melt methods), resulting in neatly arranged nanomaterials. The template synthesis method can prepare one-dimensional nanomaterials with uniform size, regular arrangement, and adjustable structure, which can effectively prevent the agglomeration of nanomaterials. The particle size and particle size distribution of nanoparticles prepared by the template synthesis method are closely related to the pore size and distribution of the template. At the same time, the formation of nanostructure arrays is also closely related to the ordering of the template. Therefore, template selection and preparation are critical. Templates only provide a mesoscopic environment for the formation of nanomaterial arrays. Nanoparticles also require other synthetic methods to prepare them, such as electrochemical deposition, electroless plating, chemical deposition, sol-gel, etc. [14]. The formation of templates on nanoparticle arrays has certain advantages. However, using certain synthetic methods to prepare nanoparticles, their morphology is not within the control range.

3.2.2. Seed Growth. The seed growth method is a new process method developed in recent years, which can effectively control the grain shape of ZnO nanoparticles and, at the same time, prepare well-arranged ZnO nanoparticle arrays. The basic idea of the seed growth method is divided into three steps: the first step is to select a suitable substrate.

TABLE 1: Properties of zinc oxide.

Chemical formula	Molar mass	Exterior	Odour	Density	Melting point	Solubility	Energy gap	Refraction
ZnO	$81.4084 \text{ g·mol}^{-1}$	White solid	Tasteless	5.606 g·cm^{-3}	1975 °C (break down)	Insoluble: 0.0004 g/100 mL (17.8°C)	3.37 eV	2.0041

In the second step, different preparation methods were used to randomly grow ZnO on the substrate covered with the crystal seed film. At this stage, the growth orientation and morphology of ZnO nanoparticles are not controlled [15]. In the third step, after the random growth of ZnO nanoparticles on the substrate, due to the crystal habit and spatial confinement effect of ZnO nanoparticles, ZnO nanoparticles grow in a specific direction on this basis to form nano-ZnO columnar arrays. The control of the morphology of ZnO nanoparticles is controlled by the choice of external catalysts and raw materials [16].

3.3. Preparations

3.3.1. Ink Preparation. First, 0.006 mol of ethylenediamine complexing agent, 15 mL of ethanol, and 8 μL of ethyl cellulose auxiliary were mixed evenly, and 0.002 mol of zinc acetate dihydrate was weighed on an electronic balance and then was added to the mixed solution; we continued to stir and dissolved it for 1 h and then filtered with a 0.22 μm microporous membrane to obtain a particle-free ZnO ink for inkjet printing [17].

3.3.2. ZnO Thin Film Preparation. The glass and PI substrates were ultrasonically cleaned with acetone for 5 min to remove oil stains on the surface of the substrates, then cleaned with deionized water, and dried for hydrophilic treatment before use. The ink was spin-coated on a 2 cm glass sheet, heated to different temperatures, and held for 30 min to form a thin film; the particle-free ZnO ink prepared by a commercial Epson inkjet printer was printed on a PI substrate and heat-treated at 300°C for 30 min on a heating plate [18].

3.3.3. Sample Characterization. The phase of the ZnO thin film was tested by a SmartLab X-ray diffractometer (Cu target, 40 kV/200 mA). The surface morphology of ZnO thin films was measured by JSM-700IF field emission scanning electron microscope [19]. Using NicoletiS5 infrared spectrometer (FTIR) combined with attenuated total reflection iD7ATR (attenuated total reflection) test ZnO thin film surface functional groups [20], the thermal decomposition behavior of ZnO ink and precursor was tested by the STA449F3 synchronous thermal analyzer. The transmittance of the film was measured with a Lambda750S UV-Vis spectrophotometer. The contact angle of the ink was tested with an SL200KS type contact angle tester. Atomic force microscopy (AFM) was used to test the roughness of the films after inkjet printing. A JEM-2100 transmission electron microscope (TEM) was used to test the morphology, diffraction spots, and high-resolution images of ZnO particles in the films [21]. The viscosity of the ink was measured at a shear rate of 26.4 s−1 using an LVDV-II + procoaxial cylindrical viscometer with a small sample cell. The electrical properties of ZnO films were measured by an HMS-5000 automatic variable temperature Hall effect tester.

4. Analysis of Results

4.1. Thermal Decomposition Behavior of Particle-free ZnO Ink. Figure 2(a) shows the TG-DSC curves of zinc acetate dihydrate precursor and particle-free ZnO ink (air atmosphere, heating rate of 10°C/min). In order to ensure that the decomposition temperature of zinc amine precursor can be seen during thermal analysis, in the experiment, the amount of solvent was adjusted to 1 mL. As can be seen from Figure 2(a), the thermal decomposition process of zinc acetate dihydrate is divided into three steps: The first step is from room temperature to 110°C, which corresponds to the endothermic peak at 105.7°C on the DSC curve, and the mass loss is 15.3%, which is caused by the loss of crystal water from zinc acetate dihydrate; the second step is 110~260°C, an endothermic peak of 255.5°C appears on the DSC curve, and its mass loss is 0, which corresponds to the melting process of zinc acetate from solid to liquid; the third step is 260~350°C, DSC. The curve appeared to have an endothermic peak at 330.8°C, and the mass loss on the TG curve was 47.1%, which was the process of the decomposition of zinc acetate into ZnO.

Figure 2(b) shows that the behavior of particle-free ZnO ink during heating is much more complex and can be divided into 5 steps: The first step is from room temperature to 80°C, and the mass loss on the corresponding TG curve is 4.6%, which is due to the loss of crystal water by zinc acetate dihydrate; The second step is 80~100°C, with the endothermic peak at 94.4°C of the DSC curve. The corresponding mass loss is 51%, which is caused by a large amount of ethanol volatilization; The third step is 100~120°C, corresponding to the endothermic peak at 100.1°C of the DSC curve, and the mass loss is 6%, corresponding to the volatilization of uncomplexed ethylenediamine; the fourth step is 120~160°C, accompanied by an endothermic peak at 154.5°C, and its mass loss is 0, which is due to the melting of the zinc amine precursor; The fifth step is 160~220°C, and the DSC curve is at 176.7. There is one absorption peak at °C, and the mass loss is 28.3%, which corresponds to the process of the decomposition of the precursor and the formation of ZnO; after the sixth step at 220°C, there is one endothermic peak at 349.8°C, with no mass loss, which corresponds to the crystallization process of ZnO.

(a)

(b)
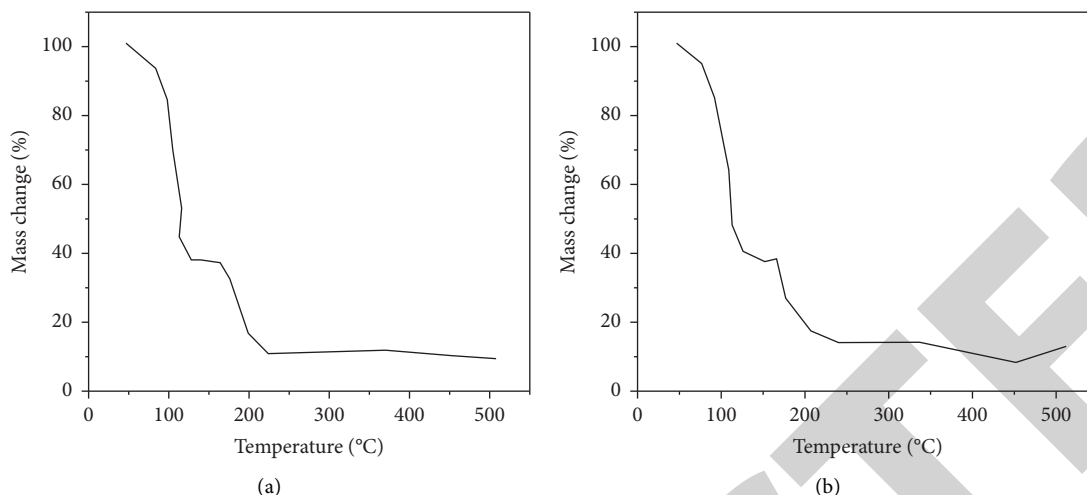
Figure 2: TG-DSC curves of zinc acetate dihydrate precursor and particle-free ZnO ink. (a) Zinc acetate dihydrate. (b) Particle-free ZnO ink.

4.2. Film-forming Properties of Particle-free Zinc-Based Conductive Ink.

Figure 3 shows the XRD spectra of the thin films of ZnO inks dried naturally at room temperature and heat-treated at 100, 200, 250, 300, 400, 600, and 800°C for 30 min, respectively. Combined with the thermal analysis results in Figure 3, the thermal decomposition temperature of the particle-free zinc-based ink is 176.7°C, so it can be seen from XRD analysis that the film that is naturally dried at room temperature and 100°C is still a crystalline precursor, and ZnO is not formed. The characteristic diffraction peaks of (100), (002), (101), (102), (110), (103), and (112) crystal planes of ZnO appeared in the thin film samples treated at 200~800°C, which were judged as standard by analysis. ZnO with hexagonal wurtzite polycrystalline structure. The intensity of diffraction peaks of the films increases with the increase of heat treatment temperature, indicating that increasing heat treatment temperature can increase the crystallinity of the films. During the low-temperature period of 200~300°C, the diffraction peak intensity of the (002) crystal plane in the film is the largest, the reason may be that the (002) plane has lower surface energy, and the film grains mainly grow along this plane, the (101) plane in the film gradually becomes the strongest diffraction peak, indicating that the (101) plane in the film may have lower surface energy at high-temperature, and the crystal grains in the film mainly grow along this plane [22].

The double peak at 3500~3000^{-1} is the vibrational stretching peak of the −NH2 functional group. The infrared spectrum 450^{-1} at 200°C and above can be considered as the characteristic absorption peak of the Zn—O bond, indicating that when the heat treatment temperature is 200°C, ZnO has been formed in the film. Among them, the absorption bands at 1588 and 1430^{-1} in the spectral lines at 200 and 250°C are caused by the antisymmetric stretching vibration and stretching vibration of C=O in the carboxyl group. Therefore, it can be judged that the precursor is not completely decomposed, the 3426^{-1} peak can be identified as being caused by the stretching vibration of hydroxyl groups
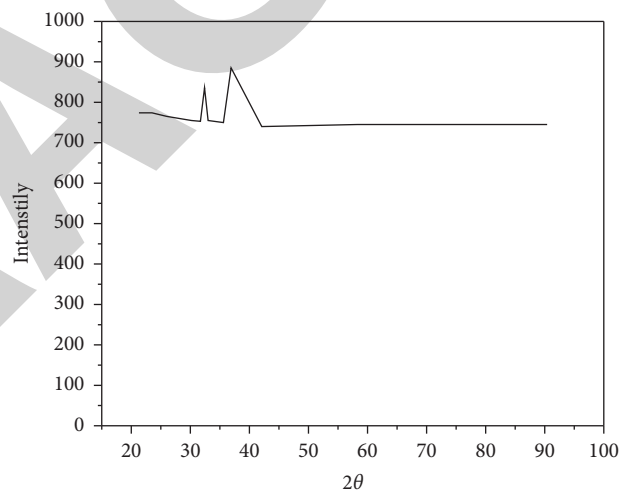
Figure 3: XRD spectra of the films obtained after heat treatment of particle-free ZnO inks at different temperatures for 30 min.

of adsorbed water in the sample. When the temperature is higher than 300°C, there is only the (Me-O) peak of Zn-O except for the vibration stretching peak of adsorbed water, indicating that there is no impurity functional group in the film after the temperature is higher than 300°C.

4.3. Printing Performance of Particle-free ZnO Ink on PI Substrate.

Printed on an inkjet printer using particle-free ZnO ink, and SEM images of patterns (300 μm) and lines with different line widths after heat treatment at 300°C for 30 min. The microstructure of the printed pattern is dense, the edge is complete, and the outline is clear. For inkjet printed lines, when the line width of the line is small (50 μm), the edge is slightly broken, mainly because when the line is small, in order to improve the resolution, the distance between the two nozzles of the printer will become larger, and the volume of the droplet ejected by the nozzle will become

TABLE 2: Resistivity, mobility, carrier concentration, and Hall coefficient of the films after heat treatment at 300°C for 30 min.

T/°C	$\rho/(\Omega * cm)$	$u/(cm^2 * V^{-1} * S^{-1})$	n/cm^{-3}	$H/(cm^3 * C^{-1})$
300	4.98×10^2	1.78	7.06×10^{15}	-8.8×10^2

smaller, due to the low viscosity of the ink, the wetting angle between the ink and the substrate is small. When the droplet falls on the substrate, it will spread out completely, the entire line is connected by the diffusion between the droplets; When the droplet volume is small, the diffusion is not complete and the edge of the line is more broken, when the line width is larger, the edge of the line is more complete and the outline is clear, mainly because the distance between the nozzles decreases and the volume of the ink droplets becomes larger, and the fusion between the ink droplets is sufficient to make the edge of the line clear and complete. The roughness of the film obtained by inkjet printing and heat treatment at 300°C is 15.2 nm, indicating that the surface is extremely smooth. The resistivity, mobility, carrier concentration, and Hall coefficient of the zinc oxide film after heat treatment at 300°C for 30 min are shown in Table 2.

The above experimental results show that

(1) A particle-free ZnO functional ink was prepared by using zinc acetate dihydrate, ethylenediamine, anhydrous ethanol, and ethyl cellulose. The thermal decomposition temperature of the ink (176.7°C) can be achieved by a complex reaction between zinc ions and amine groups, much lower than the thermal decomposition temperature of zinc acetate (330.8°C).

(2) The ink is spin-coated on the glass substrate and cured at different temperatures for 30 minutes. The film can generate ZnO with a hexagonal wurtzite polycrystalline structure when the heat treatment temperature is greater than 200°C, and the transmittance of the film is greater than 80%, among which the thin film prepared at 300°C has the tightest connection between particles and the least pores.

(3) After inkjet printing on the PI flexible substrate and heat treatment at 300°C for 30 min, the printed pattern has a dense microstructure with complete edges and clear outlines. Inkjet prints lines with different line widths. When the line width is smaller (50 μm), the edge is slightly broken. When the line width is larger, the edge of the line is relatively complete and the outline is clear. The surface roughness of the pattern after inkjet printing is only 15.2 nm, which has a good application prospect in printed electronics.

5. Conclusion

In summary, the decomposition temperature of the particle-free ZnO conductive ink studied by the author is much lower than that of the zinc acetate precursor; the film cured at 300°C for 30 min has a smooth surface, uniform particle size, good crystallinity, and transmittance of up to 80%. After inkjet printing on the PI flexible substrate, after curing at 300°C for 30 min, the pattern surface is smooth and clear, and the outline is clear. The printing method based on ZnO semiconductor nanomaterial ink has good application prospects in packaging and printing design, can be applied to flexible substrates, can prepare large-area zinc oxide films and complex zinc oxide circuits, and can be applied to solar cells and transparent conductive films, gas sensors, and other devices.

Data Availability

The data used to support the findings of this study are available from the corresponding author upon request.

Conflicts of Interest

The authors declare that they have no conflicts of interest.

Acknowledgments

References

[1] Z. Jiang, Y. Lei, Y. Lin, J. Hu, and Z. Ouyang, "Synthesis of zn 0·1 cd 0·9 s heterostructure with n-doped graphene quantum dots and graphene for enhancing photoelectric performance in uv–visible light," *Ceramics International*, vol. 46, no. 10, pp. 15801–15811, 2020.

[2] Y. Magari and M. Furuta, "Low-temperature processed metal-semiconductor field-effect transistor with in–ga–zn–o channel deposited by ar+o2+h2 sputtering," *ECS Transactions*, vol. 98, no. 7, pp. 89–95, 2020.

[3] A. G. E. Sutjipto, L. K. Ti, Y. P. Asmara, and A. Legowo, "Sample preparation of tio2 added zno using powder metallurgy route and its characteristics," *Materials Science Forum*, vol. 981, pp. 78–83, 2020.

[4] A. Ggm, A Raphael Lucas de Sousa e Silva, B. Pb, and C. Af, "Role of ga presence into the heterojunction of metal oxide semiconductor on the stability and tunability zno ceramics - sciencedirect," *Ceramics International*, vol. 46, no. 15, pp. 23390–23396, 2020.

[5] T. Onuki, Y. Okamoto, T. Aoki et al., "(invited) display and lsi applications of oxide semiconductor lsis (os lsis) using crystalline in–ga–zn oxide (igzo): applications related to coronavirus covid-19 pandemic," *ECS Transactions*, vol. 98, no. 7, pp. 185–204, 2020.

[6] H. Xu, W. Fang, L. Xu, and F. Liu, "Batch preparation of cuo/zno-loaded nanofiber membranes for photocatalytic degradation of organic dyes," *Langmuir*, vol. 36, no. 47, pp. 14189–14202, 2020.

[7] A. Das, D. Singh, A. Kaur et al., "Temperature-dependent cationic doping-driven phonon dynamics investigation in cdo thin films using Raman spectroscopy," *Journal of Physical Chemistry C*, vol. 124, no. 39, pp. 21818–21828, 2020.

Retraction

Retracted: Application of Nanofluid Electrochemistry in Heat Dissipation of Permanent Magnet Synchronous Motors

Journal of Chemistry

This article has been retracted by Hindawi following an investigation undertaken by the publisher [1]. This investigation has uncovered evidence of one or more of the following indicators of systematic manipulation of the publication process:

(1) Discrepancies in scope

(2) Discrepancies in the description of the research reported

(3) Discrepancies between the availability of data and the research described

(4) Inappropriate citations

(5) Incoherent, meaningless and/or irrelevant content included in the article

(6) Peer-review manipulation

The presence of these indicators undermines our confidence in the integrity of the article's content and we cannot, therefore, vouch for its reliability. Please note that this notice is intended solely to alert readers that the content of this article is unreliable. We have not investigated whether authors were aware of or involved in the systematic manipulation of the publication process.

Wiley and Hindawi regrets that the usual quality checks did not identify these issues before publication and have since put additional measures in place to safeguard research integrity.

We wish to credit our own Research Integrity and Research Publishing teams and anonymous and named external researchers and research integrity experts for contributing to this investigation.

The corresponding author, as the representative of all authors, has been given the opportunity to register their agreement or disagreement to this retraction. We have kept a record of any response received.

References

[1] X. Lin and G. Xie, "Application of Nanofluid Electrochemistry in Heat Dissipation of Permanent Magnet Synchronous Motors," *Journal of Chemistry*, vol. 2022, Article ID 3681749, 7 pages, 2022.

Hindawi

Research Article

Application of Nanofluid Electrochemistry in Heat Dissipation of Permanent Magnet Synchronous Motors

XiongPing Lin [ID] **and GuoDong Xie** [ID]

Chengyi University College, Jimei University, Xiamen, Fujian 361021, China

Correspondence should be addressed to XiongPing Lin; 201903304@stu.ncwu.edu.cn

In order to solve the problem of heat dissipation of permanent magnet synchronous motors, a technology using the principle of nanofluid electrochemistry is proposed. The main content of this technology is based on the characteristics and applications of nanofluids; according to the experimental system, the preparation and experimental parameters of nanofluids were determined; finally, by studying the influence of ultrasonic oscillation time and dispersant on the stability of nanofluids, it was concluded that the improvement of the thermal conductivity of nanofluids contributed to the improvement of the heat transfer rate of nanofluids. Experimental results show that when the volume fraction is 0.5, the increase rate of thermal conductivity is 1.51, the increase rate of convective heat transfer coefficient is 20.33, and the increase rate of convective heat transfer coefficient is greater than that of thermal conductivity, which shows that nanofluids have very good heat dissipation ability. It is proved that the technical research of nanofluid can meet the heat dissipation requirements of a permanent magnet synchronous motor.

1. Introduction

In recent years, the country has taken new energy vehicles as the key direction of future research and development; among them, the drive motor technology represented by a permanent magnet synchronous motor (PMSM) for electric vehicles significantly improves the performance and comfort of electric vehicles [1]. The temperature rise of the motor directly affects the performance of the motor and high temperature will destroy the insulation of the motor windings and limit the output of the motor; for permanent magnet motors, high temperature will seriously affect the magnetism of the permanent magnet and even cause irreversible demagnetization [2].

During the operation of the permanent magnet synchronous motor, in order to make it run stably and well, it is necessary to pay more attention to the heat dissipation of the motor, and this requires simulation analysis of the heat dissipation of the permanent magnet synchronous motor and further optimization, so as to solve the problem of heat dissipation of the permanent magnet synchronous motor;

the treatment is more scientific and reasonable and provides effective support and basis for ensuring the normal and stable operation of the permanent magnet synchronous motor. The development of key support fields such as new energy vehicles, robots, and high-precision CNC machine tools has put forward higher requirements for performance indicators such as motor efficiency, power density, response speed, and vibration and noise; promoting the motor to develop in the direction of high precision, high power density, miniaturization, lightweight, mechatronics, etc., has brought about problems such as a sharp increase in the internal heat generation of the motor and a serious shortage of effective heat dissipation space; therefore, the heat dissipation problem has become a further development of the motor system, the bottleneck of the development of power density direction [3].

In the actual operation and application process of the current permanent magnet synchronous motor, in order to ensure the effectiveness and stability of the permanent magnet synchronous motor operation, it is necessary to pay more attention to and study all aspects, and the heat

dissipation of the motor is a key issue that needs to be paid attention to; in the case of ideal heat dissipation of the motor, its operation can be better guaranteed. An efficient and reliable cooling system is used to quickly transfer the heat generated during the operation of the motor to the outside, which is of great significance to the life, efficiency, and operational safety of the motor [4].

2. Literature Review

With the country's vigorous development of electric vehicles, under the current background, permanent magnet synchronous motors are widely used in electric vehicles due to their small size and high power density; however, due to their high loss density and relatively closed working environment, the internal temperature is often rising too high; in severe cases, the stator insulation will fail, the permanent magnet material will be demagnetized, and the operating performance, efficiency, and life of the drive motor will be affected [5]. Therefore, a reasonable heat dissipation structure designed to control the temperature rise of the heating components of the drive motor within a safe range seems particularly important. Most modern motors use higher electromagnetic loads, so it is necessary to effectively analyze the temperature field of the motor, and on this basis, research methods to reduce motor losses and improve motor cooling are needed; in the current actual operation and application of permanent magnet synchronous motors, solving the heat dissipation problem of the motor has always been a key task, and it is also an important way and method to improve the efficiency and effectiveness of the motor. In order to effectively solve the problem of heat dissipation of permanent magnet synchronous motor, relevant researchers are required to simulate and analyze the heat dissipation of permanent magnet synchronous motor, carry out reasonable optimization according to the simulation analysis results, and carry out scientific and reasonable design for all aspects, thereby, the heat dissipation of the permanent magnet synchronous motor can achieve satisfactory results, and on this basis, the effective operation of the permanent magnet synchronous motor can be realized. We cause the motor temperature to rise further and form a vicious circle, which will seriously affect the life of the motor and the safety of the motor operation; an efficient cooling system is an important basis for restraining motor temperature rise, improving motor operation stability, and prolonging motor life [6].

In response to the abovementioned problems, the author proposed the application of nanofluids in the heat dissipation of permanent magnet synchronous motors [7]. The main content of this technology is based on the characteristics and applications of nanofluids, according to the experimental system, the preparation of nanofluids, and the determination of experimental parameters; finally, by studying the influence of ultrasonic oscillation time and dispersant on the stability of nanofluids, it is concluded that the improvement of the thermal conductivity of nanofluids contributes to the improvement of the heat transfer rate of nanofluids. It mainly analyzes and discusses the heat dissipation simulation of permanent magnet synchronous motor and realizes the optimization of heat dissipation simulation analysis from various aspects, so that the research on motor heat dissipation can obtain more ideal results and achieve the better application of permanent magnet synchronous motors [8].

3. Research Methods

3.1. Nanofluid Research

3.1.1. Characteristics and Applications of Nanofluids.
Nanofluid is a new type of heat transfer working fluid with uniform, stable, and high thermal conductivity formed by adding nanoparticles to liquid in a certain way and proportion. Since the concept of nanofluids was proposed by Argonne National Laboratory in the United States in 1995, the research on nanofluids has gradually become a research hotspot in chemical engineering, metallurgy, electronics, materials science, and other disciplines.

In the past ten years of research, it has been found that nanofluids have better thermal properties than ordinary fluids, and their potential advantages are mainly in the following aspects: ① The high heat transfer surface greatly promotes the heat transfer between the nanoparticles and the fluid; ② due to the significant Brownian motion of the nanoparticles, the nanofluid has good dispersion stability, and the sedimentation of the particles is smaller than that of the general large particles, two-phase fluid is stable; ③ the miniaturization of the equipment reduces the flow rate and operating cost of traditional fluids; ④ compared with pure fluids, under the same heat transfer intensity, nanofluids containing few nanoparticles can improve the fluid thermal conductivity and greatly reduce the pumping power; and ⑤ compared with the traditional two-phase fluid with large particles, the agglomeration tendency of particles is greatly reduced, and it can be used as a cooling fluid for microchannels [9].

Due to the abovementioned advantages of nanofluids, nanofluids are widely used in industrial production, such as in construction machinery and transportation industry engines that have a strong demand for improved cooling technology; microelectromechanical systems; heating, ventilation, and air conditioning systems [10]. In addition, it can be used in heat storage equipment, transformers, nuclear fuel reactors, etc.

3.1.2. Nanofluidic Experimental System.
According to the experimental content, the authors divided it into a nanofluid stability experimental system and a nanofluid convective heat transfer system [11].

(1) In the nanofluid stability experimental system, the author uses a combination of visual inspection and transmittance to evaluate the stability of nanofluids, and the experimental phenomenon and experimental data are verified each other, the main experimental system is a 721–100 visible spectrophotometer with
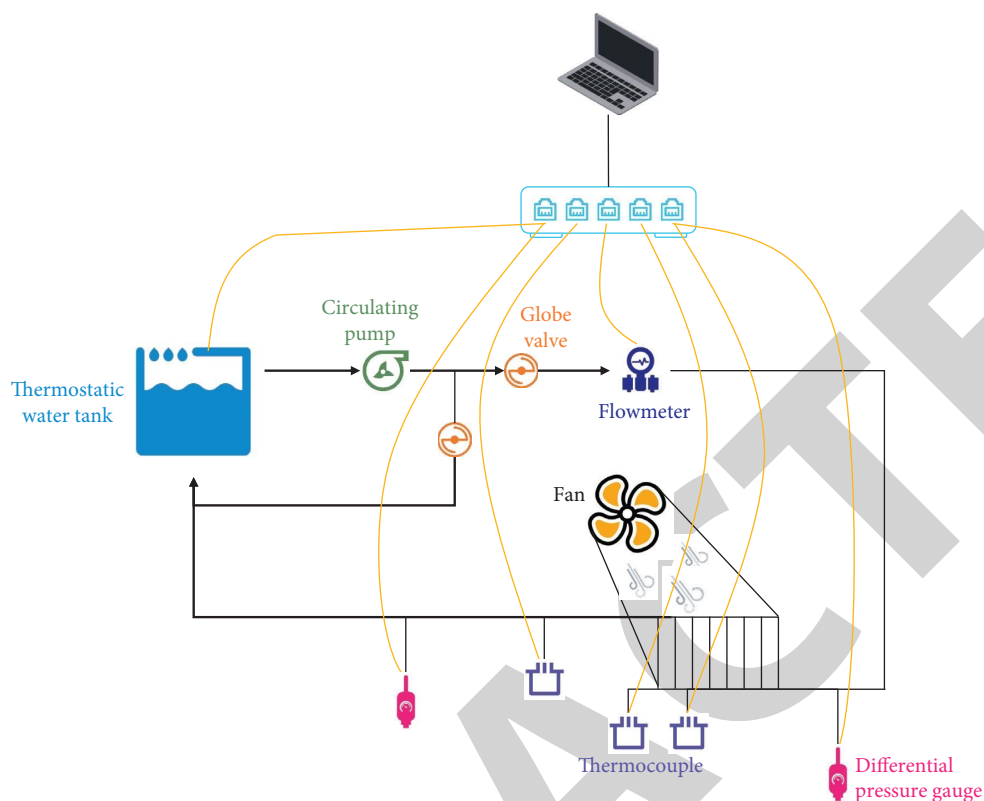
FIGURE 1: Experimental system.

accurate wavelengths, degree ±2 nm, transmittance accuracy ±1% T, stability ≤ ± 0.004 A/h [12].

(2) In the nanofluid convective heat transfer system, the experimental system is shown in Figure 1, which is divided into a working fluid circulation system, data acquisition system, constant temperature heating system, and cooling and heat dissipation system. After the nanofluid is heated to the temperature required for the experiment in the constant temperature tank, it enters the car radiator for cooling through the driving force of the circulating pump, and the cooled nanofluid re-enters the constant temperature tank for heating, thus completing the entire loop [13].

Among them, the constant temperature tank is a cylindrical glass tank with a diameter of 300 mm and a height of 490 mm, which is equipped with a 1.5 kW electric heater and is controlled and adjusted by PID. A globe valve is installed after the circulating pump to adjust the flow rate of the entire system. The cooling system is composed of a car radiator and a fan with a length of 548 mm ±2 mm and a height of 380 mm ±2 mm, inside the radiator are 54 equally spaced flat tubes separated by fins. On the opposite side of the radiator, the fan runs at constant power and the wind speed is 3 m/s. Six K-shaped thermocouples are set on the surface of the radiator to measure the surface temperature of the radiator, and one thermocouple is set at the inlet and outlet to measure the temperature at the inlet and outlet; we set up a flow meter, a Rosemount differential pressure gauge,

and a power meter in the circulation pipeline to measure the corresponding flow, differential pressure, and effective pump work, respectively. Among them are the K-type thermocouple output temperature signal, flowmeter, and Rosemount differential pressure meter output current signal [14]. These signals are collected by the data collector, processed, and fed back by the computer, and the power meter can directly read the value.

3.1.3. Preparation of Nanofluids and Determination of Experimental Parameters. MWCNT nanoparticles with different volume fractions were dispersed in an 80% water-20% ethylene glycol mixed solution [15]. The selected dispersants are sodium dodecyl benzene sulfonate (SDBS) and cetyltrimethyl ammonium chloride (CTAC); the two dispersants will have different stabilities of nanofluids due to their different properties. The author aims to prepare nanofluids with better stability; therefore, it is necessary to verify the stability of the two dispersants to nanofluids through experiments, so as to select the dispersants with better stability to nanofluids [16]. The nanoparticles and dispersant are mixed well in the base liquid and then shaken in an ultrasonic shaker. The volume fractions of nanoparticles used in the experiments were 0.05%, 0.1%, 0.15%, 0.3%, and 0.5%. The volume fraction of the nanofluid is calculated according to formula (1).

$$\varphi = \frac{1}{(100/\phi_{wt})(\rho_p/\rho_{nf})}. \tag{1}$$

The thermophysical properties of 80%:20% ethylene glycol aqueous solution at different temperatures were obtained, and the thermophysical properties of MWCNT nanoparticles were obtained according to the manufacturer. The SNB-3 digital rotational viscometer was used to measure the viscosity of the nanofluid and base fluid, and the DRE-III thermal conductivity meter was used to measure the thermal conductivity; comparing the measurement results with the relevant calculation formulas of solid-liquid two-phase flow, the error between the two is less than 5%, as mentioned in formulas (2)–(5).

$$\rho_{nf} = \varphi\rho_p + (1 - \varphi)\rho_{bf}, \tag{2}$$

$$c_{p,nf} = 1 - \varphi\frac{\rho_{bf}}{\rho_{nf}}c_{p,bf} + \varphi\frac{\rho_p}{\rho_{nf}}c_{p,p}, \tag{3}$$

$$k_{nf} = \frac{k_p + (\phi - 1)k_{bf} - \varphi(\phi - 1)\left(k_{bf} - k_p\right)}{k_p + (\phi - 1)k_{bf} + \varphi\left(k_{bf} - k_p\right)}k_{bf}, \tag{4}$$

$$\mu_{nf} = \mu_{bf}(1 + 2.5\varphi), \tag{5}$$

where φ is the shape factor, calculated from $\varphi = 3/\psi$, and ψ is the sphericity of the nanoparticle surface area (sphere, $\psi = 1.0$; rod, $\psi = 0.6$). In the text, if ψ is taken as 0.6, then φ is equal to 5.

Because the transmittance of the nanofluid measured at the optimal absorption wavelength can more accurately reflect the stability of the nanofluid, therefore, the optimal absorption wavelength of the MWCNT nanofluid should be measured first, and then, the stability of the nanofluid should be evaluated according to the change of transmittance in different time periods [17]. The method of testing the optimal absorption wavelength of nanofluid is as follows: The wavelength of the prepared MWCNT-water/ethylene glycol mixed-based nanofluid with a volume fraction of 0.15% is scanned with a spectrophotometer, the optimal absorption wavelength is selected by comparing the transmittance changes at different wavelengths, that is, the nanofluid absorbs more light at the optimal absorption wavelength, the transmission ratio is small, so the optimal absorption wavelength should appear at the position where the transmittance is in the trough, as shown in Figure 2. As can be seen from Figure 2, the optimal absorption wavelength of MWCNT-water/ethylene glycol mixed-based nanofluid is concentrated at 240 nm. In order to verify the reliability of the experiment, multiple wavelength scans were performed on the MWCNT-water/ethylene glycol mixed-based nanofluid with a volume fraction of 0.15%.

In the convective heat transfer experiment, under the control of PID, the nanofluid was heated to 45°C, 55°C, and 65°C in a constant temperature tank, and under the driving force of the circulating pump, we adjust the shut-off valve to make the nanofluid circulate in the whole system at 2 L/min, 4 L/min, and 6 L/min, respectively [18]. The fan runs with a certain constant power and the wind speed is kept at 3 m/s. The different fluid temperatures represent the engine operating at different powers, and the fluid temperature and
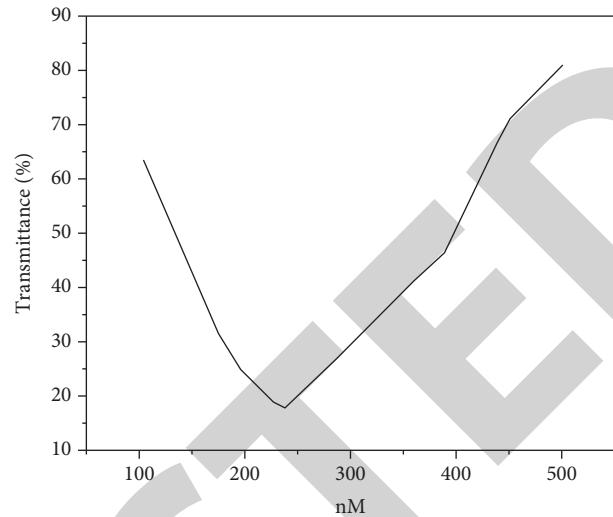
Figure 2: Wavelength scanning results of nanofluids.

flow rates were varied to better simulate engine conditions operating under real-world conditions.

When the nanofluid is heated to the temperature required by the experiment in the constant temperature tank, the circulating pump is turned on to make the nanofluid circulate through the radiator of the car and circulate in the whole system, and the flow required for the experiment can be obtained by adjusting the shut-off valve. After the whole system is stable, the surface temperature signals of 6 thermocouples, the temperature signals of 2 inlets and outlets, and the current signals of pressure difference and flow rate are recorded by the data collector, and the change of the power indicator of the power meter is recorded in real-time [19].

3.2. Nanofluid Stability Experiment

3.2.1. The Effect of Ultrasonic Oscillation Time on the Stability of Nanofluids. The MWCNT-water/ethylene glycol mixed-based nanofluid with a volume fraction of 0.15% was prepared by the "two-step method" for the ultrasonic oscillation experiment. In order to distinguish the influence of ultrasonic time on stability, the oscillation time was changed from 0 to 2 h and the interval was 30 min. However, after 3 days, the nanofluid in several test tubes showed great changes, which were 0 h, 0.5 h, 1 h, 1.5 h, and 2 h, respectively. The color of the nanofluid in the test tube has been different, and the nanofluid in the test tube at 0 h has an obvious layering phenomenon, and the state of the supernatant liquid and the lower turbid liquid appears. The nanofluid layering phenomenon in the test tube after shaking for 30 min is not obvious, but a little flocculation phenomenon can be seen. The nanofluid in the test tube after shaking for 1 h and 1.5 h still maintains good dispersion, and further experimental analysis is required. A little layering phenomenon has also appeared in the test tube after shaking for 2 hours, and a little flocculent material floats. The phenomenon shows that ultrasonic oscillation can
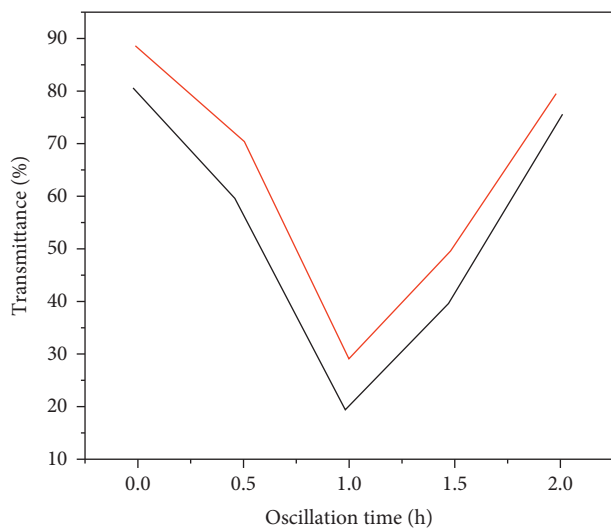
Figure 3: Variation of transmittance of nanofluids with oscillation time.

Figure 4: Stability of nanofluids in the addition of SDBS.

effectively improve the stability of nanofluids, and the effect on the stability of nanofluids varies with the oscillation time, it is not that the longer the oscillation time, the better [20].

In order to determine the oscillation time of the ultrasonic wave, the transmittance experiment was carried out on the nanofluid after oscillating for different times; by comparing the change of transmittance, the quantitative analysis could be more intuitive, and the transmittance experiment was performed again after 72 hours; the results are shown in Figure 3; with the increase of the oscillation time, the transmittance of the nanofluid shows a trend of first decreasing and then increasing; it is in a trough at 1 h, and the transmittance is the smallest, which means that the stability of the nanofluid is the best; the author chose the oscillation time of ultrasonic oscillation as 1 h. In addition, the transmittance of the just-prepared nanofluid is generally lower than that of the nanofluid after 72 hours, indicating that the stability of the just-prepared nanofluid is better; with the increase of time, the stability will be weakened, the conclusion is in line with people's general cognition [21].

3.2.2. Effects of Dispersants on the Stability of Nanofluids. In order to select a dispersant with better stability to nanofluids and appropriate dosage, a 0.15% MWCNT-water/ethylene glycol mixed-based nanofluid was prepared, and sodium dodecyl benzene sulfonate (SDBS) and hexadecane were added, respectively; cetyltrimethyl ammonium chloride (CTAC) was used as a surface dispersant, and the addition amount was increased from 0 to 0.14% by a mass fraction with an interval of 0.02%. The experimental results are shown in Figures 4 and 5.

4. Analysis of Results

Different volume fractions of nanofluids have different effects on convective heat transfer. The convective heat transfer effect of nanofluids with different volume fractions

— Standstill 0h
— Let stand for 12h
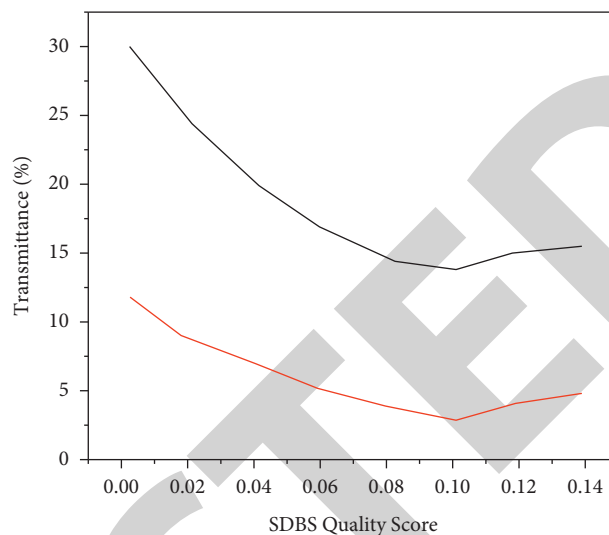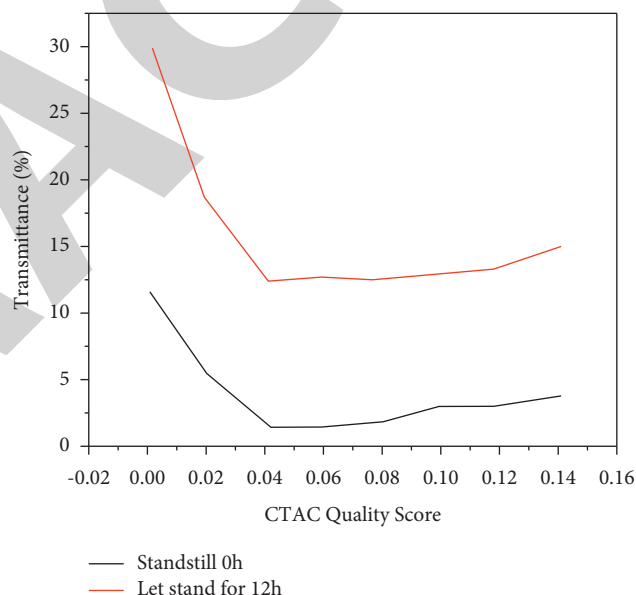
Figure 5: Stability of nanofluids in addition of CTAC.

at different flow rates was tested under constant temperature. The Nusselt number increases with the nanoparticle volume fraction and flow rate, which means that increasing the nanoparticle concentration can effectively increase the heat transfer rate [22, 23].

The improvement of the thermal conductivity of nanofluids contributes to the improvement of the heat transfer rate of nanofluids. Table 1 shows the increased rate of thermal conductivity and convective heat transfer coefficient of nanofluids (relative to the base fluid at 45°C, 2 L/min) when the volume fraction is 0.5, the thermal conductivity increase rate is 1.51, and the convective heat transfer coefficient increases rate 20.33. It can be seen that the increase rate of the convective heat transfer coefficient is greater than that of the thermal conductivity, which indicates that the improvement of the heat transfer ability of the

TABLE 1: Comparison of increases in thermal conductivity and convective heat transfer coefficients of nanofluids.

Volume fraction/%	Thermal conductivity increase rate/%	Convective heat transfer coefficient increase rate/%
0.05	0.15	5.64
0.10	0.30	8.53
0.15	0.45	10.13
0.30	0.90	17.14
0.50	1.51	20.33

nanofluid not only depends on the optimization of the thermal conductivity but also the small size effect of the nanoparticles has a significant effect, effects, such as smaller nanoparticles leading to more collisions inside the nanofluid, microconvection, etc., all help to enhance heat transfer [24, 25].

5. Conclusion

The characteristics and applications of nanofluids, according to the experimental system, determine the preparation and experimental parameters of nanofluids; finally, by studying the influence of ultrasonic oscillation time and dispersant on the stability of nanofluids, it is concluded that the improvement of the thermal conductivity of nanofluids contributes to the improvement of the heat transfer rate of nanofluids. Finally, it is proved that the technical research of nanofluid can meet the heat dissipation demand of permanent magnet synchronous motor. Thus, it is ensured that the permanent magnet synchronous motor always works at a suitable temperature, which is of great significance to the life, efficiency, and operational safety of the permanent magnet synchronous motor.

Data Availability

The data used to support the findings of this study are available from the corresponding author upon request.

Conflicts of Interest

The authors declare that they have no conflicts of interest.

References

[1] J. Qu, J. Jatskevich, C. Zhang, and S. Zhang, "Torque ripple reduction method for permanent magnet synchronous machine drives with novel harmonic current control," *IEEE Transactions on Energy Conversion*, vol. 36, p. 1, 2021.

[2] Y. Tang, X. He, and J. Cao, "Fast calculation method of transient temperature rise of motor for electro-mechanical braking," *Science Progress*, vol. 104, no. 2, pp. 19–25, 2021.

[3] Z. Zheng, J. Dai, Y. Zhang, H. Wang, and C. Chen, "Enhanced heat dissipation of phosphor film in wleds by aln-coated sapphire plate," *IEEE Transactions on Electron Devices*, vol. 67, pp. 1–6, 2020.

[4] N. Mei, X. Xu, and R. Li, "Heat dissipation analysis on the liquid cooling system coupled with a flat heat pipe of a lithium-ion battery," *ACS Omega*, vol. 5, no. 28, pp. 17431–17441, 2020.

[5] S. Espinoza, A. Poulos, H. Rudnick, J. Llera, and P. Mancarella, "Risk and resilience assessment with component criticality ranking of electric power systems subject to earthquakes," *IEEE Systems Journal*, vol. 14, pp. 1–12, 2020.

[6] Z. Liu, C. Zang, S. Zhang et al., "Atmospheric drying preparation and microstructure characterization of fly ash aerogel thermal insulation material with superhydrophobic," *Construction and Building Materials*, vol. 303, no. 17, Article ID 124425, 2021.

[7] M. R. Eid and F. Mabood, "Thermal analysis of higher-order chemical reactive viscoelastic nanofluids flow in porous media via stretching surface," *Proceedings of the Institution of Mechanical Engineers - Part C: Journal of Mechanical Engineering Science*, vol. 235, no. 22, pp. 6099–6110, 2021.

[8] C. Yang, J. Li, and J. Cao, "Simulation research on heat dissipation of the inner tank of household electric cooker based on fluent," *IOP Conference Series: earth and Environmental Science*, vol. 714, no. 4, Article ID 042002, 2021.

[9] J. Wu, B. Ma, I. Stanciulescu, H. Li, and L. Wang, "Experimental investigation of friction disc temperature field under cooling fluid," *Proceedings of the Institution of Mechanical Engineers - Part C: Journal of Mechanical Engineering Science*, vol. 235, no. 17, pp. 3377–3388, 2021.

[10] L. Kang, G. Wang, Y. Wang, and Q. An, "The power simulation of water-cooled central air-conditioning system based on demand response," *IEEE Access*, vol. 8, p. 1, 2020.

[11] R. Al-Sayagh, "Control of the free convective heat transfer using a u-shaped obstacle in an al2o3-water nanofluid filled cubic cavity," *International Journal of Advanced and Applied Sciences*, vol. 8, no. 7, pp. 23–30, 2021.

[12] R. A. Farade, N. Wahab, D. Mansour, N. B. Azis, and A. S. Murthy, "Investigation of the effect of sonication time on dispersion stability, dielectric properties, and heat transfer of graphene based green nanofluids," *IEEE Access*, vol. 9, p. 1, 2021.

[13] N. Zeidi, S. Kaziz, M. H. Said, L. Rufer, A. Cavallini, and F. Tounsi, "Partial discharge detection with on-chip spiral inductor as a loop antenna," *Review of Scientific Instruments*, vol. 92, no. 9, Article ID 094701, 2021.

[14] G. Ge and J. Liu, "The stationary response of piezoelectric cantilever beam model excited by colored noise," *Journal of Vibroengineering*, vol. 24, no. 1, pp. 190–202, 2021.

[15] J. D. Singh and G. Senthilkumar, "Measurement of volume fraction of air in water: experimental study," *IOP Conference Series: materials Science and Engineering*, vol. 1197, no. 1, Article ID 012031, 2021.

[16] Ç. Yağcı and Y. Duman, "Dispersant effect of degraded cellulase and sds on copper(ii) phthalocyanine pigment," *Biocatalysis and Biotransformation*, vol. 39, no. 4, pp. 313–321, 2021.

[17] A. Durán-Viseras, C. Sánchez-Porro, and A. Ventosa, "Natronomonas salsuginis sp. nov. a new inhabitant of a marine solar saltern," *Microorganisms*, vol. 8, no. 4, p. 605, 2020.

[18] L. Lv, D. Ye, J. Chen et al., "Circulating phosphorus concentration and risk of prostate cancer: a mendelian

Retraction

Retracted: Enhanced Performance of Sn@Pt Core-Shell Nanocatalysts Supported on Two Different Carbon Structures for the Hydrogen Oxidation Reaction in Acid Media

Journal of Chemistry

This article has been retracted by Hindawi following an investigation undertaken by the publisher [1]. This investigation has uncovered evidence of one or more of the following indicators of systematic manipulation of the publication process:

(1) Discrepancies in scope

(2) Discrepancies in the description of the research reported

(3) Discrepancies between the availability of data and the research described

(4) Inappropriate citations

(5) Incoherent, meaningless and/or irrelevant content included in the article

(6) Manipulated or compromised peer review

The presence of these indicators undermines our confidence in the integrity of the article's content and we cannot, therefore, vouch for its reliability. Please note that this notice is intended solely to alert readers that the content of this article is unreliable. We have not investigated whether authors were aware of or involved in the systematic manipulation of the publication process.

Wiley and Hindawi regrets that the usual quality checks did not identify these issues before publication and have since put additional measures in place to safeguard research integrity.

We wish to credit our own Research Integrity and Research Publishing teams and anonymous and named external researchers and research integrity experts for contributing to this investigation.

The corresponding author, as the representative of all authors, has been given the opportunity to register their agreement or disagreement to this retraction. We have kept a record of any response received.

References

[1] F. J. Rodríguez-Varela, G. Hernández-Vázquez, S. Dessources et al., "Enhanced Performance of Sn@Pt Core-Shell Nanocatalysts Supported on Two Different Carbon Structures for the Hydrogen Oxidation Reaction in Acid Media," *Journal of Chemistry*, vol. 2022, Article ID 2982594, 12 pages, 2022.

Research Article

Enhanced Performance of Sn@Pt Core-Shell Nanocatalysts Supported on Two Different Carbon Structures for the Hydrogen Oxidation Reaction in Acid Media

F. J. Rodríguez-Varela [1], **G. Hernández-Vázquez,**[1] **S. Dessources,**[2] **B. Escobar-Morales,**[3] **Aruna K. Kunhiraman** [4] **M. A. Garcia-Lobato** [5] **and I. L. Alonso-Lemus** [6]

[1]*Sustentabilidad de Los Recursos Naturales y Energía, Cinvestav Unidad Saltillo, Av. Industria Metalúrgica 1062, Parque Industrial Saltillo-Ramos Arizpe, C. P., 25900 Ramos Arizpe, Coah, Mexico*
[2]*Laboratoire des Sciences pour l'Environnement et l'Énergie (LS2E), École Normale Supérieure, Port-au-Prince, Haiti*
[3]*CONACyT, Centro de Investigación Científica de Yucatán, Km. 5.5 Carr. Sierra Papacal-Chuburná Puerto, Tablaje 31257, Sierra Papacal, Yucatán 97302, Mexico*
[4]*Rathinam Research Center, Rathinam Technical Campus, Coimbatore 641021, Tamilnadu, India*
[5]*Facultad de Ciencias Químicas, Universidad Autónoma de Coahuila, C. P., 25280 Saltillo, Coahuila, Mexico*
[6]*CONACyT, Sustentabilidad de los Recursos Naturales y Energía, Cinvestav Unidad Saltillo, Ramos Arizpe, Mexico*

Correspondence should be addressed to F. J. Rodríguez-Varela; javier.varela@cinvestav.edu.mx

Sn@Pt core-shell nanocatalysts, supported on Vulcan XC-72 and home-developed nitrogen-doped graphene (Sn@Pt/C and Sn@Pt/NG, respectively), were evaluated for the hydrogen oxidation reaction (HOR) in acid electrolyte. The nanocatalysts were synthesized by the bromide anion exchange (BAE) method. TEM characterization confirmed the nanosize nature of Sn@Pt/C and Sn@Pt/NG, with an average particle size of 2.1 and 2.3 nm, respectively. Sn@Pt/C delivered a similar mass limiting current density ($j_{l, m}$) of the HOR compared to Sn@Pt/NG, which was higher than those of Pt/C and Pt/NG (ca. 2 and 2.3-fold increase, respectively). Moreover, the Sn@Pt/C and Sn@Pt/NG core-shell nanocatalysts demonstrated a higher specific activity related to Pt/C and Pt/NG. Mass and specific Tafel slopes further demonstrated the improved catalytic activity of Sn@Pt/C for the HOR, followed by Sn@Pt/NG. The application of the nanocatalysts was proposed for polymer electrolyte membrane fuel cells (PEMFC).

1. Introduction

PEMFC have reached important niche energy markets over the past years, such as the automotive industry, stationary power applications, and the so-called poly-generation systems [1, 2]. PEMFC have relevant advantages over conventional systems based on fossil fuels, including the fact that the use of hydrogen (H_2) as the fuel leads to green electrochemical conversion devices [3], in addition to higher energy conversion efficiencies, and zero or very low greenhouse gases (GHG) emissions [1]. Moreover, the concept of green H_2 has gained a great deal of attention recently [4, 5]. On this matter, the feasibility of taking

advantage of green H_2 produced by low-temperature electrolyzers using it in PEMFC is highly relevant, because of the prospective of reaching a carbon-neutral international energy scenario.

Despite these advantages, it is acknowledged that the cost of PEMFC systems must be reduced, aiming to be more successful in reaching broader markets [2, 6]. Some breakdown studies indicate that catalysts may account for 41% of the total cost of a fuel cell stack on the basis of 500,000 units produced per year [7]. Thus, strategies to reduce the amount of Pt-group metal (PGM) catalysts in PEMFC have been implemented.

Among those approaches, the development of alloyed, metal-metal oxide, and core-shell Pt-based nanocatalysts

have demonstrated their effectiveness in reducing the amount of this noble metal, maintaining a high catalytic activity for the hydrogen oxidation reaction (HOR) and oxygen reduction reactions (ORR) at the anode and cathode of PEMFC, respectively. Core-shell nanostructures have unique properties, which are of interest for high-performance PEMFC: (i) the modification of the electronic structure of Pt by the core material, which in turn increases the catalytic activity of the nanostructures by changing the adsorption energy of species; (ii) improved electrochemical stability; and (iii) high Pt utilization because of its exposure to active species being the outermost layer [8, 9].

Pt-based core-shell nanocatalysts have probed a high catalytic activity for the ORR in acid media, employing plurimetallic, monometallic, or metal oxides cores such as Pd_3Cu_1, Ni, Ir, Co_3O_4, and $Pd_1Ir_1Ni_2$, among others [8–12]. To the best of our knowledge, the assessment of catalytic activity of Pt-based core-shell nanocatalysts for the HOR in acid media is scarce. Wang et al., report the high performance of Ru@Pt core-shell nanocatalysts with ultra-low Pt content for the HOR in acid media, having a 1 : 1 Ru : Pt atomic ratio [13]. Adzic et al. demonstrate a 2-fold enhancement in catalytic activity for the HOR of Ru@Pt core-shell nanoparticles, compared to Pt-Ru alloys. In that study, the Ru@Pt core-shell having a Pt shell thickness of two monolayers shows an increase in specific activity of the HOR by a factor of 1, compared to monometallic Pt [14].

Elsewhere, several Pt-based core-shell nanostructures having Ru, Rh, or Au as the core have shown a high performance for the HOR, however in alkaline media [15–18]. Nevertheless, the advantages of using supported metal@Pt core-shell nanostructures with a lower Pt content compared to monometallic Pt/C, yet sustaining high performance, encourages the research on those nanocatalysts for the HOR in acid media. On this matter, Sn is an element widely used as cocatalyst of Pt for fuel cell reactions. Because of its higher oxophilicity compared to Pt (0.4 vs. 0.1, respectively) [19], it forms adsorbed OH-species at more negative potentials, transferring them to Pt-sites, facilitating the electrochemical reaction taking place at the noble metal (bifunctional mechanism) [20].

Sn is also significantly cheaper than Pt [21], which results in lower cost Sn@Pt nanocatalysts, also compared to Pt/C. One of the most widely studied applications of Sn as cocatalysts is that for the ethanol oxidation reaction (EOR) at Pt-Sn/C alloys, improving the performance of monometallic Pt/C nanocatalysts through the already mentioned bifunctional mechanism and the electronic effect [22, 23]. Sn has been successfully used in the synthesis of intermetallic, random-alloy, and core-shell Pt-based nanocatalysts [24, 25].

Precisely, one of the most effective methods of synthesis of noble metal nanocatalysts is the bromide anion exchange (BAE) process. Early reports highlight the advantages of implementing this surfactant-free method, which include the following: (i) avoiding the presence of organic molecules that may prevent the adsorption of active species at the metal sites of the nanocatalysts; (ii) controlling the particle size growth, enhancing the electrochemically active surface area

(ECSA); and (iii) being a suitable and straightforward, environmentally friendly method [26–28].

In this work, Sn@Pt/C and Sn@Pt/NG nanocatalysts (where *C*: commercial Vulcan XC-72 and NG: home-synthesized *N*-doped graphene) have been synthesized by the BAE method. Their catalytic activity for the HOR is characterized by acid electrolyte and compared to that of monometallic Pt/C and Pt/NG.

2. Experimental

2.1. Heat Treatment of Vulcan XC-72 and Synthesis of Nitrogen-Doped Graphene (NG). Vulcan powders were heat treated at 400°C for 4 h in N_2 atmosphere, aiming to eliminate surface impurities [29]. NG was obtained by mixing graphite flakes and urea in a 10 : 90 wt. ratio. The mixture was submitted to ball milling using a Restch PM 200 apparatus in a balls : material weight ratio of 5 : 1, at 300 rpm for 8 h, pausing for 30 min after every hour of milling. The resulting material was passivated in N_2 for 12 h, followed by pyrolysis at 500°C in N_2 atmosphere for 1 h.

2.2. Synthesis of Core-Shell Nanocatalysts by the Bromide Anion Exchange (BAE) Method. KBr and $NaBH_4$ were used as solvents and reducing agents, respectively, [30]. Nominally, a metal : carbon weight ratio of 20 : 80 was expected for the core-shell nanostructures, with a theoretical Pt : Sn atomic ratio of 1 : 1. As an example, for the synthesis of Sn@Pt/C, in the first step Sn/C was synthesized as follows: 21.57 mg of $SnCl_6 \cdot 2H_2O$ were stirred in 95.6 mL deionized water for 5 min, followed by the addition of 16.6 mg of KBr maintaining agitation for 10 min ($n_{KBr}/n_{metallic\ salt}$ ratio = 1.46). A solution containing 120 mg of *C* was adjusted to the mixture, which was submitted to ultrasound for 45 min. Afterward, 14.3 mL of a 0.1 M $NaBH_4$ solution was added ($n_{NaBH4}/n_{metallic\ salt}$ ratio = 15), applying magnetic stirring at 40°C for 2 h. The obtained powders were filtered, washed with deionized water, and dried at 50°C for 12 h.

In a second step, the Pt shell was deposited on the core material by stirring 48.2 mg of $H_2PtCl_6 \cdot 6H_2O$ in 92.9 mL of deionized water for 5 min, with the subsequent addition of 16.15 mg of KBr keeping agitation for 20 min ($n_{KBr}/n_{metallic\ salt}$ ratio = 1.46). To this mixture, 128 mg of Sn/C were adjusted, followed by ultrasound agitation for 45 min. Then, 13.9 mL of 0.1 M $NaBH_4$ were added by applying magnetic stirring at 40°C for 2 h ($n_{NaBH4}/n_{metallic\ salt}$ ratio = 15). The powders were filtrated, washed with deionized water, and dried at 50°C for 12 h. Sn@Pt/NG, Pt/C, and Pt/NG were obtained following the same procedure.

2.3. Physicochemical and Electrochemical Characterization. Details of the physiochemical and electrochemical characterization were reported previously [31–34]. Briefly, textural properties of the supports were obtained in a Quantachrome Instruments Autosorb1 analyzer. XRD patterns were acquired in a Bruker D2 Phaser apparatus in the 2θ interval from 10 to 100°. Crystallite size was determined using the following Scherrer equation:

$$d = \frac{k \cdot \lambda}{B \cdot \cos(\theta)}, \tag{1}$$

where $k = 0.9$, λ is the wavelength of the X-rays (0.1541 nm), B is the full width at half height of the reflection, and θ is the peak maximum of the reflection. The lattice parameter a_{fcc} was calculated from the following equation:

$$a_{fcc} = \frac{\sqrt{2} \cdot \lambda}{\sin(\theta)}. \tag{2}$$

The chemical composition reported is the average of 5 micro areas analyzed by EDS in a Philips XL30 SEM microscope. Characterization by TEM was performed in a Jeol 2100 microscope, operating at 200 kV. XPS analysis was carried out using a Thermo Scientific K-Alpha + XPS apparatus (hv = 1486.68 eV).

A three-electrodes setup was used for electrochemical characterization in 0.5 M H_2SO_4, using a WaveDriver 20 bipotentiostat equipped with a rotating disc electrode setup (Pine Inst.). The reference electrode was an Ag/AgCl (saturated KCl), while the counter was a Pt coil, both placed in separated chambers from the main electrolyte. The working electrode was a 5 mm diam glassy carbon. Catalyst inks were prepared by dispersing for 30 min in ultrasound 5 μL Nafion® solution, 1 mL 2-propanol, and 10 mg of nanocatalyst powder. Aliquots of 10 μL were deposited on the glassy carbon. All potentials were reported on the RHE scale.

Cyclic voltammograms (CV) were acquired in the 0.05–1.2 V vs. RHE interval at 20 mV·s^{-1} in N_2 atmosphere. The electrochemically active surface area (ECSA$_H$) and the real area (A_r) were determined to take the charge due to the desorption of hydrogen in the hydrogen adsorption/desorption region ($H_{ads/des}$) of the CV, according to the following equations:

$$\text{ECSA}_H = \frac{Q}{Q_{H \cdot L_{Pt}}},$$
$$A_r = \frac{Q}{Q_H}. \tag{3}$$

where Q is the experimental electrical charge due to the desorption of hydrogen; Q_H is the theoretical charge due to the desorption of one monolayer of hydrogen on Pt (210 μC·cm^{-2}); and L_{Pt} is the Pt loading on the electrode.

Accelerated degradation tests (ADT) were performed on the nanocatalysts by submitting them to 1000 cycles in the same potential interval indicated above, at a scan rate of 200 mV·s^{-1}. CO-stripping polarization curves were obtained by bubbling CO for 10 min, while polarizing the working electrode at 0.05 V vs. RHE, then purging it by flowing N_2 in the electrolyte for 20 min. CV was acquired in the same mentioned potential window at 20 mV·s^{-1}.

The catalytic activity of the nanocatalysts for the HOR was evaluated in a rotating disc setup. H_2 was bubbled in the acid electrolyte for 20 min, after which polarization curves were plotted at rotation rates ω of 400, 800, 1200, 1600, and 2000 rpm, in the 0–0.65 V vs. RHE range. Curves compensated for iR drop were reported in this work. The R value

of the 0.5 M H_2SO_4 was determined from EIS measurements. Koutecky–Levich plots were obtained using the well-known Levich equation as follows:

$$\frac{1}{j} = \frac{1}{j_k} + \frac{1}{j_d}, \tag{4}$$

where j_d, j_k, and j are the diffusion-controlled, kinetic, and measured current density, respectively. The kinetic current i_k was obtained with the following equation:

$$i_k = \frac{i_d \cdot i}{i_d - i}, \tag{5}$$

where i_d and i are the diffusion-controlled and measured current, respectively. From equation (5), mass and specific Tafel plots were obtained by normalizing i_k by the Pt mass content and A_r, respectively.

3. Results and Discussion

Figure 1 shows the XRD patterns of the nanocatalysts. Pt/C has reflections ascribed to (002) due to the graphitic zones in the structure of Vulcan, and the (111), (200), (220), (311), and (222) planes of the fcc structure of Pt (PDF 00-004-0802). Sn@Pt/C shows the same peaks, with similar features. Moreover, no noticeable shift in the position of the peaks between the monometallic and the core-shell nanocatalysts has been observed. Such characteristic suggests that no atoms of the Sn core have incorporated into the Pt shell contracting it and provoking the formation of alloyed phases, as has been reported elsewhere for some other core-shell nanostructures [35, 36]. Additionally, the broadness of the reflections suggests the nanosized feature of the anode materials.

Meanwhile, Pt/NG and Sn@Pt/NG have an intense reflection due to the (002) plane characteristic of graphene-like structures, as well as the (101) and (004) peaks also ascribed to the support [37]. Moreover, both nanocatalysts show the peaks attributed to fcc Pt, also without a noticeable shift in their position.

Figure S1 in the supplementary information file shows the XRD patterns of the graphite flakes, NG, and Vulcan. The first two have high-intensity and low-intensity very narrow peaks at $2\theta = 26.5$ and 54.54°, attributed to the (002) and (004) carbon planes, characteristic of graphitic materials, respectively. These characteristics support the observations in the previous paragraph of the patterns shown in Figure 1. Vulcan shows broader peaks due to the (002) and (101) reflections of carbon at $2\theta = 25$ and 44.39°, respectively. The position of the (002) plane in Vulcan correlates well with previous reports in the literature [38]. Overall, graphite and NG show crystalline features, while Vulcan is rather amorphous in nature.

Features of the nanocatalysts from Figure 1 are shown in Table 1. The crystallite size (d_{XRD}) ranges from 3.4 to 6.1 nm, the smallest one being that of Sn@Pt/C, while the nanocatalysts supported on NG have larger values. Interestingly, there is no variation in lattice parameter (a_{fcc}) when comparing the monometallic nanocatalysts to the core-shell Sn@
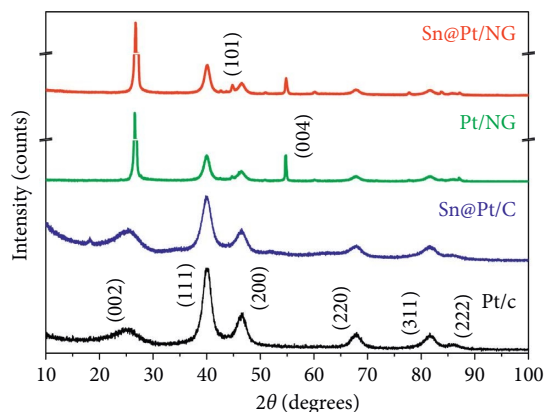
Figure 1: XRD patterns of Pt/C, Sn@Pt/C, Pt/NG, and Sn@Pt/NG.

Table 1: Parameters of the nanocatalysts from XRD and TEM analysis.

Nanocatalyst	d_{XRD} (nm)	a_{fcc} (nm)	d_{TEM} (nm)
Pt/C	4.0	0.3906	—
Pt/NG	6.1	0.3917	—
Sn@Pt/C	3.4	0.3906	2.1
Sn@Pt/NG	6.0	0.3917	2.3

Pt nanostructures on each carbon support, which indicates that the Pt lattice has suffered no contraction.

Figure S2 shows the Raman spectra of graphite, NG, and Vulcan. Peaks ascribed to the D, G, and 2D bands are observed at 1350, 1580, and 2670 cm^{-1}, respectively. The G band originates because of the stretching of sp^2 C-C bonds, and it is related to the structural order of the carbon material [39]. The D and 2D bands emerge from stretching vibrations of hybridized sp^2 and sp^3 bonds, indicating the degree of structural disorder of the samples [39]. Thus, the ratio of the relative intensities of the D and G bands (I_D/I_G) is an indicator of the degree of structural disorder or crystallinity of the materials [40].

Graphite has an I_D/I_G ratio of 0.04, confirming its highly crystalline structure. NG has the same peaks as graphite. However, the relative intensity of its D band increases considerably, resulting in $I_D/I_G = 0.86$. Such a result confirms the structural modification of NG, i.e., an increased disorder suggesting the formation of graphene layers or exfoliated graphite after ball milling. Moreover, the increased disorder observed for NG can be attributed to the doping with heteroatoms [39]. Meanwhile, Vulcan has an I_D/I_G ratio of 1.49, evidencing its disordered characteristic.

Table 2 shows the chemical composition of the nanocatalysts from EDS analysis. The Pt content at Pt/C and Pt/NG is lower than nominally expected, although the O concentration is higher than 2 wt. %. Moreover, 3.27 wt. % of N has been detected at Pt/NG, which has a C content close to 80 wt. % theoretically expected. On the other hand, the C content at Sn@Pt/C is higher than the nominal one, while Sn@Pt/NG shows 81.81 of this element, along with 5.68 (wt. %) of N. Meanwhile, the Pt:Sn ratio at Sn@Pt/C and Sn@Pt/NG is higher than theoretically expected.

Table 2: Chemical composition of the nanocatalysts by EDS.

Electrocatalizador	Pt	Sn	C	O	N	Pt:Sn at. ratio
			(wt. %)			
Pt/C	14.18	—	83.50	2.32	—	—
Pt/NG	14.89	—	79.16	2.68	3.27	—
Sn@Pt/C	8.29	1.60	86.22	3.89	—	3.1:1
Sn@Pt/NG	6.25	1.43	81.81	4.83	5.68	2.7:1

— Not determined.

Figure 2(a) (top) shows (A) the TEM micrograph of Sn@Pt/C, where the histogram (inset) indicates an average particle size $d_{TEM} = 2.1$ nm (Table 1). Figure (B) is an HRTEM micrograph of the core-shell nanocatalyst. FFT analysis allows to characterization of the nanoparticles by generating SAED patterns (inset). Two interplanar distances have been determined: (i) 0.195 nm at the center of the nanoparticle, which has been ascribed to the (211) reflection of Sn [41], even though the (200) peak of Pt may have a somehow similar value [42]; (ii) 0.220 nm at the border of the nanoparticle, attributed to the (111) plane of Pt [43]. Figure (C) shows the micrograph in dark field mode.

Figure 2(b) (bottom) shows the same analysis for Sn@Pt/NG. Inset in (A) reveals a d_{TEM} value of 2.3 nm (Table 1). Analysis by FFT in (B) also demonstrates two interplanar distances at this nanocatalyst: (i) 0.198 nm at the center ascribed to Sn (211); (ii) 0.216 nm at the border ascribed to Pt (111). Figure (C) is the dark field micrograph of the nanocatalyst. These features support the core-shell nature of nanostructured Sn@Pt/C and Sn@Pt/NG.

Table S1 depicts the surface chemical composition of the nanocatalysts by XPS. Under this perspective, the nanocatalysts have a Pt concentration between 0.68 and 2.97 (at. %). Interestingly, the Pt:Sn at. ratio of Sn@Pt/C and Sn@Pt/NG reaches a value closer to the nominal than in Table 2, more clearly seen at Sn@Pt/C (1.0:0.87). It is noteworthy that by using the XPS technique, no N species have been detected at the nanocatalysts supported on NG. Such difference compared to EDS analysis (Table 2) has been attributed to the sensitivity of XPS, which is a superficial characterization technique.

The high-resolution XPS spectra of Pt/C in the Pt 4f region is shown in Figure 3(a). Two doublets due to the spin-orbit splitting into the Pt4$f_{7/2}$ and Pt4$f_{5/2}$ states are observed. Pt^0 and Pt^{2+} species are identified at the nanocatalyst [43], the former having a higher relative concentration (Table S2). Similar doublets can be seen at Pt/NG (Figure 3(b)), also having a higher concentration of Pt^0 compared to Pt^{2+} species (Table S2).

Figures 3(c) and 3(d) are the high-resolution spectra in the Pt 4f region of Sn@Pt/C and Sn@Pt/NG, respectively. Both core-shell nanostructures show the two doublets in the Pt4$f_{7/2}$ and Pt4$f_{5/2}$ states. As in the case of the monometallic nanocatalysts mentioned above, both core-shell nanostructures develop a higher relative concentration of Pt^0 compared to Pt^{2+} (Table S2). Figures 3(e) and 3(f) show the spectra of Sn@Pt/C and Sn@Pt/NG in the Sn 3d region. In both cases, only Sn^{2+} (SnO) has been detected in the splitting into the Sn3$d_{5/2}$ and Sn3$d_{3/2}$ states, i.e., no metallic Sn has
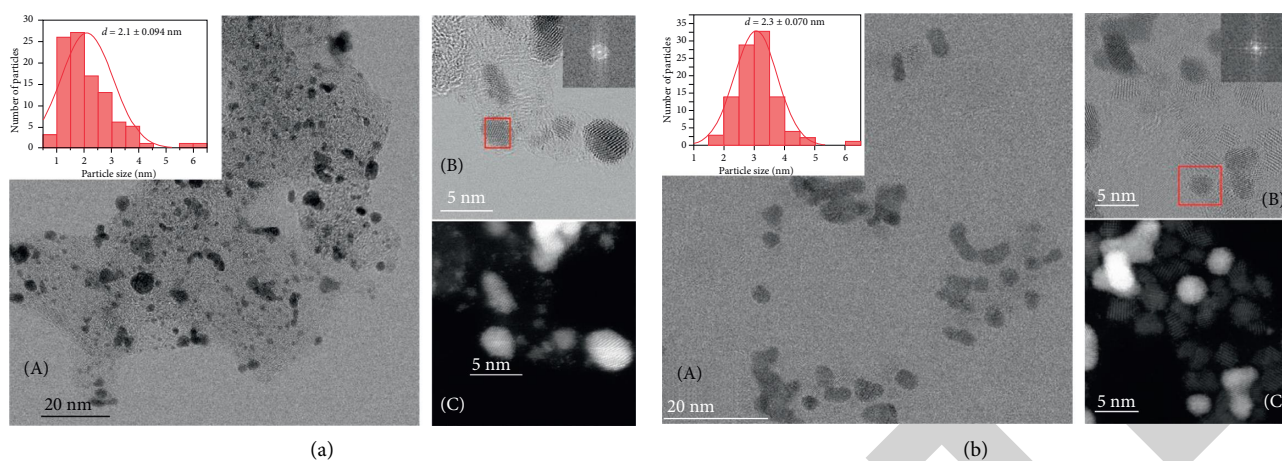
Figure 2: HRTEM micrographs of Sn@Pt/C and Sn@Pt/NG.
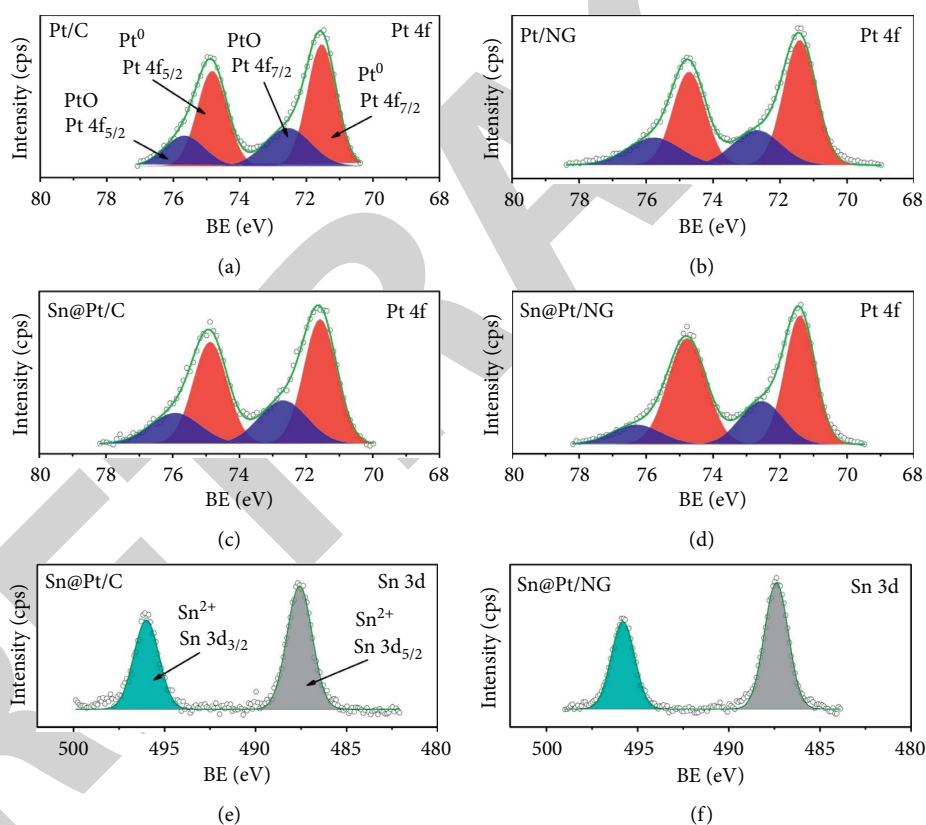
Figure 3: High-resolution XPS spectra in the Pt 4f region of (a) Pt/C, (b) Pt/NG, (c) Sn@Pt/C, and (d) Sn@Pt/NG. (e)-(f) High-resolution spectra in the Sn 3D region of Sn@Pt/C and Sn@Pt/NG.

been formed at the nanocatalysts. These results confirm the observations in Figure 1, where no reflections associated with metallic Sn have emerged.

Figures S3 and S4 show the spectra of the nanocatalysts in the C 1 s and O 1 s regions, respectively. In particular, the presence of PtO bonds at the nanocatalysts in Figure S4 correlates well with the development of Pt^{2+} species in the Pt

4f region in Figure 3. The other bonds are typically observed at carbon-supported Pt nanocatalysts [33].

Figure 4 shows CVs of (a) Pt/C, (b) Pt/NG, (c) Sn@Pt/C, and (d) Sn@Pt/NG before (1st cycle) and after (1000th cycle) ADT. Considering the chemical composition reported in Table 2, the total metal loading at the working electrodes is 72.3, 75.9, 51.2, and 39.18 mg cm^{-2} at Pt/C, Pt/NG, Sn@Pt/C,

Pt/C 1st cycle
Pt/C 1000th cycle

(a)

Pt/NG 1st cycle
Pt/NG 1000th cycle

(b)

Sn@Pt/C 1st cycle
Sn@Pt/C 1000th cycle

(c)

Sn@Pt/NG 1st cycle
Sn@Pt/NG 1000th cycle

(d)
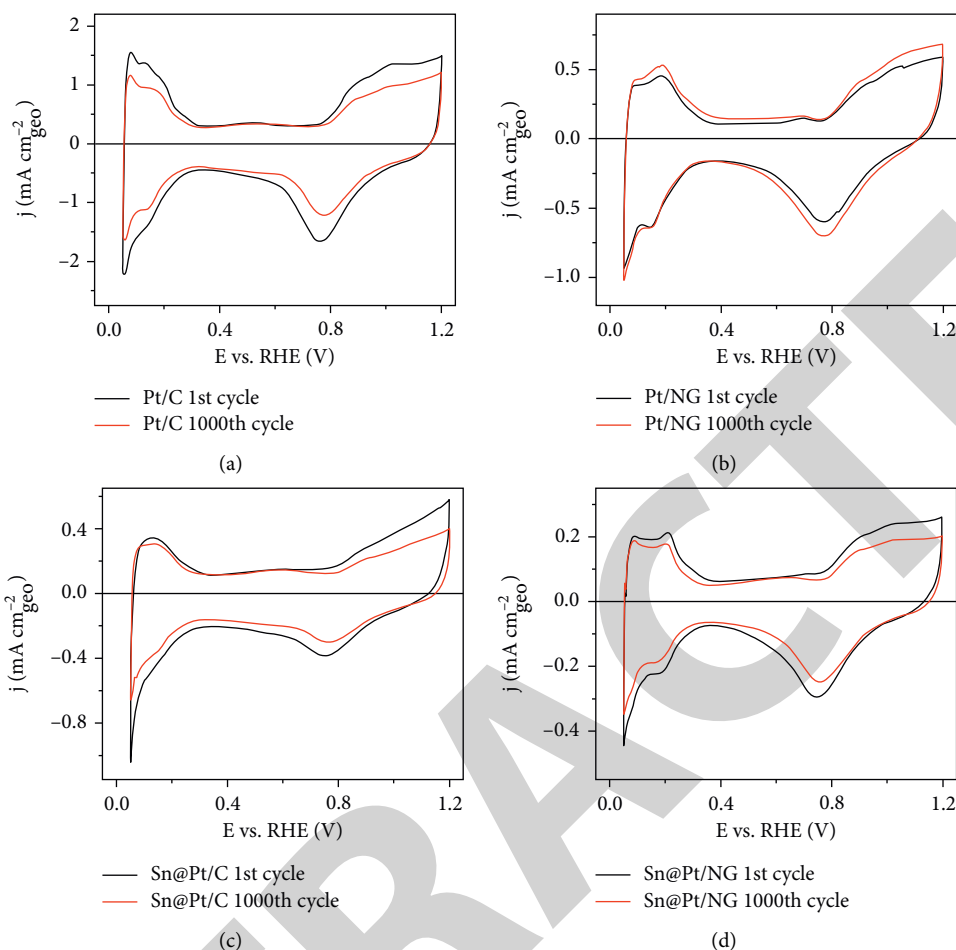
FIGURE 4: CVs of the nanocatalysts before and after ADT. (a) Pt/C, (b) Pt/NG, (c) Sn@Pt/C, (d) Sn@Pt/NG. Electrolyte: $0.5\,M\cdot H_2SO_4$ saturated with N_2. Scan rate: $20\,mV\cdot s^{-1}$.

TABLE 3: Electrochemical parameters of the nanocatalysts from CV and CO-stripping tests.

Nanocatalyst	A_r (cm_r^{-2})	$ECSA_H$ ($m^2\cdot g_{Pt}^{-1}$)	$ECSA_H^*$ ($m^2\cdot g_{Pt}^{-1}$)	Variation (%)	$ECSA_{CO}$ ($m^2\cdot g_{Pt}^{-1}$)	j_{CO} (V/RHE)	$E_{onset,\,CO}$ (V/RHE)
Pt/C	8.05	57.10	38.43	-32.7	85.17	0.76	0.54
Pt/NG	2.82	19.06	19.82	3.9	26.07	0.67,0.72	0.35
Sn@Pt/C	1.33	16.32	15.80	-3.2	21.89	0.67,0.72	0.40
Sn@Pt/NG	1.25	20.18	17.18	-14.87	22.50	0.67,0.77	0.40

*Value after ADT.

and Sn@Pt/NG, respectively. A typical negative variation in j is observed after ADT at three of the nanocatalysts ascribed to agglomeration and segregation of nanoparticles, while Pt/NG has an increase after cycling over the potential window, which suggests the activation of Pt sites due to the test.

As indicated, the electric charge due to desorption within the $H_{ads/des}$ region has been used to determine their A_r before ADT, and their $ECSA_H$ at the 1st and 1000th cycle. Table 3 shows the values of these parameters. Pt/C has the largest A_r and $ECSA_H$ values before ADT. In fact, its $ECSA_H$ is similar to previous reports elsewhere on analogous Pt/C nanocatalysts [23]. Nevertheless, Pt/C has the most important negative variation in $ECSA_H$ (-32.7%), of the same order as reported previously [23], and roughly 10 times higher than

that of the Sn@Pt/C core-shell nanocatalyst. Pt/NG shows high stability and even gains active surface area after ADT. Meanwhile, Sn@Pt/NG shows a more important negative variation in $ECSA_H$ than Sn@Pt/C.

The active surface area has also been determined from CO-stripping tests ($ECSA_{CO}$) before ADT, as shown in Figure S5, where the first cycle is the CO oxidation, while the second one indicates the behavior of the clean surface of the nanocatalysts in the N_2-saturated electrolyte. Table 3 shows the $ECSA_{CO}$ values obtained, which overall are higher than their $ECSA_H$ counterparts. The nanocatalyst with the highest $ECSA_{CO}$ value is also Pt/C, while the tendency at the other nanocatalysts resembles that of $ECSA_H$ before ADT.
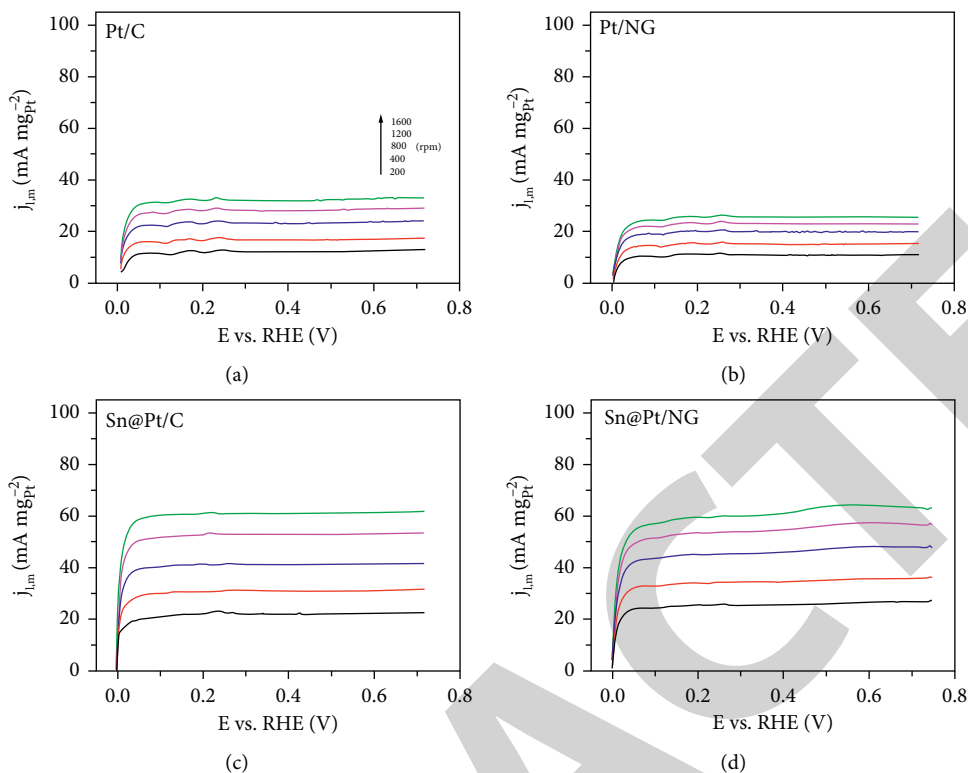
FIGURE 5: Mass activity of the HOR at (a) Pt/C, (b) Pt/NG, (c) Sn@Pt/C, and (d) Sn@Pt/NG at several ω. Electrolyte: H_2-saturated 0.5 M·H_2SO_4. Scan rate: 5 mV·s^{-1}.

Moreover, the shape of the CO oxidation plots shows the effect of both the chemical composition of the nanocatalysts and the type of support used. Pt/C has a characteristic narrow peak of monometallic Pt nanocatalysts supported on Vulcan [44], with a maximum current density peak due to the oxidation of CO (j_{CO}) at 0.76 V/RHE and an onset potential ($E_{onset, CO}$) of 0.54 V/RHE (Table 3). The use of the NG support has an important effect on Pt/NG by shifting $E_{onset, CO}$ by 0.19 V toward more negative values compared to Pt/C. Additionally, a broad shoulder with two peaks (0.67 and 0.72 V/RHE) is observed at Pt/NG, different than the sharp peak at Pt/C. This behavior of monometallic Pt has been ascribed to arbitrary nucleation of Pt nanoparticles onto sp^2 and sp^3 carbon domains [44].

Interestingly, despite being supported on Vulcan, Sn@Pt/C also shows a broad shoulder with two peaks, i.e., there is a significant effect of the chemical composition of the nanocatalyst on the oxidation of CO. Such behavior has been attributed elsewhere to two Pt states induced at a Pt shell by a Ru core [45], which is analogous to the effect of Sn on the Pt shell in this work. Moreover, the fact that the two peaks shown by Sn@Pt/C are at more negative potentials (0.67 and 0.72 V/RHE, Table 3) than that of Pt/C, indicates a displacement of the d-band center of the Pt shell due to a compressive strain effect provoked by the Sn core [45]. Additionally, $E_{onset, CO} = 0.4$ V/RHE at Sn@Pt/C, i.e., more negative than Pt/C, although 50 mV more positive than Pt/NG.

Meanwhile, Sn@Pt/NG shows peaks at 0.67 and 0.77 V/RHE, ascribed to an effect of both carbon support and

TABLE 4: Mass, specific, and geometric limiting currents of the HOR at 0.4 V/RHE and 1600 rpm on the nanocatalysts.

Nanocatalyst	$j_{l, m}$ (mA·mg_{Pt}^{-1})	$j_{l, s}$ (mA·cm_r^{-2})	$j_{l, geo}$ (mA·cm^{-2})
Pt/C	31.88	0.055	2.29
Pt/NG	25.64	0.134	1.93
Sn@Pt/C	61.08	0.376	2.55
Sn@Pt/NG	61.20	0.303	1.93

chemical composition of the nanocatalyst, with $E_{onset, CO} = 0.4$ V/RHE (Table 3). Elsewhere, CO-stripping has been proposed as an electrochemical tool to characterize core-shell nanostructures [46]. The shape of the CO-stripping curves of Sn@Pt/C and Sn@Pt/NG in Figure S5 differs completely from those of Pt-Sn/C alloyed nanocatalysts in [23], which provides more evidence that effectively core-shell nanostructures have been obtained following the synthesis procedure proposed in this work.

The iR-compensated mass polarization curves of the HOR at (a) Pt/C, (b) Pt/NG, (c) Sn@Pt/C, and (d) Sn@Pt/NG are shown in Figure 5. It should be mentioned that an R value of about 6 W has been determined for the electrolyte, in good agreement with the literature [47, 48]. A compensation of 80% of the electrolyte resistance has been considered in the plots [49]. As can be observed, at 0.4 V/RHE and 1600 rpm, the mass limiting current density ($j_{l, m}$) is significantly higher at Sn@Pt/C and Sn@Pt/NG with an almost 2-fold increase compared to Pt/C and even larger related to Pt/NG (Table 4), demonstrating an important
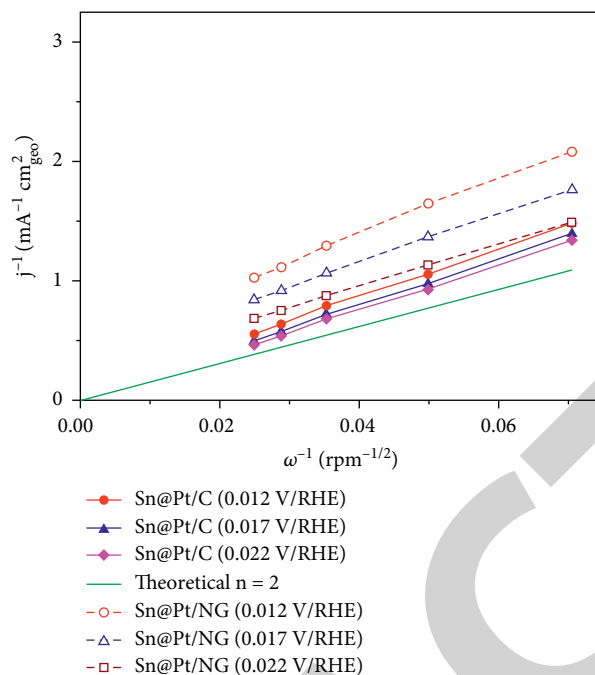
FIGURE 6: Koutecky–Levich plots of the HOR at Sn@Pt/C and Sn@Pt/NG at several ω. Potentials: 0.012, 0.017, and 0.22 V/RHE. The theoretical slope of $n = 2$ is also shown.
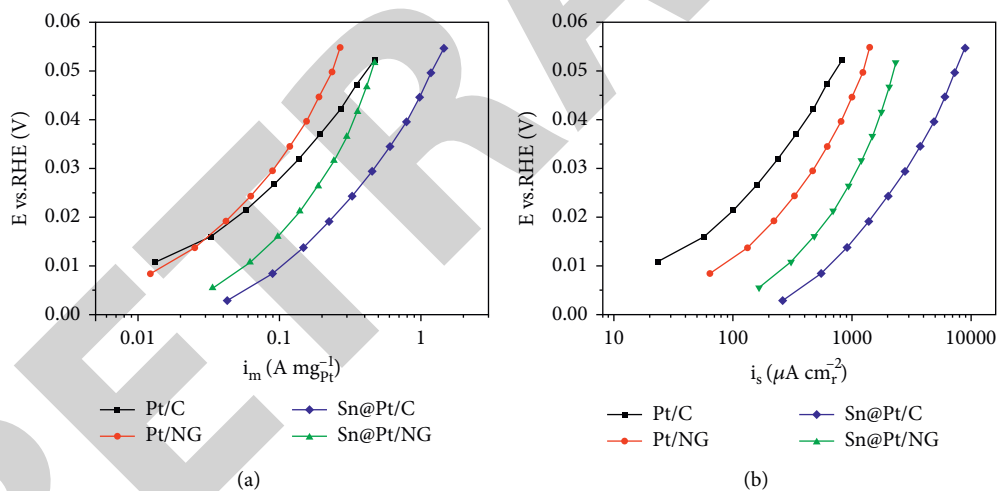
FIGURE 7: Tafel plots of (a) mass and (b) specific activity of the nanocatalysts for the HOR.

positive effect of applying the core-shell nanostructures to promote the HOR. The $j_{l, m}$ value is about the same for the two core-shell nanostructures, suggesting a dominant promotion of the reaction by the Sn@Pt nanoparticles, rather that the use of the NG support.

Furthermore, the specific activity of the nanocatalysts for the HOR is shown in Figure S6. The specific limiting current density ($j_{l, s}$) is clearly higher at Sn@Pt/C and Sn@Pt/NG, compared to Pt/C (which has the lowest performance) and Pt/NG (Table 4). In fact, Sn@Pt/C shows an almost 7 and 3-fold increase in $j_{l, s}$ related to Pt/C and Pt/NG, respectively. Moreover, Sn@Pt/C demonstrates a higher geometric catalytic activity than the other nanocatalysts, as seen in Figure S7 and Table 4. Thus, based on the mass, specific, and

geometric data in Table 4, Sn@Pt/C has the highest catalytic activity for the HOR, followed by Sn@Pt/NG.

Figure 6 shows the Koutecky–Levich plots of the HOR at Sn@Pt/C and Sn@Pt/NG, obtained from Equation (4). A theoretical Koutecky–Levich plot of a mechanism of the HOR involving a $2\,e^-$ transfer has been obtained with the following equation [50, 51]:

$$\frac{1}{B} = \frac{1}{0.2nF\nu^{-1/6}D_{H_2}^{2/3}C_{H_2}}, \tag{6}$$

where the Koutecky–Levich slope is $1/B$, while n: number of electrons transferred ($n = 2$); F: Faraday constant (96, 500°C); ν: kinematic viscosity (0.01 cm$^2\cdot$s^{-1}); D: hydrogen diffusion

TABLE 5: Comparison of performance of Sn@Pt/C with those of the literature.

Nanocatalyst	Electrolyte/rotating rate (rpm)	$j_{l,\ geo}$ (mA cm^{-2})	i_m (A mg$_{Pt}^{-1}$)	i_s (mA cm$_r^{-2}$)	Ref.
Sn@Pt/C	0.5 M H$_2$SO$_4$/1600	2.55	1.18^a	7.27	This work
TKK 46% Pt/C	0.1 M HClO$_4$/900	2.25	n.a.	n.a.	[52]
Polycrystalline Pt	0.1 M HClO$_4$/1600	2.90	n.a.	n.a.	[53]
Polycrystalline Pt	HClO$_4$ (pH = 0.2)/1600	2.75	n.a.	n.a.	[54]
RuO$_2$-Pt/C	HClO$_4$ (pH = 1.09)/1600	2.75	n.a.	n.a.	[55]
PtMo-CeOx-NAs	0.1 M HClO$_4$/1600	2.75	3.49^a	15	[56]
Pt–PdO/C	0.1 M HClO$_4$/1600	2.50	0.127^{b,c}	n.a.	[57]

^{a}At 50 mV vs. RHE; ^{b}at 200 mV vs. RHE; ^{c}total metal loading; n.a.: not available.

coefficient (3.7×10^{-5} cm$^2 \cdot$s^{-1}); and C$_{H2}$: concentration of H$_2$ in H$_2$SO$_4$ (7.14×10^{-7} mol·cm^{-3}) [38]. As can be seen in Figure 6, the experimental slopes approach the theoretical one, strongly suggesting that the HOR at the core-shell nanocatalysts undergo a mechanism involving a $2\,e^-$ transfer, in good agreement with the HOR reaction in acid media as follows:

$$H_2 \longrightarrow 2H^+ + 2e^-. \tag{7}$$
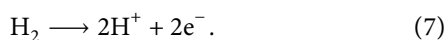
Tafel plots of mass and specific activity of the nanocatalysts for the HOR are shown in Figures 7(a) and 7(b), respectively. In both scenarios, the catalytic activity decreases in the order Sn@Pt/C > Sn@Pt/NG > monometallics. Thus, there is a significant promotion effect of the core-shell nanostructures for the reaction, which is ascribed to an electronic effect (modification of the Pt d-band center due to interactions of the shells with the Sn cores). The bifunctional mechanism, due to the oxophilicity of Sn, may have also contributed to the high performance of the core-shell nanocatalysts.

Table 5 shows a comparison of catalytic activity of Sn@Pt/C with that of some nanocatalysts reported in the literature in acid media. It should be mentioned that most of the data are rough values determined from the plots reported at each work. When considering $j_{L,\ geo}$ (which is the most widely reported), Sn@Pt/C performs very well, with a value of 2.55 mA·cm^{-2}, which is slightly higher than that reported for a TKK 46% Pt/C nanocatalyst [52]. In some cases, polycrystalline Pt [53, 54], RuO$_2$-Pt/C [55], and PtMo-CeOx-NAs [56] show a higher $j_{L,\ geo}$. Meanwhile, the value reported for a Pt-PdO/C nanocatalyst is similar to that of Sn@Pt/C [57].

Attention should be paid, however, to the mass and specific activities for the HOR. The i_m and i_s values of Sn@Pt/C are roughly one-third and one-half of those reported by Cui et al. for their PtMo-CeOx-NAs nanocatalyst, respectively, [56]. Meanwhile, the i_m of Sn@Pt/C is higher than that of the Pt-PdO/C nanocatalyst reported by Barman et al., even though the authors report the mass activity by total metal loading [57]. Thus, further studies should focus on increasing the mass and specific activities of Sn@Pt/C.

4. Conclusions

The BAE method produced nanostructured catalysts. Physicochemical and electrochemical characterizations showed the formation of Sn@Pt/C and Sn@Pt/NG core-shell nanocatalysts. From XPS analysis, Pt^0 and Pt^{2+} species were detected at all nanocatalysts, while only Sn^{2+} formed at Sn@Pt/C and Sn@Pt/NG. CO-stripping tests provided evidence of a displacement of the Pt d-band center of the Pt shells because of a strain effect attributed to the Sn cores. Such electronic modification, as well as the bifunctional mechanism due to the oxophilicity of Sn, contributed to the higher mass and specific catalytic activity of the core-shell nanocatalysts for the HOR, particularly Sn@Pt/C. Both Sn@Pt/C and Sn@Pt/NG promoted the HOR via a $2\,e^-$ transfer mechanism.

Data Availability

The data used to support this study are included within the supplementary information files.

Conflicts of Interest

The authors declare that they have no conflicts of interest.

Acknowledgments

Supplementary Materials

Figures S1 and S2 show the XRD patterns and the Raman spectra of graphite, NG, and Vulcan, respectively. Table S1 depicts the chemical composition of the nanocatalysts as determined by XPS. Table S2 shows the parameters of the nanocatalysts, obtained from XPS analysis. Figures S3 and S4 show the high-resolution spectra in the C 1s and O 1s regions of the nanocatalysts, respectively. Figure S5 depicts the CVs resulting from the CO-stripping test at the nanocatalysts. Figure S6 shows the polarization curves of the HER (specific activity) at the nanocatalysts. Figure S7 shows the polarization curves of the HER (geometric activity) at the nanocatalysts. (*Supplementary Materials*)

References

[1] J. Rodríguez-Varela, I. L. Alonso-Lemus, O. Savadogo, and K. Palaniswamy, "Overview: Current trends in green electrochemical energy conversion and storage," *Journal of Materials Research*, vol. 36, pp. 4071–4083, 2021.

[2] A. Baroutaji, A. Arjunan, J. Robinson, T. Wilberforce, M. A. Abdelkareem, and A. G. Olabi, "PEMFC poly-generation systems: developments, merits, and challenges," *Sustainability*, vol. 13, no. 21, Article ID 11696, 2021.

[3] I. Aleknaviciute, T. G. Karayiannis, M. W. Collins, and C. Xanthos, "Towards clean and sustainable distributed energy system: the potential of integrated PEMFC-CHP," *International Journal of Low Carbon Technologies*, vol. 11, no. 3, pp. 296–304, 2016.

[4] G. Squadrito, A. Nicita, and G. Maggio, "A size-dependent financial evaluation of green hydrogen-oxygen co-production," *Renewable Energy*, vol. 163, pp. 2165–2177, 2021.

[5] P. Abmann, A. S. Gago, P. Gazdzicki, K. A. Friedrich, and M. Wark, "Toward developing accelerated stress tests for proton exchange membrane electrolyzers," *Current Opinion in Electrochemistry*, vol. 21, pp. 225–233, 2020.

[6] M. M. Whiston, I. L. Azevedo, S. Litster, K. S. Whitefoot, C. Samaras, and J. F. Whitacre, "Expert assessments of the cost and expected future performance of proton exchange membrane fuel cells for vehicles," *Proceedings of the National Academy of Sciences*, vol. 116, no. 11, pp. 4899–4904, 2019.

[7] S. T. Thompson, B. D. James, J. M. Huya-Kouadio et al., "Direct hydrogen fuel cell electric vehicle cost analysis: System and high-volume manufacturing description, validation, and outlook," *Journal of Power Sources*, vol. 399, pp. 304–313, 2018.

[8] S. J. Hwang, S. J. Yoo, J. Shin et al., "Supported core@shell electrocatalysts for fuel cells: close encounter with reality," *Scientific Reports*, vol. 3, no. 1, p. 1309, 2013.

[9] Z. Yan, Y. Zhang, C. Dai et al., "Porous, thick nitrogen-doped carbon encapsulated large PtNi core-shell nanoparticles for oxygen reduction reaction with extreme stability and activity," *Carbon*, vol. 186, pp. 36–45, 2022.

[10] H.-B. Zheng, L. An, Y. Zheng et al., "Tuning the catalytic activity of Ir@Pt nanoparticles through controlling Ir core Size on cathode performance for PEM fuel cell application," *Frontiers of Chemistry*, vol. 6, p. 299, 2022.

[11] S. Hu, Y. Liu, S. Wang, X. Zhang, and P. K. Shen, "Ultrathin Co_3O_4-Pt core-shell nanoparticles coupled with three-dimensional graphene for oxygen reduction reaction," *International Journal of Hydrogen Energy*, vol. 46, no. 17, pp. 10303–10311, 2021.

[12] H. Nan, X. Tian, L. Yang, T. Shu, H. Song, and S. Liao, "A platinum monolayer core-shell catalyst with a ternary alloy nanoparticle core and enhanced stability for the oxygen reduction reaction," *Journal of Nanomaterials*, vol. 2015, Article ID 715474, 11 pages, 2015.

[13] J. X. Wang, Y. Zhang, C. B. Capuano, and K. E. Ayers, "Ultralow charge-transfer resistance with ultralow Pt loading for hydrogen evolution and oxidation using Ru@Pt core-shell nanocatalysts," *Scientific Reports*, vol. 5, no. 1, Article ID 12220, 2015.

[14] K. Elbert, J. Hu, Z. Ma et al., "Elucidating hydrogen oxidation/evolution kinetics in base and acid by enhanced activities at the optimized Pt shell thickness on the Ru core," *ACS Catalysis*, vol. 5, no. 11, pp. 6764–6772, 2015.

[15] Y.-F. Xing, Y. Zhou, Y.-B. Sun et al., "Bifunctional mechanism of hydrogen oxidation reaction on atomic level tailored-Ru@Pt core-shell nanoparticles with tunable Pt layers," *Journal of Electroanalytical Chemistry*, vol. 872, Article ID 114348, 2020.

[16] J. Hu, K. A. Kuttiyiel, K. Sasaki, C. Zhang, and R. R. Adzic, "Determination of hydrogen oxidation reaction mechanism based on Pt–H_{ad} energetics in alkaline electrolyte," *Journal of the Electrochemical Society*, vol. 165, no. 15, pp. J3355–J3362, 2018.

[17] J. Cai, X. Liao, P. Li et al., "Penta-twinned Rh@Pt core-shell nanobranches with engineered shell thickness for reversible and active hydrogen redox electrocatalysis," *Chemical Engineering Journal*, vol. 429, Article ID 132414, 2022.

[18] X.-M. Lin, X.-T. Wang, Y.-L. Deng et al., "In situ probe of the hydrogen oxidation reaction intermediates on Pt Ru a bimetallic catalyst surface by core-shell nanoparticle-enhanced raman spectroscopy," *Nano Letters*, vol. 22, no. 13, pp. 5544–5552, 2022.

[19] K. P. Kepp, "A quantitative scale of oxophilicity and thiophilicity," *Inorganic Chemistry*, vol. 55, no. 18, pp. 9461–9470, 2016.

[20] E. Antolini and E. R. Gonzalez, "The electro-oxidation of carbon monoxide, hydrogen/carbon monoxide and methanol in acid medium on Pt-Sn catalysts for low-temperature fuel cells: a comparative review of the effect of Pt-Sn structural characteristics," *Electrochimica Acta*, vol. 56, pp. 1–14, 2010.

[21] 2022, https://www.bloomberg.com/markets/commodities/futures/metals.

[22] D. González-Quijano, W. J. Pech-Rodríguez, J. I. Escalante-García, G. Vargas-Gutiérrez, and F. J. Rodríguez-Varela, "Electrocatalysts for ethanol and ethylene glycol oxidation reactions. Part I: Effects of the polyol synthesis conditions on the characteristics and catalytic activity of Pt–Sn/C anodes," *International Journal of Hydrogen Energy*, vol. 39, pp. 16676–16685, 2014.

[23] D. González-Quijano, W. J. Pech-Rodríguez, J. A. González-Quijano et al., "Performance and in-situ FTIR evaluation of Pt-Sn/C electrocatalysts with several Pt : Sn atomic ratios for the ethanol oxidation reaction in acidic media," *Chemelectrochem*, vol. 5, no. 22, pp. 3540–3547, 2018.

[24] X. Wang, L. Altmann, J. Stöver et al., "Pt/Sn intermetallic, core/shell and alloy nanoparticles: colloidal synthesis and structural control," *Chemistry of Materials*, vol. 25, no. 8, pp. 1400–1407, 2013.

[25] M. M. S. Pupo, F. E. López-Suárez, A. Bueno-López, C. T. Meneses, K. I. B. Eguiluz, and G. R. Salazar-Banda, "Sn@Pt and Rh@Pt core–shell nanoparticles synthesis for glycerol oxidation," *Journal of Applied Electrochemistry*, vol. 45, pp. 139–150, 2015.

[26] Y. Holade, C. Morais, S. Arrii-Clacens, K. Servat, T. W. Napporn, and K. B. Kokoh, "New preparation of PdNi/C and PdAg/C nanocatalysts for glycerol electrooxidation in alkaline medium," *Electrocatalysis*, vol. 4, no. 3, pp. 167–178, 2013.

[27] Y. Holade, K. Servat, T. W. Napporn, and K. B. Kokoh, "Electrocatalytic properties of nanomaterials synthesized from "bromide anion exchange" method—investigations of glucose and glycerol oxidation," *Electrochimica Acta*, vol. 162, pp. 205–214, 2015.

[28] Y. Holade, R. G. da Silva, K. Servat et al., "Facile synthesis of highly active and durable PdM/C (M = Fe, Mn) nanocatalysts for the oxygen reduction reaction in an alkaline medium," *Journal of Materials Chemistry*, vol. 4, no. 21, pp. 8337–8349, 2016.

[29] Y. Holade, N. E. Sahin, K. Servat, T. W. Napporn, and K. B. Kokoh, "Recent advances in carbon supported metal nanoparticles preparation for oxygen reduction reaction in low temperature fuel cells," *Catalysts*, vol. 5, no. 1, pp. 310–348, 2015.

[30] S. Dessources, C. Morais, T. W. Napporn, and K. B. Kokoh, "Reversible electrocatalytic activity of carbon-supported Pt_xNi_{1-x} in hydrogen reactions," *ChemPhysChem*, vol. 17, no. 23, pp. 3964–3973, 2016.

[31] J. C. Carrillo-Rodríguez, A. M. Garay-Tapia, B. Escobar-Morales et al., "Insight into the performance and stability of N-doped Ordered Mesoporous Carbon Hollow Spheres for the ORR: Influence of the nitrogen species on their catalytic activity after ADT," *International Journal of Hydrogen Energy*, vol. 46, pp. 26087–26100, 2021.

[32] O. J. Duarte-Urbina, F. J. Rodríguez-Varela, F. Fernández-Lugueño et al., "Bioanodes containing catalysts from onion waste and *Bacillus subtilis* for energy generation from pharmaceutical wastewater in a microbial fuel cell," *New Journal of Chemistry*, vol. 45, no. 28, pp. 12634–12646, 2021.

[33] A. Hernández-Ramírez, F. J. Rodríguez-Varela, P. C. Meléndez-González, and M. E. Sánchez-Castro, "Catalytic activity of Pt–CoTiO3 nanocatalysts supported on reduced graphene oxide functionalized with Cr organometallic compounds for the oxygen reduction reaction," *Journal of Materials Research*, vol. 36, pp. 4192–4206, 2021.

[34] A. A. Siller-Ceniceros, M. E. Sánchez-Castro, D. Morales-Acosta, J. R. Torres-Lubian, E. Martínez, and F. J. Rodríguez-Varela, "Innovative functionalization of Vulcan XC-72 with Ru organometallic complex: Significant enhancement in catalytic activity of Pt/C electrocatalyst for the methanol oxidation reaction (MOR)," *Applied Catalysis B: Environmental*, vol. 209, pp. 455–467, 2017.

[35] J. Shi, J. Wang, Y. Chen, Y. Sun, B. Liu, and Y. Fan, "Ag-Pd core-shell electrocatalysts for ethanol oxidation and oxygen reduction reactions in alkaline medium," *Journal of Physics: Materials*, vol. 4, no. 1, Article ID 014002, 2021.

[36] Y. Yang, C. Tan, Y. Yang et al., "Pt₃Co@Pt Core@shell nanoparticles as efficient oxygen reduction electrocatalysts in direct methanol fuel cell," *ChemCatChem*, vol. 13, no. 6, pp. 1587–1594, 2021.

[37] F. Mansoori Mosleh, Y. Mortazavi, N. Hosseinpour, and A. A. Khodadadi, "Asphaltene adsorption onto carbonaceous nanostructures," *Energy and Fuels*, vol. 34, no. 1, pp. 211–224, 2020.

[38] T. C. S. Evangelista, G. T. Paganoto, M. C. C. Guimarães, and J. Ribeiro, "Raman spectroscopy and electrochemical investigations of Pt electrocatalyst supported on carbon prepared through plasma pyrolysis of natural gas," *Journal of Spectroscopy*, vol. 2015, Article ID 329730, 2015.

[39] L. Wang, Y. Wang, M. Wu et al., "Nitrogen, fluorine, and boron ternary doped carbon fibers as cathode electrocatalysts for zinc-air batteries," *Small*, vol. 14, no. 20, Article ID 1800737, 2018.

[40] R. Wang, H. Wang, H. Li et al., "An Fe@Fe3C-inserted carbon nanotube/graphite composite support providing highly dispersed Pt nanoparticles for ethanol oxidation," *Electrochimica Acta*, vol. 132, pp. 251–257, 2014.

[41] A. U. Haq, S. Askari, A. McLister et al., "Size-dependent stability of ultra-small α-/β-phase tin nanocrystals synthesized by microplasma," *Nature Communications*, vol. 10, no. 1, p. 817, 2019.

[42] F. Trombetta, D. W. Lima, F. Fiegenbaum, M. R. Becker, M. O. de Souza, and E. M. Martini, "C16MI.OTf ionic liquid on Pt/C and PtMo/C anodes improves the PEMFC performance," *International Journal of Hydrogen Energy*, vol. 43, no. 14, pp. 6945–6953, 2018.

[43] J. C. Martínez-Loyola, A. A. Siller-Ceniceros, M. E. Sánchez-Castro et al., "High performance Pt nanocatalysts for the oxidation of methanol and ethanol in acid media by effect of functionalizing carbon supports with Ru organometallic compounds," *Journal of the Electrochemical Society*, vol. 167, no. 16, Article ID 164502, 2020.

[44] C. A. Campos-Roldán, G. Ramos-Sánchez, R. G. Gonzalez-Huerta, J. R. Vargas García, P. B. Balbuena, and N. Alonso-Vante, "Influence of sp^3-sp^2 carbon nanodomains on metal/support interaction, catalyst durability, and catalytic activity for the oxygen reduction reaction," *ACS Applied Materials and Interfaces*, vol. 8, no. 35, pp. 23260–23269, 2016.

[45] J. Zou, M. Wu, S. Ning, L. Huang, X. Kang, and S. Chen, "Ru@Pt core–shell nanoparticles: impact of the atomic ordering of the Ru metal core on the electrocatalytic activity of the Pt shell," *ACS Sustainable Chemistry & Engineering*, vol. 7, no. 9, pp. 9007–9016, 2019.

[46] P. Ochal, J. L. Gomez de la Fuente, M. Tsypkin et al., "CO stripping as an electrochemical tool for characterization of Ru@Pt core-shell catalysts," *Journal of Electroanalytical Chemistry*, vol. 655, no. 2, pp. 140–146, 2011.

[47] C. M. Pedersen, M. Escudero-Escribano, A. Velázquez-Palenzuela, L. H. Christensen, I. Chorkendorff, and I. E. L. Stephens, *Electrochimica Acta*, vol. 179, pp. 647–657, 2015.

[48] J. Zheng, Y. Yan, and B. Xu, "Correcting the hydrogen diffusion limitation in rotating disk electrode measurements of hydrogen evolution reaction kinetics," *Journal of the Electrochemical Society*, vol. 162, no. 14, pp. F1470–F1481, 2015.

[49] S. Anantharaj, S. R. Ede, K. Karthick et al., "Precision and correctness in the evaluation of electrocatalytic water splitting: revisiting activity parameters with a critical assessment," *Energy & Environmental Science*, vol. 11, no. 4, pp. 744–771, 2018.

[50] C. Wei, R. R. Rao, J. Peng et al., "Recommended practices and benchmark activity for hydrogen and oxygen electrocatalysis in water splitting and fuel cells," *Advances in Materials*, vol. 31, Article ID 1806296, 2019.

[51] Á. Selva-Ochoa, J. Su-Gallegos, P. J. Sebastian, L. Magallón-Cacho, and E. Borja-Arco, "Hydrogen oxidation and oxygen reduction reactions on an OsRu-based electrocatalyst synthesized by microwave irradiation," *Materials*, vol. 14, no. 19, p. 5692, 2021.

[52] N. Ramaswamy, S. Ghoshal, M. K. Bates, Q. Jia, J. Li, and S. Mukerjee, "Hydrogen oxidation reaction in alkaline media: relationship between electrocatalysis and electrochemical double-layer structure," *Nano Energy*, vol. 41, pp. 765–771, 2017.

[53] W. Sheng, H. A. Gasteiger, and Y. Shao-Horn, "Hydrogen oxidation and evolution reaction kinetics on platinum: acid vs alkaline electrolytes," *Journal of the Electrochemical Society*, vol. 157, no. 11, pp. B1529–B1536, 2010.

[54] W. Sheng, Z. Zhuang, M. Gao, J. Zheng, J. G. Chen, and Y. Yan, "Correlating hydrogen oxidation and evolution activity on platinum at different pH with measured hydrogen binding energy," *Nature Communications*, vol. 6, no. 1, p. 5848, 2015.

[55] S. Panigrahy, R. Samanta, P. Panda, R. Mishra, and S. Barman, "RuO_2 as promoter in Pt-RuO_2-nanostructures/carbon composite, a pH universal catalyst for hydrogen evolution/oxidation reactions," *International Journal of Energy Research*, vol. 46, no. 5, pp. 6406–6420, 2022.

Retraction

Retracted: Application of Lightweight Thermal Insulation Building Materials for Green Building Design

Journal of Chemistry

This article has been retracted by Hindawi following an investigation undertaken by the publisher [1]. This investigation has uncovered evidence of one or more of the following indicators of systematic manipulation of the publication process:

(1) Discrepancies in scope

(2) Discrepancies in the description of the research reported

(3) Discrepancies between the availability of data and the research described

(4) Inappropriate citations

(5) Incoherent, meaningless and/or irrelevant content included in the article

(6) Peer-review manipulation

The presence of these indicators undermines our confidence in the integrity of the article's content and we cannot, therefore, vouch for its reliability. Please note that this notice is intended solely to alert readers that the content of this article is unreliable. We have not investigated whether authors were aware of or involved in the systematic manipulation of the publication process.

Wiley and Hindawi regrets that the usual quality checks did not identify these issues before publication and have since put additional measures in place to safeguard research integrity.

We wish to credit our own Research Integrity and Research Publishing teams and anonymous and named external researchers and research integrity experts for contributing to this investigation.

The corresponding author, as the representative of all authors, has been given the opportunity to register their agreement or disagreement to this retraction. We have kept a record of any response received.

References

[1] L. Liu and Y. Zhai, "Application of Lightweight Thermal Insulation Building Materials for Green Building Design," *Journal of Chemistry*, vol. 2022, Article ID 7044427, 7 pages, 2022.

Hindawi

Research Article

Application of Lightweight Thermal Insulation Building Materials for Green Building Design

Lifang Liu [ID][1] **and Yuhang Zhai** [ID][2]

[1]*School of Architectural Engineering, Ningbo Polytechnic, Ningbo 315800, Zhejiang, China*
[2]*School of Architecture, Zhengzhou University, Zhengzhou 450000, China*

Correspondence should be addressed to Lifang Liu; 11231337@stu.wxic.edu.cn

In order to focus on the application of green environmental protection lightweight thermal insulation materials, an in-depth study is carried out on the basis of joint architectural design. The application of green environmental protection materials in the construction industry was successfully analyzed through methods such as layout design method, optimization design method, and scientific optimization of material selection. In the process of urbanization development in our country, the number of urban population has increased sharply, and the demand for buildings has also increased. Therefore, it is necessary to rapidly promote green building design while the construction industry is developing rapidly and complete the upgrading and transformation of the building in terms of form design. We pay attention to the needs of buildings in terms of shading and lighting, and improve the conditions of building shading and lighting through green building technology. As a result, on the basis of maintaining the residual heat of the building, the diffuse radiation of the ultraviolet rays of the sun is realized, which effectively improves the utilization efficiency of natural energy and reduces the consumption of internal energy. Architectural design under the concept of green building design not only can it meet the current functional requirements of people for architecture but also imperceptibly promote the stable development of our country's construction industry. After the research on the application of green environmental protection materials, the integration and application of green building design concepts in architectural design is of great significance not only to meet people's health and ecological needs of buildings but also to promote social stability and sustainable development.

1. Introduction

The green development strategy has become one of the main strategies of our country's current social development. With the rapid development of urbanization in our country, the society vigorously carries out engineering construction. The energy used in urban building construction is generally nonrenewable resources, and excessive use will lead to environmental damage problems, resulting in many problems such as resource depletion. The energy consumption of construction projects is relatively large; according to the survey, the total energy consumption of buildings in our country accounts for about 20.7% of the social terminal energy consumption, the energy consumption or carbon emission of the whole building process includes three

aspects, and they are the production energy consumption or carbon emission of building materials, the national construction energy consumption or carbon emission, and the national stock building operation energy consumption or carbon emission. In order to meet the goals of energy conservation, emission reduction, and environmental sustainable development in the construction field, we should fully implement the concept of green building design and do a good job in the management and control of all aspects of architectural engineering design, maximize resource utilization efficiency, and save energy and reduce emissions. Driven by the economy, the construction industry has been greatly developed, and the construction technology and materials have also been further optimized. However, in the development process of the construction industry, in order
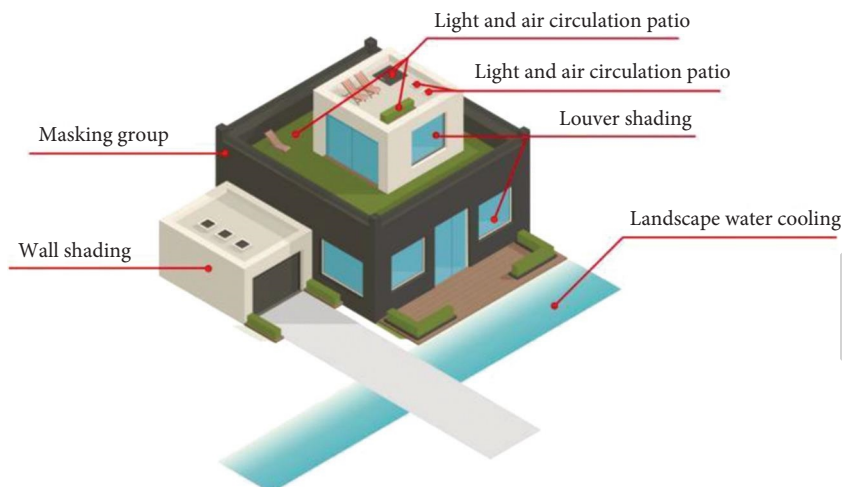
Figure 1: Sketch map of green technology application.

to meet people's material and spiritual needs, it has resulted in a large waste of resources and energy, and environmental pollution has become increasingly serious, which is not conducive to the implementation of sustainable development in our country. To this end, the integration of green concepts should be strengthened to achieve synergistic progress among people, architecture, and ecology. Green building mainly means that the concept of green environmental protection must be followed from the construction preparation, design and construction, and construction stage, including final maintenance work, to minimize the consumption of energy, building materials, costs, and environmental pollution, and to provide people with a healthy and environmentally friendly living space. Figure 1 is a schematic diagram of the application of green technology. The core of green building design is to save various resources, which mainly refers to the rational design of the entire building process with the goal of environmental protection and conservation under the premise of complying with relevant design regulations, including the adoption of advanced green design concepts and the use of green buildings, materials, and the application of renewable nonpolluting energy, and ultimately achieve the purpose of environmental protection, energy saving, and high efficiency.

2. Literature Review

Sabari et al. stated that the core of green building is based on the local natural environment, use professional knowledge to rationally organize the relationship between the building and other factors, integrate the building with the surrounding environment, and on this basis optimize the building's self-regulation, energy saving, and environmental protection performance, and prolong the service life of the building [1]. Yah and others believe that at this stage, the development of the construction industry has caused a certain degree of damage to the surrounding environment; therefore, when designing green buildings, we should fully respect the ecological principles, and implement energy

conservation and environmental protection into architectural design. Before carrying out the design work, the surrounding environment of the building should be surveyed on the spot, and the architectural design should be carried out on the premise of not destroying the original environment, and attention should be paid to the protection of the ecological environment in the later construction stage and building maintenance stage [2]. Eze and others believe that the thermal insulation materials in the construction industry are developing in the direction of light weight, high strength, and energy saving, and various new building thermal insulation materials are constantly emerging. However, it is accompanied by the problem of how to use various thermal insulation materials, so that they can be reasonably applied in the construction industry, so as to achieve the purpose of low cost, good thermal insulation performance, and waterproof and moisture-proof [3]. Liu et al. stated that for a long period of time, our country has been committed to economic development, but to a certain extent ignored the harm caused by economic development to the ecological environment, making social contradictions increasingly prominent [4]. Therefore, Jexembayeva and others believe that the construction of buildings should meet people's living and work requirements. Therefore, in the design process, in addition to scientific planning of the design content, optimizing and adjusting the overall content according to the actual situation is also an important link that cannot be ignored [5]. Sounthararajan and others believe that construction companies need to understand the future development direction of the industry in the context of the implementation of sustainable development strategies, and need to adjust construction technology and construction management methods; in this way, the ecological environment and the natural society are in a harmonious state [6]. Therefore, when Kumar et al. accumulated teaching experience, green building technology has become a key element for construction companies to achieve improvement goals, but many construction companies use green building technology inappropriately, which has a negative impact on environmental protection strategies [7]. Jena

Saubha and others said that traditional building materials need to consume a lot of natural energy, while environmentally friendly building materials only consume a small amount of resources, make full use of industrial and agricultural production and urban waste, and carry out secondary recycling to produce environmentally friendly building materials, and these building materials do not pose any hazard to human health; in a certain sense, it can be said that environmentally friendly building materials are building materials made of recycled garbage [8]. Sohel and others believe that green building is to maximize resources in the whole life cycle of construction projects, and achieve the goals of saving energy consumption, saving land, saving water, and saving building materials [9]. Xia and others believe that the rapid economic development and the wide application of Internet technology have promoted the technological innovation and reform of the construction industry, and a variety of advanced science and technology have been fully used in architectural design, construction, and other links. In the green building design, we must pay attention to scientific design principles to ensure that the building meets people's requirements for intelligent and environmentally friendly buildings in the later use process. In the specific design process, it is necessary to abandon the traditional design concept, actively introduce environmental protection science and technology, ensure the advanced science of building construction, and realize the effective combination of intelligence and green living environment [10].

3. Research Methods

3.1. Layout Design Method. In the green building design, the layout design is the most important part, which requires the designers to do a comprehensive inspection of the site resources, and increase the utilization rate of site resources and reduce the traces of artificial construction in a reasonable way, and reduce excessive consumption of nonrenewable energy. At the same time, in the building layout design, it is necessary to reduce the heat energy absorption of the building and control the indoor temperature. For green building design, the key points are as follows: first, while ensuring building functions, we optimize and adjust the internal space layout of the building, increase resource and energy utilization, and reduce energy loss caused by air conditioning, lighting, and other facilities [11]. Figure 2 shows the total output value of the construction industry and the analysis of building energy consumption in Figure 3. Second, we understand and master the characteristics of the surrounding environment, make full use of the existing terrain advantages, and complete the integration and utilization of resources. Third, we clarify the architectural design requirements, implement scientific planning for the building layout and orientation according to the characteristics of the area, make full use of natural light to enhance the indoor lighting effect, and reduce the waste of nonrenewable resources. Finally, we plan the building spacing reasonably to avoid damaging the lighting effect of the building due to excessive density, thereby reducing the
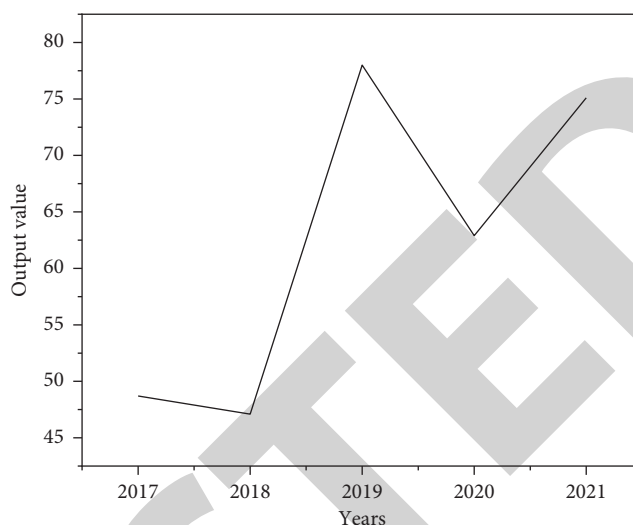
FIGURE 2: Gross output value of the construction industry.
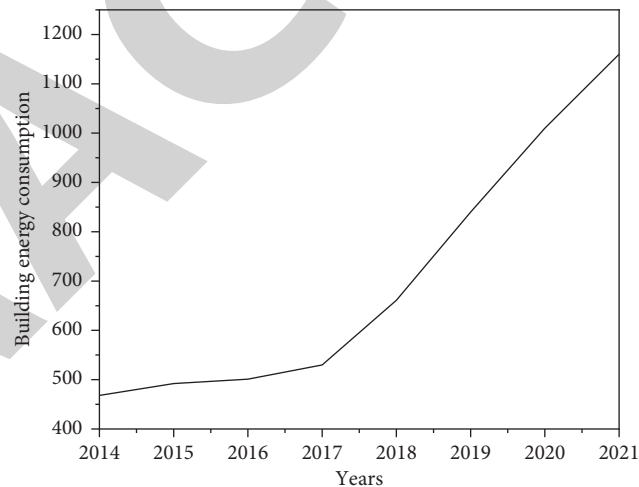
FIGURE 3: Analysis of building energy consumption.

lighting quality of the building space and improving the energy utilization rate. Combined with the current urban planning situation in our country, the process of urbanization is deepening day by day, and urban land resources are becoming more and more tense. At present, many buildings occupy a large area, but the space that can really be used by people's lives is relatively limited, which directly causes the problem of waste of land resources, and seriously compresses the urban greening area, which directly hinders the construction of urban greening [12]. In the concept of green building design, the most critical content is saving land. Therefore, in the process of building design, it is necessary to do a good job of saving land resources. In the early stage of green building design, consideration can be given to building cost, saving land resources as much as possible, reducing land area, using more land for greening, and incorporating more green elements. In the process of green building design, the designer should analyze and understand the local climate environment, geographical topography, environmental conditions, and economic development

conditions; determine the specific use of the target building; and combine the functional requirements of the building and select suitable locations within the city's jurisdiction for further development design. In architectural design, we pay attention to the envelope structure; for construction projects, we pay attention to the wall insulation design, improve the thermal insulation and confidentiality of the wall through green building technology, select materials with excellent thermal insulation performance, and complete the wall construction [13]. In addition, if there are cracks in special parts of the building, it will not only reduce the reliability of the building structure but also cause the problem of heat loss. Therefore, it is necessary to pay attention to the selection of materials for special parts and the application of technology. In terms of roof energy-saving design, you can choose to lay the thermal insulation pavement upside down, and use the waterproof membrane to improve the waterproof effect of the roof; we choose the method of laying the thermal insulation roof, and the thermal insulation material applied in this method can resist the attack of the wind and snow weather on the roof, and can also improve the effect of the roof in terms of temperature control. Except for a few rooms, preventing condensation on the inner surface of the building envelope is the minimum requirement for thermal design, and the formula for the lower limit thermal resistance is as follows:

$$q = \frac{1}{R_n} \cdot (t_n - t_{n0}). \tag{1}$$

The total thermal resistance of the envelope is as follows:

$$R_0 = \frac{t_n - t_w}{\Delta t} \cdot R_n. \tag{2}$$

The minimum thermal resistance of the building envelope is as follows:

$$R_{\min} = \frac{t_n - t_w}{\Delta t} \cdot R_n \cdot n, \tag{3}$$

where t_n is the calculated temperature of indoor air in winter, t_w is the calculated temperature of outdoor in winter, Δt is the allowable temperature difference, R_n is the heat transfer resistance of the inner surface of the enclosure, and n is the temperature correction value.

With the improvement of people's awareness of environmental protection and the development of science and technology, environmentally friendly green building materials have been widely used in the construction industry. The research and development, promotion, and application of new building materials such as foam concrete blocks and fireproof color steel plates not only ensure the quality of construction projects but also greatly reduce the energy consumption of building materials. Therefore, designers should pay attention to the use of environmentally friendly building materials in the design process and strictly control the quality of building materials [14]. It is necessary to conduct on-site inspections of manufacturers of environmentally friendly building materials, check whether the production standards are met, and conduct relevant inspections on the building materials it produces. It is

necessary to use more green building materials, such as environmentally friendly wall materials and pipes, and reduce the use of nonrenewable resources, such as replacing metal pipes with environmentally friendly plastic pipes. In addition, attention should be paid to the reuse of building materials to improve the environmental protection of the building; for example, the covering materials of the exterior walls can be reused during renovation, and clean and pollution-free solar energy and wind energy should be used more.

3.2. Optimal Design Method. Before designing a green building, a large number of materials related to the project are collected, and the designer must have a sufficient understanding of the project to design the building construction plan according to the requirements and actual conditions. Therefore, designers need to survey the site before construction, record the construction geological information at the same time, know the temperature and climate characteristics of the project work stage, have a sufficient understanding of the project, and have a purposeful and targeted approach according to the construction requirements and the project's environmental protection and green needs. Purposeful and targeted analysis and design are carried out to improve the rationality of the content of the construction plan, so that it can become a guarantee for the efficient construction of the staff. During the architectural design, it is necessary to promote the coordination between the environment and the building, increase the lighting area of the building, and ensure that the temperature in the building is suitable and the sunlight is abundant, and the purpose of controlling and reducing energy consumption can be achieved. With the rapid development of the times, green design has been widely used in current industrial buildings, and it will also attract more and more people's attention, this is due to the green design, which can not only promote the optimization of industrial structure but also prolong the service life of factory buildings [15]. Figure 4 is the application of green building materials, and Figure 5 is the usage curve of common building materials and green materials. From the economic analysis, it can be found that with the emergence of a large number of industrial buildings, new economic models will inevitably appear; therefore, we must recognize the importance of the green building solutions proposed by the design department. In the process of producing industrial products, a certain amount of substances will inevitably be consumed, and if they cannot be used in time or cannot be used correctly, certain pollutants will be produced. If these corrosive substances cannot be properly handled, it will further affect industrial production areas; at the same time, it will pollute the water source and air of the production plant. Because these phenomena will inevitably pollute the industrial production environment, the anticorrosion design must be placed in an important position in the green building design [16]. To carry out architectural design under the concept of green building design, we must follow the laws of nature, carry out architectural design in a targeted and planned way, and realize the green development of the city. At the content
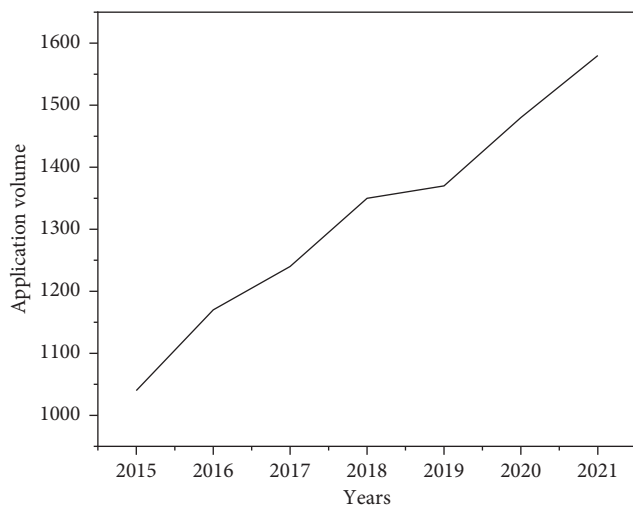
FIGURE 4: Application of green building materials.
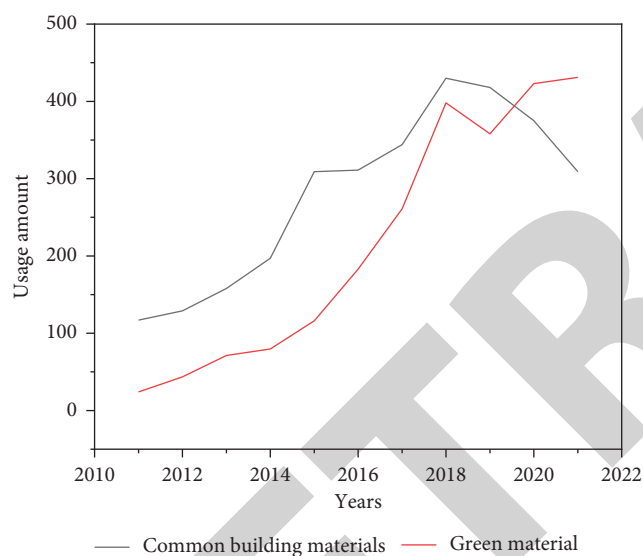
FIGURE 5: The usage curve of common building materials and green materials.

level of architectural design, natural elements and green elements should be added in the process of architectural design, in order to achieve a harmonious development of buildings between practicality and nature. Green building is a characteristic and new method, and rational application of green construction technology and green materials, and the environmental pollution caused by the construction can be controlled to a minimum level. First of all, it is necessary to conduct a comprehensive analysis and research on the building project, and design the overall structure in combination with the future use purpose of the building; second, it is determined that the types of building materials and resources meet the requirements of the building objectives, and the stability and overall applicability of the building structure are determined to meet the requirements of people's green and environmentally friendly living. In addition, in the design process, it is necessary to focus on the building's

ability to resist earthquakes, floods, and other natural disasters to ensure the service life of the building [17].

3.3. *Strengthening the Scientificity of Material Selection.* Building materials are the foundation of construction projects. The scientific selection of building materials can not only reduce capital cost loss and improve building quality, but also reduce energy consumption, achieve energy conservation and emission reduction targets, and protect the ecological environment. To this end, in the design of green buildings, the control of materials should be increased, and the scientific nature of material selection should be paid attention to. The specific measures are as follows: first, we increase the testing of materials of origin to ensure that they meet the current environmental protection standards and reduce the impact on the building environment, so as to maintain human health and improve living standards. Second, combined with its own conditions, we increase the selection rate of green environmental protection materials; on the basis of ensuring the quality of the materials themselves, we optimize the construction level of construction projects and reduce construction problems [18]. Finally, we pay attention to the research and promotion of new green building materials, and strengthen the environmental protection effect. For example, solar energy conversion can be used to reduce power loss during construction and promote the normal operation of indoor lighting and electrical equipment. In the design of architectural design, we consider architectural design methods from the perspective of energy conservation and environmental protection, design architectural forms, combine energy conservation with form design, improve the rationality of green architectural design, select quantitative analysis methods, calculate engineering quantities, simulate design plans, and analyze the energy consumption of buildings. To improve the overall design quality of green buildings in a reasonable way, we need to pay attention to the appearance of the building in architectural design, and we should also organically combine green building technology and form design, and make the building to have a good appearance while improving the energy efficiency of the building. Building construction and architectural design are closely related, so we should pay close attention to the materials of green building projects, select construction materials according to the requirements of green construction, and create green projects. In terms of architectural design, we should be clear about the construction requirements and choose green and environmentally friendly raw materials. When selecting materials, we pay attention to material suppliers, check the other party's qualifications, investigate the other party's reputation in the market, check the material samples provided by the other party, and ensure that the materials have no quality problems, and can meet the quality requirements of construction. The building materials chosen need to have environmentally friendly properties. The application of such materials will not produce toxic and harmful substances during construction [19]. Figure 6 shows the comparison of heat resistance of building
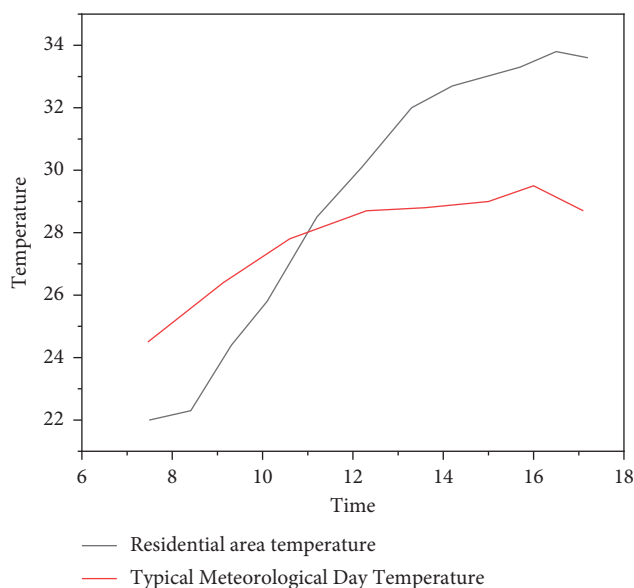
FIGURE 6: Comparison of heat resistance of building materials.

materials. In terms of building material selection, it should be considered from the aspects of material quality characteristics and cost, and through horizontal comparison, we choose the most economical one from a variety of environmentally friendly materials. The materials used in the building perimeter must have the function of automatic temperature regulation, and the use of such materials can control the indoor and outdoor temperatures at a relatively balanced level. When carrying out green building design, it is necessary to know the chemical properties of materials, test the properties of materials before construction, and prohibit the use of toxic building materials in engineering [20].

4. Results and Analysis

In recent years, our country's environmental pollution and energy problems have become increasingly serious, and various fields have continued to carry out technological innovation and research on new development ways, in order to adapt to the implementation of the national sustainable development strategy. Green building design fundamentally solves the problems of high building energy consumption and serious environmental pollution, and has been widely used in the construction industry. In the specific design process, designers should also follow certain design principles, adopt intelligent building technology, make full use of environmental protection resources and green building materials to improve the environmental protection and comfort of buildings, and then promote the sustainable development of the construction industry. There are many differences between environmentally friendly building materials and traditional building materials; first, the production raw materials are different, and the production of environmentally friendly building materials is usually the use of waste generated in people's production and life or waste generated by urban operations. Second, the production technology is different. The production of

environmentally friendly building materials requires no pollution during production, and, at the same time, no or less consumption of natural resources. Third, the production process is different. In the production of environmentally friendly building materials, catalysts that are unfavorable to the environment cannot be used. At the same time, environmentally friendly building materials are required not to contain heavy metals, and the emissions generated during the entire production process are required to meet the national environmental protection standards. Fourth, the usage is different. The purpose of producing environmentally friendly building materials is to improve people's quality of life, which not only requires environmentally friendly building materials to have a long life but also cannot cause pollution during use. Fifth, discarded is different. When the environmental protection building materials need to be dismantled to complete the historical mission, they can be recycled and reused twice without causing any pollution to the environment. To sum up, during the implementation of the environmental protection strategy, construction companies need to quickly adjust their architectural design ideas, select green building technologies in project construction, innovate building design methods, improve building energy-saving control levels, and reduce project requirements for materials and energy, while meeting the technical needs of the public, it promotes the development of social and economic cycles. Workers in the current construction industry should increase their research on various green building technologies, and organically integrate green building design and architectural design according to engineering design requirements, while optimizing the level of architectural design, in order to achieve the purpose of controlling construction costs.

5. Conclusion

In a word, the development of green design not only needs to be vigorously applied in industrial production but also needs to take into account the reduction of construction investment, in order to achieve energy conservation and emission reduction in the construction process and effectively protect the human living environment. In recent years, with the rapid development of our country's economy, countless industrial plants have emerged, which has brought huge economic benefits to the construction industry, while a large number of construction enterprises have emerged; therefore, architectural design work has also been highly valued by people. Through analysis, the author finds that when constructing a factory building, the category should be considered first, so that designers can design the factory according to the actual situation of industrial production and the different forms of the factory building develop high-quality green engineering solutions. The integration and application of green building design concepts in architectural design is of great significance, not only to meet people's health and ecological needs for buildings but also to promote stable and sustainable development of society and achieve the goal of green building development. As an important part of engineering construction, architectural design must

Retraction

Retracted: Influence of Electrochemical Anticorrosion Technology on Concrete Structure and Performance

Journal of Chemistry

This article has been retracted by Hindawi following an investigation undertaken by the publisher [1]. This investigation has uncovered evidence of one or more of the following indicators of systematic manipulation of the publication process:

(1) Discrepancies in scope

(2) Discrepancies in the description of the research reported

(3) Discrepancies between the availability of data and the research described

(4) Inappropriate citations

(5) Incoherent, meaningless and/or irrelevant content included in the article

(6) Peer-review manipulation

The presence of these indicators undermines our confidence in the integrity of the article's content and we cannot, therefore, vouch for its reliability. Please note that this notice is intended solely to alert readers that the content of this article is unreliable. We have not investigated whether authors were aware of or involved in the systematic manipulation of the publication process.

Wiley and Hindawi regrets that the usual quality checks did not identify these issues before publication and have since put additional measures in place to safeguard research integrity.

We wish to credit our own Research Integrity and Research Publishing teams and anonymous and named external researchers and research integrity experts for contributing to this investigation.

The corresponding author, as the representative of all authors, has been given the opportunity to register their agreement or disagreement to this retraction. We have kept a record of any response received.

References

[1] Q. Yang, "Influence of Electrochemical Anticorrosion Technology on Concrete Structure and Performance," *Journal of Chemistry*, vol. 2022, Article ID 5702379, 7 pages, 2022.

Research Article

Influence of Electrochemical Anticorrosion Technology on Concrete Structure and Performance

Qin Yang [iD]

Henan College of Transportation, Zhengzhou, Henan 450000, China

Correspondence should be addressed to Qin Yang; 0107025@yzpc.edu.cn

In order to solve the problem of steel bar desensitization in island concrete, which leads to steel bar corrosion and greatly reduces the service life of structures, this work studies the influence of electrochemical corrosion prevention technology on the structure and performance of concrete. Through linear sweep voltammetry (LSV) and electrochemical impedance spectroscopy (EIS), the reinforcement in seawater sand concrete and ordinary concrete under two different chloride ion erosion modes was tested electrochemically, and then, its polarization curve and electrochemical impedance spectrum were obtained and analyzed. The experimental results show that the slope ratio of anode Tafel decreases significantly under the condition of steel bar passivation. The self-corrosion potential of reinforcement is −204 MV, which is much higher than −480 MV obtained from early testing. The self-corrosion potential obtained from the L3 polarization test tends to be stable after 84 days. As the test continues, the capacitive reactance arc in L1 and L2 medium-frequency region will gradually disappear with the continuous development of corrosion. *Conclusion*. This study explains the electrochemical mechanism and rate of reinforcement corrosion in seawater and sea sand concrete.

1. Introduction

Concrete is made from cementitious materials, aggregates, water, and admixtures in one proportion. Depending on the needs of the project, some necessary additions and additives can be added to improve the performance of the stone. Stone materials have a variety of raw materials, low cost, stone has good plasticity, is resistant to compression, and can be used in combination with steel. Therefore, stone is one of the most widely used materials in civil engineering [1]. With the continuous improvement of construction in China, the construction of major projects such as Hong Kong Zhuhai Macao Sea Crossing Bridge, Shanghai Port, and Qinghai Tibet Railway will not only lead to development of the country "Belt and Belt" but also the roadmap concept, along with China's global strength. However, the environment around these large-scale projects is difficult, and the operation seems to be poor due to the impact. For long-term environment and transportation, engineering investigation shows that the service life of marine concrete structures is about 50–100 years. However, many concrete structures enter the aging period after 20 years of service, resulting in steel corrosion and other damage [2, 3]. These losses result in high financial losses, and these losses are greater than the actual cost of the project. In 2015, the Chinese Academy of Engineering implemented a large-scale technical project "China's corrosion prevention" and conducted specialized research in China's infrastructure, transportation, and other sectors. According to research, in 2014, the total cost of corrosion in China was 2.13 trillion yuan, accounting for 3.34% of the annual total products in the country.

2. Literature Review

Yu et al. used EIS to study the influence on the corrosion behavior of reinforcement in reinforced concrete structures. It is found that the impedance of steel bar shows the capacitive reactance characteristics under high frequency and low frequency, corresponding to two time constants, corresponding to electric double layer and passive film,

respectively. At the same time, the arc of the low-frequency response capacitance is flat, which shows that the charging and discharging of the two-phase voltage is not charging and discharging the equipment. Electricity is ideal, and there is a difference between the two. This is mainly due to the unevenness of the steel surface. After soaking for some time, the tail diffusion appears in the region less often, and the exchange rate refuses to decrease by two orders of magnitude, which is due to the damage in villages of passive film, which makes it low. Prevent the effect of reinforcement; corrosion of reinforcement is greatly affected by enrichment. As the concentration increases, it is easier to damage the passive film and the corrosion improvement is faster; At the same time, the author also discussed the changes of electrochemical parameters such as corrosion potential, charge transfer resistance, and Warburg impedance in the process of reinforcement corrosion [4]. Dong et al. studied the EIS characteristics of the corrosion process of reinforcement in simulated concrete pore fluid. The experimental results show that with the addition of simulated concrete pore fluid, the change characteristics of reinforcement impedance obviously show three completely different stages. In the corrosion system studied, there is a critical value of concentration. When the concentration is lower than the critical value, the passive film will not be destroyed, and the surface of the steel bar is completely passivated. The electrochemical impedance spectrum shows the characteristics of a capacitive reactance arc with a large radius. When the concentration is higher than the critical value, the radius of capacitive reactance arc decreases significantly, while the inductive reactance arc appears in the low-frequency region, and the charge transfer resistance also decreases sharply. In the last stage, the electrochemical impedance spectroscopy shows the characteristics of two time constants. Steel bars show different electrochemical impedance characteristics in the passivation stability period, pitting induction period, and pitting development period, and the time constant also changes continuously. At the same time, the charge transfer resistance decreases with the increase of concentration and with the decrease of pH value, which indicates that the corrosion rate of reinforcement is affected by both pH value and concentration [5]. Yu et al. used EIS to study the corrosion behavior of reinforced concrete structures in solution. The experimental results show that at the beginning of immersion, a capacitive reactance arc with a large radius appears on the Nyquist diagram of the electrochemical impedance spectrum, which indicates that at this time, the passive film has a good protective effect on the reinforcement, and the surface passivation of the reinforcement is good. After soaking for a period of time, the Nyquist diagram of the electrochemical impedance of the reinforcement shows the characteristics of two capacitive reactance arcs, which indicate that the passivation meter on the surface of the reinforcement has begun to damage, and the reinforcement matrix has begun to corrode. The appearance of the low-frequency capacitive reactance arc indicates that the charge transfer process has begun to occur on the surface of the reinforcement, that is, the reinforcement has begun to corrode and dissolve. When the immersion reaches the later

stage, the Nyquist diagram shows the diffusion tail, showing the characteristics of Warburg impedance, which shows that at this time, the corrosion is no longer controlled by the charge transfer process, but by the diffusion process. In the whole process, the capacitive reactance arc radius of EIS decreases gradually, which indicates that the corrosion of reinforcement is becoming more and more serious. At the same time, the author also studied the influence of pH value and concentration on reinforcement corrosion [6]. Dong et al. used EIS to study the corrosion behavior of concrete in simulated rock pore fluid with different pH in dry-wet alternating conditions. According to the test, the corrosion process of steel bars can be divided into three stages, namely, passive film dissolution stage, corrosion activation stage, and corrosion product accumulation stage. When the pH value of the solution is 1, the reinforcement mainly shows uniform corrosion behavior, while when the pH value of the solution is 3 or 7, the reinforcement mainly shows small hole corrosion behavior. The results of EIS further confirmed the existence of three stages. In the first phase, the electrochemical resistance spectrum consists of high-frequency capacitive field arcs and low-frequency capacitive field arcs and exhibits the characteristics of two-phase continuous. At this time, the capacitive reaction arc of the final frequency is an indication of the electrochemical resistance of the passive film, and the capacitive reaction arc of the minimum frequency is the embodiment of the double voltage, set of transfer fees. In the second step, electrochemical impedance spectroscopy was observed three times, that was related to the continuity of the corrosion material in steel bars. In the third stage, the arc radius of the capacitance reaction in the medium frequency is much reduced, which indicates that the corrosion protection material continues to penetrate into the rock. Then, as cl concentration increases and pH value decreases and the corrosion improvement becomes more and more severe [7].

This paper examines the effect of chlorides carried on by the aggregation and mixing of water on the substrate and after the passivation of the adsorbent. Combined with the protection spectrum obtained by the experiment, an equivalent model of corrosion improvement occurs from chloride ions at different times, and then, the process of improvement corrosion in seawater and sand-reinforced rocks is caused by electrochemical exposure. Figure 1 shows the content and process of this form.

3. Research Methods

3.1. Material and Fabrication of Test Piece. The strength level of the concrete test is C30. The coarse aggregate for sea sand-reinforced rock samples is undesalinated sea rocks with a grain size of 5–20 mm. The fine aggregate was sieved sea sand with a fineness modulus of 2.8 and a chloride ion content of 0.24%. The mixed water is formed by the oceans. Coarse aggregates for ordinary strength design are ordinary crushed stone, the size of which is 5–20 mm. The fine aggregate is natural sand sieved with a fine modulus of 2.65, and the water mixture is tap water [8, 9]. The equations of the two mixtures are the same, see Table 1 for details. The tests are
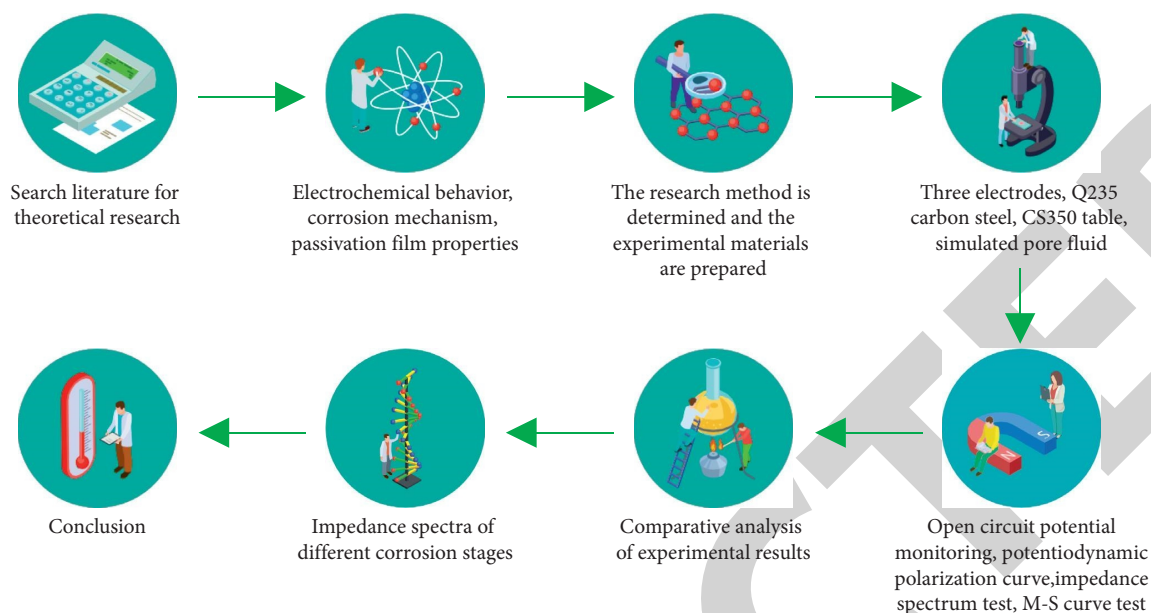
Figure 1: Article content process.

Table 1: The concrete mix proportion.

Cement/ (kg/m^3)	Water/(kg/m^3)	Sand/(kg/m^3)	Stone/(kg/m^3)	Water cement ratio
496.03	203.37	520.83	1279.76	0.41

concrete and marine rocks with dimensions × width × height = 100 mm × 100 mm × 100 mm. During casting, the rebar is embedded in the concrete electrode and 304 stainless steel is used as the auxiliary electrode. The thickness of the reinforcement protection layer is 2 cm, and the diameter between the reinforcement and stainless steel is 12 mm. A PVC pipe with a diameter of 10 cm is placed on the concrete structure and sealed with epoxy resin [10]. Inject the prepared artificial seawater into the PVC container for chloride ion penetration, connect the exposed part of the reinforcement and stainless steel with wires, and seal the remaining five surfaces of the concrete specimen with epoxy resin.

3.2. Grouping and Curing of Test Pieces. After the samples were designed and dried for 28 days, artificial seawater was put in, and a team used new film to close the hole to simulate an underwater environment. The other is to pour the ocean water after 2 days, dry it outside in the air for 3 days, and then put it in artificial water to simulate a tidal environment. The environmental performance measurement is $(20 \pm 5)^{\circ}$C. L1 and L2 are ocean rocks and L3 and L4 are white rocks and soak and dry with a wet-dry circle.

3.3. Electrochemical Test

3.3.1. Polarization Curve Test. A three-electrode system is used in electrochemical experiments. The instrument electrode is an electrochemical workstation AUTOLAB-AUT86742 developed by Wantong Co., Ltd., Switzerland,

and the material used for the electrode is saturated calomel electrode [11].

3.3.2. EIS Test. The measurement of electrochemical impedance spectroscopy was completed by the AUTOLAB-AUT86742 electrochemical workstation produced by Swiss Wantong Co., Ltd. The AC excitation signal adopts sine wave signal, the frequency range is 106~10–3 Hz, the amplitude is 10 MV, the reinforcement potential is controlled as open circuit potential during the test, and the test environment of the test piece is controlled at (20 ± 5) [12]. ZsimpWin software is used to process the impedance data of the specimen, analyze the structure of the equivalent circuit model and the parameters of each component, and use different equivalent circuits to fit according to the different corrosion conditions of the system.

4. Result Analysis

4.1. Polarization Curve Behavior. Figure 2 shows the polarization curve of corroded reinforcement in the test piece [13]. At this time, the polarization curve characteristics of the four specimens at this time are basically the same, and the curve has two obvious characteristics: first, the slope of the anode polarization curve is gentle, and the slope of the curve is small, that is, the slope β_a of the anode Tafel is significantly reduced when the reinforcement is passivated, and the anode dissolution reaction of the electrode can proceed smoothly, indicating that the reinforcement is currently in a corroded state. Second, it can be seen from the polarization curve that the self-corrosion potential E_{corr} of
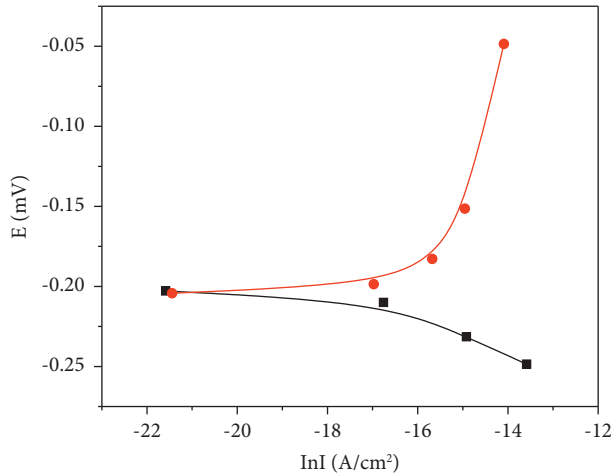
Figure 2: The rebar polarization curve of specimen L2 at 336 D.

Figure 3: Change of self-corrosion potential of reinforcement with time.

the reinforcement at this time is −204 mV, which is much higher than the −480 mV obtained in the early test.

Figure 3 shows the change in self-corrosion capacity of the test section. In the first part of the experiment, it was found that the self-corrosion resistance of L3 and L4 re-inforcements was lower than that of L1 and L2, which showed that the difference between the anode and cathode was larger and that the support is prone to corrosion. Seawater and sand concrete are obvious references of chlorides in aggregate and mixed water [14]. Reflected in the polarization curve, the self-corrosion capacity gradually increases, that is, the hardness of steel corrosion gradually increases in the next phase [15]. It is worth noting that the self-corrosion potential of L3 tends to be flat from 84 D. Combined with its impedance spectrum, we infer that since L3 is a specimen immersed in artificial seawater, it is difficult for oxygen to diffuse into it, and there is no chloride ion in the concrete mixing water and aggregate. In addition to the existence of the concrete protective layer, the chloride ion diffusion in the concrete is slow, and the thickness of the corrosion products generated by the re-action is also the thinnest among all the test pieces. For the time being, the protection effect on the reinforcement surface has not been formed, and the electrochemical corrosion on the reinforcement surface is still in the mode of large cathode and small anode. Therefore, the self-corrosion potential obtained from L3 polarization test tends to be stable after 84 days.

4.2. Electrochemical Impedance Behavior. In the study of electrochemical impedance spectroscopy, there are mainly two kinds of analysis diagrams, one is called Nyquist dia-gram, which is called Nyquist diagram for short, and the other is called Bode figure [16]. The vertical axis of the Nyquist diagram is the imaginary part Z_{Im} of the linear circuit impedance in the polarization system, and the horizontal axis is the real part Z_{Re} of the impedance. From the basic principle of EIS, we can get the real part Z_{Re} and the imaginary part Z_{Im} satisfy the relationship of the following formula:
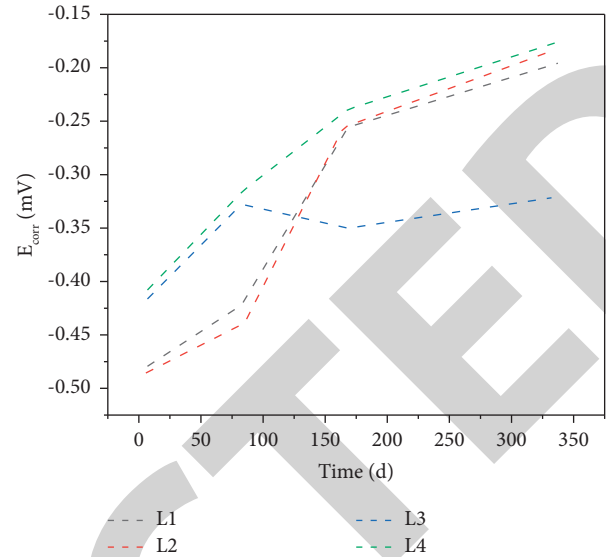
$$\left(Z_{Re} - \frac{R_t}{2}\right)^2 + Z_{Im}^2 = \left(\frac{R_t}{2}\right)^2, \tag{1}$$

where R_t describes the resistance of the equivalent element of the Faraday process on the electrode surface.

It can be seen that in the Nyquist diagram, this is a circle with $(R_t/2, 0)$ as the center and $R_t/2$ as the radius. It can be seen that the radius of the semicircle characterized in the impedance spectrum can be used to preliminarily compare the impedance of the equivalent capacitance element.

Figures 4(a) and 4(b) show the EIS diagram of the electrochemical impedance response of carbon steel elec-trode in seawater and sand concrete at different stages. Through comparison, we found that at this time, because the chloride ion in the artificial seawater has a shallow erosion depth, it has not contacted the reinforcement in the test piece at all, and the different erosion environment has not affected the development of the passive film on the surface of carbon steel for the time being. There are only chloride ions con-tained in the aggregate surface and mixing seawater around the reinforcement, so the Nyquist diagrams of L1 and L2 in the first week are completely consistent [17, 18]. In further experiments, the arc resistance of L1 and L2 capacitances in the frequency range was the difference of 84 days, indicating that during this time, the effects of differential corrosion of carbon steel begins to appear slowly. The fluidity of the whole process of corrosion protection and the migration capacity of the corrosion protection material is very weak, so the control level of the whole process is diffusion capacity of corrosion protective equipment [19].

Figure 5 shows the 84th day impedance spectrum of each specimen. By analyzing the images of L3 and L4, they found that capacitive reactance arcs also appeared in the mid-frequency range. Capacitive reactance arcing in the medium frequency is associated with pitting corrosion of steel sur-faces [20]. Compared with Figure 1, as the test continues, the capacitive reactance arc at intermediate frequency L1 and L2

(a)

(b)
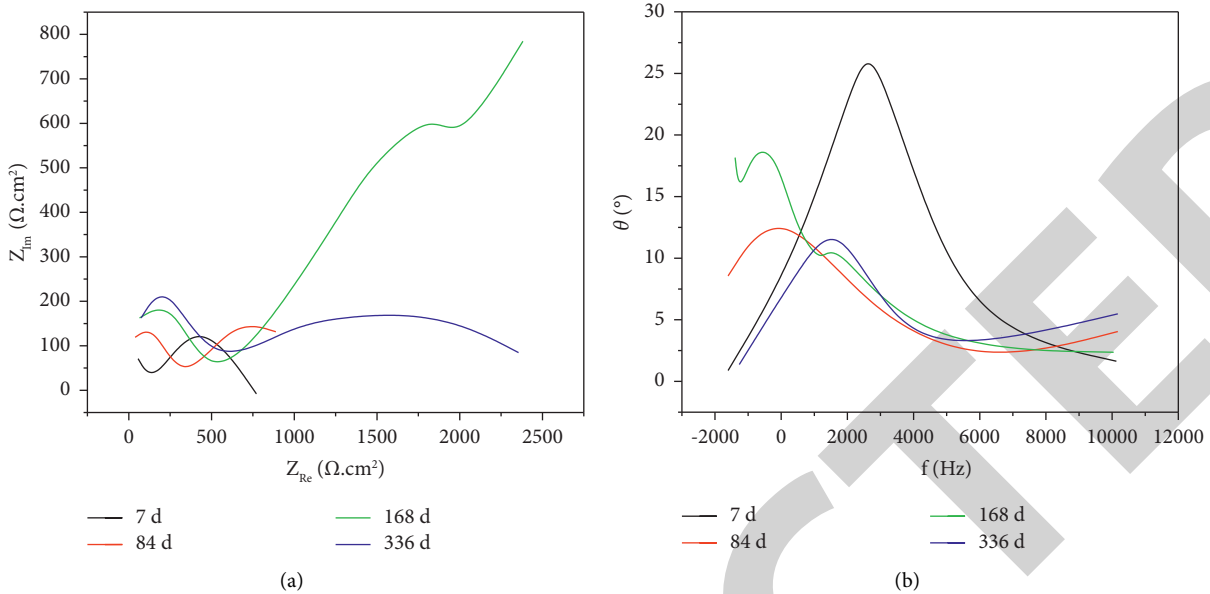
Figure 4: Nyquist diagram and Bode diagram of specimen L2.
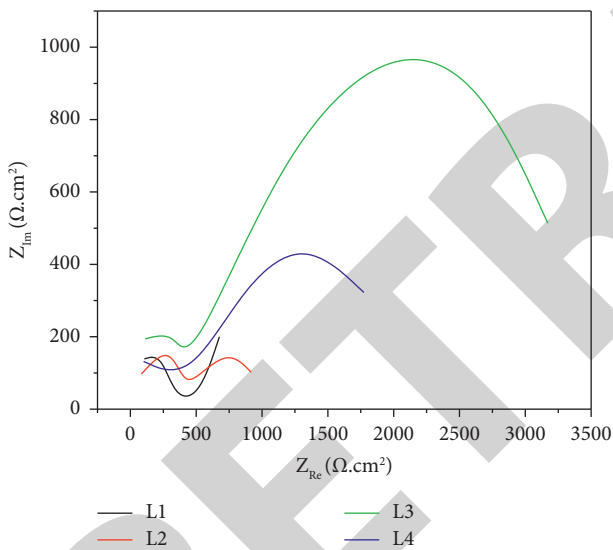
Figure 5: Nyquist diagram of the test piece at 84 D.

gradually disappears with continuous corrosion. We conclude that the occurrence of capacitive reactance arc in this section is due to the Faraday process of dissolution of iron at the bottom of the corrosion hole on the surface of the steel bar. In the first stage, there is high chloride content in the test strips and water mixture, which has a positive effect on the passive film of carbon steel. At 84 days, the effect of pitting on the surface of the steel bar begins to develop everywhere, the effect of cathode large and small anode is weak, the anode current speed of corrosion prevents the gradual decrease, and the effect of ohmic decline gradually weakens. The capacitive field arc in the medium-frequency region of the seawater and sand group is shown in the figure before disappearing, and the resistance in the low-frequency region is simultaneously lower than that of the white rock pile.

It is worth noting that we can clearly see from Figure 5 that while the capacitive reactance arc radius in the low-frequency region of L1 is smaller than L2, L3 is larger than L4. The electrochemical characterization of the above two points is that the capacitive reactance arc radius is larger [21].

4.3. Equivalent Circuit Model. From the chlorine salt corrosion Nyquist diagram above, when the armature is in the passive state (day 7), the Nyquist diagram has two capacitive reactance arcs, i.e., two constant times. When the armature is in the activated state (day 84), the capacitive reactance arc in the medium-frequency range, i.e., three times constant, is added [22]. Based on this, we conclude that the equation model in the two states is shown in Figures 6(a)-6(b), respectively.

Following the model of the experimental model and previous experience, we believe that in a similar picture of this experiment, R1 represents the solution, R2 represents the protection of the protective layer, and R3 represents the exchange rate of the protective material. The process is complete. Reinforcement at the bottom of the borehole: R4 represents the conduction resistance of two electrical layers on the surface of the reinforcement, and W represents the diffusion-related element (Warburg resistance) in the same the circuit, simulating the diffusion control effect. At this time, the passive film at the center of the support is broken, and it changes from a stable passive to a corrosively state. At this point, controlling the steps in the entire corrosion protection process is not a substitution process, but rather a major change process of the corrosion protection process or product [23, 24]. The experimental receiving impedance spectra shows that the image of most capacitive reactance arcs is flat rather than the ideal semicircle, which is called the dispersion effect. In the case of hard rocks, this phenomenon is related to the variability of the metal surface and the
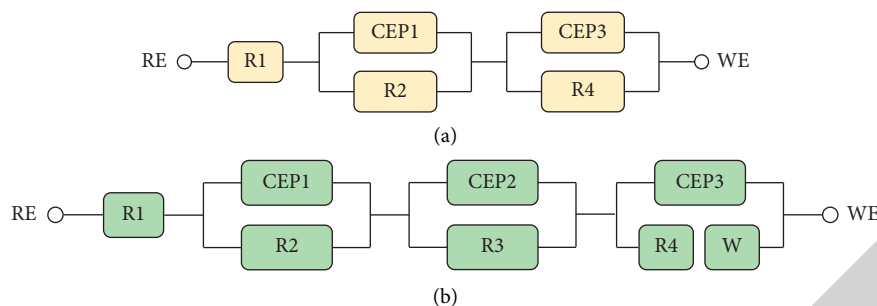
Figure 6: Equivalent circuit model under passivation and corrosion.

polyphase structure differences of the rock itself. Therefore, we use the angle-to-angle ratio (CPE) to simulate the rate and output behavior of two-layer electrodes to change the equilibrium of the electronic devices [25–30].

5. Conclusion

To investigate the special electrochemical process of corrosion improvement in seawater sand concrete in marine environment, this study used linear voltammetry (LSV) and electrochemical impedance spectroscopy (EIS) to elucidate the electrochemical mechanism and the rate of corrosion improvement in seawater sandstone by two yam, compared with ordinary stones, the following points can be drawn.

(1) The self-corrosion potential of seawater and sea sand concrete specimens increases gradually under two chloride ion corrosion modes, indicating that the subsequent corrosion reaction is more difficult with the aggravation of reinforcement corrosion degree. At the same time, the self-corrosion potential of steel bars in ordinary reinforced concrete in the soaking state gradually tends to be flat, indicating that it is always in a state of easy corrosion.

(2) When the steel bar in the rock is in a passive state, there are two capacitive reaction arcs, the capacitive reaction arc in the high-frequency region is the protective layer of rocks and the capacitive reaction arc in the low-frequency region is determined. Charge and release characteristics of two-layer electrodes on the surface of electrochemical steel bar. There are three capacitive reactance arcs in the Nyquist diagram, where the reinforcement in the sea rock and sea sand first corrodes, and the significance of the capacitive reactance arc in the high-frequency region, and in rare cases, it is the same, and the second new capacitive reactance arc in the medium-frequency region is an electrochemical characteristic of pitting corrosion.

(3) The arc radius of the reaction capacity in seawater and sand is always lower than that of normal rock, indicating that the chloride ions carried by its aggregates and water interactions mixed have a significant impact on the formation of weak rocks. The film on the surface of the armature is reflected in the parallel circuit, that is, the conduction also on the surface of the armature is reduced, and the anodic oxidation reaction is easier.

Data Availability

The data used to support the findings of this study are available from the corresponding author upon request.

Conflicts of Interest

The author declares that there are no conflicts of interest.

References

[1] T. Yu, J. F. Chen, J. Xiao, K. Zhang, J. Xiao, and Q. Zhang, "Experimental study on stress-strain curves of seawater sea-sand concrete under uniaxial compression with different strain rates," *Advances in Structural Engineering*, vol. 24, no. 6, pp. 1124–1137, 2021.

[2] V. Bhashya, G. Ramesh, S. S. Kumar, and B. Sangoju, "Performance evaluation of concretes by using recycled aggregate," *Indian Concrete Journal*, vol. 94, no. 1, pp. 51–57, 2020.

[3] G. Liu, B. Shan, D. Lai et al., "Seismic performance of seawater and sea sand concrete-filled ultra-high performance concrete tubes under low-cycle reversed lateral loading," *Advances in Structural Engineering*, vol. 24, no. 6, pp. 1221–1234, 2021.

[4] Y. L. Li, X. L. Zhao, R. S. Raman, Y. L. Li, X. L. Zhao, and R. S. Raman, "Durability of seawater and sea sand concrete and seawater and sea sand concrete–filled fibre-reinforced polymer/stainless steel tubular stub columns," *Advances in Structural Engineering*, vol. 24, no. 6, pp. 1074–1089, 2021.

[5] Z. Dong, G. Wu, X. L. Zhao, H. Zhu, and J. L. Lian, "The durability of seawater sea-sand concrete beams reinforced with metal bars or non-metal bars in the ocean environment," *Advances in Structural Engineering*, vol. 23, no. 2, pp. 334–347, 2020.

[6] Y. Huang, J. Xiao, L. Qin et al., "Mechanical behaviors of gfrp tube confined recycled aggregate concrete with sea sand," *Advances in Structural Engineering*, vol. 24, no. 6, pp. 1196–1207, 2021.

[7] Z. Dong, G. Wu, H. Zhu, Y. Wei, X. L. Zhao, and X. Shao, "Bond and flexural performance of basalt fiber–reinforced polymer bar–reinforced seawater sea sand glass aggregate concrete beams," *Advances in Structural Engineering*, vol. 24, no. 15, pp. 3359–3374, 2021.

[8] X. l. Fan, S. j. Gu, X. Wu et al., "Critical shear crack theory-based punching shear model for frp-reinforced concrete slabs," *Advances in Structural Engineering*, vol. 24, no. 6, pp. 1208–1220, 2021.

Research Article

Green Power Generation by Microbial Fuel Cells Using Pharmaceutical Wastewater as Substrate and Electroactive Biofilms (Bacteria/Biocarbon)

Ivonne L. Alonso-Lemus (ID),[1] **Carlos Cobos-Reyes,**[2] **Mayra Figueroa-Torres** (ID),[3]
Beatriz Escobar-Morales (ID),[4] **K. Kunhiraman Aruna** (ID),[5] **Prabhu Akash,**[5]
Fabian Fernández-Luqueño (ID),[2] and **Javier Rodríguez-Varela** (ID)[2]

[1]*Conacyt-Cinvestav-IPN Unidad Saltillo, Sustentabilidad de Los Recursos Naturales y Energía, Ramos Arizpe, Coahuila C.P. 25900, Mexico*
[2]*Sustentabilidad de Los Recursos Naturales y Energía, Cinvestav Unidad Saltillo, Av. Industria Metalúrgica, 1062, C.P. 25900, Ramos Arizpe, Coah, Mexico*
[3]*Universidad Autónoma de NL, Facultad de Ingeniería Civil, San Nicolás de Los Garza, Nuevo León 66455, Mexico*
[4]*Conacyt, Centro de Investigación Científica de Yucatán, Col. Chuburná de Hidalgo, Calle 43, No. 130, Mérida, Yucatán C.P. 97200, Mexico*
[5]*Rathinam Research Center, Rathinam Technical Campus, Rathinam Techzone, Pollachi Main Road, Eachanari, Coimbatore – 641021, Tamilnadu, India*

Correspondence should be addressed to Ivonne L. Alonso-Lemus; ivalemus@gmail.com

In this work, electroactive biofilms of *Bacillus subtilis* (*B. subtilis*) or *Escherichia coli* (E. *coli*) were supported on functionalized biocarbon (AB7-F), which was synthesized from waste leather and was used as catalysts to develop bioanodes for microbial fuel cells (MFCs). This way, bioanodes were fabricated and further evaluated in a three-electrode cell using pharmaceutical wastewater (PWW) as substrate. The electrochemical measurements showed a higher performance of the bioanode based on AB7-f+ *B. subtilis* to oxidize organic matter from PWW. The polarization curves in the dual-chamber MFC showed that AB7-f+ *B. subtilis* bioanode can generate an open circuit voltage of 602 mV and a power density of 77 mW m^{-2}. During long-term tests of the MFC, a variation in performance was observed, with a maximum of 96.3 mW m^{-2} on day 7. Such variation was attributed to the development of more stable biofilm as well as consumption of some compounds metabolized by bacteria grown on the bioanode. The results showed that AB7-f+ *B. subtilis* can be used as bioanode for MFCs with PWW as substrate removing around 45% of the chemical oxygen demand (COD).

1. Introduction

Water pollution has emerged as a life-threating global problem due to rapid growth of urbanization, industrialization, and irrational utilization of water resources. All the effluents from different types of industries like fertilizers, textiles, diary processing, petrochemical, beverages, and pharmaceutical have toxicated the water to such an extent that all lives on this planet are affected. In this respect,

industrial wastewater treatment is a big challenge issue. It is believed that nearly 80–90% of all industrial wastewater in developing countries is discharged untreated, causing severe environmental damage [1]. Among the various types of effluents, the one from the pharmaceutical must be treated with utmost vigilance due to the presence of organic pollutants and drug components [2]. In addition, the presence of pharmaceuticals in wastewater does not only come from industrial effluents, it is also found in domestic wastewater

[3]. Even though there are various methods for the treatment of pharmaceutical wastewater (PWW), which can be classified as physical, physicochemical, chemical, and biological methods, but all are accompanied with various challenges with low efficiency or economic infeasibility [4]. On the other hand, PWW treatment and simultaneously generating energy from it will support the waste management system, alongside sustainable means of energy generation. A vast number of research is going on bioelectrochemical systems (BES) [5]. Microbial fuel cell (MFC) has attained considerable remark due to the advantage of cost-effectiveness, high-biodegradability, and eco-friendly.

The MFCs transform the chemical energy into electrical energy by electrochemical active microorganism, known as exoelectrogens. In the anode chamber, organic matter is oxidized, producing electrons and protons. Electrons are transferred to the cathode chamber through an external circuit, where they react with oxygen and protons to form water [6]. Since electroactive bacteria can remove organic matter while generating electrical energy simultaneously, researchers focus the MFC as an alternative electrochemical technology for wastewater treatment and a sustainable energy resource. Despite this, MFCs' actual deployment has been hampered by their limited power output and expensive fabrication costs [7]. Recent research proves that modification in anaerobic anode chamber (e.g., active microorganism, bioanode configuration, and use of carbon-based catalysts) improve the total output power and performance. Since, the wastewater substrate is present in the anode chamber, the bioanode must be extremely active and electrochemically stable in wide range of pH. In this regard, a comprehensive variety of carbon material-based bioanodes has been evaluated for MFC applications [8, 9]. Biomass-derived biocarbons are rich in carbon with self-doped heteroatom, inexpensive, and eco-friendly with interesting surface chemistry and structural advantage over other precious metal material that have been used as catalysts in this application. Biocarbons from bamboo, cotton textiles, bananas, neem wood, silk cocoon, egg, and bread have been successfully demonstrated in bioanodes for MFC [8].

On the other hand, the growing interest in the development of high-efficient BES has led to the study of various exoelectrogenic cultures [9]. For example, anaerobic bacteria such as *Rhodoferax ferrireducens* and *Geobacter sulfurreducens* are studied as active microorganisms for MFC applications. When they meet exocellular solid substrates, they use outer membrane redox proteins (e.g., cytochromes) to mediate electron transfer [10]. Moreover, other bacteria like *Pseudomonas aeruginosa* and *Shewanella putrefaciens* create redox molecules as phenazine and quinones as electron carriers [11]. On the other hand, *Escherichia coli* (E. *coli*) create artificial redox molecules for extracellular electron transfer to solid substrates, and *Bacillus subtilis* (B. *subtilis*) has the advantage to be electrochemically active towards oxidation on wide range of pH in addition to being resistant to the presence of several antibiotics [12].

In our research group we have carried out previous studies for the treatment of PWW using *B. subtilis* growing on carbon-based catalyst, which improves the overall performance of MFC in terms of electricity generation and COD removal. In this concern, Duarte-Urbina et al. [12] reported decrease in chemical and biological oxygen demand (COD & BOD), total dissolved solids (TDS), and pH from 9.2–8.7 in PWW for 14 days of treatment in a dual-chamber MFC. In that work, bioanode is composed of onion waste-derived biocarbon+ *B. subtilis* showing a maximum power density (Pcell) of $30.72 \, mW \, m^{-2}$. Meanwhile, García–Mayagoitia et al. [13] reported stable bioanodes composed of functionalized ordered mesoporous carbon (f-OMC) + *B. subtilis* using PWW as a substrate (pH = 9.6). With this bioanode configuration, an open circuit voltage up to 0.62 V is obtained, with maximum current density and power density (Pcell) of $854 \, mA \, m^{-2}$ and $105 \, mW \, m^{-2}$, respectively.

In this work, we report the performance of dual-chambered H-type MFC, using a novel bioanode made with functionalized waste leather-derived biocarbon (AB7-F) plus *E. coli* and *B. subtilis* used separately as electrochemically active microorganisms and PWW as organic substrate. Whilst in the cathode chamber, a commercial Pt-based catalyst electrode and electrolyte of O_2-satured aqueous KOH solution (pH = 9.7) were used. An alkalinized Nafion membrane was used as a separator between anode and cathode chambers.

2. Experimental

2.1. Biocarbon Synthesis (Catalyst). The biocarbon was obtained based on a previous methodology reported by Alonso–Lemus et al. [14]. First, 10 g of leather waste slices were cleaned with ethanol (C_2H_5OH, Jalmek, 96%), then they were pyrolyzed at 700°C for 90 minutes at a heat rate of $10°C \, min^{-1}$ in N_2 atmosphere (Infra, 99.99%). The carbonized slices were pulverized and mixed with potassium hydroxide (KOH, Fermont, 87.5%) in a weight ratio of 2 : 1. Afterwards, this mixture was activated at 750°C for 90 minutes, at a heat rate of $8°C \, min^{-1}$ in N_2 atmosphere and cooled down to room temperature. Then, a black powder was recovered to wash it with an aqueous solution of $1 \, mol \, L^{-1}$ of hydrochloric acid (HCl, Sigma Aldrich, 37%) and dried overnight at 80°C. The biocarbon obtained was labeled as AB7.

AB7 was functionalized by intermittent microwave heating (IMH) to improve its biocompatibility [13] as follows: 300 mg of AB7 were dispersed in 30 mL of $0.15 \, mol \, L^{-1}$ methanol (CH_3OH, Sigma Aldrich, 99.8%) aqueous solution by sonication for 30 minutes. Then, the dispersion was stirred for one hour more and transferred to a modified homemade microwave maintaining magnetic stirring. The thermal treatment by IMH was for 8 minutes with 25 s on/ 15 s off pulses. The functionalized biocarbon was labeled as AB7-f.

2.2. Bioanodes Construction. As shown in Figure 1, the bioanodes were composed of three layers: support, catalytic layer, and biofilm. Carbon cloth was used as a support with a geometric area of $2 \, cm^2$ ($1 \times 2 \, cm$). A copper wire was fixed
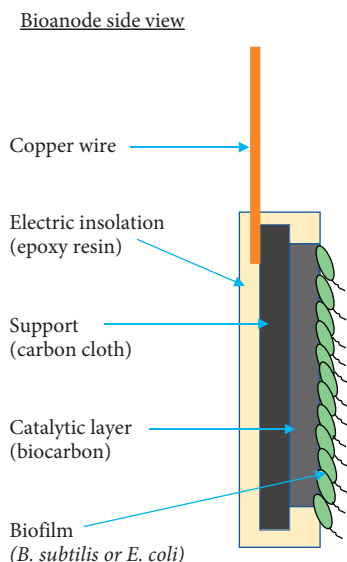
FIGURE 1: Bioanode side view with a configuration of support + catalysts + biofilm.

on its back using silver ink, then an area of $1\,cm^2$ of the carbon cloth was delimited with epoxy resin. Afterwards, the catalytic layer was deposited on the delimited area by drop-by-drop method (catalyst loading = $5\,mg\,cm^{-2}$). The catalytic ink had the following composition: 5 mg of catalyst, $64\,\mu L$ of Nafion® 117 solution (Aldrich 5 wt. %), and $64\,\mu L$ of 2-propanol (C_3H_7OH, Sigma Aldrich, 99.5%). The anodes (support + catalytic layer) were stored in a desiccator until to use them.

For the biofilm layer two bacteria were used separately: *Bacillus subtilis* (*B. subtilis*), which was obtained from the Cinvestav National Collection of Microbial Strains and Cell Cultures, whilst *Escherichia coli* (*E. coli*) ATCC® 25922™ was supplied by Microbiologics®. Inoculation of the strains from their reception until their use for the growth of the biofilm can be consulted in supplementary information. For the biofilm grown on the anodes, first, bacteria were inoculated at 30°C for 3 days using an orbital incubator (Vichi, INC-C); then the anodes were immersed into 50 mL of sterile broth media contained in an Erlenmeyer flask and inoculated for 6 days at 30°C in the orbital incubator (Figure S1(a)).

2.3. Pharmaceutical Wastewater (PWW) Substrate.
The PWW was provided by a local pharmaceutical industry. The PWW was collected and stored at -18°C to preserve it until its use. The physicochemical features of the PWW are shown in Table 1.

2.4. Physicochemical Characterization.
Morphology and elemental composition of the bioanodes were determined using a scanning electron microscope (SEM) Philips XL 30 ESEM with an EDAX detector. Moreover, the structural features of the catalysts were analyzed using a DXR-RAMAN thermo scientific spectrometer (He–Ne laser of 633 nm,

TABLE 1: Physicochemical parameters of the PWW used as substrate.

Parameter	Value
pH	9.2
Conductivity	$2870\,mS\,m^{-1}$
Chemical oxygen demand (COD)	$27{,}603\,mg\,L^{-1}$
Biochemical oxygen demand (BOD)	$10{,}433\,mg\,L^{-1}$
Nitrate nitrogen (N–NO$_3$)	$6.13\,mg\,L^{-1}$
Total phosphorus	$93.91\,mg\,L^{-1}$
Sulfate ion (SO$^{2-}_4$)	$1{,}161\,mg\,L^{-1}$
Total alkalinity	$3{,}574\,mg\,L^{-1}\,CaCO_3$
Chloride	$10{,}616\,mg\,L^{-1}$
Total dissolved solids (TDS)	$30{,}540\,mg\,L^{-1}$
Total suspended solids (TSS)	$3{,}320\,mg\,L^{-1}$

0.3 mW). Meanwhile, their functional groups were determined using a Bruker Tensor II equipment with ATR, in a range of 4000 to $500\,cm^{-1}$ with a resolution of $4\,cm^{-1}$. In addition, an ASAP 2050 equipment (Micrometrics, USA) was used to determine the textural properties of the catalysts. Prior to the measurements, the samples were degassed for 14 h at 220°C, then nitrogen was used as absorbate.

2.5. Electrochemical Measurements

2.5.1. Half-Cell.
The electrochemical measurements were performed using a Bio-Logic VSP-300 potentiostat in a three-electrode cell configuration. A platinum wire and a Ag/AgCl (NaCl $3\,mol\,L^{-1}$, 0.209 V vs. SHE) were used as counter and reference electrodes, respectively. The work electrodes (WE) were the anodes (support + catalyst) and bioanodes (support + catalyst + bacteria) previously made. Prior to the electrochemical test, the WE were stabilized for 18 hours into the N_2-saturated PW at room temperature, which was used as substrate. The Cyclic Voltammetry (CV) curves were obtained in a potential range of -0.70 to 0.45 V vs. the reversible hydrogen electrode (RHE) at a scan rate of $20\,mV\,s^{-1}$. For comparison purposes, CVs of the support and support + bacteria were obtained.

All the potential reported in this work were converted to the RHE voltage (E_{RHE}) using the following equation [15]:

$$E_{RHE} = E + 0.059\,pH + E_{ref}, \tag{1}$$

where the pH of the PWW is 9.2, E_{ref} is the potential of the reference electrode versus the standard hydrogen electrode (SHE), and E in the potential that is wanted to convert to E_{RHE}.

2.5.2. Microbial Fuel Cell Test.
The most active bioanode was tested in a dual-chambered H-type MFC (Figure S1(b)). The anode chamber contained 240 mL of N_2-saturated PW and the bioanode previously stabilized for 18 hours. Whilst in the cathode chamber a commercial Pt-based catalyst electrode (Etek, 20 wt. % Pt/C, catalyst load = $2\,mg\,cm^{-2}$) and electrolyte of O_2-saturated aqueous KOH solution (pH = 9.7) were used. A Nafion® 117 (DuPont) membrane was used as separator, which was previously alkalinized as was described in supplementary information [16]. First, the open circuit

potential (E_{OC}) was determined, then, the cell potential (E_{cell}) was registered at different external resistance values (R_{ext} = 0.01, 1, 1.2, 5, and 10 kΩ). The cell current (I_{cell}) was calculated by the Ohm's law (2)

$$I_{cell} = \frac{E_{cell}}{R_{ext}}. \tag{2}$$

Then, the current density (j_{cell}) was calculated normalizing the I_{cell} respect to the geometrical bioanode area (A_{bio}). Thus, the polarization curve (E_{cell} vs. j_{cell}) plots were obtained. Finally, the power density (P_{cell}) was calculated as follows (3):

$$P_{cell} = \frac{E_{cell}^2}{R_{ext} \cdot A_{bio}}. \tag{3}$$

Both, the polarization (E_{cell} vs. j_{cell}) and power density (P_{cell} vs. j_{cell}) plots were obtained at day 0, 1, 7, and 14.

3. Results and Discussion

3.1. Catalysts Physicochemical Properties. Figure 2(a) shows the chemical composition of the catalysts and the raw material used for their synthesis (leather), which was determined by energy-dispersive X-ray spectroscopy (EDS). As can be seen, leather was composed mainly of carbon (69.62 wt. %) and oxygen (18.89 wt. %), in addition to some heteroatoms like nitrogen (4.13 wt. %) and sulfur (3.10 wt. %). Also, other elements in less concentration were detected (e.g., Ca, Na, Mg, and Si). As it was expected, the carbon concentration of both AB7 and AB7-f catalysts increased ($C \sim 89$ wt. %) and the oxygen decreased ($O \sim 7$ wt. %) respect to leather due to pyrolysis treatment. Further, it was observed that the remaining concentration of nitrogen ($N \sim 2$ wt. %) and sulfur ($S \sim 0.1$ wt. %) was lower for both catalysts than leather, which implies that by the synthesis route proposed in this work, heteroatom self-doped catalysts could be obtained. On the other hand, it was observed that elements contained in leather in low concentration were removed from both AB7 and AB7-f, where only Mg was detected in concentrations of 0.17 and 0.14 wt. %, respectively. The chemical composition values also can be found in Table S2; meanwhile, Figure S2 shows the elemental mapping of the catalysts which demonstrate that both catalysts had a homogeneous distribution of the elements.

Figure 2(b) shows the typical morphology of leather's collagen fibers about a micron in diameter. Interestingly, the morphology of the collagen fibers was lost after the carbonization and activation treatment to which AB7 was subjected, as shown in Figure 2(c). As can be seen, collagen fibers sinterized until forming 3D particles interconnected by macropores. However, AB7-f revealed carbon particles of smaller size than the AB7 particles, which indicates that microwave heating could promote the reduction in particle size, as has been reported [12, 13].

On the other hand, the catalysis' structural and textural features were studied (Figure 3). Raman spectroscopy of AB7 and AB7-f are shown in Figures 3(a) and 3(b), respectively.

Two broad bands normally observed in amorphous carbon materials were detected, the first one at ≈ 1330 cm^{-1}, named D-band, which can be associated to defects and disorder in the graphitic lattice. The second signal at ≈ 1600 cm^{-1}, named G-band, is normally associated with sp^2 hybridization. The I_D/I_G ratio was calculated from the deconvoluted peaks showing little variation between the values found for AB7 ($I_D/I_G = 1.58$) and AB7-f ($I_D/I_G = 1.50$). However, when the ratio between D2 interband (≈ 1200 cm^{-1}) and G band was calculated, a difference was observed between AB7 ($I_{D2}/I_G = 1.12$) and AB7-f ($I_{D2}/I_G = 0.46$). The D2 interband, also called D* has been attributed sp^2-sp^3 bond in carbon lattice [17], and when its value decreases it can be assumed that the crystallinity in the nanodomains increases, therefore, AB7-f has a more crystalline nanodomain structure than AB7. This occurs because microwave heating promotes the release of carbon and oxygen from the carbon material, generating small conjugated graphitic domains, which improves crystallinity [18]. In addition, D3 interband (≈ 1500 cm^{-1}) can be related to small functional groups and SP2-bonded forms, and it has been reported that when D3 interband intensity decrease the crystallinity increase [19], which is in good agreement with our results.

Figure 3(c) shows the nitrogen adsorption/desorption isotherms of the catalyst. According to the international union of pure and applied chemistry (IUPAC) classification [20], the adsorption isotherms of both AB7 and AB7-f are type IV(a), which are commonly observed for mesoporous materials with pores greater than 4 nm. In addition, both isotherms show a hysteresis loop H4 type, indicating the filling of micropores. Therefore, it can be assumed that AB7 and AB7-f are micro-mesoporous carbon materials [21]. The specific surface area was calculated by Brunauer–Emmett–Teller method (SSA$_{BET}$). As it was expected, high surface area values were obtained for AB7 (SSA$_{BET}$ = 1890 m^{2}g^{-1}) and AB7-f (SSA$_{BET}$ = 1984 m^{2}g^{-1}) because KOH was used as a chemical activating agent and it mainly promotes the formation of micropores generating high surface area carbons. Moreover, the average pore size of AB7 and AB7-f was of 4.4 nm and 5.5 nm, respectively. The slight increase of 4% in SSA$_{BET}$ of AB7-f with respect to AB7, and the increase in the average pore size is because, as already mentioned, during microwave heating, carbon and oxygen were expelled, generating the formation of additional pores and the increase in the average pore size. On the other hand, Figure 3(d) shows the Fourier–transform infrared (FTIR) spectra of the catalysts. As can be seen, there are two broad peaks in the range of 1400–1600 cm^{-1} and 1650–1900 cm^{-1}. In the first region, the signal associated to the combined stretching of $C=C$ and C–C of aromatic compounds was observed. Meanwhile, in the second region, the corresponding $C=O$ bond can be found. The presence of C–H bond at ≈ 2600 cm^{-1} generated by aldehyde type bond also was detected [22, 23].

3.2. Bioanodes Morphology and Performance in Half-Cell. Figure 4 shows the morphology of bioanodes with different configurations. The micrographs in Figures 4(a) and 2(b)

(a)

(b)

(c)

(d)
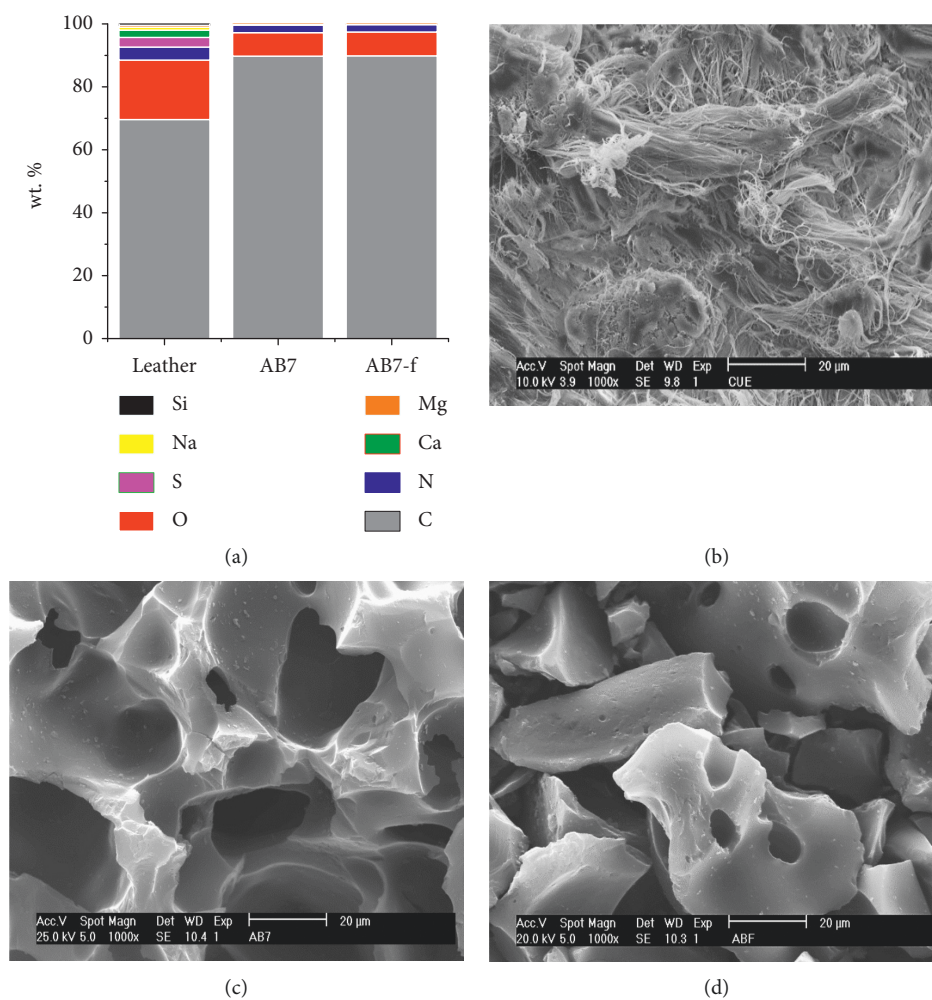
Figure 2: (a) Chemical composition of leather and catalysts determined by EDS and morphology of (b) leather, (c) AB7, and (d) AB7-f.

(a)

(b)
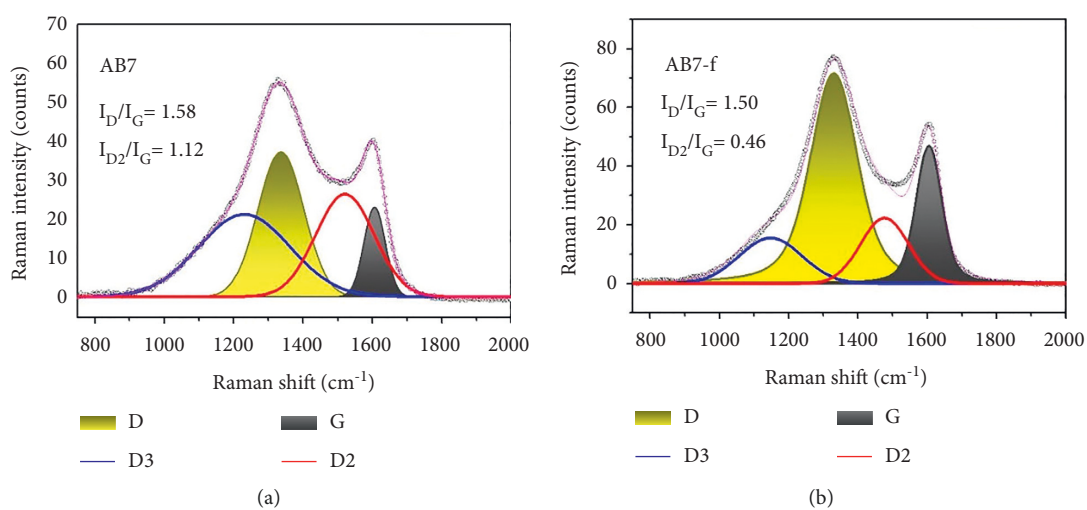
Figure 3: Continued.
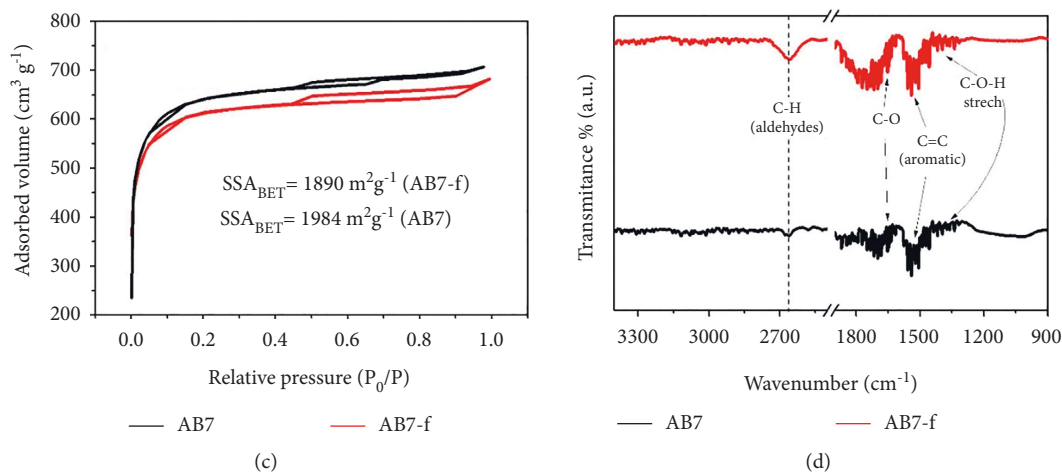
FIGURE 3: Structural and textural features of the catalysts. Raman spectroscopy of (a) AB7 and (b) AB7-f, (c) adsorption/desorption isotherms, and (d) Fourier-transform infrared spectra of the catalysts.

show the bioanodes with $S + AB7 + E.\ coli$ and $S + AB7$-$f + E.\ coli$ configurations, respectively. As can be seen, groups of bacteria are observed on the surface of the catalysts with a quasi-spherical shape, which may indicate that they are in an early stage of development, since the characteristic morphology of $E.\ coli$ is that of bacilli (smaller than those of $B.\ subtilis$). Despite the presence of these bacteria, an inhomogeneous growth of biofilm on the surface of the catalytic layer has been observed. However, for the bioanode with the $S + AB7$-$f + E.\ coli$ configuration, a greater growth of the bacteria is observed compared to the non-functionalized catalyst (Figure 4(b)). Meanwhile, the bioanode with $S + AB7 + B.\ subtilis$ configuration (Figure 4(c)) shows the presence of some isolated bacilli on a smooth surface. That change in surface texture can be attributed to polysaccharides excreted during biofilm formation [24]. Figure 4(d) shows the bioanode with $S + AB7$-$f + B.\ subtilis$ configuration. It should be noted the outstanding biocompatibility of the bioanode, the growth of the $B.\ subtilis$ biofilm on this catalyst is abundant, forming a reticular structure that almost completely covers the surface of the catalyst. Interestingly, these results indicate that functionalized catalysts improve biocompatibility, which is in good agreement with observations from our previous studies [12, 13].

The electrochemical performance of all bioanodes was evaluated in half-cell system. First, the cyclic voltammetry (CV) curves of support (S) + bacteria using N_2-saturated PWW as substrate were obtained (Figure 5(a)). In general, the electrochemical behavior of the supports with and without biofilm is very similar. The sweep in the cathodic direction had shown an increase in the current density (j) near to 0.45 V/RHE, which is more notable for $S + B.\ subtilis$. These results confirm the need to use a catalyst to promote the generation of redox couples.

In Figure 5(b) the CV of the bioanode $S + AB7$ has shown a similar shape to those CVs of Figure 5(a), although with highest values of j in the same potential range, this increase

in j can be attributed to the effect of the catalyst AB7, which increases the electrode-electrolyte interaction due to its high surface area [25]. Whilst for $S + AB7 + B.\ subtilis$ bioanode j decreases suggesting low electroactivity. Furthermore, the VC of the $S + AB7 + E.\ coli$ bioanode shows a quasi-capacitive behavior indicating a better bioelectrochemical interaction with organic matter of PWW than the previous two bioanodes.

In Figure 5(c), the VC of the anode $S + AB7$-f also shows a quasicapacitive behavior, which suggests catalytic activity of AB7-f in PWW. Remarkably, the bioanode $S + AB7$-$f + B.\ subtilis$ generates the highest values of j, with a capacitive behavior. This indicates a high catalytic activity of this bioanode to oxidize the organic matter in the PWW. In addition, this result suggests a positive effect of the functionalization treatment by modifying the surface of the catalyst, and thus, improving the biocompatibility. In contrast, the VC of the bioanode $S + AB7$-$f + E.\ coli$ has lower j values than $S + AB7$-$f + B.\ subtilis$, due mainly to the low biocompatibility between AB7-f and $E.\ coli,$ which implies a low electroactivity to oxidize PWW organic matter. In the case of this study, the electrochemical behaviors observed in Figure 5 can be attributed to the nature of both catalysts (chemical composition, morphology, specific area, structure, and texture) since it has been reported that there is not a direct relationship between the amount of biofilm and the current density generated [26]. It has also been reported that the presence of oxygenated groups in the catalysts where the biofilm grows can increase the catalyst-bacteria biocompatibility [27, 28].

3.3. Bioanodes Morphology and Performance in Half-Cell. With the results obtained from the electrochemical characterization in half-cell, it was decided to use the bioanode $S + AB7$-$f + B.\ subtilis$ for the electrochemical characterization and PWW remediation tests in a dual-chamber MFC. Figure 6(a) shows the E_{cell}-j polarization curve (black triangle) and the P_{cell}-j curve (red square) obtained at the
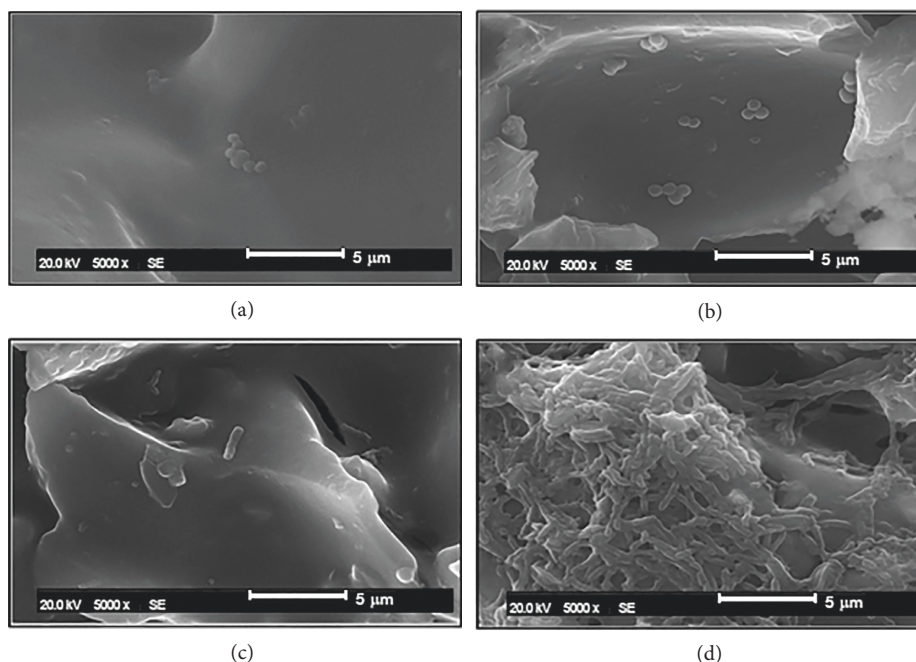
Figure 4: Bioanodes morphology with different configurations. (a) $S + AB7 + E.$ $coli$, (b) $S + AB7$-$f + E.$ $coli$, (c) $S + AB7 + B.$ $subtilis$, and (d) $S + AB7$-$f + B.$ $subtilis$.
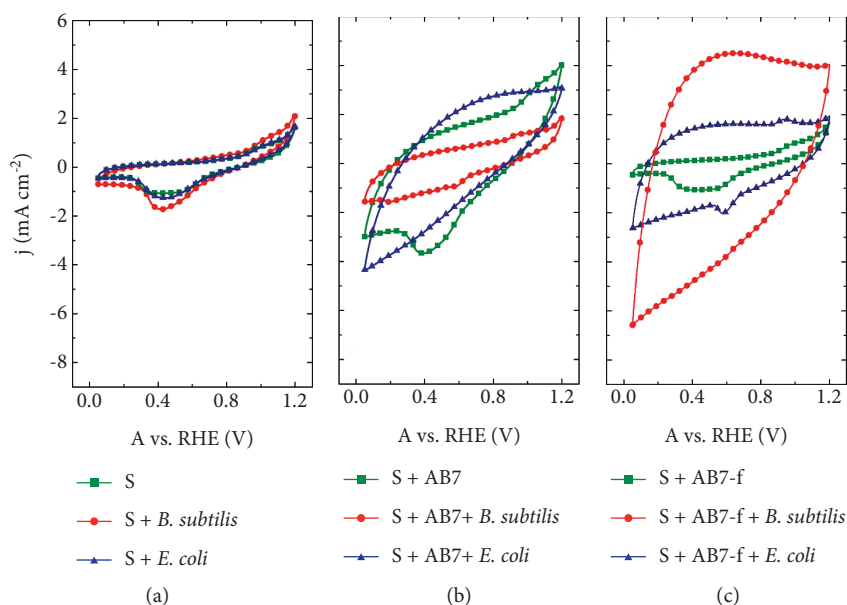
Figure 5: Half-cell characterization of the bioanodes with different configurations using N_2-saturated PWW as substrate at a scan rate of $20\,mV\,s^{-1}$ and as support (S) carbon cloth, (a) $S +$ bacteria, (b) $S + AB7 +$ bacteria, and (c) $S + AB7$-$f +$ bacteria.

beginning of the long-term test. The initial E_{cell} was of $0.60\,V$, with a maximum value of $P_{cell} = 77\,mW\,m^{-2}$ and $j = 254\,mA\,m^{-2}$. The linear tendence of the E_{cell}-j polarization curve indicates a good mass transport to the electrode, which suggests that the bioanode $S + AB7$-$f + B.$ $subtilis$ biofilm reduces the diffusional and electrochemical limitations [29]. In addition, no significant voltage drops were observed at the beginning of the test, which implies that

activation losses to carry out the redox reaction was low [30, 31], maybe due to synergic interaction of several characteristics of the bioanodes such as high specific surface area of the catalysts (AB7-f), good biocompatibility between AB7-f and $B.$ $subtilis$ and good performance in PWW substrate [30]. Figure 6(b) shows P_{cell}-j curves obtained during the long-term test (initial, day 1, 7, and 14). As can be seen, the P_{cell} generates by the MFC varies over time. The better
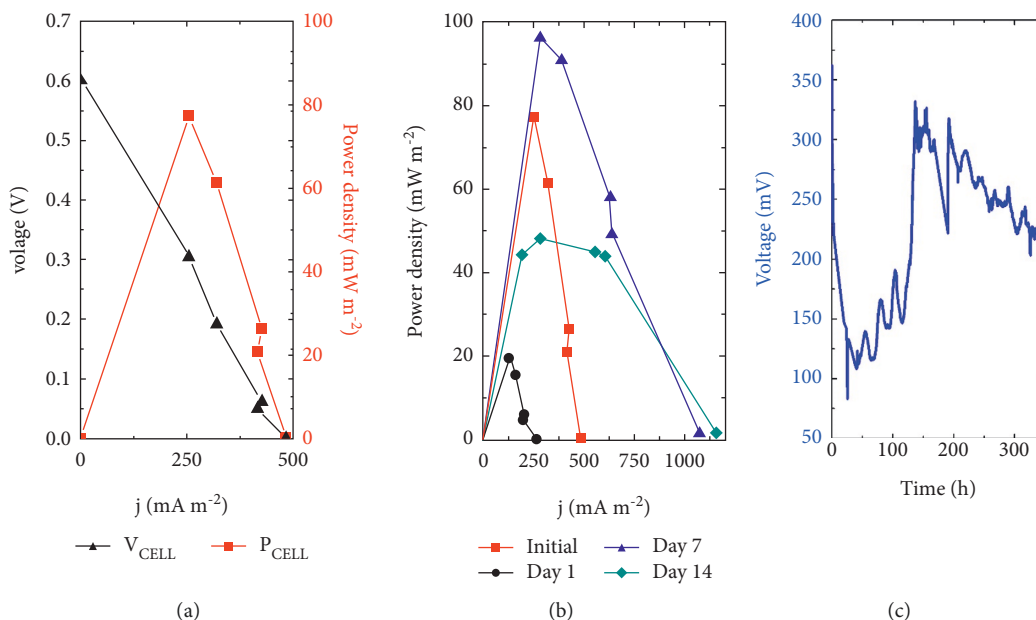
FIGURE 6: Long-term test of the MFC. Anode chamber: S + AB7-f + $B.$ $subtilis$ bioanode and PWW as substrate (pH = 9.2). Cathode chamber: 20% Pt/C catalysts in KOH (pH = 9.7) electrolyte. Nafion® 117 alkalinized membrane was used as separator. (a) E_{cell}-j and P_{cell}-j curves obtained at the initial of the test, (b) P_{cell}-j curves obtained during the initial, days 1, 7, and 14, and (c) open circuit voltage of the MFC vs. time using a R_{ext} = 10 kΩ.

TABLE 2: Electrochemical parameters of the MFC during the long-term test.

Time	E_{cell} (V)	Maximum P_{cell} (mW m^{-2})	j (mA m^{-2})	Pv (mW m^{-3})
Initial	0.60	77.4	254	38.7
Day 1	0.31	19.3	127	9.6
Day 7	0.53	96.3	283	48.1
Day 14	0.38	48.1	283	24.0

performance was observed on day 7 with a maximum of P_{cell} = 96.3 mW m^{-2}. Meanwhile, the oscillating P_{cell} generation in the MFC is because it is a dynamic system, where the biofilm of $B.$ $subtilis$ could be modified in the presence of PWW (formation/shedding of other bacteria) [32].

Table 2 summarized the electrochemical parameters obtained from Pcell-j curves at different times. The Ecell values at initial and day 7 were similar (≈0.6 V) and is consistent with previously reported MFC voltages with similar arrays (Ecell between 0.5 and 0.8 V) [33]. Therefore, it can be assumed that in these periods of time, the system was in optimal conditions.

On the other hand, the maximum P_{cell} values obtained in this work are comparable with other previously reported (Table S3). In this work, we used PWW (as received from the industry) and S + AB7-f + $B.$ $subtilis$ as bioanode, meanwhile, other reports operating the MFC with more controllable parameters (e.g., synthetic substrates and mixed cultures). However, the comparison between different types of MFC systems is complicated, since there are many variables, such as the substrate, electrodes, use of catalysts, cell configuration, temperature, pH, and bacteria [34]. Therefore, with this comparison we want to highlight that S + AB7-f + $B.$ $subtilis$ bioanode is promising to generate bioenergy even in recalcitrant media as the PWW.

Figure 6(c) shows the E_{cell}-time curve applying a R_{ext} of 10 kΩ to the MFC during the 14 days of testing. Under this condition, the initial $E_{cell(10\ kΩ)}$ was of 360 mV, which continuously decreases until 83 mV, the lowest $E_{cell(10\ kΩ)}$ value recorded at 25 h. This voltage drop may be caused by the processes of stabilization and adaptation in the bioelectrochemical system. In a period from 25 to 130 hours, a constant increase in voltage was observed until reaching voltages above 300 mV; where interestingly it can be seen that there are periods where the voltage slightly decreases, which coincides with the night periods. After 130 h, the voltage is relatively constant until 160 h, then, the voltage decreases to 224 mV. These results confirm that the best performance is between 130 and 168 h (5–7 days). Meanwhile, the voltage decreases towards the end of the long-term test may be due to decrease in nutrients assimilable by the bacteria near to the bioanode [35]. It is important to note that this is a batch process without agitation, so the diffusion of nutrients to the bioanode may be limited. This behavior has also been reported for MFC with complex organic matter such as aromatic compounds [36], paper recycling [37], and wastewater from the coke production process [38].

Finally, Table 3 shows the physicochemical parameters of PWW during the long-term test. As can be seen, there was a

TABLE 3: Physicochemical parameters of PWW at different times during the long-term test. No determined.

Parameter	Units	Long-term test			
		Initial (0 h)	Day 1 (24 h)	Day 7 (168 h)	Day 14 (336 h)
pH		9.20	9.10	8.60	8.50
Conductivity	mS m^{-1}	2,870	2,830	2,810	2,770
Chemical oxygen demand (COD)	mg L^{-1}	27,603	22,694	21,384	15,181
Biochemical oxygen demand (BOD)	mg L^{-1}	10,433	—	—	8,900
Nitrates (N–NO$_3$)	mg L^{-1}	6.13	—	—	6.76
Total phosphorous	mg L^{-1}	93.91	—	—	91.15
Sulfate ion (SO$^{2-}_4$)	mg L^{-1}	1,161	—	—	3,592
Alkalinity	mg L^{-1} CaCO$_3$	3,574	—	—	3,772
Chlorides	mg L^{-1}	10,616	—	—	9,466
Total dissolved solids (TDS)	mg L^{-1}	30,540	—	—	27,900
Total suspended solids (TSS)	mg L^{-1}	3,320	—	—	1,640

gradual decrease in pH from 9.2 to 8.5, while the electrical conductivity remains relatively constant. Regarding the chemical and biochemical oxygen demand, the removal of these in this work was of 45 and 15% of COD and BOD, respectively. The sulfates ion (SO^{-4}) increases almost three times on day 14 compared to its initial value. Meanwhile, total dissolved and suspended solids decrease 8.5 and 50.6%, respectively. Other chemical parameters such as nitrates, phosphorous, and alkalinity remains constant.

4. Conclusions

4.1. The most important findings of this work are the following. Amorphous carbon-based catalysts were successfully obtained from waste leather labeled as AB7 and AB7-f, both with a carbon content greater than 90% and high S$_{BET}$ (up to 1984 m^2 g^{-1}). Furthermore, the results prove that subjecting the catalysts to a microwave intermittent heating (MIH) treatment improves the biocompatibility between it and the bacteria.

The bioanode $S + AB7\text{-}f + B.$ *subtilis* has an outstanding performance in half-cell and MFC systems for the generation of energy and remediation of PWW. The maximum P$_{cell}$ of 96.3 mW m^{-2} was observed on day 7, achieving a removal of up to 45% of COD on day 14. Therefore, the development of catalysts made from leather waste in conjunction with PWW as a substrate and *B. subtilis* as an electroactive microorganism for use in MFCs is considered promising [39, 40].

Data Availability

No databases are included in this study.

Conflicts of Interest

The authors declare that they have no conflicts of interest.

Acknowledgments

Supplementary Materials

Figure S1. (a) Biofilm grow method and (b) dual-chambered H-Type MFC configuration used in this work. Table S2. Chemical composition of leather and leather-derived catalysts determined by EDS technique. Figure S2. Elemental mapping of the leather waste-derived catalyst AB7 and AB7-f. Table S3. Reports of different MFC configurations and the maximum power density compared with this work. (*Supplementary Materials*)

References

[1] V. V. Ranade and V. M. Bhandari, "Chapter 1: industrial wastewater treatment, recycling and reuse: an overview," in *Industrial Wastewater Treatment, Recycling and Reuse*, pp. 1–80, Butterworth-Heinemann. Copyright © 2014 Elsevier Ltd. All rights reserved, Amsterdam, Netherlands, 2014.

[2] K. Aguilar-Pérez, J. Aviles-Castillo, and G. Ruiz-Pulido, "Nano-sorbent materials for pharmaceutical-based wastewater effluents-An overview," *CSCEE*, vol. 2, Article ID 100028, 2020.

[3] D. Cecconet, D. Molognoni, A. Callegari, and A. G. Capodaglio, "Biological combination processes for efficient removal of pharmaceutically active compounds from wastewater: a review and future perspectives," *Journal of Environmental Chemical Engineering*, vol. 5, no. 4, pp. 3590–3603, 2017.

[4] G. Crini and E. Lichtfouse, "Advantages and disadvantages of techniques used for wastewater treatment," *Environmental Chemistry Letters*, vol. 17, no. 1, pp. 145–155, 2019.

[5] M. M. Ghangrekar, S. Das, and B. R. Tiwari, "11 - integration of bioelectrochemical systems with other existing wastewater treatment processes," in *Integrated Microbial Fuel Cells for Wastewater Treatment* Copyright © 2020 Elsevier Inc. All rights reserved, Amsterdam, Netherlands, 2020.

[6] T. Rashid, F. Sher, A. Hazafa et al., "Design and feasibility study of novel paraboloid graphite based microbial fuel cell for bioelectrogenesis and pharmaceutical wastewater treatment," *Journal of Environmental Chemical Engineering*, vol. 9, no. 1, Article ID 104502, 2021.

[7] M. E. Elshobary, H. M. Zabed, J. Yun, G. Zhang, and X. Qi, "Recent insights into microalgae-assisted microbial fuel cells for generating sustainable bioelectricity," *International Journal of Hydrogen Energy*, vol. 46, no. 4, pp. 3135–3159, 2021.

[8] X. Fan, Y. Zhou, X. Jin, R.-B. Song, Z. Li, and Q. Zhang, "Carbon material-based anodes in the microbial fuel cells," *Carbon Energy*, vol. 3, pp. 449–472, 2021.

[9] Y. Liu, X. Zhang, Q. Zhang, and C. Li, "Microbial fuel cells: nanomaterials based on anode and their application," *Energy Technology*, vol. 8, no. 9, Article ID 2000206, 2020.

[10] W. Yang and S. Chen, "Biomass-derived carbon for electrode fabrication in microbial fuel cells: a review," *Industrial & Engineering Chemistry Research*, vol. 59, no. 14, pp. 6391–6404, 2020.

[11] B. E. Logan, "Exoelectrogenic bacteria that power microbial fuel cells," *Nature Reviews Microbiology*, vol. 7, no. 5, pp. 375–381, 2009.

[12] T. Zhang, C. Cui, S. Chen, H. Yang, and P. Shen, "The direct electrocatalysis of *Escherichia coli* through electroactivated excretion in microbial fuel cell," *Electrochemistry Communications*, vol. 10, no. 2, pp. 293–297, 2008.

[13] F. Kracke, I. Vassilev, and J. O. Krömer, "Microbial electron transport and energy conservation - the foundation for optimizing bioelectrochemical systems," *Frontiers in Microbiology*, vol. 6, p. 575, 2015.

[14] O. J. Duarte-Urbina, F. J. Rodríguez-Varela, F. Fernández-Luqueño et al., "Bioanodes containing catalysts from onion waste and Bacillus subtilis for energy generation from pharmaceutical wastewater in a microbial fuel cell," *New Journal of Chemistry*, vol. 45, no. 28, pp. 12634–12646, 2021.

[15] S. García-Mayagoitia, F. Fernández-Luqueño, D. Morales-Acosta et al., "Energy generation from pharmaceutical residual water in microbial fuel cells using ordered mesoporous carbon and bacillus subtilis as bioanode," *ACS Sustainable Chemistry & Engineering*, vol. 7, no. 14, pp. 12179–12187, 2019.

[16] D. Lardizabal-Guitierrez, D. González-Quijano, P. Bartolo-Pérez, B. Escobar-Morales, F. J. Rodríguez-Varela, and I. L. Alonso-Lemus, "Communication—synthesis of self-doped metal-free electrocatalysts from waste leather with high ORR activity," *Journal of the Electrochemical Society*, vol. 163, no. 2, pp. H15–H17, 2015.

[17] G. Jerkiewicz, "Standard and reversible hydrogen electrodes: theory, design, operation, and applications," *ACS Catalysis*, vol. 10, no. 15, pp. 8409–8417, 2020.

[18] L. L de Souza, "Direct oxidation of ethylene glycol on PtSn/C for application in alkaline fuel cell," *International Journal of Electrochemical Science*, vol. 12, pp. 11855–11874, 2017.

[19] A. Sadezky, H. Muckenhuber, H. Grothe, R. Niessner, and U. Pöschl, "Raman microspectroscopy of soot and related carbonaceous materials: spectral analysis and structural information," *Carbon*, vol. 43, no. 8, pp. 1731–1742, 2005.

[20] P. Tang, G. Hu, Y. Gao et al., "The microwave adsorption behavior and microwave-assisted heteroatoms doping of graphene-based nano-carbon materials," *Scientific Reports*, vol. 4, no. 1, pp. 5901–5907, 2014.

[21] S. Vollebregt, R. Ishihara, F. D. Tichelaar, Y. Hou, and C. I. M. Beenakker, "Influence of the growth temperature on the first and second-order Raman band ratios and widths of carbon nanotubes and fibers," *Carbon*, vol. 50, no. 10, pp. 3542–3554, 2012.

[22] M. Thommes, K. Kaneko, A. V. Neimark et al., "Physisorption of gases, with special reference to the evaluation of surface area and pore size distribution (IUPAC Technical Report)," *Pure and Applied Chemistry*, vol. 87, no. 9-10, pp. 1051–1069, 2015.

[23] H. Marsh and F. Rodríguez-Reinoso, "Chapter 2 - activated carbon (origins)," in *Activated Carbon*, pp. 13–86, Elsevier Science, Oxford, U.K, 2006.

[24] R. Ali, Z. Aslam, R. A. Shawabkeh, A. Asghar, and I. A. Hussein, "BET, FTIR, and Raman characterizations of activated carbon from wasteoil fly ash," *Turkish Journal of Chemistry*, vol. 44, no. 2, pp. 279–295, 2020.

[25] S. Shin, J. Jang, S.-H. Yoon, and I. Mochida, "A study on the effect of heat treatment on functional groups of pitch based activated carbon fiber using FTIR," *Carbon*, vol. 35, no. 12, pp. 1739–1743, 1997.

[26] M. Schechter, A. Schechter, S. Rozenfeld, E. Efrat, and R. Cahan, "4. Anode biofilm," in *Technology and Application of Microbial Fuel Cells* InTech Open Access Books, London, U. K, 2014.

[27] S. H. Hassan, Y. S. Kim, and S. E. Oh, "Power generation from cellulose using mixed and pure cultures of cellulose-degrading bacteria in a microbial fuel cell," *Enzyme and Microbial Technology*, vol. 51, no. 5, pp. 269–273, 2012.

[28] S. A. Patil, F. Harnisch, B. Kapadnis, and U. Schroder, "Electroactive mixed culture biofilms in microbial bio-electrochemical systems: the role of temperature for biofilm formation and performance," *Biosensors and Bioelectronics*, vol. 26, no. 2, pp. 803–808, 2010.

[29] Y. Zhao, Y. Ma, T. Li, Z. Dong, and Y. Wang, "Modification of carbon felt anodes using double-oxidant HNO3/H2O2 for application in microbial fuel cells," *RSC Advances*, vol. 8, no. 4, pp. 2059–2064, 2018.

[30] X. Zhou, X. Chen, H. Li, J. Xiong, X. Li, and W. Li, "Surface oxygen-rich titanium as anode for high performance microbial fuel cell," *Electrochimica Acta*, vol. 209, pp. 582–590, 2016.

[31] V. R. Nimje, C.-Y. Chen, C.-C. Chen et al., "Stable and high energy generation by a strain of Bacillus subtilis in a microbial fuel cell," *Journal of Power Sources*, vol. 190, no. 2, pp. 258–263, 2009.

[32] B. E. Logan, B. Hamelers, R. Rozendal et al., "Microbial fuel cells: methodology and technology," *Environ. Sci. Technol.* vol. 40, no. 17, pp. 5181–5192, 2006.

[33] L. Peixoto, B. Min, G. Martins et al., "In situ microbial fuel cell-based biosensor for organic carbon," *Bioelectrochemistry*, vol. 81, no. 2, pp. 99–103, 2011.

[34] B. Min, J. Kim, S. Oh, J. M. Regan, and B. E. Logan, "Electricity generation from swine wastewater using microbial fuel cells," *Water Research*, vol. 39, no. 20, pp. 4961–4968, 2005.

[35] L. Peixoto, A. L. Rodrigues, G. Martins et al., "A flat microbial fuel cell for decentralized wastewater valorization: process performance and optimization potential," *Environmental Technology*, vol. 34, no. 13-14, pp. 1947–1956, 2013.

[36] S. Srikanth, M. Kumar, D. Singh, M. P. Singh, and B. P. Das, "Electro-biocatalytic treatment of petroleum refinery wastewater using microbial fuel cell (MFC) in continuous mode operation," *Bioresource Technology*, vol. 221, pp. 70–77, 2016.

[37] E. Herrero-Hernández, T. Smith, and R. Akid, "Electricity generation from wastewaters with starch as carbon source using a mediator less microbial fuel cell," *Biosensors and Bioelectronics*, vol. 39, no. 1, pp. 194–198, 2013.

[38] S. K. F. Marashi, H. R. Kariminia, and I. S. P. Savizi, "Bimodal electricity generation and aromatic compounds

removal from purified terephthalic acid plant wastewater in a microbial fuel cell," *Biotechnology Letters*, vol. 35, no. 2, pp. 197–203, 2013.

[39] L. Huang and B. E. Logan, "Electricity generation and treatment of paper recycling wastewater using a microbial fuel cell," *Applied Microbiology and Biotechnology*, vol. 80, no. 2, pp. 349–355, 2008.

[40] L. Huang, X. Yang, X. Quan, J. Chen, and F. Yang, "A microbial fuel cell–electro-oxidation system for coking wastewater treatment and bioelectricity generation," *J. Chem. Technol. Biotechnol.* vol. 85, no. 5, pp. 621–627, 2010.

Retraction

Retracted: Electrochemical Application of Structured Color Nanotextile Materials in Garment Design

Journal of Chemistry

This article has been retracted by Hindawi following an investigation undertaken by the publisher [1]. This investigation has uncovered evidence of one or more of the following indicators of systematic manipulation of the publication process:

(1) Discrepancies in scope

(2) Discrepancies in the description of the research reported

(3) Discrepancies between the availability of data and the research described

(4) Inappropriate citations

(5) Incoherent, meaningless and/or irrelevant content included in the article

(6) Peer-review manipulation

The presence of these indicators undermines our confidence in the integrity of the article's content and we cannot, therefore, vouch for its reliability. Please note that this notice is intended solely to alert readers that the content of this article is unreliable. We have not investigated whether authors were aware of or involved in the systematic manipulation of the publication process.

Wiley and Hindawi regrets that the usual quality checks did not identify these issues before publication and have since put additional measures in place to safeguard research integrity.

We wish to credit our own Research Integrity and Research Publishing teams and anonymous and named external researchers and research integrity experts for contributing to this investigation.

The corresponding author, as the representative of all authors, has been given the opportunity to register their agreement or disagreement to this retraction. We have kept a record of any response received.

References

[1] Z. Zhang, "Electrochemical Application of Structured Color Nanotextile Materials in Garment Design," *Journal of Chemistry*, vol. 2022, Article ID 2044265, 7 pages, 2022.

Research Article

Electrochemical Application of Structured Color Nanotextile Materials in Garment Design

Zekai Zhang

Guangdong Vocational College of Innovation and Technology, Dongguan, Guangdong 523960, China

Correspondence should be addressed to Zekai Zhang; 11231608@stu.wxic.edu.cn

In order to improve the color saturation of textile structured chromogenic photonic crystals, this paper proposes that the dye adsorbed PSt structural elements (reactive dyes/PSt microspheres) on the outer surface can be used to construct electrochemically structured chromogenic photonic crystals on mulberry fabrics by digital printing. In this method, the adsorption conditions and adsorption model of dyes on the surface of PSt colloidal microspheres were studied. The structure and morphology of reactive dyes/PSt microspheres, the arrangement of the obtained photonic crystals, and the structural chromogenic effect were characterized. The results showed that the amount of dye adsorbed on the surface of microspheres increased significantly with the increase of adsorption temperature from 25°C to 65°C. When the adsorption temperature continued to rise to 75°C, the dye adsorption capacity on the surface of PSt microspheres did not increase significantly. The adsorption model accords with the Langmuir model; reactive dye/PSt microspheres have a typical core-shell structure, and the particle size of the microspheres is slightly larger than that before adsorption. *Conclusion.* The reactive dye/PSt photonic crystal chromogenic electrochemical structure constructed on the surface of white silk fabric has a regular and orderly arrangement of microspheres, showing bright structural color.

1. Introduction

Textiles are mainly colored by applying dyes or pigments. In recent years, some new textile coloring technologies are emerging. Among them, the construction of photonic crystals on textile substrates, through the diffraction of light and other functions, to obtain the structural color effect to realize the ecological and environmental coloring of textiles has attracted the attention of researchers. As a typical physical color, the structural color produced by regularly arranged crystalline photonic crystals usually has the characteristics of high saturation, high brightness, and rainbow effect, which helps to enrich the pigment color and make the finishing point. However, it is challenging to construct photonic crystal electrochemistry structures on textile substrates to realize textile coloring. Textile is a kind of rough, porous, and flexible material with certain undulation, which can be divided into woven, knitted, and nonwoven kinds according to the weaving method [1].

Different weaving and processing methods will have different effects on the properties of textiles, which brings challenges to the construction of photonic crystal structures on textile substrates. At the same time, it is also difficult to prepare bright and colorful structural color films. Therefore, finding a textile substrate suitable for colloidal microsphere self-assembly to construct regular photonic crystals and obtain bright structural color effect will have good practical significance for realizing textile photonic crystal structure coloring, as shown in Figure 1.

The colloidal microsphere self-assembly method has the advantages of simple operation and good practicability. It is the most widely used method for preparing photonic crystals, mainly including the gravity sedimentation method, vertical sedimentation method, centrifugal deposition method, and electrophoretic deposition method. [2]. However, the above conventional colloidal microspheres self-assembly method has the disadvantages of low efficiency and long time, which greatly inhibits the application of
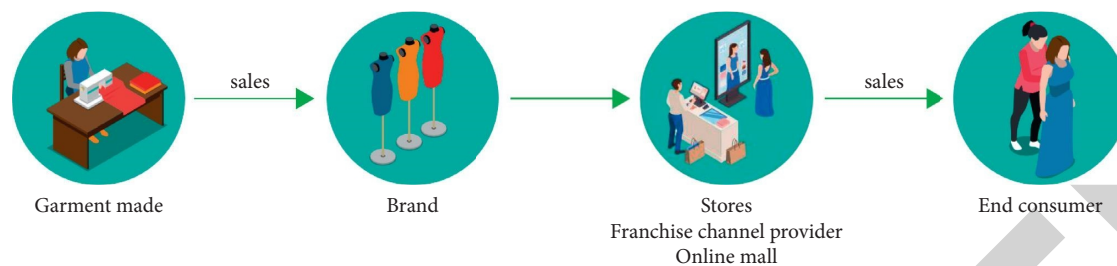
FIGURE 1: Clothing design process.

photonic crystal structure color in the textile field. Therefore, there is an urgent need to develop a colloidal microsphere self-assembly method that is practical, efficient, and suitable for the preparation of good photonic crystal chromogenic electrochemical structures. As a common method in industrial production, the spraying method has the advantages of simple operation, high efficiency, and low cost and can realize large-area rapid prototyping of materials on the plane and curved surface [3]. If the spraying method and colloidal microsphere self-assembly method can be combined, it is expected to open up a large-area, rapid, and efficient way to prepare photonic crystals, which will help to promote the practical application of photonic crystal structure color. After selecting suitable textile substrates and rapidly constructing the photochromic electrochemical structure of photonic crystals, the stability of the electrochromic structure of photonic crystals will become an important bottleneck restricting the application of the electrochromic structure of photonic crystals [4]. When undergoing simple folding, bending, washing, and friction, the photonic crystal structure is easy to fall off from the substrate and the corresponding structural color effect is easy to be reduced. Therefore, how to improve the stability of the electrochemical structure of photonic crystal color generation and retain the structural color effect is a problem that researchers in the field of photonic crystal structure color generation pay close attention to.

2. Literature Review

Graves et al. added photosensitive pigments and thermal pigments to the spinning solution through electrospinning to prepare electrospun cellulose acetate fiber with corresponding color-changing ability, which filled the research gap of photon sensor in electrospun cellulose acetate (CA) and obtained fabrics with photothermal color changing ability [5]. Guo et al. took carbon nanotube/cotton composite yarn (CCY) as the core and nanofiber polyurethane/temperature sensitive ink as the sheath and prepared skin core nanocomposite yarn with excellent mechanical properties, electrothermal properties, and electrochromic properties; that is, color change will occur when there is a charge on the fabric [6]. J. M. et al. synthesized magnetic nanosphere with magnetochromic ability by the hydrothermal method, mixed it with resin polyethylene glycol diacrylate (PEGDA), and then irradiated it with ultraviolet light to prepare cured color fiber. This magnetochromic dispersion is a kind of magnetochromic material [7]. Duaux et al. reported the preparation of thermochromic cotton fabric, that is, its smart application in children's clothing. However, some challenges still exist. The cost of thermochromic dyes or pigments is particularly high, the durability of thermochromic fibers is poor, and the manufacturing process is complex [8]. Therefore, it is still very necessary to develop a new method for continuously manufacturing thermochromic fibers. Dhiman et al. reported the use of a modular microfluidic system to manufacture alginate microfibers for magnetic response control of drug release and cell culture [9]. Syrek et al. continuously prepared carboxylated chitosan, polyvinyl alcohol, and hydrophobic ethylene vinyl alcohol copolymer (EVOH) spiral microfibers through microfluidic technology. Guo et al. prepared conductive PEDOT: PSS polymer hydrogel microfibers from multiflow microfluidic spinning [10]. Qu et al. used a new buoyancy-assisted vertical microfluidic device to produce a deformable hydrogel microfiber filled with bubbles. However, there are relatively few studies on manufacturing thermochromic fibers by microfluidic spinning [11].

In this paper, the black reactive dye was introduced into the surface of PSt colloidal microspheres by electrostatic adsorption, and the reactive dye/PSt composite colloidal microspheres were prepared. The structured reactive dye/PSt photonic crystals were constructed on mulberry silk fabrics by digital spray printing, showing bright structural colors, in order to provide a reference for the application of structural color and pigment color coupling in textiles.

3. Research Methods

3.1. Experimental Materials and Instruments. Materials used included silk fabric (electric spinning, area density 45.7), commercially available; styrene (st, analytically pure); polyvinylpyrrolidone (PVP, analytically pure); azobisisobutyl ether hydrochloride (AIBA, analytical purity); deionized water (conductivity: $18\,m\,\Omega/cm$), self-made in the laboratory; water-repellent EPF (industrial grade); and reactive black (industrial grade).

Instruments used were Lambda-35 ultraviolet visible spectrophotometer; Brook-21 zeta potentiometer; Mastersizer-2000 Malvern laser particle sizer; Altra55 field emission scanning electron microscope; Jem2100 transmission electron microscope; 600D digital camera; KH-7700 3D video microscope; Judge-II standard light source box; and 7000 d dialysis bag.

3.2. Sample Preparation Method

3.2.1. Pretreatment of Silk Fabric.
In order to prevent the seeping phenomenon in the process of digital jet printing, the mulberry silk fabric was treated with EPF solution with a mass fraction of 1% for two dipping and two rolling processes (the rolling yield was 90%) [12]. The pretreatment of mulberry silk fabric was completed by predrying at 80°C for 3 min and 130°C for 2 min.

3.2.2. Preparation of Reactive Dye/PSt Microspheres.
Using the dispersion polymerization method, we weigh 1.5 g of PVP dispersant, 10.0 g of St monomer, and 90.0 g of deionized water, respectively, and add them to the three-necked flask. We place the three-necked flask in a constant temperature water bath for heating and stirring. When the temperature rises to 75°C, we add 0.15 g of AIBA (initiator) dissolved in 10.0 g of deionized water into the three-necked flask and make them react at a constant temperature for 7 hours at a speed of 300 R/min, so as to prepare positively charged PSt microspheres with a particle size of 247 nm [13]. The positively charged PSt colloidal microspheres with good monodispersity (PDI < 0.08) and particle size in the range of 180~350 nm can be prepared by adjusting the amount of monomer and initiator. Reactive black was added to the PSt microsphere lotion of a certain concentration, stirred, and adsorbed at a specific temperature for a certain period of time, and the reactive dye/PSt microsphere was obtained after centrifugal cleaning with deionized water.

3.2.3. Self-Assembly of Reactive Dye/PSt Microspheres by Spray Printing.
The reactive dye/PSt colloidal microsphere lotion was sprayed onto the mulberry silk fabric with a desktop dispensing system (the nozzle diameter was 0.15 mm, and the printing pressure was 0.20 MPa). Reactive dye/PSt structure chromogenic photonic crystals can be obtained after the solvent is completely evaporated in a 60°C blast oven.

3.3. Testing and Characterization

3.3.1. Characterization of Physical Properties of Colloidal Microspheres.
The average particle size of colloidal microspheres was measured with a Malvin laser particle sizer, and the surface potential of colloidal microspheres was measured with a Zeta potentiometer. The structure and morphology of colloidal microspheres were observed by TEM and FESEM.

3.3.2. Drawing of Adsorption Isotherm and Calculation of Normal Deviation.
A UV visible spectrophotometer is used to test the absorbance value at the maximum absorption wavelength of reactive dye solutions with different mass fractions, and the standard working curve of dyes is drawn [14]. We determine the absorbance of dialysate of reactive dye/PSt microspheres, calculate the adsorption amount of dye on the microspheres by Lambert–Beer law, and draw the adsorption rate curve. The deviation between the experimental value and the theoretical value calculated from the

adsorption equation is called the normal deviation (ND). By judging the fitting degree between the experimental point and the adsorption model, the calculation formula is as follows:

$$\text{ND} = \left(\frac{1}{N}\right)\left(\frac{\sum_{i=1}^{N} C_{f,1}^{\text{calc}} - C_{f,1}^{\text{exp}}}{C_{f,1}^{\text{exp}}}\right), \tag{1}$$

where $C_{f,i}^{\text{calc}}$ and $C_{f,i}^{\text{exp}}$ are the calculated and experimental values of dye adsorption capacity on the microspheres, respectively, and N is the number of experimental points.

3.3.3. Morphology and Color Characterization of Structured Chromogenic Photonic Crystals.
The surface morphology of the structure colored photonic crystals prepared on the fabric was observed by FESEM. The photonic crystal structure color on mulberry silk fabric was observed with a digital camera and three-dimensional video microscope. The reflectance curve of the structured chromogenic photonic crystal constructed on the fabric in the range of 400~700 nm was measured using the UV-Vis spectrophotometer.

4. Result Analysis

4.1. Process Parameters of Reactive Dye/PSt Microspheres

4.1.1. Dye Mass Fraction.
During the polymerization of polystyrene, due to the introduction of positive initiator AIBA, the PSt colloidal microspheres synthesized in the experiment are positively charged, which can adsorb anionic reactive dyes [15]. Figure 2 shows the dye adsorption amount on the surface of PSt colloidal microspheres after adsorption at 60°C for 40 min. It can be seen that when the mass fraction of dye is less than 0.5%, the dye adsorption capacity on the surface of PSt microspheres increases significantly with the increase of the amount of dye. When the dye mass fraction was higher than 0.5%, the dye adsorption on the surface of PSt microspheres tended to be saturated and the increment was not obvious. Figure 3 shows the zeta potential curve of PSt microspheres under different dye dosages. It can be seen that the zeta potential of PSt colloidal microspheres is about +30 mV before dye adsorption. When the adsorption amount of reactive dyes increases from 0% to 0.5%, the corresponding zeta potential drops sharply. This should be driven by electrostatic attraction; many reactive dye anions are adsorbed on the surface of PSt microspheres. With the increase of dye mass fraction, the dye adsorption amount on the surface of PSt microspheres also increases. When the dye mass fraction reaches more than 0.5%, the zeta potential of the microsphere lotion tends to be stable, lower than −30 mV, showing good stability [16]. It showed that when the mass fraction of dye reached 0.5%, the adsorption of reactive dye molecules on the surface of PSt microspheres basically reached saturation. To sum up, the appropriate dye mass fraction is determined to be 0.5%.

4.1.2. Adsorption Time.
Figure 4 shows the effect of different adsorption time periods on the dye adsorption capacity on the surface of PSt colloidal microspheres at 60°C and 0.5% dye mass fraction.
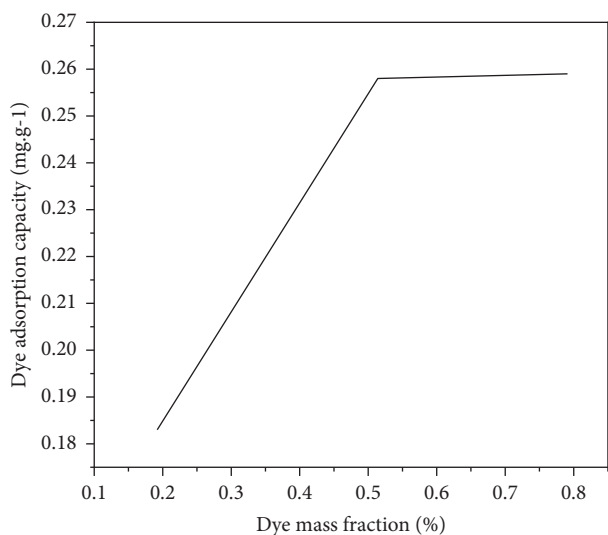
FIGURE 2: Dye adsorption capacity on the surface of PSt colloidal microspheres under different dye mass fractions.

FIGURE 3: Zeta potential of PSt colloidal microspheres with different dye mass fractions.

It can be seen that in the first 30 minutes of adsorption, the adsorption amount of reactive dyes on the surface of PSt microspheres increased linearly with the extension of adsorption time. If the adsorption time was prolonged, the dye adsorption capacity increased slowly. When the adsorption time was more than 40 min, the adsorption amount of dye did not increase significantly with the extension of adsorption time. This is mainly because, in the initial adsorption stage, there are a large number of positive charges on the surface of PSt microspheres, which makes a large number of anionic reactive dyes quickly adsorb to the surface of the microspheres; With the prolongation of adsorption time, the adsorption of anionic reactive dyes gradually reduced the positive electricity of the surface of the microspheres, and the subsequent increase in the amount of dye adsorption tended to moderate. In the later stage, the adsorption time continues to be extended, and the adsorption amount gradually reaches saturation and remains basically unchanged [17]. In conclusion, 40 min is a more suitable adsorption time.

4.1.3. Adsorption Temperature. Figure 5 shows the effect of different adsorption temperatures on the dye adsorption capacity of PSt colloidal microspheres when the dye mass fraction is 0.5% and the adsorption time is 40 min.

It can be seen from Figure 5 that the dye adsorption amount on the surface of microspheres increased significantly with the increase of adsorption temperature from 25°C to 65°C. When the adsorption temperature continued to rise to 75°C, the dye adsorption on the surface of PSt microspheres did not increase significantly. This is because the higher the adsorption temperature is, the more intense the Brownian motion of reactive dye molecules and PSt microspheres becomes. The faster the reactive dye diffuses to the surface of microspheres, the more the dye adsorbed on the surface of microspheres. However, increasing the adsorption temperature will also accelerate the desorption rate
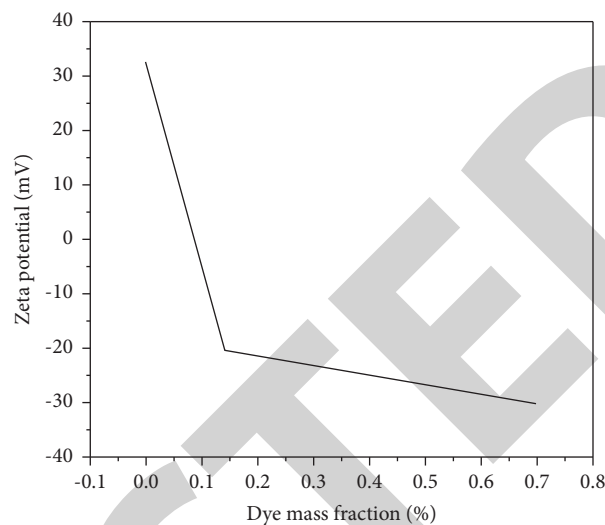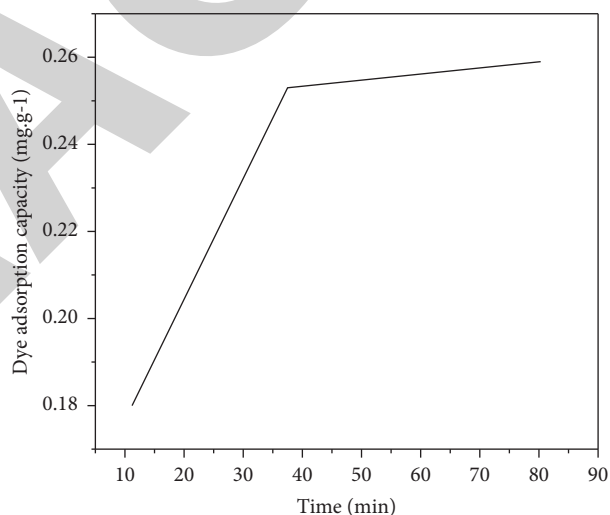
FIGURE 4: Dye adsorption amount on the surface of PSt colloidal microspheres at different adsorption time periods.

of reactive dye on the surface of microspheres [18]. According to the comprehensive analysis, the adsorption temperature should be kept at about 65°C.

4.2. Adsorption Model of Dyes on PSt Colloidal Microspheres. In order to improve the controllability of the adsorption of reactive dyes on the surface of PSt colloidal microspheres and provide better theoretical guidance for its process optimization, the adsorption model of reactive dyes on the surface of PSt colloidal microspheres was further studied. Under the conditions of dye mass fraction of 0.5% and adsorption time of 40 min, the adsorption isotherms of reactive dyes on the surface of PSt colloidal microspheres at 25°C, 45°C, and 65°C were plotted. Three common theoretical adsorption models (Nernst, Langmuir, and Freundlich) were used to fit the adsorption
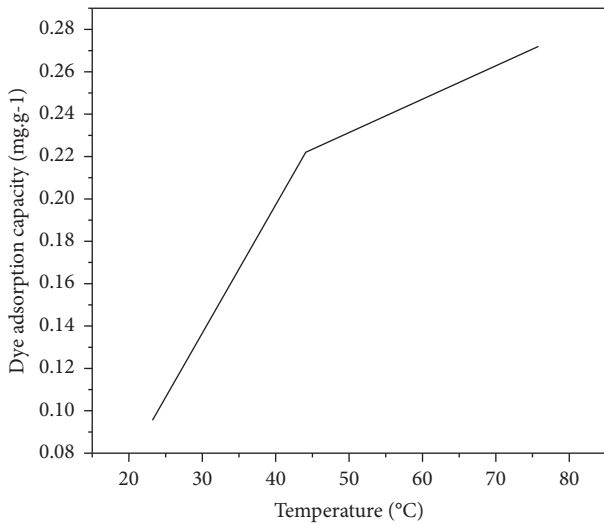
FIGURE 5: Dye adsorption capacity of PSt colloidal microspheres at different adsorption temperatures.

isotherms at different temperatures by the nonlinear least square method.

By comparing the corresponding normal deviation and fitting coefficient, the conformity degree of the three adsorption models is analyzed (see Table 1). The specific adsorption equation is shown in equations (2) to (4).

4.2.1. Nernst Type

$$[D]_f = K_1[D]_s. \qquad (2)$$

Here, $[D]_f$ is the concentration of dye on the fiber; $[D]_s$ is the concentration of the dye in the dye solution; and K_1 is the Nernst adsorption constant.

4.2.2. Langmuir Type

$$[D]_f = \frac{K_2[D]_s[S]_f}{1 + K[D]_s}. \qquad (3)$$

Here, K_2 is Langmuir adsorption constant and $[S]_f$ is the dyeing saturation value of the fiber.

4.2.3. Freundlich Type

$$[D]_f = K_3[D]_s^n. \qquad (4)$$

Here, K_3 is Freundlich adsorption constant and n is the heterogeneity factor, $0 < n < 1$.

It can be seen from Table 1 that under three different temperatures, the R^2 of Nernst type and Freundlich type are low and the ND is large. The Langmuir model has the highest R^2, which is more than 0.99, and the corresponding ND is also the lowest [19]. Therefore, the adsorption model of reactive dyes on PSt colloidal microspheres is more in line with the Langmuir model. It can be seen that reactive dyes are localized on the surface of PSt microspheres. That is, a certain number of adsorption sites are formed on the surface

TABLE 1: Simulation results of adsorption isotherms of reactive dyes on PSt colloidal microspheres.

Temperature/°C	Nernst model		Langmuir model		Freundlich model	
	ND%	R^2	ND%	R^2	ND%	R^2
25	36.2	0.853	4.1	0.990	17.0	0.943
45	40.6	0.832	2.3	0.994	17.5	0.943
65	27.1	0.904	1.1	0.997	13.8	0.968

of positively charged PSt colloidal microspheres, which promotes the localized adsorption of anionic reactive dyes, and there is an adsorption saturation value in the adsorption process. When the adsorption reaches a certain degree, the adsorption amount basically remains unchanged.

4.3. Apparent Morphology of Reactive Dye/PSt Microspheres.

From the SEM and TEM photos before and after dye adsorption on the surface of PSt microspheres, it can be concluded that after dye adsorption, the reactive dye/PSt microspheres still maintain a typical core-shell structure and the sphericity is still good. The dye adsorption has no significant effect on the sphericity of colloidal microspheres. However, after adsorption of dyes, the particle size of reactive dye/PSt microspheres increased from 184.5 nm to 196.3 nm and the shell thickness increased from 30.7 nm to 36.6 nm. This may be because a large number of dye molecules are adsorbed on the surface of PSt microspheres, which can adsorb a certain amount of water molecules at the same time, resulting in a slight increase in the particle size of the microspheres.

4.4. Application of Reactive Dye/PSt Microspheres.

From the self-assembled photonic crystal structures and corresponding structural colors of reactive dyes/PSt microspheres with different particle sizes on mulberry silk fabrics, it can be concluded that the structures of reactive dyes/PSt photonic crystals on mulberry silk fabrics are orderly arranged, showing uniform and bright structural colors; And with the decrease of the particle size of colloidal microspheres, the corresponding structural colors also show different hues such as red, orange, green, blue, and purple, and an obvious blue shift occurs [6].

Reflectivity Curves of Self-Assembled Photonic Crystals with Different Particle Sizes of Reactive Dye/PSt Microspheres on White Mulberry Silk Fabric. It can be seen that as the particle size of the reactive dye/PSt microspheres decreases from 317, 298, 247, and 201 nm to 188 nm, the maximum reflection wavelength of the structure-colored photonic crystal gradually changes from 615 nm to 418 nm, which corresponds to the color phenomenon of the self-assembled photonic crystal structure of reactive dye/PSt microspheres with different particle sizes sprayed on mulberry fabric, that is, there is an obvious blue shift, which conforms to the Bragg diffraction equation.

Before dye adsorption, the structure color of pure PSt microspheres on white mulberry silk fabric was dim, showing light blue and light green. After adsorbing the dye,

the reactive dye/PSt photonic crystal on the same substrate shows bright blue and green and the corresponding color saturation is significantly improved. This is because the white fabric can easily reflect almost all the incident light passing through the photonic crystal layer without selectivity, diluting the structural color of the selective reflection of the photonic crystal. The black dye can significantly absorb the background stray light and make the light reflected by the photonic crystal maintain good purity and saturation without the interference of additional light [20]. The results show that the structure color effect of reactive dye/PSt photonic crystal on white mulberry silk fabric is better than that of pure PSt photonic crystal. It can be concluded that the introduction of black reactive dyes into the surface of PSt microspheres to prepare composite structural units can effectively enhance the color saturation of the structure chromogenic photonic crystals on the white substrate.

5. Conclusion

(1) In this paper, reactive dye/polystyrene (PSt) composite colloidal microspheres were prepared by electrostatic adsorption. The optimum conditions for dye adsorption were determined: dye mass fraction was 0.5%, adsorption temperature was 65°C, and adsorption time was 40 min.

(2) The adsorption of active black B on positively charged PSt colloidal microspheres conforms to the Langmuir model and belongs to localized adsorption.

(3) Using the digital spray printing method and the reactive dye/PSt composite colloidal microspheres as the structural elements, the structured three-dimensional photonic crystals can be directly constructed on the white mulberry silk fabric, showing bright and beautiful structural colors, which have certain reference significance for the application of the coupling of structural colors and pigment colors in textiles.

Data Availability

The data used to support the findings of this study are available from the author upon request.

Conflicts of Interest

The author declares no conflicts of interest.

Acknowledgments

References

[1] Z. A. Razak, S. A. Rushdi, M. Y. Gadhban, S. Al-Najjar, and Z. T. Al-Sharify, "Possibility of utilizing the lemon peels in removing of red reactive (rr) dye from simulated aqueous solution," *International Journal of Green Energy*, vol. 10, no. 10, pp. 7343–7359, 2020.

[2] M. Pająk and A. Dzieniszewska, "Evaluation of the metallurgical dust sorbent efficacy in reactive blue 19 dye removal from aqueous solutions and textile wastewater," *Environmental Engineering Science*, vol. 37, no. 7, pp. 509–518, 2020.

[3] D. M. Lewis, P. J. Broadbent, C. M. Carr, and W. D. He, "Investigation into the reaction of reactive dyes with carboxylate salts and the application of carboxylate-modified reactive dyes to cotton," *Coloration Technology*, vol. 138, no. 1, pp. 58–70, 2022.

[4] S. Bapat, D. Jaspal, and A. Malviya, "Efficacy of parthenium hysterophorus waste biomass compared with activated charcoal for the removal of ci reactive red 239 textile dye from wastewater," *Coloration Technology*, vol. 137, no. 3, pp. 234–250, 2021.

[5] L. S. Graves, M. J. Goodwin, I. N. Maricar, J. A. Rebstock, and E. J. Harbron, "Maximizing amplified energy transfer: tuning particle size and dye loading in conjugated polymer nanoparticles," *Journal of Physical Chemistry C*, vol. 124, no. 48, pp. 26474–26485, 2020.

[6] Q. Guo, W. Chen, Z. Cui, and H. Jiang, "Reactive dyeing of silk using commercial acid dyes based on a three-component mannich-type reaction," *Coloration Technology*, vol. 136, no. 4, pp. 336–345, 2020.

[7] J. M. He, C. F. Xie, and J. J. Long, "Sustainable color stripping of cotton substrate dyed with reactive dyes in a developed uv/k2s2o8 photocatalytic system," *Journal of the Taiwan Institute of Chemical Engineers*, vol. 121, no. 2, pp. 241–256, 2021.

[8] G. Duaux, E. Fleury, and D. Portinha, "Biobased poly(ester-co-glycoside) from reactive natural Brønsted acidic deep eutectic solvent analogue," *Polymer Chemistry*, vol. 12, no. 38, pp. 5485–5494, 2021.

[9] G. Dhiman, V. Vinoth Kumar, A. Kaur, and A. Sharma, "Don: deep learning and optimization-based framework for detection of novel coronavirus disease using x-ray images," *Interdisciplinary Sciences: Computational Life Sciences*, vol. 13, no. 2, pp. 260–272, 2021.

[10] K. Syrek, A. Sennik-Kubiec, J. Rodríguez-López et al., "Reactive and morphological trends on porous anodic tio 2 substrates obtained at different annealing temperatures," *International Journal of Hydrogen Energy*, vol. 45, no. 7, pp. 4376–4389, 2020.

[11] Y. Qu, P. Li, P. Hou, Q. Wang, and S. Luo, "Controllable synthesis of polystyrene microspheres used as template and in-situ carbon source for li2mnsio4 cathode material to boost lithium-ion batteries performance," *International Journal of Energy Research*, vol. 46, no. 2, pp. 1711–1721, 2022.

[12] S. Shriram, B. Nagaraj, J. Jaya, S. Shankar, and P. Ajay, "Deep learning-based real-time AI virtual mouse system using computer vision to avoid COVID-19 spread," *Journal of Healthcare Engineering*, vol. 2021, Article ID 8133076, 8 pages, 2021.

[13] W. He, X. H. Dong, J. G. Zhou, and M. K. Fung, "Manipulation of the size of polystyrene spheres as the templates for internal light out-coupling structures of a white organic light-emitting diode," *Journal of Materials Chemistry C*, vol. 9, no. 21, pp. 6923–6929, 2021.

Retraction

Retracted: Application of Chemical Technology of Water-Based Acrylic Dipping Paint in Art Painting Creation

Journal of Chemistry

This article has been retracted by Hindawi following an investigation undertaken by the publisher [1]. This investigation has uncovered evidence of one or more of the following indicators of systematic manipulation of the publication process:

(1) Discrepancies in scope

(2) Discrepancies in the description of the research reported

(3) Discrepancies between the availability of data and the research described

(4) Inappropriate citations

(5) Incoherent, meaningless and/or irrelevant content included in the article

(6) Peer-review manipulation

The presence of these indicators undermines our confidence in the integrity of the article's content and we cannot, therefore, vouch for its reliability. Please note that this notice is intended solely to alert readers that the content of this article is unreliable. We have not investigated whether authors were aware of or involved in the systematic manipulation of the publication process.

Wiley and Hindawi regrets that the usual quality checks did not identify these issues before publication and have since put additional measures in place to safeguard research integrity.

We wish to credit our own Research Integrity and Research Publishing teams and anonymous and named external researchers and research integrity experts for contributing to this investigation.

The corresponding author, as the representative of all authors, has been given the opportunity to register their agreement or disagreement to this retraction. We have kept a record of any response received.

References

[1] X. Kong and X. Meng, "Application of Chemical Technology of Water-Based Acrylic Dipping Paint in Art Painting Creation," *Journal of Chemistry*, vol. 2022, Article ID 7715011, 7 pages, 2022.

Hindawi

Research Article

Application of Chemical Technology of Water-Based Acrylic Dipping Paint in Art Painting Creation

Xiangfeng Kong and **Xiangzhen Meng**

Hebei Academy of Fine Arts, Shijiazhuang, Hebei 400072, China

Correspondence should be addressed to Xiangzhen Meng; 1865400018@e.gzhu.edu.cn

In order to better sort out the superiority of water-based acrylic in painting art, explore and understand the uniqueness of water-based acrylic painting materials and apply this to art creation. The author proposes a chemical process based on water-based acrylic dipping paint, by discussing the coating and film properties of water-soluble acrylic dip paint, combined with the practical application of a casting tank; summarizing the countermeasures to solve the disadvantages of common paint films; and proving that the paint has a good comprehensive performance by comparing with other dipping paints. Experimental results show that based on the chemical process of water-based acrylic dipping paint, it has waterproof, high gloss, gloss retention, color retention, high weather resistance, and good corrosion resistance in the process of art painting; the physical parameters are better than other dipping paints, such as gloss can reach 70~80%. *Conclusion*. In art painting, water-based acrylic dip paint is a kind of comprehensive performance paint with waterproof, high gloss, gloss retention, and color retention.

1. Introduction

Looking at the development of art, it is not difficult to find that today's painting art is shifting from a single dimension to a multivalue dimension; similarly, artists are also aware that traditional art creation can no longer meet the needs of the public's aesthetics and their own artistic expression. As a result, artists began to experiment, integrate, and innovate traditional art creation from different perspectives, thereby opening up "new" breakthroughs. These breakthroughs lie in the introduction of water-based acrylic painting materials into modern art creation; although water-based acrylic painting materials have been introduced to my country for a short period of time, it has brought a huge innovative theory [1]. In terms of time, water-based acrylic painting material is a relatively young painting material, and its essence is synthetic resin material. Compared with traditional art, watercolor, and other art materials, water-based acrylic painting materials are still a baby, and their wide range of applications is obvious despite their young age. From this point of view, the uniqueness of water-based acrylic painting

materials provides more visual language for our art creation and further brings more unknown exploration space to traditional art creation, as shown in Figure 1. In the current field of painting, water-based acrylic paintings often appear in people's field of vision. On the one hand, water-based acrylic painting materials are very inclusive; they can be connected with the canvas in the process of canvas creation; and they can become part of the watercolor when they are used on paper. On the other hand, water-based acrylic painting materials can expand the painting language and visual effects of the picture. Relying on its own unique characteristics, water-based acrylic painting materials express various "new" concepts in multiple layers, angles, and all directions [2]. With the general understanding and in-depth understanding of water-based acrylic materials by painters and the effects of water-based acrylic painting materials in the practice of art, it is further proved that promoting the widespread use of water-based acrylic painting materials is a quite correct strategy. This also just makes the water-based acrylic materials better serve the fine arts. In a sense, the integration of water-based acrylic
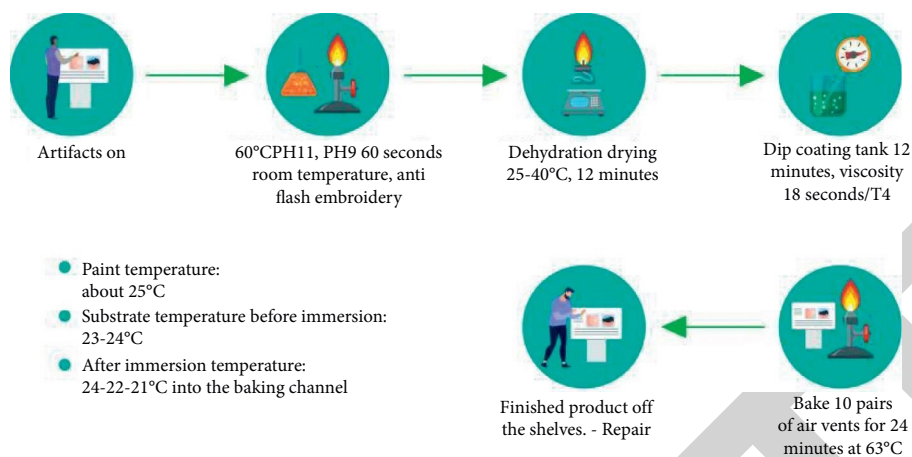
Figure 1: Chemical process of water-based acrylic dipping paint.

materials has enriched the artistic value of art, so as to better reflect the artist's creative concept and personal aesthetic orientation [3]. Therefore, we need to pass the corresponding theoretical basic research and specific material tests; only then can we understand the uniqueness of water-based acrylic painting materials and apply them to art creation. Based on the artistic creation of fine arts, with the help of the unique properties of water-based acrylic painting materials and the application of water-based acrylic painting materials in art creation as the point of convergence, this paper discussed the advantages of water-based acrylic.

2. Literature Review

Lee et al. proposed the integration of human nature, consciousness, and the human condition into visual representations. In terms of painting language, they used various means and water-based acrylic paints to create a series of painting techniques [4]. Arul et al. proposed nailing the canvas to the ground and using a stick, paintbrush, board brush, or a box with a small hole, dipped in water-based acrylic paint and dripped or flung onto the canvas [5]. He created with a series of improvisational movements, such as intuition, experience, and emotions, leaving a criss-cross of colors and patterns to express his ideas. Tafuro et al. raised the issue of garnet gel in water-based acrylic painting materials; since it is composed of mined garnet, it appears white in appearance when wet. But, after air-drying, it will be colored and become transparent [6]. In the artistic process, after unfolding it and patterning it with a paintbrush, use the palette knife to apply garnet gel only where needed; you will find that in areas where the gel coat of the coarse garnet is thinner, you can see different colors of the garnet: pink, brown, and red, where the coating is thick and deep. The gel can be seen to be a reddish-brown color close to black. Zhang et al. proposed different techniques to fully exploit the potential of water-based acrylic painting materials. While condensing the beauty of the rolling Loess Plateau terrain with irregular geometric figures, they also did not forget to express the majestic and rough northwest natural features vividly through technical effects such as color contrast, solid

edge lines, and textured brushstrokes [7]. Li et al. proposed that water-based propylene belongs to synthetic resin materials. Sprinkle appropriate amount of water on the base of different humidity or on the pigment that has not yet dried. The pigment on the top and the pigment on the bottom before or the pigment and the base are separated due to the action of water, which can form the ice crack effect similar to porcelain [8]. In the process of painting, through the control of the flow, penetration, fusion, drying, and other factors of the pigment, the interestingness of the picture shape and structure is enriched, and a modern visual painting style is formed. Pk et al. proposed that unlike oil paints, water-based acrylic paints do not turn yellow and become brittle, wrinkle, or crack. When oil paints dry and solidify, the paint layer will become hard, and it will become brittle after a long time, while acrylic paints dry and solidify very quickly, but at the same time, they can maintain their elasticity and durability; after drying, the acrylic painting painted on the canvas can be rolled up, stored somewhere, and taken out and restretched on the frame after a few years, without worrying about the color layer [9]. On the basis of the current research, the author proposes a chemical process based on water-based acrylic dipping paint, by discussing the coating and film properties of water-soluble acrylic dipping paint, combined with the application of pouring tank construction; the countermeasures to solve the common problems of paint film are summarized [10]. Compared with other dipping paints, it is proved that this paint has a good comprehensive performance in art painting.

3. Research Methods

3.1. Use Characteristics of Water-Based Acrylic Materials

3.1.1. Use Characteristics of Water-Based Acrylic Materials on Paper. The advantage of acrylic material is that it dries quickly, but the disadvantage is also that it dries quickly. This seemingly paradoxical statement sums up the embarrassment of water-based acrylic paint. Their faster setting times are better than slower drying oil paints, but there are some drawbacks. For example, soak a paintbrush in water when

not in use; otherwise, the paint will dry out on the bristles. The paint on the palette will dry quickly, so spray some water on it often. Or you can use a palette designed for water-based acrylic paints. Water-based acrylic paints can be applied to many substrates, drawing paper, canvas, wood, metal, and even exterior walls. But remember one very important thing, waterborne acrylic paints do not adhere to any oily or waxy substrates [11]. This principle excludes the possibility of painting water-based acrylic on oil painting boards and canvases, so when buying, you must ask clearly whether the painting board or canvas is prepared for water-based acrylic painting and whether it does not contain any oil-based materials. In terms of expression techniques, water-based acrylic paints show their unique flexibility. With the transparency of watercolor paints, the heaviness of oil paints, the covering power of gouache paints, and the elegance and softness of other emulsion paints, water-based acrylic paints can almost all be achieved or similar. It can be piled up repeatedly like oil paints to create a heavy feeling; add an appropriate amount of water, similar to gouache; and add a lot of water. You can draw watercolor and fine brushwork effects. Traditional techniques such as thin rubbing, thick coating, overcoating, and scratching can also be used in water-based acrylic paintings, which are more convenient and more effective than other pigments [12]. The effect of water-based acrylic works on paper is very similar to watercolor paintings, and the techniques are somewhat the same. If you are not particularly professional, you may not be able to distinguish whether it is a water-based acrylic or a watercolor painting. So many watercolor painters nowadays use water-based acrylic paint as the first step because it dries very quickly and the color is very bright after drying. But do not use too dark color in the first step; otherwise, the watercolor paint will not cover it. After drying, water-based propylene can form a plastic film. The second step is to use watercolor paint to further shape [13].

3.1.2. The Use Characteristics of Water-Based Acrylic Materials on Cloth. The thin water-based acrylic painting can reveal the original texture of the cloth. The first pass is no longer a single picture; the picture is thick and thin; and the sense of layering is clear, and the sense of picture has begun to show. The sunflower in the painting is composed of many small dots, and the paint on the pen is very full when painting. Rational thinking began to be added to the picture, and the in-depth depiction from the marquee to the picture layout and then to the framing [14]. The square frame gives a sense of stability and every step is well thought out. Including the color matching, the works of this period have high color purity and are very bright, giving people a very new feeling. The picture began to pay attention to the meaning of the dots, lines, and planes in the picture, and the painting language became richer. Water-based acrylic mineral pigments are much more delicate and can be mixed with water to become as transparent as watercolor; sprinkling paint on the wetted bottom can form an uncontrolled swimming state of the paint; it is the picture that produces a definite or uncertain relationship between the image and

color blocks; and some unexpected and accidental results are obtained; this may be the beauty of ink art and watercolor [15]. Compared to oil paints and watercolor paints, there are relatively few types of water-based acrylic paint colors because colorants such as Alizarin Crimson do not easily bond with resin binders, and these colors tend to set. In this case, other colorants have to be used instead. Between different manufacturers, there is a big difference between the types and names of colors. Water-based acrylic paints dry quickly, making it impossible to apply color over a wide range of substrates for extended periods of time, as oil paints do. This is a hassle for people who like to draw slowly and tend to evenly blend techniques. This is also a painting material that is more suitable for people to create in a modern society that pursues efficiency. But the reason why most artists choose water-based acrylic paint, that is why they can quickly apply color layer by layer, without worrying about disturbing the underlying colors [16]. Because water-based acrylic paint is water-based paint, it is easy to wipe off spills or clumps of color when it is wet. But once dry, the paint can be difficult to wash off, especially on fibers. Therefore, when painting, you can only wear old clothes, at the same time protect the surrounding furniture and floors, and put a damp cloth for an emergency.

3.1.3. The Use Characteristics of Water-Based Acrylic Materials on the Wall. The earliest use of water-based acrylic paint was to paint on walls, and due to its inclusiveness, it was gradually used to paint on various materials. There is not much difference between painting on the wall and painting on the cloth, but the area of the wall is very large, and the overall effect needs to be grasped. You cannot add too much water, and the techniques can all be used. The light and shadow effect cannot be painted by hand; it is sprayed with an airbrush; and the water-based acrylic paint can be injected into the airbrush to spray out many beautiful patterns. The walls are generally relatively large, so it is difficult to paint evenly; if half of the color is gone, it will be very troublesome; and it will be difficult to readjust the color to connect [17]. When painting on the wall, the smear is often not very even, and it will be ugly. It is not like drawing on canvas; the brushstrokes will look good when left. So, after painting it once, use a soft brush to dab some water with it while it is still dry, and the brush marks will disappear. The development of wall painting in China is getting faster and faster; in some villages, there are often many water-based acrylic paintings for publicity; now, interior decoration is often decorated with water-based acrylic paintings.

3.2. Determination of Chemical Process Parameters of Water-Based Acrylic Dipping Paint. Water-based acrylic dipping paint is a dipping paint with water as solvent, alcohol ether solvent as cosolvent, and acrylic monomer as the main film-forming material after solution polymerization. The main pigments used include strontium chrome yellow, No. 4 carbon black, silica, and precipitated barium sulfate. Additives are BYK products. The crosslinking agent is made of water-based amino resin (HMMM), which is prepared by

grinding and dispersing. It can be sprayed or dipped and is suitable for bottom-in-one coating. The main process parameters of acrylic water-based dipping paint are solid content, viscosity, PH value, paint temperature, paint dipping time, and so on. Under the condition that the PH value and paint temperature are guaranteed, the thickness of the paint film depends on the viscosity of the paint [18]. Low temperature is conducive to the stability of the paint liquid, but if the temperature is too low, the viscosity will increase, the leveling of the paint film after dipping is poor, the film thickness and flow marks increase, the mixed air bubbles are not easy to eliminate, and bubble pinholes are formed after drying, causing the paint film ills. When the temperature is higher than 30°C, the cosolvents and amines in the paint solution volatilize rapidly; the pH value drops; the paint solution system deteriorates; and the water solubility becomes poor. In order to maintain the stability of the bath liquid, the actual temperature control selection is 15~30°C [19]. The viscosity-temperature curve of dipping paint (T-4 cup) is shown in Figure 2.

It can be seen from the curve in Figure 2 that the viscosity decreases with the increase of temperature, the average temperature decreases by 1°C, and the viscosity increases for 2~4 s.

The viscosity dilution curve of dipping paint (thinner: deionized water, temperature: 25 ± 1°C, T-4 cup) is shown in Figure 3.

It can be seen from the curve in Figure 3 that from the viscosity of the original paint, with the increase of water addition, the viscosity decreases significantly, and when the addition of water continues to increase, the viscosity rises slightly (pseudothickness phenomenon), the lacquer liquid is hydrolyzed, and the system will be completely destroyed [20]. The influence of the solid content of the paint liquid on the appearance and film thickness of the paint film is shown in Table 1.

Since dip-coated parts include cold-rolled sheets, hot-rolled sheets, and castings, water-based dip coating should follow the principle of low viscosity and high solid content; if the workpiece gets a thick coating, the effect of secondary dip coating is better without increasing the viscosity. According to the test data, the parameters of the dipping process are determined as follows, and the casting is carried out: solid content: 33%~38%, dilution ratio: 2.6~3.6:1, viscosity: (30~40) $s > 25\%$, T-4 cup, paint temperature: 15~30°C, pH value: 8~10, and film thickness: 16~24 μm.

3.3. Process Management and Precautions.

(a) After degreasing, washing, surface conditioning, phosphating, and drying; the workpiece is guaranteed to be oil-free; phosphating is uniform and meticulous; sag can be reduced after dipping; and it is beneficial to improve adhesion, corrosion resistance, and film thickness and reduce the shrinkage.

(b) The dipping tank adopts a boat-shaped structure and suitable pump pressure to ensure the circulation of the tank liquid; the liquid surface flow rate is 0.5 m/min, which is beneficial to defoaming, preventing
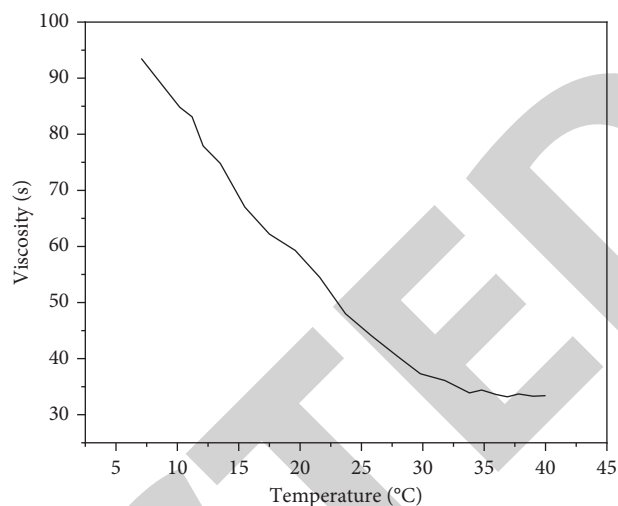
Figure 2: Viscosity-temperature curve.
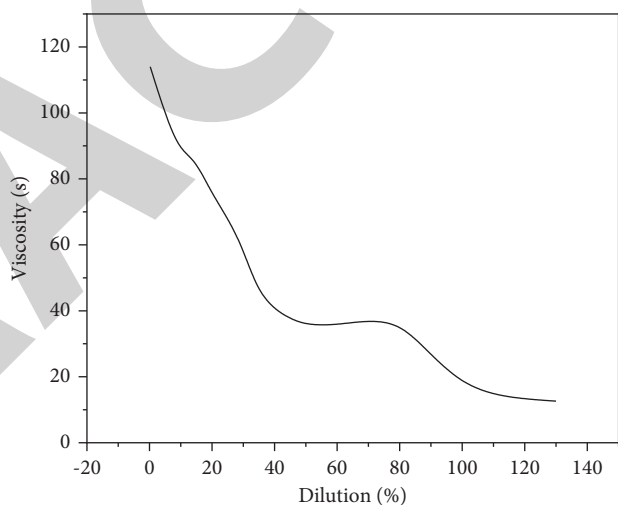
Figure 3: Viscosity-dilution curve.

pigment precipitation, and reducing viscosity; and the auxiliary tank is equipped with a 100-number copper mesh filter to remove impurities.

(c) The dip coating time is 2~3 min; the chain speed should not be too fast; and the vertical speed increase v ≤ 1 m/min; too fast is easy to produce sag and flow marks. The leveling time is guaranteed to be 10 min to facilitate leveling. The solvent of traditional solvent-based paint evaporates quickly and does not need flash evaporation, while water-based paint has a strong intermolecular hydrogen bonding force, strong cohesion, and high latent heat of evaporation; if it is directly baked at a high temperature, the internal water will evaporate and break through the paint film after the surface is cured, forming a solvent, explosion holes, and pinholes, so low temperature flashing is required.

(d) The drying temperature is guaranteed to be 140°C, and the time is 25~30 min; otherwise, it will affect the performance of the paint film [21].

TABLE 1: Effect of paint liquid solid content on paint film appearance and film thickness (25°C).

Paint liquid solids (%)	50	45	40	38	35	33	30
Reference viscosity (s)	70–100	60–90	45–70	33–40	30–36	28–33	22–30
Cold rolled sheet film thickness (μm)	35–40	30–36	24–30	20–24	18–22	15–20	13–15
Appearance of cold-rolled sheet	Difference	Difference	Better	Better	Good	Good	Good
Hot rolled sheet film thickness (μm)	45–60	40–55	30–45	25–35	22–30	20–26	18–22
Appearance of hot rolled sheet	Difference	Difference	Better	Better	Good	Good	Good
Hot rolled sheet film thickness (μm)	50–70	45–60	40–55	35–45	30–40	25–35	20–30
Appearance of hot rolled sheet	Difference	Difference	Better	Better	Good	Good	Good

TABLE 2: Control of dipping bath liquid, parameter changes, and their influence on the paint film.

Process parameters	Detection frequency	Question	Ills	Countermeasures
Solid content, 33%–40%	1 Time/day	High	Film thickness, flow marks, pinhole bubbles	Add original paint
		Low	Film Thickness, Shrinkage, Bottom Exposed	Add pure water
Viscosity, 28–45 s	2 Times/class	High	Flow marks, fat edges	Add pure water, solvent
		Low	Shrinking, film thin	Add original paint
pH, 8–10	2 Times/week	High		
		Low	Pigment settles and the system deteriorates	Refill original paint, amines
Temperature, 15–30°C	2 Times/class	High	Paint film sagging	Chilled water cooling
		Low	Flow marks, fat edges, matte paint film	Heat exchange cooling

TABLE 3: Performance index and comparative test.

Test items	Acrylic dip paint	Epoxy ester dip paint	Stoulook	Lesonal	Solvent dip paint	Asphalt dipping paint	Detection method
Original paint viscosity (s)	65~110	45~100	111	148	60~80	84	GB/T1723-93
Original paint fineness ($\leq\mu$m)	30	40	35	35	30	35	GB/T1724-89
pH	8~10	6.5~7	8~10	8~10	—	—	Precision test paper
Drying temperature (time)	140°C/30 min						GB/T1729-89
Appearance of paint film	Black, smooth						Visual inspection
Gloss (60°; %)	70 ~ 80	40~50	2	80	30~50	88	GB/T1754-88
Pendulum hardness, ($\geq$)	0.55	0.7	0.641	0.54	0.5	0.34	GB/T1730-93
Adhesion (grade)	1	3	1	1	1	1	GB/T1720-89
Flexibility (mm)	1	2	1	1	1	1	GB/T1731-93
Impact resistance (kg cm)	50	50	50	50	50	50	GB/T1732-93
Salt spray resistance (without phosphating; ($\geq$h)	96	140	32	48	60	8	GB/T1771-91
Salt spray resistance (phosphating; $\geq$ h)	206	240	206	214	144	50	GB/T1771-91
Water resistance (phosphating; $\geq$h)	650	650	650	263	500	550	
Moisture and heat resistance ($\geq$h)	240	240	—	—	350	100	GB/T1740-79
Artificial aging test (h)	260	—	—	—	—	—	GB/T1865-80
Storage stability (months)	6	6	6	6	6	6	Visual inspection
No. 70 gasoline resistance ($\geq$h)	550	168	550	550	96	550	GB/T1734-93

The following Table 2 shows the control of dipping bath liquid, parameter changes, and their effects on the paint film and their countermeasures.

4. Analysis of Results

Water-based acrylic dip paint is a thermosetting coating because the molecular chain of the polymer contains a considerable number of active functional groups such as carboxyl, hydroxyl, amine, ether, amide, and so on and guaranteed water solubility. During thermal curing, the reactive group reacts with methylol and methoxy in the crosslinking agent (water-based amino resin); it forms a coating film with a dense network structure and has the dual coating properties of acrylic and amino paint, such as high gloss, gloss retention, color retention, high weather

resistance, and good corrosion resistance, as shown in Table 3.

Through the above performance comparison, the water-based propylene of this process is used for practical drawing, and the following is the result discussion. Water-based acrylic paints dry quickly, can be diluted with water, and are waterproof when dry. In fact, they can be applied to any substrate in any thickness and by any technique, from the thinnest coat to the heavy impasto. The color is intense and vibrant, even when diluted, and the hue of the color does not change after the paint dries. The water-based acrylic paint dries to form a drab, slightly rough coating. However, the addition of water-based acrylic additives to the pigments can change the density of the pigments, resulting in different texture effects, while also making the colors brighter and deeper [22]. With the addition of additives, the diluted pigments can preserve their original adhesion, and at the same time, flow and drawability are improved. Some additives can be used to control the drying rate of pigments. There are no special regulations when using water-based acrylic paint additives. This is different from oil painting; when painting oil paintings, the colors are stacked; and the elasticity of the upper layer is better than that of the lower layer. It can paint opaque layers of color; it can also be diluted with water or solvent to form a transparent color layer. Canned paint is smoother and more fluid than tube paint and can be easily diluted with water or a solvent. This property makes water-based acrylic paints well-suited to the watercolor technique. It also works well for covering large areas of a single color. The paint dries to a smooth, even coating that is less glossy than using a tube of water-based acrylic paint. Finished paint comes in beakers, jars, or plastic bottles with spouts. All brushes suitable for oil painting and watercolor painting, whether natural or artificial, can be used for water-based acrylic painting. Liquid water-based acrylic paints flow quickly and smoothly, very close to sketch inks, compared to many colored inks that fade when exposed to light, most liquid water-based acrylic energy paints are very durable. Liquid water-based acrylic paints come in a bottle with an eyedropper, and they are suitable for expressing coating skills and detailed pen style. Liquid water-based acrylic paints are made with base resin and can be removed with an alkaline scrubber. Limit blending to two or three colors to avoid muddy colors. When the resin binder still contains moisture, it is cream-colored. So wet water-based acrylic paint will look lighter and softer than dry. When the paint dries, the binder becomes transparent, so the color appears brighter, also a little deeper.

5. Conclusion

The author proposes a chemical process based on water-based acrylic dipping paint, discusses the coating and film properties of water-soluble acrylic dipping paint, combines the application of art practice, summarizes the countermeasures to solve the disadvantages of common paint films, and proves that this paint has a good comprehensive performance by comparing with other dipping paints. The results show that the chemical process of water-based acrylic dipping paint has water resistance, high gloss, gloss retention, color retention, high weather resistance, and good corrosion resistance in the process of art painting.

Data Availability

The data used to support the findings of this study are available from the corresponding author upon request.

Conflicts of Interest

The authors declare that they have no conflicts of interest.

References

[1] N. Hara, Y. Hasegawa, H. Tanaka, M. Yoshimune, and H. Negishi, "Development of zif-8 membranes for propylene/propane separation by direct growth on a zno-modified support without activation," *Journal of Chemical Engineering of Japan*, vol. 53, no. 10, pp. 616–625, 2020.

[2] O. Ovchinnikova, Y. Polishchuk, K. Sukhyy, and E. Shembel, "Non-aqueous ionic liquids based on quaternary ammonium salts for lithium-sulfur batteries," *ECS Transactions*, vol. 105, no. 1, pp. 219–223, 2021.

[3] M. Ben Henda, "Effect of pyrrolidinium formate ionic liquid on micellization of direct and reverse pluronics in aqueous solutions," *The Journal of Physical Chemistry B*, vol. 124, no. 27, pp. 5730–5739, 2020.

[4] B. Lee, M. K. Seo, D. Kim et al., "Dissecting landscape art history with information theory," *Proceedings of the National Academy of Sciences*, vol. 117, no. 43, pp. 26580–26590, 2020.

[5] A. Arul, S. Sivagnanam, A. Dey, O. Mukherjee, S. Ghosh, and P. Das, "The design and development of short peptide-based novel smart materials to prevent fouling by the formation of non-toxic and biocompatible coatings," *RSC Advances*, vol. 10, no. 23, pp. 13420–13429, 2020.

[6] G. Tafuro, A. Costantini, G. Baratto, S. Francescato, and A. Semenzato, "Evaluating natural alternatives to synthetic acrylic polymers: rheological and texture analyses of polymeric water dispersions," *ACS Omega*, vol. 5, no. 25, pp. 15280–15289, 2020.

[7] W. Zhang, J. Bai, C. Zhou, H. Yu, and L. Wang, "Preparation and properties of water-based acrylic emulsion-assisted flexible building tiles," *RSC Advances*, vol. 12, no. 9, pp. 5340–5348, 2022.

[8] X. Li, Z. Wang, W. Li, and J. Sun, "Superstrong water-based supramolecular adhesives derived from poly (vinyl alcohol)/poly (acrylic acid) complexes," *ACS Materials Letters*, vol. 3, no. 6, pp. 875–882, 2021.

[9] A. Pk, A. Tt, A. Mmc, B. Ks, C. Cg, and A. Kj, "Development of highly performing tio2 complex thin films by novel combined physico-chemical process for enhanced photo-catalytic applications - sciencedirect," *Ceramics International*, vol. 46, no. 8, pp. 12437–12448, 2020.

[10] A. Wyl, B. Xjja, A. Xqp et al., "Functional capsules encapsulating molecular-recognizable nanogels for facile removal of organic micro-pollutants from water," *Engineering*, vol. 7, no. 5, pp. 636–646, 2021.

[11] N. Kumar, N. Kumar, and A. Bandyopadhyay, "A state-of-the-art review of laser welding of polymers - part i: welding parameters," *Welding Journal*, vol. 100, no. 7, pp. 221–228, 2021.

[12] Y. Zhang, X. Kou, Z. Song, Y. Fan, M. Usman, and V. Jagota, "Research on logistics management layout optimization and

Retraction

Retracted: Chemical Characteristics of Coil Heavy Metal Elements and Ecological Security Risks Caused by Fertilization

Journal of Chemistry

This article has been retracted by Hindawi following an investigation undertaken by the publisher [1]. This investigation has uncovered evidence of one or more of the following indicators of systematic manipulation of the publication process:

(1) Discrepancies in scope

(2) Discrepancies in the description of the research reported

(3) Discrepancies between the availability of data and the research described

(4) Inappropriate citations

(5) Incoherent, meaningless and/or irrelevant content included in the article

(6) Peer-review manipulation

The presence of these indicators undermines our confidence in the integrity of the article's content and we cannot, therefore, vouch for its reliability. Please note that this notice is intended solely to alert readers that the content of this article is unreliable. We have not investigated whether authors were aware of or involved in the systematic manipulation of the publication process.

Wiley and Hindawi regrets that the usual quality checks did not identify these issues before publication and have since put additional measures in place to safeguard research integrity.

We wish to credit our own Research Integrity and Research Publishing teams and anonymous and named external researchers and research integrity experts for contributing to this investigation.

The corresponding author, as the representative of all authors, has been given the opportunity to register their agreement or disagreement to this retraction. We have kept a record of any response received.

References

[1] Y. Ma, Q. Hao, and A. Zhong, "Chemical Characteristics of Coil Heavy Metal Elements and Ecological Security Risks Caused by Fertilization," *Journal of Chemistry*, vol. 2022, Article ID 4211602, 7 pages, 2022.

Hindawi

Research Article

Chemical Characteristics of Coil Heavy Metal Elements and Ecological Security Risks Caused by Fertilization

Yanfeng Ma [ID],[1,2] **Qingsheng Hao** [ID],[1] **and Ailin Zhong** [ID][2]

[1]*College of Economics & Management, Jilin Agricultural University, Changchun, Jilin 130118, China*
[2]*College of Foreign Languages, Jilin Normal University, Siping, Jilin 136000, China*

Correspondence should be addressed to Yanfeng Ma; 11231120@stu.wxic.edu.cn

In order to investigate the effects of fertilization on soil chemical characteristics and ecological security, the chemical characteristics and ecological security risk analysis of heavy metal elements in a certain soil caused by fertilization were proposed. The contents of Ni, V, Cr, As, Cd, Pb, Zn, and Hg in 1,065 surface soil samples collected in a district of a city in the southwest agricultural area were tested and analyzed. Multivariate statistical analysis and spatial analysis were used to clarify the geochemical distribution characteristics of these heavy metals, and the possible main sources were also discussed. The results showed that the eight heavy metals could be divided into three categories. The first category included Ni, V, Cr, and As, whose content was lower than the background value in Beijing. And the distribution was mainly affected by natural factors such as parent materials of soil formation. The second category included Cd, Pb, and Zn, whose average content was higher than the background value. And the content was the highest in residential areas. In addition to the parent material inherited from the soil, the distribution characteristics of these elements were greatly affected by human activities. And Cd was significantly more affected by human activities than Pb and Zn. The third category included Hg, and it was inferred that atmospheric deposition was the main factor affecting the distribution of Hg. It was concluded that the Hakanson method was used to evaluate the ecological risk of heavy metals in soil, and the results showed that the potential ecological risk index was low in the area.

1. Introduction

With the development of the social economy, the impact of human activities (industrial and agricultural production, transportation, etc.) on the urban natural environment tends to be strong. With the development of the city's industrial and transportation, the original inheritance of urban soil has changed in a certain intensity. The soil is widely distributed in the suburban areas, urban rivers, leisure venues, stadiums, roads and waste plant, and abandoned factories around or covered by industrial and building facilities [1]. With the acceleration of global urbanization, there are more and more heavy metals such as cadmium (Cd), and copper (Cu). Nickel (Ni), lead (Pb), zinc (Zn), mercury (Hg), chromium (Cr), iron (Fe), manganese (Mn), molybdenum (Mo), and cobalt (Co) entering the soil through various ways. At present, all countries in the world are polluted by soil heavy

metals to varying degrees, thus damaging the normal function of the ecosystem. More seriously, heavy metals will also enter animals, plants, and human bodies through the food chain and water, affecting their normal survival, which is a potential "chemical time bomb." If the human body absorbs them excessively, it will also lead to a variety of endemic diseases and even endanger human life and health. In addition, soil heavy metal pollution also has the characteristics of latency, lag, and accumulation [2, 3]. If the soil is seriously polluted by heavy metal elements, it requires a large amount of money and a long treatment cycle. The harm caused by it is more serious than the harm caused by air and water pollution and is more difficult to eliminate. In recent decades, the research on soil heavy metal pollution has attracted the attention of many scholars at home and abroad, but the focus is generally on agricultural soil. However, there are relatively few researches on heavy metal pollution in
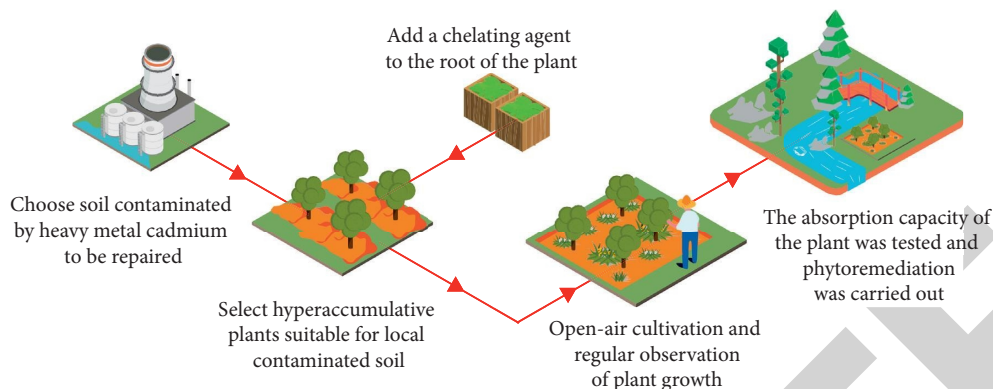
Figure 1: Chemical characteristics of soil heavy metal elements caused by fertilization by farmers.

urban soil. Therefore, the ecological and environmental effects brought by the drastic environmental changes caused by human activities should gradually become a scientific issue of concern as shown in Figure 1.

2. Literature Review

Wang and Ji used multivariate statistics and Fourier sum spectral analysis to analyze the sources of heavy metals in the surface soil samples of vegetables in a certain area and conducted safety warning research on the content of lead in soil and vegetables. The results showed that lead pollution in local vegetables may be caused by human activities (such as industrial wastewater discharge and gasoline combustion) [4]. Alobaidi et al. investigated the ecological geochemical characteristics of lead in a certain area and concluded that there was no significant relationship between lead geochemical characteristics and the cause of liver cancer prevalent in the area [5]. Sun et al. investigated the current situation of heavy metal element pollution in rural soil of the Pearl River Delta and showed that in addition to the pollution sources such as chemical fertilizer, pesticides, and livestock and poultry, industrial and other pollution also had a great impact. In addition, the industrial soil in the research area is dominated by excessive Cu, while the planting soil is dominated by excessive Cd [6]. Mukeba et al. investigated the spatial distribution and source analysis of 12 heavy metals on the surface of Lianyuan, a typical coal mining city, and the results showed that most heavy metals were related to human activities. Based on the PMF model, the influence of natural sources, atmospheric deposition, industrial activities, and agricultural activities on the source and distribution of 12 heavy metals in Lianyuan soil was 33.6%, 26.5%, 23.44%, and 16.91%, respectively. Some people also conducted quantitative research on different sources of soil heavy metals in Beijing [7]. Fouladi et al. used the MCR-WALS model to calculate quantitatively that contribution rates of atmospheric deposition, fertilizers and pesticides, and natural sources to soil heavy metals accounted for 15.5%–16.4%, 5.9%–7.7%, and 76.0%–78.6%, respectively, indicating that natural sources dominated soil heavy metals in Beijing as a whole [8]. Jwad and Abbas investigated the soil heavy metals (Cd, Hg, Cu, and Zn) in a vegetable base in

North China, and showed that the average content of each heavy metal in this area did not exceed the second-level soil quality standard. Through the calculation of exposure risks in three ways, it was found that non-carcinogenic and carcinogenic risks were low and would not cause harm to human health [9].

In the research, combined with agriculture area agriculture in southwest district neighborhood of heavy metals in the soil, which was the research object, the geochemical characteristics of eight heavy metals in soil (Ni, V, Cr, As, Cd, Pb, Zn, and Hg) were analyzed. Combined with multivariate statistics and spatial analysis discrimination, the main source of heavy metal was judged. The soil's environmental quality and its potential ecological risk were evaluated according to the relevant standards.

3. Research Methods

3.1. Sample Collection and Analysis. In this research, sampling grids were divided into $0.5 \, \text{km} \times 0.5 \, \text{km}$ in the research area. In order to reduce the random error, 5 surface soil samples were collected in each grid; the sampling depth was $0 \sim 20 \, \text{cm}$; and each sample weighed about $1.0 \, \text{kg}$. After mixing, a mixed sample was prepared, and a total of 1,065 samples were collected. GPS recorded the actual coordinates of sampling points. The collected soil samples were dried by air and ground, then passed through a nylon sieve with a diameter of 70 mesh, and then crushed through a 100-mesh sieve with an agate-grinding bowl without pollution. In order to avoid the volatilization of metal Hg, the soil samples were stored in a cool environment for future use.

The samples were analyzed and determined by National Geological Experimental Testing Center in reference to national soil environmental quality standards. The contents of Ni, V, Cr, Pb, Zn, SiO_2, Al_2O_3, and Fe_2O_3 were measured by x-ray fluorescence spectrometry (RS-1818, HORNG JAAN). The contents of Cd were determined by graphite furnace atomic absorption spectrophotometry (AA6810SONGPU), and the contents of Hg and As were determined by atomic fluorescence spectrometry (XGY-1011A). In order to ensure the accuracy of the data, the National Geological Experimental Testing Center took the relevant quality assurance and quality control (QA/QC)

measures, and the recovery rate of each standard sample was between 92% and 108%. The standard deviation of 20% of the samples was less than 5%.

3.2. Data Processing.
Geochemical statistical analysis and multivariate statistical analysis are effective tools to identify pollution sources. These methods were used to identify the main sources of heavy metals in soil. Kriging interpolation method in MapGis 6.7 was used for spatial mapping [10]. Data were analyzed by Pearson correlation analysis, principal component analysis (PCA), and cluster analysis (CA) in SPSS16.0, in which the maximum variance rotation method was adopted for principal component analysis (PCA).

3.3. Assessment Methods.
The single factor index method is widely used to evaluate the pollution of single heavy metal elements in the soil. The calculation formula is as follows:

$$P(i) = \frac{C_i}{S_i}, \tag{1}$$

where $P(i)$ is the environmental quality index of pollutants (i is an element) in soil, C_i is the measured concentration of heavy metals in soil, and S_i is the assessment standard value of heavy metals in soil. In the research, the soil background value of a city was used as the assessment standard of heavy metals in soil. The segmented assessment criteria of $P(i)$ value were as follows: $P(i) \leq 1$ means no pollution, $1 < P(i) \leq 2$ means light pollution, $2 < P(i) \leq 3$ means moderate pollution, and $P(i) > 3$ means heavy pollution.

In addition, the potential ecological hazard index method proposed by Swedish scholar Hakanson in 1980 was used to evaluate the soil environmental risk. The Hakanson index method comprehensively considered the synergistic effect of multiple elements, toxicity level, pollution concentration, and environmental sensitivity to heavy metal pollution. It could reflect the impact potential of heavy metals on the ecological environment comprehensively and was suitable for the assessment and comparison of sediment and soil in a large regional range. The calculation formula is as follows:

$$E(i) = T_i \times \left(\frac{C_i}{C_0} \right), \tag{2}$$

where $E(i)$ is the potential ecological risk coefficient of a single heavy metal and T_i is the toxicity response coefficient of a single heavy metal, and the toxicity coefficients of each metal are $Ni = Pb = 5$, $Cr = V = 2$, $As = 10$, $Cd = 30$, $Zn = 1$, and $Hg = 40$. C_i represents the concentration of heavy metals in soil. C_0 is the assessment standard value of heavy metals in soil. In the research, the soil background value of a city was used as the assessment standard of heavy metals.

The sum of the potential ecological risk coefficient $E(i)$ of each element is the potential ecological risk index (RI) of this region. The calculation formula is as follows:

$$RI = \sum E(i). \tag{3}$$

According to the potential ecological risk coefficient of each element and the comprehensive potential ecological risk index, soil quality can be divided into five grades: mild ecological pollution, moderate ecological pollution, intense ecological pollution, very intense ecological pollution, and extremely intense ecological pollution (see Table 1).

4. Result Analysis

4.1. Characteristics of Heavy Metal Content in Soil.
The enrichment coefficient is the ratio of the average content of heavy metals in soil to the background value in this area, and the enrichment ratio is the proportion of the samples exceeding the natural background value to the total samples. The average value, enrichment coefficient, and local background values of each metal element in the research area are listed in Table 2.

The results showed that the average contents of heavy metals: Ni, V, Cr, As, Cd, Pb, Zn and Hg, were 21.773 mg/kg, 70.642 mg/kg, 55.476 mg/kg, 6.957 mg/kg, 0.144 mg/kg, 24.285 mg/kg, 67.724 mg/kg, and 0.046 mg/kg, respectively. The average values of Ni, V, Cr, As and Hg were slightly lower than the background values of a city. And the enrichment coefficients (EF) of these elements were less than 1, which were 0.88, 0.89, 0.91, 0.90, and 0.78, respectively. The average values of Cd, Pb, and Zn elements were greater than the background value of a city, and the enrichment coefficients were greater than 1, which were 1.21, 1.03, and 1.18, respectively.

Box diagrams and histograms of elements are commonly used to represent the distribution characteristics of elements (see Figure 2). Some researches have shown that in the natural state; if there is no other external source, the element is normally distributed. As shown in Figure 2, Ni, V, Cr, and As are approximately normally distributed. And it is speculated that they are mainly affected by natural factors and less by exogenous factors. However, Cd, Pb, Zn, and As are not normally distributed, which means that these elements may have external input [11]. In addition, the box diagram shows that Ni, V, Cr, and As are distributed symmetrically except for a few outliers. However, Cd, Pb, Zn, and Hg elements not only have an obvious trend to the right but also appear partial outliers at both ends of the box diagram.

4.2. Spatial Distribution of Heavy Metals in Soil.
The geochemical map of heavy metal element content can provide effective information for the source and pollution range of elements. In the research, the cumulative frequency method was used to classify the elements, and the Kriging interpolation method was used to draw the spatial distribution map of each element's content combined with the location of sampling points. The contents of Ni, V, Cr, and As were low in the west but high in the east and north. The enrichment proportions of these four elements were low, which were 30.89%, 29.86%, 32.2%, and 26.67%. The vast majority of the research area was covered by Quaternary sediments, with

TABLE 1: Classification standard of potential ecological risk of soil heavy metals.

Potential ecological risk coefficient, $E(i)$	Potential ecological risk index, RI	Pollution degree
<40	<150	Mild ecological pollution
$40 \leq E(i) < 80$	$150 \leq RI < 300$	Moderate ecological pollution
$80 \leq E(i) < 160$	$300 \leq RI < 600$	Intensive ecological pollution
$160 \leq E(i) < 320$	≥600	Very intense ecological pollution
≥320	—	Extremely intense ecological pollution

TABLE 2: Statistics of soil heavy metal content in the research area (W_B/(mg/kg)).

Element	Mean ± standard deviation	Maximum	Minimum	Background value	Enrichment coefficient
Ni	21.80 ± 9.05	128.00	4.37	24.7	0.88
V	70.7 ± 17.9	223.00	16.70	79.2	0.89
Cr	55.5 ± 27.0	622.00	11.20	60.8	0.91
As	6.96 ± 2.80	30.40	1.85	7.7	0.90
Cd	0.144 ± 0.063	0.740	0.048	0.119	1.21
Pb	24.3 ± 5.27	77.90	12.20	23.7	1.03
Zn	67.7 ± 23.1	262.00	18.10	57.5	1.18
Hg	0.046 ± 0.133	3.740	0.007	0.059	0.78
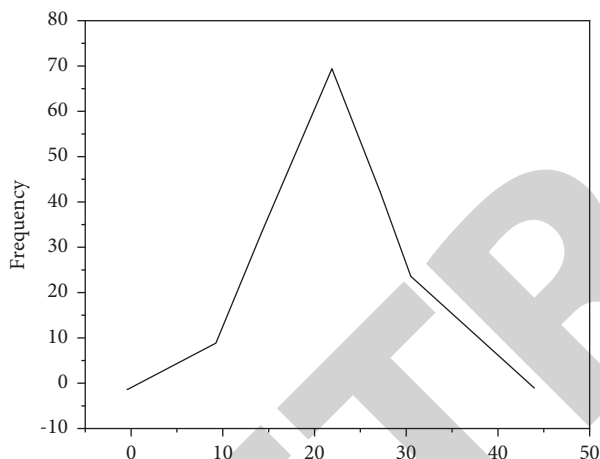
FIGURE 2: Histogram and box diagram of the heavy metal content distribution.

TABLE 3: Principal component analysis results of soil heavy metals.

Heavy metal	The principal components		
	1	2	3
Ni	0.932	0.177	0.059
V	0.906	0.098	0.017
Cr	0.899	−0.010	−0.036
As	0.524	0.413	0.245
Cd	0.111	0.878	0.069
Pb	−0.023	0.852	0.078
Zn	0.233	0.825	0.074
Hg	0.036	0.128	0.977
The eigenvalue	3.467	1.899	0.914
Variance (%)	43.342	23.743	11.427
Cumulative variance (%)	43.342	67.085	78.511

only a small range of limestone and dolomite exposed in a few areas in the north and east [12]. Because the weathering degree of rocks was controlled by environmental factors, topographic conditions, and exposure time, the more thoroughly the weathering degree is, the higher the enrichment degree of Si, Al, Fe, and other elements is. Among them, Al_2O_3/SiO_2 is a commonly used index to calculate the weathering degree, which can indirectly explain the weathering degree of rock. The higher the Al_2O_3/SiO_2 ratio is, the higher the weathering degree is. Fe_2O_3, as a product of rock weathering into the soil, is an important component of soil, and Fe_2O_3 can adsorb heavy metals in soil by affecting the charge properties of the soil surface so that Cr, As, and other elements in the surrounding soil of mountainous areas present significant high values. Similar researches have been reported in the southern area of a city. According to the spatial distribution of Fe_2O_3 and Al_2O_3/SiO_2, it can be seen that the weathering degree of rocks in the northern and eastern parts of the research area is relatively high. The area

with high Ni, V, Cr, and As contents is consistent with the area with a high degree of rock weathering, indicating that these four elements are mainly affected by rock weathering.

Compared with the above four elements, the enrichment proportion of Cd, Pb, and Zn elements was 66.29%, 45.63%, and 63.38%, respectively. The maximum content was found in a few areas in the central and northwest regions. The middle part of the research area was the area with the largest population concentration density in a county. G101 and highway ran through the area. And there were many well-known scenic spots and leisure resorts in the northwest of the research area. It was speculated that these three elements may be affected by local human activities. The enrichment proportion of Hg in soil samples in the research area was 14.37%, and the highest content was found in the central residential area. Because Hg was volatile and could be widely exchanged between soil and air, it formed unique distribution characteristics.

4.3. Principal Component Analysis and Cluster Analysis.
The principal component analysis is a method that converts multiple indexes into a few comprehensive indexes to reflect

the original data information, which is used to distinguish various metal sources in soil research. Elements with a high load on the same principal component may have similar sources [13]. Principal component analysis of heavy metal elements in the research area showed that 3 principal components were extracted from the eight heavy metal elements (see Table 3). These three groups of principal components could explain 78.51% of the total variance, which should be considered the main component. The variance of other components was less than 10%, so these three groups of factors were mainly discussed in the research.

The variance of the first principal component accounted for 43.34% of the total variable variance. Although the variance of the first principal component did not exceed 50%, the variance of the first principal component was the largest among the three principal components, indicating that the first principal component obviously affected the behavior characteristics of soil heavy metals in this area. The Ni, V, Cr, and As elements had higher loading on the first principal component, and the enrichment coefficient of the above four elements was low. The histogram showed that the Ni, V, Cr, and As elements had normal distribution and the spatial distribution of element content showed that the high values of Ni, V, Cr, and As elements appeared in the areas with high weathering degrees. These results indicated that these elements were less affected by exogenous substances and were mainly controlled by soil parent materials in this area, which was consistent with the above conclusion.

The second principal component accounted for 23.74% of the variance of the total variables. Cd, Pb, and Zn elements had a high load on the second principal component. The average values of these three elements all exceeded the background values, and their enrichment coefficients were high. The histogram showed that they were not normally distributed. The spatial distribution diagram of element content showed that the above elements had high values in the central and northwestern regions of the research area. Local agricultural activities such as planting crops and raising livestock were the main factors affecting Cd, Pb, and Zn elements in the soil. Large orchards and vegetable gardens may have been planted in the research area in order to provide an urban area with quality and sufficient agricultural products, and fertilizers and pesticides may have been used. Cd and Zn were the main additives of phosphate fertilizer and zinc fertilizer because of their insecticidal and growth-promoting effects. The application of chemical fertilizer was one of the main factors affecting the heavy metal Cd and Zn in soil. The use of Pb insecticides also significantly increased Pb content in orchard growing areas. It was very common for local agricultural planting to use plastic film, and the residual plastic film in the soil also led to the increase of Cd content in the soil [14]. In the research area, animal husbandry was developed, and livestock manure was considered to be a good supply source of soil Zn. Long-term application of organic fertilizer could increase the content of Zn in soil by 5%–30%. Other researches showed that Zn content in soil would also show a trend of accumulation with the increase of the planting years of greenhouse vegetable plots [15]. In addition, anthropogenic disturbances in scenic spots and leisure resorts could also enrich elements. In addition to the inheritance from the parent materials, the above three elements were obviously interfered with by human factors.

The third principal component of Hg accounted for 11.43% of the variance of the total variable. Hg was different from other elements because of its volatility, so it was divided into a separate category. Building facilities and medical facilities in densely populated areas greatly increased the Hg content in the environment. Meanwhile, the lifestyle of local residents such as sewage irrigation and garbage incineration was also one of the important factors affecting Hg content.

The first principal component (F1) included Ni, V, Cr, and As, which were high in the northern and eastern parts of the research area due to the influence of rock weathering and soil parent material. The second principal component (F2), including Cd, Pb, and Zn, was higher in densely populated areas of the research area and was greatly affected by human activities. The high value of Hg in the third principal component (F3) was mainly affected by atmospheric deposition in the research area.

Cluster analysis is a method to classify variables according to the degree of intimacy between variables. Through cluster analysis, variables with similar characteristics and behaviors can be grouped into a group, which has been widely used in statistical analysis [16]. The application of cluster analysis in earth science can cluster the elements from the same material source into one class and distinguish the elements from different material sources. The distance of cluster analysis represents the closeness degree between elements. The closer the clustering distance is, the closer the relationship between elements is. In this research, eight heavy metal elements were divided into three groups according to the standard distance of 15~20. The results of cluster analysis and principal component analysis were similar.

Category I: Ni, V, Cr, and As elements. The distribution of the four elements in soil samples accorded with normal distribution, and the enrichment coefficient was less than 1. They have a higher load in the first principal component, and higher values only appear in the area with a higher weathering degree of rock. This indicates that the distribution of elements Ni, V, Cr, and As in the study area is relatively uniform. The categories of heavy metals were mainly influenced by natural factors and derived from soil parent material formed by weathering of local rocks.

Category II: Cd, Pb, and Zn elements. The histogram showed that the above three elements were not normally distributed and the enrichment coefficient was greater than 1, which occupied a high load in the second principal component. This kind of element was the most seriously polluted element in soil. And the pollution of this kind of element has been reported in many literature.

Heavy metal elements Pb and Zn are known as traffic pollution elements. The closer the road is, the higher the content of Pb is. And the accumulation of Pb content is closely related to traffic flow. Pb is considered a landmark element of vehicle pollution, and vehicle exhaust becomes one of the important sources of Pb in soil due to the

Table 4: Soil element risk assessment table.

Element	Quantity of the samples				$E(i)_{\text{mean}}$
	$P(i) \leq 1$	$1 < P(i) \leq 2$	$2 < P(i) \leq 3$	$P(i) > 3$	
Ni	735	319	8	3	4.407
V	779	281	5	0	1.784
Cr	746	302	10	7	1.825
As	720	336	7	2	9.035
Cd	391	643	25	6	36.329
Pb	577	480	5	2	5.123
Zn	389	647	22	7	1.178
Hg	922	116	18	9	31.002

combustion of leaded gasoline. Although the use of leaded gasoline has been banned in China since 2000, the high content of Pb in this area obviously reflects the severity of Pb gasoline pollution in the past because of its strong stability and difficulty in degradation [17]. Pb and Zn elements in the environment have very similar sources. The driving of motor vehicles, the oxidation of motor lubricating oil, the wear of brakes and tires, and the shedding of paint all affect the accumulation of Zn in the soil. Cd is a typical element introduced into the environment by human activities. Industrial activities such as metal smelting, production of plastic stabilizers and additives and batteries, burning of fossil fuels, and production of industrial wastes in the research area can affect the content of Cd in soil [18].

Category III: Hg element. The use of coal for heating in the Beijing-Tianjin-Hebei region has increased significantly in recent decades, and Hg released by coal combustion is directly discharged into the environment, which also makes Hg remain in the soil in the form of atmospheric deposition [19].

4.4. Ecological Risk Assessment. The single pollution index and ecological hazard index of eight heavy metal elements were calculated. The potential ecological risk coefficient of each element and the number of samples under different single pollution levels were calculated. The results were listed in Table 4. The results showed that most of the sampling sites of the eight elements were not polluted, and the single pollution index ($P(i)$) of a few sampling sites of a few heavy metals was slightly greater than the range of moderate pollution. Among them, the mean value of the single pollution index of Cd element was the largest ($P(\text{Cd})_{\text{mean}} = 1.21$), followed by Zn ($P(\text{Zn})_{\text{mean}} = 1.18$) and Pb ($P(\text{Pb})_{\text{mean}} = 1.03$). Previous researches reached similar conclusions [20, 21]. The average pollution indexes of the other five elements were all less than 1 ($P(\text{Cr})_{\text{mean}} = 0.91$), ($P(\text{As})_{\text{mean}} = 0.90$), ($P(\text{V})_{\text{mean}} = 0.89$), ($P(\text{Ni})_{\text{mean}} = 0.88$), and ($P(\text{Hg})_{\text{mean}} = 0.78$). It indicates that the soil was not contaminated. According to the mean value of single factor pollution index, the order was Cd > Zn > Pb > Cr > As > V > Ni > Hg.

The potential ecological risk of eight heavy metal elements in the research area was evaluated by the Hakanson assessment method, and the potential ecological risk coefficient ($E(i)$) and potential ecological risk index (RI) of eight heavy metal elements were calculated. The results showed that the $E(i)$ values of the eight heavy metals were all lower than 40,

indicating that the single factor ecological pollution risk was low. Combined with the sampling points, the potential ecological risk index map could be drawn. RI values of more than 94% of the sampling points in the research area were lower than 150, indicating that the potential ecological harm index of local heavy metals was low and below the level of mild ecological pollution [22]. A very small number of high values occurred in local residential areas, indicating that the current soil environmental protection was good. It was suggested to maintain the current soil protection measures and create a good living environment [23–25].

5. Conclusions

In the research, 1,065 soil samples were collected in the southwest of a city and 8 heavy metals were analyzed. Spatial analysis and multivariate statistics were used to clarify the distribution characteristics of heavy metals in soil, and the main factors affecting the distribution characteristics were discussed. The results showed that the average value of Ni, V, Cr, and As elements was lower than the background value of the city. The histogram was normal distribution, and it had a high load on the first principal component of principal component analysis. The spatial distribution diagram of element content showed that the contents of Ni, V, Cr, and As elements were higher in the northern and eastern areas of the research area with a high degree of rock weathering. It showed that its distribution was mainly affected by the parent material of soil formation. Cd, Pb, and Zn element background value was higher compared to the average content of the city region. The enrichment coefficient was greater than 1. The content of the histogram did not obey the normal distribution, and the principal component analysis of the load on the second principal components was relatively high. And the three elements in densely populated and range larger regional content was higher; it may be affected by artificial factors such as local traffic, agriculture, and tourism. Hg had a non-normal distribution and was independently divided into the third principal component. Due to its volatility, its distribution characteristics were mainly affected by atmospheric deposition.

By calculating the single pollution index, potential ecological risk coefficient, and potential ecological risk index of each heavy metal element in a certain area, it could be concluded that all indexes of heavy metal elements in the local soil were low and below the level of mild pollution. However, long-term human activities may lead to continuous accumulation of heavy metals, which may pose a threat to the soil quality in the future. Therefore, attention should be paid to soil quality safety and prevention.

Data Availability

The data used to support the findings of this study are available from the corresponding author upon request.

Conflicts of Interest

The authors declare that they have no conflicts of interest.

Retraction

Retracted: Study on Early Warning of Karst Collapse Based on the BP Neural Network

Journal of Chemistry

This article has been retracted by Hindawi following an investigation undertaken by the publisher [1]. This investigation has uncovered evidence of one or more of the following indicators of systematic manipulation of the publication process:

(1) Discrepancies in scope

(2) Discrepancies in the description of the research reported

(3) Discrepancies between the availability of data and the research described

(4) Inappropriate citations

(5) Incoherent, meaningless and/or irrelevant content included in the article

(6) Peer-review manipulation

The presence of these indicators undermines our confidence in the integrity of the article's content and we cannot, therefore, vouch for its reliability. Please note that this notice is intended solely to alert readers that the content of this article is unreliable. We have not investigated whether authors were aware of or involved in the systematic manipulation of the publication process.

Wiley and Hindawi regrets that the usual quality checks did not identify these issues before publication and have since put additional measures in place to safeguard research integrity.

We wish to credit our own Research Integrity and Research Publishing teams and anonymous and named external researchers and research integrity experts for contributing to this investigation.

The corresponding author, as the representative of all authors, has been given the opportunity to register their agreement or disagreement to this retraction. We have kept a record of any response received.

References

[1] D. Chen, "Study on Early Warning of Karst Collapse Based on the BP Neural Network," *Journal of Chemistry*, vol. 2022, Article ID 1799772, 7 pages, 2022.

Research Article

Study on Early Warning of Karst Collapse Based on the BP Neural Network

Dongqin Chen (ORCID)

ChangJiang Polytechnic, Wuhan, Hubei 430074, China

Correspondence should be addressed to Dongqin Chen; 31115401@njau.edu.cn

In order to comprehensively grasp the dynamics of karst collapse, promote the comprehensive prevention and control level of karst collapse, and prevent secondary disasters caused by lava collapse, this study presents a method of karst collapse early warning based on the BP neural network. This method does not need to set the sliding surface in the finite element calculation model. The stress of the sliding surface is fitted according to the spatial stress relationship of the deep karst layer through the improved BP neural network PID control algorithm and BP neural network algorithm, which avoids the modeling and mesh generation of the complex sliding block and has good accuracy and ease of use. According to the basic theory of the BP neural network, the calculation formulas of multilayer feedforward and error back propagation processes are derived, and the two-dimensional and three-dimensional finite element models of gravity dams without and with sliding blocks are established, respectively. Finally, according to the common formulas of viscoelastic artificial boundary and equivalent load, the two-dimensional and three-dimensional input programs of the karst fluid state are compiled, and a neural network early warning model is obtained. The experimental results show that the process karst state simulated by the algorithm is very close to the actual situation, and the minimum value of antisliding coefficient and its occurrence time can be accurately predicted, with an error range of less than 3%. *Conclusion.* BP neural network prediction can effectively predict karst collapse, with higher prediction accuracy, and can effectively simulate the actual collapse risk.

1. Introduction

The distribution area of karst in China is more than 3.4 million, accounting for about 36% of the land area. Karst area is rich in mineral resources, groundwater, and tourism resources. At the same time, it is also faced with serious geological environment problems such as karst collapse, tunnel water inflow, drought and waterlogging, water and soil pollution, and so on. As one of the most important geological environment problems in the karst area, karst collapse is widely distributed in the world [1]. The formation of karst collapse requires three basic conditions as follows: karst space, a certain thickness of caprock, and trigger factors. Caprock is the main body of collapse. Karst cave gap provides storage and migration space for collapse, which determines the location of collapse to a certain extent, and the trigger factor is the dynamic condition of collapse. There

are stress transfer and material transportation among the three, which is comprehensively manifested in the interaction of "rock-soil-water," in which water is of great importance. The changes in groundwater level, velocity, and flow will produce many mechanical effects such as potential corrosion, dissolution, absorption, and water hammer, which will cause the deformation and damage of rock and soil mass and eventually form collapse. In addition to groundwater, gravity and dynamic load are also common factors causing collapse. In recent years, under the double background stress of human engineering activities and extreme climate, karst collapse geological disasters have shown a high-frequency trend, and their spatial and temporal distribution, loss degree, depth, and breadth of impact have also undergone new changes. The concealment, abruptness, repetition, and unpredictability are becoming increasingly prominent [2]. Throughout the study of karst collapse, the

five in one technical and theoretical framework system of "genetic mechanism, identification and evaluation, monitoring and alarm, emergency response and risk management" has been formed. So far, however, the problem of "where, when, and how to collapse" has not been well solved [3]. The prevention and control of karst collapse is still a world-class technical problem in the field of geoscience, which is mainly reflected in the insufficient quantification of the genetic mechanism and the identification and evaluation method of hidden dangers. That is to say, the early warning mechanism and algorithm are still imperfect.

Therefore, the combination of the BP neural network algorithm can avoid the modeling of the sliding block. Only the coordinate information of the sliding surface can be extracted to fit the internal stress value of the karst, which greatly reduces the workload of fluid calculation. It can more effectively monitor the risk of lava and give early warning.

2. Literature Review

For the research on early warning of karst collapse, Wang et al. and others proposed to combine the characteristics of biological neurons receiving and transmitting signals and put forward the mathematical model MP model of neurons, creating a new era of human research on neural networks. The change of connection strength between neurons is analyzed, and the idea of the neural network learning Hebb learning rule is proposed [4]. Zhao et al. and others proposed a learning algorithm that can simulate the human learning process, which is called perceptron, which means that the neural network has the learning ability [5]. Abdelfatah and others put forward the Hopfield network model, which makes the research of the neural network enter the next stage of development. This is a single-layer interconnection. The improved backpropagation algorithm is introduced into the multilayer perceptron, and the BP neural network learning algorithm is proposed. The research on the neural network has become a hot spot again [6]. Chen et al. and others put forward the analysis of the performance of the BP neural network nonlinear function and proved that the feedforward neural network with only one hidden layer and any continuous S-type nonlinear function can approximate any complex function [7]. Mahmoudabadbozchelou et al. and others put forward the Delphi method for quantification and conducted the empirical analysis. It can be seen that the fuzzy neural network model has advantages in coal mine safety evaluation. The fuzzy neural network model combined with fuzzy theory and neural network technology not only has the ability of learning, connection, and adaptation but also has fuzzy thinking, which can make the evaluation results more objective [8]. Mazzi et al. and others put forward the coal mine safety early warning evaluation method based on a neural network and genetic algorithm. The neural network has good self-learning, adaptive, parallel processing, and nonlinear computing capabilities, so it has been widely used in intelligent control, nonlinear optimization, signal processing, and other aspects [9]. Yilmaz and Koyuncu others proposed a genetic algorithm to optimize neural network weights and thresholds to establish a coal

mine accident prediction model [10]. They found that compared with the traditional algorithm, it has better prediction accuracy and faster convergence speed. They concluded that a genetic algorithm to optimize the neural network is feasible and effective.

In this study, the BP neural network algorithm can avoid the modeling of the sliding block. Only the coordinate information of the sliding surface can be extracted to fit the stress value in the karst, which greatly reduces the workload of fluid calculation. In this study, the improved BP neural network PID control algorithm is used to simulate, so as to monitor and warn the lava quickly and effectively.

3. Research Methods

3.1. Karst Collapse Hidden Danger Identification and Evaluation System and Data Acquisition. The identification of hidden danger of karst collapse is generally divided into two scales as follows: regional scale and site scale. On the regional scale, with the continuous improvement of the resolution of satellite images and the development of new aviation technologies such as laser radar and synthetic aperture radar, remote sensing has become a major technical method. It has the advantages of wide coverage and rapid identification in the investigation and description of the status quo of collapse pits and the comparative analysis of development trends. At the site scale, geophysical prospecting is a common and effective technical means. In recent years, with the development of electrical seismic and other joint geophysical exploration technologies, the accuracy and depth of karst collapse detection have been significantly improved. For example, the comprehensive application of different methods such as ground geological radar, resistivity imaging, seismic refraction, and microgravity has effectively solved the problem of detection at different depths. At the same time, the application of cross-hole CT, borehole radar, and other technical methods has also effectively solved the problem of precision depiction from coarse to fine. The evaluation of karst collapse can be divided into three levels as follows: susceptibility, risk, and risk. Susceptibility assessment is to evaluate the geological background of karst collapse. Risk assessment is to study the stability of karst collapse under the action of trigger factors on the basis of susceptibility assessment. Risk assessment needs to comprehensively consider the risk and risk of loss of personnel and property. For the evaluation of karst collapse, the key is to establish an evaluation model and determine the weights and interrelations of various factors. Commonly used methods include decision tree, stepwise regression analysis, AHP, fuzzy mathematics, and neural network. Different methods have their own advantages and disadvantages. The accuracy depends critically on the knowledge and quantification of the genetic mechanism of karst collapse. The most important data to be obtained mainly includes the following four aspects: first, karst collapse triggered by subgrade and underground space engineering; second, the rapid change of hydrodynamic conditions has seriously damaged the equilibrium state of rock and soil mass and induced karst collapse. The main reasons for the sharp change in

hydrodynamic conditions are rainfall, reservoir water storage, underground water filling, irrigation leakage, serious drought, underground drainage, and high-intensity pumping; third, additional load; and fourth, acid-based solution corrosion caused by waste liquid [11].

3.2. BP Neural Network Structure.

The structure of the BP neural network is shown in Figure 1. It uses a three-layer structure of output layer, hidden layer, an input layer, and j, i, and l represent the input layer node, the hidden layer node, and the output layer nodes, respectively. The number of input nodes in the input layer is 4, the number of hidden nodes in the hidden layer is 5, and the number of output nodes in the output layer is 3. The input node corresponds to the system's expected value, actual value, deviation, and control size, and the output layer node corresponds to the parameters K_p, K_i, and K_d, one by one, of the PID control algorithm (Figure 1).

The BP (back-propagation) neural network is one of the many artificial neural networks that the teacher learns, usually consisting of a data input layer, a hidden layer of nonlinear activation function, a linear output layer, and a BP neural network. The structure of the model is shown in Figure 1 [12]. The first is the forward multilayer feedforward process: the network randomly assigns the initial connection weight and threshold (also known as deviation) to each neuron according to the number of hidden layers and hidden layer units set by the user. The input layer data are processed by linear weighing of the net input of the latent layer, the weight, and the threshold. Output layer input: after the linear conversion of weight and threshold from layer to layer, the output layer results in a nonlinear activation function of neurons in the output layer. Then, there is the process of error redistribution: the loss function is used to calculate the total error between the output layer result and the expected output result, and then according to different optimization algorithms, the loss function is used to calculate the partial derivatives of the neurons, weights, and other parameters of each layer, so as to obtain the parameter update direction to reduce the error. Set the descent step size and repeatedly adjust the error of the weight and threshold, so that the error is continuously reduced until it reaches an acceptable level or the preset learning times [13]. The algorithm of the BP neural network is shown in Figure 2.

BP neural networks are often used to address adjustment and classification problems. Depending on the complexity of the problem, the number of latent layers, the number of neurons in each layer, and the activation function of the neurons in each layer can be flexibly adjusted.

3.3. Sample Data Division and Learning Rate.

To prevent overconfiguration of the neural network by relying too much on the training package data, we divide the sample input data into training packages, validation packages, and test packages, and the validation packages and test packages are not included in the training packages neural network. When the neural network updates the parameters such as weight and deviation for each iteration of the training set data, it checks
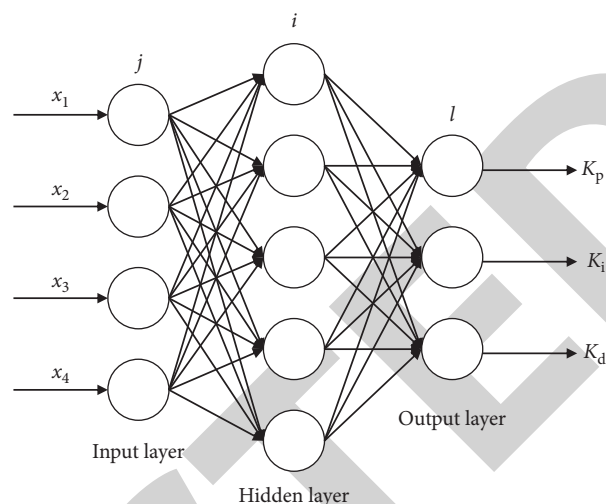
FIGURE 1: BP neural network structure.

the verification set error under the current parameters [14]. As the neural network continuously reduces the error of the training set through multiple iterations, it is prone to overfitting. At this time, the error of the verification set will increase with the occurrence of overfitting. When the error of the verification set does not continue to decrease after multiple iterations, the neural network will stop training in advance and save the weight and deviation before the error increases as the optimal network parameters [15]. There are two main functions of the test set. On the one hand, the test set can be used to evaluate the generalization ability of the neural network after the training. On the other hand, it can indicate whether the division of the dataset is reasonable to a certain extent according to whether the number of iterations required for the test set to reach the minimum value is roughly the same as that required for the verification set to reach the minimum value [16].

The methods of dividing training, verification, and test sets generally include random data division, continuous data division, staggered selection of data division, according to index [17]. This study uses the method of randomly dividing data to further strengthen the disorder of the training set and improve the generalization ability of the network. In the follow-up training process, it can be seen that the number of iterations when the error of the validation set and the test set reaches the minimum value is the same, indicating that the method of randomly dividing data is reasonable [18, 19].

In practical application, it is difficult to quickly determine the optimal learning rate. With the development of the BP neural network, the learning rate is no longer a fixed value. The generation of variable learning rate overcomes the traditional disadvantage of difficulty to determine the initial learning rate, speeds up the search speed, effectively improves the accuracy of the results, and also solves the oscillation phenomenon in the later stage of network training [20]. The commonly used learning rate setting method is the exponential decay learning rate method, that is, the learning rate is large at the initial stage of training, and the learning rate decreases continuously with the progress of training until the model converges.
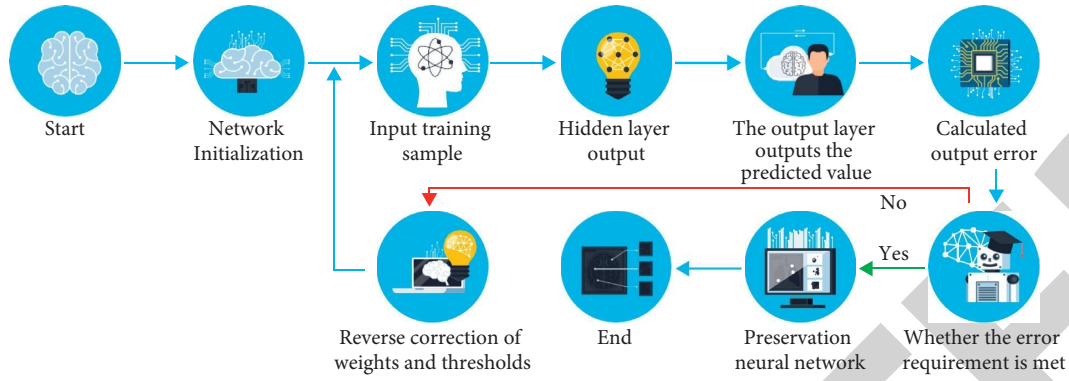
Figure 2: Flowchart of the BP neural network algorithm.

3.4. BP Neural Network PID Controller. The BP neural network unit and PID controller unit are combined to form a BP neural network PID controller. Its principle is that the BP neural network outputs the optimal PID control parameters through self-learning and weight coefficient adjustment according to the current operating state of the system, so that the three adjustable parameters of the PID controller can adapt to changes. Its structure is shown in Figure 3.

The input quantity of the BP neural network input layer is shown in the following formula:

$$o_j^{(1)} = x(j),$$
$$j = 1, 2, 3, 4. \tag{1}$$

The input and output quantities of the BP neural network hidden layer are, respectively, shown in the following formulas:

$$\mathrm{net}_i^{(2)}(k) = \sum_{j=0}^m w_{ij}^{(2)} O_j^{(1)}(k), \tag{2}$$

$$o_i^{(2)}(k) = f\left[\mathrm{net}_i^{(2)}(k)\right], \quad i = 1, 2, \ldots, 5. \tag{3}$$

The hyperbolic tangent function is used as the excitation function of hidden layer neurons, as shown in the following formula:

$$f(x) = \frac{e^x - e^{-x}}{e^x + e^{-x}}. \tag{4}$$

The input and output quantities of the BP neural network output layer are, respectively, shown in the following formulas:

$$\mathrm{net}_i^{(3)}(k) = \sum_{i=0}^q w_{li}^{(3)} O_i^{(2)}(k), \tag{5}$$

$$o_l^{(3)}(k) = g\left(\mathrm{net}_l^{(3)}(k)\right). \tag{6}$$

It is obtained from the following formula:

$$o_1^{(3)}(K) = K_p,$$
$$o_2^{(3)}(K) = K_i, \tag{7}$$
$$o_3^{(3)}(K) = K_d,$$

where $\omega_{li}^{(3)}$ is the weighting coefficient from hidden layer to output layer; $g(x)$ is the activation function of neurons in the output layer, expressed in the following formula:

$$g(x) = \frac{1 + \tanh(x)}{2} = \frac{e^x}{e^x + e^{-x}}. \tag{8}$$

The performance index function is

$$E(k) = \frac{1}{2}[r(k+1) - y(k+1)]^2. \tag{9}$$

In order to speed up the convergence, an inertia term is added to make the search converge to the global minimum quickly. The formula of the neural network weight coefficient is modified according to the gradient descent method, as shown in the following formula.

$$\Delta\omega_{li}^{(3)}(k+1) = -\eta \frac{\partial E(k)}{\partial \omega_{li}^{(3)}} + \alpha\Delta\omega_{li}^{(3)}(k), \tag{10}$$

where η is the learning rate; α is the momentum factor. The following equation can be obtained from equation (7).

$$\begin{cases} \dfrac{\partial u(k)}{\partial o_1^{(3)}(k)} = e(k) - e(k-1), \\[3mm] \dfrac{\partial u(k)}{\partial o_2^{(3)}(k)} = e(k), \\[3mm] \dfrac{\partial u(k)}{\partial o_3^{(3)}(k)} = e(k) - 2e(k-1) + e(k-2). \end{cases} \tag{11}$$
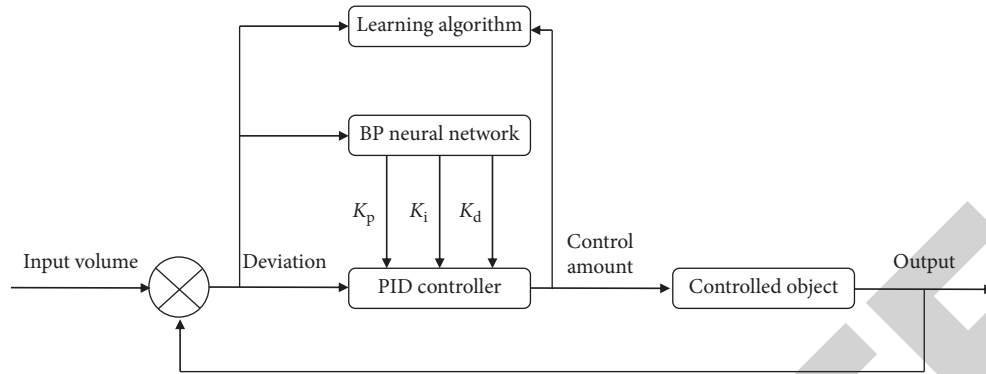
Figure 3: Structure of the BP neural network PID controller.

Thus, the output layer weight calculation formula of the BP neural network can be obtained as

$$\Delta\omega_{li}^{(3)}(k+1) = \eta e(k+1)\mathrm{sgn}\left(\frac{\partial y(k+1)}{\partial u(k)}\right)$$

$$\frac{\partial u(k)}{\partial o_l^{(3)}(k)} g\left[\mathrm{net}_l^{(3)}(k)\right] o_j^{(2)}(k) + \alpha\Delta\omega_{li}^{(3)}k,$$

$$j = 1, 2, 3, 4,$$

$$i = 1, 2, 3.$$

$$(12)$$

Calculation formula of the classical incremental PID controller is

$$\mu(k) = \mu(k-1) + K_p[e(k) - e(k-1)]$$
$$+ K_i e(k) + K_d[e(k) - 2e(k-1) + e(k-2)], \quad (13)$$
$$e(k) = r(k) - y(k),$$

where K_p, K_i, and K_d are the proportional, integral, and differential coefficients of PID controller, respectively; $\mu(k)$ is the output of the PID controller; $y(k)$ is the actual output value of the controlled object; $r(k)$ is the expected value of the system; $e(k)$ is the system deviation [21].

3.5. Improved BP Neural Network PID Control Algorithm. The rate of learning remains the same during the study of traditional BP neural networks. If the rate of learning is too high, increasing the weight will cause the network to fluctuate with minimal error and make it impossible to integrate the network.

In order to improve the performance of the BP neural network, the term impulse was added and improved in this study. The function of the torque term is to remember the direction of change in the weight of the connection at the last moment. Increasing the momentum term can obtain a larger learning rate coefficient and improve the learning speed. The oscillation phenomenon may occur in the training process of the neural network, and the "inertia effect" of the momentum term can inhibit the oscillation and buffer. The correction of weight is

$$\Delta\omega(n) = -\eta\frac{\partial E_{(n)}}{\partial_\omega} + \alpha_1\Delta\omega(n-1). \quad (14)$$

Combining the above improved BP neural network with a PID controller, a new BP neural network PID controller (NBPPID) was created, the structure of which is shown in Figure 4.

The steps of the improved algorithm are as follows:

(1) Determine the structure of the BP neural network, initialize the weight coefficients of the input layer, hidden layer, and output layer of the BP neural network, and select appropriate momentum factors α_1, α_2 and learning rate η to make $k = 1$;

(2) The input and output are obtained by sampling, and the deviation is calculated;

(3) The inputs and outputs of the neurons in the input layer, hidden layer, and output layer of the BP neural network are determined. The control parameters K_p, K_i, and K_d of the PID controller are determined by the outputs of the output layer;

(4) PID controller outputs control quantity

(5) The BP neural network adaptively adjusts PID control parameters by adjusting weighting coefficients online

(6) Let $k = 1$ and return to step 1

4. Result Analysis

The improved monitoring algorithm (NBPPID) was compared with the traditional BP neural network PID control algorithm (BPPID) and BP neural network PID control algorithm (MBPPID) through the performance of the improved BP neural network PID control algorithm. The simulation experiment is carried out with MATLAB, and the time-varying nonlinear simulation system is taken as

$$y(k) = \frac{\alpha(k)y(k-1)}{1 + y^2(k-1)} + \mu(k-1), \quad (15)$$

where $\alpha(k) = 1.3(1 - 0.6e^{-0.2k})$.

The structure adopted by the BP neural network has a learning rate of $\eta = 0.2$, $\alpha_1 = 0.5$, $\alpha_2 = 0.1$. Compared with
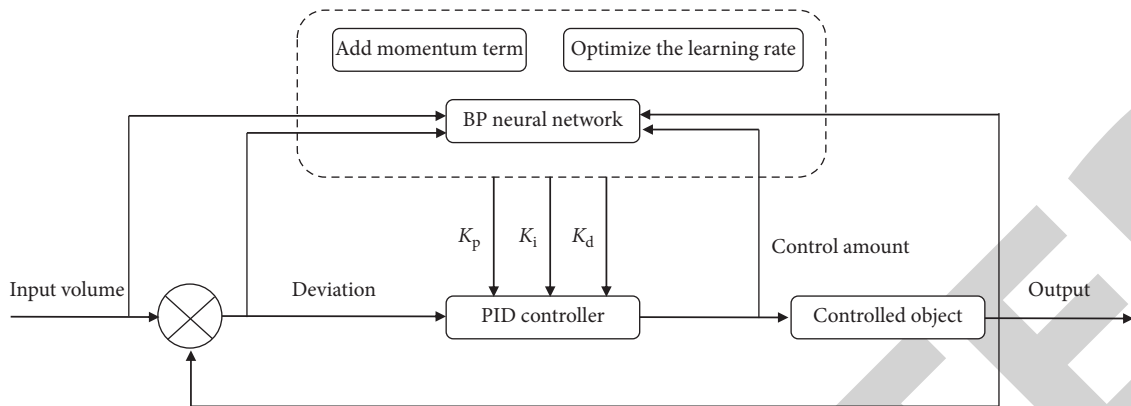
Figure 4: Improved BP neural network PID controller structure.
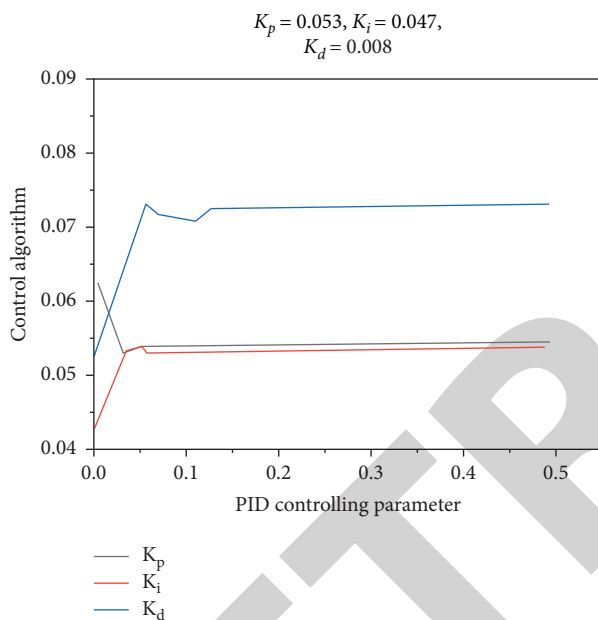
Figure 5: PID control parameter curve of three control algorithms.

Forecast daily actual load value
6 Heavy MapReduce-BP model predicted values

Figure 6: Load forecasting results of the neural network.

the traditional BP neural network PID control algorithm, NBPPID and MBPPID algorithms can effectively alleviate the oscillation phenomenon, and NBPPID reaches the expected value before the MBPPID algorithm, which speeds up the convergence speed. Figure 5 shows the control parameter curves of three control algorithms PID. It can be seen from Figure 5 that the optimal value of PID control parameters of the NBPPID control algorithm is as follows:

$$K_p = 0.053,$$
$$K_i = 0.047, \qquad (16)$$
$$K_d = 0.008.$$

By improving the learning rate and momentum factor, the algorithm uses the momentum factor to optimize the learning rate and increase the momentum term to suppress the possible oscillation in network training. In the control process, the NBPPID control algorithm adaptively adjusts PID parameters. Input the monitoring data into the BP neural network to obtain the corresponding curve, as shown in Figure 6.

5. Conclusion

Experimental results show that the PID neural network algorithm can effectively alleviate the phenomenon of fluctuations and accelerate the integration rate of the algorithm. When using the BP neural network method to calculate deep melting stability, regression coefficient, and mean squared error, it is not possible to determine the effective force and slip protection coefficient of the sliding surface, used as a measuring neural network. Compared with the antisliding coefficient calculated by the sliding block model, this index can represent the error level between the predicted value and the accurate value of the ground subsidence coefficient. Compared with the preset sliding surface model, the neural network repeated the prediction scheme 12 times, and taking the mean value at each time can be used as the final early warning result, and the karst state in the whole experimental simulation process is very close to the actual situation. The minimum value of antisliding coefficient and its occurrence time can be accurately predicted, and the error range is within 3%. It also shows that the BP neural network is very accurate in the early warning of karst collapse and can effectively simulate the actual collapse risk.

Hindawi

Retraction

Retracted: Research Progress of Polycyclic Aromatic Hydrocarbons Pretreatment Methods and Application of Computer Simulation Technology for Prediction and Degradation of Electrochemical Concentration Detection

Journal of Chemistry

This article has been retracted by Hindawi following an investigation undertaken by the publisher [1]. This investigation has uncovered evidence of one or more of the following indicators of systematic manipulation of the publication process:

(1) Discrepancies in scope

(2) Discrepancies in the description of the research reported

(3) Discrepancies between the availability of data and the research described

(4) Inappropriate citations

(5) Incoherent, meaningless and/or irrelevant content included in the article

(6) Peer-review manipulation

The presence of these indicators undermines our confidence in the integrity of the article's content and we cannot, therefore, vouch for its reliability. Please note that this notice is intended solely to alert readers that the content of this article is unreliable. We have not investigated whether authors were aware of or involved in the systematic manipulation of the publication process.

Wiley and Hindawi regrets that the usual quality checks did not identify these issues before publication and have since put additional measures in place to safeguard research integrity.

We wish to credit our own Research Integrity and Research Publishing teams and anonymous and named external researchers and research integrity experts for contributing to this investigation.

The corresponding author, as the representative of all authors, has been given the opportunity to register their agreement or disagreement to this retraction. We have kept a record of any response received.

References

[1] H. Chang and Y. Lu, "Research Progress of Polycyclic Aromatic Hydrocarbons Pretreatment Methods and Application of Computer Simulation Technology for Prediction and Degradation of Electrochemical Concentration Detection," *Journal of Chemistry*, vol. 2022, Article ID 6288072, 16 pages, 2022.

Hindawi

Research Article

Research Progress of Polycyclic Aromatic Hydrocarbons Pretreatment Methods and Application of Computer Simulation Technology for Prediction and Degradation of Electrochemical Concentration Detection

He Chang [iD] and Yang Lu [iD]

School of Computer Science, Jilin Normal University, Siping, Jilin 136000, China

Correspondence should be addressed to Yang Lu; 15071001210013@hainanu.edu.cn

Polycyclic aromatic hydrocarbons (PAHs) are a class of organic compounds that are composed of aromatic rings containing only carbon and hydrogen atoms. They are one of the widespread environmental pollutants in the world. In recent years, many scholars have focused on the inhibition, formation mechanism, content of active components, and biodegradation effect of polycyclic aromatic hydrocarbons. They summarized the research progress of pretreatment methods for detection, but rarely discussed the experimental dataset for comprehensive analysis of pollution sources and the impact of different pretreatment technologies on the extraction of different substrates. What is more, computer simulation has not been mentioned. In this study, the pollution sources of polycyclic aromatic hydrocarbons (PAHs) are reviewed, and the related applications of various pretreatment methods such as gel permeation chromatography (GPC) are summarized. Finally, the computer simulation of the response surface method is introduced. The concentration of polycyclic aromatic hydrocarbons is tested or predicted by combining the neural network with the alternating trilinear decomposition (ATLD) algorithm, artificial population algorithm (ABC), and hierarchical genetic algorithm (HGA). Its future development trend is discussed and prospected, which provides a reference for solving the pollution problem. We look forward to providing help for the follow-up research of scholars in this field.

1. Introduction

There are two main sources of PAHs. The first is the natural source, mainly from the green vegetation of natural fire, volcanic eruption sediments, aquatic and terrestrial plants, and biosynthesis. The second is the man-made sources, mainly from incomplete combustion of coal, oil, natural gas and other fossil fuels, industrial processing, wood, traffic emissions, and road dust.

Among more than 100 kinds of polycyclic aromatic hydrocarbons (PAHs) that have been discovered and detected in nature, 16 PAHs have been listed as "priority pollutants under control" by EPA and the European Union. The nature and form of carcinogenic compounds cause a variety of degradation products that widely exist in the

atmosphere, soil, and other environment, thus causing a wide variety of food or supplies such as dairy products, meat, seafood, nuts, and other pollution, which can be listed as one of the important pollutants. They will not only cause harm to ecological environment but also will pose a threat to human health.

In recent years, many scholars have summarized and discussed the inhibition, formation mechanism, content of active components, and biodegradation effect. There are few detection pretreatment methods to summarize the research progress, but these methods are not perfect. The impact of pollution sources and different substrates extracted by different pretreatment technologies on experimental data has been intensively analyzed, but computer simulation has rarely been mentioned and applied. In this study, the

domestic and foreign literature on high temperature oil fume baked food, food packaging materials, atmospheric environment, water contact separation, detection, and extraction of polycyclic aromatic hydrocarbons in recent years were reviewed. Besides, their pretreatment was studied. This study reviews the research progress of correlation analysis technology in instrumental testing experiments and discusses and prospects the computer simulation of the response surface method and the application of the neural network in polycyclic aromatic hydrocarbons extraction. Besides, the future development trend of polycyclic aromatic hydrocarbons is discussed and prospected, which will be helpful to the research work of the scholars in this field.

2. Sources of Contamination by Polycyclic Aromatic Hydrocarbons

2.1. Contamination of High Temperature Smoked Food. Many studies have shown that barbecue and smoked foods in the process of production may induce the formation of polycyclic aromatic hydrocarbons. In particular, a certain amount of polycyclic aromatic hydrocarbons may be contained or produced in the pyrolysis of adipose tissue, incomplete combustion, high temperature fuming, and thermal polymerization of food fats; these will result in some residue on the surface of the food. Fasano and others found that when the temperature of the smoked products was higher than 200°, polycyclic aromatic compounds were produced and gradually migrated from the casing to the interior of the smoked products [1]. Chen and others studied and measured the content of PAHs in the smoke generated by heating model lipids and edible lipids; they found that PAHs and their derivatives were produced in the smoke generated by heating model lipids, and the content of the latter was significantly higher than that of the former [2]. Merlo and others analyzed five kinds of smoked bacon meats on the market and found that trace PAHs carcinogens were produced in the process of wood heating and the preparation of smoked bacon samples [3]. Shen and others found that during the smoking process, PAHs would be adsorbed on the meat surface in gaseous form or attached to the meat surface as particles. When the smoking process continues, PAHs that remain on the surface will penetrate into the internal part of the meat [4]. Kafouris and others analyzed PAHs in char-roasted pork and poultry, smoked pork, smoked hams, smoked sausages, and bacon. They found that 96% of the samples were contaminated with at least one PAH. Among these contaminated samples, 12% of the smoked products and 15% of the roasted meat samples exceeded the maximum level of EU legislation [5].

2.2. Contamination of Food Packaging Materials. In recent years, the safety of food packaging material has been greatly improved. More PAHs may be introduced into food packaging materials (such as impure paraffin oil) during the process of fluorescent whitening, bleaching, printing, printing, and waxing, thus affecting their safety [6]. Studies have shown that the use of food packaging contact materials

contaminated with PAHs may lead to the spread of paHs to food, resulting in the contamination of packaged food. Therefore, the food industry should of course avoid improper use of packaging in the food production process. Moreover, the polluted plastic packaging materials should be processed centrally to prevent their indirect pollution to the natural environment [7]. Conchione and others were the first to investigate the presence of PAHs in pizza boxes containing recycled fibers and to assess the potential migration by conducting migration tests using the Tenax® animitator. The results showed that the high content of PAHs in the samples, especially chrysene, confirmed the migration potential of these pollutants [8]. Li and others detected eight kinds of PAHs in 21 samples of polystyrene food contact materials and evaluated the migration of PAHs by using the stochastic migration model. It was concluded that the migration rate of PAHs depends on the molecular structure and agglomeration properties of plastic materials [9].

2.3. Atmospheric Pollution. The PAHs mixture in the air is mainly accompanied by coal tar, automobile exhaust, and smoking smoke. In particular, the occurrence of haze is often characterized by a sharp increase in the concentration of particulate matter, which not only pollutes the natural environment such as agricultural products and soil but also causes great trouble to human production and life, as well as poses a great threat to human health. In addition, PAHs are also important organic components of environmental particulate matter (PM2.5) with diameter less than 2.5 microns. Among PAHs' derivatives, PAHs and hydroxyl PAHs have been detected in high concentrations of PM2.5 samples. It is an important way to enter the human lungs. He and others found in their studies that persistent organic pollutants (pops) such as polycyclic aromatic hydrocarbons (PAHs) in suspended particulate matter in the atmosphere will have a coupling effect with harmful algal blooms in the aquatic environment, thus causing pollution to lake water environment [10]. From September 2012 to August 2013 in China, Japan, South Korea, and other five Asian countries, Hong and others measured the concentrations of 47 kinds of PAHs in 176 sites in different seasons for four consecutive months, all of which were detected [11]. When studying the polycyclic aromatic hydrocarbons, Baek and others found that its concentration change has certain law in the spatial and seasonal distribution.

The polycyclic aromatic hydrocarbons' content shows obvious seasonal variation and the highest content appears in winter, so they concluded that the factors affecting the concentration of polycyclic aromatic hydrocarbons may have a direct relationship with home heating, fuel combustion in automobile exhaust, and industrial activity in its pollution sources [12]. Ma and others described 16 kinds of PAHs and 16 kinds of nitropolycyclic aromatic hydrocarbons (NPAHs) combined with inhalable particles in cold areas of China and analyzed their sources and health risks. They proposed that the main source of PAHs is combustion, and controlling the combustion of coal and biomass would

be an effective measure to improve the air quality in Harbin during the heating period. And in addition to the direct emissions, about 20% of polycyclic aromatic hydrocarbons are from the second generation. According to the weather conditions on the influence of polycyclic aromatic hydrocarbons and unsaturated fatty acid concentration, it can be found that in the heating period, PAHs pollutants are more vulnerable to the influence of meteorological condition than in the non-heating period. The highest health risks caused by contacting PM10-PM2.5 with polycyclic aromatic hydrocarbons are also prone to happen in the winter. Health risk assessments have shown that there is a potential cancer risk associated with prolonged exposure to such environments [13].

2.4. Water Pollution. Studies have shown that organic pollutants such as PAHs exist in all kinds of aquatic systems, trace residues in sewage treatment plant inlet and outlet water, groundwater, surface water or seawater, and other water bodies [14]. Although the content is very low, it will have an impact on the natural environment and human health due to its persistence and accumulation. Chen Jiang et al. detected PAHs in mine drainage and underground water collected from many places. After analysis, they found the enrichment reason might be that PAHs and others organic substances are not easy to photodegradation in the dark and closed underground environment and are not easy to py-rolysis due to the constant underground temperature. In addition, some pollutants, including them, may be accumulated by the adsorption of deposits, coal, and rocks in the mine [15]. Ambade and others detected a trace amount of 16 PAHs in drinking water samples. After analyzing the physical and chemical parameters of all the samples, they believed that the pollution might be caused by the surface water pollution caused by industrial and domestic waste-water discharge, the precipitation and deposition of com-bustion sources, and the infiltration of PAHs from surface water sources to groundwater [16].

From the above analysis, it is not difficult to find that the pollution problem of PAHs is affecting our daily life, and the consequences will be hard to imagine if it is not controlled. However, with the rapid development of science and technology, the application of computer has gradually ex-panded up to a domain, represented by deep learning and machine learning. Cooperation with the relevant learning algorithm in compound properties prediction and treatment showed a better ability to frequently predict the simulation of various compounds in the experiments. In particular, the application of the artificial neural network in chemical analysis and other fields has emerged, which not only avoids repeated and redundant experimental operations but also saves experimental operation costs and effectively improves work efficiency. In addition, the computational simulation method can also describe the adsorption separation process at the microscopic level, which cannot be replaced by ex-periments. In this study, response surface methodology and neural network are reviewed. It is not difficult to find that it is very important to choose appropriate pretreatment technology and detection method for further effective

monitoring of PAHs. In this study, through a large number of literature reviews, this study compares and summarizes several commonly used new pretreatment application technologies. Advantages, disadvantages, and adaptability are integrated to make a comprehensive and systematic review.

3. New Pretreatment Application Technology for Polycyclic Aromatic Hydrocarbons Concentration Detection

3.1. Gel Permeation Chromatography (GPC). Gel permeation chromatography (GPC), as one of many new separation technologies, is mainly used in the detection of multi-pollutant residues in agricultural residues, food, and oil and has been applied to the detection of polycyclic aromatic hydrocarbons. In the determination and analysis of PAHs in edible oil samples, Wang and others [17] used gel perme-ation chromatography to remove triglycerides in the samples before treatment. Lian and others [18] used gel permeation chromatography to reduce matrix interference in the pre-treatment of determination of 16 PAHs in cigarette samples, which can obtain cleaner final extract than traditional solid-phase extraction technology, making the analysis results more accurate and ensuring reliable routine determination at a low level. Shao and others [19] took agricultural land in the suburbs of Tianjin as the research object to analyze the content of 16 kinds of PAHs in typical soil samples and purified them by gel permeation chromatography and other technologies before treatment. Through analysis, it is found that some sites near the city are seriously polluted by polycyclic aromatic hydrocarbons. Coal burning is still the main pollution source in Tianjin. Data from the experiment can be further used to assess the health risks associated with PAH-contaminated soils and help local governments find appropriate ways to reduce PAH-contaminated soils; Kong and others [20] used gel permeation chromatography to purify samples in the pretreatment experiment of 15 PAHs in the determination of adipose tissue, and the determi-nation results met the verification criteria.

It can be seen from the above examples that gel per-meation chromatography, as a pretreatment technology, is often combined with GAS chromatography-tandem mass spectrometry to detect PAHs in the matrix, which effectively avoids the volatilization of reagents, and has the advantages of strong resistance to matrix interference and high sensi-tivity. Besides, it can be continuously and automatically analyzed to improve the accuracy of results. It can also be seen from Table 1 that the average recovery rate of samples is at a high level, and other coefficients are within the standard range. Therefore, gel permeation chromatography can be used for purification when the extracted PAHs samples contain lipids, pigments, alkaloids, polymers, and other pretreatment methods.

3.2. Molecular Imprinting (MIP). Molecular imprinting (MIP) technology, which is based on simulating the inter-action between receptors and antibodies in nature to prepare

TABLE 1: Effect of gel permeation chromatography on the determination of polycyclic aromatic hydrocarbon in different substrates.

Substrate	Method	LOD (μg/kg)	Recovery (%)	R^2	RSD (%)	References
Oil	UHPLC-DAD-FLD	0.0025–0.01	73–110	>0.999	<10	[17]
Cigarette	GC-MS	0.1–0.8	83–104	*	<10	[18]
Soil	GC-MS	0.16–9.36	64.6–111.9	0.99 (B [a] p)	1.3–16.5	[19]
Fat	GC-MS	0.1–6.6	120–130	≥0.99	8.48–20.3	[20]

molecularly imprinted polymers with specific selectivity for specific target molecules, has obvious advantages especially in the trace analysis of complex matrix samples in the fields of food safety, environmental, and pharmaceutical analysis. Known as the manufacture of "molecular key" "artificial lock" technology, more and more attention are given at home and abroad. In addition, molecularly imprinted SPE column can be reused, and the experimental cost can be saved because of its resistance to strong acid and alkali and other adverse environmental damage. Rajendran et al. [21] selected four biological samples from cereals, animals, and humans as representative lipids to explore the potential application of MIP adsorbent in the analysis of PAHs in lipid matrix biological samples. They compared it with the commonly used gel permeation chromatography. The results show that MIP can be used for the analysis of PAHs in biological samples of various lipid substrates. Compared with the traditional GPC method, the MIP method has less experimental time and solvent consumption. In addition, the recovery rate of 16 PAHs homologues by the MIP method is similar to that by the GPC method. The results show that the MIP method can be used as an alternative method for the analysis of PAHs in biological samples with various lipid substrates (Figure 1). Geiss et al. [22] developed a simple, rapid, and economical method for the determination of eight preferred PAHs in rubber and plastic materials, which can improve extraction and cleaning procedures. The purification performance of silica gel packed column and MIPs solid-phase extraction column was qualitatively evaluated, and the superiority of solid-phase extraction based on MIP compared with the traditional silicification purification method was emphasized. Combined with gas chromatography-mass spectrometry (GC-MS) analysis of selective ion mode, it was found that the method had high extraction efficiency, purity, and speed. Zhou et al. [23] proposed a novel purification method based on the combination of molecularly imprinted polymer (MIP) and polycyclic aromatic hydrocarbons (PAHs) to determine 24 PAHs in edible oil. Under the optimized conditions, the coefficient indexes are good. Krupadam et al. [24] selected molecular-imprinted poly (vinylpyridine-co-ethylene glycol dimethacrylate) as the experimental pretreated solid-phase extraction material to determine five carcinogenic polycyclic aromatic hydrocarbons in atmospheric dust, which is easy to operate and has high stability. In addition, organic matter in air dust has no influence on MIP extraction, which can be used for trace determination.

By comparing the data in Table 2, it was found that the detection method for PAHs was mostly gas chromatography-mass spectrometry (GC-MS) when molecularly imprinted solid-phase extraction (MISPE) was applied. The sample recovery was also at a high level with good parameters. The technique is formed by the copolymerization of cross-linked monomers, which can absorb specific PAHs through noncovalent interactions, allowing rapid, accurate, and highly selective extraction of target analytes from complex matrices during preprocessing of samples. It can be used in the selective determination of pesticide residues, drugs, organic dyes, mycotoxins, and persistent organic pollutants in food substrates in the pretreatment of samples. Through reading the above literature, it can be found that the molecularly imprinted solid-phase extraction method is similar to the GPC method in terms of impurity removal, polycyclic aromatic hydrocarbon recovery, total cost of materials, and reagents. However, Sun and others found in the experiment that some impurities could not be completely removed by using the GPC method. Therefore, molecularly imprinted technology is more appropriate to protect the GC-MS system. In addition, this method can process samples in batches, while the GPC method can only process one sample at a time, and MIP technology can avoid excessive time consumption.

3.3. Accelerated Solvent Extraction (ASE). Accelerated solvent extraction (ASE) has been widely applied in many fields, which has the characteristics of less solvent, high selectivity, high extraction efficiency, and simplified operation steps. Zhang and others [25] used a combination of rapid solvent extraction and solid-phase extraction to determine the content of seven polycyclic aromatic hydrocarbons (PAHs) in soil and earthworm samples for sample pretreatment, then purified by solid-phase extraction column, and evaporated by a rotary evaporator to dry. This method has high recovery rate and good reproducibility and can be used for quantitative analysis of PAHs in soil and earthworm samples. Dinović-Stojanović and others [26] verified the detection methods of several PAHs in smoked meat products. The accelerated solvent extraction method and solid-phase extraction method were used for further purification of target substances. Experimental results showed that this method could be used for the analysis and detection of several PAHs in smoked meat products. Suranová and others [27] used accelerated solvent extraction equipment such as separation and extraction and presmoked meat samples in lipid compounds and oily impurity such as interference. The method is simple to operate, and the recovery rate is in line with relevant standards. The applicability of the method is verified on the final food analysis performance evaluation program certification material (smoked meat products), and the data results are consistent;
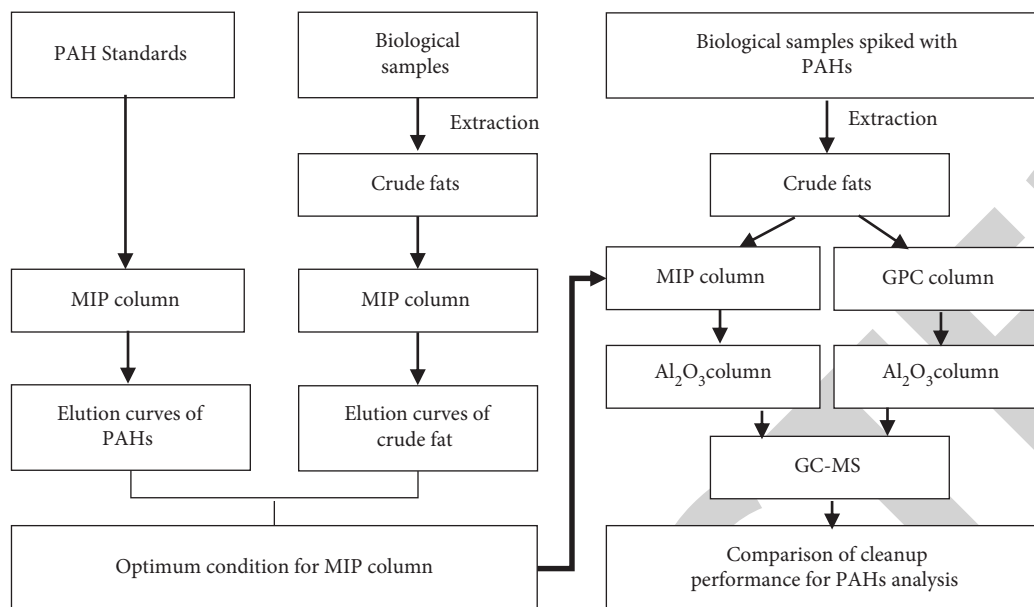
FIGURE 1: The schematic flowchart of the experimental design.

TABLE 2: Effect of molecular imprinting-gas chromatography on the determination of polycyclic aromatic hydrocarbon in different substrates.

Substrate	Method	LOD (μg/kg)	Recovery (%)	R^2	RSD (%)	References
Biological sample	GC-MS	*	75–120	*	*	[21]
Rubber plastic material	GC-MS	*	79–99	>0.99	1.4–10.8	[22]
Oil	GC-MS	0.1–1.0	86–116	≥0.9990	≤10.8	[23]
Atmospheric dust	GC-MS	0.5–0.9	5–97	0.998	1.8–2.7	[24]

Tan and others [28] determined polycyclic aromatic compounds such as phenanthrene, pyrene, and acenaphthene in fish by stable isotope dilution gas chromatography-tandem mass spectrometry and extracted fish samples by an improved accelerated solvent extraction method to eliminate the influence of potential matrix interference. The results showed that the method met all the standards stipulated by the European Commission legislation.

After reading the above literature, it is found that rapid solvent extraction technology is a technology with higher extraction rate than traditional solvent. By increasing the temperature and pressure, the solvent is in liquid form, which accelerates the extraction power of solvent, improves the extraction efficiency of sample, and reduces the extraction time and reagent of target substance. Due to the semivolatile and nonvolatile characteristics of PAHs, rapid solvent extraction technology can be selected as the sample pretreatment technology.

It should be noted that this kind of pretreatment technology has high requirements for testing instruments, and the extraction agent, eluent, and volume ratio also have a certain influence on experimental results. It is mainly used for testing the residues of polycyclic aromatic hydrocarbons and pesticides in food in physical and chemical testing. As can be seen from Table 3, the rapid solvent extraction method is mostly used in combination with the high performance liquid chromatography-fluorescence detection method, and the linear relationship coefficients are all at a high level.

3.4. Matrix Solid-Phase Dispersion Extraction (MSPD).

Matrix solid-phase dispersion (MSPD) is used to fully mix the sample and adsorbent and grind it into a semisolid column for elution. MSPD has the functions of dispersion, extraction, and purification and has the characteristics of simple and quick operation and strong resistance to matrix interference. So far, MSPD has been widely used in the analysis of various compounds in various matrices. Sharma et al. [29] established a rapid method for simultaneous determination of 4 PAHs in bovine tissues. The matrix solid-phase dispersion technique was used to collect samples from the bovine muscle, liver, and lung that died of free pathological injury, and the results of various parameters obtained were within the standard range. Liu et al. [30] analyzed and determined 16 kinds of PAHs in soil samples by using matrix solid-phase dispersion technology to purify and elution soil samples, eliminating most of the interfering matrix components. In order to obtain a higher recovery rate, the results show that the method can be used for soil PAHs analysis and save the solvent consumption, material cost, sample operation, and required time. When analyzing polycyclic aromatic hydrocarbons (PAHs) in fish tissues, Huang et al. [31] used matrix solid-phase dispersion technology to treat

Table 3: Effect of accelerated solvent extraction chromatography on the determination of polycyclic aromatic hydrocarbon in different substrates.

Substrate	Method	Extraction solvent (v/v)	Eluent (v/v)	LOD (µg/kg)	Recovery (%)	R^2	RSD (%)	References
Soil earthworm	HPLC-FLD	N-Hexane-O-acetone (4 : 1)	N-Hexane-dichloromethane (9 : 1)	0.15–0.85	83.5–110.2 (soil); 81.2–97.1 (earthworm)	0.9998–1.000	1.1–4.6 (soil); 1.6–4.2 (earthworm)	[25]
Smoked meat	HPLC-FLD	N-Hexane (*)	N-Hexane (*)	0.03–0.2	>96.3	0.993–0.997	*	[26]
Smoked product	HPLC-FLD	Acetone-n-hexane (*)	Acetone-n-hexane (*)	5 0.11–0.23	74 ± 7–109 ± 11	0.99988–0.9999	4.4–11.6	[27]
Fish	GC-MS	Dichloromethane-n-hexane (4 : 1)	Dichloromethane-n-hexane (4 : 1)	0.06–2.28	44.8–133.7	0.9968–0.9998	3.1–9.6	[28]

Table 4: Effect of the matrix solid-phase dispersion method on the determination of polycyclic aromatic hydrocarbon in different substrates.

Substrate	Method	Dispersant	Substrate: dispersant	Eluent	LOD (ng/g)	Recovery (%)	R^2	RSD (%)	References
Cattle tissues	HPLC-FLD	C_{18}	4 : 1	Acetonitrile + water	0.012	96.4–98.8	0.998	≤10	[29]
Soil	HPLC-FLD	Florisil® + SiO_2	2 : 1 : 1	Acetone + hexane	0.01–0.6	94.3–103.9	0.9996	0.6–1.9	[30]
Fish tissue	HPLC-FLD	Florisil + C_{18} + Na_2SO_4	6 : 10 : 20 : 5	Hexane + dichloromethane	0.04–0.32	80.4–105.4	*	2.14–7.87	[31]
Microbial culture solution	HPLC-FLD	C_{18}	1 : 20	Acetonitrile + water	0.02–0.03	>90	>0.99	3.6–4.1	[32]

samples and investigated the suitability of different solid carriers and their influence on the extraction efficiency of natural fat content in samples. The reproducibility of the experimental results is good, and the detection and quantification limits are far below the maximum allowable levels stipulated by European Union and national regulations. Therefore, MSPD can be used as a good alternative method to extract PAHs from fish tissues in the pretreatment experiment. Llasera and others [32] used the high performance liquid chromatography and fluorescence detection method to quantitatively detect PAHs in microbial liquid culture of ciliate protozoa. Since there are few analytes extracted from microorganisms and insoluble organics in the sample, the MSPD method is selected for pretreatment (Table 4).

After reading the above literature, it can be found that the matrix solid-phase dispersion method can integrate the process of sample crushing, homogenization, extraction, purification, and separation into one step, which is green, simple, and efficient. The advantages of this method are reflected in the consumption of samples and organic solvents, environmental protection, experimental cost, simplicity of extraction process, and time consuming. In addition, there is no need to use ultrasonic, microwave, and other auxiliary extraction methods, without heating, so as to avoid the degradation of the target analyte.

Second, if this method is used to obtain the maximum extraction efficiency of the target component, the molecular structure of the target analyte, the type of dispersant elution solvent, and the volume ratio should be taken into account. Experimental selection should be optimized; the obtained

linear relationship detection limit precision stability recovery data should also be integrated in the form of tables.

In addition, it was found that in the extraction of PAHs, if the matrix components are complex, gel permeation chromatography, rapid solvent extraction, pressurized solvent extraction, and solid-phase extraction (SPE) may be needed to assist purification, so as to establish a new method of dispersed matrix SPE. In summary, MSPD can be considered as the purification method if the plan is to extract PAHs from complex solid and semisolid samples such as insoluble lipophilic substances and organic matter.

3.5. Magnetic Solid-Phase Extraction (MSPE). Magnetic solid-phase extraction (MSPE) technology is to select a specific magnetic or magnetized material as the adsorbent, through the effect of magnetic field to separate the sample from the matrix, in addition, considering that there may be a small amount of sample residue on the magnetic adsorbent, so the final need to elute it, to get more accurate results. Qin et al. [33] chose Fe_3O_4@PDA@PCD as the adsorbent and used magnetic solid-phase extraction to analyze 6 PAHs in soil. When the adsorption efficiency of Fe_3O_4@PDA@PCD and Tenax resin is 90%, the time required for PAHs to reach adsorption equilibrium is compared. It is found that Fe_3O_4@PDA@PCD (5 min) is much smaller than Tenax resin (30 min). Compared with the latter, the former has higher dispersion in aqueous solution, so it takes less time to reach adsorption equilibrium. The MSPE method was used to determine the cumulative concentration of PAHs in

TABLE 5: Effect of magnetic solid-phase extraction on the determination of polycyclic aromatic hydrocarbon in different substrates.

Substrate	Method	Adsorbent	Adsorption equilibrium time	Recovery (%)	R^2	RSD (%)	LOD (μg/kg)	References
Soil	GC-MS	Fe$_3$O$_4$@PDA@PCD	5 min	86–98	$R^2 = 0.98$	<10	*	[33]
Milk product	GC-MS	MWCNT-MNP	5 min	>86.1	0.981–0.992	3.2–10.1	0.04–0.075	[34]
Water	HPLC-FLD	Fe$_3$O$_4$@SiO$_2$@MMTA-Au	90 s	87.8–120	0.9919–0.9985	1.14–3.45	0.25–37.5	[35]
Water	HPLC-FLD	Fe$_3$O$_4$@MIL-101	<30 min	*	0.9978–0.9992	3.3–4.8	*	[36]

earthworms, and the correlation analysis was conducted with the extracted amount. The applicability of the MSPE method in biological feasibility assessment earthworms proved that the method can be used to predict and analyze PAHs in soil. Nabi et al. [34] studied 16 kinds of PAHs in dairy products by MSPE/GC-MS and discussed the influence of different factors on the content of PAHs in different types of dairy products. MWCNT-MNP complex of CNTs surface modified by adsorbent was quantitatively analyzed by SIM. The results showed that the linear relationship of the method was good and the recovery rate was high. Except for few milk powder samples, the content of PAHs in other samples was lower than the EU standard limit. Yang et al. [35] prepared a new magnetic adsorbent and utilized the 90s magnetic solid-phase extraction method to complete the adsorption, which greatly saved the time of sample pretreatment. Li and others [36] chose to use metal-organic skeleton composite material (Fe$_3$O$_4$@MIL-101) as magnetic solid-phase extraction adsorbent to determine PAHs in tap water samples. They combined the high-performance liquid chromatography-fluorescence method for qualitative and quantitative analyses, avoiding cumbersome operations such as filtration and optimizing experimental operations.

Searching keywords "PAHs" and "MSPE" in Web of Science database, it can be found that in recent years, magnetic solid-phase extraction has been widely used in the determination and analysis of PAHs. Magnetic adsorbents were prepared according to the characteristics of extraction environment. Due to its unique discrete properties and the effect of external magnetic field, easy to operate, high efficiency, and green environmental protection, extraction efficiency is also considerable. In addition, the number of adsorbent cycles is also beneficial to reduce the cost of the experiment. In addition, through the analysis of the data given in Table 5, it can be seen that the standard recovery rate of the sample after the application of this technology is high, and the linear relationship and other parameters are in the standard range. In conclusion, as one of the most promising sample pretreatment technologies, magnetic solid-phase extraction (MSPE) will be applied more widely in food safety and other fields in the future.

3.6. Cloud Point Extraction (CPE).

Cloud point extraction (CPE) is a green extraction technology based on the phenomenon of cloud point and the solubility of micelle solution to achieve the separation of water-soluble substances

from hydrophilic or oily substances. Matsuura and others [37] used the turbidity point extraction method and selected Brij30 as a nonionic surfactant to separate phenanthocyanin from soil. In the experiment, the effect of two salt additives on promoting phase separation in CPE was investigated. It was found that the turbidity point temperature decreased by about 30°C with the addition of sodium chloride, while the turbidity point temperature decreased by about 45°C with the addition of sodium sulfate, so sodium sulfate was selected. In addition, the gravity sedimentation method was used to replace centrifugal separation in the separation of PAHs in the washing solution, so that a large number of samples could be processed at a lower cost. The experimental results show that the sample recovery rate is high, which also proves that the method is economical and effective for treating a large amount of contaminated soil. Soares and others [38] used turbidity point extraction and OPEO30 surfactant phase derivations and gas chromatography-mass spectrometry to detect PAHs in groundwater samples. According to the multiple response, Pareto diagram, curvature test and chromatographic data analysis, the experimental scheme was designed using central point experimental conditions and the optimal conditions were determined. The multiple response was calculated using the following equation:

Multiple response

$$= \sum \left(\frac{\text{PAH area}}{\text{Maximum PAH area obtained in design}} \right). \quad (1)$$

Compared with LLE, this method has the main advantages of using nontoxic solvent in small volume and low volume samples and conforms to the principle of green chemistry. Jia et al. [39] established a turbidity point extraction method based on the hexafluoro-isopropanol (HFIP) mediated TX-100 water system. The results proved that the HFIP-mediated CPE enrichment factor and extraction rate were better. This method is simple, rapid, and reliable and can be used for the extraction and detection of polycyclic aromatic hydrocarbons organic pollutants in water.

Through the analysis of Table 6 content, it was found that the turbidity point extraction method could be used to detect trace PAHS pollutants in the pretreatment of food, water samples, and soil. The HPLC-UV method was mostly used for detection. Low toxicity and nonvolatile nonionic

TABLE 6: Influence of cloud point extraction on determination of polycyclic aromatic hydrocarbon in different substrates.

Substrate	Method	Surfactant	Temperature (°C)	Recovery (%)	LOD (μg/L)	References
Soil	HPLC-UV	Brij30	25	58–88	*	[37]
Water	GC-MS	OPEO30	70	70–98	0.02–0.05	[38]
Water	HPLC-UV	HFIP-TX-100	26	79.4–110.8	0.04–0.38	[39]

surfactants were widely used in the preconcentration process. Initiation initiates the separation of the aqueous phase close to the critical micelle concentration from the surfactant rich phase. In order to improve the extraction efficiency, the selection of surfactant is particularly important.

3.7. Other Technologies. Manzano et al. [40] used two-dimensional gas chromatography-time-of flight mass spectrometry to quantitatively analyze complex PAHs mixtures in NIST SRMs. High orthogonality column combination (LC50 × NSP-35) was used to quantify complex PAHs mixtures in NIST SRMs, achieving better chromatographic resolution and greater orthogonality. In addition, it can be used to accurately quantify complex PAHs mixtures in environmental extracts and comprehensively determine their complex PAHs composition. Ramos-Contreras and others [41] developed a green method based on pressurized hot water extraction (PHWE), micromembrane-assisted solvent extraction (MASE), and temperature programmed evaporation gas chromatography-ion trap tandem mass spectrometry (PTV-GC-MS/MS) for the analysis of 16 polycyclic aromatic hydrocarbons (PAHs) and 8 related compounds in atmospheric particulate matter. The critical water extraction-membrane microextraction method is proved to be reliable and effective for the determination of trace PAHs in atmospheric particulate matter. Cochran and Kubatova [42] proposed an effective method for simultaneous extraction of polycyclic aromatic hydrocarbons (PAHs) and their polar oxidation products from atmospheric particulate matter by pressurized fluid extraction (PFE).

In recent years, donor-acceptor complex chromatography (DACC) has been used for the detection of PAHs as a new technology, which can reduce the amount of solvent and save the analysis time in the purification of tested samples. Windal et al. [43] used donor-receptor complex chromatography (DACC) combined with high-performance liquid chromatography-ultraviolet/fluorescence detection to analyze 16 European priority PAHs in fish oil and dried plants, and the results showed that the detection of most of them showed good linear relationship. Barranco et al. [44] compared the purification method based on the donor-acceptor composite chromatography column (DACC) with the standardized method widely used in food industry (low-pressure column chromatography with alumina as the stationary phase) in the pretreatment analysis of polycyclic aromatic hydrocarbons (PAHs) in edible oil, and the results showed that DACC is used to control the type of mobile phase and the flow rate, which not only optimizes the pretreatment operation and saves the elution time but also cleans the sample, facilitates the follow-up detection, and

makes the experimental results reach a more accurate and higher level.

4. Application of Computer Simulation in Concentration Detection, Prediction, and Degradation of Polycyclic Aromatic Hydrocarbons

4.1. The Response Surface Method. The response surface method first appeared in the 1950s. The history is not long, but it develops rapidly. It was proposed by Box and Hunter in 1951. Hill, Hunter, Draper, Khuri, Comell, and other scholars have conducted some preliminary application studies and preliminary definitions of response surface methodology successively and made a relatively comprehensive and systematic discussion.

In this method, the response surface model and function relationship are fitted by finite number of tests and test data. Through optimization calculation, the best combination of test variables and the best process parameters is found. In recent years, RSM has been widely used in food, Chinese medicine, engineering, ecology, biological engineering, and many other fields.

The prediction based on the RSM statistical model not only provides the best prediction for parameter optimization but also reduces a lot of laboratory work. Abd Manan and others used response surface methodology (RSM) to study the optimal conditions for photofenton oxidation to degrade polycyclic aromatic hydrocarbons in drinking water. The drinking water samples were prepared with an aqueous solution at a water treatment plant in Perak, Malaysia, in September 2016. The reaction time, pH value, and molar concentration of H_2O_2 and $FeSO_4$ were determined by the RSM method. The influences and interactions of these parameters were evaluated by using a five-stage central composite design of the quadratic model. The response variable was the total organic carbon (TOC) removal rate, and the quantitative analysis of polycyclic aromatic hydrocarbons was performed by gas chromatography-mass spectrometry [45]. Gitipour and others established a mathematical model with response surface methodology to quantify the influence of three parameters, including washing temperature, washing time, and detergent, on the washing process of PAH-contaminated soil. In the experiment, the DOE method was used to carry out 20 experiments to maximize the removal efficiency of PAHs by combining research variables. The three factors studied varied within a predetermined range, and the output (i.e., removal rate) was evaluated to compare the removal process of each PAH, so as to obtain the model of the total removal rate of PAHs and finally obtain the optimal conditions related to the

parameters studied. In addition, the established secondary model for removing PAHs also has a high correlation coefficient [46]. Ramalhosa and others established a micro-wave-assisted extraction (MAE)-liquid chromatography-photodiodearray (LC-PDA) combined fluorescence detection method and used response surface methodology to find the optimal extraction parameters. They analyzed and determined 18 PAHs in the food tissues of three common edible and commercial fishes (sardines, mackerel, and horsemackerel) from the Atlantic Ocean. Different levels of naphthalene and other PAHs were detected in the samples analyzed, and none of the samples contained benzo [a] pyrene, a marker used to evaluate the occurrence and carcinogenesis of PAHs in food. The application of the RSM method can fully consider the possible interaction between variables, while avoiding the method of one-factor experiment. This method is sensitive, efficient, simple, and robust and can be used for routine analysis [47]. Gfrerer and others used the response surface design method to optimize the extraction of PAHs using the new process, taking the changes of extraction cycles and holding time after reaching the heating temperature as experimental variables. The comparison shows that fluidized bed extraction is an effective alternative method to extract PAHs from soil and sediment. The recoveries and relative standard deviations are in the acceptable range. The results provided by this method are similar to those of the standard Soxhlet extraction method. Compared with traditional methods, this method has the advantages of short extraction time, less solvent consumption, and higher efficiency and precision [48]. Hui et al. prepared poly-β-cyclodextrin ionic liquid FF using n-octanol as supramolecular solvent as a new extractant. In combination with GC-FID, the main variables of FF formation time (min), volume of SUPRAs (LAIRL), and extraction time (min) were optimized by variation-by-variable (OVAT) analysis and response surface methodology (RSM). It was successfully applied in dispersive liquid phase microextraction of seven representative PAHs. The application of magnetic separation avoids the traditional microextraction techniques such as centrifugation or filtration, which greatly improves the separation rate. OFAT analysis is used to screen and determine the variables that affect the extraction efficiency, and the optimized method has been successfully applied to the content safety study of polycyclic aromatic hydrocarbons in a variety of commercial food and beverage in Malaysia [49].

Central combination design based on the response surface method is an effective method to seek optimal conditions for multivariable systems. This method not only reduces the number of experiments and improves the possibility of statistical interpretation but also indicates whether the parameters interact. Lu et al. used a physiology-based method to simulate human digestion in vitro and analyzed the effects of soil/liquid ratio (S/L), pH value, and culture time on the bioacceptability of PAHs in simulated gastrointestinal soil using response surface methodology combined with the central composite design method [50]. Chen and others used response surface methodology designed by Box–Behnken to study the effects of substrate

concentration, inoculation amount, and temperature on the degradation of polycyclic aromatic hydrocarbons (PAHs) in petroleum-contaminated soil. The influencing factors were determined by variance analysis. This proves that the interaction between key factors in the bioremediation process can be modeled, optimized, and studied by Box–Behnken design using RSM technology, which can maximize the biodegradation capacity of PAHs in soil and achieve the maximum degradation efficiency [51]. Rostampour and others used response surface methodology to study and optimize important parameters such as ethanol ratio, salt content, extraction volume, and dispersant solvent in the extraction process. Microwave-assisted extraction (MAE) technology was used in the pretreatment stage to improve the release of solid samples in aqueous solution and shorten the extraction time [52]. Marta et al. analyzed 14 PAHs in grilled and smoked muscle foods using acetonitrile as an extraction agent using response surface methodology. Matrix matching calibration curves were developed and weighted least square calibration was used to determine the optimal dosage of magnesium sulfate and sodium chloride to facilitate liquid phase separation of PAH-containing acetonitrile extraction. The results showed that the recovery rate was high and the repeatability and reproducibility met the relevant standards. Compared with the traditional method, the experimental extraction is simple and does not require adsorbents or special equipment [53]. Mohammadi et al. separated and determined PAHs in edible oil, and microwave technology was used to complete the rapid release of PAHs in the sample. Response surface methodology based on central composite design was used to study the influencing factors of the extraction process. This method is an accurate, rapid, and reliable sample pretreatment method for the extraction and determination of PAHs from different edible oil samples [54]. Dalvand et al. prepared silica/polyaniline nanofiber adsorbent to prevent the aggregation of polyaniline in the process of polymerization by combining in situ polymerization and electrospinning. The prepared NTD and gas chromatography-flame ionization detector were combined with response surface methodology to simultaneously analyze PAHs and benzene series in soil. The effective experimental variables were evaluated by introducing the RSM method designed by Box–Behnken, and the influencing experimental variables were optimized. Under the optimized conditions, a lower detection limit, a wider detection limit, an acceptable recovery rate, and reproducibility were obtained [55]. Yang et al. used 1,3,5-tris (4-aminophenyl) benzene and triformyl chloride (TAPBTMC-COF) for amide coupling reaction at room temperature, combined with solid-phase microextraction technology and response surface methodology to determine the influence of parameters on SPME efficiency. The results show that the method has a high recovery rate and can be used for the determination of PAHs in actual water samples [56]. In the experiment of simultaneous determination of 16 PAHs in barbecue samples, Kamankesh et al. used response surface methodology to optimize the factors related to microextraction efficiency. Compared with other methods, this method is simple and feasible, with short total analysis

time, low solvent consumption, high recovery rate, high enrichment coefficient, good repeatability, good precision, and high feasibility [57]. Hosseini and others established a gas chromatography-flame ionization detector (GC-FID), floatation-assisted liquid-liquid microextraction (HLLME-FA) method for the determination of PAHs in water samples and designed a special extraction pool for the first time to facilitate the extraction and collection of four PAHs in water samples with low-density solvents. The data were analyzed by a regression program based on the FCCD response surface method (RSM). The optimal conditions of each variable and the effects of different factors on the extraction efficiency were studied, and the method obtained satisfactory results [58]. Mohammadi and others measured the content of 16 polycyclic aromatic hydrocarbons (PAHs) in 80 samples of 4 traditional smoked fish and found that there was a significant interaction between the volume of hydrolysate and the amount of ethanol ratio extractant and dispersant. In this study, RSM was used to describe the complete effect of each parameter in the process and evaluate the influence of the interaction between the selected variables on the extraction conditions, which can effectively extract and measure the residual PAHs in smoked fish [59]. Christopoulou and others established a matrix solid-phase dispersion extraction (MSPD) method for the determination of 16 preferred PAHs in indoor dust samples from the Environmental Protection Agency (EPA). In this study, response surface methodology based on experimental statistical design is applied. Satisfactory results are obtained in linear accuracy range and precision of the optimized experimental method. All the target analytes have high recoveries and are suitable for the analysis of PAHs in specific matrix [60]. In the determination of PAHs in smoked rice samples, Fazeli et al. designed experiments using the CCD method and investigated the effects of extraction solvent volume factor, purification cylinder type, purification solvent type, and volume on the reaction rate (BAP recovery rate). ANOVA was used to analyze the variance of 72 test data. RSM describes the full effect of each parameter in the process and includes the interaction between the variables. The BAP index of Hashmi and local Domesia smoked rice samples was determined by the optimized selection method. The BAP index of most smoked rice samples was lower than the maximum allowed level in the European Union [61]. Mollahosseini and others used mechanical stirring bar adsorption extraction MSBSE-PAN combined with GC/FID to extract and determine some low-molecular weight polycyclic aromatic hydrocarbons (PAHs) in water samples. The response surface methodology (RSM) based on central composite design (CCD) was used to optimize the adsorption time, desorption time, sample volume, and stirring speed. Under the optimum conditions, the limits of detection (LOD) and limits of eligibility (LOQ) were in reasonable range, respectively. The relative standard deviations (RSDs) of the analytes including acenaphthene (ACE), anthracene (Ant), naphthene (NAP), and phenanthrene (PHE) were less than 12.7%, and the relative recovery (RRS) was at a high level. The application of the coating saves cost and time, and the method of extracting PAHs from water

samples is economical and time saving. The results show that this method is a time efficient, economic, and effective method to obtain the best extraction conditions [62].

4.2. Artificial Neural Network.
The artificial neural network (ANN) is a kind of flexible mathematical structure. It can extract the basic interaction between dependent variables and independent variables with high precision by simulating the human brain's organizational structure and thinking mode. It endows computer programs with self-learning ability and can be used as a method to predict the optimization of the microchemical research process. The artificial neural network can be used as a method to predict the optimization of the microchemical research process because of its unique characteristics of nonlinearity, self-adaptation, generalization, and model independence, and some satisfactory results have been obtained in some studies.

The BP neural network is a kind of the neural network which adopts the error backpropagation training algorithm. It is a one-way propagating multilayer feedforward network composed of input layer, hidden layer, and output layer. The BP neural network adopts the supervised learning method. The process of learning algorithm is divided into two stages: the first stage is the forward propagation process, in which the actual output value of nodes at each layer is calculated from the input layer through the hidden layer, layer by layer, and nodes at each layer only accept the input of the previous node. It only affects the state of the next node. The second stage is the backpropagation process. If the output layer fails to obtain the desired output value, the error between the actual and expected output is recursively calculated layer by layer, and the error signal tends to be minimized according to this error.

The backpropagation artificial neural network model is considered as a potential application for predicting PAH concentrations in soils, and its application can help reduce the frequency of chemical analysis for on-site remediation monitoring purposes and support the decision of the end point of remediation. Huanyu et al. studied the influence of corn stalks on PAHs diffusion in soil and its related mechanism, modeled the relationship between soil properties and PAHs concentration in soil by using the backpropagation artificial neural network, and determined the predictive ability of the artificial neural network model on PAHs concentration in soil after straw returned to field. The performance of the neural network models was quantified by root mean square error (RMSE):

$$\text{RMSE} = \sqrt[2]{\frac{\sum_{i=1}^{n} (x_i - y_i)^2}{n}}. \tag{2}$$

It was found that the addition of 6% corn straw amount could significantly increase the dissipation of PAHs in soil, and the addition of corn straw increased the solubility and migration of PAHs, thus improving the biodegradation of PAHs in soil. This provides a feasible option for remediation of PAHs contaminated soil [63].
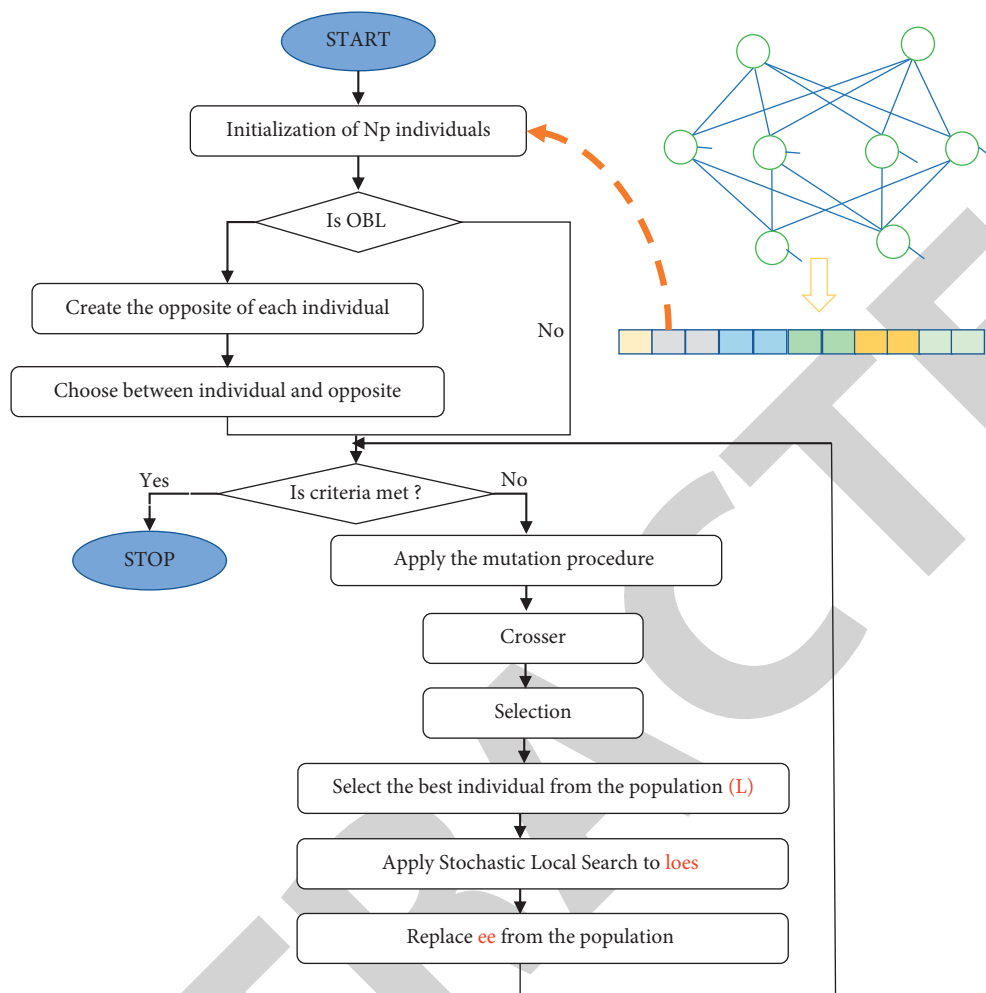
FIGURE 2: Scheme of the DE algorithm used to evolve the ANN parameters.

Chen et al. used the backpropagation artificial neural network to predict the content of benzo [a] pyrene in smoked sausage. The effects of smoking temperature, smoking time, and fat/lean meat ratio on BAP content were analyzed, and the nonlinear regression model and BP-ANN model were established, respectively. The BP-ANN can better explain the uncertainty and nonlinear relationship of BAP content in sausage under different smoking conditions, which further shows that the ANN model is an ideal model for predicting BAP content [64]. Xu et al. established the parameter-biodegradation relationship model of polycyclic aromatic hydrocarbons hypoxic Andrews model using the BP-ANN method, and the results showed that the backpropagation artificial neural network had high prediction accuracy and ability [65].

As one of the optimization algorithms, the differential evolution algorithm is getting more and more attention. Using Visual Studioc\Network Framework 4.0, Pirsaheb et al. modeled the formation of PAHs in meat products using artificial neural networks (ANNs) optimized by the differential evolution algorithm. The type of meat (the animal that provides the meat), the meat cut (the specific part of the animal that cuts the meat), the presence of skin, the barbecue temperature, and the time were taken as input parameters, and the output was the total PAHs value. In addition, in order to improve the quality of the initial solution, the author adopts objection-based learning (OBL), and the optimal network results are in good agreement with the experimental data. Therefore, this method can replace experiments used to predict PAH levels in various meats and reduce the consumption of resources in terms of time, experienced human resources and materials. The scheme of the DE algorithm and its integration with ANNs is shown in Figure 2 [66].

Principal component analysis is often used to extract the main characteristic variables of data. Cauchi et al. used the artificial neural network (ANN) method to qualitatively and quantitatively determine some key pollutants in drinking water at the same time and successfully determined the contents of cadmium, lead, copper, and polycyclic aromatic hydrocarbons (PAHs) such as anthracene, phenanthrene, and naphthalene in special water samples. Principal component analysis (PCA) was used as the data preprocessing technology before ANNS modeling, and the root mean square error (RMSEP) was used to measure the difference between the predicted concentration and the actual

concentration, so as to obtain the optimal ANN model. This method greatly improves the ability of accurate prediction of pollutants and can be effectively used to obtain quantitative data of pollutant concentration in drinking water [67]. Wesolowski et al. used two different types of the neural network multilayer perceptual sensor (MLP) and self-organizing map (SOM) to identify changes in urban air pollutant levels throughout the year, where MLP was used to predict which heating season a sample was collected in, and SOM was used to map all samples to identify any similarities between them [68].

In recent years, along with the vigorous development of social economy and science and technology, ocean and soil also suffered from pollution in different degree; the existence of various pollutants (such as PAHs) poses a threat to the environment and biota. Therefore, how to promote the effective degradation of PAHs to design the bioremediation strategy has become one of the focuses of attention in recent years. Jing et al. established an artificial neural network model to predict the removal effect of polycyclic aromatic hydrocarbons (PAHs) in marine oil-bearing wastewater by ultraviolet radiation. Naphthalene was selected as the representative of polycyclic aromatics; 12 neurons in the hidden layer and Levenberg–Marquardt backpropagation algorithm were used to find that the number of neurons in the hidden layer would significantly affect the convergence and prediction accuracy of the network (Figure 3). The removal rate was taken as the model output. The injection rate, salinity, temperature, initial concentration, and reaction time were simulated as functions of five independent input variables. It is concluded that the neural network model can effectively predict the degradation behavior of PAHs induced by light, and the removal rate of the established neural network model is close to the measured value validation and test subset, which can accurately simulate the naphthalene removal process and reproduce the experimental results (Figure 4). The experiment operation time and material cost are saved, and the mechanism of photodegradation of PAHs is further understood, which provides a scientific basis for Marine and offshore oil and gas industry to develop corresponding treatment technology [69].

In recent years, central composite design based on the response surface methodology and artificial neural network combined with the genetic algorithm model have been used more and more in the detection of PAHs. Sachaniya et al. compared the biodegradation levels of PAHs by the response surface method and artificial neural network. The results showed that the degradation rate of PAHs predicted by the neural network model based on the mean absolute deviation and other error functions was higher than that of RSM, and the error function values of the ANN were lower. Therefore, the artificial neural network is proved to be a more reliable bioengineering tool with the best structure [70]. Moham-madi et al. used the response surface method (RSM) and artificial neural network (ANN) combined with the genetic algorithm (GA) to model and optimize the removal of pyrene from sorghum contaminated soil. In the experiment, the LM algorithm was chosen as the best training algorithm to determine the best and worst conditions for removing
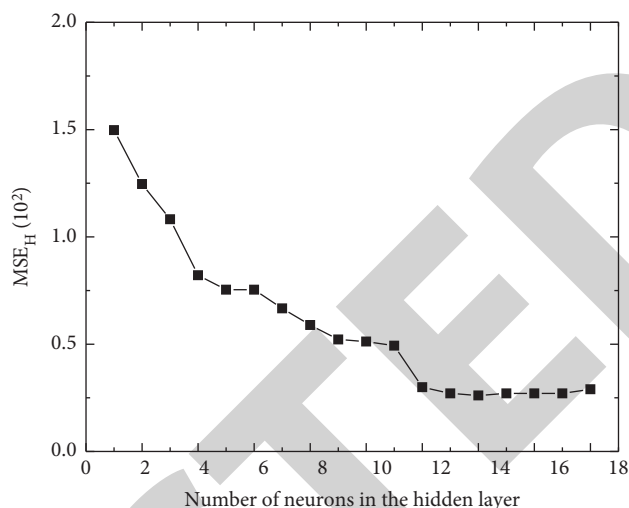
FIGURE 3: Relationship between the number of hidden neurons and MSE.

pyrene. The results showed that using indoleacetic acid and *Pseudomonas* could improve the removal efficiency of pyrene in soil of sorghum plants, and the prediction ability of the neural network model was obviously better than that of the RSM model [71]. Subashchandrabose et al. established the artificial neural network (ANN) and genetic algorithm (GA) models to analyze the toxicological interactions of phenanthrene and benzo [a] pyrene, as well as two kinds of heavy metals (HMS) on *Chlorella* MM3 oxidative stress. The validation of experimental data and biochemical prediction results showed that the model established by the combination of the neural network and genetic algorithm could effectively predict the toxicity of PAHs and HMS mixture to microalgae, and the relative error was only 10%. This study provides biochemically based mechanical toxicity information of microalgae exposed to mixtures of organic and inorganic pollutants, thus laying a foundation for future studies on the mechanism of microalgae mixed toxicity and the development of a better toxicity prediction model for polycyclic aromatic hydrocarbons and HMS mixtures [72].

5. Summary and Prospect

After reading a lot of literature, it is found that the pollution of polycyclic aromatic hydrocarbons (PAHs), which is one of the pollutants under optimal control in the EU, should not be underestimated. This article first introduces the characteristics and sources of polycyclic aromatic hydrocarbons and summarizes the four main sources: high temperature fume bake food contamination, food packaging contact material pollution, air pollution, and water pollution on the testing and analysis of polycyclic aromatic hydrocarbon compounds extracted or separation of the literature, through the search of pollutant source and select reasonable method for effective control of them.

In this increasingly "intelligent" era, various technologies emerge at the historic moment, which not only improve our thinking mode and methods but also make our
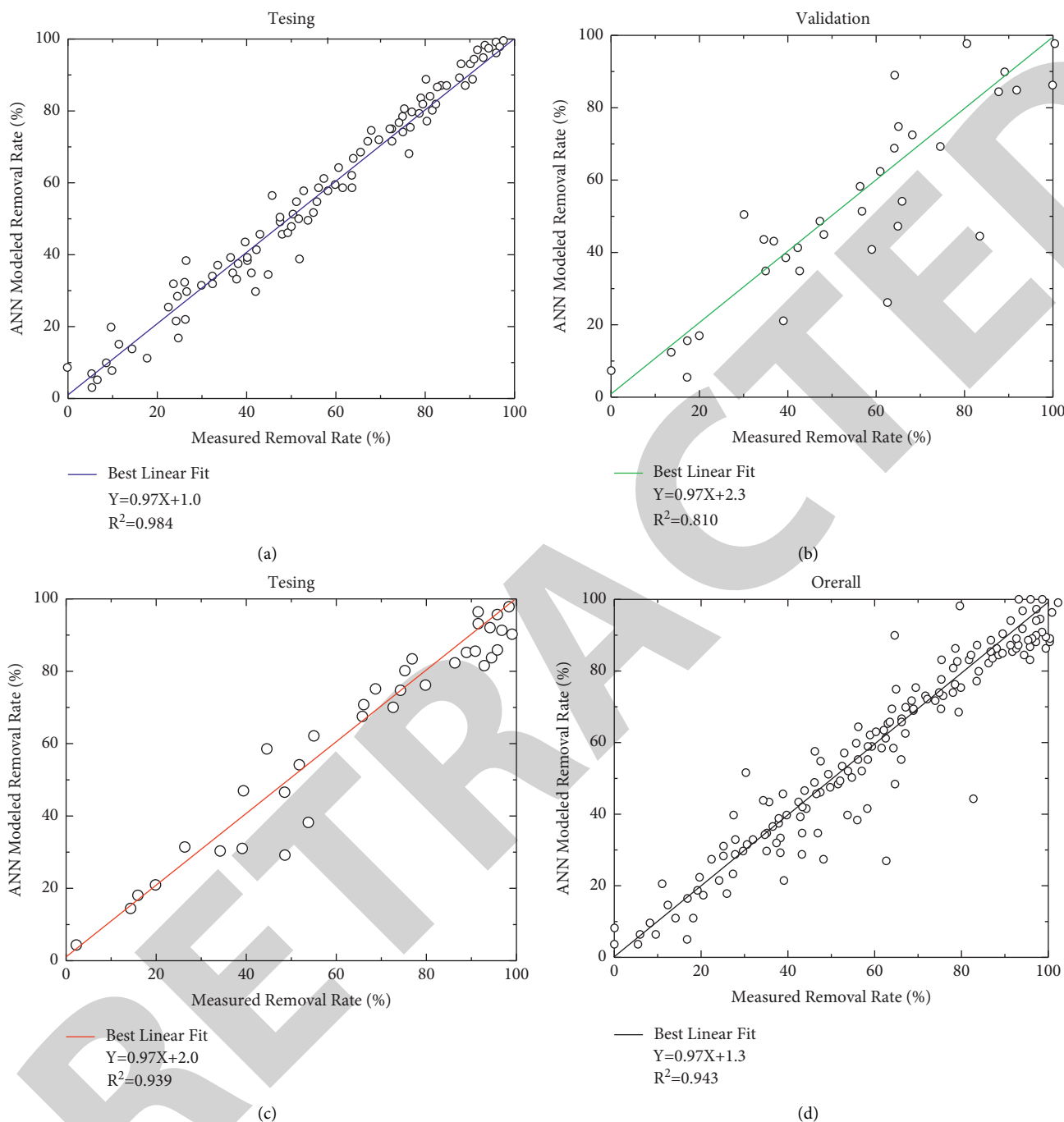
Figure 4: Comparison between ANN modeled and experimentally measured values of naphthalene removal rate for the (a) training, (b) validation, (c) testing, and (d) overall data.

experimental work more convenient. In the tens of thousands of experimental data, combined with hundreds of thousands of years ago, the computer has shown unparalleled advantages. The numerical simulation method and response surface can be used to process the data in batches and select the optimal solution among the numerous data. The emergence of the artificial neural network makes the computer have the ability of self-learning, simplifies the complex experimental operation, and saves time. It has strong learning ability and fault tolerance and can adapt to

various evaluation environments. The prediction can be made through the establishment of the model, so as to provide a way and help for the targeted pollution prevention and control in advance.

In a word, with the development of computing hardware and theoretical methods, big data, deep learning, and artificial intelligence will continue to play an increasingly important role in the field of chemistry and chemical engineering and will develop towards a more intelligent and efficient direction.

Data Availability

The data used to support the findings of this study are available from the corresponding author upon request.

Conflicts of Interest

The authors declare that they have no conflicts of interest.

Acknowledgments

References

[1] E. Fasano, I. Yebra-Pimentel, E. M.-C. rballo, and J. Simal-Gándara, "Profiling, distribution and levels of carcinogenic polycyclic aromatic hydrocarbons in traditional smoked plant and animal foods," *Food Control*, vol. 59, 2016.

[2] B. H. Chen and Y. C. Chen, "formation of polycyclic aromatic hydrocarbons in the smoke from heated model lipids and food lipids," *Journal of Agricultural & Food Chemistry*, vol. 49, p. 5238, 2001.

[3] T. C. Merlo, L. Molognoni, R. B. Hoff, H. Daguer, I. Patinho, and C. J. Contreras-Castillo, "Alternative pressurized liquid extraction using a hard cap espresso machine for determination of polycyclic aromatic hydrocarbons in smoked bacon," *Food Control*, vol. 120, Article ID 107565, 2021.

[4] G. Shen, Y. Chen, S. Su et al., "Contamination and distribution of parent, nitrated, and oxygenated polycyclic aromatic hydrocarbons in smoked meat," *Environmental Science and Pollution Research*, vol. 21, no. 19, pp. 11521–11530, 2014.

[5] D. Kafouris, A. Koukkidou, E. Christou, M. Hadjigeorgiou, and S. Yiannopoulos, "Determination of polycyclic aromatic hydrocarbons in traditionally smoked meat products and charcoal grilled meat in Cyprus," *Meat Science*, vol. 164, Article ID 108088, 2020.

[6] G. Purcaro, L. Barp, and S. Moret, "Determination of hydrocarbon contamination in foods a review," *Analytical Methods*, vol. 8, 2016.

[7] K. Kuzmicz and A. Ciemniak, "Assessing contamination of smoked sprats (Sprattus sprattus) with polycyclic aromatic hydrocarbons (PAHs) and changes in its level during storage in various types of packaging," *Journal of Environmental Science and Health, Part B*, vol. 53, pp. 1–11, 2017.

[8] C. Conchione, C. Picon, R. Bortolomeazzi, and S. Moret, "Hydrocarbon contaminants in pizza boxes from the Italian market," *Food Packaging and Shelf Life*, vol. 25, Article ID 100535, 2020.

[9] S. Q. Li, H. G. Ni, and H. Zeng, "PAHs in polystyrene food contact materials: an unintended consequence," *Science of the Total Environment*, vol. 609, pp. 1126–1131, 2017.

[10] Y. He, N. Qin, W. He, and F. Xu, "The impacts of algae biological pump effect on the occurrence, source apportionment and toxicity of SPM-bound PAHs in lake environment," *Science of the Total Environment*, vol. 753, Article ID 141980, 2021.

[11] W. J. Hong, H. Jia, W. L. Ma et al., "Distribution, fate, inhalation exposure and lung cancer risk of atmospheric polycyclic aromatic hydrocarbons in some asian countries," *Environmental Science and Technology*, vol. 50, no. 13, pp. 7163–7174, 2016.

[12] K. M. Baek, Y. K. Seo, J. Y. Kim, and S. O. Baek, "Monitoring of particulate hazardous air pollutants and affecting factors in the largest industrial area in South Korea: The sihwa-banwol complex," *Environmental Engineering Research*, vol. 25, 2019.

[13] L. Ma, B. Li, Y. Liu et al., "Characterization, sources and risk assessment of PM2.5-bound polycyclic aromatic hydrocarbons (PAHs) and nitrated PAHs (NPAHs) in Harbin, a cold city in Northern China," *Journal of Cleaner Production*, vol. 264, Article ID 121673, 2020.

[14] C. Grandclement, I. Seyssiecq, A. Piram et al., "From the conventional biological wastewater treatment to hybrid processes, the evaluation of organic micropollutant removal: a review," *Water Research*, vol. 111, pp. 297–317, 2017.

[15] Q. J. Jiang, Y. Y. Li, X. X. Hu, B. Lu, and R. Wang, "Estimation of annual emission and distribution characteristics of polycyclic aromatic hydrocarbons (PAHs) in Taiyuan," *China Environmental Science*, vol. 33, pp. 14–20, 2013.

[16] B. Ambade, S. S. Sethi, A. Kumar, T. K. Sankar, and S. Kurwadkar, "Health risk assessment, composition, and distribution of polycyclic aromatic hydrocarbons (PAHs) in drinking water of southern Jharkhand, east India," *Archives of Environmental Contamination and Toxicology*, vol. 80, pp. 120–133, 2021.

[17] J. Wang, L. Jia, W. Wei, S. Lang, P. Shao, and X. Fan, "Determination of polycyclic aromatic hydrocarbons in edible oil by gel permeation chromatography and ultra-high performance liquid chromatography coupled with diode array detector and fluorescence detector," *Acta Chromatographica*, vol. 28, no. 3, pp. 415–427, 2016.

[18] W. Lian, F. Ren, L. Tang, and D. Dong, "Analysis of polycyclic aromatic hydrocarbons in cigarette samples using gel permeation chromatography clean-up by gas chromatography-tandem mass spectrometry," *Microchemical Journal*, vol. 129, pp. 194–199, 2016.

[19] X. Shao, Y. Xu, W. Zhang, and J. Lv, "Polycyclic aromatic hydrocarbons (PAHs) pollution in agricultural soil in Tianjin, China," *Soil and Sediment Contamination: International Journal*, vol. 24, no. 3, pp. 343–351, 2015.

[20] D. Kong, N. Wang, Z. Shan et al., "Simultaneous determination of pesticides, polycyclic aromatic hydrocarbons, polychlorinated biphenyls and phthalate esters in human adipose tissue by gas chromatography-tandem mass spectrometry," *Journal of Chromatography B*, vol. 898, pp. 38–52, 2012.

[21] A. Rajendran, N. Balakrishnan, and P. Ajay, "Deep embedded median clustering for routing misbehaviour and attacks detection in ad-hoc networks," *Ad Hoc Networks*, vol. 126, Article ID 102757, 2022.

[22] O. Geiss, C. Senaldi, I. Bianchi, A. Lucena, S. Tirendi, and J. Barrero-Moreno, "A fast and selective method for the determination of 8 carcinogenic Polycyclic Aromatic Hydrocarbons in rubber and plastic materials," *Journal of Chromatography A*, vol. 1566, pp. 13–22, 2018.

[23] H. Zhou, X. Wu, D. Chen et al., "Simultaneous determination of 24 polycyclic aromatic hydrocarbons in oils by gas chromatography-mass spectrometry using an improved clean-up procedure," *Food Analytical Methods*, vol. 12, no. 9, pp. 1957–1963, 2019.

[24] R. J. Krupadam, B. Bhagat, and M. S. Khan, "Highly sensitive determination of polycyclic aromatic hydrocarbons in ambient air dust by gas chromatography-mass spectrometry after molecularly imprinted polymer extraction," *Analytical and Bioanalytical Chemistry*, vol. 397, no. 7, pp. 3097–3106, 2010.

[25] Y. N. Zhang, X. L. Yang, Y. R. Bian, G. U. Cheng-Gang, D. Z. Wang, and X. Jiang, "An accelerated solvent extraction-solid phase extraction-high performance liquid chromatographic method for determination ofpolycyclic aromatic hydrocarbons in soil and earthworm samples," *Chinese Journal of Analytical Chemistry*, vol. 44, 2016.

[26] J. M. Dinović-Stojanović, J. M. Stišović, A. R. Popović, D. M. Nikolić, and S. D. Janković, "Benzo [a]pyrene, benz[a] anthracene, benzo[b]fluoranthene and chrysene in smoked meat and smoked meat products --validation of the method," *Hemijska Industrija*, vol. 70, 2016.

[27] M. Suranová, J. Semanová, B. Skláršová, and P. Simko, "Application ofAccelerated solvent extraction for simultaneous isolation and pre-cleaning up procedure during determination of polycyclic aromatic hydrocarbons in smoked meat products," *Food Analytical Methods*, vol. 8, no. 4, pp. 1014–1020, 2015.

[28] J. Tan, X. Lu, L. Fu, G. Yang, and J. Chen, "Quantification of Cl-PAHs and their parent compounds in fish by improved ASE method and stable isotope dilution GC-MS," *Ecotoxicology and Environmental Safety*, vol. 186, Article ID 109775, 2019.

[29] A. Sharma, R. Kumar, M. W. A. Talib, S. Srivastava, and R. Iqbal, "Network modelling and computation of quickest path for service-level agreements using bi-objective optimization," *International Journal of Distributed Sensor Networks*, vol. 15, no. 10, Article ID 155014771988111, 2019.

[30] X. Liu, C. Ma, and C. Yang, "Power station flue gas desulfurization system based on automatic online monitoring platform," *Journal of Digital Information Management*, vol. 13, no. 6, pp. 480–488, 2015.

[31] R. Huang, S. Zhang, W. Zhang, and X. Yang, "Progress of zinc oxide-based nanocomposites in the textile industry," *IET Collaborative Intelligent Manufacturing*, vol. 3, no. 3, pp. 281–289, 2021.

[32] M. Llasera and J. Olmos-Espejel, "Methodology for quantitative determination of polycyclic aromatic hydrocarbons in Protozoa cultures," *Journal of the Mexican Chemical Society*, vol. 55, pp. 113–119, 2011.

[33] S. Qin, S. Qi, X. Li et al., "Magnetic solid-phase extraction as a novel method for the prediction of the bioaccessibility of polycyclic aromatic hydrocarbons," *Science of the Total Environment*, vol. 728, Article ID 138789, 2020.

[34] C. Nabi, M. Dadgar, Y. Fakhri et al., "Levels of polycyclic aromatic hydrocarbons in milk and milk powder samples and their likely risk assessment in Iranian population," *Journal of Food Composition and Analysis*, vol. 85, 2020.

[35] X. Yang, Y. Yin, Y. Zong, T. Wan, and X. Liao, "Magnetic nanocomposite as sorbent for magnetic solid phase extraction coupled with high performance liquid chromatography for determination of polycyclic aromatic hydrocarbons," *Microchemical Journal*, vol. 145, pp. 26–34, 2019.

[36] Y. Li, X. Zhou, L. Dong et al., "Magnetic metal-organic frameworks nanocomposites for negligible-depletion solid-phase extraction of freely dissolved polyaromatic hydrocarbons," *Environmental Pollution*, vol. 252, 2019.

[37] Y. Matsuura, T. Sekikawa, and M. Sakata, "A simple method for separating phenanthrene from soil by cloud-point extraction," *Soil and Sediment Contamination*, vol. 28, pp. 1–11, 2019.

[38] S. A. R. Soares, C. R. Costa, R. G. O. Araujo, M. R. Zucchi, J. J. Celino, and L. S. G. Teixeira, "Determination of polycyclic aromatic hydrocarbons in groundwater samples by gas chromatography-mass spectrometry after pre-concentration using cloud-point extraction with surfactant derivatization," *Journal of the Brazilian Chemical Society*, vol. 26, 2015.

[39] X. Jia, Y. Li, L. Cao, Z. Rui, and Y. Xiao, "Hexafluoroisopropanol-mediated cloud point extraction of organic pollutants in water with analysis by high-performance liquid chromatography," *Analytical and Bioanalytical Chemistry*, vol. 409, pp. 1–11, 2017.

[40] C. Manzano, E. Hoh, and S. L. M. Simonich, "Quantification of complex polycyclic aromatic hydrocarbon mixtures in standard reference materials using comprehensive two-dimensional gas chromatography with time-of-flight mass spectrometry," *Journal of Chromatography A*, vol. 1307, pp. 172–179, 2013.

[41] C. Ramos-Contreras, E. Concha-Graña, P. López-Mahía, F. Molina-Pérez, and S. Muniategui-Lorenzo, "Determination of atmospheric particle-bound polycyclic aromatic hydrocarbons using subcritical water extraction coupled with membrane microextraction," *Journal of Chromatography A*, vol. 1606, Article ID 460381, 2019.

[42] R. E. Cochran and A. Kubatova, "Pressurised fluid extraction of polycyclic aromatic hydrocarbons and their polar oxidation products from atmospheric particles," *International Journal of Environmental Analytical Chemistry*, vol. 95, no. 5, pp. 434–452, 2015.

[43] I. Windal, L. Boxus, and V. Hanot, "Validation of the analysis of the 15 + 1 European-priority polycyclic aromatic hydrocarbons by donnor-acceptor complex chromatography and high-performance liquid chromatography-ultraviolet/fluorescence detection," *Journal of Chromatography A*, vol. 1212, no. 1-2, pp. 16–22, 2008.

[44] A. Barranco, R. M. Alonso-Salces, E. Corta et al., "Comparison of donor-acceptor and alumina columns for the clean-up of polycyclic aromatic hydrocarbons from edible oils," *Food Chemistry*, vol. 86, no. 3, pp. 465–474, 2004.

[45] T. S. B. Abd Manan, T. Khan, S. Sivapalan et al., "Application of response surface methodology for the optimization of polycyclic aromatic hydrocarbons degradation from potable water using photo-fenton oxidation process," *Science of The Total Environment*, vol. 665, pp. 196–212, 2019.

[46] S. Gitipour, A. Mohebban, S. Ghasemi, M. Abdollahinejad, and B. Abdollahinejad, "Evaluation of effective parameters in washing of PAH-contaminated soils using response surface methodology approach," *International Journal of Environmental Science and Technology*, vol. 17, no. 2, pp. 683–694, 2019.

[47] M. J. Ramalhosa, P. Paiga, S. Morais et al., "Analysis of polycyclic aromatic hydrocarbons in fish: optimisation and validation of microwave-assisted extraction," *Food Chemistry*, vol. 135, no. 1, pp. 234–242, 2012.

[48] M. Gfrerer, M. Serschen, T. Wenzl, B. M. Gawlik, and E. Lankmayr, "Optimized extraction of polycyclic aromatic hydrocarbons from contaminated soil samples," *Chromatographia*, vol. 53, pp. 467–473, 2002.

[49] B. Y. Hui, N. N. M. Zain, S. Mohamad, P. Varanusupakul, H. Osman, and M. Raoov, "Poly (cyclodextrin-ionic liquid) based ferrofluid: a new class of magnetic colloid for dispersive liquid phase microextraction of polycyclic aromatic

Retraction

Retracted: Durability Test and Mechanical Properties of CFRP Bolt under Accelerated Corrosion Conditions

Journal of Chemistry

This article has been retracted by Hindawi following an investigation undertaken by the publisher [1]. This investigation has uncovered evidence of one or more of the following indicators of systematic manipulation of the publication process:

(1) Discrepancies in scope

(2) Discrepancies in the description of the research reported

(3) Discrepancies between the availability of data and the research described

(4) Inappropriate citations

(5) Incoherent, meaningless and/or irrelevant content included in the article

(6) Peer-review manipulation

The presence of these indicators undermines our confidence in the integrity of the article's content and we cannot, therefore, vouch for its reliability. Please note that this notice is intended solely to alert readers that the content of this article is unreliable. We have not investigated whether authors were aware of or involved in the systematic manipulation of the publication process.

Wiley and Hindawi regrets that the usual quality checks did not identify these issues before publication and have since put additional measures in place to safeguard research integrity.

We wish to credit our own Research Integrity and Research Publishing teams and anonymous and named external researchers and research integrity experts for contributing to this investigation.

The corresponding author, as the representative of all authors, has been given the opportunity to register their agreement or disagreement to this retraction. We have kept a record of any response received.

References

[1] Q. Li, X. Li, and L. Guo, "Durability Test and Mechanical Properties of CFRP Bolt under Accelerated Corrosion Conditions," *Journal of Chemistry*, vol. 2022, Article ID 2094640, 7 pages, 2022.

Hindawi

Research Article

Durability Test and Mechanical Properties of CFRP Bolt under Accelerated Corrosion Conditions

Qi Li [ID], Xianglan Li [ID], and Li Guo [ID]

College of Urban Construction, Jiangxi University of Technology, Nanchang, Jiangxi 330098, China

Correspondence should be addressed to Qi Li; 201804323@stu.ncwu.edu.cn

In order to study the influence of acid corrosion on the quality, elastic modulus, tensile strength, elongation, and other properties of epoxy mortar test block and CFRP bolt, the durability test and mechanical properties test of CFRP bolt under accelerated corrosion conditions were proposed. An epoxy mortar test block was soaked in acidic solution for 90 d, and the quality, elastic modulus, tensile strength, elongation, and other properties of CFRP bolt were analyzed. Through the analysis of test data, the load-slip relationship curve of bolt was obtained and the Arrhenius equation was used. The relationship curve between tensile strength retention and logarithm of time in test environment was obtained, and the concept of conversion factor TSF was introduced to predict the strength retention of anchor corroded by acid rain for 20 years in service. The experimental results show that the maximum loss rates of mass, elastic modulus, and compressive strength of epoxy mortar test block are 1.98%, 2.81%, and 11.25%, respectively, during 90 d immersion in acidic solution. The maximum loss rates of mass, elastic modulus, tensile strength, and elongation of CFRP bolt are 0.65%, 3.29%, 6.51%, and 5.06%, respectively. Based on the analysis of the test data, the load-slip curve of the bolt is obtained, which indicates that acid corrosion reduces the bond performance of CFRP bolt. The bond-slip curve of bolt after 90 d acid corrosion was obtained by further analysis of experimental data. *Conclusion.* The experiment has certain engineering application values.

1. Introduction

Anchor rod is the rod system structure of rock and soil reinforcement. It uses an anchor rod body to exert longitudinal tension on rock and soil mass to overcome the shortcoming that the tensile capacity of rock and soil mass is far lower than the compressive capacity. Bolt anchoring is an important field in civil engineering. In geotechnical engineering, bolt anchoring can reduce the size and weight of the structure. It greatly improves the strength and stability of the rock and soil structure and effectively reduces the deformation of rock and soil structure. In 1912, the bolt was first used in the support of coal mine tunnel in Scheretz Mine in Germany, which opened the era of the use of bolt in civil engineering.

At present, the United States, Europe, and Japan have taken the anchor as an important means of underground excavation engineering construction. The number of bolts in

use is more than 500 million every year and the usage is increasing year by year. Foreign bolt manufacturers led by Henkel and Firep export a large number of rock and soil bolts to emerging regions such as South America and Asia, and the export volume is also increasing year by year [1]. In recent decades, rock and soil anchoring technology has been greatly developed in China, and many new theories and technologies have been put forward, which are widely used in civil engineering construction such as slope, foundation pit, dam, waterway, mine and airport, and many bolt production companies with independent intellectual property rights have emerged. With the construction of infrastructure in China, especially water conservancy, transportation, energy, and urban infrastructure construction, rock and soil anchorage will show a broad development prospect. In the process of use, materials are affected by the environment and their performance degrades, their state changes, until they are damaged and deteriorated, which is usually called corrosion
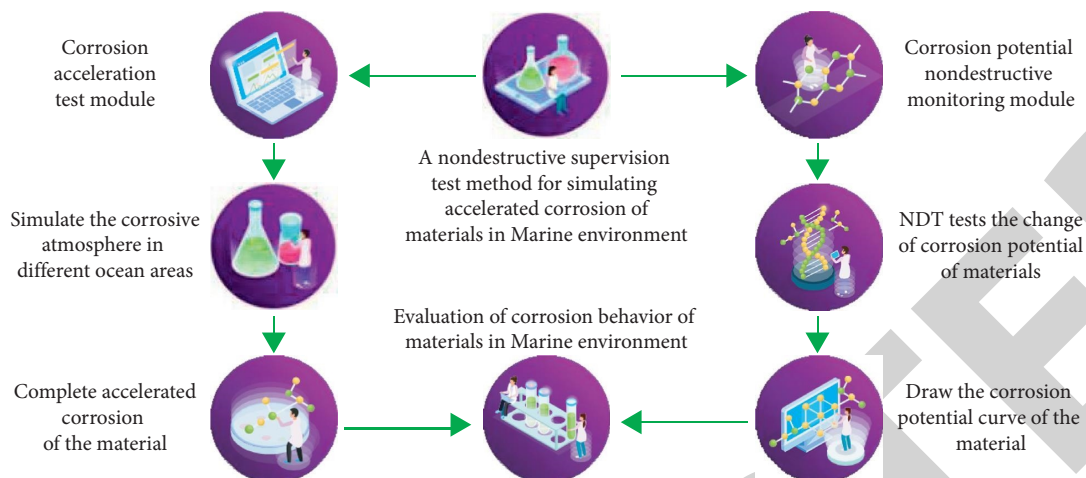
Figure 1: CFRP anchor.

[2]. Material corrosion not only brings great economic loss and a large amount of resources and energy consumption to the country but also threatens equipment, equipment, buildings, and personal safety.

We carry out corrosion tests of materials, accumulate corrosion data, and combine with laboratory analysis and research, which is of great significance to control the natural environment corrosion of materials and to provide scientific basis for the research and development of new materials, especially for the rational selection of materials, the adoption of corresponding protection measures, and the assurance of engineering quality and reliability for national key engineering construction and national defense construction, as shown in Figure 1:

2. Literature Review

Krishnadasan et al. conducted temperature cycling and humidity exposure tests on carbon fiber sheets and glass fiber sheets in 1997, and the results showed that the tensile strength, elastic modulus, and ultimate strain of CFRP are not decreased but increased, and the interface between the carbon fiber and epoxy composites is damaged and the bond between the fiber and matrix is reduced. After temperature cycling, the tensile strength and elastic modulus of GFRP do not decrease, but the ductility decreases and the embrittlement trend occurs. Under the condition of humidity exposure, the tensile strength of GFRP decreases obviously. After temperature cycling, the tensile strength and elastic modulus of epoxy resin are improved, but under humidity, the tensile strength and elastic modulus decrease significantly [3]. Yang et al. in 1994 studied the durability of reinforced concrete beams externally reinforced with aramid fiber, E-glass fiber, and graphite fiber fabrics under freeze-thaw and dry-wet cycles. The results show that the reinforced beams with aramid, E glass, and graphite are degraded in different degrees and their ultimate strength is reduced. The strength advantage of aramid and E-glass reinforced beams is almost invisible, with a loss of one-half, but graphite still retains the advantage and the strength loss is not large [4]. In

1997, Liu et al. studied the effects of FRP sheets on the performance and bond properties of concrete beams reinforced with FRP sheets in a saline dry-wet cycling environment. The research results show that the bearing capacity of FRP externally pasted concrete beams is improved when subjected to tensile surface, and the durability of the binder has a great influence on the durability of FRP reinforced concrete [5]. Castillo et al. conducted an experimental study on the dry-wet cycle and freeze-thaw cycle durability of CFRP- and GFRP-reinforced concrete cylindrical structures in salt water. The results showed that the strength, ductility and stiffness of CFRP reinforced specimens decreased under the dry-wet cycle. The strength, ductility, and stiffness of GFRP-reinforced specimens are reduced. The strength and ductility of both are reduced and the stiffness is basically unchanged under freeze-thaw cycles. However, in general, CFRP- and GFRP-reinforced structures still show good performance in harsh environment, and the effect of freeze-thaw cycle is greater on CFRP and GFRP than that of the dry-wet cycle [6]. Elgohary et al. simulated the long-term working environment around concrete beams repaired by FRP through the short-term acceleration test. During the simulation process, the specimens were soaked in boiling water and irradiated by an ultraviolet lamp for seven days. The test structure showed that the efficiency of FRP reinforcement could be reduced by more than 50% and the stiffness could be reduced by nearly 50% under harsh environment conditions. The superiority of CFRP reinforcement is reduced. The leading role of the FRP polymer matrix on the long-term performance of FRP is proposed [7]. Nabipour and Akhoundi mainly studied the overall durability of CFRP-reinforced structures from the durability of CFRP and the durability of the bond between CFRP and concrete. The research structure shows that the bond performance between CFRP and concrete is improved under ultraviolet and water leaching environment conditions [8]. Memon et al. conducted repeated freeze-thaw cycle tests on concrete members reinforced by fiber materials. The effect of the freezing-thawing cycle on the durability of a bond interface was studied by comparing with the reinforced system

in a common environment. In addition, they analyzed the changing trend of interface bond strength and initial cracking load with the increase of freezing-thawing cycles, studied the damage mechanism of new and old concrete bond surface, and gave suggestions for bond repair of concrete structures damaged by freezing-thawing. It provides a theoretical basis for structural reinforcement in cold regions [9].

FRP bars have high tensile strength and corrosion resistance, light dead weight and easy construction, so since the 1990s, FRP bars have been used in engineering and replaced steel bolts [10]. At present, the widely used FRP bars mainly include CFRP, AFRP, GFRP, and so on. The working environment of the anchor bolt is relatively bad, such as the erosion of anchor bolt by acid rain, electrochemical corrosion of sodium and calcium salt in rock and soil, etc., which will affect the safety of the use of the anchor bolt. Based on the durability test research of CFRP bolt in an acidic corrosion environment, there are still few relevant research studies in China [11]. The test of the CFRP bolt in an acidic corrosion environment was carried out by using the method of high concentration solution acceleration. The test results have certain guiding significance for the design and engineering application of the CFRP bolt.

3. Research Methods

3.1. Test Materials and Equipment. CFRP bolt: 7 mm diameter light round steel bar produced by a company is used in the test, and the length of anchor is 245 mm, 300 mm, and 350 mm.

Epoxy mortar test block: the main components are epoxy resin + curing agent + filler, curing agent, and filler are mixed in a certain proportion, and the epoxy mortar test block is made according to the requirements of GB 50203-2011 Code for Construction Quality Acceptance of Masonry Structure Engineering. The tensile test equipment is a hydraulic universal testing machine.

3.2. Test Method. In this corrosion test, 98% concentrated sulfuric acid was diluted to design a strong acid environment with pH = 3. In order to avoid corrosion of the immersion container, a PEVA corrosion resistant material was used to seal the immersion container with multiple layers. Butter the surface of the anchor before soaking to avoid serious corrosion of the anchor that would affect the mechanical properties of the test. On the 10th, 20th, 30th, 40th, 50th, 60th, 70th, 80th, and 90th days, the physical properties such as mass and size were measured. We test the pH of the soaking solution once a week to ensure that the pH is constant. Mechanical properties of the epoxy mortar test block and bolt were tested on an universal testing machine without soaking and after soaking for 30, 60, and 90 days [12]. The compressive strength of the epoxy mortar block was tested by a compressive failure test and its elastic modulus was calculated by stress and strain. The tensile strength of the CFRP bolt was tested by tensile failure test, and its physical properties such as elongation and elastic
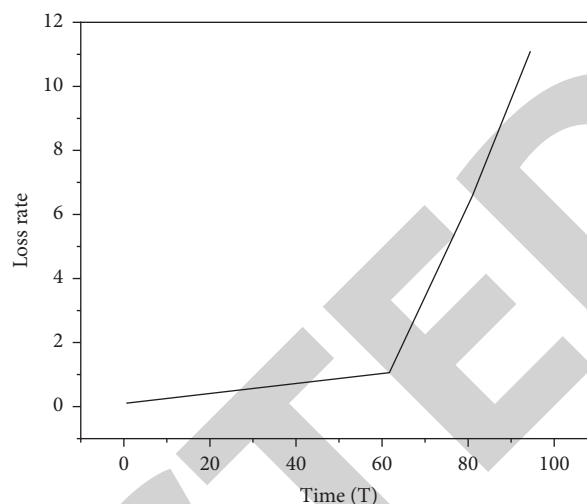
FIGURE 2: Loss ratio of performance index of the epoxy mortar test block in an acid corrosion process.

modulus were calculated by test data. Finally, the bond performance of bolt is analyzed by test data.

4. Result Analysis

4.1. Epoxy Mortar Test Block. During the test, the change of the outer color of the test block cannot be observed with the naked eye. When it was taken out every 10 days, there were water drops on the surface of the test block, indicating that the immersion solution only eroded its surface and failed to erode into the inside of the test block [13]. It can be seen that the epoxy mortar test block has good compactness inside, and the adhesive layers can be tightly cemented. In the test process, performance index loss of epoxy mortar test block is shown in Figure 2.

It can be seen from Figure 2 that the mass loss of epoxy mortar test block is small, and the mass remains basically unchanged 30 days before the test, with the maximum mass loss rate of about 1.98%. The elastic modulus changed little during the test, and the maximum loss was about 2.81%. The compressive strength changes slightly in the first 60 days, and the maximum loss rate is 11.25% from the 60th day to the 90th day.

4.2. CFRP Anchor. The loss rate of surface performance index of CFRP bolt during acid corrosion process is shown in Figure 3.

As can be seen from Figure 3, after soaking for 30 days, the quality of the CFRP bolt is basically unchanged, but a protective layer has been formed on its surface, so it can be considered that corrosion has not started yet. After soaking for 60 days, the protective layer coated on the bolt has disappeared, and the anchor has corrosion phenomenon, but the reinforcement has no corrosion phenomenon, and the quality is reduced compared with that before 30 days. After soaking for 90 days, the corrosion of anchor is further aggravated, and the reinforcement appears swelling. Compared with soaking for 60 days, the mass of anchor increases,
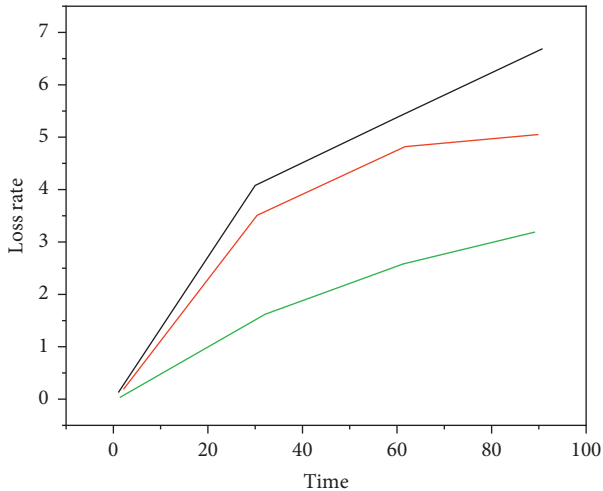
Figure 3: Performance index loss rate of the CFRP bolt in an acid corrosion process.

Figure 4: Load-slip curve of acid corrosion.

Figure 5: Comparison curve of fitting between the test curve and acid environment.

which can be interpreted as the corrosion liquid has penetrated into the interior of anchor from its surface, resulting in an increase in its mass [14, 15]. In the process of acid corrosion, the mass loss of bolt is small, and the maximum mass loss rate is about 0.65% on the 60th day. The loss rates of elastic modulus, tensile strength, elongation, and other indicators increased with the extension of soaking time. On the 90th day, the maximum loss rates of the above three physical performance indicators were 3.29%, 6.51%, and 5.06%, respectively.

4.3. Bond Slip Change of the CFRP Bolt. The total displacement of the bolt and the elastic deformation of THE CFRP rod are calculated through the test, and the difference between them is the slip of the bolt. The load-slip relationship curves of anchor bolts were drawn (see Figure 4) when they were not corroded by acid, corroded for 60 days, and corroded for 90 days.

It can be seen from Figure 4 that, under the same load, the rock bolt with 90 d acid corrosion has the largest slip, followed by the rock bolt with 60 d acid corrosion, and the minimum is the rock bolt without corrosion [16]. It can be seen that the bond slip of the CFRP bolt increases with the progress of corrosion test, and acid corrosion has a negative effect on its bond performance.

4.4. Fitting of Bond-Slip Curve for 90 d Acid Corrosion. The bond stress-slip curve of three anchorage lengths after acid corrosion for 90 d was sorted out and fitted. The curve fitting equation was as follows

$$\tau = 0.004S^4 - 0.0688S^3 + 0.3358S^2 + 0.8776S + 0.005. \quad (1)$$

The correlation parameters of linear regression can be obtained from equation (1), among which, correlation coefficient $R = 0.992$ and determination coefficient $R^2 = 0.984$. Figure 5 shows the comparison between the test curve and the fitting curve in an acidic environment.
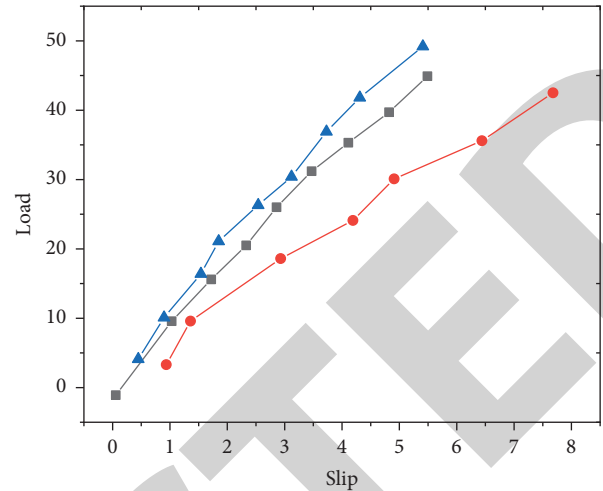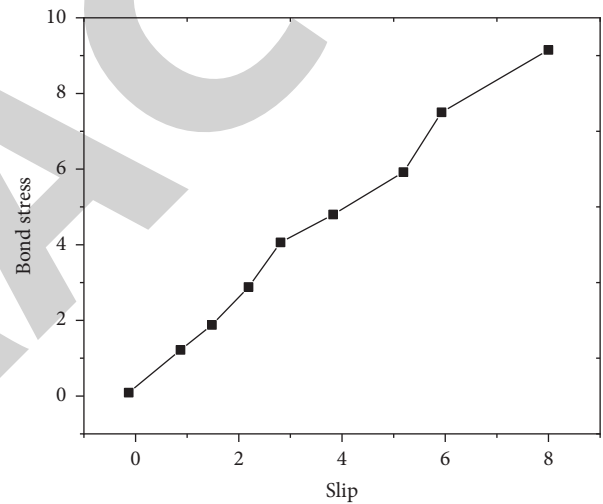
The results in Figure 5 are used to compare bolts with 245, 300, and 350 mm anchor lengths, and the errors are all within 10%. The pseudosynthetic results can be used to predict the slip values of CFRP bolts with arbitrary anchorage length and diameter under the same acidic environment and different loads.

4.5. CFRP Bolt Working Life Prediction

4.5.1. Arrhenius Equation. Arrhenius equation is the most commonly used method to predict the long-term service life of CFRP bolt using short-time test data. According to the Arrhenius equation, the degradation rate of tensile strength of CFRP bolt in the acidic corrosion environment is shown in equation (2)

$$k = \frac{\mathrm{d}f}{\mathrm{d}t} = A\exp\left(\frac{-E_\alpha}{RT}\right). \quad (2)$$
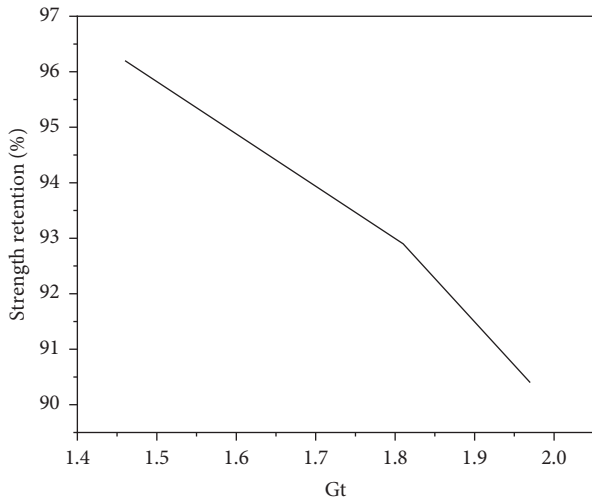
Figure 6: Logarithmic relationship of tensile strength retention rate of the CFRP bolt with time.

Table 1: Average annual pH value of rainfall in a province in recent 5 years.

Year	In 2011	In 2012	In 2013	In 2014	In 2015
pH value	4.81	4.50	4.52	4.76	4.57

Table 2: Strength retention rate prediction of bolt after service life by Arrhenius.

Acid rain erosion time/year	1.82	3.63	5.45	10.00	20.00
Convert to soak time/d in the test environment	30	60	90	165	330
Anchor strength retention rate/(%)	96.2	94.35	92.85	91.14	88.56

Among which, k is the degradation rate of tensile strength of CFRP bolt; f is the tensile strength of CFRP bolt; t is the time. A are the constants related to material properties; E_α is the activation energy leading to degradation of tensile strength of the CFRP bolt; R is the molar gas constant, 8.3145 J/(mol·K); and T is the absolute temperature, K.

The FHWA method given by the Federal Highway Administration of the United States is a life prediction method based on Arrhenius equation (see Formula (3)). Many researchers have also shown through experimental studies that the retention rate of tensile strength of bolt Rt basically maintains a linear relationship with the logarithm of time [17]. As the Figure 3 shows

$$R_t = a\lg t + b, \tag{3}$$

where R_t is the retention rate of tensile strength of CFRP bolt, (%); t is the time; and a, b are constants.

The loss rate of tensile strength of CFRP bolt in Figure 6 can be transformed into the retention rate of tensile strength, and the values of a and b can be obtained by curve fitting according to the least square method. The fitting curve is shown in equation (4).

$$R_t = -6.927\lg t + 106.5. \tag{4}$$

According to equation (4), the regression correlation coefficient $R = 0.996$, and the determination coefficient $R^2 = 0.992$.

Relevant studies show that the Arrhenius equation can be introduced into the concept of conversion factor TSF to calculate the time required for CFRP bolt corrosion to the same degree at two different temperatures [18]. The conversion factor is further studied, and the conversion factor model with pH value as a parameter is established through experiments, as shown in equation (5)

$$TSF = e^A \left(10^{-pH1} - 10^{-pH0} \right), \tag{5}$$

where TSF is the conversion factor; A is the undetermined coefficient can be obtained from the test; e is the natural

constant; and $10^{-pH}10^{-pH}$ is the corresponding pH value solution hydrogen ion concentration.

According to the results of this study, TSF = 1 when pH = 3; $TSF = 1.459$ when pH = 4.5. The tensile strength loss of bolt soaked in pH = 3 for 90 d was 6.51%, corresponding to the soaking days of bolt soaked in pH = 4.5 with 6.51% loss of tensile strength was $90 \times 1.459 = 131.31$ d.

4.5.2. Influence of Acid Rain on Durability of the CFRP Bolt. As a large amount of carbon dioxide in nature is soluble in water, the pH value is about 5.6 when the solution reaches gas-liquid equilibrium. Therefore, when the pH value of rainfall is less than 5.6, it can be defined as acid rain [19]. Acid rain has become one of the serious environmental problems in China. The average annual pH value of rainfall in a province in recent five years is shown in Table 1, in which the average annual pH value of acid rain in a city is close to that in a province. The basic pH value of acid rain in a city is 4.5 [20–22].

Relevant data show that the average number of rainfall days in a city from 1951 to 2007 is 144.58 d. Considering that CFRP bolts cannot be dried immediately after rainfall, it is assumed that CFRP bolts are corroded by acid rain for 4 h on average every day during the 144.58 d. It is equivalent to soaking CFRP bolts in pH = 4.5 solution 578.32 h a year, soaking 90 d in pH = 4.5 solution is equivalent to 5.449 years of acid rain erosion of exposed CFRP bolts in a certain area. After 20 years of acid rain erosion, the strength retention rate was 88.56% (see Table 2). It is consistent with the research in literature that CFRP bolts have good acid corrosion resistance, and CFRP bolts are slightly corroded in an acid rain corrosion environment [23–25].

5. Conclusion

The following conclusions were obtained from the study:

(1) The size and appearance color of the epoxy mortar test block did not change significantly during 90 d immersion in acidic solution. The mass, elastic modulus, and compressive strength decreased, and the maximum loss rate was 1.98%, 2.81%, and 11.25%, respectively. With the extension of soaking time, the compressive strength loss of the epoxy mortar test

block is large, and the acid corrosion environment for a long time will have a significant adverse effect on the epoxy mortar test block.

(2) The size and appearance color of the CFRP bolt do not change significantly during 90 d immersion in acid solution. The maximum mass loss occurred on the 60th day and the mass loss rate was 0.65%. The maximum loss rates of elastic modulus, tensile strength, and elongation were 3.29%, 6.51%, and 5.06%, respectively, on the 90th day. The test results show that the decrease of the above physical properties is small, and the acid corrosion resistance of the CFRP bolt is good.

(3) According to the load-slip relationship curve of the bolt, the bond slip of CFRP bolt increases with the progress of corrosion test, and acid corrosion has a negative effect on its bond performance.

(4) The bond slip curve was fitted after 90 days of acid corrosion. The fitted curve can reflect the change of bond performance of the CFRP bolt and epoxy mortar after acid corrosion. The test curve has certain engineering application value and can provide reference for revising related engineering specifications.

(5) Using the Arrhenius equation, the relationship curve between the tensile strength retention rate and logarithm of time in test environment was obtained. By introducing the concept of conversion factor TSF, the experimental environment was converted to an acid rain erosion environment, and the strength retention rate of anchor corroded by acid rain for 20 years was predicted.

Data Availability

The data used to support the findings of this study are available from the corresponding author upon request.

Conflicts of Interest

The authors declare that they have no conflicts of interest.

Acknowledgments

References

[1] W. Xu and D. Wang, "Static and dynamic impact performance optimization of cfrp/al bolt joint coupling structure–lay-up–connection parameters," *Archives of Civil and Mechanical Engineering*, vol. 22, no. 3, p. 118, 2022.

[2] M. Kumar, J. S. Saini, H. Bhunia, and S. R. Chowdhury, "Behavior of mechanical joints prepared from eb cured cfrp nanocomposites subjected to hygrothermal aging under bolt preloads," *Applied Composite Materials*, vol. 28, no. 2, pp. 271–296, 2021.

[3] C. K. Krishnadasan, N. S. Shanmugam, B. N. Rao, and B. Sivasubramonian, "Experimental investigation and numerical simulation on the strength of carbon-fiber-reinforced polymer–metal bolted and bonded interfaces," *Journal of Materials Engineering and Performance*, vol. 30, no. 12, pp. 9440–9454, 2021.

[4] J. Q. Yang, S. T. Smith, Y. F. Wu, and P. Feng, "Strengthening single-bolt timber joints with externally bonded cfrp composites," *Structures*, vol. 28, pp. 2671–2685, 2020.

[5] Q. Liu, H. Sun, Y. Chai, J. Zhu, T. Wang, and X. Qing, "On-site monitoring of bearing failure in composite bolted joints using built-in eddy current sensing film," *Journal of Composite Materials*, vol. 55, no. 14, pp. 1893–1905, 2021.

[6] D. Castillo, T. H. Nguyen, and J. Niiranen, "Spatially random modulus and tensile strength: contribution to variability of strain, damage, and fracture in concrete," *International Journal of Damage Mechanics*, vol. 30, no. 10, pp. 1497–1523, 2021.

[7] D. H. Elgohary, Y. Amaim, and S. Reda, "Improving the protection of architecture textiles against uva radiation on the grab tensile strength test coated polyurethane," *Journal of the Textile Association*, vol. 81, no. 5, pp. 288–293, 2021.

[8] M. Nabipour and B. Akhoundi, "An experimental study of fdm parameters effects on tensile strength, density, and production time of abs/cu composites," *Journal of Elastomers and Plastics*, vol. 53, no. 2, pp. 146–164, 2021.

[9] G. M. Memon, R. Ahmed Jhatial, I. Ali Sahito, and A. Ayoub Arbab, "Impact of types of orthophthalic unsaturated polyester matrix on tensile strength of woven roving fibers as reinforcement," *Journal of Industrial Textiles*, vol. 50, no. 7, pp. 1006–1019, 2021.

[10] D. G. Zisopol, I. Nae, A. I. Portoaca, and I. Ramadan, "A theoretical and experimental research on the influence of fdm parameters on tensile strength and hardness of parts made of polylactic acid," *Engineering, Technology & Applied Science Research*, vol. 11, no. 4, pp. 7458–7463, 2021.

[11] T. E. Abioye, H. Zuhailawati, A. S. Anasyida, S. P. Ayodeji, and P. K. Oke, "Effects of particulate reinforcements on the hardness, impact and tensile strengths of aa 6061-t6 friction stir weldments," *Proceedings of the Institution of Mechanical Engineers - Part L: Journal of Materials: Design and Applications*, vol. 235, no. 6, pp. 1500–1506, 2021.

[12] J. Cunha, T. C. Silva, M. L. Costa, and M. C. Rezende, "Ageing effects after ozone and water immersion on tensile strength at room and high temperatures of carbon/epoxy f8552 laminates," *Journal of Composite Materials*, vol. 55, no. 1, pp. 145–156, 2021.

[13] T. Ono, A. Ishikawa, and E. Yonemochi, "Selection of small amounts of glidant capable of improving the tensile strength of ibuprofen tablets," *Chemical & Pharmaceutical Bulletin*, vol. 69, no. 4, pp. 374–382, 2021.

[14] S. H. Kim, K. S. Yom, and S. M. Choi, "Evaluation of simple tensile strength of internal diaphragm according to cross sectional shape," *Journal of Korean Society of Steel Construction*, vol. 33, no. 3, pp. 171–179, 2021.

[15] J. Cwik, L. A. Gonzalez, X. Shi, C. C. Spirgel, and S. Yankell, "Plaque reduction and tensile strength evaluations of three dental floss products," *American Journal of Dentistry*, vol. 34, no. 3, pp. 123–126, 2021.

[16] E. M. Sokolova and N. I. Neshev, "Arrhenius equation in analysis of the mechanism of erythrocyte hemolysis," *Biophysics*, vol. 65, no. 3, pp. 448–451, 2020.

Hindawi

Retraction

Retracted: The Adsorption of VOCs by Honeycomb Ceramics Loaded with Molecular Sieves

Journal of Chemistry

This article has been retracted by Hindawi following an investigation undertaken by the publisher [1]. This investigation has uncovered evidence of one or more of the following indicators of systematic manipulation of the publication process:

(1) Discrepancies in scope

(2) Discrepancies in the description of the research reported

(3) Discrepancies between the availability of data and the research described

(4) Inappropriate citations

(5) Incoherent, meaningless and/or irrelevant content included in the article

(6) Peer-review manipulation

The presence of these indicators undermines our confidence in the integrity of the article's content and we cannot, therefore, vouch for its reliability. Please note that this notice is intended solely to alert readers that the content of this article is unreliable. We have not investigated whether authors were aware of or involved in the systematic manipulation of the publication process.

Wiley and Hindawi regrets that the usual quality checks did not identify these issues before publication and have since put additional measures in place to safeguard research integrity.

We wish to credit our own Research Integrity and Research Publishing teams and anonymous and named external researchers and research integrity experts for contributing to this investigation.

The corresponding author, as the representative of all authors, has been given the opportunity to register their agreement or disagreement to this retraction. We have kept a record of any response received.

References

[1] P. Zhang, "The Adsorption of VOCs by Honeycomb Ceramics Loaded with Molecular Sieves," *Journal of Chemistry*, vol. 2022, Article ID 7207403, 7 pages, 2022.

Research Article

The Adsorption of VOCs by Honeycomb Ceramics Loaded with Molecular Sieves

Ping Zhang [ID]

Yantai Yunfeng Ecological Environment Industry Development Co. Ltd., Yantai, Shandong 264000, China

Correspondence should be addressed to Ping Zhang; 1710300625@hbut.edu.cn

In order to improve the adsorption performance of molecular sieve honeycomb ceramics for VOCs, the author proposes a research method for the adsorption performance of VOCs based on the honeycomb ceramics loaded with molecular sieves. The method prepared cordierite honeycomb ceramic-supported HY, Na Y, USY, ZSM-5-300, and ZSM-5-360 monolithic adsorption materials by the coating method. Using toluene, ethyl acetate, isopropanol, and acetone as adsorbates, the adsorption properties of single-component and mixed-component organic compounds on the supported molecular sieve honeycomb ceramics were investigated. The result shows ZSM-5-300 has the largest adsorption capacity for the four adsorbates, which are toluene 68.0 mg/g, ethyl acetate 118.7 mg/g, isopropanol 70.9 mg/g, and acetone 72.5 mg/g. The test results show that ZSM-5-300 molecular sieve has high saturated adsorption capacity and is an ideal VOCs adsorption material.

1. Introduction

The development of modern industry, while bringing us good quality and cheap goods, also brings environmental problems. In recent years, the frequent occurrence of haze weather has seriously affected people's life and health; volatile organic compounds are one of the main reasons for the formation of haze. Volatile organic compounds (VOCs) refer to the saturated vapor pressure greater than 70 Pa at room temperature, an organic compound with a boiling point below 260°C under normal pressure. According to chemical structure, it can be divided into alkanes, alkenes, alkynes, aldehydes, acids, esters, alcohols, benzene series, halogenated hydrocarbons, ketones, acids, and others, a total of 12 kinds of substances. It has the characteristics of many types, complex components and long release period; it is a kind of chemical substance with "three hazards" (carcinogenic, teratogenic, and mutagenic) to the human body; it participates in photochemical reactions and causes the greenhouse effect; at the same time, it is also the main material for the formation of atmospheric particulate matter, which is harmful to the atmospheric environment and human body [1]. Volatile organic compounds (VOCs) are

toxic and polluting organic compounds; it comes from various fields of industrial production, motor vehicle emissions, and human activities, and the emissions are huge. The catalytic combustion method is clean and efficient, with low reaction temperature and low energy consumption, and is an effective means to control the emission of VOCs [2].

According to amendments to the Clean Air Act passed by the United States in 1990, of the nearly 190 air pollutants that are strictly controlled, about 70% are volatile organic compounds. In May 2010, the General Office of the State Council forwarded the "Notice of Guiding Opinions on Promoting Joint Prevention and Control of Air Pollution to Improve Regional Air Quality" (Guobanfa (2010) No. 33) issued by the Ministry of Environmental Protection and other departments; for the first time, the pollution prevention and control of VOCs was proposed at the national level. The guidance states "engaged in production operations that emit VOCs such as spray painting, petrochemicals, shoe industry, and electronic products, pollution control should be carried out in accordance with specific relevant technical specifications." The treatment of VOCs has become one of the major problems to be solved urgently in contemporary environmental pollution [3].

2. Literature Review

Due to the harm of VOCs to the environment and human body, all countries in the world have formulated relevant laws and regulations on the emission of VOCs and minimize or even eliminate the emission of VOCs [4]. Although it is possible to transform the production process and process, improve the production equipment, so that it can achieve zero emissions in the production process. However, limited by the level of production technology and cost pressure, most ways to control the emission of VOCs can only be in the exhaust gas treatment stage. There are two general methods for controlling VOCs emission content: recycling technology and destruction technology [5]. The so-called recycling technology is to recover and recycle VOCs, which are generally used for VOCs with high concentration or relatively economical value. Destruction technology is to degrade and destroy VOCs to generate CO_2 and H_2O and other harmless substances, which are suitable for medium and low concentrations of VOCs [6]. Common technologies for recovering VOCs mainly include adsorption technology, absorption technology, condensation technology, and membrane separation technology. Common technologies for destroying VOCs mainly include combustion technology, photocatalytic degradation technology, biodegradation technology, and plasma technology. These technologies for removing VOCs have their own advantages and disadvantages; in actual operation, one or a combination of several is selected according to the specific conditions of the air volume, concentration, type, and economic value of VOCs in the exhaust gas [7].

Adsorption is the process of converting a mixture into two or more products with different components using an adsorbent. Adsorbents are often porous solid materials. The adsorption method is widely used in the treatment of organic waste gas; due to its low adsorption capacity, the adsorption method is mainly used for the purification of organic waste gas with low concentration and large air volume [8]. Organic waste gases that have been successfully treated by adsorption are the painting process (toluene, xylene, and benzene), organic solvent volatilization, acetone waste gas, ethyl acetate, paint production waste gas styrene, and xylene. The key to adsorption technology is the adsorbent. Commonly used adsorbents for adsorbing organic waste gas are activated carbon particles, activated carbon fibers, molecular sieves, and adsorption resins. The advantages of adsorption technology are high removal rate, the removal rate can reach more than 95%, no secondary pollution, high purification efficiency, convenient operation, and automatic control [9].

Molecular sieve is a natural zeolite or synthetic aluminosilicate, which has the functions of sieving molecules, adsorption, ion exchange, and catalysis; it is mainly composed of silicon, oxygen, aluminum, and other metal cations, and it has high thermal stability and chemical stability [10, 11]. Since the 1970s, a large number of artificial zeolite molecular sieves have been synthesized; because of their unique channel zeolite molecular sieves, they have become indispensable catalytic materials and adsorption materials in petrochemical and fine chemicals and are used in more and

more fields. In the 1940s, zeolite molecular sieves were artificially synthesized for the first time; up to now, more than 200 kinds of zeolite molecular sieves with framework structures have been found. Sodium silicate and sodium aluminate are commonly used as raw materials to synthesize molecular sieves. However, due to the problems of high energy consumption, high environmental pollution, and low efficiency in the synthesis process, it is gradually replaced by the synthesis method using kaolin and diatomite as raw materials.

Yda et al. synthesized ZSM-5 molecular sieve with kaolin as raw material by the nonorganic template method; the samples were characterized by XRD, SEM, FTIR, N_2 adsorption and desorption, and temperature-programmed elution, and its catalytic cracking performance was studied, and the results showed that the molecular sieve has high hydrothermal stability and strong acidity, which is beneficial to the formation of propylene and butene in oil [12]. Enesca A. et al. developed three molecular sieve adsorption runners for the separation and concentration of different VOCs and pointed out that Y-type molecular sieves were used for amines, esters, ethers, and macromolecular VOCs; Y-type and ZSM composite molecular sieves are used for aromatic hydrocarbons, ethers, alcohols, and aldehydes; ZSM molecular sieves are used for ketones and chlorinated alkanes (alkenes) [13].

The authors prepared cordierite honeycomb ceramic-supported HY, Na Y, USY, ZSM-5-300, and ZSM-5-360 monolithic adsorption materials by the coating method. Using toluene, ethyl acetate, isopropanol, and acetone as adsorbates, the adsorption properties of single-component and mixed-component organic compounds on the supported molecular sieve honeycomb ceramics were investigated, which has an important value for industrial application.

3. Research Methods

3.1. VOCs Control Technology. The pollution prevention and control of VOCs mainly manages the source and process of pollution sources by formulating standards, improving systems, improving energy structure, changing raw materials, and improving technological processes; however, most of the exhaust gas emitted in the production process adopts terminal treatment, which is mainly divided into two technologies: destruction and recycling [14, 15]. Destruction technology mainly converts toxic and harmful organic pollutants into nontoxic, harmless, or low-toxic substances through chemical reactions and discharges them into the atmosphere, including the catalytic combustion method, photocatalytic method, biodegradation method, and low temperature plasma method, the recovery technology mainly separates and enriches organic pollutants through physical methods such as temperature, pressure, and filtration and realizes the resource utilization of VOCs, including the adsorption method and condensation method [16, 17]. There are many types of VOCs with different properties; according to the types, concentrations, and emission methods of VOCs, VOCs treatment technologies

have different applications in actual production, and even a combination of several treatment technologies is used. Different treatment technologies have different characteristics and application ranges; in actual projects, the most suitable technology is selected according to the type of VOCs, gas flow, and concentration; condensation and membrane separation technologies are mostly used to treat VOCs gases with a concentration greater than 10000 mg/m^3; catalytic combustion and adsorption are mostly used to treat VOCs gases with a concentration of 2000–10000 mg/m^3, and biodegradation and plasma technologies are mostly used to treat concentrations less than 2000 mg/m^3 VOCs gas [18]. Figure 1 shows common VOCs treatment technologies:

3.2. Preparation of Loaded Honeycomb Ceramics.
Commercial powder HY molecular sieve (Si/Al = 5.1, specific surface area 548 ㎡/g), NaY (Si/Al = 3.0, specific surface area 581 ㎡/g), US (Si/Al = 7.8, specific surface area 545 ㎡/g), ZSM-5-300 (Si/Al = 300, specific surface area 358 ㎡/g), and ZSM-5-360 (Si/AI = 360, specific surface area 346 ㎡/g) were taken.

Weigh an appropriate amount of the above 5 kinds of molecular sieves with an electronic balance and put them in a 200 mL beaker, add silica sol binder, dilute to a certain concentration with deionized water, stir for 30 min, slowly immerse the prepared honeycomb ceramics in the above solution, soak for 15 min, dry at 100°C for 1 h, roast in a muffle furnace at 400°C for 2 h, and cool to room temperature for later use.

3.3. Characterization of Adsorbents.
The specific surface area of molecular sieves was measured by N$_2$ adsorption on the JW-BK200C specific surface and pore size analyzer; before the measurement, the samples were degassed at 200°C for 6 hours and calculated by the BET multipoint method.

3.4. Adsorption Experiments.
The entire adsorption system of the experiment consists of a VOCs generator, a gas flow control system, a temperature control system, and an adsorption device. The size of the honeycomb ceramics used in the experiment is 100 × 100 × 50 mm, and the pore density is 200 holes/i㎡; the abovementioned honeycomb ceramics are processed into cylinders with a diameter of 2.0 cm, and 4 pieces are one unit, which are placed in a quartz glass tube with a diameter of 2.2 cm. The VOCs adsorption experiment uses air as the carrier gas; after being dried and purified by the air purifier, it is divided into 3 paths through a four-way pipe and enters the flowmeter of the 3 gas paths, respectively; one of them passes through a mass flow meter and an organic gas generator (placed in an ice-water bath) bring out a certain concentration of VOCs gas; 1 pass through the mass flow meter into the water vapor generator (placed in a 40°C waterbath) and bring out a certain concentration of water vapor. The first route is the dilution gas, and the last 3 routes are merged into 1 route gas. Adjust the flow of the 3-way gas through the flow meter to prepare the inlet gas with a certain VOCs concentration, relative humidity, and air velocity.

When the VOCs content and relative humidity at the inlet concentration no longer change, it is connected to the adsorption device for experiments. The inlet concentration of VOCs before the reaction and the outlet concentration after the reaction were detected by a gas chromatograph (GC1120). The total gas flow rate is 0.32 m^3/h, the single-component organic matter experiment, and the adsorbate concentration is 500 mg/m. In the multicomponent organic matter experiment, the concentration of each adsorbate is 125 mg/m^3, the outlet VOCs concentration reaches 10% of the inlet concentration as the breakthrough point, and when it reaches 90%, it is saturated adsorption, and the VOCs adsorption amount is calculated through the integration of the breakthrough curve; the formula is

$$q = \frac{F \times C_0}{60 \times W} \left[t_s - \int_0^{t_s} \frac{C_i}{C_0} dt \right].$$ (1)

In the formula, q is the adsorption amount of organic gas, mg/g; F is the total gas flow rate, m^3/h; C_0 is the initial concentration of inlet VOCs, mg/m^3; t_s is the adsorption time, min; C_i is the concentration of VOCs at the min exhaust outlet, mg/m^3; W is the adsorbent loading, g.

4. Results Analysis

4.1. Phase Confirmation of Molecular Sieves.
Figure 2 shows that HY, NaY, USY, ZSM-5-300, and ZSM-5-360 molecular sieves are mixed with silica sol (mass ratio is 9:1), respectively; XRD pattern after calcination is at 400°C. It is completely consistent with the corresponding Y-type molecular sieve XRD spectrum (PDF45-0112) and ZSM-5 molecular sieve XRD spectrum (PDF44-0003), and no SiO$_2$ diffraction peak is observed; it shows that SiO$_2$ is in a highly dispersed state, only for bonding. Molecular sieves are calcined at 400°C and their structures remain stable [19].

4.2. Adsorption Performance of Molecular Sieves for Single-Component VOCs.
Using toluene and ethyl acetate as adsorbates, the adsorption properties of five molecular sieves were determined, respectively. Figure 3 shows that the five molecular sieves have obvious "shoulder peaks" in the toluene penetration curves, the reason may be that the polarities of toluene and water are quite different, and the Y-type molecular sieves with low silica-alumina ratio are in the presence of a large amount of water vapor, great competition relationship, and the more polar water will replace part of the toluene adsorbed on the molecular sieve. There is no "shoulder peak" in the toluene breakthrough curves of ZSM-5-300 and ZSM-5-360, indicating that the high-silicon ZSM-5 molecular sieve has the adsorption breakthrough curves of benzene and ethyl acetate. As shown in Figures 3 and 4, the saturated adsorption time sequence of five molecular sieves for toluene and ethyl acetate is USY > ZSM-5-300 > HY > ZSM-5-360 > NaY, and NaY has the worst adsorption performance. HY, NaY, and USY have strong hydrophobicity, and water vapor has no effect on the adsorption of toluene. Ethyl acetate also has no obvious "shoulder peak" on the five adsorption materials, which may
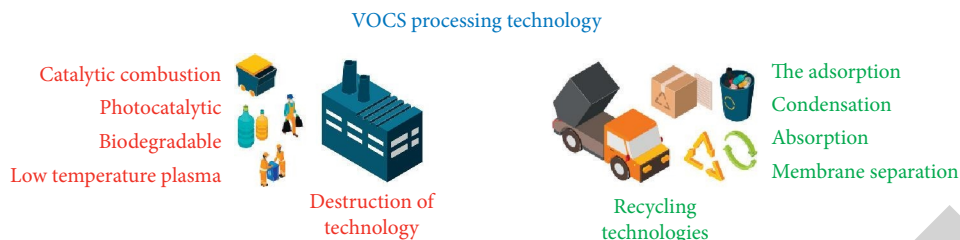
Figure 1: Common VOCs treatment technology.
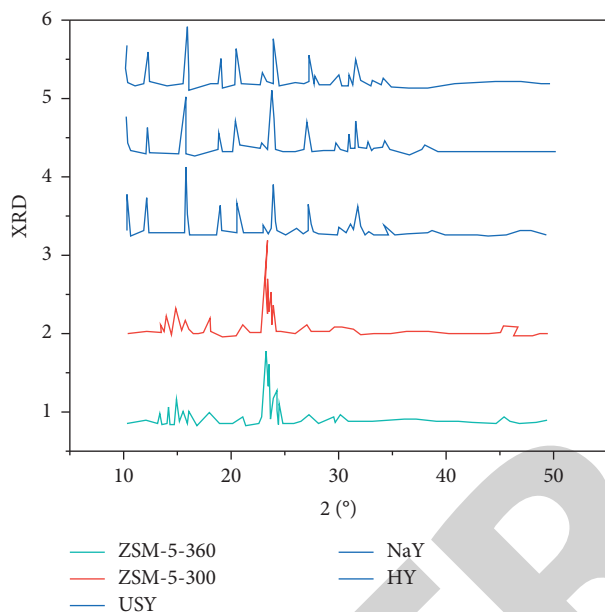
Figure 2: XRD patterns of the mixture of HY, Na Y, USY, ZSM-5-300, and ZSM-5-360 molecular sieves and silica sol.

Figure 3: Adsorption breakthrough curve of molecular sieve for toluene. Note: Airspeed 5000 h^{-1}. The adsorption conditions are normal pressure, (35 ± 2) °C, molecular sieve loading 2.0 g, toluene and ethyl acetate concentration 500 mg/m^3, and water vapor RH = 60%.

be due to the similar polarity of ethyl acetate and water, and the substitution effect is not obvious [20].

Table 1 provides the saturated adsorption capacity of 5 kinds of adsorption materials for toluene, ethyl acetate, isopropanol, and acetone [21]. It can be seen that ZSM-5-300 has the largest adsorption capacity for the four adsorbates, which is closer to USY. The adsorption capacity of HY and ZSM-5-300 is in the middle. The saturated adsorption capacity of NaY is the smallest because there is a large competitive adsorption relationship between toluene and water vapor in NaY with a low Si/Al ratio; in the presence of a large amount of water vapor, the adsorption capacity of VOCs decreased significantly compared with the dry gas condition [22].

4.3. Adsorption Performance of Multicomponent VOCs. In the actual industrial VOCs adsorption, the components are often complex, so it is necessary to investigate the adsorption performance of molecular sieves for mixed VOCs [8]. Figure 5 shows the adsorption breakthrough curve of ZSM-5-300 molecular sieve to the mixed components of toluene, ethyl acetate, isopropanol, and acetone. As shown in Figure 5, the adsorption process of the four mixed

components is more complicated than that of a single component; the adsorption process of the mixed components is roughly divided into three stages: in the initial stage (before 50 min), the four mixed components are equally adsorbed on the molecular sieve, each occupying the "active site" of the molecular sieve. As the adsorption process continued, the outlet concentrations of acetone, toluene, isopropanol, and ethyl acetate gradually increased, the outlet concentration of ethyl acetate rose relatively slowly, and acetone, toluene, and isopropanol all showed a downward trend after reaching the highest point successively and then gradually tended to balance; there is an obvious "hump" on the breakthrough curve, that is, the outlet concentration of acetone is greater than the inlet concentration within a certain breakthrough time, which is in line with the typical two-component adsorption process curve. In the saturation equilibrium stage, the concentration of the mixed components no longer increases or decreases and tends to be stable [23]. During the adsorption process, the boiling point of acetone is 56°C, which is relatively low, so the adsorption strength of acetone on the surface of molecular sieve is weak
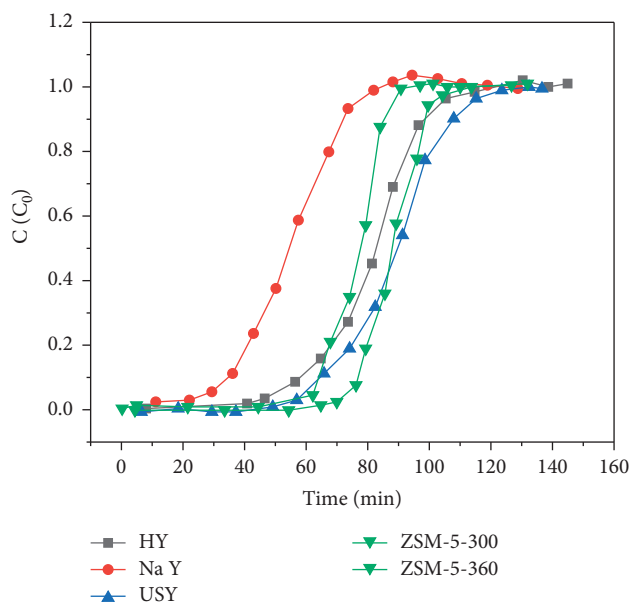
FIGURE 4: Adsorption breakthrough curve of molecular sieve for ethyl acetate. Note: Airspeed 5000 h^{-1}. The adsorption conditions are normal pressure, (35 ± 2) °C, molecular sieve loading 2.0 g, toluene and ethyl acetate concentration 500 mg/m^3, and water vapor RH=60%.

FIGURE 5: Adsorption breakthrough curve of ZSM-5-300 molecular sieve for mixed components of toluene, ethyl acetate, isopropanol, and acetone. Note: Airspeed 5000 h^{-1}. The adsorption conditions were normal pressure, (35 ± 2) °C, molecular sieve loading 2.0 g, four VOCs concentrations were 125 mg/m^3, and water vapor RH = 60%.

TABLE 1: The saturated adsorption capacity of VOCs adsorbed by molecular sieves (mg/g).

Molecular sieve	Toluene	Ethyl acetate	Isopropyl alcohol	Acetone
HY	62.7	108.0	63.4	67.3
NaY	24.0	73.1	37.2	63.4
USY	65.3	117.3	68.6	71.2
ZSM-5-300	68.0	118.7	70.9	72.5
ZSM-5-360	58.6	101.9	59.6	64.7

TABLE 2: Adsorption parameters of mixed VOCs on ZSM-5-300 molecular sieve.

VOCs	Saturated adsorption capacity/(mg·g^{-1})	Breakthrough adsorption/(mg·g^{-1})
Toluene	22.3	17.1
Ethyl acetate	45.0	35.8
Isopropyl alcohol	25.0	19.8
Acetone	19.0	16.5

at a certain temperature, and it is easily replaced by other adsorbates under the drive of airflow; there is also an obvious "hump" on the breakthrough curves of toluene and isopropanol because the polarity of ethyl acetate is stronger than that of toluene and isopropanol; acetone, toluene, and isopropanol adsorbed in the molecular sieve channels are replaced by ethyl acetate, resulting in an obvious "hump." The pore size of ZSM-5-300 is 0.51–0.56 nm, and the molecular diameters of toluene, ethyl acetate, isopropanol, and acetone are 0.60, 0.52, 0.47, and 0.50 nm, respectively, under the combined action of the surface polarity of molecular sieve and the superposition of pore walls, with the completion of the "hump" of acetone, toluene, and isopropanol, the outlet concentration of ethyl acetate slowly increased; finally, adsorption saturation was reached, and it can be seen from the breakthrough curve that there was a competitive adsorption between the four components. Table 2 provides the adsorption parameters of mixed VOCs on ZSM-5-300 molecular sieves [24]. Comparing Table 1 and Table 2, it can be seen that the saturated adsorption amount of mixed VOCs is significantly reduced compared with that of single

component, and the decline range is 67.2% of toluene, isopropyl alcohol 64.7%, acetone 73.8%, and ethyl acetate 62.1%, indicating that when the molecular sieve surface area "effective adsorption site" remains unchanged, the adsorption capacity of each adsorbate will be significantly reduced when the molecular sieve adsorbs mixed VOCs.

5. Conclusion

The author studied the adsorption performance of VOCs on the honeycomb ceramics loaded with molecular sieve and screened out the optimal adsorption material, which achieved the expected research purpose; the development of a new type of adsorption material with a good coating effect, excellent adsorption performance, and good regeneration is of great value for industrial application. The results of the study are as follows: the order of saturated adsorption capacity of single-component organics toluene, ethyl acetate, isopropanol, and acetone on the supported molecular sieve honeycomb ceramics is ZSM-5-300 > USY > HY > ZSM-5-360 > NaY, ZSM-5-300 It is a more suitable adsorption material for adsorbing complex

VOCs. Compared with the single-component adsorption of ZSM-5-300 molecular sieve for the adsorption of mixed-component VOCs, the saturated adsorption of mixed VOCs is significantly reduced; this indicated that the adsorption capacity would change significantly when the mixed VOVs were adsorbed, which was attributed to the coadsorption and competitive adsorption between the four VOCs. The research on the adsorption performance of VOCs on the supported molecular sieve honeycomb ceramics can be further considered in the following aspects: the loading, dispersibility, and adsorption strength of ZSM-5-300 molecular sieve on honeycomb ceramics have an important influence on improving its adsorption of VOCs; it is necessary to further study the molecular sieve coating process, such as stirring speed and stirring time, pH, type of binding material, molecular sieve ratio, and other conditions during the experiment, in order to prepare honeycomb ceramic adsorption materials with strong stability and good adsorption effect. Further research was conducted to synthesize porous ZSM-5 molecular sieve adsorption materials by the template method, nanograin method, and postprocessing method or composite ZSM-5 molecular sieve and mesoporous molecular sieve to form mesoporous-microporous composite materials, adsorption and desorption performance of industrial waste gas.

Data Availability

The data used to support the findings of this study are available from the corresponding author upon request.

Conflicts of Interest

The author declares that there are no conflicts of interest.

References

[1] D. Chen, Z. Xu, S. Zhong, Z. Chen, and C. Cen, "Preparation and application of VOC s adsorption materials in textile industry," *IOP Conference Series: Earth and Environmental Science*, vol. 450, no. 1, Article ID 012041, 2020.

[2] J. Liu and G. Zheng, "Emission of volatile organic compounds from a small-scale municipal solid waste transfer station: ozone-formation potential and health risk assessment," *Waste Management*, vol. 106, no. Apr, pp. 193–202, 2020.

[3] M. Wei, S. Wu, L. Zhu, N. Li, and C. Yang, "Environmental impact on VOC s emission of a recycled asphalt mixture with a high percentage of rap," *Materials*, vol. 14, no. 4, p. 947, 2021.

[4] B. Deng, H. Zhang, and J. Wu, "Modeling VOC s emission/sorption with variable operating parameters and general boundary conditions," *Environmental Pollution*, vol. 271, no. 1, Article ID 116315, 2021.

[5] W. Abou Saoud, A. Kane, P. Le Cann et al., "Innovative photocatalytic reactor for the degradation of VOC s and microorganism under simulated indoor air conditions: cu-ag/tio2-based optical fibers at a pilot scale," *Chemical Engineering Journal*, vol. 411, no. 15, Article ID 128622, 2021.

[6] A. Mahmood, X. Wang, X. Xie, and J. Sun, "Degradation behavior of mixed and isolated aromatic ring containing VOC s: langmuir-hinshelwood kinetics, photodegradation, in-situ

[7] A. V. Chistyakov, G. I. Konstantinov, M. V. Tsodikov, and A. L. Maximov, "Rapid conversion of methane to hydrogen stimulated by microwave irradiation on the surface of a carbon adsorbent," *Doklady Physical Chemistry*, vol. 498, no. 1, pp. 49–53, 2021.

[8] X. Liu, J. Liu, J. Chen, F. Zhong, and C. Ma, "Study on treatment of printing and dyeing waste gas in the atmosphere with ce-mn/gf catalyst," *Arabian Journal of Geosciences*, vol. 14, no. 8, p. 737, 2021.

[9] W. Donphai, N. Kunthakudee, S. Munpollasri et al., "Application of magnetic field to co hydrogenation using a confined-space catalyst: effect on reactant gas diffusivity and reactivity," *RSC Advances*, vol. 11, no. 7, pp. 3990–3996, 2021.

[10] B. Li, K. M. Kwok, and H. C. Zeng, "Versatile hollow zsm5 nanoreactors loaded with tailorable metal catalysts for selective hydrogenation reactions," *ACS Applied Materials & Interfaces*, vol. 13, no. 17, pp. 20524–20538, 2021.

[11] M. Xu, S. Lei, R. Dong, and C. Jin, "Zsm-5 zeolite support for ptau toward ethanol oxidation," *Journal of the Electrochemical Society*, vol. 168, no. 5, Article ID 056507, 2021.

[12] B. Yda, A. Bw, A. Rs, A. Lc, and W. Wei, "Potassium titanate whiskers on the walls of cordierite honeycomb ceramics for soot catalytic combustion - sciencedirect," *Ceramics International*, vol. 47, no. 24, pp. 34828–34835, 2021.

[13] A. Enesca and L. Isac, "Photocatalytic activity of cu2s/wo3 and cu2s/sno2 heterostructures for indoor air treatment," *Materials*, vol. 14, no. 13, p. 3656, 2021.

[14] A. Mottaghitalab, A. Khanjari, R. Alizadeh, and H. Maghsoudi, "Prediction of affinity coefficient for estimation of voc adsorption on activated carbon using v-matrix regression method," *Adsorption*, vol. 27, no. 6, pp. 963–978, 2021.

[15] S. Wu, Y. Wang, C. Sun et al., "Novel preparation of binderfree y/zsm-5 zeolite composites for VOC s adsorption," *Chemical Engineering Journal*, vol. 417, no. 2, Article ID 129172, 2021.

[16] N. Yi, M. Fang, W. Di, Z. Xia, T. Wang, and Q. Wang, "Aerosol emissions of amine-based co2 absorption system: effects of condensation nuclei and operating conditions," *Environmental Science & Technology*, vol. 55, no. 8, pp. 5152–5160, 2021.

[17] Q. Ma, J. Lu, J. Yao, J. Yin, R. Zhang, and F. Luo, "The synergistic role of acidic molecular sieve on flame retardant performance in pla/mf@app composite," *Journal of Polymer Research*, vol. 29, no. 5, p. 192, 2022.

[18] C. Y. Chuah, J. Lee, J. Song, and T. H. Bae, "Carbon molecular sieve membranes comprising graphene oxides and porous carbon for co2/n2 separation," *Membranes*, vol. 11, no. 4, p. 284, 2021.

[19] J. Liu, S. Zhu, L. Zhang, Z. Liu, Q. Cui, and H. Wang, "Study on characterization and coke compositions of deactivated 5 a molecular sieve for adsorption separation of industrial naphtha," *ChemistrySelect*, vol. 5, no. 42, pp. 12844–12852, 2020.

[20] C. Guo, Y. Wang, F. Wang, and Y. Wang, "Adsorption performance of amino functionalized magnetic molecular sieve adsorbent for effective removal of lead ion from aqueous solution," *Nanomaterials*, vol. 11, no. 9, p. 2353, 2021.

[21] R. Kumar and A. Sharma, "Risk-energy aware service level agreement assessment for computing quickest path in computer networks," *International Journal of Reliability and Safety*, vol. 13, no. 1/2, p. 96, 2019.

Retraction

Retracted: Simulation of the Electro-Superconducting System Based on the H Equation

Journal of Chemistry

This article has been retracted by Hindawi following an investigation undertaken by the publisher [1]. This investigation has uncovered evidence of one or more of the following indicators of systematic manipulation of the publication process:

(1) Discrepancies in scope

(2) Discrepancies in the description of the research reported

(3) Discrepancies between the availability of data and the research described

(4) Inappropriate citations

(5) Incoherent, meaningless and/or irrelevant content included in the article

(6) Manipulated or compromised peer review

The presence of these indicators undermines our confidence in the integrity of the article's content and we cannot, therefore, vouch for its reliability. Please note that this notice is intended solely to alert readers that the content of this article is unreliable. We have not investigated whether authors were aware of or involved in the systematic manipulation of the publication process.

Wiley and Hindawi regrets that the usual quality checks did not identify these issues before publication and have since put additional measures in place to safeguard research integrity.

We wish to credit our own Research Integrity and Research Publishing teams and anonymous and named external researchers and research integrity experts for contributing to this investigation.

The corresponding author, as the representative of all authors, has been given the opportunity to register their agreement or disagreement to this retraction. We have kept a record of any response received.

References

[1] J. Zhang, "Simulation of the Electro-Superconducting System Based on the H Equation," *Journal of Chemistry*, vol. 2022, Article ID 6831771, 7 pages, 2022.

Hindawi

Research Article

Simulation of the Electro-Superconducting System Based on the H Equation

Jun Zhang 🄳

College of Computer and Information Engineering, Guizhou University of Commerce, Guiyang 550014, Guizhou, China

Correspondence should be addressed to Jun Zhang; 202007000289@hceb.edu.cn

In order to reduce the levitation energy consumption and increase the levitation air gap, a simulation study of the electrochemistry superconducting magnetic levitation system based on the H equation is proposed. Through finite element simulation, the magnetic field distribution, current distribution, force, and other characteristics of the magnetic suspension system in the superconducting gravimeter are obtained; the relationship between the force of the superconducting ball in the magnetic field and the height of the suspension body and the current of the suspension coil is analyzed; and the penetration rate, the magnetic gradient, penetration depth, and maximum magnetic induction intensity of the superconducting spherical surface of the single-coil electrochemistry superconducting magnetic levitation system are obtained by simulation calculation. Simulation results show that, at 1 s, we start to use 0.2 s, 0.4 s, 0.6 s, and 0.8 s time, respectively, to pass current into the floating coil until it reaches 4.4 A. The magnetic gradient of the electrochemistry superconducting magnetic levitation system using a single coil is too large to meet the requirements of gravity measurement, the penetration depth is much smaller than the thickness of the superconducting sphere, and the maximum magnetic field on the surface of the superconducting sphere is much smaller than the critical magnetic field value of the superconducting material, and no loss will occur. The critical magnetic field value of the superconducting sphere is much smaller than that of the superconducting sphere. The critical magnetic field value of the material will not quench, which verifies that the H equation can simulate the superconducting magnetic levitation system well and has a high simulation accuracy and efficiency.

1. Introduction

With the continuous development of society, the future development trend of rail transit will have the characteristics of energy saving, environmental protection, safety and comfort, fast, and convenience. In addition to technological innovations in existing rail transportation vehicles, rail transit in the twenty-first century, it is also necessary to vigorously develop new rail transportation vehicles, and the maglev train was born [1]. At the same time, with the continuous development of superconducting materials, combining superconducting materials and magnetic levitation trains makes the maglev train faster, develops operational reliability, high safety, low loss and noise, and is comfortable and environmentally friendly [2]. According to its working principle and technical characteristics, traditional maglev trains can be divided into electromagnetic

attraction type (EMS) and electrodynamic repulsion type (EDS) [3]. Electromagnetic attraction (EMS) maglev trains mainly use electromagnets installed on the bogies on both sides of the train and magnets laid on the rails of the line; the attractive force generated under the action of a magnetic field attracts the long stator core under the guide rails to make the train levitate; the magnets on both sides of the guide rail and the magnets on both sides of the train generate attractive force to achieve guiding and braking functions [4, 5].

At present, conventional gravimeters mainly use mechanical springs to achieve the suspension of inspection quality. In the long-term measurement process, mechanical springs will have problems such as creep, hysteresis, and nonlinearity, and as a result, the accuracy of gravity measurement continues to decrease. With the continuous development of low temperature and superconducting

technology, it has become possible to apply superconducting magnetic levitation technology to gravity measurement. The superconducting gravimeter utilizes the zero resistance and Meissner characteristics of the superconductor, which can make the superconductor stably suspended in the magnetic field without energy loss. Since the system is working at low temperature, the thermal noise and expansion coefficient of the system are greatly reduced; this makes the superconducting gravimeter have extremely high measurement accuracy, very low noise, and drift rate, and it can solve a series of problems existing in conventional mechanical gravimeters [6]. Moreover, for the simulation of the magnetic levitation system in the superconducting gravimeter, due to the need to obtain a large amount of simulation data to guide the experiment, the simplified A-equation static magnetic field model is usually used for simulation. We set the permeability of the superconducting sphere to 0 or set the surface of the niobium sphere as a magnetic insulation boundary condition; the virtual displacement method or the magnetic pressure formula can be used to quickly obtain the force and magnetic force gradient of the superconducting niobium ball in the magnetic field [7]. This method is an ideal model, unable to obtain the magnetic field and shielding current distribution inside the superconducting sphere; through our experiments, it is found that there is a large deviation from the simulation, which will lead to deviations in the design of the suspension system. The H equation based on the magnetic field strength is a new method for solving superconducting systems. There are few related studies at present; we apply it to the simulation of the magnetic levitation system in the superconducting gravimeter, and it can solve the magnetic field distribution, shielding current, force, and AC loss in the superconducting sphere; on the other hand, the H equation is easier to implement in the finite element software COMSOL, this can improve the simulation efficiency and accuracy of the magnetic levitation system in the superconducting gravimeter. Fujii et al. proposed a three-phase permanent magnet motor drive using only a three-phase inverter and a degree of freedom controlled magnetic levitation drive method. The suspension winding is connected between the neutral point of the Y-connected motor winding and the middle point of the voltage source. Therefore, the levitation force is actively controlled by the zero sequence current. The experimental results show that under the load state of the motor, the vibration of the magnetic suspension is increased compared to that under no load. Vibration mainly includes the driving frequency, the basic, and third components of 1F and 3F. We focus on the improvement of the positioning accuracy of the magnetic levitation system. We found that the vibration 1F is caused by the detection error of the current sensor and the three-phase unbalanced resistance and inductance, and the vibration 3F is caused by PWM driving. In order to improve positioning accuracy, we studied current detection methods and observer-based voltage disturbance compensation. Experimental results show that these compensations improve the positioning accuracy of magnetic levitation [8].

Based on this research, taking the magnetic levitation system in the superconducting gravimeter as the research object, we discussed the structure of the magnetic levitation system in the superconducting gravimeter, introduced the basic principles of H equation finite element simulation; the shielding current, magnetic field distribution, and levitation characteristics of the magnetic levitation system in the superconducting gravimeter are analyzed. The results are compared with experimental results and the A equation static magnetic field method, the error causes are analyzed. It lays a theoretical foundation for further improving the design precision of the superconducting gravimeter and also provides a certain reference significance for improving the simulation efficiency and precision of the superconducting system.

2. Research Methods

2.1. The Structure of the Superconducting Magnetic Levitation System Applied to Gravity Measurement. A typical application of the superconducting magnetic levitation system is a superconducting gravimeter [9]. In a low temperature environment, utilizing the zero resistance characteristics of superconductors can produce unchanged current in the superconducting coil; this produces a very stable background magnetic field. We place a high-precision superconducting niobium ball in the background magnetic field, and the Meissner effect of superconductors can equivalently act as a "spring" in a mechanical gravimeter, the superconducting ball is forced and suspended. Because it does not use mechanical springs and works in a 4.2 K liquid helium environment, the superconducting gravimeter can achieve extremely high measurement accuracy, very low noise, and drift rate [10]. The structure of the superconducting magnetic levitation system for gravity measurement is mainly composed of a superconducting levitation coil, a superconducting niobium ball, and a displacement detection capacitor. The superconducting ball floats under the Meissner effect and the suspension force and gravity reach a balance; by adjusting the current in the upper and lower superconducting coils, the magnetic force gradient in the space area can be adjusted, that is, the stiffness of the "spring". When the gravity changes slightly, the superconducting ball will be displaced in the vertical direction, reach a new equilibrium position, so the distance between the upper and lower capacitor plates will change, and the measurement of gravity can be completed by the differential capacitance detection circuit [11].

2.2. The Basic Principle of the H Equation Finite Element Simulation. A two-dimensional rotational axis symmetric transient field model is used to model the superconducting Maglev system for gravity measurement. From Faraday's law of electromagnetic induction and the B-H constitutive relationship, the following equation can be obtained:

$$\nabla \times \overrightarrow{E} = -\frac{\partial \overrightarrow{B}}{\partial t} = -\mu_0 \frac{\partial \left(\mu_r \overrightarrow{H} \right)}{\partial t}. \tag{1}$$

In the formula, μ_0, μ_r are the vacuum permeability and the relative permeability of the material, respectively, for

superconductors, take its relative permeability $\mu_r = 1$, the shield current model is used to describe its superconductivity. In a two-dimensional rotational axisymmetric model, we use the cylindrical coordinate system (r, z, φ); since the current flowing into the floating coil only has a circular component, therefore, there are only H_r, H_z, E_φ, J_φ components in the spatial region. The curl vector equation (1) can be decomposed into two scalar equations in the r and z directions as shown in fd2:

$$\begin{bmatrix} -\dfrac{\partial E_\varphi}{\partial_z} \\[2mm] \dfrac{E_\varphi}{r} + \dfrac{\partial E_\varphi}{\partial r} \end{bmatrix} = -\mu_0 \dfrac{\partial}{\partial t} \begin{bmatrix} \mu_r H_r \\[1mm] \mu_r H_z \end{bmatrix}. \tag{2}$$

For nonsuperconducting regions, Ohm's law $E_\varphi = \rho J_\varphi$, where ρ is the resistivity of the material; for the superconducting region, using the classic E-J equation to describe the nonlinear constitutive relationship in the second type of superconductor, we obtain as follows:

$$E = E_0 \left(\dfrac{J}{J_c} \right)^n. \tag{3}$$

Among them, E_0 is the critical electric field strength, n is a constant, and both affect the speed of the superconductor's zero resistivity transition, determined by the superconducting material, $E_0 = 0.0001\ V/m, n = 21$ is selected in this simulation.

J_c is the critical current density of the superconductor, susceptible to external magnetic field and temperature; the classic Kim model is used to describe the relationship between the critical current density and the external magnetic field as follows:

$$J_c(B) = \dfrac{J_{c0}}{\left(1 + \left|\mu_0 \mu_r H/B_0\right|\right)^\alpha}. \tag{4}$$

Among them, J_{c0} is the critical current density of the superconductor when the external magnetic field is zero, B_0 is the superconducting material parameter, and α is the Kim coefficient. Since the superconducting magnetic levitation system of this model is in a 4.2 K constant temperature liquid helium environment, and the magnetic field used for levitation changes very little; therefore, the influence of external temperature and magnetic field changes on the critical current density of superconducting niobium spheres can be ignored; we take it as a fixed value. In this simulation, the critical current density is taken as $10^8\ A/m^2$.

From Ampere's loop law $\overrightarrow{J} = \nabla \times \overrightarrow{H}$, it can be obtained as follows:

$$J_\varphi = \dfrac{\partial H_r}{\partial z} - \dfrac{\partial H_z}{\partial r}. \tag{5}$$

Incorporating formulas (3) and (5) into formula (2), the governing equation of the superconducting region can be obtained as follows:

$$\begin{bmatrix} -\dfrac{\partial}{\partial z}\left(E_0\left(\dfrac{\partial H_r/\partial z - \partial H_z/\partial r}{J_c} \right)^n \right) \\[3mm] \dfrac{1}{r}E_0\left(\dfrac{\partial H_r/\partial z - \partial H_z/\partial r}{J_c} \right)^n + \dfrac{\partial}{\partial r}E_0\left(\dfrac{\partial H_r/\partial z - \partial H_z/\partial r}{J_c} \right)^n \end{bmatrix}$$
$$= -\mu_0 \dfrac{\partial}{\partial t} \begin{bmatrix} \mu_r H_r \\[1mm] \mu_r H_z \end{bmatrix}. \tag{6}$$

As for the nonsuperconducting area, we simply put Ohm's law and formula (5) into formula (2); thus, the governing equation of the magnetic field intensity H in the entire region is obtained. From the governing equations and boundary conditions, the H distribution in the entire spatial domain can be obtained, then we use the B–H constitutive relationship and formula (5) to obtain the magnetic field distribution and current distribution in space. Finally, the Lorentz force equation can be used to obtain the force of the superconducting sphere in the magnetic field as follows:

$$\overrightarrow{F} = \int_V \overrightarrow{J}_{sc} \times B\ dV. \tag{7}$$

Among them, J_{sc} is the shielding current density in the superconductor, B is the magnetic induction intensity, and V is the volume area of the superconductor.

Because COMSOL's "Magnetic Field Formula" interface can set material properties with obvious nonlinear E-J characteristics, the finite element simulation of the model can be performed in COMSOL. It should be noted that the "conduction current relationship" of the superconductor should be selected as the "E-J characteristic" and input into equation (3).

Another thing to note is that, in the process of finite element meshing, it is necessary to divide the mesh close to the surface of the superconductor to be particularly small; because according to the London equation, the magnetic field and shielding current only exist within a few angstroms to hundreds of angstroms on the surface of the superconductor and decay exponentially. After many simulations, it was found that if the mesh on the surface of the superconductor is too large, it will not be able to accurately reflect the magnetic field and shield current distribution on the superconductor or affect the accuracy of the solution; this is also difficult to achieve using MATLAB to write finite element programs [12].

2.3. The Principle and Classification of High-Temperature Superconducting Linear Motors.

Introducing high-temperature superconducting materials into traditional linear motors, then combining with the diamagnetism of high-temperature superconducting materials, strong capture field characteristics, and self-suspension and self-direction characteristics, it laid a theoretical and technical foundation for the development of practical high-temperature superconducting linear motor technology. At present, many

countries have conducted in-depth research on high-temperature superconducting linear motor technology, through theoretical analysis, established related models, and developed a variety of prototypes. Among them, the more extensive research is the high-temperature superconducting linear synchronous motor, according to the different types of superconducting materials used and the different application principles, it is classified as follows: (1) High-temperature superconducting bulk magnet secondary linear synchronous motor; (2) primary linear synchronous motor with high-temperature superconducting coil; (3) high-temperature superconducting coil magnet secondary linear synchronous motor; (4) high-temperature superconducting block linear reluctance synchronous motor; and (5) full-superconducting high-temperature superconducting linear synchronous motor. According to its structural composition, it can be divided into 69–7: (1) unilateral type; (2) bilateral type; and (3) cylindrical type.

Different types of high-temperature superconducting linear synchronous motors have their practical application scenarios and advantages and disadvantages. The above types of high-temperature superconducting linear synchronous motors can be divided into semi-superconducting and full-superconducting types. Compared to the fully superconducting type, the semi-superconducting structure is simpler, less materials are used, the superconducting cooling system is simpler, and maintenance is simpler. The full-superconducting structure and cooling system are more complicated, but the thrust generated is greater and the efficiency is higher [13, 14]. For the unilateral type, the primary and secondary will produce a lot of normal force. In order to solve this problem, a two-sided structure can be used.

3. Result Analysis

In the actual process, both the superconducting niobium ball and the suspension coil are in a 4.2 K liquid helium environment. It is impossible to directly measure the force of a superconducting ball, only indirectly verifying the simulation results can be adopted. When the superconducting ball is in the middle position, the distance to the upper and lower capacitor plates is 0.5 mm. In the initial state, the ball falls on the lower capacitor plate due to gravity, with the gradual increase of the floating coil current, the suspension force of the ball is also gradually increasing; when the levitation force reaches the gravity of the ball, the ball starts to leave the lower capacitor plate to achieve magnetic levitation, and the suspension force of the superconducting ball in each suspension position is equal to the gravity of the ball [15]. The relationship between the floating height of a fixed-mass superconducting ball (gravity of 0.12828 N) and the current of the floating coil can be measured through experiments; in order to reduce the variable, only the lower coil current is passed. For simulation, the same structure size is used for modeling, the suspension height of the ball is adjusted, and different currents are applied to the levitation coil until the levitation force obtained by the simulation is equal to the gravity 0.1828 N. Figure 1 shows the relationship between
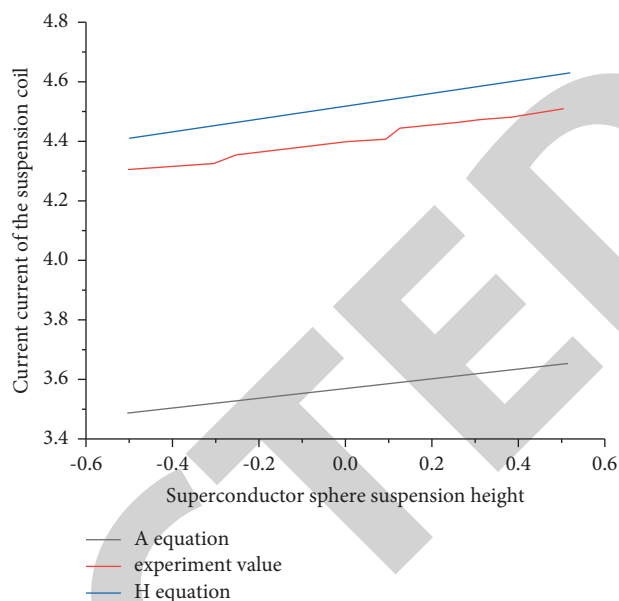
Figure 1: The relationship between the levitation height and coil current.

the floating height of the ball and the current of the floating coil obtained by the experiment and the simulation using the H equation, and it is compared with the data obtained from the static magnetic field model of Equation A.

As you can see from the figure, within −0.5 mm and 0.5 mm, the floating height obtained by experiment and simulation is basically linear with the coil current; but to suspend superconducting balls of the same mass at a certain height, the suspension current obtained by H equation simulation is more close to the actual current. It is only 2.7% higher than the actual current, which is very helpful for designing the suspension coil in the superconducting gravimeter. However, the current simulated by the static magnetic field model of Equation A is 23.6% lower than the actual value, this is mainly because under the same current, the ideal model with a permeability of 0 is used to calculate that the force on the superconductor is greater than the actual value, therefore, under the same height and force, the current required for simulation using the A-equation static magnetic field model is much smaller than the actual value. In contrast between the two, using the H equation simulation can indeed improve the simulation accuracy of the magnetic levitation system in the superconducting gravimeter [16, 17].

By bringing the floating height and current data obtained from the experiment into the H equation simulation model, it can simulate and calculate the suspension force of the ball as shown in Table 1. Compared with the actual force value 0.1828 N, it can be seen that the force calculated by the simulation of the H equation is only 6-7 mN lower than the actual force, the error is about 5%, within our tolerance range. The reason for the analysis error may be that our suspension coils are not wound uniformly and regularly, the machining, assembly, and measurement errors of superconducting niobium balls, and meshing during simulation,

TABLE 1: Suspension force obtained by the simulation.

Experiment through human coil current (A)	Experimentally measured floating position (mm)	Suspension force obtained by simulation (N)
4.3	−0.4	0.112115
4.34	−0.25891	0.111552
4.36	−0.18398	0.11217
4.38	−0.08524	0.11163
4.4	0.002501	0.111556
4.42	0.072633	0.111697
4.44	0.108347	0.112343
4.46	0.244902	0.111748
4.48	0.371653	0.111251
4.51	0.4	0.111674
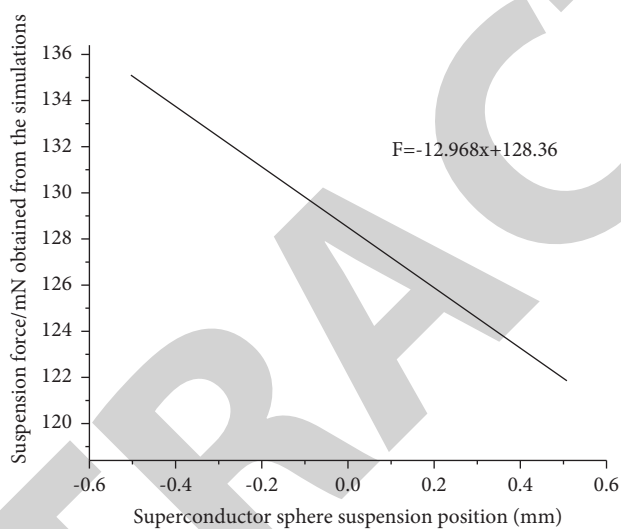
FIGURE 2: The relationship between the suspension force and the suspension position of the ball.
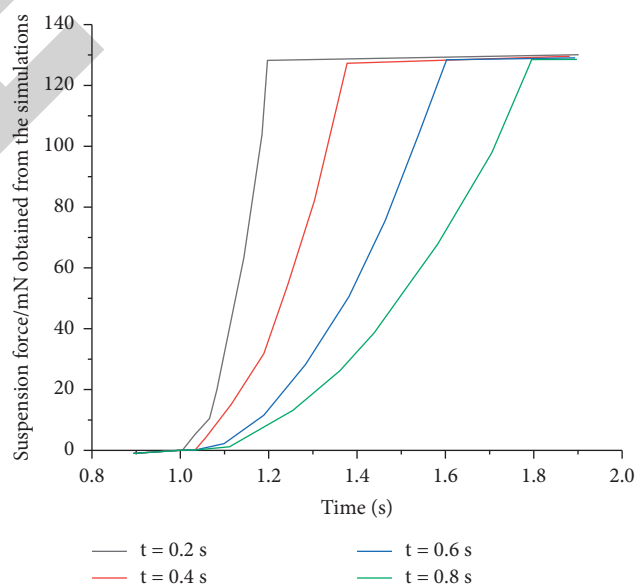
FIGURE 3: Levitation force obtained by applying current at different times.

the use of single-turn wire instead of the actual multiturn coil caused, in the future experiments and simulation process, we need to find ways to improve to further improve the simulation accuracy.

We fix the current when the superconducting ball is in the center position; by suspending the ball at different heights, the relationship between the levitation force and the levitation position of the ball can be simulated, as shown in Figure 2, so as to calculate the rigidity of the magnetic levitation system. As can be seen from the figure, in the range of −0.5–0.5 mm, the levitation force received by the ball is negatively related to the levitation height [18]. Through the levitation force-displacement curve, the magnetic force gradient of the system can be obtained, that is, the "spring" stiffness is about 12.968 N/m. Obviously, the use of a single-coil levitation system cannot meet the need for a small stiffness of $10−2$ N/m in the superconducting gravimeter; a double-coil suspension system is needed to improve the design accuracy of the superconducting gravimeter.

Figure 3 shows the curve of the force of the superconducting ball obtained by simulation with time; at 1 s, we start to use 0.2 s, 0.4 s, 0.6 s, and 0.8 s time, respectively, we pass current into the floating coil until it reaches 4.4 A. It can be found from the figure that the rate of current flow only affects the rate of change of the force on the superconducting ball, but it does not affect the magnitude of the final force. When the magnitude of the applied current remains the same, the force on the ball no longer changes, but it is not necessarily zero, which is different from the force of a conventional conductor in a changing magnetic field. The results of experiment and simulation are basically the same.

Through the comparison of experiment and simulation, it is verified that the H equation can better simulate the superconducting magnetic levitation system, and it has higher simulation accuracy and efficiency [19]. Through finite element simulation, the magnetic field distribution of the magnetic levitation system in the superconducting gravimeter, current distribution, force, and other characteristics are obtained, the force and levitation height of the superconducting ball in the magnetic field are analyzed, and the current size of the floating coil, the rate of access, the simulation calculation has obtained the magnetic force gradient, the penetration depth, the maximum magnetic induction intensity on the surface of the superconducting sphere [20]. Simulation results show that the magnetic force gradient of the superconducting magnetic levitation system using a single coil is too large to meet the requirements of gravity measurement; the penetration depth is much smaller than the thickness of the superconducting ball, moreover, the maximum value of the magnetic field on the surface of the superconducting sphere is much smaller than the critical magnetic field value of the superconducting material, so quenching will not occur.

4. Conclusion

The current simulation of the magnetic levitation system in the superconducting gravimeter mainly adopts the A-equation static magnetic field method; the data obtained by simulation are quite different from the experimental results. In order to improve simulation accuracy and efficiency, a new simulation model was established in COMSOL using the H equation. The data obtained by simulation has a small deviation from the experimental results, and it is verified that this method can improve the simulation accuracy and efficiency of the superconducting magnetic levitation system. The simulation obtained the magnetic field distribution of the magnetic levitation system in the superconducting gravimeter, shielding current distribution, force, penetration depth, and other characteristics analyzed the levitation force and levitation height of the superconducting ball in the magnetic field. The relationship between the suspension force of superconducting balls in the magnetic field and the current passing rate of suspension coil at suspension height is analyzed. The magnetic gradient of the superconducting Maglev system is calculated. The rationality and correctness of the designed magnetic levitation system are verified.

Data Availability

The data used to support the findings of this study are available from the corresponding author upon request.

Conflicts of Interest

The authors declare that they have no conflicts of interest.

Acknowledgments

References

[1] S. Suzuki and A. Satoh, "Influence of the cluster formation in a magnetic particle suspension on heat production effect in an alternating magnetic field," *Colloid and Polymer Science*, vol. 297, no. 10, pp. 1–9, 2019.

[2] S. Yook, S. S. Shams Es-haghi, A. Yildirim, Z. Mutlu, and M. Cakmak, "Anisotropic hydrogels formed by magnetically-oriented nanoclay suspensions for wound dressings," *Soft Matter*, vol. 15, no. 47, pp. 9733–9741, 2019.

[3] H. E. Mollabashi and A. H. Mazinan, "Incremental smc-based cnf control strategy considering magnetic ball suspension and inverted pendulum systems through cuckoo search-genetic optimization algorithm," *Complex & Intelligent Systems*, vol. 5, no. 3, pp. 353–362, 2019.

[4] X. Liu, G. Ying, X. Liao et al., "Cytometric microbead magnetic suspension array for high-throughput ultrasensitive detection of aflatoxin b1," *Analytical Chemistry*, vol. 91, no. 1, pp. 1194–1202, 2019.

[5] A. Mertelj, B. Lampret, D. Lisjak, J. Klepp, J. Kohlbrecher, and M. Čopič, "Evolution of nematic and ferromagnetic ordering

Retraction

Retracted: Chemical Regulation Effect of Water Use Efficiency of Maize Intercropping

Journal of Chemistry

This article has been retracted by Hindawi following an investigation undertaken by the publisher [1]. This investigation has uncovered evidence of one or more of the following indicators of systematic manipulation of the publication process:

(1) Discrepancies in scope

(2) Discrepancies in the description of the research reported

(3) Discrepancies between the availability of data and the research described

(4) Inappropriate citations

(5) Incoherent, meaningless and/or irrelevant content included in the article

(6) Peer-review manipulation

The presence of these indicators undermines our confidence in the integrity of the article's content and we cannot, therefore, vouch for its reliability. Please note that this notice is intended solely to alert readers that the content of this article is unreliable. We have not investigated whether authors were aware of or involved in the systematic manipulation of the publication process.

Wiley and Hindawi regrets that the usual quality checks did not identify these issues before publication and have since put additional measures in place to safeguard research integrity.

We wish to credit our own Research Integrity and Research Publishing teams and anonymous and named external researchers and research integrity experts for contributing to this investigation.

The corresponding author, as the representative of all authors, has been given the opportunity to register their agreement or disagreement to this retraction. We have kept a record of any response received.

References

[1] H. Chen and L. Huang, "Chemical Regulation Effect of Water Use Efficiency of Maize Intercropping," *Journal of Chemistry*, vol. 2022, Article ID 2914749, 8 pages, 2022.

Hindawi

Research Article

Chemical Regulation Effect of Water Use Efficiency of Maize Intercropping

Hongwei Chen [ID] and Ling Huang [ID]

School of Life Science and Technology, Henan Institute of Science and Technology, Xinxiang, Henan 453003, China

Correspondence should be addressed to Hongwei Chen; 1412020119@st.usst.edu.cn

In order to solve the practical problems of large water demand and shortage of water resources in traditional wheat/maize intercropping, a planting method of changing stubble retention method is proposed in this paper. This method was used to study the effects of three stubble retention methods of traditional wheat straw incineration, straw return, and straw stubble on grain yield, water use efficiency (WUE), and economic benefits of wheat/maize intercropping. The results showed that, compared with the grain yield of burning and returning, the single cropping of wheat increased by 7.2% and 5.1%, the intercropping of wheat increased by 6.2% and 5.1%, the single cropping of corn increased by 4.7% and 2.5%, and the intercropping of corn increased by 7.2% and 3.3%, respectively; compared with the burned and returned WUE, wheat monoculture increased by 20.4% and 16.2%, respectively, wheat intercropping increased by 17.9% and 14.6%, respectively, corn monoculture increased by 16.7% and 10.9%, respectively, and corn intercropping increased by 11.8% and 17.0%, respectively. In terms of the average value of monoculture wheat, monoculture corn, and wheat/corn, the net benefits of incineration, turning, and stubble treatment are 10946, 11471, and 13454 yuan ● hm^{-2}, respectively. Considering the grain yield, water use efficiency, and net income, the standing stubble planting mode is the best planting mode of wheat/maize in this area.

1. Introduction

With the rapid development of China's economy, resource consumption is becoming more and more serious, the available land area and freshwater resources are decreasing, the cultivated land area is insufficient, and the temporal and spatial distribution of water resources is uneven. Therefore, how to make rational use of limited cultivated land and freshwater resources has become the focus of attention. Intercropping has the characteristics of making full use of resources and greatly increasing yield. At present, it has important practical significance to solve the contradiction between continuous population growth and continuous reduction of cultivated land [1].

China is a country with a large population. Food has always been the focus of China's attention. Water resources are a necessary condition for crop growth. Different spatial layout has a certain impact on crop canopy structure [2]. The canopy leaf area index decreased with the increase of row spacing. The canopy opening increases with the increase of

row spacing: the row spacing configuration can also change the wheat canopy microenvironment, and the light interception and extinction coefficients at different levels of the canopy decrease with the increase of row spacing. Figure 1 shows a special corn chemical herbicide [3]. Different spatial layout has an impact on the resource utilization of intercropping. The planting modes with different field spacing have different conditions such as group ventilation and light transmission. The degree of competition and complementarity is different, and the utilization of space and nutrients is different, so the yield increase and value-added effect are also different [4]. A reasonable intercropping structure can not only reduce the competition between the two crops and make effective use of land resources but also make the group make full use of natural climate and other conditions, improve the utilization rate of light energy, and obtain better economic benefits [5, 6].

This paper analyzes the change law of water use efficiency in different spatial layouts and carries out a quantitative
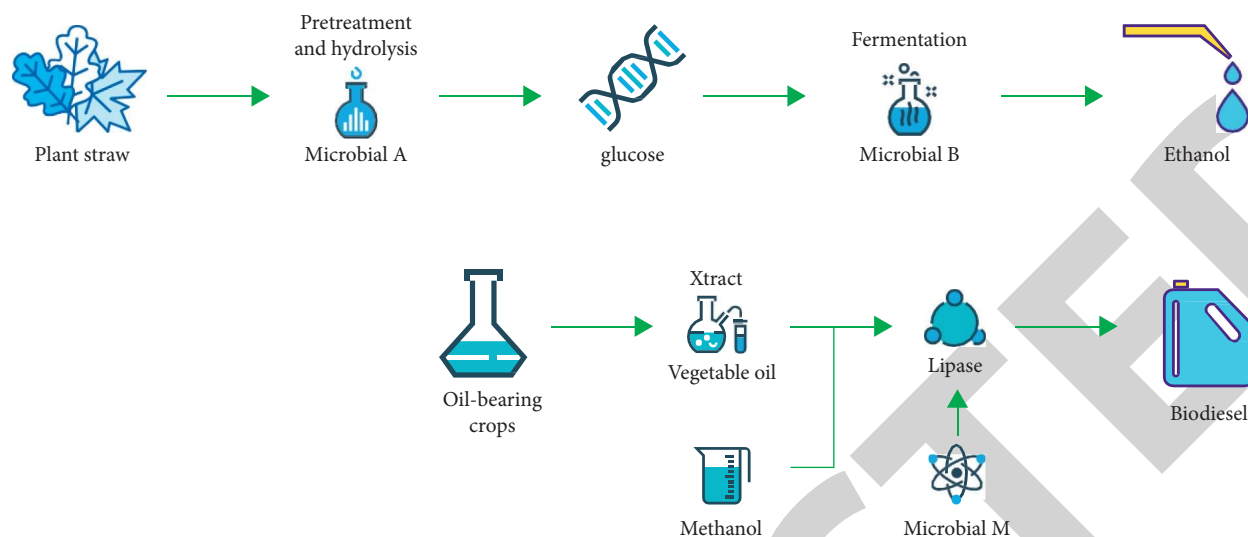
Figure 1: Atrazine, a special chemical weeding for corn.

analysis of the relative interspecific competitiveness of the two crops, so as to explore how to change the aboveground spatial structure of corn/wheat composite population, reasonably coordinate the competition and complementarity of the two crops, realize the efficient utilization of water and fertilizer resources, and provide experimental and theoretical support for improving the economic and ecological benefits of corn/wheat planting mode in Hexi oasis irrigation area.

2. Literature Review

Intercropping refers to the way that two or more crops with similar growth seasons are planted in rows or strips (multiple rows) on the same field. Interplanting refers to the planting method of planting crops between plants and rows in the late growth stage of previous crops or transplanting postseason crops [7]. The planting method of intercropping has a long history. As early as the 1st century BC, China has recorded the intercropping of melons and beans in the book of Pan Sheng in the Western Han Dynasty [8]. *Qi min yao shu* in the 6th century described the experience of intercropping mulberry with mung beans, as well as intercropping adzuki beans and shallots with coriander [9]. After the Ming Dynasty, wheat intercropping, soybean intercropping, cotton intercropping, and potato intercropping have been more common, and the intercropping of other crops has also been developed [10]. Since the 1960s, the intercropping area has expanded rapidly, including intercropping of high and low stem crops and intercropping of different crop types, such as intercropping of grain crops and cash crops, green manure crops, and feed crops. In particular, corn/bean crops are the most common and widely distributed in the northeast, north China, northwest, and southwest. In addition, there are corn/peanut intercropping, wheat/broad bean intercropping, sugarcane/peanut, sugarcane/soybean intercropping, sorghum/millet, and so forth [11]. In forest grain intercropping, mulberry, fruit tree, or *Paulownia* are more intercropped with annual crops [12]. In India and many African countries, intercropping of beans, corn, sorghum, millet, and cassava is also common [13].

China is one of the countries with serious shortage of water resources in the world, and the geographical distribution of water and soil resources is extremely uneven, with more in the south and less in the north, as well as more in the east and less in the west. The per capita share of water resources in most areas is far lower than the warning line of serious water shortage. The most serious problem of water shortage is in north China and northwest China. Due to the shortage of water resources, the contradiction between industrial and agricultural production and domestic water of urban residents and the ecological environment is becoming more and more serious in some areas. The phenomenon of river cutoff also occurs from time to time, the groundwater level is also declining, and the ecological environment is deteriorating day by day. Water conservation and water-saving technology began to be paid more and more attention [14, 15].

From the 1970s, the research and application of water-saving agricultural technology began to receive attention in northern China [16]. Since the 1980s, water-saving technology has been widely studied and applied in engineering, facility agriculture, crop cultivation, and other fields, with outstanding research results. It also provides effective technical support for efficient water use and water conservation in farmland at the micro level. However, in comparison, the research results on the optimization of agricultural water use structure and water resources management are not very significant [17, 18]. The technological development in this field is relatively lagging behind. At the macro level, efficient water use and water-saving technologies are still generally insufficient.

At present, Chinese scholars' research on water-saving technology of intercropping mainly focuses on multicropping and irrigation technology. Zhao et al. found that wheat/maize is the main planting mode in Hexi and

northwest oasis irrigation areas of Gansu Province. When the irrigation quota of wheat and maize is 6750 m^3/hm^2, the yield can reach 15000 kg/hm^2 [19]. Rolls used micro ridge and furrow irrigation technology. When the irrigation amount of wheat intercropping maize was 6000 m^3/hm^2, the yield reached 12800 kg/hm^2, which was 23.79% higher than that of flat cropping [20]. Kaabar et al. proposed that when the traditional flood irrigation is adopted, the irrigation amount of the "belt field" along the Hexi Desert with the highest water use efficiency is 8775 m^3/hm^2 [21]. These studies provide a strong basis for systematically studying the water consumption characteristics of intercropping system and developing water-saving irrigation technology [22].

Based on the current research, this paper arranges experiments in a certain area, studies the effects of different stubble retention methods on crop yield and WUE under the wheat maize intercropping mode, puts forward the stubble retention planting mode suitable for this area, further improves the water-saving and protective farming system in the oasis irrigation area, reduces the pollution and resource waste caused by straw incineration, and promotes the recycling of resources in this area, so as to provide a theoretical basis for the development of circular agriculture in this area.

3. Research Methods

3.1. Overview of the Study Area. The test was conducted at a local test station. The area relies on river water and groundwater for irrigation. The groundwater level is below 65 m. The terrain is flat. It has a temperate continental arid climate with sufficient sunshine, abundant heat, and dry climate. It is windy and sandy in spring with dry and hot wind in summer. The average altitude is 1776 m, the average annual precipitation is 160 mm, and the interannual and seasonal changes of precipitation are large. It is dry in winter and spring, the annual evaporation is 2021 mm, the average annual temperature is 7.7°C, ≥10°C, the annual accumulated temperature is 2985.4°C, the annual frost-free period is 156 d, the total solar radiation is 140–158 kj • cm^{-2}, and the annual sunshine hours are 3051 h. The soil is mainly irrigated and silted soil in northwest inland irrigation area, with silty loam and deep soil layer. The basic physical and chemical properties of the soil in the test area are shown in Table 1.

3.2. Test Design. The first crop in this experiment is spring wheat, which is harvested with high stubble. The stubble height is 30 cm (stubble biomass is 3847 kg • hm^{-2}). No tillage is carried out after harvest, and the stubble is treated before planting [23]. The experiment adopts split zone design. The stubble treatment is the main area and the planting mode is the subarea. There are three kinds of stubble treatment. The stubble treatment is standing stubble (s, no overwhelming measures are taken for the wheat stubble; crops are directly sown between the wheat stubble rows), incineration (b, tillage after stubble incineration), and return (R, turning the stubble back to the field with rotary cultivator). There are three planting modes: monoculture

wheat, monoculture corn, and wheat/corn intercropping. There are nine treatments and three repetitions. The plot area is 28.2 m^2 (6.0 m × 4.7 m). A 1 m corridor is set between each plot. Manage crops according to local fertilization, irrigation management experience, and crop growth characteristics [24]. Due to the large soil porosity and deep disturbance layer in the return and incineration treatment, the irrigation amount is slightly higher than that in the stubble treatment. The irrigation amount in the wheat growth period of the return, incineration, and stubble treatment is 300, 300, and 270 mm, respectively, and the corn growth period is 390, 390, and 360 mm, respectively. The rainfall during the growth period of wheat and maize is 58.8 mm and 117.9 mm, respectively. The fertilization time of different planting modes is different, but the total fertilization amount is the same [25].

The sowing time of wheat is March 24, and the variety is Yongliang No. 4. It is flat planting, the sowing density is 375 kg • hm^{-2}, planted in branches, and the row spacing is 12 cm. The sowing time of maize is April 20. The variety is Wuke No. 2. It is flat planting, with a sowing density of 82500 plants • hm^{-2}, a row spacing of 39 cm, and plant spacing of 24 cm. The sowing time and density of spring wheat and maize in wheat/maize intercropping system are the same as those in monoculture. The wheat belt width is 72 cm, the species are 6 rows, the row spacing is 12 cm, the maize belt width is 78 cm, the species are 2 rows, the row spacing is 39 cm, and the plant spacing is 24 cm. The wheat belt accounts for 48% and the maize belt accounts for 52%. All treatments were applied with 112.5 kg • hm^{-2} pure P (calcium superphosphate, containing P_2O_5, 46%) and pure K (potassium sulfate, containing K_2SO_4, 50%). The amount of nitrogen applied during the growth period of spring wheat and spring maize was 225 kg • hm^{-2}, of which 112.5 kg • hm^{-2} was the base fertilizer. The wheat was applied with 112.5 kg • hm^{-2} after the first irrigation at the tillering stage, and the maize was applied with 56.25 kg • hm^{-2} before irrigation at the jointing stage and the big bell mouth stage. The harvest dates of wheat and corn are July 24 and October 5, respectively.

3.3. Determination Items and Methods. During the emergence period of wheat and maize, the soil temperature was measured regularly with a geothermometer at a depth of 25 cm, stratified by 5 cm, and measured at 8:00, 14:00, and 18:00. The soil mass water content of 0–150 cm soil layer was measured by drying method. It was stratified by 20 cm, and the last layer was 30 cm. The measurement dates were May 4, May 30, June 12, August 24, and 1 day before and 1 day after wheat and corn sowing. Samples were taken from wheat belt and corn belt, respectively, and the soil water storage in each period was calculated according to the soil mass water content. The dry matter of wheat and maize plants is determined on May 11, May 28, June 15, July 2, July 24, August 3, and October 5, respectively. 15 plants from each plot of wheat and 5 plants from each plot of maize are taken, and the relative growth rate (RGR) is calculated as shown in the following formula:

Table 1: Physical and chemical characteristics of soil in the test area.

Soil layer (cm)	Unit weight $(g \cdot cm^{-3})$	Field capacity (%)	Total nitrogen $(g \cdot kg^{-1})$	Total phosphorus $(g \cdot kg^{-1})$	Total potassium $(g \cdot kg^{-1})$	Available phosphorus $(mg \cdot kg^{-1})$	Available potassium $(mg \cdot kg^{-1})$	Organic matter $(g \cdot kg^{-1})$	pH
0~20	1.47	21.50	0.95	0.40	5.73	8.14	125.80	11.49	8.66
20~40	1.49	18.25	0.72	0.37	6.71	7.35	112.84	9.58	8.76

$$\mathrm{RGR} = \frac{\left(\ln W_{t_1} - \ln W_{t_2} \right)}{(t_2 - t_1)}, \tag{1}$$

where W_{t_1} is the dry matter mass at time t_1 and W_{t_2} is the dry matter mass at time t_2. When harvesting, the economic output is calculated according to the plot after removing the side row, and the economic benefit is calculated according to the input-output.

Crop water use efficiency (WUE) is shown in the following formula:

$$\mathrm{WUE} = \frac{Y}{\mathrm{ET}}, \tag{2}$$

where Y is the grain yield and ET is the water consumption during the whole growth period of crops.

$$\mathrm{ET} = I + P - R_0 - D_P + C_R \pm \Delta S_F \pm \Delta S_W, \tag{3}$$

where I is the amount of irrigation, which is measured by water meter; P is the precipitation, provided by the local meteorological bureau; R_0 is surface runoff; D_P is the displacement of the lower boundary; C_R is the amount of water in the shallow groundwater level transported upward through the capillary; ΔS_F is the horizontal movement of water in the root zone; ΔS_W is the change of soil water storage:

Soil water storage W (mm) = soil volume water content $*$ $*$soil layer thickness (mm)

Soil volume moisture content (%) = soil mass moisture content $*$ $*$soil bulk density

Soil mass moisture content (%) = [(wet soil mass + box mass) − (dry soil mass + box mass)]/dry soil mass $*$ $*$100%

R_0 and ΔS_F of flat land can be 0. The groundwater in the test area is deeply buried, and its recharge is generally negligible, $C_R = 0$; ΔS_W is calculated according to the soil water content during crop sowing and harvest; the lower boundary drainage is not detected in the test; $D_P = 0$.

3.4. Data Processing.

SAS8.1 and Excel software were used for analysis of variance and significance test ($\alpha = 0.05$). The difference between single tailed test repetitions was significant, and the difference between treatments was significant by the new complex difference method.

4. Result Analysis

4.1. Effects of Stubble Retention Methods on Soil Temperature, Crop Emergence Rate, and Emergence Period.

It can be seen from Table 2 that, under the intercropping mode, the soil temperature of wheat and maize at the seedling emergence stage is significantly lower than that of incineration and return treatment, which is reduced by 0.5 and 0.4°C in wheat and by 1.0 and 0.6°C in maize, respectively. There is no significant difference between incineration and return treatments (the laws of monoculture and intercropping are similar, which is not listed in the paper). The number of seedlings per unit area of wheat stubble treatment was significantly lower than that of incineration and turning, and there was no significant difference between turning and burning. Although the emergence rate of maize stubble treatment decreased slightly, there was no significant difference among treatments. The emergence period of wheat stubble was 3 and 5 days later than that of turning and burning, and that of corn was 6 and 5 days later. The main reason for the low emergence rate of wheat is that the soil bulk density of no tillage planting is larger, the compactness is significantly higher than that of turning and incineration, and stubble will also hinder the contact between seeds and soil. Corn is a sparsely planted crop, so straw has little impact on its emergence rate, mainly reflected in the delay of seedling stage. On the one hand, the undisturbed compactness of surface soil is high, which affects the growth of seedlings. On the other hand, stubble reduces the solar radiation reaching the ground, the soil moisture content is high, and the recovery of ground temperature is slower than incineration and turning.

4.2. Effect of Stubble Retention on Soil Water Storage.

During crop growth, there was no significant difference in soil water storage between different stubble retention methods in early May. From the end of May, the soil water storage of standing stubble treatment was significantly higher than that of returning and incineration treatment, with an average of 9.2% and 12.8% higher than that of returning and incineration treatment in the whole growth period (as shown in Table 3), while the returning treatment was significantly higher than that of incineration treatment only on June 12, and there was no significant difference in other growth periods. Although the irrigation amount of standing stubble treatment is slightly lower than that of the other two treatments, because standing stubble reduces solar radiation and water exchange between soil and atmosphere, the loss of soil water evaporation is reduced, so that standing stubble treatment has relatively high soil water storage. The difference in the early stage is small, mainly because the stubble before this experiment is wheat with high stubble (30 cm), and each treatment is carried out before wheat sowing. Therefore, the difference of soil water storage on May 4 is not significant.

Table 2: Effects of stubble retention methods on emergence number, emergence period, and soil temperature of intercropping wheat and maize.

Crops	Stubble retention method	Soil temperature (°C)	Emergence number (plant · m^{-2})	Emergence time
Wheat	B	10.3	724a	04–10
	R	10.4	716a	04–12
	S	9.9	708b	04–15
Corn	B	11.1	8.13a	05–20
	R	11.5	8.13a	05–21
	S	10.5	8.12a	05–26

Table 3: Effects of stubble retention methods on soil water storage in different growth periods.

Treatment	Date					
	05-04	05–30	06–12	07–24	08–24	10-05
B	346	320	346	228	342	310
R	354	356	352	250	346	334
S	372	410	378	274	398	362

Table 4: Effects of stubble retention methods on relative growth rate of crops.

Treatment	Stubble retention method	Determination period					
		05.11–05.28	05.28–06.15	06.15–07.02	07.02–07.24	07.24–08.03	08.03–10.05
Monoculture wheat	B	0.036	0.056	0.013	0.009		
	R	0.035	0.059	0.007	0.011		
	S	0.032	0.065	0.009	0.011		
Monoculture corn	B		0.108	0.055	0.019	0.023	0.014
	R		0.103	0.076	0.022	0.014	0.014
	S		0.100	0.083	0.021	0.020	0.015
Wheat/corn	B	0.023	0.084	0.024	0.034	0.071	0.014
	R	0.018	0.077	0.042	0.023	0.082	0.015
	S	0.006	0.074	0.051	0.024	0.096	0.015

4.3. Effect of Stubble Retention Methods on Relative Growth Rate of Crops. It can be seen from Table 4 that, in wheat monoculture planting, the relative growth rate of stubble treatment in middle and late May is lower than that of stubble returning and incineration treatment. From the end of May to the middle of June, it shows stubble returning > incineration, and then each treatment rises alternately. The relative growth rate of stubble treatment was lower before the middle of June and higher than that of turning and incineration treatment after the middle of June. In wheat/maize, from the middle of May to the middle of June, the relative growth rate of standing stubble treatment was lower than that of returning and incineration. From the middle of June to early July and after early August, the relative growth rate of standing stubble treatment was higher than that of returning and incineration. The reason for the inconsistency between single and intercropping treatment is that the crop growth of intercropping treatment is affected by both crops. The main reason for the low relative growth rate of crops in the early growth stage of stubble treatment is that stubble treatment absorbs less light radiation and less water loss, so the soil temperature is low. After the temperature rises in the middle and late stage, it will no longer become the main factor restricting crop growth.

4.4. Effects of Stubble Retention and Planting Mode on Crop Yield and Water Use Efficiency. In wheat monoculture, the grain yield of standing stubble treatment increased by 7.2% and 5.1%, respectively, compared with incineration and return treatment (as shown in Table 5). In wheat intercropping, the grain yield of standing stubble treatment increased by 6.2% and 5.1%, respectively, compared with incineration and return treatment, but there was no significant difference in wheat seed yield among different stubble retention methods.

The water consumption of crop under various planting modes is different (wheat monoculture, wheat intercropping, corn monoculture, and corn intercropping). Compared with different stubble retention methods, standing stubble treatment was significantly lower than turning and incineration treatment. Wheat monoculture decreased by 8.6% and 12.1%, respectively, wheat intercropping decreased by 8.3% and 10.0%, respectively, corn monoculture decreased by 7.6% and 10.3%, respectively, and corn intercropping decreased by 7.6% and 8.6%, respectively. In wheat monoculture, the WUE of standing stubble treatment was significantly higher than that of incineration and turnover treatment, and there was no significant difference between incineration and turnover treatments. The WUE of standing stubble treatment increased by 20.4% and 16.2%,

TABLE 5: Effects of stubble retention and planting patterns on crop yield and water use efficiency.

Planting method	Stubble retention method	Grain yield ($kg \cdot hm^{-2}$)		Biological yield ($kg \cdot hm^{-2}$)		Economic coefficient		Crop water consumption (mm)		Water use efficiency ($kg \cdot hm^{-2} \cdot mm^{-1}$)	
		Wheat	Corn	Wheat	Corn	Wheat	Corn	Wheat	Corn	Wheat	Corn
Monoculture	B	6490a	11590a	19091a	22251b	0.33b	0.52a	511a	621a	12.9b	18.7b
	R	6621a	11840a	17713b	25238a	0.37a	0.47b	491a	603a	13.3b	19.6b
	S	6956a	12136a	18762a	25544a	0.37a	0.48b	449b	557b	15.5a	21.8a
Intercropping	B	8052a	13146b	19221a	21221b	0.42a	0.62a	490a	562a	16.5b	23.4b
	R	8142a	13642ab	19904a	24461a	0.41a	0.56b	481a	557a	16.9b	24.5b
	S	8553a	14098a	19768a	24744a	0.43a	0.57b	441b	515b	19.4a	27.4a
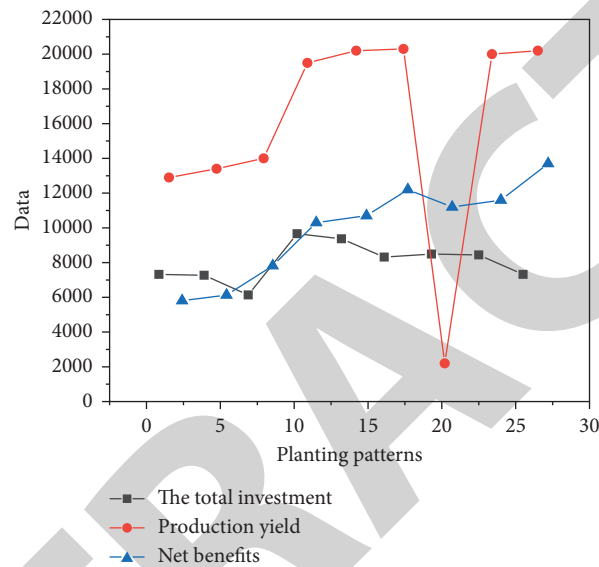
FIGURE 2: Effects of stubble retention and planting mode on crop economic benefits.

respectively. In wheat intercropping, WUE of standing stubble treatment increased by 17.9% and 14.6%, respectively, compared with incineration and turnover treatment.

4.5. Impact of Stubble Retention and Planting Mode on Crop Economic Benefits. The analysis of input and output benefits of different stubble and planting modes (Figure 2) shows that, in wheat monoculture, the net benefits of turning back and burning and standing stubble treatment are 5960, 5698, and 7815 yuan $\bullet$ hm^{-2}, respectively, and the income of standing stubble is 31.1% and 37.2% higher than that of turning back and burning, respectively; in maize monoculture planting, the net incomes of returning, burning, and stubble treatment were 10686, 10260, and 12373 yuan $\bullet$ hm^{-2}, respectively, and the income of stubble treatment was 15.8% and 20.5% higher than that of returning and burning, respectively; in wheat/maize intercropping, the net income of returning, burning, and stubble was 11471, 10946, and 13454 yuan $\bullet$ hm^{-2}, respectively, and the income of returning and stubble was 17.3% and 22.9% higher than that of burning, respectively. Under the three planting modes, stubble treatment has the highest economic benefit, followed by turning and incineration treatment, which is mainly due to the fact that stubble treatment eliminates the procedures

of soil rotation before sowing, land preparation, and middle tillage, and has better effects of water storage and moisture conservation, and the grain yield is also higher than the other two treatments, which finally makes the economic yield significantly higher than turning and incineration treatment. Under the stubble treatment, the yield gain of wheat or maize intercropping was 6761 yuan higher than that of wheat monoculture, and the difference was small compared with that of maize monoculture. Compared with wheat monoculture and maize monoculture; the economic benefit increased by 5639 yuan hm^{-2} and 1081 yuan hm^{-2}, respectively.

5. Conclusion

Through the comparison of different planting methods of corn, we can get the most scientific and economic benefits for the development of wheat. The conclusions are as follows: This study found that, in various planting modes, the relative accumulation rate of dry matter in the early stage of stubble treatment was lower than that of incineration and return treatment and gradually caught up with and exceeded that of incineration and return treatment in the middle and later stage, but there was also an alternating rise phenomenon. It is mainly because the stubble treatment absorbs

less light radiation and less water loss in the early growth stage, so the soil temperature is low, while the soil temperature increases in the middle and later stage, and the temperature no longer becomes the main factor restricting crop growth. Conservation tillage can effectively inhibit soil water evaporation and improve crop water use efficiency. This study shows that the soil water storage of standing stubble treatment is 9.2% and 12.8% higher than that of turning and incineration treatment in the whole crop growth period, while the turning treatment is significantly higher than incineration treatment only on June 12. Although the irrigation amount of standing stubble treatment is slightly lower than that of the other two treatments, standing stubble reduces the solar radiation and water exchange between soil and atmosphere, reduces the loss of soil water evaporation, and improves the water use efficiency (WUE). Conservation tillage can save costs and increase benefits. The results of this experiment show that, under the three planting modes, the economic benefit of stubble treatment is the highest, followed by turnover, and the economic benefit of incineration treatment is the lowest. The main reason is that stubble treatment eliminates the procedures of soil rotation before sowing, land preparation, and middle tillage and has a good effect of water storage and moisture conservation, and the crop grain yield is also higher than those in the other two treatments. Finally, the economic yield is significantly higher than those of turnover and incineration treatment. It is concluded that, in addition to high yield and WUE, the no tillage stubble planting mode has significant ecological effects on straw recycling, water storage and moisture conservation, and increasing soil organic matter in Hexi oasis irrigation area, but the effects of climate and year type on it need to be further studied.

Data Availability

The data used to support the findings of this study are available from the corresponding author upon request.

Conflicts of Interest

The authors declare that they have no conflicts of interest.

Acknowledgments

References

[1] Y. Huang, Z. Zhang, Z. Li, D. Dai, and Y. Li, "Evaluation of water use efficiency and optimal irrigation quantity of spring maize in hetao irrigation district using the noah-mp land surface model," *Agricultural Water Management*, vol. 264, no. 3, Article ID 107498, 2022.

[2] H. Liu, B. Yuan, X. Hu, and C. Yin, "Drip irrigation enhances water use efficiency without losses in cucumber yield and economic benefits in greenhouses in north China," *Irrigation Science*, vol. 40, no. 2, pp. 135–149, 2022.

[3] J. Zou, J. Ding, M. Welp, S. Huang, and B. Liu, "Assessing the response of ecosystem water use efficiency to drought during and after drought events across central Asia," *Sensors*, vol. 20, no. 3, p. 581, 2020.

[4] T. Wang, H. Zhang, J. Zhao, X. Guo, and S. Tong, "Estimation of water-use efficiency based on satellite for the typical croplands," *IEEE Access*, vol. 8, no. 99, p. 1, 2020.

[5] N. Liu, J. Kala, S. Liu et al., "Drought can offset potential water use efficiency of forest ecosystems from rising atmospheric CO_2," *Journal of Environmental Sciences*, vol. 90, no. 4, pp. 265–277, 2020.

[6] S. Ghosh, B. P. Bloom, Y. Lu, D. Lamont, and D. H. Waldeck, "Increasing the efficiency of water splitting through spin polarization using cobalt oxide thin film catalysts," *Journal of Physical Chemistry C*, vol. 124, no. 41, pp. 22610–22618, 2020.

[7] L. Han-Saem, J. Hur, and H.-S. Shin, "Enhancing the total organic carbon measurement efficiency for water samples containing suspended solids using alkaline and ultrasonic pretreatment methods," *Journal of Environmental Sciences*, vol. 90, no. 4, pp. 23–31, 2020.

[8] L. Monteiro, R. Cristina, and D. Covas, "Water and energy efficiency assessment in urban green spaces," *Energies*, vol. 14, no. 17, p. 5490, 2021.

[9] X. Qin, T. Huang, C. Lu et al., "Benefits and limitations of straw mulching and incorporation on maize yield, water use efficiency, and nitrogen use efficiency," *Agricultural Water Management*, vol. 256, no. 3, Article ID 107128, 2021.

[10] M. Cheng, H. Wang, J. Fan, F. Zhang, and X. Wang, "Effects of soil water deficit at different growth stages on maize growth, yield, and water use efficiency under alternate partial root-zone irrigation," *Water*, vol. 13, no. 2, p. 148, 2021.

[11] N. K. Lenka, S. Lenka, D. S. Yashona, and D. Jat, "Elevated temperature and low nitrogen partially offset the yield, evapotranspiration, and water use efficiency of winter wheat under carbon dioxide enrichment," *Agricultural Water Management*, vol. 250, no. 2, Article ID 106856, 2021.

[12] L. Yu, X. Zhao, X. Gao et al., "Effect of natural factors and management practices on agricultural water use efficiency under drought: a meta-analysis of global drylands," *Journal of Hydrology*, vol. 594, no. 3, Article ID 125977, 2021.

[13] Z. Ding, Y. Liu, L. Wang et al., "Effects and implications of ecological restoration projects on ecosystem water use efficiency in the karst region of southwest China," *Ecological Engineering*, vol. 170, no. 2, Article ID 106356, 2021.

[14] X. Liu, Z. Wei, Y. Ma, J. Liu, and F. Liu, "Effects of biochar amendment and reduced irrigation on growth, physiology, water-use efficiency and nutrients uptake of tobacco (*Nicotiana tabacum* l.) on two different soil types," *Science of the Total Environment*, vol. 770, no. 3, Article ID 144769, 2021.

[15] M. Cheng, H. Wang, J. Fan Zhang et al., "A global meta-analysis of yield and water use efficiency of crops, vegetables and fruits under full, deficit and alternate partial root-zone irrigation," *Agricultural Water Management*, vol. 248, no. 12, Article ID 106771, 2021.

[16] Y. Chen, Z. Ding, P. Yu et al., "Quantifying the variability in water use efficiency from the canopy to ecosystem scale across main croplands," *Agricultural Water Management*, vol. 262, no. 3, Article ID 107427, 2022.

[17] S. Yang, J. Zhang, J. Han et al., "Evaluating global ecosystem water use efficiency response to drought based on multi-model analysis," *Science of the Total Environment*, vol. 778, no. 20, Article ID 146356, 2021.

Hindawi

Retraction

Retracted: Numerical Simulation of Fine Blanking Die Wear and Die Performance Analysis

Journal of Chemistry

This article has been retracted by Hindawi following an investigation undertaken by the publisher [1]. This investigation has uncovered evidence of one or more of the following indicators of systematic manipulation of the publication process:

(1) Discrepancies in scope

(2) Discrepancies in the description of the research reported

(3) Discrepancies between the availability of data and the research described

(4) Inappropriate citations

(5) Incoherent, meaningless and/or irrelevant content included in the article

(6) Peer-review manipulation

The presence of these indicators undermines our confidence in the integrity of the article's content and we cannot, therefore, vouch for its reliability. Please note that this notice is intended solely to alert readers that the content of this article is unreliable. We have not investigated whether authors were aware of or involved in the systematic manipulation of the publication process.

Wiley and Hindawi regrets that the usual quality checks did not identify these issues before publication and have since put additional measures in place to safeguard research integrity.

We wish to credit our own Research Integrity and Research Publishing teams and anonymous and named external researchers and research integrity experts for contributing to this investigation.

The corresponding author, as the representative of all authors, has been given the opportunity to register their agreement or disagreement to this retraction. We have kept a record of any response received.

References

[1] Y. Li, Y. Zhao, and Y. Hao, "Numerical Simulation of Fine Blanking Die Wear and Die Performance Analysis," *Journal of Chemistry*, vol. 2022, Article ID 9893356, 7 pages, 2022.

Research Article

Numerical Simulation of Fine Blanking Die Wear and Die Performance Analysis

Yamin Li [ID],[1] **Yali Zhao** [ID],[1] **and Yongxing Hao** [ID][2]

[1]*School of Mechanical and Electrical Engineering, Zhongyuan Institute of Science and Technology, Zhengzhou,
Henan 450000, China*
[2]*School of Mechanical Engineering, North China University of Water Resources and Electrical Power, Zhengzhou,
Henan 450045, China*

Correspondence should be addressed to Yamin Li; 20148480@stu.sicau.edu.cn

In order to study the die wear law of rotary fine blanking helical cylindrical gear, a three-dimensional rigid plastic finite element model of rotary fine blanking helical cylindrical gear is established on the Deform-3D software platform. Based on the Archard wear model, this paper analyzes the die wear in the fine blanking process, obtains the wear distribution of each point on the working surface of the die, determines the maximum wear area, and makes a comparative analysis with the fine blanking die wear of spur gear. Through the single factor variable method, this paper studies the effects of reverse jacking force, blank holder force, blanking speed, punch and die clearance, die fillet radius, and die initial hardness on die wear. The test results show that when the punch reduction is the same, the wear of the female die of fine blanking helical cylindrical gear is greater than that of fine blanking spur cylindrical gear. When the counter jacking force increases from 100 kN to 200 kN, the maximum wear of the die gradually increases from 6.91×10^{-6} mm to 9.38×10^{-6} mm; when the blank holder force increases to 3/4 of the blanking force, the die wear decreases with the increase of blank holder force; it is ideal when the blanking clearance is 0.5% t (0.02 mm). *Conclusion*. The wear model can accurately predict the relationship between main process parameters and wear in the process of rotary fine blanking, and the measures to reduce die wear are put forward from the aspect of process design.

1. Introduction

Using fine blanking technology to replace the current cutting processing to manufacture precision plate parts can greatly promote the production of automobile, electronic instruments, and other industries; drive the development of the whole machinery manufacturing industry in China; and achieve better economic and social benefits [1]. Fine blanking die is not only the key equipment for producing fine blanking parts but also the core of fine blanking technology, which directly determines the precision of fine blanking parts and the productivity of the factory. The die life is one of the important indicators to measure the die quality. With the rapid development of China's industrial modernization, the structure of fine blanking parts is becoming more and more complex, the accuracy requirements are higher, the application range is wider and wider, and

higher requirements are put forward for the service life of fine blanking die. The large-scale, complex, high-precision, and high-efficiency of molds all depend on the improvement of mold life [2]. However, the structure of fine blanking die is complex. Engineers often design a set of die according to experience, resulting in unqualified product quality, low die life, low production efficiency, and greatly improved production cost. Therefore, the simulation analysis and estimation of fatigue life of fine blanking die has important scientific and practical significance for improving the design level of fine blanking die, improving the accurate theoretical basis for engineers to design die, improving the service life of die, improving factory production efficiency, and reducing production cost.

Fine blanking is the abbreviation of precision blanking, which belongs to noncutting processing technology. Precision blanking technology is to cut and separate the

sheet along the required contour under three-dimensional pressure on a special press or a modified general press through a precision blanking die and finally obtain a plate-like precision contour part with smooth section, good perpendicularity, flatness, and high-precision [3]. Using precision blanking process instead of cutting process to manufacture plate-shaped precision contour parts, the main technical indexes of parts can reach or even exceed cutting and other machining methods, and the machining efficiency can be increased more than ten times, which greatly reduces the production cost. It is one of the development directions of manufacturing technology at present.

2. Literature Review

In terms of fine blanking process optimization, the common means are as follows: improving the design structure of fine blanking press or die, using orthogonal experiment, or finite element simulation to obtain the optimal results of different process parameters. Fine blanking press needs high strength, high stiffness, and good dynamic performance to ensure fine blanking accuracy. Ji used finite element simulation and topology optimization technology to optimize the structure of 12000 kN fine stamping machine and finally realized the improvement of performance while reducing the weight of the press [4]. Lubis analyzed the theoretical mechanism of stamping sheet metal with stepped punch without V-shaped blank holder by experiment and finite element simulation. The stepped punch structure increases the hydrostatic stress and material flow in the shear zone, so a bright shear surface can also be obtained. For precision gear parts with high dimensional requirements, the problem of fine punching collapse angle can be solved by using negative punch and die clearance. The larger the negative die clearance is, the smaller the part collapse angle is until it tends to a fixed value [5].

There are many factors affecting the wear of fine blanking die, including blank holder force, reverse jacking force, blanking speed, die chamfer, punch and die clearance, die hardness, and other physical parameters. It is difficult to determine the relationship between these physical parameters and die wear through experiments. The correlation between wear and these physical parameters can be obtained through finite element simulation. Zheng, combined with Archard model and using DEFORM-3D simulation, concluded that die wear is positively correlated with blank holder force, reverse jacking force, blanking speed, and die chamfer and negatively correlated with punch die clearance and die hardness [6]. Liu further trained the internal relationship between these main parameters and wear through neural network and then calculated the total wear through MATLAB platform. The total wear was obtained through the superposition of single wear. After each wear, the fillet, hardness, and clearance of punch and die are updated. Under the condition of wear, the next wear is calculated. The results are in good agreement with the experiment. The fine blanking process is studied by the finite element method, and the simplified model of undamaged punch is generally used [7]. Zhang compared the undamaged punch with the worn punch by finite element method. It is concluded that the stress and strain of the simplified model are relatively

more concentrated, so the proportion of bright bands on the shear surface of parts obtained by undamaged punch is higher and there are fewer burrs [8].

In this paper, the DEFORM-3D wear analysis module is used to analyze the die wear in the rotary fine blanking process, obtain the wear distribution diagram of each point on the die surface, and determine the die wear distribution and the maximum wear area. Through comparative analysis, the effects of reverse jacking force, blank holder force, blanking speed, punch and die clearance, die fillet radius, and die initial hardness on die wear were studied. The research results show that the wear model accurately reflects the relationship between the main process parameters and wear in the process of rotary fine blanking, as shown in Figure 1, which provides a theoretical basis for die design.

3. Research Methods

3.1. Basic Concept of Fatigue. The load of most mechanical parts used in engineering varies with time, and fatigue is the main failure form. Fatigue refers to the process that parts or structures gradually produce local permanent structural or performance changes at a certain point or some points under cyclic load, form cracks after a certain number of cycles, and continue to expand under load until complete fracture.

The process of fatigue failure can be summarized as follows: under the action of cyclic load, microcracks are formed on the local maximum stress and the weakest and most stressed grains and then develop into macrocracks, which continue to expand and eventually lead to fatigue fracture. From the fracture of fatigue failure, we can find that the fatigue failure of parts has experienced three stages as follows: crack formation, propagation, and instantaneous fracture. Starting from the process of fatigue failure, we divide the fatigue life into fatigue crack formation life and fatigue crack propagation life.

From the characteristics of fatigue failure, it can be seen that, in the actual working conditions, fatigue is often difficult to detect, and it is very sensitive to the performance and processing of the material itself. Therefore, fatigue analysis is a very important part in part design and manufacturing. A complete fatigue analysis should include fatigue stress analysis, fatigue failure form analysis, antifatigue performance measurement, and the theory of estimating fatigue life, including fatigue cumulative damage theory and fatigue crack growth theory [9]. The fatigue analysis needs to collect the structural shape, material properties, and loading of relevant parts and obtain the estimated value of the working life of parts through theoretical analysis and calculation on the basis of actual working conditions. For the study of material properties, tensile and fatigue tests need to be carried out to obtain the basic parameters of the material. On the basis of consulting relevant books and calculating through empirical formula, the load situation is mainly based on the actual loading history.

Damage refers to the change degree or damage degree of material performance under fatigue load. When the material bears the stress higher than the fatigue limit, a certain amount of damage will be produced on the material every
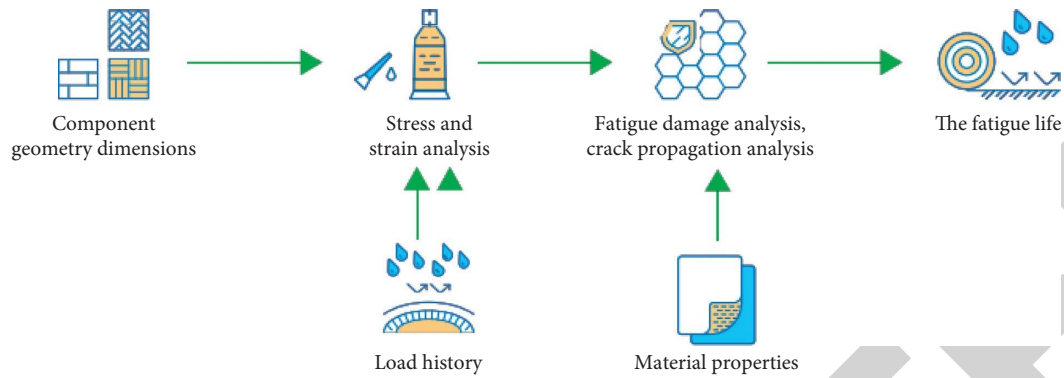
FIGURE 1: Wear performance analysis of fine blanking die.

cycle, and this damage can be accumulated. When the damage accumulates to the critical value, the material will undergo fatigue failure, which leads to a variety of fatigue cumulative damage theories.

3.2. Establishment of the Wear Model.

In order to study the die wear law of rotary fine blanking helical cylindrical gear, this paper selects a helical cylindrical gear (geometric parameters are shown in Table 1) for finite element analysis [10] and analyzes and calculates the gear ring pressing and punch rotary blanking process. The blank material is 45 steel, and the die is D2 steel (corresponding to the domestic brand Cr12Mo1V1). The material model in DEFORM-3D software is used for analysis and calculation in the simulation. In order to improve the precision of rotary fine blanking calculation, the total number of grids of the blank is 200000, and the shear zone is locally refined.

Archard wear model predicts the wear amount of die in the forming process, and the expression is as follows [11]:

$$\omega = \int K \frac{P^a v^b}{H^c} \, dt, \tag{1}$$

where ω is the wear depth; P is the positive pressure on the die surface; v is the sliding speed; and a, b, and c are standard constants. For steel, a and b are 1 and c is 2; K is the constant related to material properties, $K = 2 \times 10^{-8}$; H is the initial hardness of the mold (HRC); and t is the blank thickness.

Enter the Deform-3D preprocessing module to set the simulation control, select the heat conduction mode and Lagrange incremental algorithm, check the tool wear item in the data definition between objects, and select the Archard model to provide a theoretical algorithm for subsequent calculation. After the simulation analysis, select the tool wear item in the analysis option of the postprocessing module to analyze the wear results of the die. The size of each parameter can be determined according to the empirical formula of fine blanking parameters. Table 2 shows the basic conditions of finite element simulation. In this model, $t = 4$ mm.

4. Result Analysis

4.1. Comparative Analysis of Wear Amount.

The precondition of fine blanking die wear is the friction between the die and the material working surface during fine blanking [12],

but the severity of die working surface wear mainly depends on the normal force acting on the die surface, sliding speed, the state of the friction surface, and the hardness of the die surface according to the Archard wear model.

Through the comparative study, it is found that the wear of fine blanking die is mainly in the edge area, whether spur cylindrical gear or helical cylindrical gear. This is because in the process of gear fine blanking, the plastic deformation is mainly concentrated in the gap area at the edge, the range of plastic deformation is narrow, the stress is highly concentrated in the die edge area, the new shear area is first formed in the edge area, and the local high temperature caused by plastic deformation is also concentrated here. Therefore, the working conditions of the die edge are the worst in the process of fine blanking. Under such very bad conditions, friction with materials is easy to cause wear, so the wear of fine blanking die is mainly concentrated on the end face and side around the die edge.

Outside the cutting edge area, although the pressure acting on the end face of the working surface of the die is very large, there is no material relative displacement and friction, so there is no wear [13]. The lateral deformation of the die is much smaller than that of the die due to the friction force on the side of the die. If there are good lubrication conditions, there will be little or no wear.

The maximum wear of straight and helical teeth is shown in Figure 2. For the fine blanking model of spur gear, when the reduction of male die is 1, 2, 3, and 4 mm, respectively, the maximum wear of female die is 1.84×10^{-6}, 3.42×10^{-6}, 5.74×10^{-6} and 7.13×10^{-6} mm, respectively. For the fine blanking model of helical cylindrical gear, when the reduction of male die is 1, 2, 3, and 4 mm, respectively, the maximum wear of female die is 3.11×10^{-6}, 4.56×10^{-6}, 7.05×10^{-6}, and 8.39×10^{-6} mm, respectively.

For helical cylindrical gears, when the punch reduction is the same, the wear of fine blanking helical cylindrical gear die is greater than that of fine blanking spur cylindrical gear die. This is because in the fine blanking process of helical cylindrical gear, due to the increased rotation movement of the die, the material flow in the fine blanking process of helical cylindrical gear is more intense [14].

4.2. Analysis on the Relationship between the Change of Process Parameters and Wear.

The wear of fine blanking die is the result of the comprehensive action of many factors,

TABLE 1: Geometric parameters of reference helical cylindrical gear.

Parameter	Number of teeth, z	Normal modulus, mm	Pressure angle, $\alpha/(°)$	Helix angle, $\beta/(°)$	Tooth width, b/mm
Numerical value	18	2.5	20	10	4
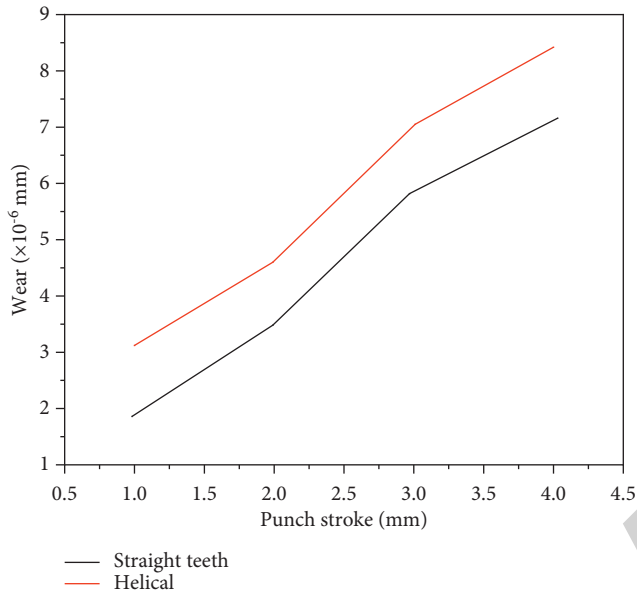
FIGURE 2: Comparison of wear amount of straight tooth and oblique tooth dies under different punch stroke conditions.

TABLE 2: Basic conditions of finite element model simulation.

Name	Description
Part type	Workpiece: plastic body
	V-shaped blank holder: rigid body
	Punch/die: rigid bodies
	Antiroof: rigid body
Workpiece material	AISI-1045
Die material	AISI-D2
Fillet radius of die edge (mm)	R_P, 0.01; R_d, 0.2
Blanking clearance (mm)	0.5% t (0.02 mm)
Blank holder force (kN)	500
Counter jacking force (kN)	150
Feed rate (mm·s^{-1})	10
Initial hardness of dieHRC	62
Rotation speed (RAD·s^{-1})	0.077
Friction factor	0.12
Fracture criterion	Oyane
Critical fracture value	2.5
Wear model	Archard wear model

including part material, die material, die structure, fine blanking process, and lubrication [15, 16]. From the perspective of process parameters, blank holder force, reverse jacking force, and blanking speed not only affect the section quality of blanking parts, but also affect the wear of dies [17]. In the rotary fine blanking model, six factors such as blank holder force, reverse jacking force, blanking speed, die fillet radius, blanking clearance, and die initial hardness are selected for analysis (Table 3), and the influence law of each factor on wear is studied. The selected method is single factor variable method. When one parameter is changed, the size of other process parameters is determined by Table 3.

4.2.1. Influence of Antijacking Force. In order to study the influence of antijacking force on the wear of the rotary fine blanking die, the wear of the die was simulated when the antijacking force was 100,125,150,175, and 200 kN. When the counterjacking force increases from 100 kN to 200 kN, the maximum wear of the die gradually increases from 6.91×10^{-6} mm to 9.38×10^{-6} mm, as shown in Figure 3.

4.2.2. Influence of Blank Holder Force. Figure 4 shows the influence of blank holder force on the wear amount of die. It can be seen that the wear amount of die increases with the increase of blank holder force. When the blank holder force increases to 3/4 of the blanking force, the wear amount of die

decreases with the increase of blank holder force. This is because when the blank holder force increases, the three-dimensional hydrostatic stress increases, and the quality of the blanking section becomes better. But when the blank holder force exceeds a certain amount [18], it will cause the change of the stress direction, and the material is prone to fracture, in the case of material tearing earlier, the relative friction between the material and the die becomes smaller and the wear degree of the die decreases [19].

4.2.3. Influence of Punch Feed Speed. The influence of punch feed speed on die wear is shown in Figure 5. With the increase of punch feed speed, the wear amount of die also increases. This is because, under the condition of a certain blank holder force and reverse jacking force, the increase of punch feed speed requires a greater blanking force. As a result, the surface pressure of the blank and the die increases, and the flow speed of the blank and the die also increases. According to the Archard wear model, the wear amount increases [20].

4.2.4. Impact of Blanking Clearance. One of the main differences between fine blanking and ordinary blanking lies in the difference of blanking clearance. The blanking clearance of fine blanking is much smaller than that of ordinary blanking. With the increase of blanking clearance, the wear amount of the female die decreases [21–23] as shown in Figure 6. This is because the blanking clearance increases and the hydrostatic pressure in the fine blanking process decreases, so the positive pressure on the inner side of the die and the edge decreases. According to the Archard wear model, the wear amount decreases. However, if the blanking

TABLE 3: Model process parameters and numerical settings.

Blank holder force (kN)	Counterjacking force (kN)	Feed speed (mm·s⁻¹)	Blanking clearance, % (t)	Die fillet radius (mm)	Initial hardness of die, HRC
400	100	6	0.1	0.2	58
450	125	8	0.3	0.3	60
500	150	10	0.5	0.4	62
550	175	12	0.7	0.5	64
600	200	14	0.9	0.6	66
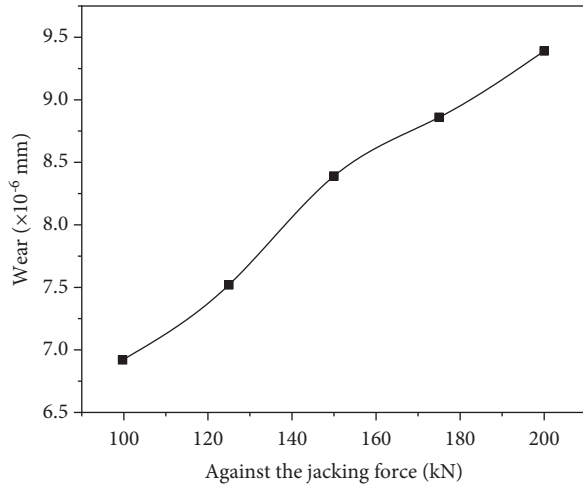
FIGURE 3: Effect of antijacking force on die wear.
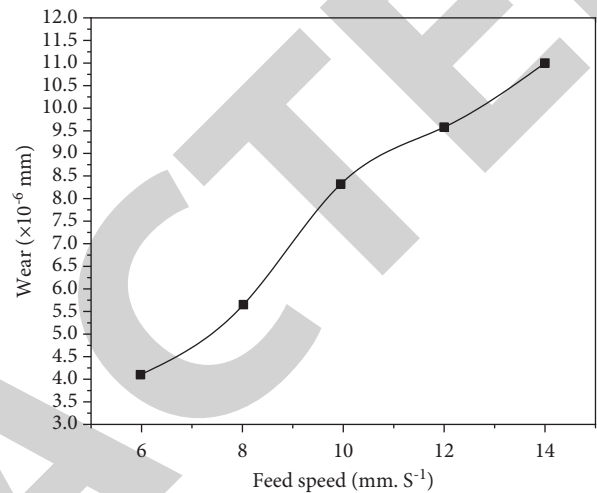
FIGURE 5: Effect of punch feed speed on die wear.
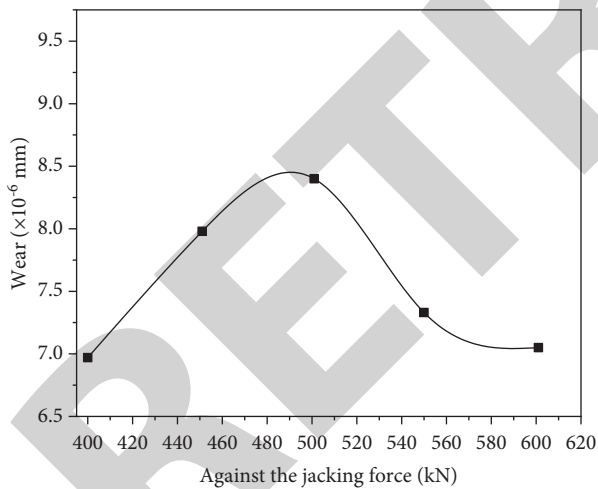
FIGURE 4: Effect of blank holder force on die wear.
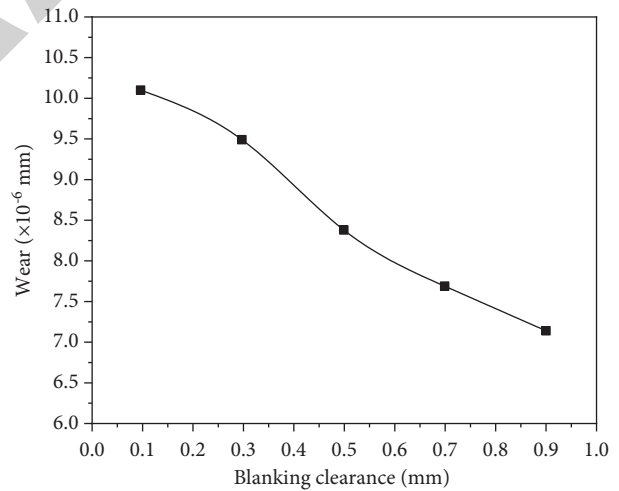
FIGURE 6: Effect of blanking clearance on die wear.

clearance is too large in the process of fine blanking, the surface quality of fine blanking parts will become worse. Therefore, selecting the appropriate blanking clearance is a key factor to improve the service life of the die and ensure the quality of fine blanking parts. For this model, considering the die life and blanking quality, it is ideal when the blanking clearance is 0.5% t (0.02 mm).

4.2.5. Influence of Die Fillet Radius. In the process of fine blanking, the fillet radius of the die is another factor affecting the quality of fine blanking parts. Through research, it is

found that the fillet radius of the die also has an important impact on the service life of the die, as shown in Figure 7. As can be seen from the figure, with the increase of the fillet radius of the die, the wear amount of the die increases. This is because the increase of the fillet radius of the die improves the stress state of the material at the transition fillet, so as to reduce the plastic deformation degree of the material and prolong the plastic deformation time, resulting in the longer wear time of the die. According to the Archard wear model, the wear amount increases. As the increase of the fillet radius of the die will increase the step angle of the workpiece
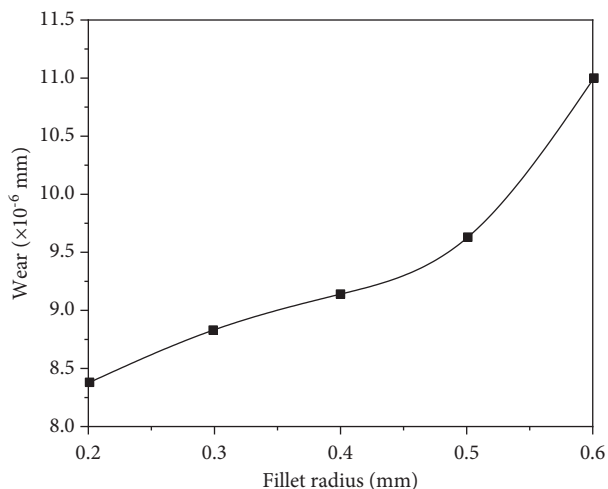
FIGURE 7: Effect of die fillet radius on die wear.
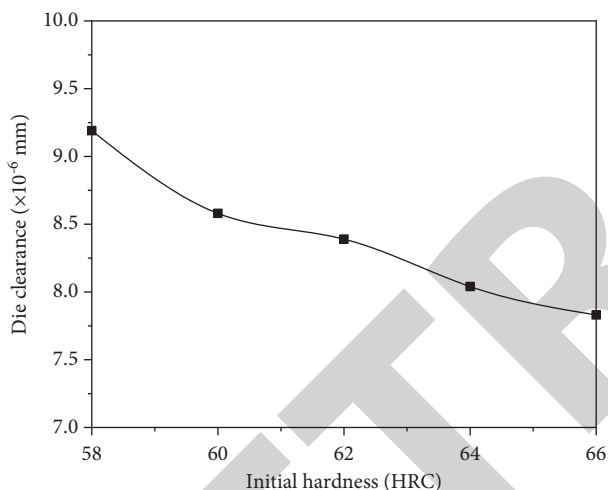
FIGURE 8: Effect of initial hardness of die on die wear.

accordingly, considering the die wear, section quality and step angle, it is ideal to take 0.2 mm as the fillet radius of the die.

4.2.6. Effect of Initial Hardness of Die. Die hardness is an important factor affecting die life. Figure 8 shows the effect of initial die hardness on die wear. It can be seen from the figure that the maximum wear of die decreases with the increase of initial die hardness. Therefore, the service life of the die can be improved by increasing the initial hardness of the die. At the same time, in order to prevent edge collapse and die fracture, the die also needs to have certain toughness. At present, the surface hardness of the die is generally provided through surface treatment technology, and the matrix has certain toughness, such as coating TiN or TiAlN coating on the die surface, so as to increase the die hardness within a certain range, so as to reduce the wear of rotary fine blanking die and increase its service life [24, 25].

5. Conclusion

No matter the spur gear or helical gear, the most worn part in the die blanking process is the die edge. For helical cylindrical gears, in the fine blanking process of left-hand helical cylindrical gears, the material flow is mainly concentrated on the right side of the spiral teeth of the die, and the wear on the right side of the tooth top circle of the spiral teeth of the die is more serious than that on the left side. Increasing the reverse jacking force, punch feed rate and die fillet radius will aggravate the wear of rotary fine blanking die and reduce its service life. Increasing the blanking clearance and the initial hardness of the die can reduce the wear of the die and increase the service life of the die.

Data Availability

The data used to support the findings of this study are available from the corresponding author upon request.

Conflicts of Interest

The authors declare that they have no conflicts of interest.

Acknowledgments

References

[1] Y. Liu, Y. Xiong, L. Hua, L. Yang, and W. Zeng, "Mechanical characteristic analysis of a separable stator fabricated by fine-blanking process with numerical and experimental methods," *International Journal of Advanced Manufacturing Technology*, vol. 112, no. 4, pp. 1–11, 2021.

[2] M. Sahli, X. Roizard, M. Assoul, G. Colas, S. Giampiccolo, and J. P. Barbe, "Finite element simulation and experimental investigation of the effect of clearance on the forming quality in the fine blanking process," *Microsystem Technologies*, vol. 27, no. 3, pp. 871–881, 2021.

[3] Y. Suzuki, T. Shiratori, M. Yang, and M. Murakawa, "Influence of strain-induced martensitic transformation of austenitic stainless steel sheet in precision blanking on cut-surface quality," *Materials Transactions*, vol. 61, no. 2, pp. 295–299, 2020.

[4] K. Ji, Y. Liu, S. Liu, and Y. Zhang, "A review on the microblanking technology of metallic foils," *International Journal of Advanced Manufacturing Technology*, vol. 114, pp. 1–16, 2021.

[5] D. Z. Lubis, Aminnudin, and A. H. Perwira, "Punch tool speed and material effect on keychain cranioplasty plate dimensions using finite element method," *Key Engineering Materials*, vol. 851, pp. 105–110, 2020.

[6] J.-Y. Zheng, J. Wang, and M. W. Fu, "Experimental and numerical study of the size effect on compound meso/ microforming behaviors and performances for making bulk

Retraction

Retracted: Monitoring of Nitrogen Transport in Pear Trees Based on Ground Hyperspectral Remote Sensing and Digital Image Information

Journal of Chemistry

This article has been retracted by Hindawi following an investigation undertaken by the publisher [1]. This investigation has uncovered evidence of one or more of the following indicators of systematic manipulation of the publication process:

(1) Discrepancies in scope

(2) Discrepancies in the description of the research reported

(3) Discrepancies between the availability of data and the research described

(4) Inappropriate citations

(5) Incoherent, meaningless and/or irrelevant content included in the article

(6) Peer-review manipulation

The presence of these indicators undermines our confidence in the integrity of the article's content and we cannot, therefore, vouch for its reliability. Please note that this notice is intended solely to alert readers that the content of this article is unreliable. We have not investigated whether authors were aware of or involved in the systematic manipulation of the publication process.

Wiley and Hindawi regrets that the usual quality checks did not identify these issues before publication and have since put additional measures in place to safeguard research integrity.

We wish to credit our own Research Integrity and Research Publishing teams and anonymous and named external researchers and research integrity experts for contributing to this investigation.

The corresponding author, as the representative of all authors, has been given the opportunity to register their agreement or disagreement to this retraction. We have kept a record of any response received.

References

[1] Z. Fan, D. Wang, N. Zhang, and B. Zhou, "Monitoring of Nitrogen Transport in Pear Trees Based on Ground Hyperspectral Remote Sensing and Digital Image Information," *Journal of Chemistry*, vol. 2022, Article ID 7590846, 7 pages, 2022.

Research Article

Monitoring of Nitrogen Transport in Pear Trees Based on Ground Hyperspectral Remote Sensing and Digital Image Information

Zehua Fan [ID],[1] **Desheng Wang** [ID],[2] **Nannan Zhang** [ID],[1] **and Baoping Zhou** [ID][1]

[1]*College of Information Engineering, Tarim University, Alar, Xinjiang 843300, China*
[2]*College of Plant Sciences, Tarim University, Alar, Xinjiang 843300, China*

Correspondence should be addressed to Baoping Zhou; 2013071138@stu.zjhu.edu.cn

To study nitrogen transport monitoring in pear trees based on ground-based hyperspectral remote sensing and digital image information. First, based on ground hyperspectral remote sensing and digital image information, combined with the characteristics of visible and near-infrared spectral data and digital image data, a beet nitrogen nutrition diagnosis model based on visible and near-infrared spectral and digital image information was established. The results showed that under water and nitrogen management conditions, the marked nitrogen use efficiency at soil profiles 15, 45, and 75 cm was 28.2%, 22.3%, and 16.3%, respectively. From the analysis of soil and plant nitrogen measured in this experiment, it can be seen that nitrogen nitrate fertilizer should be properly applied to pear trees in the future.

1. Introduction

Hyperspectral data acquisition is mainly completed by two sensors: a nonimaging spectrometer and an imaging spectrometer. The nonimaging spectrometer can measure the reflection spectrum of the target object in the field or indoors and generate the spectral reflectance curve. The user can directly see the spectral characteristics of the target object and process the data by the hyperspectral analysis method to achieve qualitative or quantitative monitoring [1]. An imaging spectrometer integrates spectral technology and imaging technology to achieve "Atlas integration," which can not only obtain the shape and position information of the target object in the image but also record the spectral information of the object. Each pixel point on a hyperspectral image contains a continuous reflection spectrum curve, which realizes the collection of spectral information from point to surface. It has richer spectral information and is an upgraded version of nonimaging spectrometer.

Nitrogen is the most significant nutrient element affecting crop growth and development, yield, and quality formation (Figure 1). The total nitrogen content in crops is about 0.3–5.0% of dry weight. Nitrogen participates in the composition of chlorophyll. It is not only the main component of protein, but also an important component of nucleic acid and many enzymes in plants [2]. In addition, some vitamins, some alkaloids, and some plant hormones such as auxin and cytokinin in plants contain nitrogen. In production, under nitrogen deficiency, the growth of aboveground and root systems of crops is significantly inhibited, the formation and development of reproductive organs are also limited, the plants mature in advance, and the seeds and fruits are small but not full, which significantly affects the yield and quality of crops. On the contrary, increasing the application of nitrogen fertilizer can increase crop yield and improve the quality of crop products, so the input of nitrogen fertilizer increases year by year. China is the country with the largest consumption of nitrogen fertilizer. The average annual consumption per unit of cultivated land area is three times the world average. It is expected to continue to increase in the next 10 years. With the large increase of nitrogen fertilizer applications, the nitrogen use efficiency gradually decreases. On an average, the utilization efficiency of several nitrogen fertilizers by wheat crops is 27%–34%, which is far lower than that of corn, cotton, rice, and other crops. Due to the unscientific
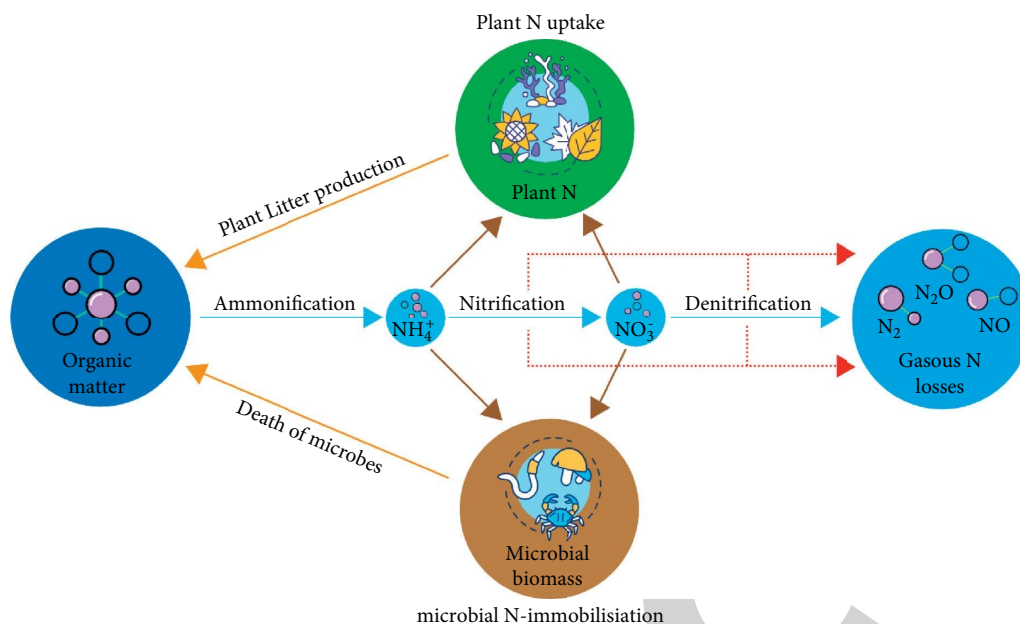
FIGURE 1: Nitrogen transport monitoring.

application of nitrogen fertilizer, nitrogen is often lost by leaching, denitrification, and nitrogen volatilization. The loss rate of wheat crops is 14%–55%, and that of autumn crops is 18%–55%. Most of the lost nitrogen enters groundwater and surface water, resulting in the continuous increase of nitrate nitrogen in groundwater and surface water, resulting in water eutrophication, resulting in a series of environmental problems, such as the destruction of water resources and aquatic resources, the reduction of the use value of water, the increase of the cost of water treatment, and even a threat to human health [3].

In short, nitrogen fertilizer is not only an important factor in agricultural production but also one of the most important factors polluting the environment. Rapid and effective tracking and monitoring of crop nitrogen status and determining scientific fertilization management measures are of great significance to improving nitrogen utilization efficiency, making rational use of resources, improving crop yield, improving quality, and protecting the environment. Therefore, with the deepening of people's understanding of the severity of survival security problems such as resources and the environment, how to improve nitrogen use efficiency and reduce the impact on the agricultural ecological environment is a major problem that needs to be studied and solved urgently. Precision agriculture represents the development direction of modern agriculture and is also the key field of agricultural science and technology research. Compared with traditional agriculture, precision agriculture is characterized by the exchange of high and new technology and scientific management for the maximum conservation of natural resources and the minimum pollution of the ecological environment. Its core is to properly divide the whole field into several small plots, timely obtain the information on the small plots, make decisions according to the plot in

consideration of the differences in natural conditions, and accurately carry out agricultural operations in each plot, that is, carry out real-time monitoring and diagnosis of the spatial differences of soil characteristics and crop conditions, and implement regular, positioning and quantitative prescription farming on this basis, so as to fully obtain the highest benefits. Therefore, the rapid acquisition and quantitative diagnosis of crop growth information is an important key technology in today's precision agricultural technology system. At present, there is an urgent need for low-cost, high-density, high-precision, and high-reliability farmland information acquisition technology to achieve rapid, real-time, accurate, and economic access to accurate information such as crop growth and development, plant diseases and pests, water and fertilizer status, and corresponding environmental conditions [4].

Cui Y. et al. believe that nitrogen is an important nutrient element affecting the growth, development, yield, and quality of pear trees. Nitrogen is a synthetic element of protein, nucleic acid, amino acid, and other life substances, which can promote photosynthesis, improve pear quality, and increase yield [5]. Fricker et al. believe that improving the availability of nitrogen can increase ecosystem biomass at least in the short term. At present, China is the country with the largest consumption of nitrogen fertilizer in the world. Excessive application of nitrogen fertilizer will not only affect the quality and yield of pear trees but also cause a series of environmental pollution problems [6]. Therefore, Marcinkowska-Ochtyra et al. believe that the formulation of a scientific nitrogen application scheme and improvement of fertilizer utilization efficiency are not only conducive to the growth of pear trees and increase production and income, but also protect the environment, reduce pollution, and realize the common development of economic and ecological benefits [7]. Booysen et al. found that the traditional

method of measuring leaf nitrogen content is time-consuming and laborious and requires destructive sampling, which makes it difficult to achieve large-area monitoring. In recent years, with the rapid development of hyperspectral remote sensing technology based on vegetation spectral characteristics, it has become possible to monitor crop nitrogen content in real-time and quickly within the region [8]. D. Kopeć et al. believe that the massive and rich spectral information carried by hyperspectral data accurately analyzes the vegetation from the macro level to the micro level of monitoring vegetation physiological parameters, which has become the development trend of modern precision agriculture. Monitoring crop growth and nutrition diagnosis by hyperspectral remote sensing will be an important basis for field management and yield and quality prediction [9]. Zhang et al. believe that due to different internal structures, natural features have different degrees of reflection, absorption, transmission, and radiation of electromagnetic waves, resulting in great differences in the reflected spectrum of electromagnetic waves between different features, which is the spectral characteristics of features. The electromagnetic wave reflection spectrum of ground objects is the manifestation of remote sensing information [10]. Liu et al. believe that both multispectral and hyperspectral can be used to estimate crop nitrogen abundance and deficiency, and the accuracy is high. The hyperspectral technology overcomes the shortcomings of discontinuous band and insufficient information in wide band, which makes the accuracy of rapid nondestructive detection of crop nitrogen content greatly improved. But at the same time, there may be a problem that massive data has not been fully utilized. It is necessary to explore more spectral analysis methods in future research to mine the effective information in hyperspectral data [11]. Luo et al. used the image of rice leaves to map the nitrogen content of a single plant, which intuitively displayed the component information distribution of a single leaf. The crop nitrogen content monitoring model based on leaf hyperspectral data has high accuracy, but the model is not unified and ignores the vertical distribution form of crop canopy, which is not suitable for other forms of the crop nitrogen prediction and has certain limitations [12]. Sun et al. believe that because the surface spectral source is mixed composite information, the canopy spectrum is mainly determined by plant biochemical components, LAI, light layer structure, soil background and other factors. People take a variety of means to process the spectrum to improve their ability to identify target information and the accuracy of the monitoring model [13].

2. Method

2.1. Image Color Feature Information Extraction. The extraction of image color features is the process of converting image data into digital data. It is the necessary data basis for the diagnosis of pear nitrogen nutrition by using pear canopy image information [14]. The processing process includes two steps: image preprocessing and color feature extraction. Image preprocessing includes image filtering and image segmentation. The extraction flow chart of image feature information is shown in Figure 2.

At present, digital image technology is widely used in crop scientific research, including crop shape information extraction, image segmentation, foreign object recognition, crop identification, nutrition diagnosis, and so on. The color value information of the image should be considered in the process of image processing [15], especially in crop nutrition diagnosis based on image color feature information.

In this study, a unified standard fixed shooting mode was adopted in the process of obtaining pear canopy images. On the one hand, the interference of random factors is inevitable, and the inherent information of pear canopy will be affected by the change of image brightness and the interference of environmental noise; On the other hand, an important step in canopy image processing is to remove irrelevant background information in the image, such as soil and shadow. [16]. Therefore, preprocessing the original image obtained in the field is a very important link in the application research of digital image technology.

By selecting an appropriate threshold limit T, the target image and the background image are divided into two different threshold intervals. When the threshold of image pixel $f(x, y) \leq T$, the point is defined as the target area point, and when the threshold $f(x, y) > T$, the point is defined as the background area point. The calculation formula can be expressed as:

$$
\begin{aligned}
T(x, y) &= 1, \quad f(x, y) \leq T, \\
T(x, y) &= 0, \quad f(x, y) \leq T.
\end{aligned}
\tag{1}
$$

Among them, the set of $T(x, y) = 1$ is the target image area, and the set of $T(x, y) = 0$ is the background image area.

In this paper, the segmentation object contains green leaves, shadows, soil, withered grass, and a sun plate. The final research object is the green leaves, and the gray value difference between the leaves and the background is obvious, so the threshold segmentation method based on gray value is adopted. The image segmentation processing flow is shown in Figure 3.

Otsu method is used to calculate the segmentation threshold, which can be realized by the graythresh operation of its own function in the MATLAB software function library. Through the formula analysis of a high discrete probability density function, as shown in the following formulas:

$$
p_r(r_q) = \frac{n_q}{n},
\tag{2}
$$

$$
q = 0, 1, 2, \ldots, L - 1,
\tag{3}
$$

in the formula, n is the total number of pixels in the image, n_q is the number of pixels with gray level r_q, and L is all gray levels in the image. Suppose we set a threshold value k, C_O is a group of pixels with gray level $[0, 1, \ldots, k - 1']$, and C_1 is a group of pixels with gray level $[k, k + 1, \ldots, L - 1]$. The Otsu

FIGURE 2: Flow chart of image color feature information extraction.

FIGURE 3: Flow chart of image segmentation.

2.2. Hyperspectral Vegetation Index. A vegetation index is a combination of spectral data in different bands, which can reflect crop growth and can be used to estimate a series of biophysical and biochemical parameters. It has been successfully applied to the estimation of plant nitrogen content, LAI, biomass, and chlorophyll. Vegetation index information can better reflect the plant growth status [17]. Researchers have successfully applied it to the analysis of crop nutrition status. Referring to the previous research results, this study selected some representative vegetation indexes with better application analysis results and processed the data to diagnose the nitrogen nutrition of pear trees.

In order to establish a better correlation between vegetation index and nitrogen, SPSS data analysis software is used to select modeling set data, combined with multiple stepwise regression to establish a multiple linear regression equation. The established multiple stepwise regression equation is as follows:

$$\hat{y} = -5115.844 - 765.20 x_{NDRE} + 128.81 x_{R-M}, \tag{6}$$

where $\hat{y}$ is the nitrogen content; x_y is the data corresponding to the selected vegetation index (λ).

The results show that the combination of multiple stepwise regression can improve the accuracy of nitrogen diagnosis the correlation has been greatly improved and the prediction accuracy of canopy nitrogen content has been greatly improved. Figure 4 shows the verification results of the vegetation index combined with SMLR on the nitrogen content of pear trees in the verification set data [18].

2.3. Migration and Residual Law of Nitrate Nitrogen in Different Soil Layers. In addition to being absorbed by crops, some soil residual nitrogen continues to remain and move in the soil. However, from the dynamics of 0–100 cm soil water during the growth period, with the passage of time, due to the influence of crop water consumption and soil surface evaporation, the overall trend of soil profile water is wavy and gradually depleted [19]. Moreover, due to the water absorption of crop roots, the water depletion of the lower layer is serious, and there is no obvious free water flow through the depth of 100 cm of the soil profile. Therefore, there will be no strong leaching of NO3-N in the crop growth season, and the marked nitrate nitrogen does not migrate out of the root zone with the water mass flow. There were significant differences in the distribution of labeled nitrogen in each layer of the profile after harvest. Both the residual nitrogen in the upper part of the soil profile and the residual nitrogen in the lower part of the soil profile moved downward under the action of soil moisture, and formed a cumulative peak at a certain position. The accumulation peaks of 15 and 45 cm labeled nitrogen of the two pear varieties appeared at 60–80 cm of the soil profile, which was directly related to the two times of irrigation in the rejuvenation period and flowering period, so that the labeled nitrate nitrogen migrated significantly with the water and mass flow [20]. There was almost no accumulation peak of labeled nitrogen in the section at 15 cm after harvest, and the % ndff value of the whole section was very low. The

method selects the closed value k of the maximum interclass variance σ_B^2, and the interclass variance formula is expressed as:

$$\sigma_B^2 = \omega_0 (\mu_0 - \mu_T) + \omega_1 (\mu_1 - \mu_T)^2. \tag{4}$$

The function graythresh finds the threshold of maximizing σ by calculating the histogram of—images. The threshold returns a normalized value between 0.0 and 1.0. The calling syntax of function graythresh is:

$$T = \text{graythresh}(f), \tag{5}$$

where f is the input image and T is the generated threshold.

Figure 4: Verification results of vegetation index combined with SMLR nitrogen prediction value.

accumulation peak of 45 cm labeled nitrogen also appeared at 60–80 cm of the soil section. The CM labeled nitrogen of the two crops did not migrate significantly only diffused downward about 20 cm centered on the labeled area, and the accumulation peak appeared at 80–100 cm of the soil profile. Due to the water absorption of crop roots, the water in the lower layer moves upward, and the residual nitrogen in different marker positions moves upward. 15.45 cm labeled nitrogen moved up to the surface layer in the soil, and the upward distance was 15 cm and 45 cm, respectively. The soil marker nitrogen at the depth of 75 cm moved up to 40 cm and 35 cm. It shows that the deeper the level of residual nitrogen marker, the weaker its redistribution ability in soil and the more concentrated the residue.

3. Experimental Analysis

The experimental site is located in the digital pear garden experimental base of the 16th regiment of the first division in southern Xinjiang, which belongs to a typical temperate continental arid climate. The buried depth of groundwater is 15 m, and the precipitation is mainly distributed from July to August. During the pear test period, the precipitation from October 2017 to September 2019 was 204 mm, which was 86 mm higher than the average precipitation in previous years. The soil of the test site is alluvial tidal soil in the Piedmont Plain [21]. According to the fertility classification standard of Southern Xinjiang, the test site belongs to high fertility soil.

3.1. Experimental Scheme.
The experiment was designed with multiple factors. The main treatment is the marking position, and three ^{15}N marking positions are set, that is, 45, 75, and 105 cm away from the surface. The by-treatment is crop species and varieties, namely pear trees, including 2 varieties of pear trees. There were 9 treatments in total, and each treatment was repeated 3 times. The microarea is 1 m × 1 m and the interval between cells is 1 m to prevent

mutual influence between cells. Because the crops planted in the previous seasons of the test plot are consistent with the fertilization and other factors, the test microarea is small, so the square gradient of the soil will not be considered. The field experiment arrangement adopts crop species or varieties as the district group. There are 3 ^{15}N marker positions in the district group, for a total of 9 microareas, which are randomly arranged [22]. At the same time, a 2 m × 2 m dynamic sampling area of pear trees is set. The crop variety, sowing rate, and fertilization method are the same as those of the ^{15}N microarea, but the ^{15}N mark is not made, and it is also repeated 3 times, for a total of 9 plots.

3.2. Marking Method.
^{15}N in the treatment microarea 15 cm away from the ground surface, drill 4 holes vertically between the crop rows with a soil drill to 15 cm of the soil layer, place a PVC pipe with an inner diameter of 0.5 cm and a length of 15 cm in each hole, inject 4156 g potassium nitrate dissolved in 10 ml water into it, and then rinse the appliance with 40 ml water for 4 times. Then backfill and compact the soil in the soil drill according to the original state, and mark the injection position with a marker post. The ^{15}N marking method of the other two treatment microareas is the same except that the drilling depth is 45 and 75 cm of the soil layer, respectively [23].

The test data were statistically analyzed and analyzed for variance according to ANOVA program (LSD test $p < 0105$) in SAS software (version 6112) and t-test in Excel [24].

3.3. Result Analysis.
With the deepening of ^{15}N marker level, the uptake of ^{15}N marker by aboveground parts of crops decreased significantly, and there were significant differences among the three marker treatments (Tables 1 and 2). It shows that pear trees have a high ability to absorb nitrate nitrogen in soil profile under the experimental conditions. Pear trees have significant differences in the total absorption of soil profiles marker ^{15}N, resulting in very significant differences in the utilization of soil marker nitrogen. The utilization rate of labeled nitrogen in different positions of the soil profile decreased significantly with the deepening of the soil profile depth. The utilization rates of labeled nitrogen at 15, 45, and 75 cm of soil profile were 28.2%, 22.3%, and 16.3%, respectively. The utilization rates of marker nitrogen of pear variety Xiaoyan 54 were 21.8%, 17.4%, and 11.5%, respectively, while those of Jing 4.1 were 21.8%, 11.6% and 7.4%. The difference of crop utilization rate of labeled nitrogen at different positions of soil profile also reached a very significant level ($p < 0.01$), but there was no interaction between crop and labeled position.

Canopy reflectance spectrum can reflect the nonpoint source information of crop population, which has good representativeness. In addition, plant hyperspectral has the characteristics of continuity and precision and has a stronger ability to detect the physical and chemical parameters of the pear canopy. On the basis of previous studies, making full use of hyperspectral parameters such as REPle, MND705, SDR/SDB, and FD742, which are sensitive to chlorophyll and biomass of different vegetation, a hyperspectral model

TABLE 1: ^{15}N absorption and utilization rate of aboveground parts treated with different markers.

N	Utilization (%)	
	Pear	
28.2a	21.8a	21.8a
22.3b	17.4b	11.6b
16.3c	11.5c	7.4c
22.3	16.9	13.6

TABLE 2: Nitrogen uptake and utilization.

Tagged depth	N absorbed dose	
	Small weir 54	411
15	2.80a	2.18a	2.18a
45	2.23b	1.74b	1.16b
75	1.63c	1.15c	0.74c
Mean value	2.22	1.69	1.36

which can well monitor the nitrogen nutrition status of pear leaves in the later stage of jointing and filling was established. The model test results show that the model can eliminate or reduce the impact of different nitrogen levels, varieties, growth periods, and differences between different years on the model estimation, has good accuracy and universality, and has important application value in pear nitrogen monitoring and diagnosis [25]. In order to solve the shortcomings of the prediction model of protein content based on plant nitrogen nutrition and the method of inferring protein content by leaf color card, a prediction model that can really calculate protein content quickly and accurately without damage is constructed. In this study, the protein content prediction model based on plant nitrogen nutrition with a strong agronomic mechanism and the plant nitrogen nutrition monitoring model based on hyperspectral remote sensing with physical principles were linked, and the prediction model of pear grain protein content based on hyperspectral characteristic parameters was established. The prediction error was about 8%, and the results were accurate and reliable.

4. Conclusion

Based on the ground hyperspectral remote sensing and digital image information, this paper studies the nitrogen diagnosis methods of pear trees, analyzes the research progress of crop nitrogen nutrition diagnosis at home and abroad, and, combined with the characteristics of digital image data and visible near-infrared spectrum data collected in the field experiment in this study, establishes a pear nitrogen diagnosis model based on visible near-infrared spectrum and digital image information, so as to further establish a complete field pear nitrogen fertilizer recommendation system. Nitrogen is an important component of organic nitrogen-containing substances such as amino acids, proteins, nucleic acids, coenzymes, chlorophyll, hormones, vitamins, and alkaloids in plants. It is not only the structural material of cells but also the basis of material metabolism. Its content directly affects the growth and development process of fruit trees and the formation and quality of fruits. Therefore, it is of great significance to accurately grasp the nitrogen content in soil and leaves through nutritional diagnosis.

In this study, only one pear variety test sample was studied. Due to the different genetic characteristics of each pear variety, the external characteristics of different nutrient supply modes will also be different. At the same time, there are many kinds of nutrient elements that affect the growth of pear trees. The differential supply mode of these nutrient elements will also have a differential impact on the growth of pear trees, and the absorption of one nutrient element will also affect the absorption of another nutrient element. Especially for the changes of pear growth characteristics under different nutritional conditions of nitrogen, phosphorus, and potassium, it is necessary to further study and summarize diagnostic rules and quantitative experience in order to identify nutrition more accurately.

Data Availability

The data used to support the findings of this study are available from the corresponding author upon request.

Conflicts of Interest

The authors declare that there are no conflicts of interest.

References

[1] E. M. Gorbunova, A. N. Besedina, N. V. Kabychenko, I. V. Batukhtin, and S. M. Petukhova, "Response of water-saturated reservoirs to a dynamic impact based on the data of groundwater-level monitoring by precision measurements," *Izvestiya—Physics of the Solid Earth*, vol. 57, no. 5, pp. 644–658, 2021.

[2] T. Li, Z. Zhu, J. Cui, J. Chen, and H. Wang, "Monitoring of leaf nitrogen content of winter wheat using multi-angle hyperspectral data," *International Journal of Remote Sensing*, vol. 42, no. 12, pp. 4676–4696, 2021.

[3] H.-B. Jiang, H.-X. Li, M.-X. Zhao et al., "Strategies for timing nitrogen fertilization of pear trees based on the distribution, storage, and remobilization of ^{15}N from seasonal application of (^{15}NH$_4$)$_2$SO$_4$," *Journal of Integrative Agriculture*, vol. 19, no. 5, pp. 1340–1353, 2020.

[4] A. Wang, Y. Wang, and Y. Chen, "Hyperspectral image classification based on convolutional neural network and random forest," *Remote Sensing Letters*, vol. 10, no. 11, pp. 1086–1094, 2019.

[5] Y. Cui, H. Wang, and H. Zhu, "Superpixel-based local collaborative sparse unmixing for hyperspectral image," *Journal of Applied Remote Sensing*, vol. 13, no. 1, p. 1, 2019.

[6] G. A. Fricker, J. D. Ventura, J. A. Wolf, M. P. North, F. W. Davis, and J. Franklin, "A convolutional neural network classifier identifies tree species in mixed-conifer forest from hyperspectral imagery," *Remote Sensing*, vol. 11, no. 19, p. 2326, 2019.

[7] A. Marcinkowska-Ochtyra, K. Gryguc, A. Ochtyra, D. Kopeć, A. Jarocińska, and Ł. Sławik, "Multitemporal hyperspectral data fusion with topographic indices-improving classification of natura 2000 grassland habitats," *Remote Sensing*, vol. 11, no. 19, p. 2264, 2019.

Retraction

Retracted: Experimental Study on Compressive Strength of Ultrahigh Performance Concrete Prefabricated Wall Structure

Journal of Chemistry

This article has been retracted by Hindawi following an investigation undertaken by the publisher [1]. This investigation has uncovered evidence of one or more of the following indicators of systematic manipulation of the publication process:

(1) Discrepancies in scope

(2) Discrepancies in the description of the research reported

(3) Discrepancies between the availability of data and the research described

(4) Inappropriate citations

(5) Incoherent, meaningless and/or irrelevant content included in the article

(6) Peer-review manipulation

The presence of these indicators undermines our confidence in the integrity of the article's content and we cannot, therefore, vouch for its reliability. Please note that this notice is intended solely to alert readers that the content of this article is unreliable. We have not investigated whether authors were aware of or involved in the systematic manipulation of the publication process.

Wiley and Hindawi regrets that the usual quality checks did not identify these issues before publication and have since put additional measures in place to safeguard research integrity.

We wish to credit our own Research Integrity and Research Publishing teams and anonymous and named external researchers and research integrity experts for contributing to this investigation.

The corresponding author, as the representative of all authors, has been given the opportunity to register their agreement or disagreement to this retraction. We have kept a record of any response received.

References

[1] J. Cao, Y. Dai, L. Hu, Y. luo, F. Long, and S. Ding, "Experimental Study on Compressive Strength of Ultrahigh Performance Concrete Prefabricated Wall Structure," *Journal of Chemistry*, vol. 2022, Article ID 3380144, 7 pages, 2022.

Research Article

Experimental Study on Compressive Strength of Ultrahigh Performance Concrete Prefabricated Wall Structure

Jianfeng Cao ,[1] Yunfei Dai ,[1] Liqiang Hu ,[1] Yu luo ,[1] Fang Long ,[1] and Shiying Ding [2]

[1]*Guangxi Xinfazhan Communications Group Co. Ltd., Nanning 530000, Guangxi, China*
[2]*Guangxi Road and Bridge Engineering Group Co. Ltd., Nanning 530000, Guangxi, China*

Correspondence should be addressed to Liqiang Hu; 1400440530@xs.hnit.edu.cn

In order to study the influence of two parameters, height-thickness ratio and reinforcement ratio, on the compressive performance of prefabricated recycled concrete block-filled core walls, the author proposes a test method for the compressive strength of wall structures. In this method, 9 walls of dry and full-fill masonry are used, and the test measuring device and the arrangement of measuring points are designed to carry out the loading test. The results showed that reinforcement can significantly improve the axial compressive bearing capacity of the wall, but the out-of-plane displacement of the unreinforced wall is smaller than that of the reinforced wall. The larger the height-to-thickness ratio, the better the ductility of the reinforced core wall; the measured value of the axial compressive bearing capacity of the core-filled wall and the mean and coefficient of variation of the ratio to the standard calculated value were 1.49 and 0.13, respectively. The measured value is 34% to 68% higher than the standard calculated value. In conclusion, based on the test data and GB 50003–2011 "Code for Design of Masonry Structures," the theoretical calculation formula of the compressive bearing capacity of the prefabricated recycled concrete block-filled core wall is given.

1. Introduction

Since the 1920s, prefabricated buildings have become an important direction for the construction industry. In the 1960s, Britain, France, the Soviet Union, and other countries began to study and build prefabricated buildings. Since then, prefabricated buildings have developed rapidly and have been promoted around the world. Since 2015, my country has comprehensively promoted prefabricated buildings across the country, and there have been breakthroughs in recent years [1]. Prefabricated wall is an important part of prefabricated buildings, and it is widely used in prefabricated single buildings and fences. The prefabricated wall refers to the parts of the wall that are prefabricated by the factory and wall form for uniform installation at the construction site (Figure 1). The prefabricated wall is mainly constructed in the form of dry work, which has the advantages of short construction period, high efficiency, less labor, simple assembly, low manufacturing cost, and disassembly and reuse [2], it has a wide range of application prospects and has been

widely explored at home and abroad, and many experiences are worth learning from.

At present, most of the rural houses in my country are mainly built by farmers, and there are many problems such as lack of effective earthquake resistance measures, uneven construction quality, and poor thermal insulation function. The prefabricated concrete structure has the advantages of low energy consumption, easy quality control, fast construction speed, good construction site environment, and less shrinkage cracks. To this end, the use of prefabricated concrete structures to build rural houses can effectively improve the construction quality of the house, save energy consumption, speed up construction, reduce construction waste, and fundamentally improve the quality of rural housing.

2. Literature Review

Meng X. et al. designed a precast concrete frame with welded and bolted joints, the low-cycle reciprocating load test was carried out with the cast-in-place concrete frame, and the
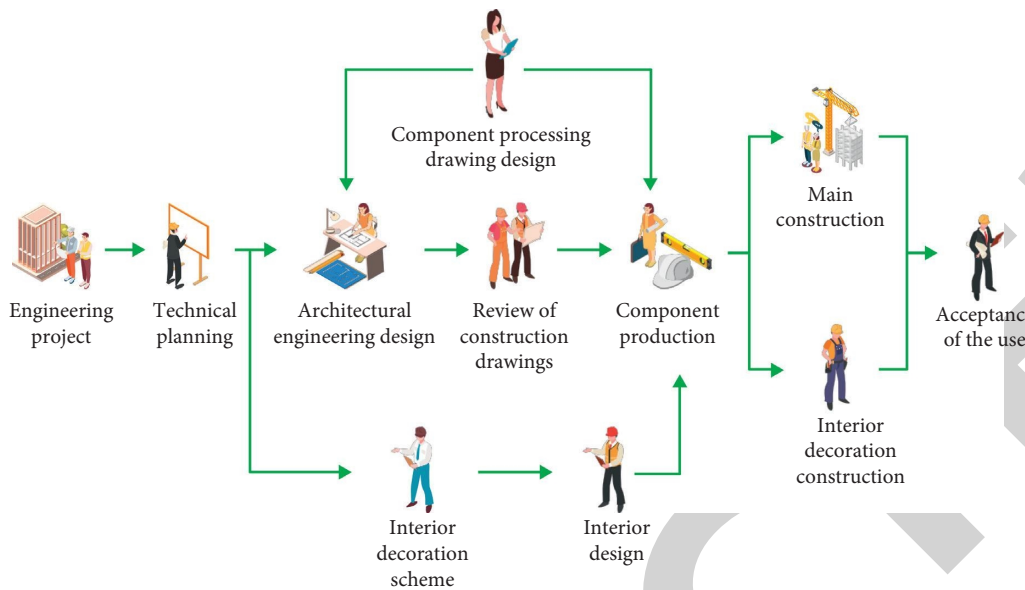
FIGURE 1: Assembly construction process.

responses of different connection types under the same loading mode were compared. It is shown that the improved bolted connection may be suitable for high-intensity areas [3]. Liu R. et al. conducted a low-cycle reciprocating loading test on composite plate shear wall specimens and cast-in-place specimens, and the result shows that, compared with the cast-in-place shear wall, the composite plate shear wall is slightly worse in stiffness degradation, and the stiffness degradation of the composite plate shear wall is more serious. Bonding properties between prefabricated wall panels and cast-in-place concrete are an important factor affecting the overall performance of the laminated plate shear wall, and the connection between the surface layers has less influence on it [4]. Jiang A. Q. et al. conducted axial and eccentric compression tests on 6 composite wallboards, combined with finite element analysis [5], and the test results showed that the overall performance of the laminated plate shear wall is better, the prefabricated layers on both sides are coordinated in force, and the bearing capacity increases with the increase of the slenderness ratio. Through the finite element modeling analysis, the bearing capacity formulas of the axial compression and eccentric compression of the laminated plate shear wall are given. Dai G. through a low-cycle reciprocating loading test study on a multilayer fabricated shear wall with vertical joints [6], considering factors such as horizontal longitudinal bars in vertical joints, shear keys in horizontal joints, and dowel bars in horizontal joints, studied its bearing capacity, stiffness, hysteresis, ductility, energy dissipation. The result showed that the ultimate bearing capacity of the fabricated shear wall specimen is related to the boundary constraints; when the shear key is set in the horizontal joint of the wall specimen, the setting of the dowel bar does not have a large effect on the peak point stiffness. Ding X. studied the finite element modeling of the fabricated shear wall structure and its seismic performance, and the finite element results show that setting vertical joints has little effect on the seismic performance of prefabricated

shear walls. When designing vertical joints, the shear bearing capacity of the vertical joints should be calculated and analyzed [7]. Ismail S. et al. performed quasistatic loading on 4 hollow shear wall specimens connected by inserts, monotonic loading was carried out with two specimens, and extended analysis was carried out in combination with the finite element software ABAQUS. The result showed that the hollow form shear walls with single and double rows of inserted reinforcement meet the seismic requirements, and the seismic performance of the wall with double-row reinforcement is slightly better than that of the wall with single-row reinforcement; when the axial pressure is relatively large, the compression damage area of the wall increases [8].

Among the many studies, there are few studies on the mechanical properties of prefabricated recycled concrete block-filled core walls; therefore, it is of certain significance to study the mechanical properties of prefabricated recycled concrete block-filled core walls under axial compressive loads.

3. Research Methods

3.1. Dry Connection Prefabricated Wall Structure. The prefabricated panel structure by dry connectors (PPSDC) is proposed for rural housing. The structure is composed of prefabricated walls, prefabricated floor slabs, and prefabricated corner columns. For the vertical and horizontal joints of the wall, both are connected dryly, while the upper and lower corner posts are connected by grouting sleeves. There are two types of dry connections, bolted and welded. Due to the regular size and simple structure of prefabricated walls, it has the advantages of standardized design and industrialized production. At the same time, the four corners of the prefabricated floor slab are recessed inward to ensure that the prefabricated corner columns are connected up and down. The prefabricated corner columns are divided into

three cross-section forms, T-shaped, L-shaped, and cross-shaped, set at the intersection of vertical and horizontal walls to ensure the connection between vertical and horizontal walls and strengthen the force at the corners of the structure.

The dry joints of PSDC are divided into two types, vertical joints and horizontal joints, which are arranged in the connection area between the prefabricated components, and the prefabricated components are connected by steel connectors. Steel connectors are divided into two types: bolted connectors and welded connectors. Bolted connectors are composed of ordinary bolts and connecting steel plates, while welded connectors are composed of embedded steel sleeves and connecting steel plates.

3.2. Experimental Design

3.2.1. Test Material. The block used by the author is made by crushing and processing construction waste, and the block strength grade is MU10. The mix ratio of core-filled concrete refers to JC861-2000 "Small Hollow Block Concrete for Concrete," the strength grade of core-filled concrete is C20, the bottom beam and ring beam use ordinary concrete, and the strength class is C30.

3.2.2. Specimen Design and Production. A total of 9 wall specimens were used in the test, all of which were masonry with dry base and full filling [9]. The lowest one-skin block of the core-filled wall uses a sweeping block to simulate the masonry process of such a wall in an actual project. The core-filled wall is built without mortar, layer by layer, and the main masonry process [10, 11] is as follows: (1) Check whether the upper surface of the bottom beam is level with a laser line projection instrument. (2) According to the actual size of the wall, use the template as a corner to ensure the verticality of the wall. (3) During the dry laying of the wall, use a level to level the wide side of the wall. (4) After the 9 pieces of walls are all dry, check and calibrate the verticality of the walls with a laser line projector, and use wood to reinforce the adjacent 3 walls into a whole and restrict each other to prevent the wall from tilting when pouring the core concrete. (5) Consolidate self-compacting concrete with a strength grade of C20 to the wall holes. The height of the surface after the core concrete is poured, it should be about 3 cm lower than the height of the highest skin block of the core-filled wall, and a certain depth should be reserved to make the ring beam concrete and the core-filled wall mesh with each other. (6) After the initial setting of the core-filled concrete, fix the formwork and the holding angle of the ring beam together, and pour the ring beam concrete. (7) After 3 days, the core-filled wall is demolded, its surface is cleaned, and the core-filled wall specimen is masonry completed.

The specific design scheme of the test piece is shown in Table 1.

3.2.3. Test Measuring Device and Measuring Point Arrangement. A total of 6 strain gauges and 7 displacement sensors are arranged on the core-filled wall. Two strain gauges are, respectively, arranged on the two wide sides of the core-filled wall [12], and one strain gauge is arranged on the narrow sides, respectively, for physical alignment of the specimen during preloading. One displacement sensor is arranged at each of the upper, middle, and lower positions of the wide side, used to measure the out-of-plane displacement of the core-filled wall. Two displacement sensors are arranged on the two narrow sides, respectively, 2 displacement sensors inside, used to measure the axial deformation from the first skin block to the highest skin block at the bottom of the core-filled wall, and 2 displacement sensors on the outside, used to measure the axial displacement between the upper surface of the bottom beam and the bearing plate on the press. The wall reinforcement takes one wall as an example, and the odd-numbered skins of the core-filled wall are arranged with transverse reinforcement mesh.

3.2.4. Loading System. The test was carried out on a 20,000 kN press in a structural laboratory. The loading system is continuous loading; before the formal loading, the specimen is preloaded (10% estimated load) for 3 to 5 times; in the early stage of specimen loading, the control method of equipment loading is test force control, and the control loading rate is 2.0 ± 0.5 kN/s; when the load is applied to 70% of the estimated load, the control method of equipment loading is switched to displacement loading [13], the loading rate was maintained at 0.2 ± 0.01 mm/min, and the load increasing rate was not much different from that when the test force was controlled. The specific test steps are carried out in accordance with GB/T 50129–2011 "Standards for Test Methods of Basic Mechanical Properties of Masonry."

4. Analysis of Results

4.1. Destruction Analysis. The stress process of the 9 core-filled walls is basically similar; when the applied load is small, no cracks appear on the surface of the specimen, which is basically in the elastic working stage. When cracks appear in the core-filled wall, the specimen is considered to have entered the failure stage, and the failure process [14] is divided into three stages.

4.1.1. Stage 1. When the load is applied to the initial crack load of the wall, that is, 70% to 85% of the ultimate load, a vertical crack first appears on the upper part of the narrow side of the core-filled wall, there are no obvious cracks on the wide side, and this stage is regarded as the elastic-plastic stage of the core-filled wall.

4.1.2. Stage 2. Continue to load, the axial deformation of the specimen continues to increase, and a second vertical crack appears on the narrow side of the core-filled wall. The two main vertical cracks widened and developed downward. A few vertical cracks appeared at the vertical gray joints on the wide side of the core-filled wall. Explain the stress

TABLE 1: Specimen design scheme.

Specimen number	Number of test pieces (piece)	Dimensions (W × D × H) (mm)	Whether to reinforced	Test content
CW1-S	2	$1018 \times 100 \times 1800$	Yes	Research on the effect of height-thickness ratio on the compressive strength of walls
CW2-S	2	$1008 \times 100 \times 1900$	Yes	
CW3-S	2	$1038 \times 100 \times 2300$	Yes	
CW-4	1	$1028 \times 200 \times 1600$	No	Study on the effect of reinforcement ratio on the compressive strength of the wall
CW-5	1	$1028 \times 200 \times 2000$	No	
CW-6	1	$1028 \times 200 \times 2400$	No	

Note. The specimen number with the letter S is the reinforced wall; otherwise, it is the unreinforced wall.

concentration here. This stage is regarded as the plastic stage of the core-filled wall.

4.1.3. Stage 3. After the applied load reaches the ultimate load, the bearing capacity of the irrigated core wall decreases rapidly, the vertical cracks at the vertical ash joints on the wide side develop rapidly and penetrate the entire block, and the number of vertical cracks increases significantly. The corners of the blocks fall off, and the core-filled wall is brittle and broken. In the stage of decreasing compressive bearing capacity, the 2.4 m height of the irrigated core wall showed the phenomenon of block wall collapse, the block plays a good role in constraining the core column concrete, and the two could work well together.

4.2. Test Results. The 9 pieces of the core-filled wall all show the characteristics of brittle failure; with the increase of the height-to-thickness ratio of the core-filled wall, the axial deformation capacity of the wall increases, and the specific test data are shown in Table 2.

4.3. Wall Compressive Bearing Capacity. The author refers to GB 50003–2011 "Code for Design of Masonry Structures," the formula for calculating the compressive bearing capacity of the normal section of the reinforced block masonry member under axial compression [16], and the formula of the average compressive strength of the masonry; the calculation formula (1) of the axial compressive bearing capacity of the prefabricated recycled concrete block-filled core wall is derived [17]:

$$N = \phi\left(f_{gm}A + 0.8f_y'A_s'\right). \tag{1}$$

Here, $\phi = 1/(1 + 0.001\beta^2)$.

$$f_{gm} = k_1 f_1^\alpha (1 + 0.07 f_2) k_2 + 0.63\delta\rho f_{cu,m}, \tag{2}$$

where N is the axial compressive bearing capacity of the core-filled wall; ϕ is the stability coefficient of the axial compression wall; f_{gm} is the average compressive strength of the perforated block masonry; A is the cross-sectional area of the core-filled wall; f_y' is the average compressive strength of the vertical reinforcement; A_s' is the cross-sectional area of all vertical reinforcement bars; β is the height-to-thickness ratio of the core-filled wall; f_1 is the average compressive strength of the block; α, k_1, and k_2 are all parameters related to the block, concrete block α takes 0.9, k_1 takes 0.46, the test

blocks are mortar-free masonry, so f_2 is taken as 0, and k_2 is taken as 0.8; δ is the porosity of the block [18]; ρ is the porosity of the masonry; $f_{cu,m}$ is the average compressive strength of the porosity concrete cube.

Based on the test data, it is suggested that the formula for the axial compressive bearing capacity of the prefabricated recycled concrete block-filled wall is the following formula (3):

$$N = \phi\left(1.42 f_{gm}A + 0.8f_y'A_s'\right). \tag{3}$$

In the formula, the calculation method of the parameters of ϕ and f_{gm} is the same as formula (1). Using formula (3) to calculate the axial compressive bearing capacity of the wall, the results are shown in Table 2.

It can be seen from Table 2 that the average value of the ratio of the measured value of the axial compressive bearing capacity of the core-filled wall to the calculated value in GB 50003–2011 and the coefficient of variation are 1.49 and 0.13, respectively. The measured value is 34%–68% higher than the calculated value in GB 50003–2011.

It can also be seen from Table 2 that the measured value of the axial compressive bearing capacity of the core-filled wall and the mean and coefficient of variation of the ratios to the values calculated by the proposed formula were 1.06 and 0.13, respectively. It shows that this suggested formula has a certain reference value.

4.4. Wall Load-Displacement Curve. According to the vertical displacement of the wall and the total load of the press measured by the displacement sensor [19], the following can be seen from Figures 2(a) and 2(b): (1) The data in the rising stage of the bearing capacity of the irrigated wall are in good agreement; after the ultimate load, the data are more discrete. The reason may be the brittle failure of the irrigated wall. On the other hand, it may be that the construction quality of the core-filled wall causes data dispersion. (2) Increasing the height-to-thickness ratio of the irrigated wall with steel reinforcements [20], its ductility is improved to a certain extent.

It can be seen from Figure 2(c) that the height-to-thickness ratio is the same, and the axial compressive bearing capacity of the reinforced wall, compared with the unreinforced wall, is increased by 11% to 15%.

4.5. Out-of-Plane Displacement-Load Curves of Walls. Out-of-plane displacement-load curves of 9-piece core-filled walls show the following: (1) As the height-to-thickness ratio

TABLE 2: Wall test results.

Specimen number	(Size) (mm)	Height-to-thickness ratio	(Fcr) (kN)	(Fm) (kN)	(Fn) (kN)	(Fc) (kN)
CW1-S-1	1032 × 200 × 1535	6.7	1400	2018	1874	2748
CW1-S-2	1050 × 200 × 1530	7.8	2150	2872	1974	2848
CW2-S-1	1042 × 200 × 1926	8.7	2520	2934	1945	2850
CW2-S-2	1050 × 200 × 1915	10.3	2300	3282	1945	2830
CW3-S-1	1043 × 200 × 2310	12.6	2900	3068	1866	3599
CW3-S-2	1046 × 200 × 2305	10.6	2040	3234	1766	5799
CW4	1051 × 200 × 1535	7.2	2450	2524	1788	3667
CW5	1039 × 200 × 1930	8.6	2130	2642	1901	2158
CW6	1030 × 200 × 2310	10.6	2560	2795	1819	2441

Note. (1) F_{cr} is the cracking load of the wall; F_m is the test value of the ultimate load of the wall; F_n is the ultimate load value of the wall calculated by the formula of the masonry code [15]; F_c is the theoretical value of the ultimate load of the wall calculated by the proposed formula. (2) The relative limit displacement is the relative displacement of the upper and lower measuring points on the narrow side of the wall under the ultimate load. (3) The compressive strength of the core-filled concrete is the average value of the compressive strength of three 150 mm³ test blocks and the wall specimens after curing under the same conditions, which is about 20 MPa. (4) The block strength is the average compressive strength of the gross cross-sectional area of the five blocks after leveling, 8.54 MPa. (5) The specimen number with the letter S is a reinforced wall; otherwise, it is an unreinforced wall.

(a)

(b)

(c)
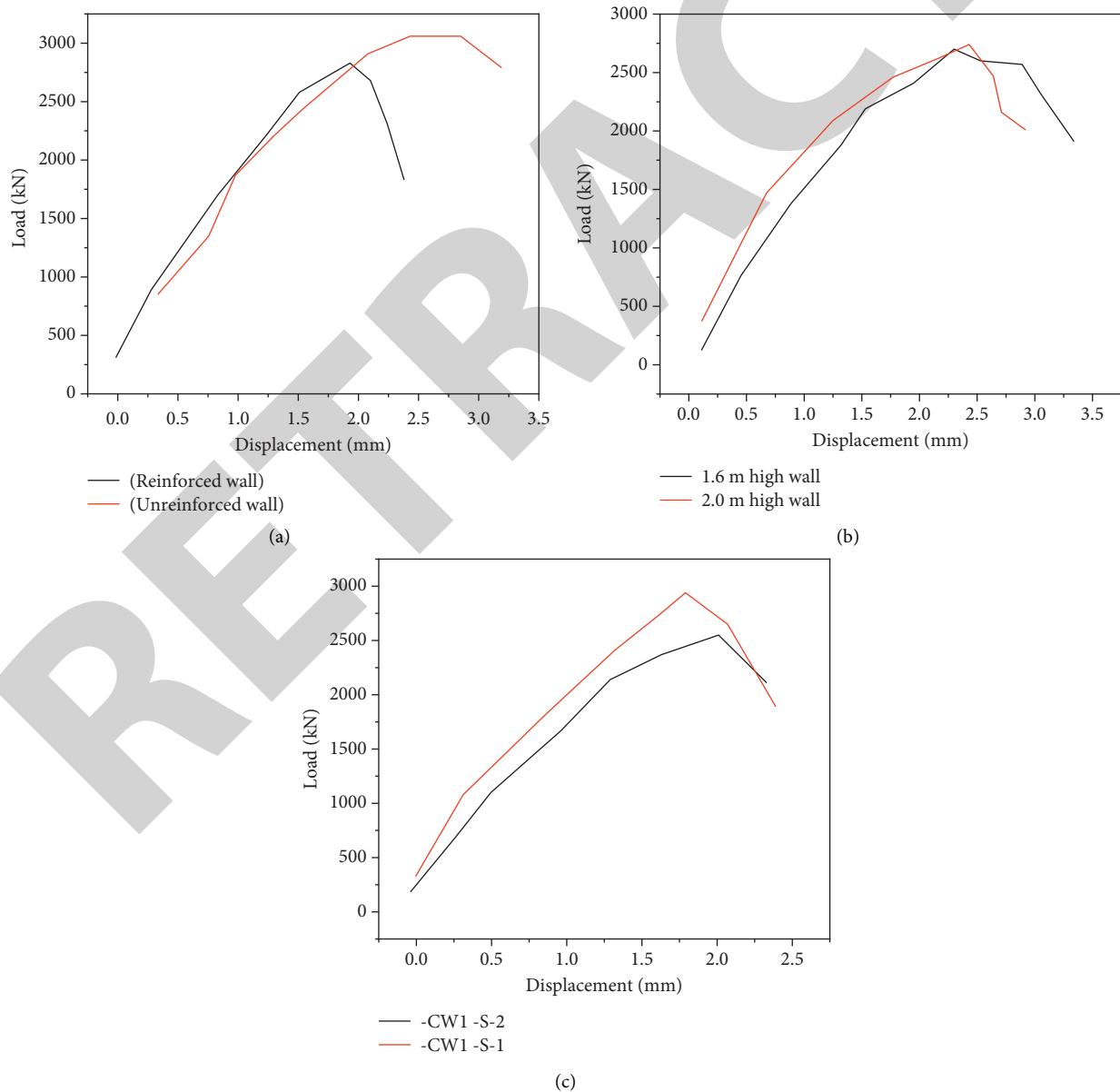
FIGURE 2: Wall load-displacement curve.

of the core-filled wall increases, the maximum out-of-plane displacement of the highest one-skin block under the ultimate load increases. (2) The out-of-plane displacement of the reinforced core wall is larger than that of the unreinforced core wall. (3) There is basically no out-of-plane displacement at the bottom of the core-filled wall, and the ratio of out-of-plane displacements in the middle and upper parts increases nonlinearly. (4) The maximum out-of-plane displacement of the highest skin block of the irrigated core wall is only 5 mm under the ultimate load, and this test is close to the axial compression test.

4.6. Design Principles of PPSDC Ductile Nodes. From the analysis of the above failure mechanism and test results, it can be seen that the failure area of PPSDC is mainly concentrated in the node area at the bottom of the structure, and the failure mode is different from the cast-in-place structure or the equivalent cast-in-place fabricated structure [21]; the existing seismic methods of concrete structures cannot be used for design; therefore, it is necessary to establish the PPSDC calculation theory and ductility design concept based on joint performance.

The results showed that the failure mode of the bolted structure is the punching failure of the concrete around the bolts in the bottom node area. The failure mode of the welded connection structure is the anchor failure of the steel embedded parts at the bottom of the wall. Both failures are dry joint failures and belong to the brittle failure mode, and the realization of the expected ductile failure mode under earthquake action is one of the main factors in ensuring the seismic performance of the structure. Therefore, in order to realize the ductile failure of PPSDC, the plasticity of the connecting steel plate should be fully utilized, ensure punching failure of concrete and anchor failure of steel embedded parts, and not occur before yielding of the connecting steel plates, improving the ductility of dry joints [11].

Therefore, the design principle of ductile joints of PPSDC is proposed as "strong anchorage, strong surrounding, and weak steel plate." The purpose is to take advantage of the good ductility of steel connectors, the connecting steel plate is selected as the main energy-consuming component, and in order to make the failure first occur at the connecting steel plate, the hinge-out sequence, damage degree, and energy-dissipation mechanism of the plastic hinges in different parts of the dry joint area should be controlled properly. In order to ensure that there will be no concrete punching failure in the node area, anchor failure of the steel embedded parts should be avoided. Only by achieving this, the ductile failure mode of the structure can be realized. For bolted connection structures, the punching shear resistance of the concrete in the node area can be enhanced by increasing the minimum end distance and minimum side distance of the bolt holes of the wall panel or using new materials such as high ductility concrete to improve the brittle performance of the node area. For welded connection structures, the connection between anchor bars and steel embedded parts can be improved, such as the use of threaded connections, in order to improve the anchoring capacity of steel embedded parts in the wall.

5. Conclusion

Through the experimental study and analysis of the mechanical properties of the 9-piece prefabricated recycled concrete block-filled wall under axial load, the following conclusions can be drawn:

(1) The axial compression limit load of the reinforced wall is 11% to 15% higher than that of the unreinforced wall; due to the effect of the internal reinforcement of the core-filled wall, the out-of-plane displacement of the highest block of the reinforced wall is larger than that of the unreinforced wall.

(2) Increase the height-to-thickness ratio of the reinforced prefabricated recycled concrete block-filled wall; its ductility is improved to a certain extent.

(3) Based on the suggested formula given in GB 50003–2011 and test data, it can be used to calculate the axial compressive bearing capacity of the prefabricated recycled concrete block-filled wall, and the experimental values are in good agreement with the calculated results.

Data Availability

The data used to support the findings of this study are available from the corresponding author upon request.

Conflicts of Interest

The authors declare that they have no conflicts of interest.

Acknowledgments

References

[1] C. L. Wang, S. Jiang, B. C Li, and S. Li, "Research on mechanical properties of a new fabricated wall material in building with light steel structure," *Materials Science Forum*, vol. 1001, pp. 145–154, 2020.

[2] V. K. Dragunov, A. P. Sliva, A. L. Goncharov et al., "Specific features of electron-beam welding of iter blanket first wall components," *Thermal Engineering*, vol. 67, no. 6, pp. 387–395, 2020.

[3] X. Meng, K. Liu, Z. Li, and L. Sha, "Experimental study on seismic performance of prefabricated beam wall out-of-plane connection nodes with different anchoring measures," *KSCE Journal of Civil Engineering*, vol. 26, no. 2, pp. 770–780, 2021.

[4] R. Liu, H. Huang, Z. Sun, A. Alexander-Katz, and C. A. Ross, "Metallic nanomeshes fabricated by multimechanism directed self-assembly," *ACS Nano*, vol. 15, no. 10, pp. 16266–16276, 2021.

[5] A. Q. Jiang, W. P. Geng, P. Lv, J. W. Hong, and C. S. Hwang, "Ferroelectric domain wall memory with embedded selector realized in linbo3 single crystals integrated on si wafers," *Nature Materials*, pp. 1–7, 2020.

Retraction

Retracted: Application of Visual Communication Combined with Electrochemistry in Ceramic Carving Product Design

Journal of Chemistry

This article has been retracted by Hindawi following an investigation undertaken by the publisher [1]. This investigation has uncovered evidence of one or more of the following indicators of systematic manipulation of the publication process:

(1) Discrepancies in scope

(2) Discrepancies in the description of the research reported

(3) Discrepancies between the availability of data and the research described

(4) Inappropriate citations

(5) Incoherent, meaningless and/or irrelevant content included in the article

(6) Peer-review manipulation

The presence of these indicators undermines our confidence in the integrity of the article's content and we cannot, therefore, vouch for its reliability. Please note that this notice is intended solely to alert readers that the content of this article is unreliable. We have not investigated whether authors were aware of or involved in the systematic manipulation of the publication process.

Wiley and Hindawi regrets that the usual quality checks did not identify these issues before publication and have since put additional measures in place to safeguard research integrity.

We wish to credit our own Research Integrity and Research Publishing teams and anonymous and named external researchers and research integrity experts for contributing to this investigation.

The corresponding author, as the representative of all authors, has been given the opportunity to register their agreement or disagreement to this retraction. We have kept a record of any response received.

References

[1] J. Geng, "Application of Visual Communication Combined with Electrochemistry in Ceramic Carving Product Design," *Journal of Chemistry*, vol. 2022, Article ID 5768966, 7 pages, 2022.

Research Article

Application of Visual Communication Combined with Electrochemistry in Ceramic Carving Product Design

Jian Geng [ID]

Xijing University, Xi'an, Shaanxi 710123, China

Correspondence should be addressed to Jian Geng; 202018000893@hceb.edu.cn

In order to improve the design of ceramic carving products, the author proposes a visual communication, combined with electrochemistry, laser engraving technology, using superpixel imaging technology, carry out laser engraving ceramic reticulation imaging processing, build a binary laser engraving image model, using image edge feature matching method, carry out the edge contour feature detection of the laser engraved ceramic reticulated image, and extract the local information feature quantity of the laser engraved ceramic mesh image. The fuzzy adaptive segmentation method is used for the extracted features and to perform grid area segmentation. The experimental results show that the greater the laser output power, the deeper the engraving depth. As the laser output power increases, the depth of the hole formed by a single pulse laser is enlarged, the etched area formed by the dense hole group also deepens. However, the experiment found that after the laser power is increased to a certain value (17 A), the temperature of the light spot rises sharply, reach the melting point of ceramics, and produce slag that is not easy to remove on the engraved surface, decrease the effective engraving depth. It proves that visual communication, combined with electrochemistry, can effectively realize the design of ceramic carving products.

1. Introduction

Visual communication design is in the continuous development of new media technology, ushered in its own important period of reform. Today's visual communication design has formed a book including book-binding design, printing technology, publicity display, public environment design, digital art design, and comprehensive artistic expression system such as digital photography and videography. This is traditional graphic design, retaining the unique advantages of one's own excellent traditions, and the continuous development of new media technology, the result of mutual learning and fusion [1]. As shown in Figure 1, specifically, in the visual communication design of new media technology, the diversified applications are mainly reflected in.

First, the design tool changes. Traditional visual communication design is mainly drawn by hand. In the design process, paper becomes the main design tool, and in book binding design, painting design, logo design, text design, and

commercial promotion design are the main design content. Also, with the development of digital technology, the visual communication design has changed in the design tools; with the continuous development of digital technology and related software technology, the traditional paper hand-drawn design method, replaced by computer software, specifically, contains digital drawing tools, digital photography image shooting tools, etc. [2]. For example, the well-known Dreamweaver, Photoshop, AutoCAD, etc. are all specific application software for digital drawing in web page drawing, image processing, and industrial drawing. Paperless design has changed the design stage in the past, which required a lot of paper to draw in inefficient working conditions; at the same time, the continuous development of digital photography and camera technology also makes visual communication design gradually moved towards the direction of multidimensional dynamic visual communication [3].

Second, the status of the media has changed. We all know the traditional visual communication design and the degree of dependence on paper makes its dissemination
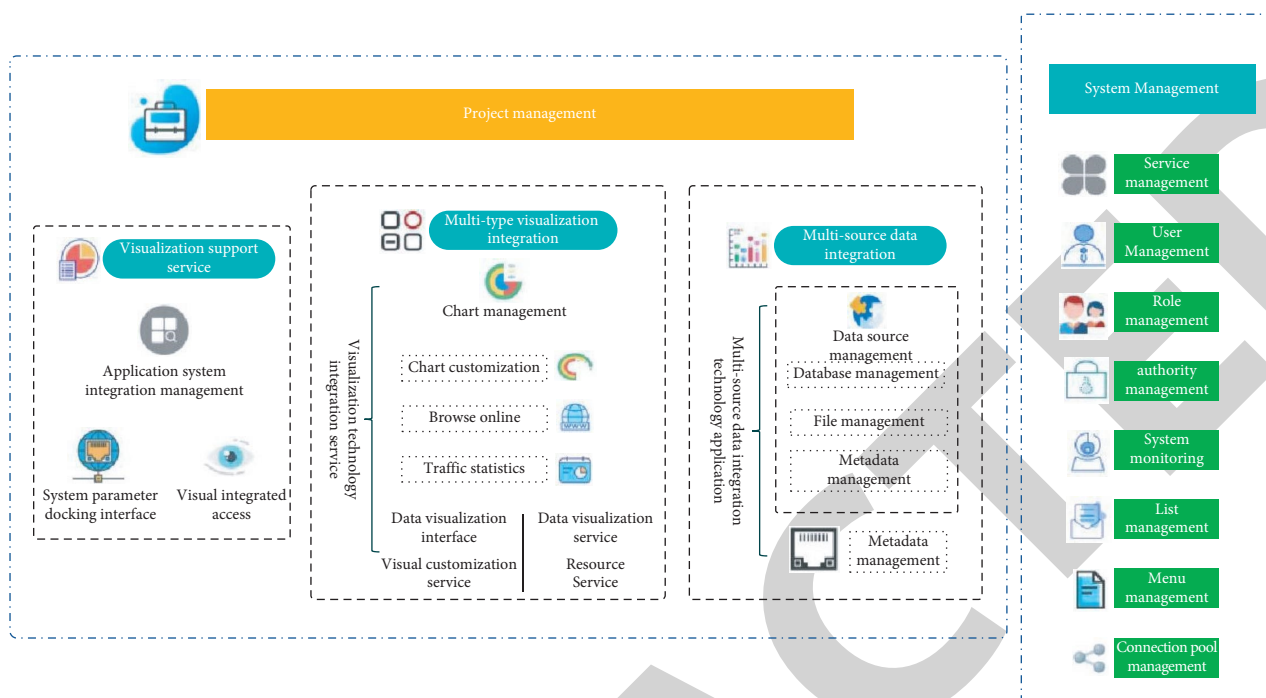
Figure 1: Visual communication combined with electrochemistry.

carrier still stay in the era of printing technology. As a result, printing technology has become an important factor in the development of traditional visual communication design. Product packaging design is also in the innovation of printing technology, an important topic that has been paid attention to by the industry. With the popularity of the Internet and the rise of digital media, in the technological revolution of digital technology, visual communication design under the impact of digital control technology and a variety of digital communication media have also emerged at the historic moment [4]. The new media can realize the visual transmission effect of pictures, texts, characters, and sounds; at the same time, the characteristics and advantages of the times displayed by the new media also makes digital technology in the field of visual communication design much favored; at the same time, the continuous development of digital control technology has also had a wide-ranging impact in the printing industry. Therefore, under the background of the sudden emergence of new media and the integration of new and old media, the status of the media of visual communication design has quietly changed [5].

2. Literature Review

Zheng, with the help of visual symbols, transferred and used information resources. In this process, the use of technology plays an important role. With the continuous improvement of the level of social science and technology, multimedia technology has been well developed and applied to visual communication design. With the effective combination of the two, the quality and efficiency of visual communication design have been improved to a certain extent [6]. Liu et al. proposed that multimedia technology has a visual guidance

function, can promote the memory of the audience, and facilitate the refinement and screening of useful information by the audience. Multimedia technology not only to a certain extent promote the prosperity and development of art but also provides a platform for the inheritance of traditional art [7]. Yang et al. stated that in the context of the development of the era of integrated media, multimedia technology is widely used in visual communication design. It not only improves the quality of visual communication design but also promotes the innovative development of visual communication design. Applying multimedia technology to visual communication design [8], Yan combined Sketchup, Auto-CAD, and other software for laser engraving, performed 3D modeling of ceramic reticulated defects, used association matching and template detection methods, and carried out the detection of ceramic reticulation defects in laser engraving [9]. Corrales-Garcia et al. proposed a laser engraving based on differential scanning of key points, ceramic reticulation defect detection, and positioning method, used infrared feature scanning and holographic projection technology, performed image segmentation and scanning of ceramic anilox defects in laser engraving, improved the defect detection ability. This method is not good for the detection performance of small defects [10]. Bera et al. proposed a differential scan based on moving frames, adaptive compensation laser engraving, and ceramic reticulation defect detection method. This method uses block technology, in order to achieve the reconstruction of the three-dimensional contour and the matching of the image template; however, during the detection process of this method, there is a problem of weak adaptive repair ability [2]. Choi et al. used lasers to perform complex forming and processing of ceramics, and it has always been a difficult point in laser processing [11]. Liao et al., using laser technology and

processing microtexture on the surface of aluminum substrate, successfully manufactured a low-adhesion double sparse surface, with excellent performance in anti-icing and self-cleaning [12]. Bourdonnec et al., using lasers, on the surface of polydimethylsiloxane, successfully prepared a superhydrophobic surface imitating reed leaves [13]. Ladeesh and Manu used laser engraving, on the surface of composite insulator silicone rubber, processing various textures, and the effect of texture shape, spacing and depth on hydrophobicity is obtained [14].

Based on the current research, we propose a laser engraving based on Harris corner detection and automatic detection method of ceramic reticulation defects, using superpixel imaging technology, and carry out laser engraving ceramic reticulation imaging processing and build a binary laser engraving image model, by extracting the feature vector, combined with fuzzy adaptive segmentation method. The segmentation of the grid area is realized.

3. Image Collection and Feature Preprocessing of Ceramic Reticulated Defects in Laser Engraving

3.1. Laser-Engraved Ceramic Reticulation Image Collection. In order to realize the detection of ceramic anilox defects in laser engraving, combining image restoration and 3D multimedia reconstruction methods, and realize laser engraving defect detection and positioning, the first step is to use the ray-casting image feature scanning method, construct 3D multimedia contours of defect images, realize the image collection of ceramic reticulated defects in laser engraving, use the image space scanning method of ceramic reticulated defects in laser engraving (common ones such as cell projection and splatting), use the feature scanning method to extract brightness features and texture features according to the feature extraction results, carry out automatic detection of defective parts based on the difference of the brightness feature to the moving frame of the superpixel, and perform template registration, thereby improving the detection ability of ceramic reticulation defects in laser engraving [15].

Assuming that the local noise reduction domain near each point in the image is Ω, engraving ceramic mesh image $I(x, y)$ on grayscale laser, use dividing line C to divide into two areas R_1 and R_2. The total number of blocks on both sides of the target boundary of the image is K. Using the GMM Gaussian Mixture Model, describe the marking process of laser-engraved ceramic mesh image pixels. The imaging output of the laser-engraved ceramic mesh image is

$$\frac{\partial u(x, y; t)}{\partial t} = \frac{\partial^2 u(x, y; t)}{\partial \xi^2} + c^2 \frac{\partial^2 u(x, y; t)}{\partial \eta^2}. \quad (1)$$

Relying on the neighborhood segmentation curve for pixel feature matching, the texture subspace of the superpixel laser-engraved ceramic mesh image is expressed as

$$\begin{bmatrix} x \\ y \end{bmatrix} = \begin{bmatrix} \cos\theta & -\sin\theta \\ \sin\theta & \cos\theta \end{bmatrix} \begin{bmatrix} \xi \\ \eta \end{bmatrix}. \quad (2)$$

In the above formula,

$$\theta = \arctan\left(\frac{\dfrac{\partial u}{\partial y}}{\dfrac{\partial u}{\partial x}}\right). \quad (3)$$

By presetting the correlation K, in the laser engraving, the sparse linear equations for matching the image template of the ceramic anilox defect image are as follows:

$$g(x, y) = h(x, y) \times f(x, y) + \eta(x, y). \quad (4)$$

In formula (4), $h(x, y)$ represents the parallax function of the ceramic reticulated defect, and $\times$ represents convolution. Using the edge detection algorithm to realize image information fusion, we get

$$c = \sqrt{\exp\left[-\frac{1}{K} |\nabla u(x, y; t)|\right]}. \quad (5)$$

In order to realize the region merging after superpixel segmentation, the laser-engraved ceramic mesh image area is divided into various sub-blocks. The scale of the sub-block is M, and M-1 iterations are performed. The iterative formula for saliency superpixel discrimination is as follows:

$$d_{i+1} = 2F\left(x_{i+1} + \frac{1}{2}, y_i + 2\right)$$
$$= \begin{cases} 2\left[\Delta x(y_i + 2) - \Delta y\left(x_{i,r} + \dfrac{1}{2} - \Delta xB\right)\right], & d_i \le 0, \\ 2\left[\Delta x(y_i + 2) - \Delta y\left(x_{i,r} + \dfrac{1}{2} - \Delta xB\right)\right], & d_i > 0. \end{cases} \quad (6)$$

Calculated in the laser engraving under texture mapping transformation and chromatic aberration, the difference pixel value of the image feature extraction of ceramic anilox defect was obtained and then get the laser engraving. The estimated value of the edge pixel of the ceramic reticulation defect is

$$\hat{f}(x, y) = \beta F(x, y) + (1 - \beta)m_l + \delta_l^2. \quad (7)$$

The strong texture concentration of laser-engraved anilox defect image was calculated. (x, y) represents the scanning point, $F(x, y)$ represents the pixel value, δ_l^2 represents the local variance, and m_l represents the weak texture set of the defect location [16].

3.2. Image Edge Contour Feature Detection. Based on template matching and image block processing, through the realization of image training samples, the main feature vector space is constructed. In the process of image laser engraving and image reconstruction processing of ceramic reticulation defects, establish the local gradient energy distribution function of ceramic reticulated defects as follows:

$$x_{i,d}^{k+1} = \begin{cases} 1, & \rho_{i,d}^{k+1} \le \text{sig}\left(v_{i,d}^{k+1}\right), \\ 0, & \rho_{i,d}^{k+1} \le \text{sig}\left(v_{i,d}^{k+1}\right). \end{cases} \tag{8}$$

In the above formula, $\rho_{i,d}^{k+1} \in [0, 1]$ is a geometric feature, $\text{sig}(\cdot)$ is the Sig-moid function. Use metrics to control superpixels denoted as $C = \{(x, y) \in \Omega: \phi(x, y) = 0\}$ and get the brightness characteristics of the image:

$$\text{sig}\left(v_{i,d}^{k+1}\right) = \frac{1}{1 + e^{-v_{i,d}^{k+1}}}. \tag{9}$$

Use pixel i as the base point to achieve image segmentation. The scope is carried out in the affine invariant area of the image. Suppose the geometric feature vectors $e_1, e_2, \ldots, e_l$, of the first l laser-engraved ceramic mesh image. In the overlapping area, the iterative equation of the image reconstruction error in the holographic projection area is as follows:

$$v_{i,d}^{k+1} = w \cdot v_{i,d}^k + c_1 \cdot \text{rand}() \cdot \left(c_3 \cdot \text{rand}() \cdot p\text{best}_{i,d}^k - x_{i,d}^k\right) \\ + c_2 \cdot \text{rand}() \cdot \left(c_2 \cdot \text{rand}() \cdot g\text{best}_d^k - x_{i,d}^k\right). \tag{10}$$

Among them, $c_3 \cdot \text{rand}()$ and $c_4 \cdot \text{rand}()$ are called the Harris corners of the reticulated image, and the expression is

$$c_3 \cdot \text{rand}() = \begin{cases} 1, & e_p > e_{0p}, \\ c_3 \cdot \text{rand}(), & e_p \le e_{0p}, \end{cases} \\ c_4 \cdot \text{rand}() = \begin{cases} 1, & e_g > e_{0g}, \\ c_4 \cdot \text{rand}(), & e_g \le e_{0g}. \end{cases} \tag{11}$$

$x_{ij} \in [x_{\min}, x_{\max}]$ and $\overline{X}_i = (\overline{x}_{i1}, \overline{x}_{i2}, \ldots, \overline{x}_{ij}, \overline{x}_{iD})$ are called the difference feature of image edge contour feature detection [17]. For the gray sample set (x_i, y_i) of the image of the ceramic anilox defect in laser engraving, use x_i for input and y_i for corresponding output. In the laser engraving, the characteristic distribution function of ceramic reticulated defects is

$$f(x) = w^T \phi(x) + b. \tag{12}$$

In the formula, W is the image edge contour feature detection and b is the offset. The distance between each pixel point and cluster center was calculated, and the partial detection information of ceramic mesh defect image in laser engraving was obtained according to the similarity of different features [18]. Thus, the image constraint control 3D multimedia reconstruction model is obtained:

$$\min_{w,b,e} J(w, e) = \frac{1}{2} W^T W + \frac{C}{2} \sum_{i=1}^{n} e_i^2, \\ \text{s.t. } y_i = w^T \phi(x) + b + e_i, \\ i = 1, 2, \ldots, l. \tag{13}$$

In the formula, C is the penalty parameter and e_i is the defect detection error. According to the above analysis, the template matching and 3D multimedia edge contour segmentation are carried out by using the block technique, and the feature location of ceramic reticular defect in laser engraving is carried out according to the regional sample attributes of 3D multimedia contour [19].

4. Experimental Results and Analysis

Under the condition that the laser scanning speed is 25 mm/s and the repetition frequency is 2 kHz, the relationship curve of the influence of laser power (characterized by current, the same below) on the depth of engraving, is shown in Figure 2. The results show, the greater the laser output power, the deeper the engraving depth. With the increase of laser output power, the depth of the hole formed by a single pulse laser increases and the etched area formed by dense hole groups also deepens. However, the experiment found that after the laser power is increased to a certain value (17 A), the temperature of the light spot rises sharply, when the melting point of ceramics is reached, and slag that is not easy to be removed is generated on the engraving surface, which reduces the effective engraving depth [20].

As shown in Figure 3, under the conditions of a laser power of 12 A and a repetition frequency of 2 kHz, the law of engraving depth changes with the laser scanning speed. As can be seen, if the laser scanning speed is too large or too small, the engraving depth will be reduced; only when the scanning speed is moderate (15 mn/s at this time), the engraving depth increases significantly. If the laser repetition frequency remains the same, increasing the scanning speed will cause the overlap of the laser spot to decrease, and the engraving depth will decrease significantly [21]. Too small scan speed will cause unit time, the laser energy received by the engraving surface increases, and slag is produced, which also reduces the depth of engraving [22]. Under the condition that the laser scanning speed is 25 m-n/s and the laser power is 12 A, engraving depth and the relationship with the change of laser pulse repetition frequency is shown in Figure 4. The engraving depth increases with the increase of the repetition frequency, after reaching a certain value (2.0 kHz), and the engraving depth began to show a downward trend. Increase in repetition frequency means that the energy received by the carving area at the same time increases and the number of interactions between the laser and the material increases, resulting in partial melting of the ceramic, and slag is generated on the engraving surface, which reduces the effective engraving depth.

On the original ceramic surface and the surface of each texture sample with the best hydrophobic performance, drop $40 \mu L$ droplets, affix the label and serial number for future use. The TEMI880 series humidity temperature programmable controller was used for temperature setting at $-10°C$, and the humidity is 80%. When the temperature in the instrument stabilizes at $(-10 \pm 0.5)°C$, put the samples to be tested in the order of the labels, and start the timing. Observe through the window until the droplet becomes completely white. Take it out and end the timing [23]. When the time is 80 s, the water droplets on the surface of the original ceramics is observed, and ice crystals have begun to appear; however, the water droplets on the surface of the three
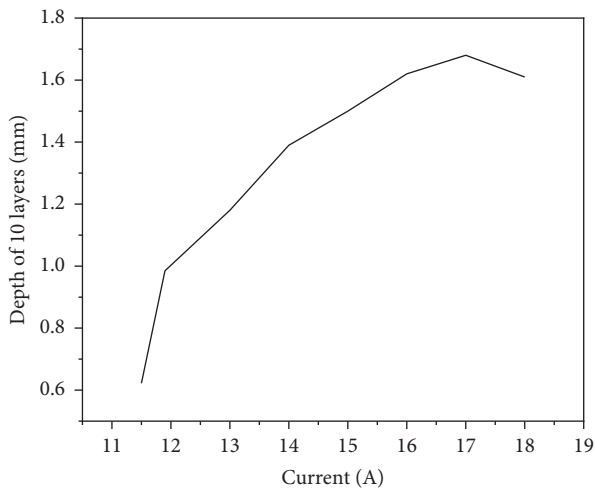
FIGURE 2: The relationship between laser power and engraving depth.
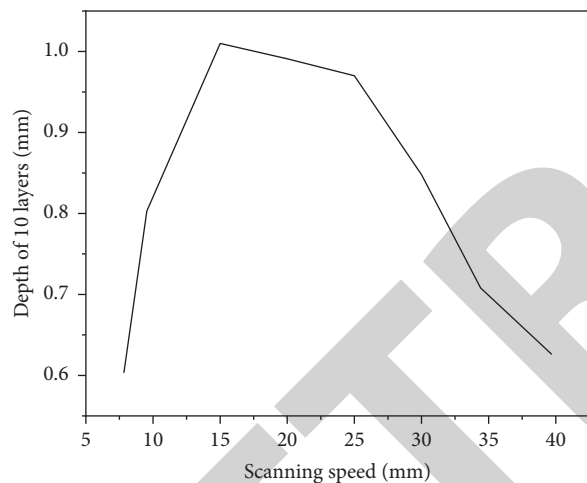
FIGURE 3: The relationship between scanning speed and engraving depth.
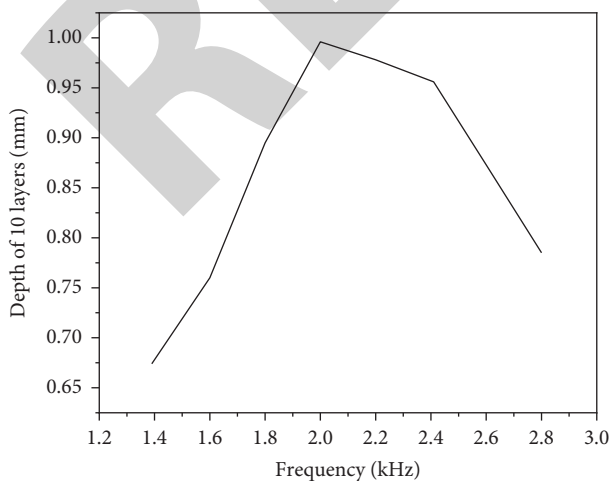
FIGURE 4: The relationship between laser pulse frequency and engraving depth.
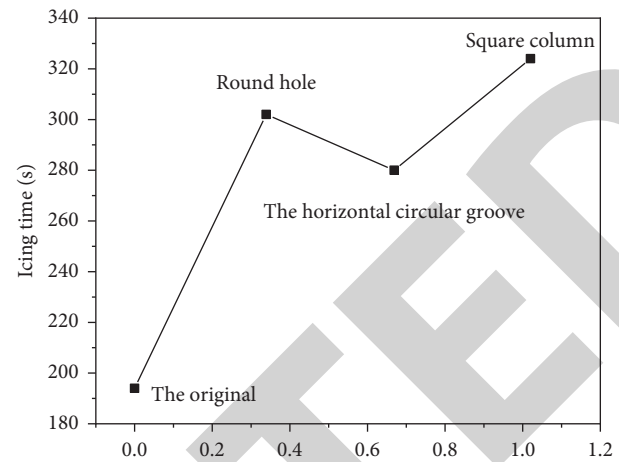
FIGURE 5: Comparison of average freezing time on textured surface.
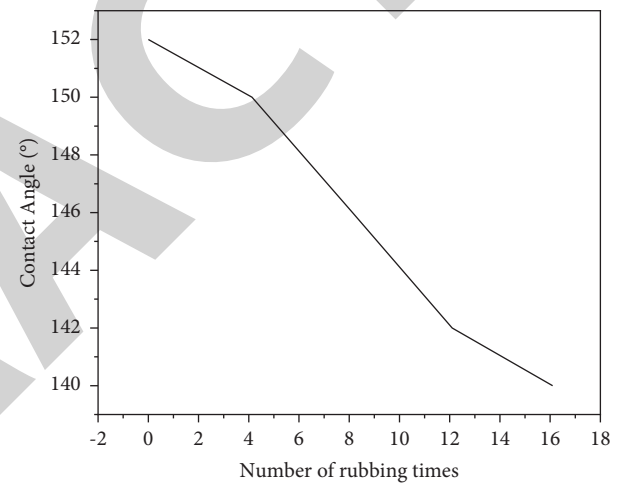
FIGURE 6: The contact angle of the surface of the transverse groove changes with the number of friction.

textures remained unchanged. When the time is 220 s, the water droplets on the textured surface gradually begin to become ice crystals. When the time is 280 s, the water droplets on the surface of the transverse groove texture are completely frozen, and the test results are shown in Figure 5. The results showed that, after the texturing treatment, the anti-icing performance of the sample is obviously improved with delayed freezing time. This is due to the small contact angle of water droplets on the original ceramic surface. The contact area between the two is larger, so the heat transfer speed is faster. The contact angles of water droplets on the textured ceramic surface are all greater than 150°. Reduce the contact area between water droplets and the ceramic surface, delay the heat transfer, and then delay the freezing time.

In order to study the superhydrophobicity of the prepared surface and durability of anti-icing properties, conduct abrasion resistance tests on samples of various types of optimal textures. The author uses an accelerated test method, in order to make the surface friction greater. A weight of 200 g was used to pressurize the sample, and move back and forth on the sandpaper of model number 3000. After moving
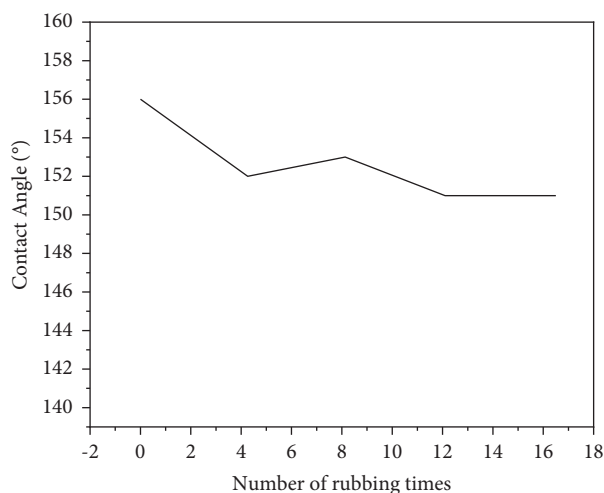
FIGURE 7: The contact angle of the surface of the square column varies with the number of frictions.
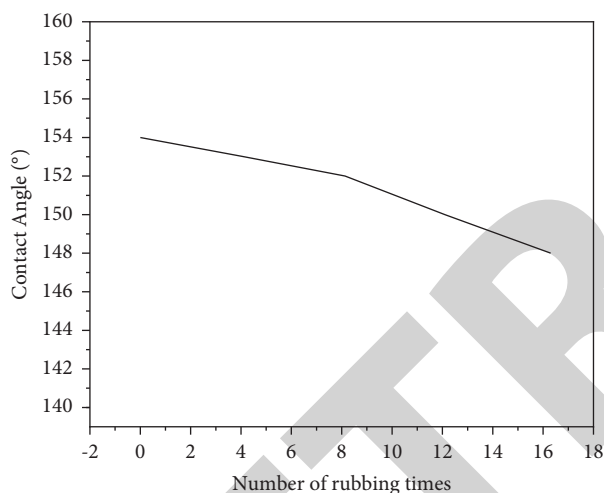
FIGURE 8: The contact angle of the surface of the round hole changes with the number of friction.

15 cm to the right, returning to the original path is a friction. After each rubbing, clean the surface, the contact angle of the test surface [24]. The contact angle and 3-dimensional multimedia topography after 10 times of friction are shown in Figures 6, 7, and 8. The contact angle changes after the friction times are 0, 4, 8, 12, and 16, respectively.

The test results show that as the number of frictions increases, the contact angle of each texture surface decreased slightly but not much. The square column texture surface is within the friction times of the test, still maintaining a super-hydrophobic state; however, when the surface of the transverse groove texture is rubbed more than 12 times, the texture loses its hydrophobicity, and when the round hole texture surface is rubbed more than 16 times, superhydrophobicity is lost.

5. Conclusion

The thickness of single-layer slices must be ensured to be equal to the actual depth of each layer engraved by the laser.

It is the key to the process of laser 3D multimedia engraving. For a selected engraving material, as long as the process parameters are properly selected, under the premise of ensuring the quality of engraving, obtain a precise single-layer engraving depth. Explore the laser engraving depth and the law of changes with process parameters, and establish a mathematical model of engraving, which helps in the experiment, quickly obtain the parameter data that meets the needs of the process, and provide data basis for laser 3D multimedia engraving. The successful engraving of three-dimensional multimedia five-pointed star graphics not only shows that the principle of layered forming can be applied to the field of laser engraving but also provides an industrial verification for the laser 3D multimedia engraving system.

Data Availability

The data used to support the findings of this study are available from the corresponding author upon request.

Conflicts of Interest

The author declares that there are no conflicts of interest.

References

[1] Y. C. Wang, Y. Ma, W. Z. Yu, Y. F. Li, and Y. H. Liu, "Application of the computer assisted virtual reduction combined with 3d printing technique in acetabular fractures," *China Journal of Orthopaedics and Traumatology*, vol. 30, no. 7, pp. 627–632, 2017.

[2] S. Bera, S. N. Sur, and R. Bera, "Multimedia communication using dvb technology over open range," *Procedia Computer Science*, vol. 70, pp. 282–288, 2015.

[3] F. He, "Industrial product graphic design based on visual communication concept," *Acta Technica CSAV (Ceskoslovensk Akademie Ved)*, vol. 62, no. 1, pp. 269–278, 2017.

[4] X. Xi, "Design and manufacture of pe multimedia network courseware under the web environment," *Agro Food Industry Hi-Tech*, vol. 28, no. 1, pp. 1621–1626, 2017.

[5] Q. Zhou, X. Li, K. He, Y. Sheng, and N. Zhang, "Application of intraoperative mri combined with neuronavigation in microsurgical resection for insular glioma," *Journal of Central South University. Medical Sciences*, vol. 43, no. 4, pp. 383–387, 2018.

[6] D. Zheng, "Research on application of computer 3d modeling technology in ceramic tea set design," *Journal of Physics: Conference Series*, vol. 1961, no. 1, Article ID 012058, 2021.

[7] D. Liu, Z. Wu, X. Lin, and R. Ji, "Towards perceptual video cropping with curve fitting," *Multimedia Tools and Applications*, vol. 75, no. 20, pp. 12465–12475, 2016.

[8] Q. Yang, H. Wang, M. Dohler, Y. Wen, and G. Xue, "Guest editorial multimedia communication in the internet of things," *IEEE Internet of Things Journal*, vol. 4, no. 2, pp. 484–486, 2017.

[9] R. Yan, "The rise of multimedia for online communication startups," *IEEE Multimedia*, vol. 22, no. 4, pp. 100–104, 2015.

[10] A. Corrales-Garcia, R. Rodriguez-Sanchez, J. L. Martínez, G. Fernandez-Escribano, and F. J. Quiles, "Multimedia communications using a fast and flexible dvc to h.264/avc/svc transcoder," *Journal of Signal Processing Systems*, vol. 79, no. 3, pp. 211–232, 2015.

[11] J.-H. Choi, U. S Kim, and W.-S. Cho, "Study on ceramic pattern carving by using laser—focused on glaze's melting

Retraction

Retracted: Application of CAD/CAM Technology in Electrochemical Relief Design and Processing of Ceramic Art

Journal of Chemistry

This article has been retracted by Hindawi following an investigation undertaken by the publisher [1]. This investigation has uncovered evidence of one or more of the following indicators of systematic manipulation of the publication process:

(1) Discrepancies in scope

(2) Discrepancies in the description of the research reported

(3) Discrepancies between the availability of data and the research described

(4) Inappropriate citations

(5) Incoherent, meaningless and/or irrelevant content included in the article

(6) Peer-review manipulation

The presence of these indicators undermines our confidence in the integrity of the article's content and we cannot, therefore, vouch for its reliability. Please note that this notice is intended solely to alert readers that the content of this article is unreliable. We have not investigated whether authors were aware of or involved in the systematic manipulation of the publication process.

Wiley and Hindawi regrets that the usual quality checks did not identify these issues before publication and have since put additional measures in place to safeguard research integrity.

We wish to credit our own Research Integrity and Research Publishing teams and anonymous and named external researchers and research integrity experts for contributing to this investigation.

The corresponding author, as the representative of all authors, has been given the opportunity to register their agreement or disagreement to this retraction. We have kept a record of any response received.

References

[1] H. Li, "Application of CAD/CAM Technology in Electrochemical Relief Design and Processing of Ceramic Art," *Journal of Chemistry*, vol. 2022, Article ID 8190143, 6 pages, 2022.

Research Article

Application of CAD/CAM Technology in Electrochemical Relief Design and Processing of Ceramic Art

Hongyan Li [ID]

Office of Educational Administration, Chongqing City Vocational College, Yongchuan, Chongqing 402160, China

Correspondence should be addressed to Hongyan Li; 20160197@ayit.edu.cn

Ceramic relief modeling design and CNC machining programming have a wide range of applications in industrial production and daily life. In view of the actual needs of enterprises, this research studies the CAD simulation technology of ceramic relief and achieves the modeling of other pieces of relief based on the geometric outline of the plane breakthrough. According to geometric relief modeling, bitmap relief modeling, tool path selection, and relief simulation processing, the establishment of a ceramic relief model is realized. Finally, the simulation processing is carried out on the ArtCAM software platform, and reasonable processing parameters are obtained to realize the CNC engraving processing of ceramic relief. The experimental results show that the machining efficiency of the ceramic relief model established in this study is improved by 11.3% and 42.8%, respectively, compared with the two traditional methods, which verifies the correctness and superiority of the designed model.

1. Introduction

Ceramic carving is one of the most important traditional ceramic art decoration techniques. It has a long history in China. Its development process embodies the wisdom and hard work of potters of all dynasties. Aesthetic development track [1]. In recent years, people's living standards have been continuously improved, and the real estate industry has developed rapidly, which has brought about an increase in the demand for ceramic art. Interior decoration crafts, mainly lamps and carved vases, are more and more popular among people. At present, the traditional ceramic engraving method is still in the manual processing stage, and the patterns that can be engraved are relatively simple, which is far from meeting the deep needs of the market [2]. Based on market demand and production needs, the introduction of CAD/CAM technology into ceramic engraving processing and the use of CNC engraving processing technology to replace traditional manual engraving processing methods will greatly improve production efficiency and product quality. Figure 1 shows a typical case designed and manufactured by the CAD/CAM platform [3].

2. Literature Review

Geometric relief is to model a three-dimensional relief surface for a given two-dimensional contour area. This method is widely used in relief design, but there is no certain formula to specify the height value of each point in the contour area. Generate geometric relief for a given graphic, and different engraving softwares have different effects. For example, the relief effect of ArtCAM is smoother than that of Type 3. But the basic principle is to define the point in the area as the ordinate according to a certain rule from the boundary to the center and determine the height value of the point by giving the section line, so as to shape the three-dimensional surface relief model.

At present, a 3D modeling technology based on hand-drawn sketches has been developed in the design field [4, 5], which has a strong reference value for the improvement of geometric relief functions. It is a conceptual design-based modeling approach that models hand-drawn sketches directly. The process is that the user draws a free curve on the screen, and then, the system closes it and quickly calculates a three-dimensional model with this contour line. Some advanced algorithms also support cross-section shape
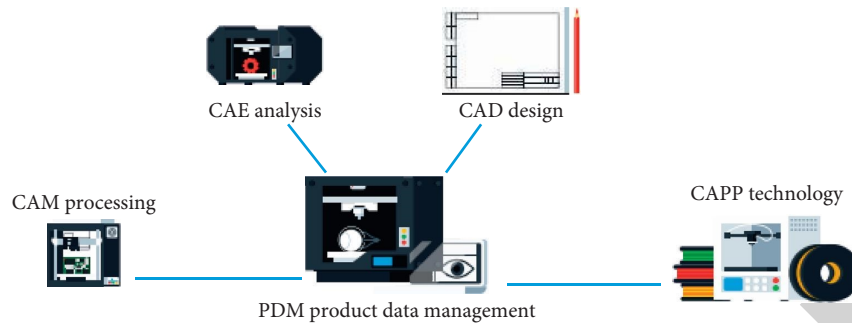
Figure 1: Typical case of CAD/CAM platform design and manufacturing.

modeling, that is, one curve is used as the outline and the other is the cross-section shape for fast 3D modeling. It can be seen that the hand-drawn sketch modeling technology is very similar to the geometric relief technology in principle, but it is more free and open than the geometric relief.

Bitmap relief is also called picture relief or grayscale relief. Its purpose is to obtain a three-dimensional relief model through the three-dimensional information reflected in the picture [6]. Since a picture cannot reflect the complete three-dimensional information, the picture relief is actually based on the picture data, relying on the artistic level of the designer to create a relief model that is artistically expressive but not necessarily accurate in the engineering sense. At present, popular relief software such as TYPE3 and ArtCAM do not provide processing of pictures but only extract grayscale information from pictures, convert them into heights according to the grayscale mapping relationship, and finally generate a 3D model [7]. Bitmap relief designers use the image processing software to process images into grayscale images that reflect three-dimensional shapes, that is, grayscale art images. The relief CAD software directly shapes relief from grayscale art images without making any changes to the three-dimensional information reflected in the grayscale art images. The JDpaint engraving CAD/CAM software developed by Beijing Jingdiao Technology Co., Ltd. is aware of its shortcomings and provides some functions of relief editing, but due to its simple technology, it still cannot change the current bitmap relief design. It is completed on the image processing software for the embarrassing situation [8].

The purpose of relief CNC machining programming is to generate a noninterference tool processing path according to different tool types and according to the cutting strategy proposed by the user and generate processing instructions after postprocessing to control the CNC engraving machine for processing. To realize the relief NC machining programming, the following problems need to be solved [9]: how to represent the relief model in the computer; how to generate the relief model according to the designer's intention; and how to generate an accurate and efficient CNC machining tool path according to the relief model. There is no essential difference between relief CNC machining programming and general CNC machining programming, so there are a lot of literature for reference. Chengdu University of Electronic Science and Technology takes the

relief of the furniture [10] industry as the research object and carries out relief design and processing from the two-dimensional outline. The software is implemented based on the secondary development of AutoCAD and can only generate line-cutting and circular-cutting tool paths for 2D area milling. In the research, it was found that the commercial engraving CAD/CAM software at home and abroad mostly uses discrete facets to represent the relief model. The projection of the vertices of these facets on the XY plane is a regular lattice, so the NC machining programming of the relief can be considered. Drawing on the existing research results, tool path generation technology is based on a discrete point cloud or STL model [11]. British scholar RJ. Cripps [12] analyzed and compared the difference between discrete CAD/CAM systems and analytical CAD/CAM systems and used the inverse tool offset (ITO) method to generate the finishing tool path of discrete point data. Taiwanese scholars AC. Lin [13] and others first established the Z-map representation of the starting point cloud and then carried out rough and fine path planning according to the Z-map model. In order to improve efficiency, the algorithm does not calculate the discrete set of tool position points but adopts some special processing for ball-end tools to avoid overcutting.

On the background of the topic selection, this study refers to a company in Nanjing that has been engaged in the development and sales of engraving machines for a long time [14]. In order to expand the business scale and expand the market, the company hopes to have engraved CAD/CAM software with independent intellectual property rights, so it has established a cooperative relationship with the CAD/CAM Engineering Research Center of Nanjing University of Aeronautics and Astronautics to jointly develop the software. This study participated in this project in the CAD/CAM Engineering Research Center of Nanjing University of Aeronautics and Astronautics and undertook the research of relief CAD/CAM technology and the development of related modules. The software conducts demand analysis and function analysis through detailed demonstration in the system design process. During the development process, experienced senior engineers from the factory were hired as guidance to refine the software functions and make the software conform to the operating habits of the engineers [15]. After the software function module is completed, the software quality is tested in cooperation with the factory

technicians, and the actual processing is carried out on the factory-produced engraving machine using the processing path generated by the software, which verifies the correctness of the algorithm and the practicability of the software.

3. Research Methods

The traditional ceramic carving process, from conception and design to final glazing and firing, is generally completed independently by a single worker. Before engraving, it is necessary to outline a hard pen sketch according to the design requirements, so the pattern can only be relatively simple [16]. The engraving process requires workers and masters to have high manual skills, which will have two impacts: first, the processing process is too affected by human factors, and the product quality is difficult to unify; second, there is a certain degree of inherited personal carving skills. The difficulty of changing the workers will make some products unsustainable. In the whole production process, the two links of engraving and engraving need to take a long time, and ceramic products are easily damaged during the engraving process, which leads to low production efficiency [17].

With the development of engraving CAD/CAM software, relief CAD/CAM technology is generally integrated as an important functional module. Currently, the relief models involved are mainly built through bitmap relief modeling and geometric relief modeling obtained using the modulo technique. The geometric relief modeling studied in this study is the relief surface modeling technology based on plane geometry. The bitmap relief modeling is the relief surface modeling technology based on geometric information and grayscale information, and the modeling of bitmap relief generally uses images first. The processing software preprocesses the picture and then uses the relief CAD software for editing, in order to obtain the perfect relief effect [18].

3.1. Geometric Relief Modeling. Geometric relief modeling refers to the process of constructing a three-dimensional relief from flat geometric figures. A three-dimensional relief model with complex details is often formed by the fusion of several small curved patches, which are called relief surfaces. The relief surface is jointly determined by a two-dimensional region and a cross-section function [19]. Taking the offset t of the equidistant ring as the independent variable and the height value h of the contour line as the function value, there are countless function mapping relationships, and each mapping relationship corresponds to a section function. The algorithm currently supports two types of section functions: linear functions and circular functions. As shown in the figure, the linear function is defined by the abscissa of the transition point and the inclination angle of the straight line in Figure 2; the circular function is defined by the abscissa of the transition point and the central angle of the arc segment, as shown in Figure 3. When the two-dimensional area of the relief surface intersects, the overlapping area can be defined by surface fusion. There are currently eight fusion methods:
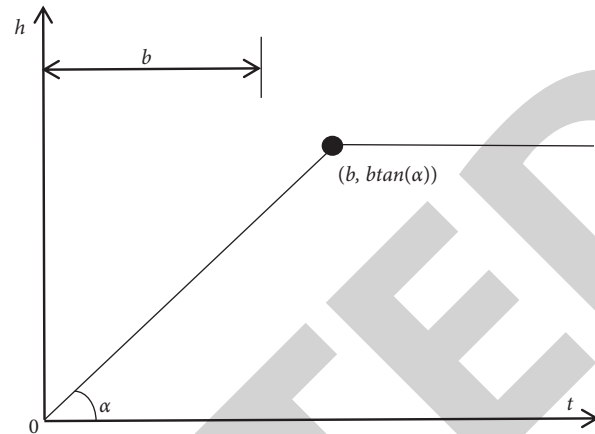
Figure 2: Schematic diagram of cross-section function (linear function).
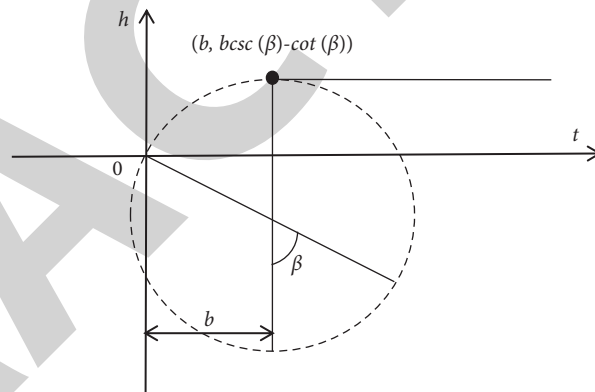
Figure 3: Schematic diagram of cross-section function (circular function).

negative substitution fusion, subtractive fusion, additive fusion, positive substitution fusion, highest fusion, lowest fusion, vector external zero fusion, and zero fusion [20].

By defining the section function and changing the surface blending method, the 3D relief model can be constructed from the plane outline.

3.2. Bitmap Relief Modeling. Bitmap relief modeling refers to reconstructing 3D relief models from bitmap images through a series of special processing. Through various digital image processing techniques (such as grayscale, embossing, filtering, and denoising), ordinary RGB photos are processed into grayscale art images, so that the grayscale information of each pixel in the RGB photo can be converted. For the height information of the relief, the relief model is finally obtained [21].

The empirical formula can make the conversion of a color bitmap to a grayscale image:

$$H_{ij} = 0.299R_{ij} + 0.578G_{ij} + 0.114B_{ij}. \tag{1}$$

Among them, H_{ij} represents the grayscale value of the converted grayscale image; R_{ij}, G_{ij}, and B_{ij} represent the red, green, and blue color components of the pixel in the ith row

and the jth column of the color bitmap; bitmap relief modeling also supports eight fusion functions. Through the fusion of relief surfaces, it is convenient to combine the functions of bitmap relief modeling and geometric relief modeling in the same relief model, thus greatly enriching relief design methods.

4. Result Analysis

4.1. Toolpath Selection. There are two commonly used cutting methods in engraving processing: one is the line-cutting method, that is, the tool is processed along the straight line and the other is the circular cutting method, which is the sequential processing of the tool along the contour [22, 23]. In the process of circular-cutting, since the processing method of the engraving tool is always the same, that is, the cutting state of down milling has been maintained or the cutting state of upcut milling has been maintained, so the engraving processing accuracy of the blank is high, but this algorithm is quite complicated. When the tool path file is generated, it will waste a lot of time; in the process of back and forth cutting, the machining process will alternately show down milling and up milling. Although the processing quality of this processing method is not as good as that of circular cutting, it is not suitable for most parts. Material removal and row cutting have high cutting efficiency, and to a certain extent, this algorithm is very simple. In the CNC engraving of ceramic blanks, the ring cutting method is generally used in the relief engraving of flat ceramic plates; the line cutting method is generally selected in the CNC engraving of ceramic revolving workpieces. If the ring cutting method is used, the processing time is long and the yield is low.

4.2. Embossing Simulation Processing. With the completion of the relief design and the selection of the machining path, the tool path needs to be simulated. The ultimate purpose of machining simulation is to debug a satisfactory and efficient tool path file and finally generate standard machining instruction code [24]. In this study, ArtCAM, which is widely used by the British company Delcam, is used as the embossing simulation software [25]. Before simulation processing, the material setting of the workpiece to be processed is first required, that is, the X, Y, and Z values of the workpiece blank to be processed are set. It should be noted that the X and Y values of the blank must be the same as the size of the established 3D model, and the Z value is set according to the model parameters. In addition, it is necessary to set the Z-axis zero point of the material. The material Z-axis zero point is also called the machining origin, which can be set at the bottom or top of the material blank.

The thickness of the blank chosen in this study is 5 mm, and the Z-axis zero point of the material is at the top. Set the processing parameters; the area to be processed is the set selected vector area; the processing strategy selects parallel processing; the tool is selected as a flat-bottomed tip; the spindle speed is 20000 r/min, the feed rate is 2000 mm/min,
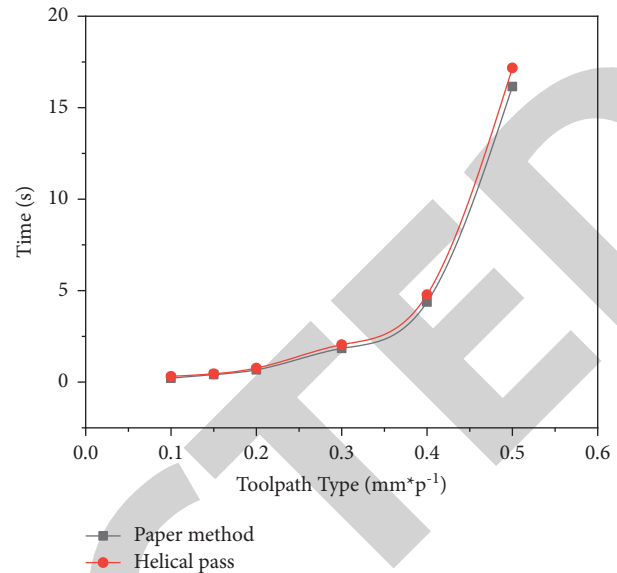
Figure 4: Comparison of processing path calculation efficiency (helical pass).

and the cutting speed is 600 mm/min; the model size is set to 100×1002 mm, and the resolution is 0.5 mm/pixel. The toolpath spacing is to go to 50% coverage. In this experiment, the calculation efficiency of machining paths was observed according to different path types of different tools. The experimental results are shown in Figures 4 and 5.

From the experimental results, the ceramic relief model established in this study is 11.3% and 42.8% higher than the two traditional methods in terms of machining path efficiency. The analysis is as follows: in theory, the calculation of different tool paths is mainly the generation of tool location datasets, so the calculation speed will not have much difference. It can be seen from the test results that the speed variation rules generated by the three machining paths are consistent, and the difference is limited, which is consistent with the theoretical prediction. For the last set of data, the data calculation time can be considered to have exceeded the user's tolerance. As the radius of the flat bottom of the tool increases, in order to avoid overcutting, the embossed details gradually disappear on the tool surface, and with the increase of the machining step, the tool marks on the embossed surface also increase significantly. Therefore, in the processing process, the tool radius should be selected as small as possible, and the step distance should be as small as possible.

For a given relief model, the reciprocating machining path is used to test, and different tools are used, and the calculation efficiency is given in Table 1.

It can be seen from the table that the computational efficiency of the algorithm decreases as the tool diameter increases. One of the main features of this algorithm is that the calculation speed has nothing to do with the complexity of the surface nor with the complexity of the tool shape. Most of the relief surfaces are free and complex surfaces. The diameter of the tools used for relief processing is small, and the shapes of the tools are many shapes with engraving characteristics. Therefore, the relief processing
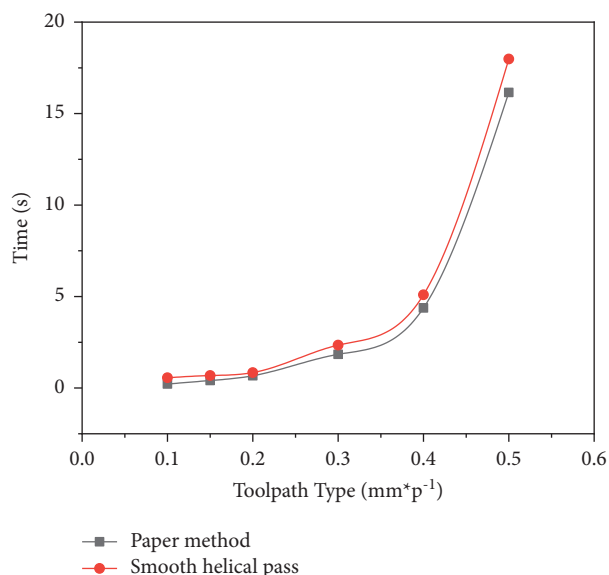
Figure 5: Comparison of processing path calculation efficiency (smooth helical pass).

Table 1: The relationship between calculation efficiency and tool diameter change.

Tool diameter	1 mm	2 mm	4 mm	8 mm	12 mm	16 mm
N_R	2	4	8	16	24	32
Operation time (s)	0.219	0.234	0.453	1.344	2.829	4.969

N_R is the number of points covered by the tool diameter.

programming module introduced in this article is suitable for relief finishing.

5. Conclusion

This study introduces relief CAD/CAM technology into ceramic engraving, which not only improves the efficiency and quality of engraving to a certain extent but also greatly expands the ceramic relief library. Finally, the feasibility of this technology is proved through example processing. The application of this technology fundamentally gets rid of the status quo of the manual engraving operation of ceramic engraving and relieves people from heavy manual labor. At the same time, ceramic engraving products have also been widely promoted.

The rapid development of relief art puts forward higher requirements for relief CAD/CAM software, and the continuous improvement of relief CAD/CAM software can better promote the development of the relief industry. Therefore, combined with the experience in relief research in this study, some work prospects are put forward: (1) learn from the hand-drawn sketch modeling technology and study the geometric relief modeling technology based on free-form curves. Improve the algorithm of smooth relief and improve its computational efficiency. (2) Expand the editing function of relief, such as adding functions, surface transition, and free-form surface fitting for the local modeling technology of relief surfaces. (3) Combined with the current development

characteristics of GPU, further study the hardware acceleration technology of inverted tool based on the Z-Map data model and study the application of programmable GPU in relief modeling, display, and lighting.

Data Availability

The data used to support the findings of this study are available from the corresponding author upon request.

Conflicts of Interest

The authors declare that they have no conflicts of interest.

References

[1] L. Xiong, "Application of computer virtual technology in ceramic packaging design," *Journal of Physics: Conference Series*, vol. 1961, no. 1, Article ID 012057, 2021.

[2] A. Skorulska, P. Piszko, Z. Rybak, M. Szymonowicz, and M. Dobrzyński, "Review on polymer, ceramic and composite materials for cad/cam indirect restorations in dentistry-application, mechanical characteristics and comparison," *Materials*, vol. 14, no. 7, 2021.

[3] J. Chen, "Application of computer 3D modeling technology in ceramic tea set design," in *Proceedings of the 2021 7th International Symposium on Mechatronics and Industrial Informatics (ISMII)*, Zhuhai, China, 2021.

[4] D. Zheng, "Research on application of computer 3D modeling technology in ceramic tea set design," *Journal of Physics: Conference Series*, vol. 1961, no. 1, Article ID 012058, 2021.

[5] J.-C. Durand, P. Slangen, S. Montresor et al., "Behavior of CAD/CAM ceramic veneers under stress: a 3D holographic study," *Journal of the Mechanical Behavior of Biomedical Materials*, vol. 118, no. 27, Article ID 104436, 2021.

[6] R. O. Pilecco, F. Dalla-Nora, L. F. Guilardi et al., "In-lab simulation of CAD/CAM milling of lithium disilicate glass-ceramic specimens: effect on the fatigue behavior of the bonded ceramic," *Journal of the Mechanical Behavior of Biomedical Materials*, vol. 121, Article ID 104604, 2021.

[7] K. Nowosad, M. Sujka, U. Pankiewicz, and R. Kowalski, "The application of PEF technology in food processing and human nutrition," *Journal of Food Science and Technology*, vol. 58, 2021.

[8] M. Embaireeg, "Effect of finish line design on the fit accuracy of CAD/CAM monolithic polymer-infiltrated ceramic-network fixed dental prostheses: an in vitro study," *Polymers*, vol. 13, 2021.

[9] B. Liu, J. Zhao, Y. Liu et al., "Application of high-throughput first-principles calculations in ceramic innovation," *Journal of Materials Science and Technology*, vol. 88, no. 29, 2021.

[10] C. H. Lu, Y. T. Tsai, T. L. Tsai, T. S. Chan, X. Zhang, and C. C. Lin, "Cr 3+-Sphere effect on the whitlockite-type NIR Phosphor Sr 9 Sc(PO 4) 7 with high heat dissipation for digital medical applications," *Inorganic Chemistry*, vol. 61, 2022.

[11] X. Y. Chan, C. Chua, S. Tan, and H. L. Ferrand, "Energy dissipation in composites with hybrid nacre-like helicoidal microstructures," *Composites Part B: Engineering*, vol. 232, 2022.

[12] W. Yanzheng and W. Xiaohong, "Design and application of information system and technology in business management:

Hindawi

Retraction

Retracted: Mechanical Performance Analysis of Steel Beam-Column Joints in Fabricated Multirise Steel Structures after Fire

Journal of Chemistry

This article has been retracted by Hindawi, as publisher, following an investigation undertaken by the publisher [1]. This investigation has uncovered evidence of systematic manipulation of the publication and peer-review process. We cannot, therefore, vouch for the reliability or integrity of this article.

Please note that this notice is intended solely to alert readers that the peer-review process of this article has been compromised.

Wiley and Hindawi regret that the usual quality checks did not identify these issues before publication and have since put additional measures in place to safeguard research integrity.

We wish to credit our Research Integrity and Research Publishing teams and anonymous and named external researchers and research integrity experts for contributing to this investigation.

The corresponding author, as the representative of all authors, has been given the opportunity to register their agreement or disagreement to this retraction. We have kept a record of any response received.

References

[1] F. Liu, X. Wang, B. Cai, X. Li, and L. Yang, "Mechanical Performance Analysis of Steel Beam-Column Joints in Fabricated Multirise Steel Structures after Fire," *Journal of Chemistry*, vol. 2022, Article ID 7425801, 8 pages, 2022.

Research Article

Mechanical Performance Analysis of Steel Beam-Column Joints in Fabricated Multirise Steel Structures after Fire

Fang Liu [iD],[1,2] Xiuli Wang,[1,2] Bin Cai,[1,2] Xuguang Li,[1,2] and Liqi Yang[1,2]

[1]*School of Civil Engineering Jilin Jianzhu University, Jilin, China*
[2]*Jilin Province Zhongrun Steel Structure Technology Co.,Ltd, Jilin, China*

Correspondence should be addressed to Fang Liu; 2015080@qhnu.edu.cn

This study aims to analyze the mechanical properties of fabricated multistory and high-rise steel structures and steel beam-column joints after fire. Considering that the steel structure building has the characteristics of good seismic resistance, flexible structural layout, short construction period, and good safety, first, the thermal and mechanical properties of steel are analyzed. They are thermal conductivity, the thermal expansion coefficient of steel, yield strength, and elastic modulus of ordinary steel. Next, the thermal conduction principle of steel under fire environment is analyzed, including thermal conduction, thermal convection, and thermal radiation. Then, the three-story and three-span reinforced concrete is selected as the experimental object. The local frame calculation model is established through the finite element software Abaqus. It is found that when the axial compression ratio is 1.0 and the fire time of the steel body is 180 min, the vertical deformation speed of the middle column and side column of the frame will increase rapidly. Besides, the bending moment at the bottom of the side column of the frame will increase inversely. The change is not obvious when the axial compression ratio is other values. The axial deformation of the universal beam is obvious under the condition of different fire load ratios. When the load ratio increases, the maximum fire resistance of the universal beam will decrease rapidly. Meanwhile, when the steel body is subjected to the same load ratio, different bearing capacity β has little effect on the fire resistance limit of the steel body. This thesis focuses on a series of changes in the steel of fabricated multistory and high-rise steel buildings after the fire, hoping to provide a reference for the relevant teams of steel construction and make the future housing construction safer.

1. Introduction

In the 18th century, steel structure buildings first appeared in Britain. Up to now, steel has become the most important building material among multiple building materials. The emergence of steel structures has changed people's understanding of building materials and changed the designer's concept of architectural design in the whole industry. Since the reform and opening up, China's scientific and technological level has developed by leaps and bounds, and the field of steel structure has also seized this development opportunity [1]. During this period, China has improved both in construction technology and production technology, making the application of steel structure in China increasingly widely. For example, Shanghai World Expo Exhibition Hall, National Stadium in Beijing, Shanghai World Financial

Center, and Canton Tower represent China's application level in steel structure [2]. At present, steel structure buildings show good safety, quality, and earthquake resistance characteristics and are favored by multiple engineering enterprises. However, there are some limitations, such as poor fire resistance of steel structures [3]. The reason is that the performance of steel will decline significantly in a high-temperature environment or when a fire occurs. The yield strength of steel will change and gradually decrease when the temperature of steel structure building is above 200°C. When the temperature rises to 400°C, steel's elastic modulus and yield strength will decrease by more than 50%. If the ambient temperature rises to 600°C, the strength and stiffness of steel will be basically lost [4]. It suggests that when a fire occurs, the steel structure building is easy to be damaged if it has not been protected. According to the statistics of relevant

research teams, most steel structure buildings will be damaged as a whole within 15–20 minutes of the fire. In addition, steel buildings will also have apparent thermal expansion and cold contraction, and thermal expansion will occur in a high-temperature environment. In the fire fighting process, the steel shrinks due to the decrease of ambient temperature. Such a change will significantly change the stress state of steel, so that the steel structure building cannot meet the use requirements. At present, the rapid development of urbanization has also promoted the continuous progress of the construction industry. Under this situation, all kinds of new architectural forms come into being. Large space structures and high-rise structures have been loved and pursued by more and more people because of their unique charm. However, due to the improvement of the building function demand, the demand for other aux-iliary facilities, such as power and heat, has also increased a lot. It has led to a significant increase in the potential fire hazards inside the building. In the past decades, there have been many steel structure collapse accidents caused by the fire in China.

Chan et al. studied the effects of several factors on the functionally graded concretes (FGCs) bonding quality of steel fiber and recycled aggregate in multistory and high-rise steel structure buildings. The test results show that the in-fluence of aggregate type and casting delay between layers on the quality of layer transition zone (LTZ) in the studied FGC is greater than that of fiber content. In addition, the FGC studied can be produced when the interlayer casting delay time is less than 24 hours without losing mechanical properties, increasing the potential for large-scale produc-tion of low-bearing capacity structures [5]. Ahmad et al. studied the effects of different amounts of steel fiber on the mechanics and durability of concrete. The compressive strength and splitting tensile strength of steel structures cured for 7 and 28 days were studied. Various parameters such as water absorption, acid corrosion resistance, and permeability were studied to evaluate the durability of each mixture. The results show that the strength of the composite increases to 2% and then decreases gradually with the ad-dition of steel fiber. When the content of steel fiber is 2.0%, the durability parameters such as water absorption, per-meability, and acid corrosion resistance of concrete are significantly improved. Therefore, it is recommended to mix steel fibers at 2.0% of the weight of cement to achieve maximum benefits [6].

This thesis is to analyze the mechanical and thermal performance of steel structure and steel beam-column joints in fabricated multistory and high-rise steel structure buildings after the fire. By establishing a three-story and three-span reinforced concrete model and selecting a local frame, the deformation of its side column, middle column, and beam is analyzed. The research innovation is to analyze the steel structure joints through the combination of thermal and mechanical properties, which significantly improves the accuracy of the conclusion. It is hoped that this thesis can help relevant design teams to complete the design of steel structures better and reduce the impact of fire factors on steel structures.

2. Research Scheme Design

2.1. Performance of Semirigid Joints. Nowadays, urban life fires occur frequently, and the research on the fire resistance of steel structure buildings has become extremely important. Therefore, in steel structure buildings, it is more necessary to focus on the analysis of joint performance under fire:

(1) In a high-temperature environment, steel yield strength will gradually decrease, which will change the internal force redistribution of each joint of the steel structure. In general, the change of internal force redistribution will seriously impact steel structure buildings. If it is in a high-temperature environment for a long time, the steel structure will be seriously deformed, resulting in collapse [7].

(2) Under the action of high temperature or fire, due to the thermal expansion effect of steel, the member produces large deformation and great additional stress to the joints, resulting in joint failure.

(3) Joint is an essential component in the joint con-nection structure. The research on joint performance can more effectively grasp the overall performance of the structure. The research on the fire resistance performance of the joint can reduce or avoid the damage of the structure in fire or make the structure have a certain fire resistance period to ensure the safety of life and property.

2.2. Thermal Properties of Steel

2.2.1. Thermal Conductivity λ_s. Generally, the higher the temperature is, the lower the thermal conductivity of the steel itself is. When the temperature reaches a certain value, the thermal conductivity of the steel body will not change. Therefore, China has made a specified value for the thermal conductivity of the steel body:

$$\lambda_S = \frac{45W}{(m^2 \cdot {}^\circ C)}.$$ (1)

2.3. Specific Heat Capacity of Steel C_S. It represents the ability of the steel body to release and absorb energy. China also stipulates the value of specific heat capacity of steel body:

$$C_S = \frac{600J}{kg \cdot {}^\circ C}.$$ (2)

When the temperature of the steel body is higher, the specific heat capacity of the steel will also increase. When the steel temperature reaches 600°C~700°C, sudden change will occur and the specific heat capacity will decrease. The reason why the specific heat capacity of steel changes suddenly is that when the steel reaches 600°C~700°C, the crystal lattice vibration inside the steel body changes from the previous orderly movement to disordered movement, resulting in the disappearance of magnetism, and finally, the specific heat capacity of steel changes [8]. When the temperature of the

steel body increases gradually, the steel is also gradually completing the disordered transformation, so the specific heat capacity of the steel decreases.

2.3.1. Steel Density ρ_s.

Steel density ρ_s will not change due to external temperature change, which is determined by the steel itself. Therefore, China uniformly sets the density of steel as $\rho_s = 7850 \, kg/m^3$.

2.3.2. Thermal Expansion Coefficient of Steel α_s.

The coefficient of thermal expansion represents the ratio between the change of unit length of steel and the original length when the temperature of steel increases by 1°C, and its unit is m/(m•°C). When the thermal-mechanical coupling method is used to analyze the steel structure, the coefficient of thermal expansion is an essential physical quantity [9]. Although the thermal expansion coefficient α_s of steel will change with temperature to a certain extent, the overall change range is not large. Therefore, China also stipulates the value of thermal expansion coefficient of steel at high temperature:

$$\alpha_S = \frac{1.4 \times 10 - 5m}{(m \cdot °C)}. \tag{3}$$

2.4. Mechanical Properties of Steel

2.4.1. Yield Strength f_y of Ordinary Steel.

Steel has no yield strength at high temperature, but on the contrary, the yield strength at room temperature is apparent [10]. Therefore, China has also made a standardized definition of this:

$$\frac{f_{yT}}{f_y} = 1 \quad 20°C \leq T \leq 300°C,$$

$$\frac{f_{yT}}{f_y} = 1.24 \times 10 - 8T3 - 2.096 \times 10 - 5T2 + 9.228$$

$$\times 10 - 3T - 0.2168 \cdot 300°C \leq T \leq 800°C, \tag{4}$$

$$\frac{f_{yT}}{f_y} = \frac{0.5 - T}{20000} \quad 800°C \leq T \leq 1000°C,$$

where $f_{yT}/f_y = 1.24 \times 10 - 8T3 - 2.096 \times 10 - 5T2 + 9.228 \times 10 - 3T - 0.2168$ $f_{yT}/f_y = 0.5 - T/20000 f_{yT}$ represents the yield strength when the external temperature of the steel is T. f_y represents the yield strength of steel under normal temperature.

2.4.2. Elastic Modulus E of Ordinary Steel.

The elastic modulus of steel will decrease obviously under high-temperature conditions, and the steel will deform obviously under the action of external load [11, 12]. Therefore. China has formulated the following specifications for the calculation of elastic modulus of ordinary steel under high-temperature conditions:

$$\frac{E_T}{E} = \frac{7T - 4780}{6T - 4760} \quad 20 \leq T \leq 600°C,$$

$$\frac{E_T}{E} = \frac{1000 - T}{6T - 2800} \quad 600°C \leq T \leq 1000°C, \tag{5}$$

where $E_T/E = 1000 - T/6T - 2800 E_T$ represents the elastic modulus of steel at temperature T (N/mm²) and E represents the elastic modulus of steel at room temperature (N/mm²).

2.5. Heat Transfer Principle of a Steel Structure under Fire.

When the outside temperature is too high or a fire occurs, the steel structure mainly realizes heat exchange through the outside air and the steel surface to complete heat transfer. The heat transfer inside the structure is realized by the thermal conduction capacity of the steel body [13–15]. Therefore, in the analysis process with the ANSYS software, the temperature load will be transmitted according to the following three channels.

2.5.1. Thermal Conduction.

The meaning of thermal conduction of steel is the process that the steel body transfers energy from a high-temperature environment to a low-temperature environment [16]. In this process, heat transfer needs to be completed through contact. This thesis mainly studies the contact between universal beam and beam flange, universal beam and bolt, and universal beam and side column. In addition, the heat transfer calculation among components shall be completed in strict accordance with the following equation:

$$\frac{Q}{t} = \frac{kA(T_2 - T_1)}{d}, \tag{6}$$

where k represents the thermal conductivity of the material. Q is the heat transferred between objects in t time. T represents the external temperature of the material. A represents the surface area of the material. d represents the distance between two objects when completing heat transfer [17].

2.5.2. Thermal Convection.

The meaning of thermal convection is the heat transfer process that occurs when the object surface contacts with other fluids under different temperature conditions. This thesis will analyze the heat exchange between air and steel frame surfaces. Equation (7) is to calculate thermal convection:

$$Q = h(T_1 - T_2), \tag{7}$$

where h represents the heat transfer coefficient of the object, T_1 represents the temperature of the external fluid, and T_2 represents the temperature of the object's own surface after contact with the fluid.

2.5.3. Thermal Radiation.

Thermal radiation is the heat transfer of objects through electromagnetic waves. As long as the object has temperature, the object will continuously radiate heat energy [18].

(a)

(b)

(c)

(d)
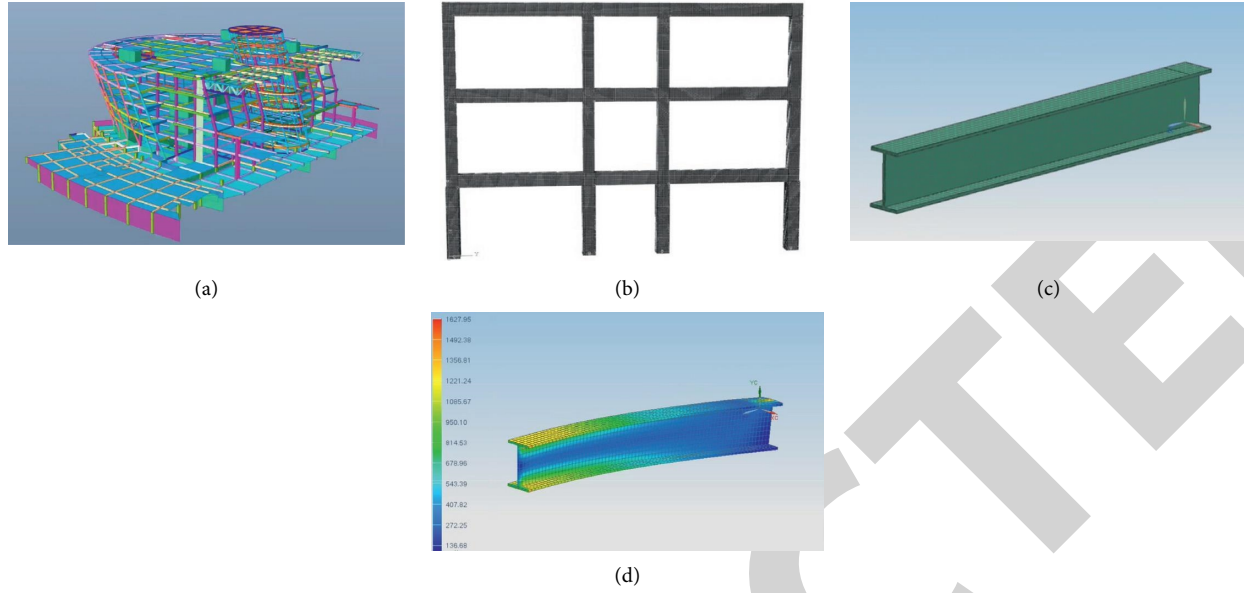
FIGURE 1: Finite element analysis model. (a) multistory and high-rise steel structure model; (b) grid division of reinforced concrete frame strengthened with local universal beam; (c) local universal beam model; (d) local universal beam grid.

$$Q = \varnothing \cdot \varepsilon_r \cdot 5.67^{-8} \cdot \left[\left(T_g + 273 \right)^4 - \left(T_b + 273 \right)^4 \right], \tag{8}$$

where $\varnothing$ represents the component shape coefficient, which is usually 1.0. T_g and T_b represent the temperature of steel components, and Q represents the heat transferred from air to steel in unit time; ε_r represents the radiation coefficient.

2.6. Establishment of Finite Element Model. A three-story and three-span reinforced concrete plane frame is taken as the research object. The Abaqus software performs the finite element analysis and calculation of the local frame. Figure 1 shows the finite element analysis model of the steel structure.

ISO834 standard temperature rise curve is adopted. The bottom floor of the frame is under fire, the bottom side column is under fire on three sides, the middle column is under fire on four sides, and the lower part of the bottom beam is under fire [19]. The convective heat transfer coefficient of the fire surface is 25, and the comprehensive radiation coefficient is 0.5; the heat transfer coefficient of heat convection of nonfire surface is 9; the comprehensive radiation coefficient is 0.

In the temperature field analysis, cement mortar and concrete are simulated by DC3D8 element, the steel bar is simulated by DC1D2 element, and angle iron and gusset plate are simulated by DS4 element. Tie constraints are adopted between concrete and concrete, between steel bar and concrete, between angle iron and concrete, between concrete and cement mortar, and between gusset plate and angle iron, regardless of the thermal resistance and slip between contact surfaces.

During mechanical analysis, cement mortar and concrete are simulated by the C3D8R element, the steel bar is simulated by the T3D2 element, and angle iron and gusset plate are simulated by the S4R element [20]. Regardless of

the mechanical action of the cement mortar protective layer, tie constraints are adopted between concrete beams and columns and sliding action is considered between angle iron and concrete columns. The contact surface between structural steel and concrete is defined as hard contact in the normal direction and classical Coulomb friction in the tangential direction. The friction coefficient is 0.3, and separation after contact is allowed. The steel bar cages of beams and columns are embedded into beams and columns by means of embedded constraints. It is assumed that there is complete coupling between reinforced joints and concrete joints. Equation (9) is to calculate the axial compression ratio of the steel body:

$$n = \frac{N_c}{\left(f_{ck} A \right)}. \tag{9}$$

where Nc represents the axial load of the calculated section, f_{ck} is the standard value of concrete compressive strength, and A is the section area of the concrete column. Equation (10) is the load ratio:

$$m = \frac{P_0}{P_u}, \tag{10}$$

where P_0 represents the axial force of the column under the frame under the normal temperature environment, and P_u represents the ultimate bearing capacity of the steel structure frame column under the normal temperature environment.

3. Analysis of Experimental Results

3.1. Temperature Field Analysis. Figure 2 shows the comparison of temperature field analysis results.

The change curve in Figure 2(a) suggests a certain difference between the finite element analysis results and the
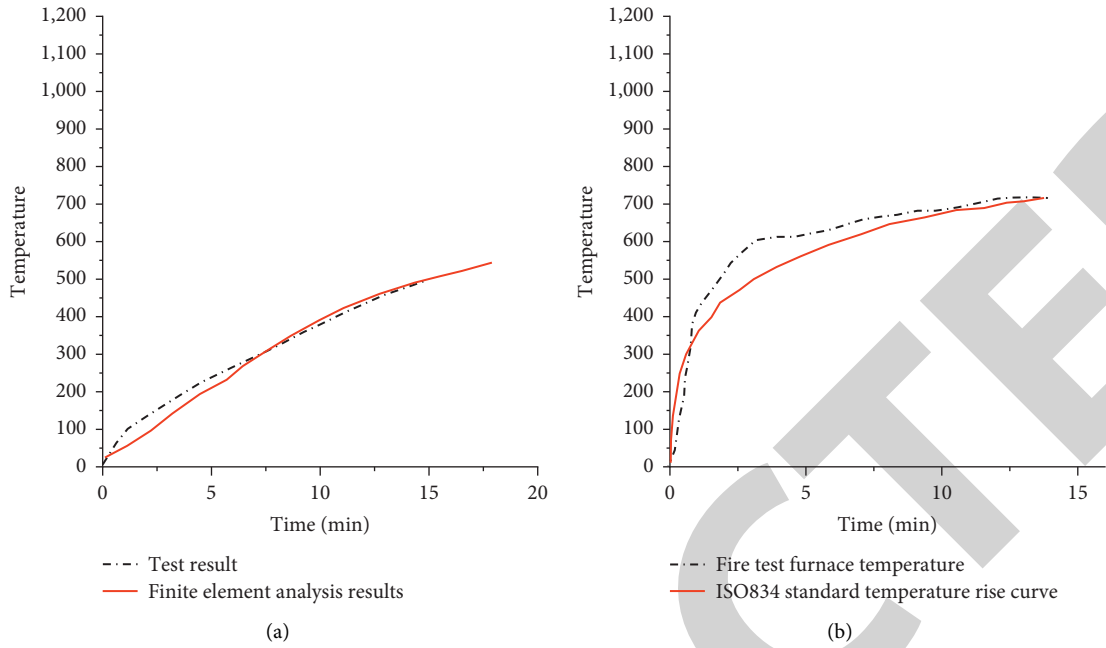
Figure 2: Comparison of temperature field analysis results. (a) Comparison between finite element analysis results and test results; (b) comparison between ISO834 standard temperature rise curve and test furnace temperature.
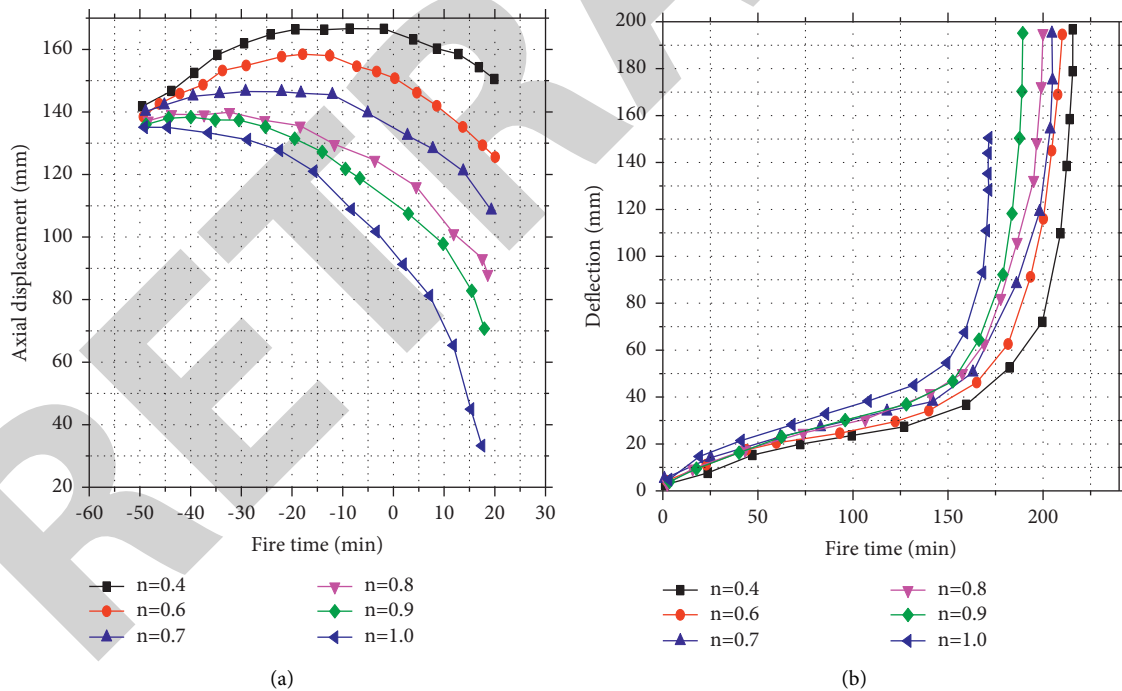
Figure 3: Analysis of axial compression ratio results. (a) Axial displacement analysis diagram of column top in the fire; (b) deflection of side span on fire.

test results within 5 minutes after the fire. However, this difference gradually decreases with the increase of fire time, and finally the two change curves tend to be consistent. In Figure 2(b), within three minutes of the fire, the ISO834 temperature rise curve is lower than the test temperature,

and the gap between them gradually increases. At the seventh minute after the fire, the gap gradually decreases. During the subsequent temperature rise, the two curves are almost close. It means that the ANSYS software has good calculation ability in simulating the temperature field of steel

(a)

(b)

(c)

(d)
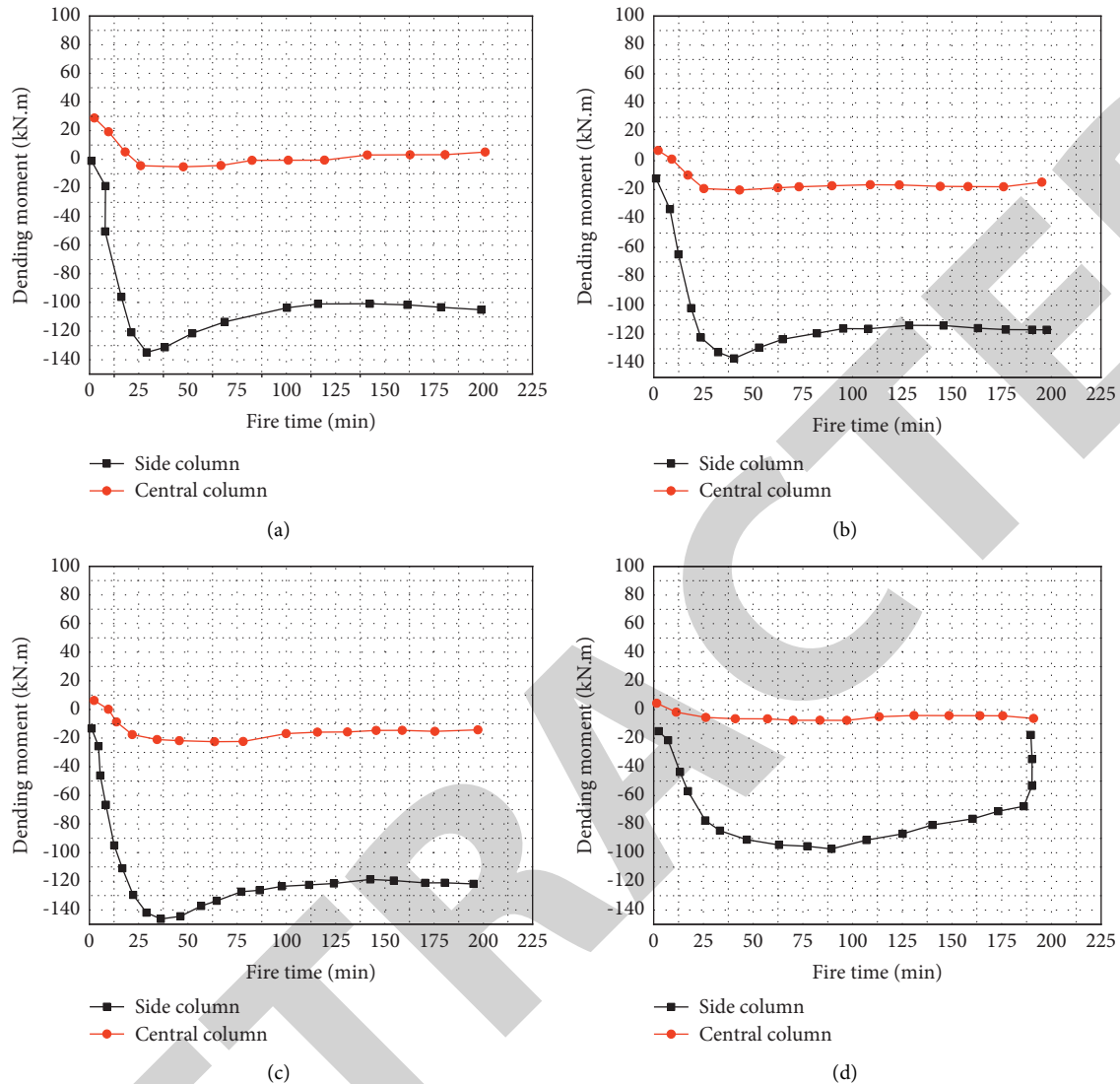
Figure 4: Variation of bending moment at the bottom of the reinforced column under different axial compression ratios. (a) Axial compression ratio $n = 0.4$; (b) axial compression ratio $n = 0.6$; (c) axial compression ratio $n = 0.8$; (d) axial compression ratio $n = 1.0$.

structure and steel beam-column. The test results are basically close to the calculation results.

3.2. Influence Analysis of Axial Compression Ratio. Figure 3 is the result of the axial compression ratio of the steel body.

The result data in Figure 3(a) reveal that when the axial compression ratio is 0.4, 0.6, 0.7, 0.8, and 0.9, the displacement change rate of the column top in the vertical direction is generally small. When the axial compression ratio increases gradually, the transverse deformation rate of the steel body will increase gradually. When the axial compression ratio is 1.0 and the fire time of the steel body is 180 min, the deformation speed of the whole middle column and side column in the vertical direction will increase rapidly. Figure 3(b) proves that there is no obvious difference in the initial fire of steel beams and columns when

different axial compression ratios are loaded. The reason is that the deflection of the steel beam itself is affected by its load level, and the influence of the steel beam-column on the steel beam is not very obvious. However, when the axial compression ratio is 1.0 and the fire time is 135 min, the deflection of the steel beam decreases rapidly because the fire resistance of the steel beam and column has reached the limit. Figure 4 shows the bending moment analysis of the bottom end of the reinforced column under different axial compression ratios.

Figure 4 suggests that the bending moment change of the middle column is much smaller than that of the side column bottom because the steel beam restrains each joint of the middle column. When the axial compression ratio is 0.4, 0.6, and 0.8, the bending moment at the bottom of the side column of the whole frame basically has the same change trend. At the beginning of the fire, the growth rate is fast. When the fire time increases, the rate also decreases

(a)

(b)
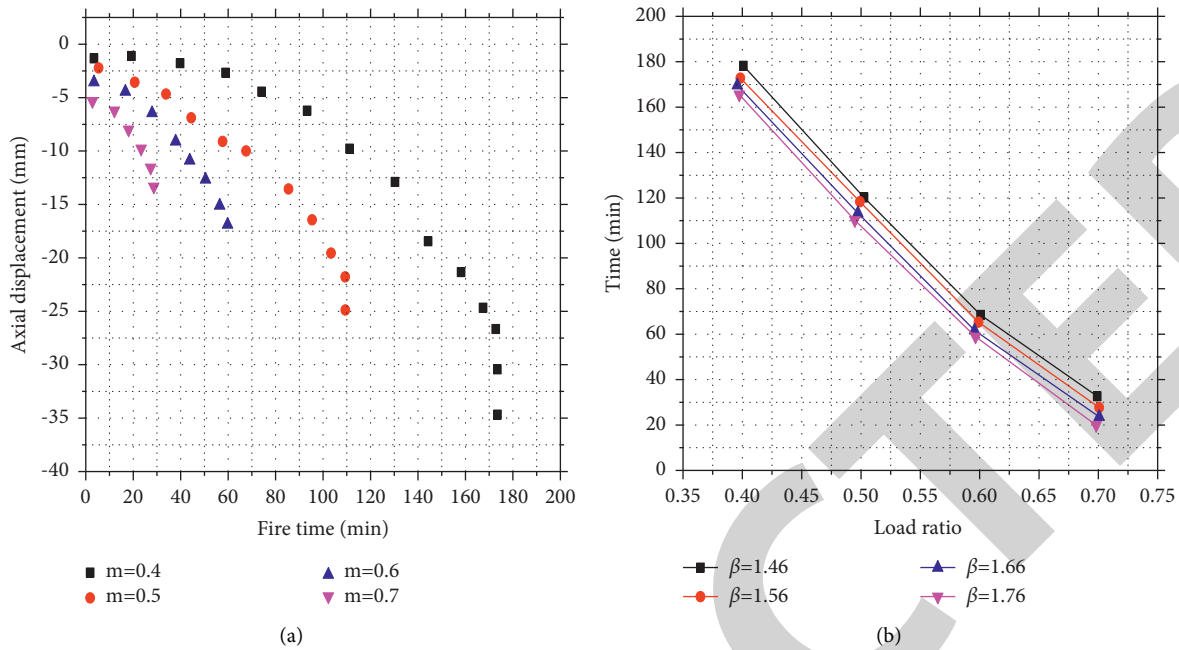
Figure 5: Analysis results of different load ratios of steel body. (a) Variation diagram of lateral displacement of middle column top when the bottom layer is in the fire; (b) fire resistance rating curve of steel frame under different load ratios.
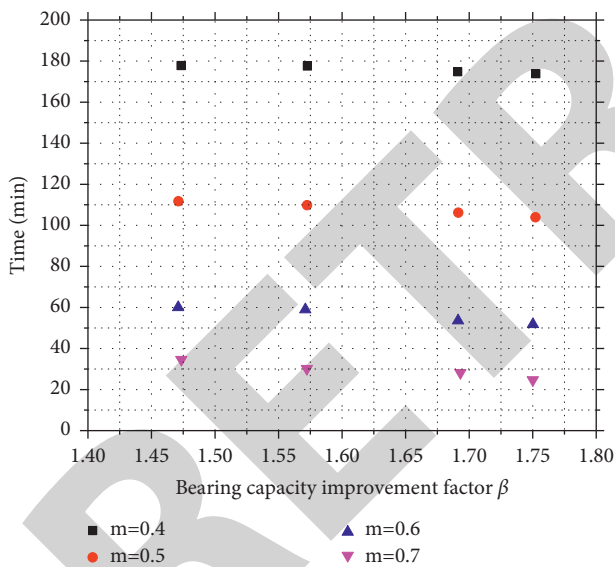
Figure 6: The effect of different bearing capacities on the fire resistance of the steel body.

gradually. When the axial compression ratio is 1.0, the bending moment at the bottom of the side column of the frame increases inversely. It is because the temperature of the steel body increases gradually with the increase of fire time. In the later stage, when the fire time reaches 190 min, the deflection of the beam reaches the maximum, resulting in the tension of the side column to the frame.

3.3. Influence Analysis of Load Ratio. Figure 5 shows the analysis results of different load ratios of the steel body.

The result data in Figure 5(a) show that the axial deformation of the universal beam is obvious under different fire load ratios. When the load ratio increases, the maximum fire resistance of the universal beam will decrease rapidly. Figure 5(b) reveals that when the load ratio increases, the fire resistance of the steel body shows a linear downward trend.

3.4. Influence Analysis of Bearing Capacity Improvement Coefficient. Figure 6 shows the effect of different bearing capacities on the fire resistance of the steel body.

Figure 6 shows that when the steel body is subjected to the same load ratio, different bearing capacities β have little effect on the fire resistance limit of the steel body. It is because the steel itself has good thermal conductivity, and the steel surface has a protective layer, which will make the impact on the steel body when the heat is transferred from the surface to the concrete almost negligible. Therefore, when the whole steel frame is in the same temperature field, the fire resistance of each column is basically the same.

4. Conclusion

The purpose is to analyze the mechanical properties of fabricated multistory and high-rise steel structures and steel beam-column joints after the fire. The thermal performance analysis of steel support is supplemented to improve the comprehensiveness of the research conclusion. First, the thermal and mechanical properties of steel are understood through theoretical research, including thermal conductivity, the thermal expansion coefficient of steel, yield strength, and elastic modulus of ordinary steel. Next, the thermal conduction principle of steel under fire environment is analyzed, including thermal conduction, thermal

Retraction

Retracted: Electrochemical Seismic Design and Artificial Intelligence System Modeling of High-Rise Steel Structure Buildings

Journal of Chemistry

This article has been retracted by Hindawi following an investigation undertaken by the publisher [1]. This investigation has uncovered evidence of one or more of the following indicators of systematic manipulation of the publication process:

(1) Discrepancies in scope

(2) Discrepancies in the description of the research reported

(3) Discrepancies between the availability of data and the research described

(4) Inappropriate citations

(5) Incoherent, meaningless and/or irrelevant content included in the article

(6) Peer-review manipulation

The presence of these indicators undermines our confidence in the integrity of the article's content and we cannot, therefore, vouch for its reliability. Please note that this notice is intended solely to alert readers that the content of this article is unreliable. We have not investigated whether authors were aware of or involved in the systematic manipulation of the publication process.

Wiley and Hindawi regrets that the usual quality checks did not identify these issues before publication and have since put additional measures in place to safeguard research integrity.

We wish to credit our own Research Integrity and Research Publishing teams and anonymous and named external researchers and research integrity experts for contributing to this investigation.

The corresponding author, as the representative of all authors, has been given the opportunity to register their agreement or disagreement to this retraction. We have kept a record of any response received.

References

[1] W. Xia, "Electrochemical Seismic Design and Artificial Intelligence System Modeling of High-Rise Steel Structure Buildings," *Journal of Chemistry*, vol. 2022, Article ID 8693110, 8 pages, 2022.

Hindawi

Research Article

Electrochemical Seismic Design and Artificial Intelligence System Modeling of High-Rise Steel Structure Buildings

Wenjie Xia [ID]

Jinan Engineering Polytechnic, Jinan City, Shandong Province 250000, China

Correspondence should be addressed to Wenjie Xia; 20162103771@mails.imnu.edu.cn

This study aims to improve the mechanical earthquake-resistance ability of high-rise buildings' steel structures so that their safety performance is improved and their service life is prolonged. The simulation experiments on the response of the staggered truss steel structure are conducted in high-rise buildings to earthquake energy waves. First, MATLAB is used to build an experimental platform for earthquake-resistance evaluation of high-rise residential buildings. Through the high-rise building model training, it is found that the model meets the needs of the study. Second, the earthquake-resistance performance parameters, deformation recovery capacity, and dynamic response speed of the staggered truss steel structure are simulated and tested. After earthquake energy waves with different intensities are posed on the high-rise building model, the performance parameters of the staggered truss structure are tested, and the changes in the parameters of the structure are analyzed. Finally, the earthquake-resistance performance and post-earthquake recovery ability of the staggered truss structure are tested through comparative analysis. The results show that the interlayer displacement fluctuation of the staggered truss steel structure is the smallest, and the earthquake resistance performance is better than others under the energy waves of all kinds of earthquakes. Although its earthquake-resistance ability decreases with the duration of earthquakes, the reduction speed is slow. When the quake lasts 12 s, the resistance of the staggered truss structure is still greater than 2500 MPa. This study provides a reference for the staggered truss structure of high-rise buildings.

1. Introduction

With the improvement of China's economic level, urbanization is also accelerating rapidly, and residential areas in the city are becoming increasingly insufficient. In response to solving the problem, some real estate developers tend to build high-rise buildings, which can save development costs and also attract residents. As China's geographical location is in the earthquake zone, many cities are near the earthquake zone. This brings challenges to the development of high-rise buildings. Therefore, the mechanical earthquake resistance of steel structures of high-rise buildings attracts more and more attention.

Steel materials are widely used in high-rise buildings because of their lightweight, high strength and hardness, good environmental protection, and earthquake resistance [1]. The earthquake-resistance ability, deformation

performance, and dynamic response of the steel structure are analyzed. When the earthquake occurs, the load bearing of the steel structure is the response of external load and the strong inertia based on its mass [2]. The steel structure with a good deformation ability and excellent elasticity can protect the main body of the building because it can dissipate the energy generated by the earthquake.

With the optimization and development of architectural design, the steel structure applied in high-rise buildings is also developed [3]. A mathematical model of the structure of high-rise buildings is established, and the numerical simulation of each structural material under the action of earthquake energy waves is analyzed. The earthquake-resistance performance of the structure of high-rise residential buildings is evaluated from vertex displacement, interlayer preparation, and base shear force. Based on the experimental results, the static elastic-plastic analysis of the structure is

made using finite element analysis software, and the earthquake-resistance performance of the structure under different intensities is calculated. The results show that high-rise buildings' staggered truss steel structure has good earthquake resistance, deformation recovery, and rapid-response ability. This study provides a reference for studying the steel structure of high-rise buildings.

2. Mechanical Earthquake-Resistance Ability of the Steel Structure

This research on earthquake resistance of high-rise buildings responds to the influence of natural disasters such as earthquakes. The way to improve high-rise buildings' earthquake-resistance ability is to design an earthquake-resistant structure as the main body of the building. Generally, architects select the steel structure with good performance in constructing high-rise buildings. The steel structure has a good bearing capacity and deformation ability, reducing damage and avoiding casualties and economic loss in natural disasters.

2.1. Staggered Truss Steel Structure. In high-rise buildings, the staggered truss steel structure mainly takes the building panel, truss structure, and load-bearing column as the basis [4]. The unilateral truss is arranged along the vertical direction of the interlayer, and the adjacent truss is staggered [5]. One side is connected to the top, and the other is connected to the bottom of the adjacent truss. The two ends of the truss are supported on the bearing column of the main building [6].

Such a unique structure can give the staggered truss steel structure a good deformation performance. The building staircase load in the vertical direction is transmitted and concentrated on bearing columns [7], avoiding deformation [8, 9]. The horizontal load on the building is transmitted to the floor through the staggered truss mechanism. Since the staggered truss mechanism in the interlayer provides sufficient lateral stiffness for the building body, there will be no excessive displacement in the horizontal direction under the action of horizontal load. The staggered truss steel structure is shown in Figure 1.

The vertical load on the main body acts on the upper and lower chords of the staggered truss structure, which can concentrate the load to the nodes of the truss. The extreme load should be considered in the joint design of the staggered truss structure. In the calculation, it is supposed that the ends of diagonal web members and vertical members are hinged, and the upper and lower chord members are the continuous beams hinged with columns at the ends. The truss uses the tension monoclinic web member system to clarify the transmission direction of forces. There is no inclined rod between midspan nodes and its shear force is borne by a chord. The walkway should be placed at the part with small shear forces, and it can be located at the quarter-point to meet the needs of setting suites. Because there is no vertical bar between the fasting nodes, the chord cannot be regarded as a member only

bearing axial force. When subjected to the transverse load, the chord will bend. The shear and bending moment of the chord shall be calculated and its bearing capacity shall be checked. However, under the action of vertical loads, the shear force on the chord in the middle node is zero, while the shear force on the chord in the other nodes is also very small and can be ignored, so the truss is simplified into a statically determined structure.

In the calculation, the end reaction can be calculated, and then, the section or node method can be used to calculate the truss. The structural lateral displacement curve shows the influence of high-order vibration modes based on the static elastoplasticity of the model and the structural uncoupled vibration theory, displacement response spectrum theory, and the transformation relationship between the multi- and single-degree-of-freedom system. From the elastic natural vibration period and corresponding vibration modes under each vibration mode, the equivalent and lateral displacement curves of the equivalent single degree of each vibration mode are obtained; the overall elastic lateral displacement is also obtained. According to the assumption, the lateral displacement curve under a certain performance level is determined.

2.2. Earthquake Resistance of High-Rise Buildings. The evaluation of the earthquake-resistance ability of high-rise residential buildings needs to establish the dynamic equilibrium equation of the multi-degree-of-freedom system of the original structural column under ground acceleration and calculate the equivalent mass of the equivalent single-degree-of-freedom system, the equivalent restoring force, and the equivalent damping. According to the calculated results, the calculation equation of base shear and displacement at the yield point of an equivalent single degree-of-freedom system is given. Finally, the spectral velocity and spectral displacement are calculated. The performance evaluation of the building's structural columns is realized by the superposition of the two [10, 11].

If the deformation vector of the earthquake-resistance response of a high-rise residential building is $|\Phi|$, the dynamic equilibrium equation of the multi-degree-of-freedom system of the original structure column under ground acceleration is as follows:

$$[M]|\ddot{x}| + [C]|\dot{x}| + [Q] = -[M][I]\ddot{x}_\varepsilon, \tag{1}$$

where $[M]$ and $[C]$ represent the mass and damping matrix of multi-degree of freedom, respectively, $|\ddot{x}|$ and $|\dot{x}|$ represent the relative acceleration and relative velocity vector, respectively, $[Q]$ represents the restoring force vector, $[I]$ represents the unit vector, and $\ddot{x}_\varepsilon$ represents the motion acceleration of structural columns relative to the ground.

According to equation (1), the equivalent damping of the building structure column can be calculated. The expression equation is as follows:

$$C^\varepsilon = |\Phi|^\tau [C]|\Phi| \frac{|\Phi|^\tau [M][I]}{|\Phi|^\tau [M]|\Phi|}, \tag{2}$$
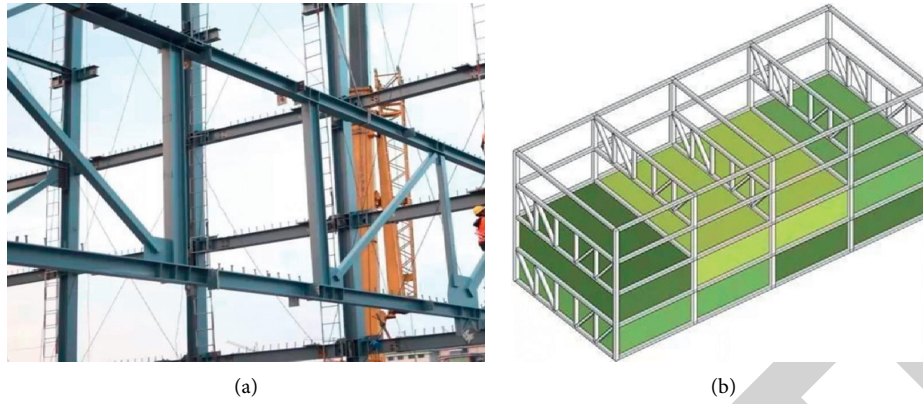
Figure 1: Staggered truss steel structure. (a) The staggered truss steel structure in reality; (b) a 3D model of the staggered truss steel structure.

where $|\Phi|^\tau$ is the deformation vector of the structure column in energy wave dissipation.

According to the pushover analysis of the multi-degree-of-freedom structure of the original structure column, the relationship between force and deformation of the equivalent single-degree-of-freedom system of the building structure column can be calculated. The relationship between the base shear force and displacement at the yield point is calculated by using the following formula:

$$x_y^\varepsilon = \frac{|\Phi|^\tau [M] |\Phi|}{|\Phi|^\tau [M] |I| x_{k,y}}, \tag{3}$$

where x_y represents the vertex displacement of the building structure column and x_k represents its base displacement.

The demand spectrum curve of the building structure column is established. The 5% damping elastic acceleration response spectrum of the building structure column transforms the relationship between spectral acceleration S_0 and the inherent period T of the building structure column to its acceleration-displacement response spectrum. The calculation equation of the displacement spectrum of the building structure column is as follows:

$$S_k = \frac{T^2}{4\pi^2} S_0. \tag{4}$$

Equation (4) can calculate the earthquake resistance of the structure column.

First, the earthquake-resistance ability index of the building structure column is calculated, including the strength index and ductility index of the vertical components and the horizontal lateral bearing ability of the vertical components. Then, the total horizontal lateral bearing ability of the building structure column is determined according to the condition of the lateral displacement and deformation of the residential floor. The strength index of the structure column is calculated by the vertical components of the residential floor. The ductility index is the contribution of each component to the earthquake resistance ability of the structural columns.

If the assessed high-rise residential buildings have different vertical components, their components should be calculated separately. The calculation is determined according to the vertical component with the slightest. The total horizontal lateral bearing ability to build structure columns is determined according to the lateral deformation degree of residential floors. If the ductility index of building structural columns is $F = 1.0$, the building structure is calculated according to the area of the residential building walls [12]. The calculation equation of the earthquake-resistance ability index of building structural columns is as follows:

$$I_n' = \frac{\tau_\omega (nA_\varepsilon + A_\omega)}{\omega \sum A_f}, \tag{5}$$

where ω represents the value of the gravity load per unit area of the building structure column, A_ε represents the area of the building structure column of the residential floor, A_ω represents the area of the whole wall of the floor after the window hole and door hole of the residential building are deducted, $\sum A_f$ represents the sum of the area of the calculation layer of the residential building and the structural column of the superstructure, n represents the ratio of the shear modulus of the high-rise residential concrete to the structural column, and τ_ω is the standard earthquake and shear strength value of the structural columns damaged along the residential ladder sections.

The earthquake-resistance ability of the structural column is evaluated according to the calculation results of the earthquake-resistance ability index of building structural columns [13], the cumulative damage model of structural columns [14], the total dissipated strain energy of the structural column system, and the damage index of the building structural columns [15].

The cumulative damage model of the structure columns is implemented according to the life curve (N-s relationship) and the Miner criterion. Low-cycle fatigue life N of a parameter of the building structure column is calculated at any j cycle. The equation of the cumulative damage model of the structure column is as follows:

$$D_f = \sum \frac{1}{2N}. \tag{6}$$

A low-cycle fatigue model of structural columns under constant cyclic loading is implemented. The equation is as follows:

$$u_m - u_y = \left(\dot{u}_m - u_y \left(\left(\dot{2} N_f \right)^2 \right) \right), \qquad (7)$$

where u_m and $\dot{u}_m$ represent the peak displacement of the building structure column under the constant amplitude cyclic load and the peak displacement of the building structure column under the constant amplitude monotonic load, respectively, and u_y represents the yield displacement of the building structure column. N_f represents the low-cycle fatigue life of the building structure column (or the number of load cycles of the building structure column).

The damage index of the building structure column is compared with specific values [16]. When the damage index is between 0 and 0.15, it indicates that the building structure column is slightly damaged, showing that the earthquake-resistance ability of the building structure is good. When the damage index of the building structure is between 0.15 and 0.30, it indicates that there is a medium degree of damage in the building structure. When the damage index of the building structure is more significant than 0.80, it suggests that the building structure has been seriously damaged. The main body of the building has the risk of collapsing at any time, and its earthquake resistance is worst [17].

According to the requirements of "two stages and three levels," the earthquake-resistance effect calculated under the "good use" level is combined with the corresponding constant and live load effect (wind load effect and vertical seismic effect are considered when necessary). The component strength and stability are checked according to the combined internal force, and static elastic-plastic analysis is carried out after the section value is adjusted to check whether the designed structure meets the "personal safety" and the deformation limit requirements under the performance level of "preventing collapse." If it does not meet the requirements, readjust the member section and repeat the above design process.

In the MATLAB 8.0 environment, a test platform to evaluate the earthquake-resistance ability of the structural column is built, and simulation experiments are carried out using SeismoStruct.

2.3. Earthquake-Resistance Ability of High-Rise Buildings with the Staggered Truss Structure.

Through the test platform for evaluating the earthquake-resistance ability, the earthquake resistance ability of the staggered truss structure under energy waves is tested. The specific experimental process is shown in Figure 2.

Figure 2 shows that the earthquake-resistance ability of high-rise buildings with the staggered truss structure is studied. First, the staggered truss structure is added to the high-rise building model. Then, the changes in the material properties of the staggered truss structure and the changes in the interlayer displacement angle of the structural column are tested under energy waves with different intensities. Thus, the response performances of other structures under energy waves with different intensities are obtained, and the earthquake-resistance performance of each structure is obtained. Finally, the stable performance of each structure is achieved by testing the energy dissipation rate of the structural columns in high-rise buildings.

The experiment is to explore the influence of relevant components and structural parameters on the deformation capacity, energy dissipation capacity, and reasonable failure mechanism of the staggered truss structure under earthquakes. According to the experiment and example analysis, the earthquake-resistance performance of the staggered truss structure is evaluated, and the design suggestions are put forward. The dynamic characteristics of the staggered truss structure and its response in elastic and elastoplastic stages under different records and strengths are summarized, including the internal force and deformation state in the earthquake-resistance response and the formation and development sequence of plastic hinges. The parts where stress and plastic deformation exist determine the yield mechanism's mechanism weak links and possible damage of the structure.

3. Analysis of Experimental Results

3.1. Relationship between Shear Stress and Time Variation under Different Accelerations.

The change curves of shear stress and time of the simulation model under different accelerations are shown in Figure 3.

Figure 3 shows that under different accelerations, the changing trend of the shear stress of the staggered truss steel structure is the same, and the waveform is similar. the time of shear stress in positive and negative directions is consistent. The relationships between shear stress and the staggered truss steel structure time under different accelerations are compared. The results show that the time nodes of the maximum shear stress of the staggered truss steel structure on energy waves are inconsistent. If they are more than 5 s, there will be a gradual declining trend after the appearance of the peak.

3.2. Displacement Angle of Different Earthquake Resistance Structures under External Force.

The interstory displacement angle of the structural column is calculated by the elastic method of the wind load, or the ratio of the maximum horizontal displacement between the residential floors and their heights under energy waves. It is an important index to measure the earthquake-resistance ability of structural columns. Four different methods are used to analyze the interstory displacement angles of the building structure columns, and their results are compared. The experimental results are shown in Figures 4 and 5.

Figures 4 and 5 show that when there is a small earthquake, the interstory displacement of the building structure without steel structure is largest, indicating that the earthquake-resistance ability of the structure is worst; under a large earthquake, the inter-story displacement fluctuation of high-rise buildings with the truss steel structure is most significant, proving that the earthquake-resistance ability of
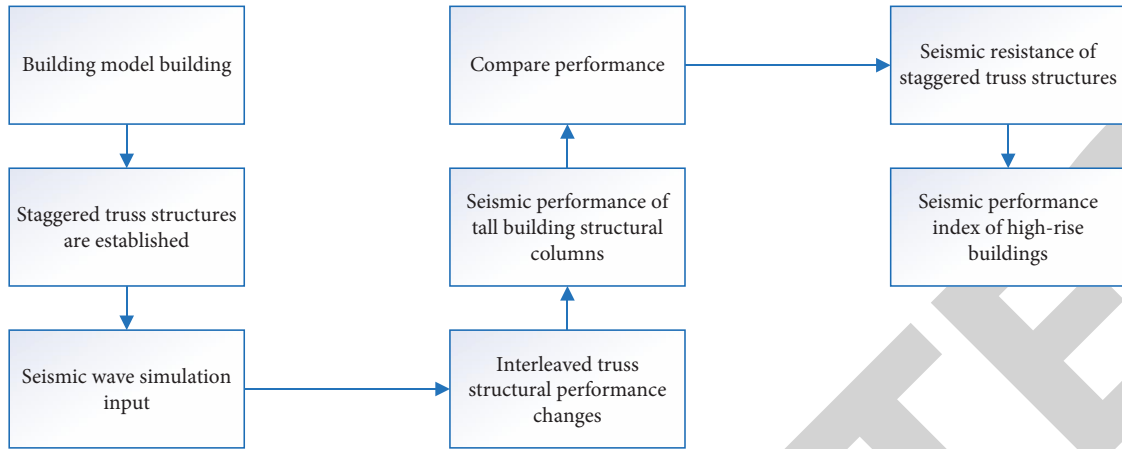
Figure 2: Experimental process of evaluating the earthquake-resistance ability of the structure column.

(a)

(b)
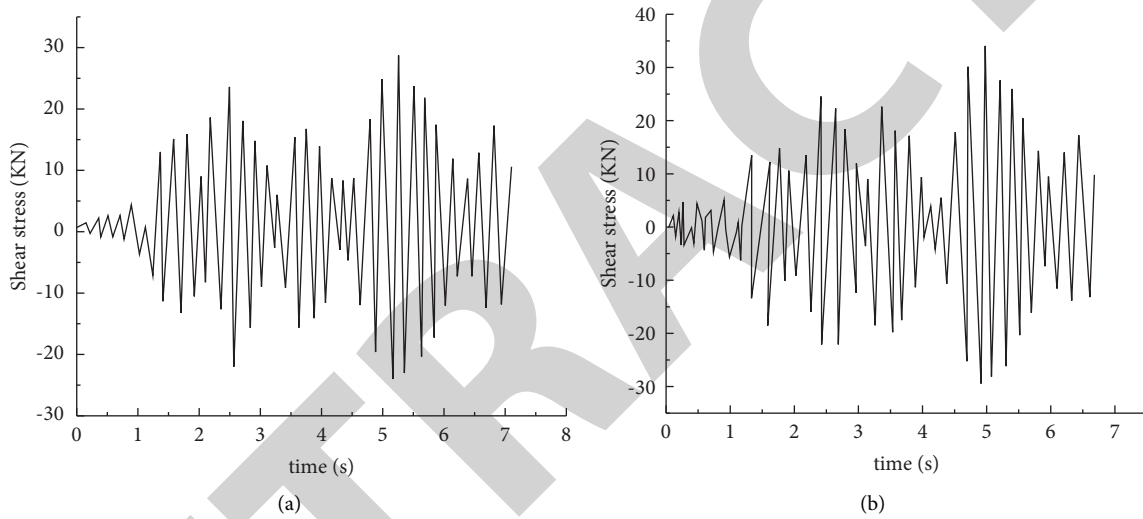
Figure 3: Relationship between shear stress and time under different accelerations. (a) The shear stress change at an acceleration of 50 gal; (b) the shear stress change at an acceleration of 100 gal.
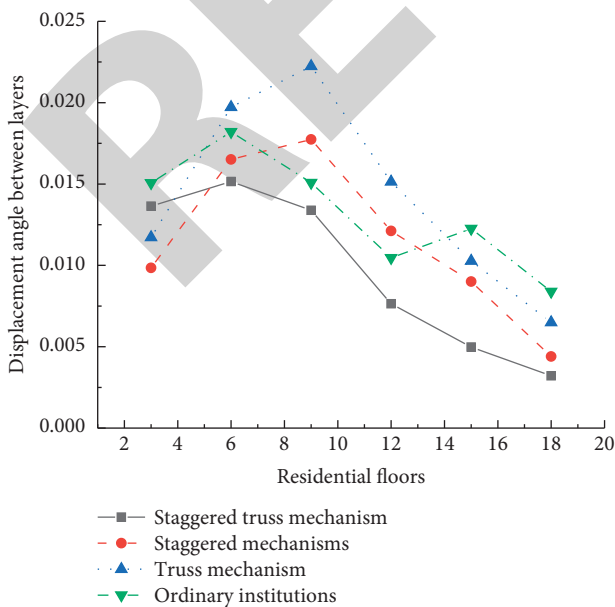
Figure 4: Interstory displacement angles of different floors under small earthquakes.
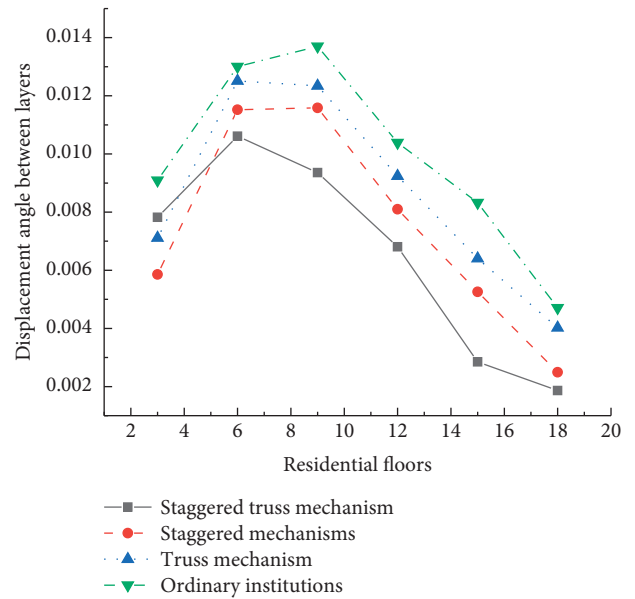
Figure 5: Interstory displacement angles of different floors under large earthquakes.

(a)   (b)
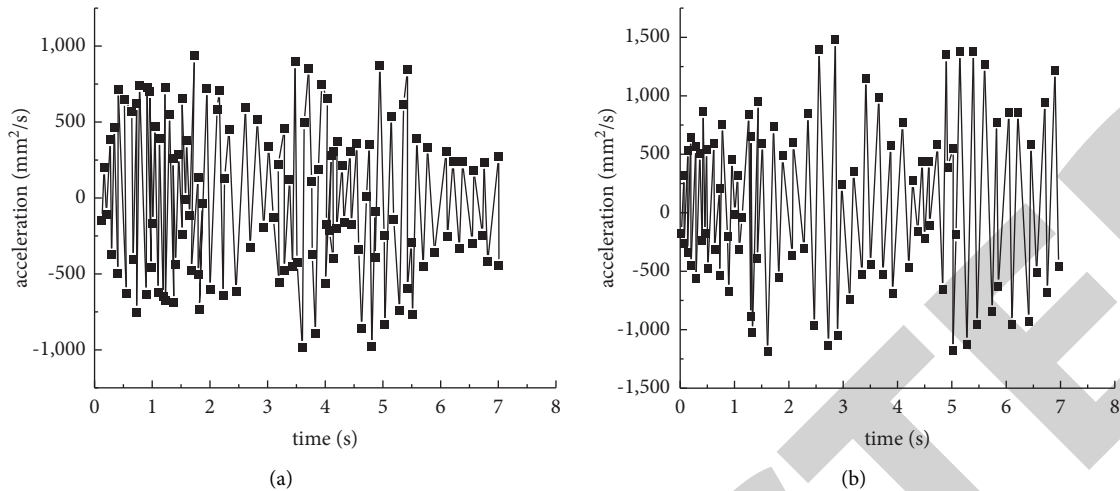
FIGURE 6: Acceleration-time curve of the staggered truss structure. (a) The time curve with a peak acceleration of 50 gal; (b) the time curve with a peak acceleration of 100 gal.

(a)   (b)
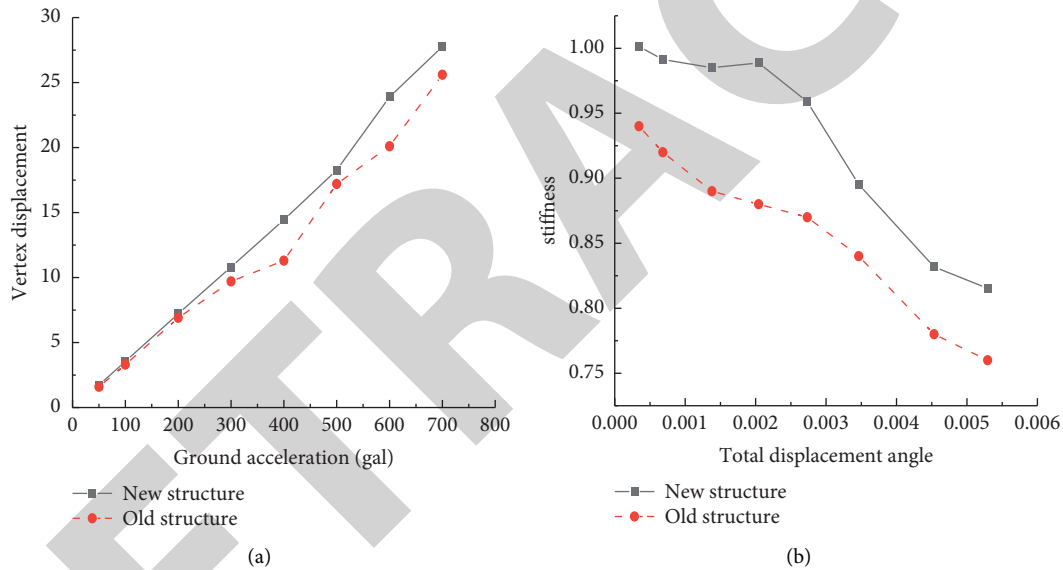
FIGURE 7: Relationship of total displacement, total displacement angle, and stiffness. (a) The relationship between ground acceleration and vertex displacement; (b) the relationship between total angular displacement and stiffness.

the structure is worst under large earthquakes; the interstory displacement of building structure columns with the staggered truss steel structure is stable under large earthquake and a small earthquake. However, its performance under moderate damage is not ideal; the interstory displacement of building structural columns is the smallest, and its performance is the best.

3.3. Effect of Earthquake Waves on Acceleration.
There are different accelerations under different earthquake waves, as shown in Figure 6.

The peak time of the top-level response acceleration is inconsistent with the peak time under the earthquake wave, and the former is lagged. This is because the natural vibration period of the structure is related to its earthquake

wave period. The staggered truss structure has different conduction effects on different forces.

The relationship of total displacement, whole displacement angle, and stiffness in the staggered truss mechanism is shown in Figure 7.

Figure 7 shows that the structure is in an elastic state during the test, and the stiffness changes little. When the peak acceleration increases from 50 gal to 700 gal, the hysteresis curve of the structure is linear, and the energy consumption is less. The displacement response of the structure increases with the increase of the peak acceleration. When the peak acceleration is 600 gal, the structure first yields at the foot of the column. The slope of the hysteresis curve decreases and the stiffness degrades; the shape of the hysteresis curve shows that when the displacement is negative, the hysteresis curve deviates. This is because the
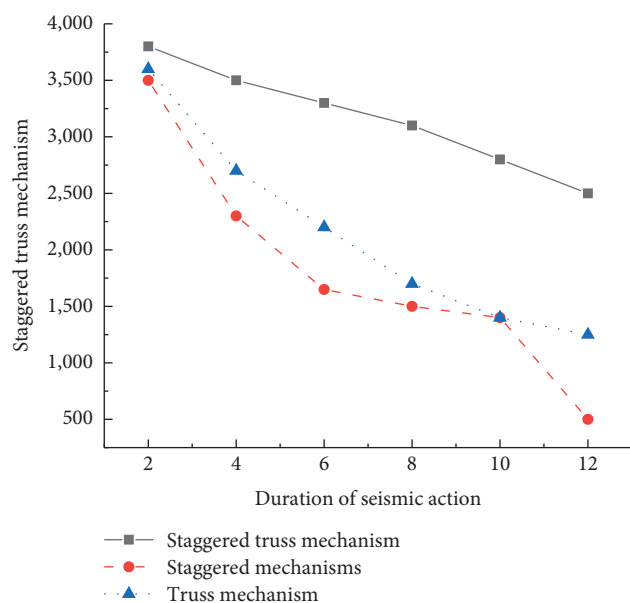
FIGURE 8: Stress changes of building columns with different structures.

elastic-plastic deformation caused by the round steel rod of the two loading beams on the top floor consumes part of the load, resulting in the displacement error of the actuator when it is pulled back. When the peak acceleration is 700 gal, the area of the hysteresis curve of the structure increases, indicating that the energy of the structure begins to dissipate and enters the elastic-plastic working stage.

3.4. Stress Changes of Building Structures. The stress of the structure column of high-rise residential buildings refers to the internal force generated by the interaction between the components of the building structure column when the building structure column is deformed under external forces (such as earthquakes, temperature changes, and humidity changes). The effect of the external force and the recovery of the structure column from deformation should be analyzed, and the effectiveness of the proposed method needs to be tested. Different methods are used to analyze the stress changes of building structural columns, and the results are compared. The comparison results are shown in Figure 8.

Figure 8 shows that the stress changes of the building structure column in the steel truss structure decreases the fastest with respect to the duration of earthquakes; when earthquake lasts 12 s, the stress of the building structure column decreases less than 1000 MPa; when the duration of the earthquake is 8 s, the stress of the building structure column tends to be stable; when the earthquake lasts 12 s, the stress of the building structure column is reduced to less than 1500 MPa, and the resistance of the building structure column of the staggered steel structure is not ideal. In short, the stress changes of the building structure column of the staggered truss steel structure are reduced with the earthquake's duration, but the reduction rate is slow. When the earthquake duration reaches 12 s, the stress of the other two methods is less than 1500 MPa, and the stress of the building

structure column is still maintained at 2500 MPa, which shows that the earthquake resistance of the structure column is best.

4. Conclusion

System modeling of the mechanical earthquake-resistance ability of high-rise buildings is studied. After a staggered truss mechanism is constructed, the earthquake-resistance ability of high-rise buildings is improved. Through the modeling and simulation based on MATLAB software, the simulation results show that the staggered truss mechanism has a strong load resistance and elastic performance along the direction of the truss, and its stiffness is not degraded under the action of the load. The staggered truss steel structure has excellent transferability for the stress generated by the load inside the building structure, which can significantly protect the building body. Under different earthquake waves, the staggered truss steel structure significantly affects high-rise buildings, which greatly improves the stability and bearing ability of high-rise building structural columns. However, there are some shortcomings that need to be improved. For example, only one type of the high-rise building model is selected in the simulation experiment, and the experiment results are not universal because there are few experimental samples. Besides, the staggered truss structure may influence the resistance ability of high-rise buildings, and the materials may also have a certain influence on the resistance of the staggered truss structures. A series of comparative experiments are needed to explore the influencing factors and the resistance of the structure of high-rise buildings.

Data Availability

The data used to support the findings of this study are available from the corresponding author upon request.

Conflicts of Interest

The authors declare that they have no conflicts of interest.

References

[1] B. Chen, W. Cheng, H. Ma, and Q. Yang, "Wind interference effects from one high-rise building and similar low-rise flat-roof buildings," *Journal of Structural Engineering*, vol. 147, no. 9, Article ID 04021138, 2021.

[2] S. Chapain and A. M. Aly, "Vibration attenuation in high-rise buildings to achieve system-level performance under multiple hazards," *Engineering Structures*, vol. 197, Article ID 109352, 2019.

[3] Y. M. Bazhenov, S. A. Murtazaev, D. S. Bataev, A. H. Alaskhanov, T. Murtazaeva, and M. Saydumov, "High-strength concretes based on anthropogenic raw materials for earthquake resistant high-rise construction," *Engineering Solid Mechanics*, vol. 9, no. 3, pp. 335–346, 2021.

[4] M. Sarcheshmehpour and H. E. Estekanchi, "Life cycle cost optimization of earthquake-resistant steel framed tube tall buildings," *Structures*, vol. 30, pp. 585–601, 2021.

Retraction

Retracted: Study on the Color Genesis of South Red Agate and the Geological Characteristics of the Siliceous Gravel Layer

Journal of Chemistry

This article has been retracted by Hindawi following an investigation undertaken by the publisher [1]. This investigation has uncovered evidence of one or more of the following indicators of systematic manipulation of the publication process:

(1) Discrepancies in scope

(2) Discrepancies in the description of the research reported

(3) Discrepancies between the availability of data and the research described

(4) Inappropriate citations

(5) Incoherent, meaningless and/or irrelevant content included in the article

(6) Peer-review manipulation

The presence of these indicators undermines our confidence in the integrity of the article's content and we cannot, therefore, vouch for its reliability. Please note that this notice is intended solely to alert readers that the content of this article is unreliable. We have not investigated whether authors were aware of or involved in the systematic manipulation of the publication process.

Wiley and Hindawi regrets that the usual quality checks did not identify these issues before publication and have since put additional measures in place to safeguard research integrity.

We wish to credit our own Research Integrity and Research Publishing teams and anonymous and named external researchers and research integrity experts for contributing to this investigation.

The corresponding author, as the representative of all authors, has been given the opportunity to register their agreement or disagreement to this retraction. We have kept a record of any response received.

References

[1] K. Li and Y. Yuan, "Study on the Color Genesis of South Red Agate and the Geological Characteristics of the Siliceous Gravel Layer," *Journal of Chemistry*, vol. 2022, Article ID 9157753, 7 pages, 2022.

Hindawi

Research Article

Study on the Color Genesis of South Red Agate and the Geological Characteristics of the Siliceous Gravel Layer

Kongliang Li [ID] [1] and Ye Yuan [ID] [2]

[1]*Anhui Technical College of Industry and Economy, Hefei, Anhui 230051, China*
[2]*China University of Geosciences (Beijing), Beijing 430074, China*

Correspondence should be addressed to Kongliang Li; 11233311@stu.wxic.edu.cn

The aim of the study was to explore the gem mineralogical characteristics of southern red agate and then analyze its structural characteristics and color causes. The mineral composition, structure, and chromogenic minerals of Nanhong agate were tested by a conventional gemmological test and observed under the microscope, infrared spectrum, and microlaser Raman spectrum. It is found that the color of southern red agate samples is mainly dark red or orange red, and colorless, white or yellow bands can be seen in some samples; the relative density is in the range of 2.59~2.65. The matrix structure of the sample is mainly long fiber and short fiber, and some of them are fine-grained and crystalline plasmid. There are concentric ring-banded structures, and some horizontal banded and vein structures can also be seen. The analysis and test results show that the south red agate has a typical radial fiber structure, and the main chemical component is SiO_2; Under the orthogonal polarizing microscope, a large number of round reddish brown mineral inclusions with banded distribution can be seen, the spot-colored mineral is iron oxide hematite, and calcite of the late hydrothermal origin can be seen in the cracks. In addition, the study shows that the formation of south red agate is multistage and the formation of hematite inclusions is also multistage.

1. Introduction

The application history of southern red agate can be traced back to the period of Hongshan culture. It has been used by royal families and nobles as early as the northern and southern dynasties. From the Ming and Qing dynasties to now, high-quality Nanhong agate has always been an important material for jewelry. It is one of the jade varieties with a long history in China. Nanhong agate is a unique species in China. It is named for its main mining area in Baoshan, Yunnan, in history. However, it is not only produced in Yunnan that it is called Nanhong agate [1]. In a broad sense, southern red refers to the general name of red agate with bright colors produced in southwest China. Its three major producing areas are Baoshan southern red in Yunnan (southern Yunnan red), Liangshan southern red in Sichuan (southern Sichuan red), and Diebu southern red in Gansu (southern Gansu red). The common Nanhong agate

in the market is mainly produced in Baoshan, Yunnan, and Liangshan, Sichuan. Sichuan Nanhong is a variety of Nanhong that has been developed in large quantities in recent years. It is produced in Meigu area of Liangshan Prefecture, Sichuan province. It was discovered and mined in 2009 [2]. The discovery of Sichuan Nanhong has greatly alleviated the problems of low output, many grain cracks, and exhausted mining of Baoshan Nanhong and led to a new "Nanhong fever." For a time, the price of Nanhong agate soared and became the darling of the collection industry again. Nowadays, the price of southern red agate has soared all the way, while similar Mongolian red agate, Xinjiang red agate, and African red agate do not have such a high price. The gemstone mineralogical characteristics and chromogenic mechanism of southern red agate need to be studied. What is the difference between southern red agate and red agate from other producing areas and how to distinguish it from imitations in the market are worthy of our discussion

[3]. The research on the south red agate will help people better understand south red agate and play a certain role in the identification work and the prospecting work of the south red agate.

2. Literature Review

Redlisiak et al. said that south red agate, often referred to as "south red," is a general term for a natural red agate that is mainly red and moist and thick in appearance produced in southwest China in recent years [4]. Kondratyeva et al. said that in China, south red agate has a long application history and its earliest use can be traced back to the period of Hongshan culture [5]. Lu et al. said that the earliest surviving south red product is the south red shell coin unearthed at the Jinsha site in Chengdu, which follows the tradition of using shell coins by the ancestors of Sanxingdui [1]. Zheng– Sheng et al. said that in the tombs of the nobles of the ancient Dian state during the Warring States period, many strings of Nanhong agate and two Nanhong agate carvings of beetles and cow heads were also unearthed [6]. Wang et al. found through investigation that until the Ming and Qing dynasties, Nanhong agate once became a substitute for red coral and was known as one of the "seven treasures of Buddhism." It has an extremely special position in Tibetan Buddhism and is widely used in Buddha beads and bracelets [7]. Zhu et al. said that during the Qianlong period of the Qing dynasty, Nanhong agate won the favor of the royal family, so a large number of Nanhong agates were paid as tribute to the court. So far, it reached its first heyday. The beautiful color carvings of Nanhong agate such as "double fish dragon flower arrangement" and "bat peach tree flower arrangement" in the Qing dynasty are still collected in the Palace Museum [8]. Golovanova and Pitieva believed that in terms of metallogenic environment, Chinese agate often occurs in volcanic rock series, and its mineralization is mainly magmatic hydrothermal alteration and hydrothermal filling. And common agate deposits occur in basalt formation, neutral volcanic rock formation, acid TUFF formation, and residual slope alluvial clastic formation, which provides suggestions for the prospecting direction of agate [9]. Huang et al. carried out a field investigation in the mining area of Nanhong agate and performed a specific analysis on the metallogenic environment. Among them, the Nanhong agate deposit in Liangshan, Sichuan province, belongs to the magmatic hydrothermal deposit, which takes the hydrothermal formed by basalt magmatic eruption as the material source. The metallogenic process mainly includes primary and secondary ore. At present, the mined deposits are sedimentary conglomerate deposits [10]. Wang et al. believe that the deposit type of Nanhong agate in Baoshan, Yunnan, belongs to the low-temperature hydrothermal colloidal deposit formed in the later stage of magma, which is mainly produced in the Quaternary strata and often filled in the almond pores and fractures of basalt [11]. Combined with the study of metallogenic environment and basic gem mineralogical characteristics, Krasilnikov et al. also performed a specific analysis on the color genesis of south red agate. They believed that south red agate is mainly colored by inclusions [12].

3. Method

3.1. South Red Agate Samples Are Selected for Testing.
A total of 8 samples of Nanhong agate (hereinafter referred to as "combined material") used in this paper are produced in the mine mouth of Lianhe Township, Meigu County, Liangshan Prefecture, Sichuan Province, and provided by an Auction Co., Ltd. The samples are numbered from L-101 to L-108. Samples L-101, L-102, L-105, and L-107 have epidermis. The part of sample L-107 is crystalline white quartz particles, and the other three are southern red agate with uniform appearance [13]. The basic characteristics are shown in Table 1.

Through the observation of the specimen, it can be seen that the color of the "combined material" of south red agate is mainly red with an orange or pink hue. The "cherry red" (also known as "water red") in the color classification of south red agate comes from the "combined material". Transparency is translucent-transparent. In addition, some white areas appear in sample L-106 and the white part is slightly transparent and opaque. The south red agate combined material has a conch fracture, which is oily and shiny because it contains cryptocrystalline-microcrystalline aggregate. It can be seen to the naked eye that densely distributed red granular mineral inclusions are distributed in the whole sample. The red mineral runs through almost the whole sample. For samples with bands, red granular inclusions gather along the bands, while the distribution of red minerals is relatively sparse at non-bands. The diameter of red mineral particles in most samples is between 10 and 80 μm, and the naked eye needs to observe with the help of transmitted light. In sample L-104, the diameter of some red mineral particles reaches $100 \sim 200$ μm, while the diameter of red minerals in samples L-107 and L-108 even reaches 400 μm, which is clearly visible to the naked eye under natural light [14]. In addition, some areas of sample L-107 are crystalline white quartz. At the transition between quartz and agate, some positions are red. Different from the surrounding red granular inclusions, the red part cannot distinguish particles and is cryptocrystalline. It is not difficult to find that the color of the "combined material" of south red agate is closely related to the distribution of red mineral inclusions. In areas where red inclusions are densely distributed, the thicker the red, the thinner the particles are distributed, and the lighter the color or even become colorless.

3.2. Geological Characteristics of the Siliceous Gravel Layer

3.2.1. Profile Description.
The tectonic location in the area is the Yangtze carbonate platform tectonic area of the upper Yangtze block, which mainly exposes Cambrian-Triassic strata, and the structural features are mainly NE trending folds and faults. The elevation of this section is 1125 m, the highest part of the mountain top is 1500 m, and the average slope angle is 37°. The gravel layer is located at the gentle slope of the depression. The exposed width of the gravel layer is about 20 m, the thickness is 10 m, and the exposed length is 30 m. The lower part is damaged by denudation and highway construction, and its exposed characteristics are unknown. The material composition of each layer of the gravel layer is mainly gravel, and only the 4th and 7th layers

TABLE 1: Basic characteristics of "combined material".

Sample number	Size (cm)	Color	Mass (g)	Relative density
L-101	4.51 × 4.28 × 2.61	The center is red, the band is red or orange red, and the band gap is orange yellow or colorless	52.5	2.6
L-102	3.37 × 2.07 × 1.16	Red	9.0	2.6
L-103	3.31 × 1.73 × 1.32	Red	10.9	2.6
L-104	3.22 × 4.28 × 2.61	The strip is red, and other areas are colorless or light red	18.0	2.7
L-105	3.81 × 2.70 × 12.61	Red	16.9	2.6
L-106	2.91 × 2.59 × 1.41	Red, white appears in some areas, and there is no obvious boundary with red	16.9	2.6
L-107	4.35 × 3.44 × 1.61	Red	31.2	2.6
L-108	2.80 × 2.21 × 1.86	Red	11.3	2.6

are gravelly sand clay layers. The overall gravel diameter is relatively coarse, mostly 2~8 cm. The gravels are mostly angular and basically not rounded. The composition of gravel is relatively single, which is basically composed of dolomite [15]. The boundary between layers is obvious. According to the characteristics of the gravel combination and gravel diameter change, it is divided into 9 layers from bottom to top. Generally speaking, the larger the gravel diameter of the gravel layer, the stronger its hydrodynamic force. According to the gravel diameter, the gravel layer in the survey area is divided into four sedimentary cycles and the circular column diagram is established. Cycle 1 is layer 2–4. The gravel diameter of the lower part is 10 cm, and the average gravel diameter is 2 cm in the upward transition. It has obvious binary structure characteristics of coarse at the bottom and fine at the top, and the sand clay and gravel of layer 4 are mixed and accumulated, showing the characteristics of sharp weakening of water flow power. Cycle 2 is the fifth layer, with a gravel diameter of 8 cm and upward to 2 cm. Cycle 3 is the 8th layer, which is distributed in the lenticular shape, the lower part is supported gravel, basically without the matrix, and the upper part is gravelly sand clay layer. Cycle 4 is 9–10 layers, with a gravel diameter of 12 cm in the lower part and 5 cm in the upper part, with obvious changes. The gravel diameter of each cycle decreases from bottom to top, reflecting the gradual reduction of hydrodynamic force of each cycle [16]. The gravels in the gravel layer are characterized by poor roundness and single gravel composition, which reflect that the material source is close. The gravel layer has a certain sorting property, and there is no matrix in the layer, which reflects that its deposition process has a certain duration, which is speculated to be the characteristics of intermountain flood alluvial deposition.

3.2.2. Gravel Particle Size Characteristics.

The particle size analysis of the gravel layer adopts a manual direct measurement method. According to the horizon direction of the gravel layer, samples shall be taken from bottom to top in the vertical bedding direction. Each layer shall be sampled with a 50 cm × 50 cm grid, and the length of the gravel axis in the grid shall be counted. By measuring 9 groups of samples in the gravel layer, the gravel in the gravel layer is mostly concentrated in 3~12 cm, accounting for more than 70%. Only sample 6 is mainly composed of fine particles such as

sand and clay, and the gravel content is 42%. The particle size parameters are calculated according to the Folk–Ward formula, as shown in Table 2, and the results are shown in Table 3. The overall average particle size of the gravel layer is −4.26 (19 mm). The average particle size of sample 13 decreased gradually. The average particle size of samples 4–6 decreased from −5.7 to −1.62, indicating that the water flow velocity decreased gradually.

The average particle size of samples 1, 2, 4, 5, 8, and 9 is $\varphi < -4$ (> 16 mm), and the sorting coefficient is between 1 and 2, indicating that its sorting property is medium. While the field outcrop of the corresponding layer shows that each layer is supported by particles, and there is little matrix deposition such as clay and sand. The average particle size ϕ in samples 3, 6, and 7 is −1~−4 (2 ~ 16 mm), and its particle size is relatively small. The sorting coefficient is between 2 and 4, and the sorting property is poor. The absolute values of skewness are >10, and there are two asymmetric particle size peaks and the sorting property is poor [17]. Combined with the field outcrop identification, the fourth layer corresponding to sample 3 is the grayish yellow coarse gravel layer containing sand and clay and the fine particles such as sand and clay are significantly increased. The frequency accumulation curve shows that the sediment has two obvious peaks, as shown in Figure 1.

4. Results and Analysis

4.1. Structural Characteristics of South Red Agate.

Nanhong agate particles are closely combined and have a near aphanitic structure. Its structural characteristics cannot be accurately observed under a 10× magnifying glass. In order to observe the structural characteristics more clearly, the raw stone samples are converted into mineral flakes and observed under a polarizing microscope. The samples under an orthogonal polarizer have a typical radial fiber structure. Due to multiple crystals in the same structural layer, the crystals are perpendicular to the base and extend synchronously to the opposite side since the microcrystalline bud, resulting in the radioactive growth of the crystals from a point or a mineral edge. Due to the poor fluidity of SiO_2 colloid, the crystal can only grow into fine fibrous crystals with radial structure. The color of southern red agate is related to the red dot minerals that are roughly banded and densely distributed. Under a 1000× microscope, it is a small

Table 2: Particle size parameter formula.

Name	Folk and Ward
Median	$M_{d\varphi} = \varphi_{50}$
Average particle size	$M_Z = (\varphi 16 + \varphi 50 + \varphi 84/3)$
Sorting	$\sigma_1 = (\varphi 84 - \phi 16/4) + (\phi 95 - \phi 5/6.6)$
Skewness	$SK_1 = (\varphi 16 + \varphi 84 - 2\varphi 50/2(\varphi 84 - \varphi 16)) + (\varphi 5 + \varphi 95 - 2\varphi 50/2(\varphi 95 - \varphi 5))$
Kurtosis	$K_G = (\varphi 95 - \varphi 5/(2.44(\varphi 75 - \varphi 25)))$

Table 3: Gravel composition and particle size parameters.

Sample number	Layer number	Average particle size (φ)	Sorting coefficient (σ_1)	Skewness (SK_1)	Kurtosis (K_G)
1	2	−4.97	1.6	−2.19	0.73
2	3	−4.71	1.63	5.47	1.24
3	4	−3.51	2.4	11.47	0.59
4	5	−5.7	1.14	3.46	0.75
5	6	−4.21	1.03	1.25	1.21
6	7	−1.42	2.17	−20.34	0.71
7	8	−3.1	2.23	14.26	0.51
8	9	−5.7	1.35	2.37	0.74
9	10	−4.9	1.37	2.33	0.71

nearly spherical reddish brown chromogenic mineral with incomplete crystal morphology and the existence of nearly hexagonal particles. Fourier near infrared spectroscopy was used to test three bead samples with good surface polishing in different areas [18]. Test conditions: room temperature, reflection method, the measurement range is set to 400~2000 cm^{-1}, the resolution is 4 cm^{-1}, and 30 scans. The comparison results of infrared absorption spectra are shown in Figure 2.

In Figure 2, south red agate has five obvious absorption peaks, namely, 496, 541, 783, 1099, and 1195 cm^{-1}, that is, the main mineral composition of south red agate is α-quartz. Due to the fine structure of Nanhong agate, it is difficult to determine the species of some minerals using the microscope and laser Raman analysis technology is often used for qualitative and quantitative analysis of small areas of rock and mineral analysis. Therefore, Raman spectroscopy is used to further determine the species of nearly spherical chromogenic minerals. The spectrum obtained from the laser Raman test of reddish brown punctate minerals with banded and dense distribution seen by the naked eye is shown in Figure 3.

The test conditions are as follows: argon ion laser 532 nm; the test range is 100~3000 cm^{-1}; scanning 3 times, laser scanning spot 1 μm. Figure 4 shows the Raman spectrum of south red agate chromogenic minerals.

According to Figure 4, the test samples have 228.93, 248.44, 295.48, 413.56, 467.33, 501, 613.84, and 1320.50 cm^{-1} obvious scattering peaks. The Raman spectra of reddish brown near spherical minerals in southern red agate are very similar; the scattering peaks around 467 cm^{-1} and 1320 cm^{-1} are strong, and the other peaks are mainly distributed between 130 and 620 cm^{-1}. Comparing the test data with the Raman data of minerals in the RRUFF database, the absorption of scattering peaks near 130, 210, and 468 cm^{-1} is α-quartz. The absorption mineral of the scattering peak near 225, 245, 294, 410, 499, 501, and 61ll cm^{-1} is hematite, that is,
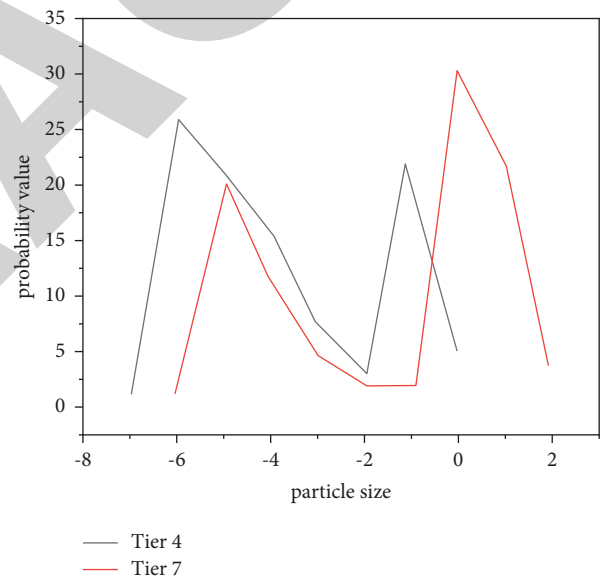
Figure 1: Grain size frequency curve of sediments in layers 4 and 7.

the red nearly spherical mineral inclusions distributed in strips are iron oxide hematite, the absorption peak at 501 cm^{-1} is the strong scattering peak of SiO$_2$, 1320 cm^{-1} in the form of clinopyroxene, and the absorption is the characteristic absorption peak spectrum of calcite [19]. The results of Raman scattering peaks show that the main mineral of south red agate is α-quartz, the nearly spherical chromogenic mineral distributed in a strip is iron oxide hematite, and the fissure is filled with calcite and other minerals of the late hydrothermal origin.

4.2. Discussion on Color Causes and Influencing Factors of South Red Agate. Through the comprehensive test and analysis of south red agate and yellow and white comparison samples, it can be determined that the main chromogenic
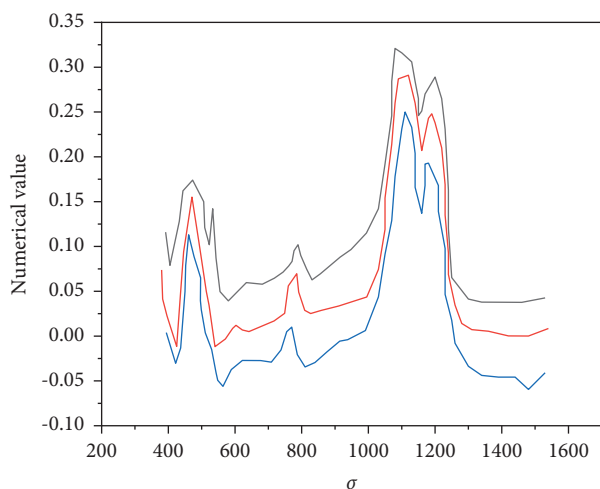
Figure 2: Comparison of infrared absorption spectra of south red agate.

Figure 3: B-1 Raman spectra of chromogenic minerals of south red agate.

mineral of south red agate and comparison samples is goethite, and there is also a very small amount of hematite. The evidence is as follows:

(1) The polarizing microscope observed that the spot-colored minerals and disseminated distribution areas of Nanhong agate are orange red. On the whole, the color tone is yellowish and translucent, which is consistent with the common color of goethite in nature.

(2) X-ray powder diffraction analysis showed that a small amount of the goethite phase was detected in central south red agate, but no obvious goethite phase was detected in yellow and colorless agate.

(3) The existence of the goethite phase was detected in the color region of dot chromogenic minerals and disseminated distribution in Raman spectroscopy.

(4) The UV-Vis absorption spectra of red and yellow samples are the superposition of typical absorption spectra of goethite and hematite.

(5) In the whole rock chemical composition analysis, the average iron content of red samples > the average iron content of yellow samples > the iron content of white comparison samples. These pieces of evidence show that red and yellow colors of Nanhong agate and the comparison sample are mainly related to the existence and content of the goethite phase, and there may be a small amount of hematite.

In addition to the content of chromogenic minerals, the color difference between goethite and hematite also affects the color of agate. When the particle size of goethite or wurtzite is $0.3 \sim 1.0 \, \mu$m, the appearance is yellow, and when the particle size is $0.05 \sim 0.8 \, \mu$m, the color is dark yellow. As the particle becomes smaller, the appearance color will gradually darken. When the particle size of hematite is less than $0.1 \, \mu$m, the color is orange, and when the size is $0.1 \sim 0.5 \, \mu$m, the color is red. When a single particle is larger than $1.5 \, \mu$m, it will appear purple. When goethite and
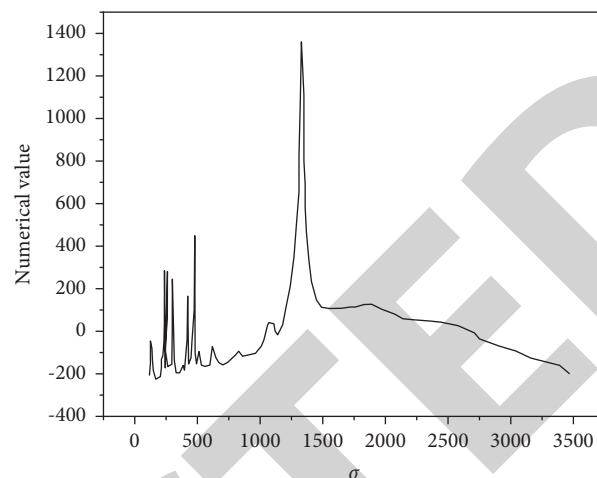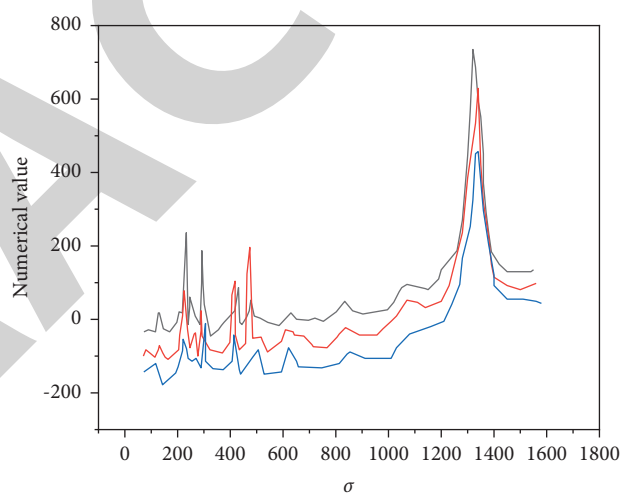
Figure 4: Raman spectra of chromogenic minerals of Nanhong agate.

hematite are combined in a very dense way, the whole combination will appear black or dark brown. In this paper, the size of the spot-colored minerals is about $10 \, \mu$m. According to the above theory, it is speculated that the appearance of agate should be opaque black. However, under the polarizing microscope, the colored minerals are translucent orange red, with fuzzy particle boundaries and no complete monocrystal characteristics. Therefore, it is speculated that the spot-colored minerals observed under the polarizing microscope are an aggregate composed of submicron goethite and a very small amount of hematite particles. In addition, there are some translucent orange red areas with disseminated distribution in Nanhong agate; no single chromogenic mineral particles can be observed, but the Raman spectrum and UV-Vis absorption spectrum show that this area is goethite with a very small amount of hematite minerals. Therefore, it is speculated that the chromogenic areas with disseminated distribution are similar to the chromogenic minerals with dot distribution, which are

an aggregate composed of submicron goethite and a small amount of hematite particles.

5. Conclusion

South red agate has a typical radial fiber structure, and there are parallel fiber crystal structures in each layer. The color of Nanhong agate in Baoshan city, Yunnan province, and Liangshan Prefecture, Sichuan province, is roughly distributed in strips, which is consistent with the distribution of nearly hexagonal reddish brown minerals. Baoshan south red agate has orange hues and developed fissures. Liangshan south red agate has rich colors and few fissures. The conventional gemmological characteristics of south red agate are similar to ordinary cryptocrystalline quartzite, but a large number of nearly red spherical inclusions are densely distributed through magnification observation. Combined with the infrared spectrum and Raman spectrum, the main mineral is α-quartz, in which the nearly hexagonal reddish brown spherical mineral inclusion is iron oxide hematite and the calcite at the crack is a mineral of late hydrothermal origin. During enlarged inspection, goethite and a small amount of hematite in Beihong agate exist in orange red punctate and disseminated forms. The size of the punctate goethite and hematite is about $10\,\mu m$, but they do not have an obvious crystal shape, and the particle boundary is fuzzy. It is speculated that it is an aggregate formed by the aggregation of submicron goethite and a small amount of hematite. The particle size of orange red goethite and hematite with disseminated distribution is not visible during magnification inspection. It is speculated that the particle size is similar to the colored minerals with dot distribution, both of which are submicron size but do not aggregate to form a dot aggregate visible under the microscope. On the whole, the content of goethite and hematite in Beihong agate is more than that in the yellow comparison sample. The higher the content of chromogenic minerals, the more red the color tone of Beihong agate. The comprehensive use of the Raman spectrum and UV-Vis absorption spectrum is of great significance for nondestructive analysis of phase composition of jewelry and jade, origin differentiation, and color classification of quartz jade.

Data Availability

The data used to support the findings of this study are available from the corresponding author upon request.

Conflicts of Interest

The authors declare that they have no conflicts of interest.

Acknowledgments

References

[1] Z. Lu, X. He, and Q. Guo, "Color and genesis of beihong agate and its spectroscopic characteristics," *Guang pu xue yu guang pu fen xi*, vol. 40, no. 8, pp. 2531–2537, 2020.

[2] K. N. Tkachenko, "Nutrition of the red fox (vulpes vulpes) in bol'shekhekhtsirskii nature reserve and its environs (southern part of the Amur river region)," *Biology Bulletin*, vol. 48, no. 8, pp. 1424–1433, 2021.

[3] A. V. Maslov, "Volcanic tuffs, red- and usual-colored clayey rocks in upper riphean–vendian deposits in the middle and southern urals: comparison of lithochemical characteristics," *Lithology and Mineral Resources*, vol. 56, no. 2, pp. 132–151, 2021.

[4] M. Redlisiak, A. Mazur, and M. Remisiewicz, "Size dimorphism and sex determination in the song thrush (turdus philomelos) migrating through the southern baltic coast," *Annales Zoologici Fennici*, vol. 57, no. 1-6, 2020.

[5] L. G. Kondratyeva, M. S. Dyachkova, and A. V. Galchenko, "The origin of genetic code and translation in the framework of current concepts on the origin of life," *Biochemistry*, vol. 87, no. 2, pp. 150–169, 2022.

[6] Y. Y. Zheng and J. Sheng, "The origin of translation," *Nature Chemistry*, vol. 13, no. 8, pp. 725-726, 2021.

[7] X. Wang, B. Li, X. Yang et al., "Characteristics of "guangyuan-wangcang" trough during late middle permian and its petroleum geological significance in northern Sichuan basin, sw China," *Petroleum Exploration and Development*, vol. 48, no. 3, pp. 655–669, 2021.

[8] T. Zhu, W. Li, Q. Wang, and Y. Hu, "Engineering geological and petrological characterization of paleoweathered rock in the k1/j2 contact zone in the ordos basin, China," *Environmental Earth Sciences*, vol. 81, no. 6, 2022.

[9] O. V. Golovanova and K. E. Pitieva, "The neopleistocene aquifer system in the region of the development of the astrakhan gas condensate field: characteristics, structures, and formation models," *Moscow University Geology Bulletin*, vol. 76, no. 6, pp. 646–655, 2022.

[10] Y. Huang, C. Tao, J. Liang et al., "Geological characteristics of the qiaoyue seamount and associated ultramafic-hosted seafloor hydrothermal system (52.1˚E, southwest Indian ridge)," *Acta Oceanologica Sinica*, vol. 40, no. 11, pp. 138–146, 2022.

[11] Y. Wang, G. Zhai, G. Liu et al., "Geological characteristics of shale gas in different strata of marine facies in South China," *Journal of Earth Sciences*, vol. 32, no. 4, pp. 725–741, 2021.

[12] S. S. Krasilnikov, A. T. Basilevsky, M. A. Ivanov, and A. S. Krasilnikov, "Geological and geomorphological characteristics of high-priority landing sites for the luna-glob mission," *Solar System Research*, vol. 55, no. 2, pp. 83–96, 2021.

[13] H. J. Brink, "The variscan deformation front (VDF) in northwest Germany and its relation to a network of geological features including the Ore-Rich Harz Mountains and the European Alpine belt," *International Journal of Geosciences*, vol. 12, no. 05, pp. 447–486, 2021.

[14] E. H. Al-Khersan, S. A. Al-Taei, and A. A. Al-Zubaidi, "Marine geophysical study to explore the seafloor bathymetry and geological features at the Iraqi corridors, northwestern Arabian gulf," *Pure and Applied Geophysics*, vol. 179, no. 2, pp. 747–764, 2022.

Retraction

Retracted: Art Design of Ceramic Sculpture Based on 3D Printing Technology and Electrochemistry

Journal of Chemistry

This article has been retracted by Hindawi following an investigation undertaken by the publisher [1]. This investigation has uncovered evidence of one or more of the following indicators of systematic manipulation of the publication process:

(1) Discrepancies in scope

(2) Discrepancies in the description of the research reported

(3) Discrepancies between the availability of data and the research described

(4) Inappropriate citations

(5) Incoherent, meaningless and/or irrelevant content included in the article

(6) Peer-review manipulation

The presence of these indicators undermines our confidence in the integrity of the article's content and we cannot, therefore, vouch for its reliability. Please note that this notice is intended solely to alert readers that the content of this article is unreliable. We have not investigated whether authors were aware of or involved in the systematic manipulation of the publication process.

Wiley and Hindawi regrets that the usual quality checks did not identify these issues before publication and have since put additional measures in place to safeguard research integrity.

We wish to credit our own Research Integrity and Research Publishing teams and anonymous and named external researchers and research integrity experts for contributing to this investigation.

The corresponding author, as the representative of all authors, has been given the opportunity to register their agreement or disagreement to this retraction. We have kept a record of any response received.

References

[1] J. Zhu and W. Liu, "Art Design of Ceramic Sculpture Based on 3D Printing Technology and Electrochemistry," *Journal of Chemistry*, vol. 2022, Article ID 3190499, 9 pages, 2022.

Research Article

Art Design of Ceramic Sculpture Based on 3D Printing Technology and Electrochemistry

Junxi Zhu and **Weiyu Liu**

Ceramic Art Design Department, Jingdezhen Ceramic Institute, Jingdezhen, Jiangxi, 333000, China

Correspondence should be addressed to Junxi Zhu; 321045119103@stu.suse.edu.cn

In order to solve the artistic design of ceramic sculpture, we proposed a method based on 3D printing technology for ceramic sculpture. First, using ANSYS ICEMCFD simulation software, we verified the effectiveness of the ceramic sculpture design method based on 3D printing technology in this study. Second, the design method of this study is recorded as the experimental group A. The two traditional design methods are recorded as experimental group B and experimental group C, respectively. Finally, we determined and compared the effect, size error, and precision error of the three groups of design methods to design the product. Ceramic sculptures are designed by proving the design method, high pattern definition, and small surface precision error. In the three directions of x-axis, y-axis, and z-axis, the relative size error generated is small, and the error is maintained below 1.0, and the effect of the finished product is consistent. So, the surface roughness of the ceramic sculpture designed this time is low, which will not affect the dimensional accuracy of the ceramic sculpture.

1. Introduction

3D printing, commonly known as additive manufacturing, is the process of 3D printing by a computer-controlled printer. First, build a model of the part data to be printed. It is decomposed into several plane data, and then, the print head of the 3D printer is controlled by the computer, using rollers to spread powder or other technology. Powder materials such as metals or ceramics are sintered into flat shapes according to flat data, turning multidimensional manufacturing into a bottom-up two-dimensional layer-by-layer process, thereby forming a multidimensional solid object. 3D printing technology combines cutting-edge technologies in many fields such as digital modeling, material technology, and information collection, it has profoundly changed the process and method of object manufacturing and is known as "the most iconic production tool of the third industrial revolution," which has attracted more and more attention at home and abroad [1].

3D printing uses traditional 3D software to shape the 3D data of the design draft and then print the three-dimensional data through a 3D printer, and the model of the three-dimensional data can be quickly converted into a solid template. The shape of the product is designed through the computer, as shown in Figure 1. This not only saves a lot of cost and time but also provides convenient modifiability, experimentation, and creativity to produce ceramic models. It has a great impetus for the future development of the industry. However, due to the limitations of current printing materials and cost calculation considerations, generally, the design of ceramic modeling is completed through printed metal or resin models, combined with traditional reproduction and casting techniques, the shaped gypsum mold is used for grouting, and finally, the shape design of the ceramic is completed.

2. Literature Review

In today's rapid technological development, 3D printing and virtual reality technology rely on its own efficient and convenient characteristics, and it has penetrated into all fields of all walks of life. It is playing an increasingly
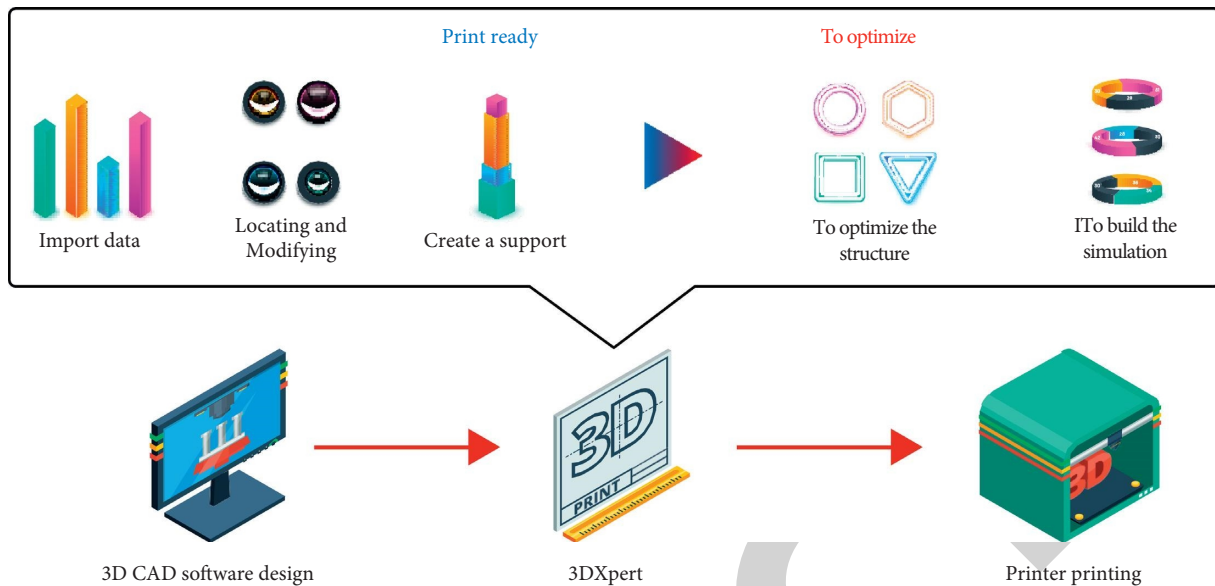
Figure 1: 3D printing.

important role in the manufacturing sector. With the accelerated development of urbanization, the demand for ceramic sculpture as a spiritual carrier is increasing day by day. At this time, the existing technical means are too single. By analyzing the status of virtual reality technology and 3D printing technology and comparing the old and new manufacturing methods, it aims to establish a digital intelligent sculpture system, combined with specific cases, it demonstrates the rationality and effectiveness of new technologies in the design and manufacture of ceramic sculptures.

3D printing technology has been developed abroad for a long time; it has been gradually applied in various fields of the manufacturing industry. At present, the widely used materials on the market are mainly polymer resins and metals, such as aerospace composite materials mainly printed with thermoplastic/short fiber materials. This stable network cross-linked polymer has been widely used in many parts of aerospace optical remote sensors. The material products prepared by 3D printing have the advantages of light weight and high strength, realizing the integration of concept design, technical verification, and manufacturing. It greatly shortens the manufacturing time and saves materials, and the printed parts with complex shapes can be directly used for the assembly and repair of the whole machine, convenient. Du, J. et al. showed that the traditional microfluidic chip manufacturing technology is a labor-intensive industry, which is not conducive to the rapid iteration and rapid manufacturing of chip design in the laboratory [2]. Lin, C. et al. first proposed that the basic idea is applicable to almost all 3D printing methods, the main process is to first use the CAD method to slice and divide complex three-dimensional components, convert it into computer-recognized code instructions, and then print the ceramic powder to be molded into a solid unit with the help of an output device [3]. Pinargote, N. et al. took the lead in

proposing water-based colloidal slurry to prepare three-dimensional functional ceramics. The advantage of this type of paste is that the viscoelasticity can be regulated over multiple orders of magnitude, and lines with patterns and spans can be formed [4]. Zhao, B. et al. first used polyetherimide- (PEI-) coated monodisperse $SiO2$ microspheres with a diameter of $1.17\,\mu$m as the raw material. A suspension was prepared by dispersing it in deionized water [5]. Zheng, D. first proposed to combine the photocuring molding technology with the preparation process of ceramic materials, and the material used in the photocuring molding technology is a slurry composed of photosensitive resin and ceramic powder [6]. Li, P. et al. fabricated high-performance porous β-TCP bone tissue engineering scaffolds by 3D printing technology [7]. Zou, Q. et al. prepared manganese-tricalcium phosphate (Mn-TCP) bioceramic scaffolds with ordered macroporous structure by 3D printing method [8]. Yan, J. et al. prepared ZrO2–Al2O3 ceramic samples by SLM technology, the density of ZrO2–Al2O3 ceramic samples can reach 100% without sintering and posttreatment, the bending strength is 500 MPa, and there is no crack [9]. Shi, L. et al. used the organic polymer precursor polycarbosilane to crack to prepare SiC ceramic fibers, creating a precedent for the preparation of ceramics and composite materials by the transformation of precursors [10]. Zhang, L. et al. used conventional light curing technology (SLA) to obtain polymer ceramic precursors, and thermal cracking transformed the ceramic precursors into ceramic parts [11]. Cho, S. N. et al. studied in detail the effects of dispersant, diluent concentration, and other factors on the viscosity of ceramic slurry and determined the optimal component content, a new water-based ceramic slurry based on silica sol was successfully developed, and a silica ceramic slurry with a solid content of up to 50% was prepared [12].

On the basis of the current research, the author proposes a ceramic sculpture based on 3D printing technology, the

designed ceramic sculpture has high pattern definition and small surface precision error, the resulting relative size error is small, and the error is maintained below 1.0, which is consistent with the effect of the finished product. Therefore, the surface roughness of the ceramic sculpture designed this time is low, which will not affect the dimensional accuracy of the ceramic sculpture.

3. Ceramic Sculpture Art Design Based on 3D Printing Technology

3.1. 3D Printing Technology Background. 3D printing is a process of creating three-dimensional objects by adequately preparing materials, where diagonal shapes are designed. This printing technique has an often-used term called "rapid prototyping," so this formulation technique uses several layers of sediment material to construct a 3D model. The different shapes and forms of objects are created by additively processing the sequence of different materials, one layer on top of the other. The process begins by creating a virtual object with 3D modeling software, or a replica object with a 3D scanner. After years of exploration and development, 3D printing technology has made great progress; at present, it has been able to achieve a fine resolution of 600dpi on a single layer thickness of 0.01 mm. At present, the most advanced products in the world can achieve a vertical rate of 25 mm thickness per hour and can achieve 24-bit color printing [13]. 3D printers use different methods. Significant differences manifest in the way one layer is applied to another. The American Society for Testing and Materials (ASTM) defines the technical procedures for seven different additives, stereolithography, material jetting, adhesive jetting, material extrusion, powder layer fusion, sheet lamination, direct energy deposition, which enables it to create 3D objects. 3D technology is suitable for printing different 3D objects; therefore, it can also be successfully used to print communication tools for the blind and visually impaired, such as Braille and 3D maps. Until recently, Braille was mainly printed in relief, less by screen printing and other printing techniques. Today, 3D printing technology is becoming more and more popular, not only for printing Braille but also for printing tactile objects, maps, and floor plans.

3.2. Ceramic Sculpture

3.2.1. Basic Type. There are various types and forms of ceramic sculptures, which can be classified from multiple angles. There are the following two main classifications (see Figure 2). In these two categories, decorative sculpture and garden sculpture are the most commonly used creation methods by designers [14].

(1) Decorative Sculpture. It is an artistic creation of decorating and beautifying buildings that follows the general layout of the building but has its own specific content. Decorative sculptures can be divided into folk sculptures, decorative sculptures, religious sculptures, monument sculptures, and functional sculptures according to their different functions. With its diverse forms and shapes, it perfectly plays the role of beautifying the urban environment and enriching people's culture, such as the sculptures in front of the gymnasium and those designed around the building. It can express a wide range of themes and flexible forms, such as characters, animals, ancient myths, and legends. It is characterized by the small scale of sculpture, which can enrich people's spiritual and cultural world while beautifying the surrounding environment.

3.2.2. The Production Process of Traditional Sculpture

(1) Project production is an important means for works to convey ideas and information exchange to people, everyone has a different understanding of a real object, and designers need to express their creative intentions to partners through scheme design and determine the style, shape, texture, material, and layout. Of the work according to the scheme information, the advantage is that it can greatly reduce the probability of rework in the later stage [15].

(2) A sculpture is a three-dimensional form of art. In addition to its beauty, the safety of its structure should also be considered. This link is difficult to fully demonstrate on the two-dimensional drawings, and it is necessary to make a three-dimensional sketch model. The production of the draft is mainly on the premise of respecting the first draft, fully considering the feasibility of processing and the rationality of the structure, recreating from the three-dimensional structure and artistic form.

(3) Building the inner skeleton and making the skeleton is one of the key steps in making a sculpture. It can determine the dynamics of the sculpture, support the inner structure of the sculpture and the mud on the surface, for large sculptures, and reduce its own weight and save materials. In the selection of skeleton materials, there are mainly wood and metal (lead wire, iron nails, steel bars, etc.), and titanium alloy materials can be selected if funds allow.

(4) On the big clay, the enlargement of the clay sculpture occurs after the original small draft is finalized. The works are made according to the actual size. The whole sculpture is shaped from the inside to the outside. The enlarged clay sculpture should be consistent with the small draft [16].

(5) Regarding the in-depth shaping, after the large shape is determined, the designer needs to carry out in-depth characterization, starting from the depiction of local details to the whole sculpture, repeated observation, and modification. The designer adjusts the relationship of each part until the final molding and prepares for the next step of reproducing the mold.

(6) Regarding sculpture overturning, clay sculpture needs to be stored for a long time after it is completed, which requires the work to be turned into a more rigid material. This requires the use of
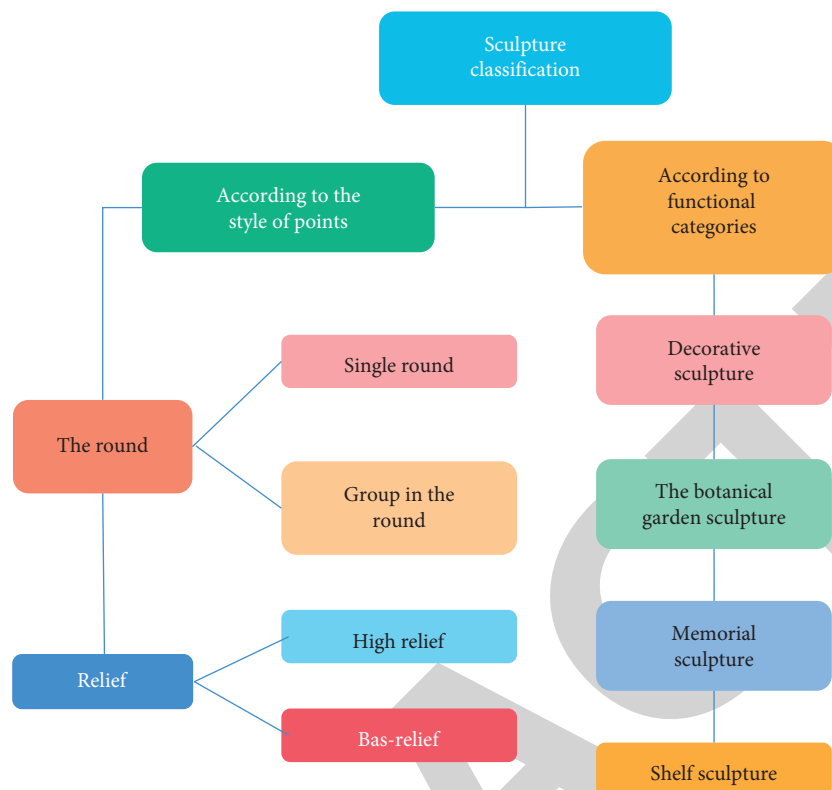
FIGURE 2: Basic types of sculpture.

traditional model making techniques, and small sculptures can be completed independently by the creators, and large-scale sculptures require the co-operation of several professional technicians. The level of technicians is very important; if there is a mistake, the previous work in the clay sculpture stage may be for nothing. Because the work at this stage is too meticulous and requires a lot of time, it is easy to cause the problem of an excessively long production cycle.

(7) After the reproduction is completed, wait for the work to air dry and then manually knock out the mold to take out the sculpture. At this time, the sculpture is already a semifinished product, and the surface needs to be treated manually: grinding, repairing, and polishing. Finally, the artistic creators will color the work according to the design requirements.

(8) Transport to site for installation. The overall process is shown in Figure 3

3.3. Development Status of 3D Printing and Digital Technology in Ceramic Sculpture

3.3.1. Development Status of 3D Printing Technology. 3D printing technology first appeared in the mid-to-late 1980s, invented by the Massachusetts Institute of Technology, later transferred to the 3M company in the United States, and developed the first 3D printing equipment in 1986. At that
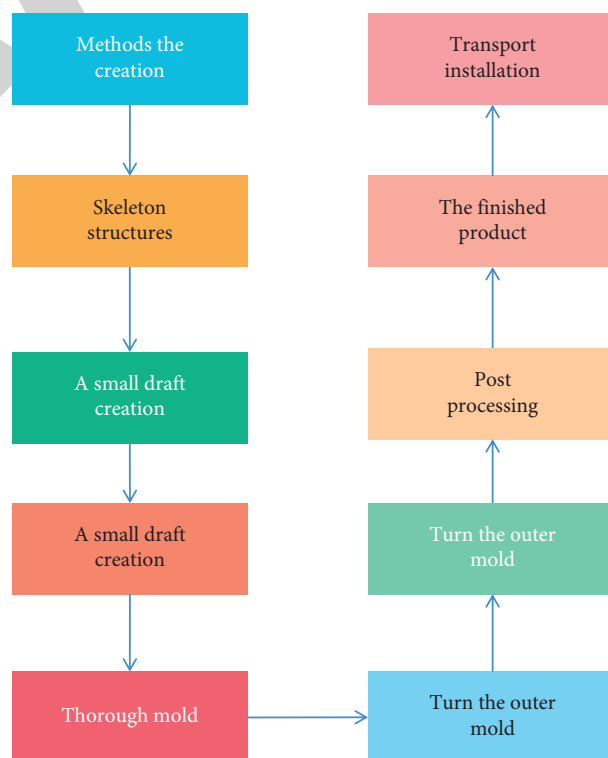
FIGURE 3: Flowchart of traditional sculpture production.

time, the application and popularity of this technology in the industry was slow, but it already had a prototype, and the comparison with future commercial applications was

inseparable. After entering the new century, 3D printing technology has gradually matured and perfected and has developed rapidly. The data shows that the global market value of 3D printing in 2012 was 2 billion US dollars, a year-on-year increase of 29%, and the market demand increased by 25% year-on-year. The U.S. accounted for 38 percent of that, and about 10 percent came from China. As shown in Figure 4, we can more intuitively understand the changes in the size of the global 3D printing market, showing an upward trend. In 2012, the British "Economics" magazine published an article "3D printing promotes the third industrial revolution." It has attracted the attention of the whole world and has caused heated discussions in the world [17]. In terms of technical equipment, Zcop developed the first color 3D printer in 2005. In 2012, Scottish experts and scholars used 3D printers and biological materials to process human liver tissue. In 2014, the International Space Organization (ISS) deployed the first 3D printer, and workers were able to print their own daily necessities and machine parts as needed. In the past few years, the application and popularization of 3D printing technology were on the rise, and it has had a significant impact on traditional industries.

3.4. Application and Embodiment of 3D Technology in Contemporary Ceramic Sculpture Design.

The use of digital technology in the development of ceramic sculpture is relatively late, and 3D technology is also an auxiliary technology that has gradually begun to flourish in recent years. At first, some sculptors began to experiment with 3D digital painting and 3D modeling with the help of computers and software, so as to see the image works very close to the final product through the drawing. Compared with traditional sketching, mud drafting, and other methods, 3D digital technology and final image imaging are more direct, accurate, and beautiful and have obvious advantages compared with traditional drawing methods. The application of 3D technology in all aspects of contemporary ceramic sculpture and plastic production continues to expand. Many cities require 3D stereoscopic presentation when making sculptures and rendering effects in real scenes, even simulating different background elements, such as day, night, lighting changes, and surrounding scenery, to add to the dynamism of the final sculpture. The design and production of traditional ceramic sculptures may consume a lot of manpower, material resources, and financial resources, but the results are very small. 3D digital technology can not only avoid the above risks well but also add icing on the cake for sculpture works. At the same time, it can also reflect the public's demand for ceramic sculpture works to the greatest extent and give full play to the aesthetic function of ceramic sculpture in public resources. Therefore, this technique has been widely favored since it was applied in ceramic sculpture. With the in-depth application of 3D digital technology in ceramic sculpture, its value is not only a single simulation tool and provides a new idea and artistic language for ceramic sculpture designers, effectively broadening the way of diversified development of sculpture works [18]. Before 3D technology
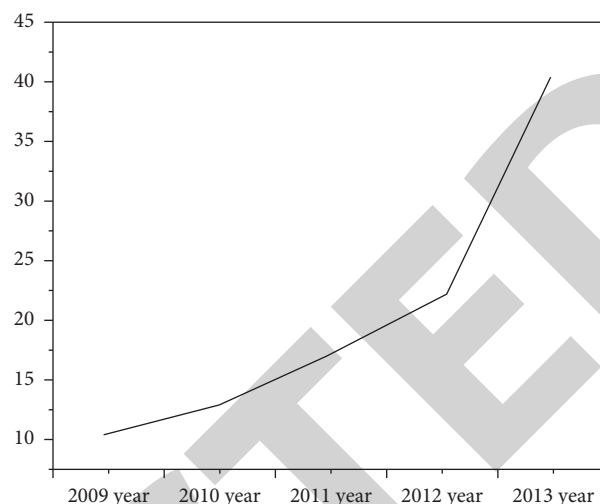
FIGURE 4: Growth rate of global 3D printing market size.

was officially put into use, the design of sculpture works could only show the effect roughly in the form of strokes. With the large-scale use of 3D technology, sculpture works can be more vividly presented in front of the designer in the early stage, which is beneficial to complete the designer's artistic conception from the perspective of tools and discretion. In addition, 3D digital technology also provides a broader experimental space for designers of ceramic sculptures with the support of virtual technology. The final effect of the sculpture works is tested before the formal construction. The sculpture material can be evaluated according to the printed 3D renderings, without the need for a physical structure. Details such as sculpture suspension can be processed through digital technology models, and the possibility of reversibility has not been designed and constructed at the same time; by inversely correcting the rendering of the effect, the final sculpture is brought to a perfect state. The limit reflects the public's demand for urban public sculpture works and gives full play to the aesthetic function of urban public sculpture in public resources. Therefore, this technology has been widely favored since it was applied in urban public sculpture in my country [19].

3.5. Efficiency and Reliability of 3D Printing and Digital Technology in Ceramic Sculpture Design.

In terms of efficiency, the emergence of the combination of 3D printing and digital technology reduce the workload of designers, improve work efficiency, and free the staff from the tedious and complicated design and manufacturing process. The application of digital technology has made the difficult problems in the design of ceramic sculptures easy to solve. For repeated work that needs to copy an object, adjust the angle, scale proportionally, it can be easily solved by digital virtual reality technology. In the virtual environment, the designer can modify and design the work in an all-round way; it further inspired the creative staff, greatly shortened the design cycle, and effectively improved the quality of the

work. At the same time, compared with the complex production process of traditional ceramic sculptures, 3D printing technology is more convenient and efficient, a new work can be easily "printed," and within a reasonable range, complex designs can be formed, no matter how precise the size can be grasped, no matter how many materials can be realized in a sculpture work [20].

In terms of reliability, 3D printing and digitization technology is programmed based on its own data. Unlike manual operations, as long as the system works properly, there will be no errors in the results. For example, in model construction, the size of the model can be accurate to a few decimal places, and then, the model data information is extracted to the 3D printing device for printing. This workflow enables the manufacture of ceramic sculptures with a level of reliability that is simply unmatched by traditional ceramic sculpture techniques [21].

4. Experimental Demonstration Analysis

The experimental demonstration analysis adopts the method of comparative experiment and selects the ceramic sculpture in the product as the research object of this experiment, using ANSYS ICEMCFD simulation software to simulate the design of ceramic sculpture, in order to verify the effectiveness of the ceramic sculpture design method based on 3D printing technology in this study [22]. The ceramic sculpture design method studied in this study is recorded as the experimental group A. The two traditional ceramic sculpture design methods were recorded as experimental group B and experimental group C, respectively. The ceramic sculpture design parameters, dimensional measurement tools, and calculation formulas were determined, and the effects, dimensional errors, and precision errors of the three groups of design methods were compared.

4.1. Experiment Preparation.
Based on this experiment, the selected experimental object is ceramic sculpture. There are many complicated patterns in the ceramic sculpture, the overall shape is generous and beautiful, the details are exquisite, and the workmanship is fine, which can meet the needs of this experiment. Using ANSYS ICEMCFD simulation software, as the design software of three groups of methods, after completing the ceramic sculpture design, its running environment in the computer is shown in Table 1.

Based on the experimental parameters, the ceramic thickness was set to 6 mm, and the overall height was set to 300 mm. Set the printing speed device of the 3D printer to 40 mm/s, the layer thickness (the thickness of each layer of entities printed) is 0.2 mm, the nozzle temperature of the printer is 210–240°C, and the printing filling rate is 100% and is a solid pattern When the print fill rate is 0%, it is a hollow pattern. Based on the experimental parameters of the previously mentioned equipment, the design effects of the three groups of methods were compared [23].

TABLE 1: Simulation software operating environment.

Operating environment	Configure	Parameter
Hardware environment	CPU	Intel Core i5-9400
	Frequency	2.90 GHz
	printer	3D printer
	Number of digits	64 bit
Software environment	Analog software voice	APDL
	3D printer control software	3D printer

4.2. Experimental Results

4.2.1. Comparison of Design Effects.
Based on the experimental environment, experimental objects, and experimental parameters set up in this experiment, using three groups of methods, the ceramic sculpture design was completed in the ANSYS ICEMCFD simulation software, and the effect of the ceramic sculptures designed by the three groups of methods was compared. The ceramic sculpture designed by experimental group B has obvious break marks in the pattern on the back, which affects the overall appearance. Although the patterns on the ceramic sculptures designed by experimental group C are intact, the overall design has a strong sense of roughness and has not reflected the fineness and roundness of ceramic sculptures. The ceramic sculptures designed by experimental group A have complete patterns, rounded overall, and no roughness. It can be seen that because of the design method of ceramic sculpture in this study, the designed ceramic sculpture has high pattern definition and low roughness, which is consistent with the effect of the finished product [24].

4.2.2. Measurement Size Error.
Based on the results of the first set of experiments, a second set of experiments was carried out to measure three sets of methods. The result of designing the ceramic sculpture is to establish a coordinate system (x, y, z) with the connection point of the back and seat surface of the ceramic sculpture as the center, as shown in Figure 5.

Along the three directions of x-axis, y-axis, and z-axis, a universal dimension measuring instrument, vernier caliper, measure the size of the ceramic sculpture designed by three methods and the actual size of the ceramic sculpture and record the dimensions in three directions. In order to ensure the rigor of the experiment, the dimensions of the ceramic sculptures designed by each group of methods are in three directions, measure the size of the ceramic sculpture 10 times, and calculate the relative error of the ceramic sculpture designed by the three groups of design methods and the actual product of the ceramic sculpture in three directions. The measurement results are shown in Figure 6.

As can be seen from Figure 6, the ceramic sculptures designed by experimental group B have the largest relative errors in the three directions. The relative error in the three directions of the ceramic sculptures in the experimental group C is smaller than that in the experimental group B but
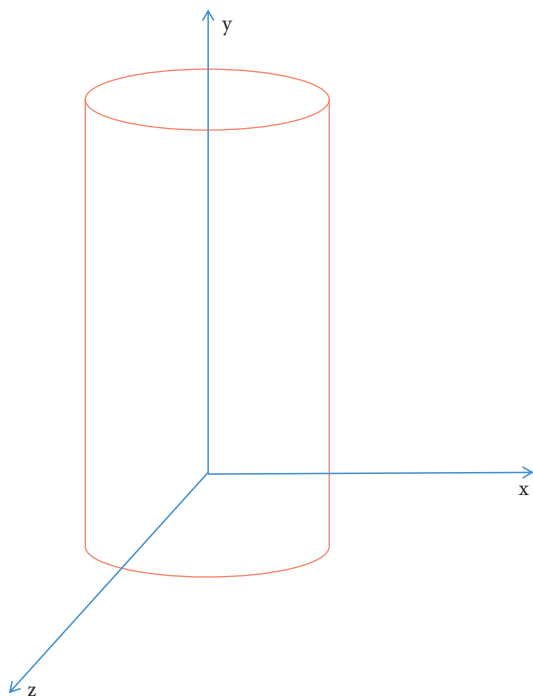
Figure 5: Ceramic sculpture coordinate system.
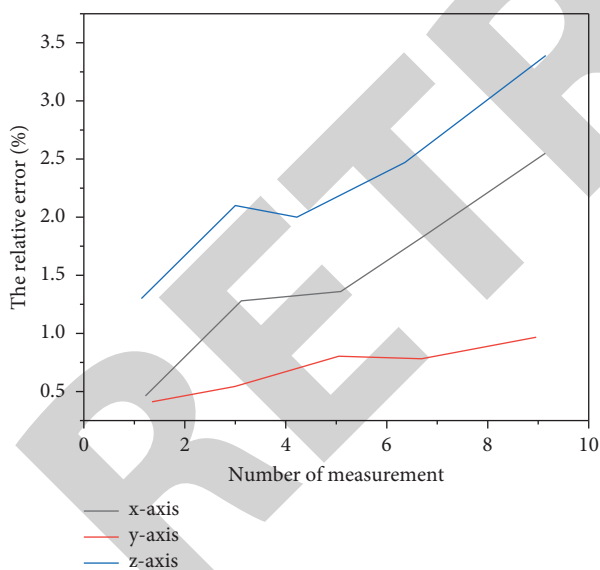
Figure 6: Dimensional errors in three horizontal directions.

is still more than 2.6%. In only the experimental group A, the designed ceramic sculpture, the relative error in the three directions has always been less than 1.0%. From this, it can be seen that the ceramic sculpture designed by the ceramic sculpture design method of this research has small relative dimensional errors in the three directions of x-axis, y-axis, and z-axis and will not affect the dimensional accuracy of the ceramic sculpture [25].

Table 2: Surface relative accuracy error (mm^2).

Testing frequency	Experiment group a	Experiment group B	Experiment group C
1	0.624	1.521	3.380
2	0.656	2.149	2.715
3	0.343	1.934	2.660
4	0.354	2.305	2.547
5	0.537	1.463	2.947
6	0.565	2.457	3.445
Mean	0.512	1.947	2.970

4.2.3. Measuring Surface Accuracy Error. Based on the first set of experimental results, a virtual design drawing is obtained, and the surface accuracy of the ceramic sculpture designed by the three groups of methods is measured. The calculation formula (1) is as follows:

$$\Delta S = \frac{1}{2}\mu \cdot h^2. \tag{1}$$

In formula (1), ΔS represents the surface accuracy error of ceramic sculpture (mm2); μ represents the dimensionless scale factor; h represents the layer height (mm) that the ceramic sculpture needs to be processed.

The general dimension measuring instrument, vernier caliper, was used to measure the area, processing layer height, and total height of the ceramic sculpture, which were used as the calculation data of this group of experiments. In order to ensure the rigor of the experimental results, each group of data was measured six times, and the relative accuracy results of the three groups of ceramic sculpture surfaces were calculated according to formula (1), and the average value of the six measurement accuracy errors was obtained. The experimental results are shown in Table 2.

It can be seen from Table 2 that the surface accuracy error of the ceramic sculpture designed by the experimental group C is the largest. Compared with the mean value of surface accuracy error of experimental group A, it is 2.458 mm^2 higher, and it is 0.999 mm^2 higher than the mean value of surface accuracy error of experimental group B. The surface precision error of the ceramic sculpture designed by the experimental group B is smaller than that of the experimental group C, but it is 1.459 mm^2 higher than the average surface precision error of the experimental group A. It can be seen that, in the ceramic sculpture designed by the ceramic sculpture design method of this study, the surface accuracy error is small and maintained below 1.0 mm^2, and the surface roughness is low. Based on the three sets of experimental results, it can be seen that, in the ceramic sculptures designed by the ceramic sculpture design method of this study, the pattern has a high definition, and the surface accuracy error is small. In the three directions of x-axis, y-axis, and z-axis, the resulting relative size error is small, and the error is maintained below 1.0, which is consistent with the effect of the finished product. Therefore, the surface roughness of the ceramic sculpture designed this time is low, which

will not affect the dimensional accuracy of the ceramic sculpture.

5. Conclusion

To sum up, in the ceramic sculpture designed by the design method of this research, the pattern has a high definition, and the surface accuracy error is small. In the three directions of x-axis, y-axis, and z-axis, the resulting relative size error is small, and the error is maintained below 1.0, which is consistent with the effect of the finished product. Therefore, the surface roughness of the ceramic sculpture designed this time is low, which will not affect the dimensional accuracy of the ceramic sculpture. Make full use of 3D printing technology to design ceramic sculpture shapes, print ceramic sculpture patterns, and improve the design accuracy of ceramic sculptures. However, in the design method of ceramic sculpture in this study, the influence of the product design raw materials selected in the design of ceramic sculptures on the product design results has not been considered. Therefore, in future research, it is necessary to further study the design method of ceramic sculpture, consider the material properties of the product, improve the equivalent stress of ceramic sculpture design, and further improve the practicability of ceramic sculpture.

Data Availability

The data used to support the findings of this study are available from the corresponding author upon request.

Conflicts of Interest

The authors declare that they have no conflicts of interest.

References

[1] Y. He, "Research on the role of art creation in ceramic material product design based on the perspective of innovation," *E3S Web of Conferences*, vol. 251, no. 4, Article ID 01033, 2021.

[2] J. Du, "Research on optimization of portrait sculpture data based on 3d image and mobile edge computing," *IEEE Access*, vol. 8, no. 99, p. 1, 2020.

[3] L. Cai, "Research on the design of multicolored ceramic cultural creative products based on computer vr technology," *Journal of Physics: Conference Series*, vol. 1744, no. 3, Article ID 032160, 2021.

[4] N. W. Solís Pinargote, A. Smirnov, N. Peretyagin, A. Seleznev, and P. Peretyagin, "Direct ink writing technology (3d printing) of graphene-based ceramic nanocomposites: a review," *Nanomaterials*, vol. 10, no. 7, p. 1300, 2020.

[5] B. Zhao, "Research on the application of ceramic 3d printing technology," *Journal of Physics: Conference Series*, vol. 1827, no. 1, Article ID 012057, 2021.

[6] D. Zheng, "Research on application of computer 3d modeling technology in ceramic tea set design," *Journal of Physics: Conference Series*, vol. 1961, no. 1, Article ID 012058, 2021.

[7] P. Li, "Research on visual art design method based on virtual reality," *International Journal of Gaming and Computer-Mediated Simulations*, vol. 13, no. 2, pp. 16–25, 2021.

[8] Q. Zou, "Research on the design of digital media art display platform based on dynamic visual recognition," *International Journal of Arts and Technology*, vol. 12, no. 2, p. 118, 2020.

[9] Y. Jun and S. X. Xian, "Research on landscape design based on digital technology," *Journal of Physics: Conference Series*, vol. 1651, no. 1, Article ID 012071, 2020.

[10] L. Shi, "Application research of 3d digital technology in sculpture creation," *E3S Web of Conferences*, vol. 236, no. 5, Article ID 05101, 2021.

[11] L. Zhang, X. Yang, Y. Xu, and Q. Yu, "Research on the models and implementation techniques of ceramic mes system based on isa95," *E3S Web of Conferences*, vol. 236, no. 12, Article ID 02030, 2021.

[12] S. N. Cho, "A study on the extension of traditional formative ceramic art through convergence of design mediums," *The Korean Society of Science & Art*, vol. 38, no. 5, pp. 463–475, 2020.

[13] W. H. Lee, Y. F. Wu, Y. C. Ding, and T. W. Cheng, "Fabrication of ceramic moulds using recycled shell powder and sand with geopolymer technology in investment casting," *Applied Sciences*, vol. 10, no. 13, p. 4577, 2020.

[14] H. Y. Durak, M. Saritepeci, and F. B. Çam, "Examination of university students' opinions on use of augmented reality technology in archeology field," *Journal of Qualitative Research in Education*, vol. 8, no. 1, pp. 156–179, 2020.

[15] D. Selva, B. Nagaraj, A. Rajendran, A. Nair, and A. Nair, "Intelligent network intrusion prevention feature collection and classification algorithms," *Algorithms*, vol. 14, no. 8, p. 224, 2021.

[16] R. Wilk, W. Likus, A. Hudecki, M. Syguła, A. Różycka-Nechoritis, and K. Nechoritis, "What would you like to print? students' opinions on the use of 3d printing technology in medicine," *PLoS One*, vol. 15, no. 4, Article ID e0230851, 2020.

[17] M. Fan and A. Sharma, "Design and implementation of construction cost prediction model based on svm and lssvm in industries 4.0," *International Journal of Intelligent Computing and Cybernetics*, vol. 3, no. 2, pp. 145–157, 2021.

[18] A. Xu, "Application of 3d printing technology in the field of ceramic material manufacturing," *IOP Conference Series: Earth and Environmental Science*, vol. 440, no. 2, Article ID 022070, 2020.

[19] X. Liu, J. Liu, J. Chen, and F. Zhong, "Degradation of benzene, toluene, and xylene with high gaseous hourly space velocity by double dielectric barrier discharge combined with Mn3O4/activated carbon fibers," *Journal of Physics D: Applied Physics*, vol. 55, no. 12, Article ID 125206, 2022.

[20] T. Ishida and K. Kinomura, "Outline of 3d printing technology with cement based materials and its impact on the construction industry," *Concrete Journal*, vol. 58, no. 1, pp. 45–51, 2020.

[21] R. Huang, P. Yan, and X. Yang, "Knowledge map visualization of technology hotspots and development trends in China's textile manufacturing industry," *IET Collaborative Intelligent Manufacturing*, vol. 3, no. 3, pp. 243–251, 2021.

[22] K. Miyamoto, H. Koga, M. Izumi, M. Mizui, and H. Nishiguchi, "Study on fabrication of anodes for sofcs with 3d printing technology," *ECS Transactions*, vol. 96, no. 1, pp. 219–226, 2020.

Retraction

Retracted: Electrochemical Preparation of Recycled Self-Compacting Concrete Composite Beams and Their Application in Prefabricated Buildings

Journal of Chemistry

This article has been retracted by Hindawi following an investigation undertaken by the publisher [1]. This investigation has uncovered evidence of one or more of the following indicators of systematic manipulation of the publication process:

(1) Discrepancies in scope

(2) Discrepancies in the description of the research reported

(3) Discrepancies between the availability of data and the research described

(4) Inappropriate citations

(5) Incoherent, meaningless and/or irrelevant content included in the article

(6) Peer-review manipulation

The presence of these indicators undermines our confidence in the integrity of the article's content and we cannot, therefore, vouch for its reliability. Please note that this notice is intended solely to alert readers that the content of this article is unreliable. We have not investigated whether authors were aware of or involved in the systematic manipulation of the publication process.

Wiley and Hindawi regrets that the usual quality checks did not identify these issues before publication and have since put additional measures in place to safeguard research integrity.

We wish to credit our own Research Integrity and Research Publishing teams and anonymous and named external researchers and research integrity experts for contributing to this investigation.

The corresponding author, as the representative of all authors, has been given the opportunity to register their agreement or disagreement to this retraction. We have kept a record of any response received.

References

[1] Y. Yuan and Y. Zhu, "Electrochemical Preparation of Recycled Self-Compacting Concrete Composite Beams and Their Application in Prefabricated Buildings," *Journal of Chemistry*, vol. 2022, Article ID 4748456, 8 pages, 2022.

Hindawi

Research Article

Electrochemical Preparation of Recycled Self-Compacting Concrete Composite Beams and Their Application in Prefabricated Buildings

Yuan Yuan and **Yongchao Zhu**

Railway Engineering College, Zhengzhou Railway Vocational and Technical College, Zhengzhou, Henan 451460, China

Correspondence should be addressed to Yongchao Zhu; 15081200210008@hainanu.edu.cn

In order to solve the problems of electrochemical preparation of recycled self-compacting concrete composite beams and their application in prefabricated buildings, we need to meet the requirements of national housing industrialization and green buildings, make up for the low development capacity of prefabricated buildings, and improve the speed of housing construction and the rapid development of the construction industry. Now the prefabricated building has entered a period of rapid growth. However, the research on the construction technology of the prefabricated building is still in its infancy, and there are many difficulties and challenges in the construction. The deformation and internal force of a prefabricated residential laminated floor slab in the construction process of prestressed PK slab transportation, stacking, hoisting, and the laminated cast-in-situ layer will affect the normal use of the building. However, at present, there is less mechanical analysis of its construction process, so there is blindness in the formulation, implementation, and inspection of the construction scheme. Through the social survey of 200 people, 179 people believe that prefabricated buildings will be better than traditional buildings. Therefore, by participating in the practice of prefabricated housing engineering, the key mechanical problems in the construction of the composite floor slab of prefabricated housing are explored and found.

1. Introduction

In China, for a long time, frame structure, frame shear wall structure, shear wall structure, steel-concrete structure, and other concrete buildings mainly adopt the traditional construction method of the on-site binding beam, slab, and column reinforcement pouring concrete. The degree of industrialization is low, the product rate of building structural components is low, the quality of building residential products is poor and unstable, the labor production efficiency is poor, the design and construction is extensive, the loss of building materials is large, and the amount of construction waste is large. In the past ten years, China's scientific research work on prefabricated concrete buildings has gradually increased. A number of enterprises have cooperated with scientific research institutions such as colleges and universities to carry out mechanical analysis and related technical research and applied it in development projects, which has been demonstrated on a certain scale [1]. Compared with the cast-in-situ concrete buildings constructed by traditional construction methods, the construction process of prefabricated concrete buildings has the advantages of saving resources, small on-site operation, improving on-site construction conditions, convenient construction, and so on. In the construction process, the transportation and hoisting process of the prestressed PK plate are relatively convenient and feasible. The prestressed PK plate laminated floor does not need formwork, which effectively reduces the amount of formwork, reduces the amount of work on the construction site, shortens the construction period, saves materials, and reduces the project cost [2].

Due to the variability of the concrete tensile strength, with the increase in stress in the component, there will be one or several cracks in the weak part of concrete at the same time. At the same time, the tension on the crack section will no longer be borne by the concrete but by the reinforcement. The stress of the reinforcement at the crack will suddenly increase, and the concrete at the crack will retract to both sides. At the same time, the slip and bonding stress between the reinforcement and the concrete will appear [3]. The function of bond stress is to transfer the tensile part of the reinforcement to the concrete until the distance from the crack increases, the strain of concrete and reinforcement gradually becomes equal, and the bond force is zero. With the continuous increase in the external load, new cracks will appear in concrete members and the stress between reinforcement and concrete will also change with the change in distance from cracks. Among them, the stress variation diagram of reinforcement and concrete of axial stressed members is shown in Figure 1.

2. Literature Review

Ihsan et al. said that in the early 1960s [4], the former Soviet Union used the assembled integral concrete laminated floor in the floor of buildings. Its structural structure is to use the prefabricated flat ribbed and grooveless prestressed concrete thin plate as the formwork, use manual rough treatment on the upper surface of the prestressed concrete thin plate, and then pour ceramsite concrete on the prestressed concrete thin plate. Its strength is generally C7.5~C10. The artificial rough surface treatment on the upper surface of the prestressed concrete sheet ensures the combination of precast slab concrete and cast-in-situ concrete. Wu et al. said that the assembled integral concrete composite floor has been successfully applied in the seismic building engineering in the southern region of the former Soviet Union [5]. Huang et al. of France widely used the assembled monolithic concrete composite floor from 1970 to 1979 and configured reinforcement on the composite section to bear the shear force of the composite section so as to make the precast slab and cast-in-situ concrete work better together [6]. In recent years, Wender et al. studied and developed a new type of the reinforced concrete structure system, that is, semi-precast structure system. Its structure is to place the *U*-shaped semi-precast beam on the *I*-shaped semi-precast column and connect the lower reinforcement [7]. Yang et al. reported that PC laminated floors are widely used in the floors of public industrial buildings and multistorey and high-rise buildings [8]. According to the research, Imaz-Lueje et al. believed that the PC laminated floor can be applied in seismic areas and strong seismic areas [9]. Li et al. said that the FP laminated floor slab is a form of the PC laminated slab, and its structural structure is the prefabricated thin plate with high strength and low relaxation female thread reinforcement. The prefabricated thin plate is not only a part of the FP laminated floor slab structure but also a template for the construction of the cast-in-situ concrete layer. The FP laminated floor slab can be formed by pouring concrete on
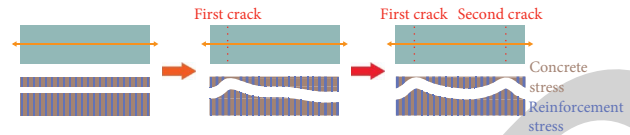
Figure 1: Axial stressed member.

its prefabricated thin plate [10]. In 1961, Bodehou et al. studied and manufactured the assembled integral multi-ribbed floor slab. The beam adopts the prefabricated "I" shaped small beam, and the precast concrete thin plate is placed on the beam. The precast concrete thin plate and the beam are poured with concrete to form a whole after curing, and the precast thin plate is placed on the flange at the lower part of the beam as the ceiling flat roof [11]. The Beijing Civil Aviation Office Building and the Beijing National Hotel are the first two high-rise buildings with assembled integral concrete composite structure in China.

3. Method

3.1. Failure Criteria of Concrete. The failure criterion of concrete is very important in the finite element analysis of reinforced concrete structures. The failure of concrete materials is defined by the use of ultimate strength. The ultimate strength of concrete has a variety of strength criteria with different parameters, such as one to five parameters. At present, the Willam–Warnke five-parameter strength criterion model is often used in finite element analysis. The meridian of the model is a more general tension and compression parabolic meridian [12].

The failure surface expression of the Willam–Warnke five-parameter failure criterion is shown as follows:

$$\frac{F}{f_c} - S \geq 0. \tag{1}$$

When the Willam–Warnke five-parameter model is used for finite element analysis, the concrete failure surface is continuous and convex without an inflection point and the failure surface is nonlinear on the meridian plane. The model analysis results are consistent with the experimental data. The parameters in the failure criterion of the model can be determined by standard tests. Therefore, the Willam–Warnke five-parameter model can better describe the failure characteristics of concrete [13]. The meridian equations of pressure and tension are shown in formulas (2) and (3):

$$\frac{\tau m1}{fc} = a0 + a1\left(\frac{\sigma m}{fc}\right) + a2\left(\frac{\sigma m}{fc}\right)^2, \tag{2}$$

$$\frac{\tau m1}{fc} = b0 + b1\left(\frac{\sigma m}{fc}\right) + b2\left(\frac{\sigma m}{fc}\right)^2. \tag{3}$$

The pull meridian and the pressure meridian intersect on the hydrostatic pressure coordinate axis. In the aforementioned formula, only five parameters are independent. The five parameters are determined through the material test [14].

The basic premise of elastoplastic analysis of concrete is to determine the stress-strain relationship. In the case of multiaxial stress, due to the limitation of test conditions, the stress-strain relationship of concrete is often simulated and determined by the equivalent uniaxial stress-strain relationship. The full curve of concrete under uniaxial compression and uniaxial tension is obtained by the test [15]. The stress-strain relationship of concrete under uniaxial compression is shown in Figure 2, and the stress-strain relationship of concrete under uniaxial tension is shown in Figure 3.

The Hognestad formula and the Saenz formula are often used in the stress-strain curve of concrete under uniaxial compression. The Hognestad formula is often used in specifications, and the Saenz formula is often used in finite element analysis. The following is the expression of the Saenz formula, as shown in formulas (4)–(6):

$$\sigma = \frac{E0\varepsilon}{1 + (a + (E0/ES) - 2)(\varepsilon/\varepsilon0) - (2a - 1)(\varepsilon/\varepsilon0)^2 + a(\varepsilon/\varepsilon0)^3}, \tag{4}$$

$$a = \frac{(E0/Es)((\sigma0/\sigma N) - 1)}{((\varepsilon N/\varepsilon0) - 1)^2} - \frac{\varepsilon N}{\varepsilon0}, \tag{5}$$

$$Es = \frac{\sigma0}{\varepsilon0}. \tag{6}$$

In finite element analysis, the stress-strain curve of reinforcement is often simplified. When the reinforcement has an obvious yield point, the ideal elastic-plastic model is generally adopted, and the mathematical expression is shown in the following formulas:

$$\sigma = E\varepsilon, \tag{7}$$

$$\sigma = f_y. \tag{8}$$

When the reinforcement does not have the obvious yield point, the broken line model is generally adopted, which has two slopes (elastic slope and plastic slope). The mathematical expression is shown as follows:

$$\sigma = E\varepsilon. \tag{9}$$

3.2. Treatment of Prestressed Reinforcement.
The stress characteristics of the structure change due to the application of prestress. In the process of structural deformation, the stress of prestressed reinforcement also changes all the time, which makes the restraint effect on the structure also change. Therefore, the basis of prestressed concrete structure analysis is to accurately grasp the treatment method of the prestressed reinforcement [16]. There are two methods in ANSYS.

3.2.1. Equivalent Load Method.
The effect of the prestressed reinforcement on the structure is simplified into an equivalent external load applied to the structure. The
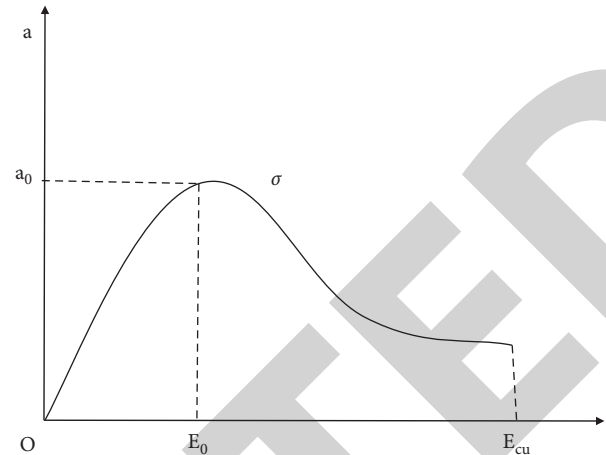
Figure 2: Stress-strain relationship of concrete under uniaxial compression.
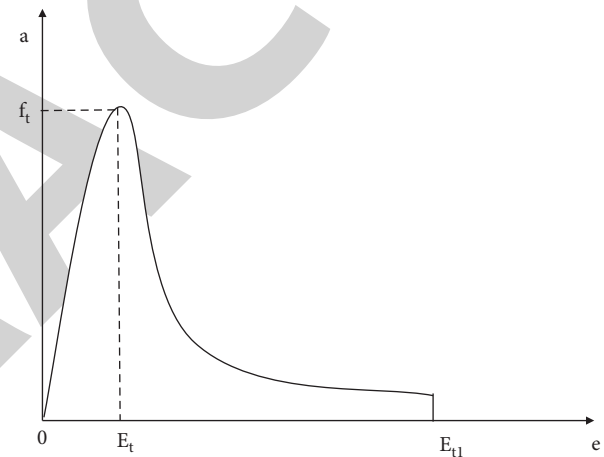
Figure 3: Stress-strain relationship of concrete under uniaxial tension.

equivalent load method is mainly used in relatively simple structural analysis. This processing method can meet the accuracy requirements of engineering and is widely used. Because it does not need to consider the position of reinforcement, the model is simple and the calculation process is easy to converge, but there is no way to analyze the internal force of reinforcement and its influence on concrete deformation and internal force. It is difficult to consider the influence of the synergistic effect of the prestressed reinforcement and the external load on the concrete deformation and internal force, and there is no way to analyze the influence of the external load on the stress increment of prestressed reinforcement [17].

3.2.2. Solid Reinforcement Method.
In the process of establishing the model, the concrete adopts the solid element and the prestressed reinforcement adopts the link element, which makes the influence of reinforcement and concrete in the model to be considered at the same time. The solid reinforcement method can consider the influence of several

factors and can be applied to the analysis of complex structures. It can also be used when engineering analysis needs high accuracy. There are two main methods to apply prestress in model analysis: one is the initial strain method, and the other is the temperature reduction method. The initial strain method is to set an initial strain for the prestressed reinforcement to replace the effect of prestress, and the two functions are the same. The cooling method is to cool the rod element link and shrink the rod element link to apply prestress in this way [18].

Compared with the initial strain method, the cooling method is simple, and the influence of many factors can be considered, such as stress loss and stress increment of the external load on the prestressed reinforcement. In the model, the prestress is applied by the cooling method, and the temperature change value corresponding to the prestress value needs to be calculated in advance, as shown in the following formula:

$$\Delta T = \sigma l E a. \tag{10}$$

In the convergence criterion of ANSYS, the relative measure of convergence based on displacement and the absolute measure of convergence based on force are given. It is better to use the force or moment as the basis of convergence tolerance in the process of model analysis. Element size, convergence criterion, and substeps are three main factors affecting the convergence of the SOLID65 element. In the process of establishing the model, the elements should be divided appropriately. If the element division is too small, the calculation may be unable to continue due to stress concentration. Hexahedral elements should be used as much as possible. When setting the convergence criteria, the convergence conditions can be relaxed appropriately. Generally, it should not exceed 5% and the force based convergence conditions are adopted [19].

Generally, when the crushing of concrete is not considered in the model calculation, it is easy to converge in the calculation. If the normal structure or the member is calculated and analyzed, the uniaxial compressive strength uncompst should be set to −1, and the option of concrete crushing should be turned off. "Concr + miso" shall be used when calculating the limit of the analyzed structure or member, and the crushing inspection of concrete shall be closed. In the process of modeling, to avoid the failure of solution due to the damage of concrete caused by stress concentration, it is advisable to appropriately increase the element size near the support or add some elastic cushion blocks or change the element at the support to solid45 and give steel properties so as to avoid stress concentration. The Solid45 unit provided by ANSYS is similar to the SOLID65 solid unit. The Solid45 unit has no cracking and crushing performance.

From the current test of composite beams in the world, the final deformation characteristics and crack development of composite beams under the concentrated load are very close to those of general cast-in-place beams. It is also shown that there are mainly vertical cracks in the middle of the beam span, and the spacing distribution is basically the same; there are obvious inclined cracks near the supports at both ends. Finally, the inclined cracks pass through the composite surface until the beam is damaged. However, due to the secondary pouring and two-stage stress of this structural member, its development process is different from that of general cast-in-place beams. When the first load is applied, the section of the precast part of the beam presents a distribution similar to that of the oblique crack of the abdominal shear: it is distributed as many thin and short vertical cracks, but the width of the crack is small, the extension height of the crack is small, and there is no oblique crack. After the load is applied in the second stage after superposition until the beam is damaged, its crack is called the critical oblique crack and after many experimental studies conducted by scholars, it is found that the critical oblique crack is always along the connecting line between the load action point and the bearing cushion block [20].

The crack development process of the composite beam is different from that of the cast-in-place beam, which is mainly caused by its two-stage construction and two-stage stress. When the composite beam is stressed f for the first time, the prefabricated part is compressed on the upper side and tensioned on the lower side. At this time, the compressive stress is generated on the upper side of the prefabricated part, that is, the composite surface. When the composite beam is formed, the compressive stress on the composite surface is solidified by the postcast part. For the later load of the whole composite beam, this part of the compressive stress is equivalent to prestress, so scholars vividly call it "load prestress." When the composite beam is stressed F1 for the second time, with the continuous increase in F, the stress state on the composite surface will change from compression to tension. In the process of mutual offset between tensile stress and load preload, the internal force on the composite surface will be redistributed until the load prestress disappears. Therefore, the load prestress inhibits the deformation of concrete and reinforcement so that when the inclined crack develops near the superposition surface, the speed becomes slow and even stagnates, which delays the main inclined crack from passing through the superposition surface, resulting in the crushing and destruction of the concrete in the shear compression area of the inclined section, thus improving the shear bearing capacity of the beam [21].

The two-stage stress characteristics of composite beam also determine that the stress distribution on its section is different from that of the cast-in-place beam. Under the action of F, because the height of the prefabricated part is relatively low compared with the overall beam, the phenomenon of "normal stress advance" of longitudinal reinforcement and "shear stress advance" of the stirrup will appear under the same external load, which is also the reason for the early occurrence of cracks in the composite beam. After the postcast concrete reaches its design strength, it begins to bear external forces. Under the action of $F2$, the concrete stress of the laminated layer starts from zero, so there is a phenomenon of "shear stress lag." The stress of the precast concrete is quite complex. Some of the original stress on its section and the stress caused by F offset each other and some overlap each other. With the increase in the number

and length of inclined cracks, the stress on the section is constantly redistributed. When the inclined cracks approach the superposition surface, they develop slowly and stagnate when they reach the superposition surface. In this way, the influence of the load applied in the first stage on the precast part is weakened. At this time, all the loads on the beam are gradually borne by the whole beam and the whole deformation pattern of the composite beam is gradually close to that of the general cast-in-place beam until it is finally damaged.

To sum up, the phenomena of "load prestress" and "shear stress lag" are beneficial to composite beams and we should pay attention to and make rational use of them. For the early and rapid crack development caused by "stress lead" and "shear lead," we should take appropriate measures in design and structure to reduce or avoid as much as possible.

The development pattern of the cracks in the composite beam is basically consistent with the research of scholars: because of the characteristics of the double stress of the composite beam, the cracks appear earlier and the earlier cracks are caused by the stress in one stage; the cracks in the precast part are mainly vertical cracks, with a small width and small height of crack extension. Compared with the whole cast-in-place beam, the stress of the composite beam remains unchanged in the first stage. When the whole bears the same load, vertical cracks appear at the supports of the composite beam and the whole cast-in-place beam. The cracks at the supports of the composite beam develop faster than that of the whole cast-in-place beam, and inclined cracks appear faster. However, the inclined cracks of the composite beam develop more intensively and roughly develop into two main inclined cracks, which connect the load and the bearing cushion block. However, the inclined cracks of the whole cast-in-place beam developed from the support are scattered and random. In the midspan part, "load prestress" makes the development of cracks in the composite beam slow with the increase in load and the development of cracks in the midspan of the whole cast-in-place beam is almost synchronous with the inclined cracks. Generally speaking, the cracks of composite beams appear earlier than those of cast-in-place beams, which are disadvantageous in the normal use stage of components, but their cracks develop slowly and have their advantages in the limit use stage [22].

The reason for the slow development of cracks near the composite surface of the bending area in the midspan of the composite beam is as follows: the load preloading stress is generated at the composite surface due to the loading in the first stage. When the second stage force is applied, the stress redistribution occurs on the composite surface, that is, from the compression area to the tensile area. At this time, the load preloading stress and tensile stress offset each other with the increase in the load and the cracks in the midspan do not begin to develop again until the tensile stress gradually offsets the load preloading stress. Therefore, the development of midspan cracks in the crack development process of composite beams is relatively slow, which is the so-called "compression stress lag" phenomenon, so it has a

good inhibitory effect on the crack development of composite beams.

In the simulation, it is also found that the crack development speed at the support of the composite beam is faster than that of the cast-in-place beam, which is due to the lower height of the prefabricated part of the composite beam without support (compared with the cast-in-place beam). The construction load generated in the construction stage is borne by this part, so there is an obvious phenomenon of "shear stress advance" in the stirrup in the precast part of the composite beam, and the stress of the same stirrup in the cast-in-place part (composite layer) is "shear stress lag" compared with the stirrup in the same position of the whole cast-in-place beam.

According to the crack development characteristics and the development mechanism of composite beam components under normal use, some influencing factors of crack development of the composite beam are explained. Then, the cracks of the composite beam and the whole beam are simulated and compared by ANSYS finite element software. The simulation results are consistent with the theory, which proves that the cracks of composite beam can be studied by ANSYS. By simulating the effects of several main parameters αh and aM affecting the composite beam and the concrete grade difference between the precast part and the composite part on "load prestress," "stress advance," and "stress lag," then, we analyze and study its advantages and disadvantages on crack development. Through comparative analysis, it can be seen that in order to control the height of the precast part and the size of the one-stage load, the concrete strength of the precast part and the composite beam and the difference between the two parts of concrete should be controlled, which can be paid attention to in the design and engineering of the composite beam. The change in the concrete strength of the precast layer is shown in Table 1, and the list of the concrete strength change in the cast-in-situ layer is shown in Table 2.

Stress analysis is mainly used to determine the stress concentration and peak stress and strain at the dangerous point related to component failure. It is very necessary to analyze the location selection of fabricated joints. The maximum compressive stress under the action of seismic force is used to judge how to select the segment position [23]. The variation of unit stress is shown in Figure 4.

4. Results and Analysis

The composite beam has the advantages of convenient construction of the prefabricated structure, short construction period, integrity of cast-in-situ structure, and good seismic performance, which makes it widely used in engineering construction. On the contrary, its two-stage pouring and two-stage stress make the mechanical performance and deformation pattern of the composite structure different from those of the whole pouring structure [24].

Based on the in-depth research theory of composite beams by many scholars, the numerical simulation of reinforced concrete composite beams under the concentrated load is carried out by using ANSYS large-scale finite

TABLE 1: Change in the concrete strength of the precast layer.

| Concrete strength of the cast-in-situ layer | C30 | C30 | C30 | C30 |
| Concrete strength of the precast layer | C25 | C30 | C40 | C50 |

TABLE 2: List of concrete strength changes in the cast-in-situ layer.

| Concrete strength of the cast-in-situ layer | C25 | C30 | C25 | C40 |
| Concrete strength of the precast layer | C30 | C30 | C30 | C30 |
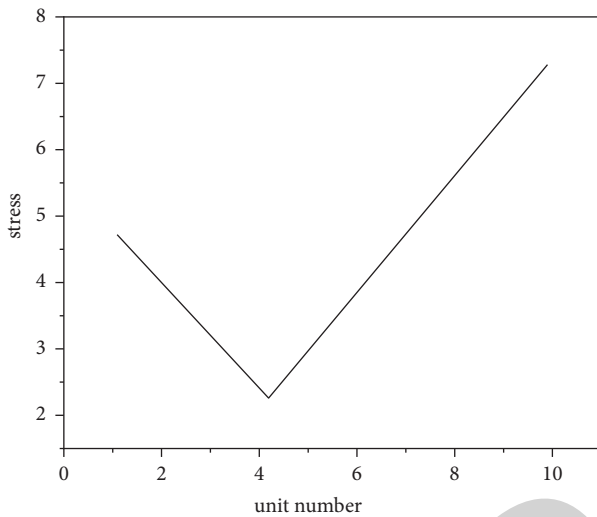
FIGURE 4: Variation of unit stress.

element software. The influential laws of these factors on the generation and development of component cracks and deflections are summarized by in-depth analysis of the stress changes in longitudinal reinforcement, stirrups, and concrete caused by superposition parameters α_h and a_{gy}, and the strength grade of old and new concrete. Then, through the analysis of the simulated deflection value and influencing factors, the relationship between the above factors and the deflection value of the composite beam are fitted. It can be concluded as follows: in order to prevent excessive deflection in one stage from affecting the normal use of composite beams in the later stage, the height of prefabricated parts in the design and construction of composite beams should be controlled. The size of the stage load, and the use of new and old concrete grade composite beam should be considered [25].

On the basis of the crack development mechanism of the composite beam and the simulation results of the normal composite beam by ANSYS [26], it is proved that the cracks of composite beams can be studied by ANSYS. Through the simulation of several main parameters α and α affecting the composite beam and the impact analysis of the concrete grade difference between the precast part and the composite part on "load prestress," "stress advance," and "stress lag," it can be seen that the height of the precast part and the size of the first stage load should be controlled. At the same time, the difference of concrete strength between the precast part and composite part should be controlled, and attention should be paid to the design and engineering of the composite beam to control the speed of crack development [27].

Through the comparison of deflection values, it is proved that the simulation of displacement and deformation of the composite beam by ANSYS is accurate and it is also concluded that the influencing factors affecting the stiffness and deflection of the composite beam are mainly the strength of the stressed reinforcement, precast part, and cast-in-situ part of concrete [28]. The deflection value and influencing factors obtained from the simulation are analyzed, and the relationship between the superposition parameters αh and aM and the concrete strength of the precast part and the superposition part on the deflection value of the composite beam are fitted. During the design and construction of the composite beam, it must be noted that the height of the precast part cannot be too small, which is generally taken as 0.55–0.6 and the load in the first stage should not be too large. These two cases are mainly to prevent the excessive deflection in the first stage from affecting the normal use of the composite beam in the later stage. In addition, the old and new concrete of the composite beam shall not be of the same grade as far as possible because both theoretical and simulation results tell us that when the concrete of the same grade is used, the deflection of the composite beam is relatively large.

5. Conclusion

By comparing the results of ANSYS finite element simulation analysis with the theoretical calculation results of the reverse arch value and the detection test results of the detection center, it is proved that the ANSYS finite element analysis model is reasonable and feasible.

In the mechanical simulation analysis of the prestressed PK slab composite floor construction process, the simplification of the finite element analysis model has a great impact on the simulation results. The two skids under the bottom plate of the prestressed PK plate are simplified into linear fixed support and linear sliding support, respectively, and two special lifting appliances are simplified into linear sliding support, four ordinary lifting points are simplified into four-point sliding support, and two temporary supports are simplified into linear sliding support, which makes the simulation analysis results closer to the actual situation. Through experiments, it is proved that the electrochemical preparation of the recycled self-compacting concrete composite beam and its application in prefabricated buildings are feasible, which effectively solves the requirements of national housing industrialization and green buildings, makes up for the lack of low development power of prefabricated buildings, and improves the construction speed of

the construction industry and the rapid development of the construction industry.

Data Availability

The data used to support the findings of this study are available from the corresponding author upon request.

Conflicts of Interest

The authors declare that they have no conflicts of interest.

Acknowledgments

References

[1] C. Hui, K. Li, Y. Li, Y. Bian, R. Hai, and C. Li, "Experimental study and analysis on axial compression performance of high—strength recycled concrete—filled steel tube column in corrosive environments," *International Journal of Steel Structures*, vol. 22, no. 2, pp. 450–471, 2022.

[2] S. Kumar, G. Rao, and P. M. Raju, "Strength and durability studies on ggbs concrete," *Malaysian Construction Research Journal*, vol. 30, no. 1, pp. 17–34, 2020.

[3] H. Sun, X. Ge, W. He, and L. Zhao, "A reconfigurable antenna with sum—and difference—patterns for wlan access points," *IEEE Antennas and Wireless Propagation Letters*, vol. 19, pp. 1073–1077, 2020.

[4] F. Ihsan, L. Daniault, S. Bellanger et al., "Coherent beam combining of 61 femtosecond fiber amplifiers," *Optics Express*, vol. 28, no. 14, 2020.

[5] D. Wu, Z. Y. Zhang, G. Fu, X. Shi, and X. Li, "Rotman lens-fed antenna for generating multiple orbital angular momentum (Oam) modes with gain enhancement," *IEEE Access*, vol. 99, p. 1, 2020.

[6] T. Huang, D. Zhang, Y. Huang, C. Fan, Y. Lin, and F. Zhang, "Flexural bearing capacity and failure mechanism of CFRP-aluminum laminate beam with double-channel cross-section," *Science and Engineering of Composite Materials*, vol. 28, no. 1, pp. 139–152, 2021.

[7] S. A. Wender, J. M. Odonnell, L. Zavorka, and B. Bhuva, "Measured energy dependent neutron attenuation through the stacked printed circuit boards," *IEEE Transactions on Nuclear Science*, vol. 67, pp. 1114–1117, 2020.

[8] J. Yang, S. S. Qi, W. Wu, and D. G. Fang, "A novel sum and difference conical beam—scanning reflector antenna," *IEEE Access*, vol. 99, 2020.

[9] B. Imaz-Lueje, D. R. Prado, M. Arrebola, and M. R. Pino, "Reflectarray antennas: a smart solution for new generation satellite mega—constellations in space communications," *Scientific Reports*, vol. 10, no. 1, 2020.

[10] S. Li, Z. N. Chen, T. Li, F. H. Lin, and X. Yin, "Characterization of metasurface lens antenna for sub-6 GHz dual-polarization full-dimension massive mimo and multibeam systems," *IEEE Transactions on Antennas and Propagation*, vol. 68, no. 3, pp. 1366–1377, 2020.

[11] M. Bodehou, E. Martini, S. Maci, I. Huynen, and C. Craeye, "Multibeam and beam scanning with modulated metasurfaces," *IEEE Transactions on Antennas and Propagation*, vol. 68, no. 3, pp. 1273–1281, 2020.

[12] S. Ibrahim and N. B. Mabrouk, "Integrated ism-fuzzy micmac approach based factor analysis on the implementation of safety program in construction industry," *Decision Science Letters*, vol. 10, no. 2, pp. 139–150, 2021.

[13] B. Liao and L. Li, "How can green building development promote carbon emission reduction efficiency of the construction industry? based on the dual perspective of industry and space," *Environmental Science and Pollution Research*, vol. 29, no. 7, pp. 9852–9866, 2021.

[14] R. Q. Zhang, A. Ma, X. Liang, L. M. Zhao, H. Zhao, and Z. Y. Yuan, "Cobalt nanoparticle decorated *n*-doped carbons derived from a cobalt covalent organic framework for oxygen electrochemistry," *Frontiers of Chemical Science and Engineering*, vol. 15, no. 6, pp. 1550–1560, 2021.

[15] N. U. Yusupdjanova and M. S. Asadova, "Clusters in the construction industry—integration, innovation and criteria for economic growth (on the example of the republic of Uzbekistan)," *Theoretical and Applied Science*, vol. 97, no. 5, pp. 611–614, 2021.

[16] S. Nazari, F. Borrelli, and A. Stefanopoulou, "Electric vehicles for smart buildings: a survey on applications, energy management methods, and battery degradation," *Proceedings of the IEEE*, vol. 109, pp. 1128–1144, 2021.

[17] X. Meng, K. Liu, Z. Li, and L. Sha, "Experimental study on seismic performance of prefabricated beam wall out—of—plane connection nodes with different anchoring measures," *KSCE Journal of Civil Engineering*, vol. 26, no. 2, pp. 770–780, 2021.

[18] G. Yao, M. Wang, Y. Yang, and J. Li, "Development and analysis of prefabricated concrete buildings in Chengdu, China," *International Journal of Sustainable Development and Planning*, vol. 15, no. 3, pp. 403–411, 2020.

[19] A. Benyahia, "Bond behavior of self-compacting mortar containing construction and demolition waste under elevated temperatures," *Asian Journal of Civil Engineering*, vol. 22, no. 3, pp. 405–415, 2020.

[20] M. S. Nair and K. G. Jayaraj, "Self-compacting concrete using recycled coarse aggregate—a feasible solution for waste demolished concrete," *International Journal of Advanced Research*, vol. 8, no. 7, pp. 836–847, 2020.

[21] T. M. Hasan and A. S. Ali, "Flexural behavior of fiber reinforced self—compacting rubberized concrete beams," *Journal of Engineering*, vol. 26, no. 2, pp. 111–128, 2020.

[22] R. D. Kumar, P. T. Ravichandran, and K. D. Krishnan, "Use of quarry dust with recycled coarse aggregate in sustainable self compacting concrete," *Journal of Green Engineering*, vol. 10, no. 4, pp. 1297–1311, 2020.

[23] H. Amara, N. Arabi, and A. Perrot, "Unconventional tools for the study of the flow properties of concrete equivalent mortar based on recycled concrete aggregates," *Environmental Science and Pollution Research*, vol. 29, no. 18, pp. 26739–26758, 2021.

[24] D. R. Seshu, C. Manjula, T. Rao, C. Rao, and K. Kumar, "A novel means of improving the performance of reinforced concrete beams using the welded wire mesh as core zone reinforcement," *Asian Journal of Civil Engineering*, vol. 21, no. 6, pp. 1–7, 2020.

[25] R. Huang, P. Yan, and X. Yang, "Knowledge map visualization of technology hotspots and development trends in China's textile manufacturing industry," *IET Collaborative Intelligent Manufacturing*, vol. 3, no. 3, pp. 243–251, 2021.

Retraction

Retracted: Electrochemical Mechanical Properties of Beam-Column Joints of Building Steel Structures under Impact Loads

Journal of Chemistry

This article has been retracted by Hindawi following an investigation undertaken by the publisher [1]. This investigation has uncovered evidence of one or more of the following indicators of systematic manipulation of the publication process:

(1) Discrepancies in scope

(2) Discrepancies in the description of the research reported

(3) Discrepancies between the availability of data and the research described

(4) Inappropriate citations

(5) Incoherent, meaningless and/or irrelevant content included in the article

(6) Peer-review manipulation

The presence of these indicators undermines our confidence in the integrity of the article's content and we cannot, therefore, vouch for its reliability. Please note that this notice is intended solely to alert readers that the content of this article is unreliable. We have not investigated whether authors were aware of or involved in the systematic manipulation of the publication process.

Wiley and Hindawi regrets that the usual quality checks did not identify these issues before publication and have since put additional measures in place to safeguard research integrity.

We wish to credit our own Research Integrity and Research Publishing teams and anonymous and named external researchers and research integrity experts for contributing to this investigation.

The corresponding author, as the representative of all authors, has been given the opportunity to register their agreement or disagreement to this retraction. We have kept a record of any response received.

References

[1] L. Qian, "Electrochemical Mechanical Properties of Beam-Column Joints of Building Steel Structures under Impact Loads," *Journal of Chemistry*, vol. 2022, Article ID 4942187, 9 pages, 2022.

Hindawi

Research Article

Electrochemical Mechanical Properties of Beam-Column Joints of Building Steel Structures under Impact Loads

Liu Qian ID

Anhui Vocational and Technical College, Hefei 230062, Anhui, China

Correspondence should be addressed to Liu Qian; 31115302@njau.edu.cn

To optimize the seismic performance in high-rise buildings, the performance changes of beam-column joints of high-rise steel structures of buildings when they are impacted are analyzed to obtain the optimal choice of joint combination. The most commonly used steel beam and steel column joints are selected as the research objects. Firstly, the finite element model and the shell element model of the force are established and then the model of the finite element combination of six kinds of steel beam and steel column joints is established. Secondly, the applied data of common impact force in actual buildings are collected, and the simulated impact force in this experiment is established according to the sampled data. Then, the changes in each performance of the joints under the action of the impact external force are deeply explored through simulation. Finally, the accuracy of the model is confirmed by calculation. The experimental results comprehensively show that the transmission mechanisms of the impact force are different for the six joints. Through calculation and comparison, the bending stiffness, strength, deformation, the displacement degree of the joints, and the bearing degree of the impact external force are comprehensively analyzed. It is concluded that the bolt-type and external diaphragm-type steel tube column concrete and steel-beam concrete composite joints have better seismic resistance than the other five joints. The bolt-type does not need to be welded on site, and the on-site construction workers only need to assemble, which can reduce the technical requirements for construction workers, improving the practicability and applicability. Therefore, it shows reliable reference significance for the joint selection of building steel structures.

1. Introduction

Steel structures are widely used in buildings [1]. When subjected to other external forces, steel structures can withstand very good compressive bearing capacity because steel has strong toughness and plasticity. Steel usually appears in the form of construction or formwork in construction, which can effectively save the time and manpower and material resources of repeated disassembly and assembly of formwork on the construction site and improve the construction efficiency. Because the general steel is very thin, it is often easy to process and reuse, which saves a lot of construction costs. The research results of many architectural scholars have shown that steel structure is the preferred material, with light weight and good seismic performance. In recent years, steel structures have become the mainstream materials in the construction field

[2] and are often used as important building structures such as beam-column joints.

Many scholars in the world have simulated in-depth experimental research on beam-column joints of steel structures through a large number of experimental data and theoretical analysis and analyzed and summarized the relevant calculation theories, design methods, and calculation equations of steel structures. With the application and expansion of the theory in engineering, the relevant specifications and recommended standards for steel have been promulgated [3], and the steel structure technology has been listed as one of China's scientific and technological achievements. In addition, the calculation equation of the joint's bearing limit was also deduced; the beam-column joint type with better seismic performance was studied through the experimental mechanism. Some researchers have conducted experiments on compressive, flexural, and

impact bearing capacity for different types of beam-column joints [4] and simulated and analyzed them and obtained calculation formulas that can be extended to actual construction projects.

As the performance of building steel structures is gradually excavated and tested, there is a choice of welding materials for joints on the combined modules of steel structures. At present, there is no more accurate optimal solution because there is no comprehensive conclusion on the stability, seismic resistance, and impact resistance of building beams or building column joints. Therefore, the cross-shaped member of the concrete-filled steel tube (CFST) beam and column is undertaken as an example in this work to establish the experimental basis and carry out the finite element calculation. Firstly, separate experiments are carried out on CFST beams and CFST columns [5] to study their endurance and resistance under load. Secondly, the bearing force, stress distribution, energy consumption, the curve state of the connecting skeleton, and the degree of degradation and damage are analyzed. Finally, the impact resistance advantages and disadvantages of each combination module are obtained through various experimental studies. In addition, the applicable environment of the steel structure joint module is summarized, which provides an important technical support for the selection of the steel structure beam-column joint combination mode. Results here can provide reference significance for the selection of joints of building steel structures.

2. Mechanical Properties of the Impact Load Based on CFST Beam-Column Joints

2.1. Establishment of the Force Finite Element Model for Beam-Column Joints. Four joint-reduced general shell element models are used to construct the steel pipe element model [6]. The selection of this kind of the shell element model can facilitate us to solve the problem through two theories of thin shell and thick shell in the experiment. It also has good plasticity and elasticity. For simulation experiments, it has been able to extremely realistically restore the deformation and stress of the steel pipe under pressure during specific construction. After the steel pipe element model is selected, it is necessary to add a baffle plate with a baffle plate and the material adopts the element model of eight joint reductions. The baffle is added at the end of the steel column or steel beam to provide a carrier for the impact force in the later experiment. This element model will have a slight distortion of the mesh, but it does not affect the experimental results and still meets the error range. The model of the CFST is constructed by the C3D8R element of the Open System for Earthquake Engineering Simulation (OpenSEES) software [7]. The advantage of this unit is that it can realistically simulate the state and the working state of the improved performance of concrete under the mixing of steel tubes. The steel pipe unit model and the C3D8R unit model are shown in Figure 1 and 2, respectively.

Each joint in the steel pipe element model contains 6 dimensions, including the direction of movement along the A, B, and C axes in the plane and the direction of rotation
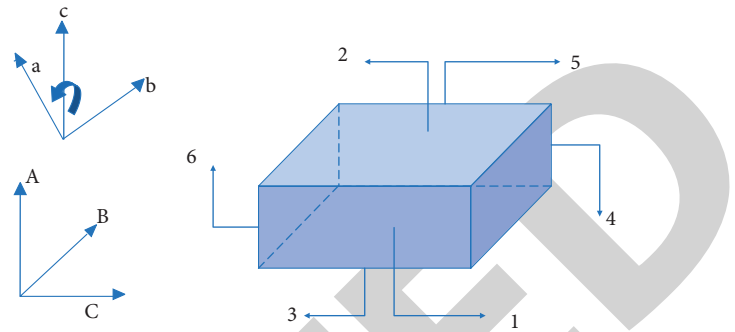
Figure 1: The steel pipe unit model.
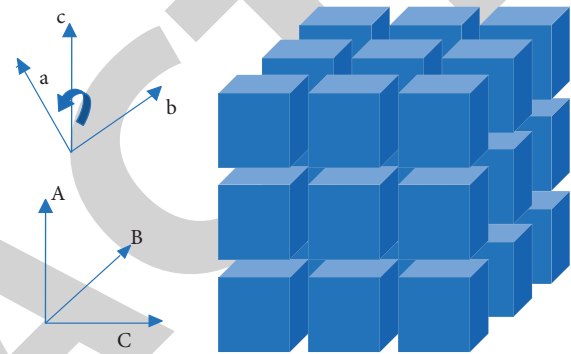
Figure 2: The C3D8R unit model.

around the A, B, and C axes. The 6 joints are, respectively, represented in the figure, which can accurately and clearly show the change in the mechanical properties of the steel pipe under the impact force. The eight joint three-dimensional solid model of the baffle and the concrete-filled steel tubular element model are both based on the C3D8R element model, which can effectively reduce the degree of freedom and improve the efficiency [8]. The obtained data can be more accurate, each joint also has 6 dimensions, which is the same as the dimension direction of the steel pipe unit model. The element is capable of simulating nonlinear materials and can clearly study their elastic and plastic deformation and damage.

For the finite element joint model established in this work, there are six types of simulation combinations, as shown in Figure 3.

The figure shows the joint forms of the three column top shafts under pressure and the load and the sequential combined model diagram of the two connection methods. The three joints are steel tube column and steel beam, CFST column and steel beam, and CFST column and CFST beam. The two connection methods are the bolt-type and the external diaphragm-type [9].

2.2. Parameter Selection and Simulation Calculation of the Finite Element of Each Test Piece. The ingredients of concrete in this simulation experiment are water, cement, fine sand, crushed stone, and water reducer, and the ratio is $1:2.4:3.4:4.1:0.0005$. The parameters of the selected steel pipe are the
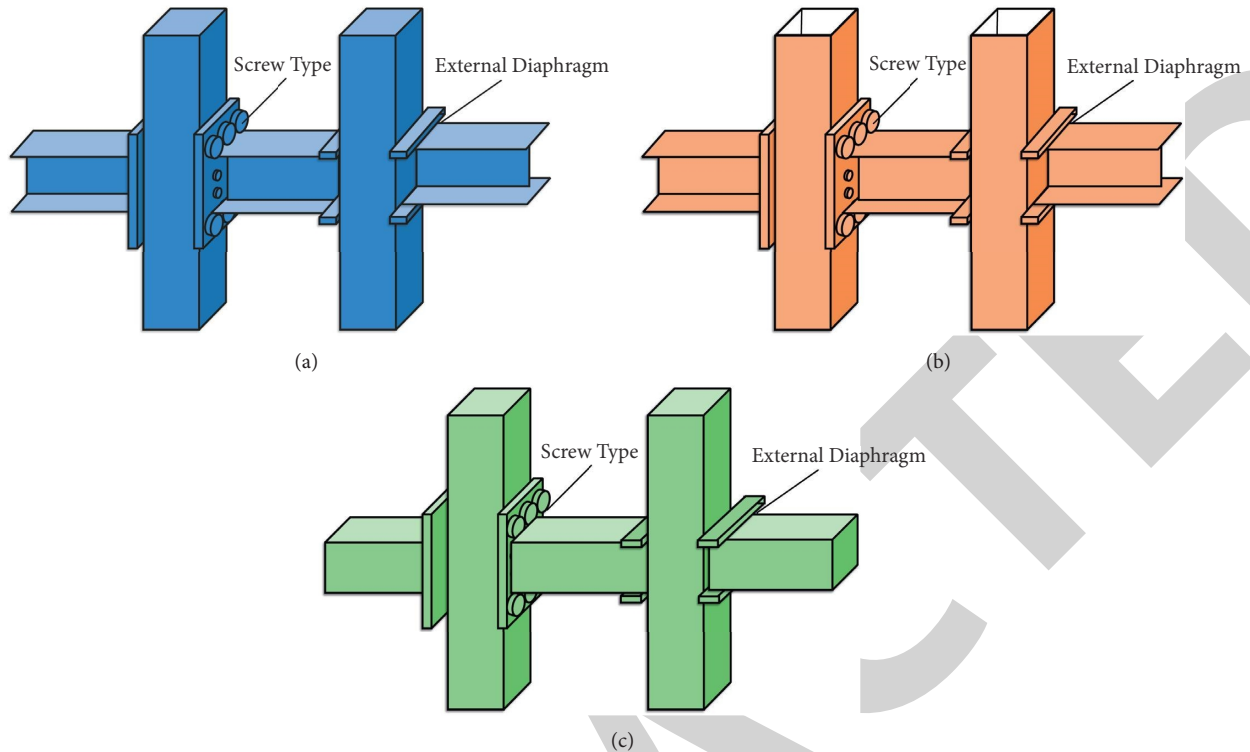
Figure 3: Model diagrams of six types of simulated combination modes: (a) steel tube column and steel beams; (b) CFST columns and steel beams; (c) CFST columns and steel-tube-beam.

wall thickness of 6 mm and the perimeter of the section of the pipe string of 250 mm. After the predetermined value is set, the calculation is carried out according to the relevant regulations, the material of the steel pipe in practical application and the strength of the concrete prepared in this experiment. The calculation equation of the bearing pressure value of the pipe string is given as follows:

$$N_\rho = f_s A_s. \tag{1}$$

In the above equation, N_ρ is the bearing pressure value of the pipe string, f_s is the yield strength of the pipe, and A_s represents the variance value of the pipe string. When the beam-column joint is subjected to an impact force, in addition to the displacement deformation, there is also the deformation amount at yielding that needs to be considered [10]. For the convenience of research, the analysis and calculation of displacement ductility is set up in this paper, that is; the ratio between the deformation degree and the yield deformation is calculated by the equation. If the ductility is large, it means that the impact resistance is good; otherwise, it means that the resistance is not good. The equation for the calculation of the displacement ductility is expressed as follows:

$$m = \frac{\Delta x}{\Delta y}. \tag{2}$$

The difference in x is the deformation, the difference in y is the deformation at yield, and m is the displacement ductility.

The calculation equations for the bending stiffness value of the cross section of the steel tube column and the bending stiffness value of the steel beam are the same, expressed as follows:

$$EI = E_s I_s. \tag{3}$$

In aforementioned equation (3), EI is the bending stiffness of the CFST column, E_s is the elastic modulus, and I_s refers to one-twelfth of the side length of the steel tube column to the fourth power.

The equation for calculating the bending bearing capacity of the beam is as follows:

$$M_{uk} = [0.5A_s(h - 2t - d_n) + bt(t + d_n)]f_y. \tag{4}$$

In equation (4), A_s is the longitudinal reinforcement area, h is the beam height, b is the beam width, and f_y is the flexural strength.

The calculation results of each index of the bearing pressure value of the pipe string, the bending stiffness value of the cross section, the bending resistance value, and the bending stiffness value are shown in Table 1.

2.3. Establishment of the Finite Element Model of Beam-Column Joints under Impact Force. The impact force set in the experiment is to apply an impact force along the direction of the steel column at the top of the steel column model and gradually increases the impact force value until the test joint is damaged. The force distribution, local

TABLE 1: Various properties of steel.

Parameter type	CFST column	Steel pipe column	CFST beam	Steel beam
String bearing load pressure value (KN)	357.0	369.9	—	—
Cross-section bending stiffness value (N•mm^2)	1.99×10^{13}	2.49×10^{13}	—	—
Bending resistance value (kN•m)	—	—	129	121.0
Resistance to bending stiffness value (N•mm^2)	—	—	6.89×10^{12}	6.66×10^{12}

deformation, and the impact load limit are analyzed through the simulation results. Each element to be analyzed is set with a corresponding duration predetermined, and each simulation experiment is set to automatically repeat and stack 1000 instructions [11]. The error range of each superposition is strictly controlled to ensure that the system will not be interrupted during the simulation. If interrupted, the system defaults to the end of the trial and the simulation fails or to success if looping normally. The schematic diagram of the direction in which the impact force is applied is shown in Figure 4.

In the experiment, it should be noted that in addition to the impact force we set in the actual building, there will also be three adhesion forces on the contact surface between the steel pipe and the concrete that need to be considered. These three forces must be damaged before the entire specimen can be completely damaged [12]. The first is the adhesive force between the steel pipe wall and the gel material produced by mixing the cement powder with water, and the second is the occlusal force between the rough protrusions and depressions on the steel pipe wall and the concrete [13]; the third is that there is a friction coefficient between the steel pipe wall and the concrete, so there will be friction. Then, under the action of the impact force, it is not damaged at the same time but has a certain regularity and process in sequence. First, the impact force is small and there is no relative displacement of the joint sliding [14]. Therefore, the friction force and the bite force have no effect for the time being, and the stick force is being pulled. Secondly, after the viscous force reaches the limit, the occlusal part between the pipe wall and the concrete begins to be damaged, resulting in a certain viscous resistance. Then, the impact force continues to increase and the friction force starts when the occlusal surface can no longer keep its relative static until the impact force increases again; the friction force and the part of the occlusal force counteract the impact force.

2.4. Impact Force Parameter Value Setting.

In the impact experiment, since it needs to preset a force or equation, a lot of research and sampling are performed before the simulation experiment. The collected data show that the impact force does not grow linearly but is divided into several stages [15]. The first stage is the pulse stage, that is, when it is subjected to the external force, it never touches the contact and the force area increases rapidly. Then, the joint begins to move downward under the impact, the contact surface becomes smaller rapidly, and the impact force also decreases rapidly, resulting in a high-intensity fluctuation. The second stage is platform Section 1. When the impact object touches the joint for the second time, it starts to contact with the joint specimen
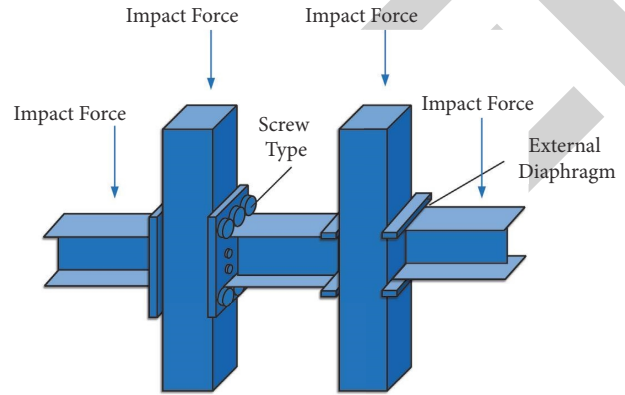
FIGURE 4: Schematic diagram of the direction of the impact force.

and falls together and then passes through the first stage of a small amplitude and contacts and falls at the same time. Such a reciprocating process forms a relatively stable and gentle impact force. The third stage is the subpulse stage, and when the impact force reaches a certain limit, the specimen and alluvium begin to have tendency to rebound upward because this will slow down the return speed of all flexible joints. Because the impactor's velocity is faster than the element's lower velocity, reducing the recovery speed of each component, this section has reduced its impact. The fourth stage is the platform segment 2. At this time, the impact force is not reduced to zero, the impact object and the joint are relatively static and vibrate with a small amplitude, and the impact force is relatively stable [16]. The size is similar to the second stage.

From the above four-stage force conditions of the actual building impacted, it can simulate an experimental parameter curve. The sampling curve and the simulation curve are shown in Figure 5.

Figure 5(a) is the sampled data, and Figure 5(b) is the simulation curve. The whole simulation curve is a nonlinear curve [17], but it is subdivided into four stages to see that each stage is a linear element. The value corresponding to 4.5 t is set as the limit value of the impact force in the first stage, and the value corresponding to 8.5 t is set as the limit value in the third stage. The action time of the first stage is set to 4 t–5 t, the action time of the second stage is set to 5 t–8 t, the action time of the third stage is set to 8 t–9 t, and the action time of the fourth stage is set to 9 t–12 t.

3. Experimental Results and Analysis

3.1. Analysis on the Limit of the Impact Force of Beam-Column Joints.

A unidirectional downward impact force is applied on the top of the column, and the simulation results of the impact bearing limit of the steel beam joint are shown in Figure 6.

(a)

(b)
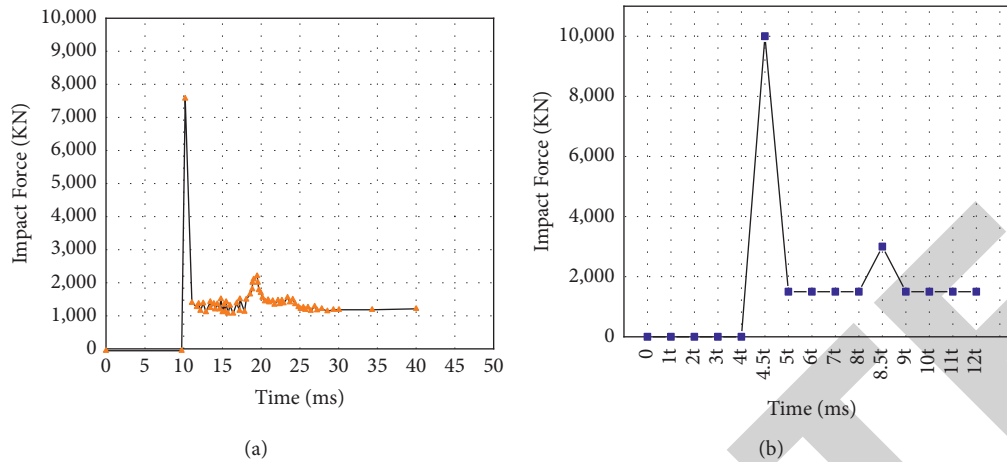
Figure 5: Impact force curve: (a) experimental parameter curve; (b) sampling curve and simulation curve.

The joint bearing capacity image studies the two connection methods separately, namely, the bolt-type and the external diaphragm-type. Figure 6(a) is the bolt-type, and Figure 6(b) is the external diaphragm-type. Corresponding to the three combinations of specimens, the images can be clearer and easier for us to analyze and compare. The general law can be seen from the image, that is, in the initial stage of impact force application, which is the pulse stage, and the force on the joint presents a linear progressive trend. When the impact force is in platform 1, 2, and subpulse stages, the joint force tends to be gentle and stable. After analysis, the following conclusions can be drawn. For bolt-type joints, the combination of CFST columns and steel beams has a higher impact bearing capacity; for external diaphragm-type joints, the combination of CFST columns and steel beams has a higher impact bearing capacity. Finally, the two methods are compared and found that their impact bearing capacity is almost similar.

A unidirectional downward impact force is applied to the steel beam, and the simulation results of the limit bearing capacity of the steel beam joint are shown in Figure 7.

Figure 7(a) is the bolt-type, and Figure 7(b) is the external diaphragm-type. The general law can be seen from the image, that is, in the initial stage of impact force application, which is the pulse stage, and the force on the joint presents a linear progressive trend. When the impact force is in platform 1, 2, and subpulse stages, the joint force tends to be gentle and stable. After analysis, the following conclusions can be drawn. For bolt-type joints, the combination of CFST columns and steel beams has a higher impact bearing capacity; for external diaphragm-type joints, the combination of CFST columns and steel beams has a higher impact bearing capacity. Finally, it is found by comparing the two methods that the combination of bolt-type CFST columns and steel beams has a higher impact bearing capacity.

3.2. Skeleton Displacement Analysis of Beam-Column Joints under Impact. When the impact force is cyclically superimposed to increase the peak value of the pulse phase, the

magnitude of the joint displacement indicates the bearing degree of the joint specimen for the impact force. The simulation results of the ultimate bearing capacity of the steel beam joint are shown in Figure 8.

The displacement curve can represent the relationship between the applied impact force and the joint damage displacement. When the impact force is cyclically superimposed to increase the peak value of the pulse phase, the magnitude of the joint displacement indicates the bearing degree of the joint specimen for the impact force. Figure 8(a) is the bolt-type, and Figure 8(b) is the external diaphragm-type. After analysis, the following conclusions can be drawn. For bolt-type joints, the combination of CFST columns and steel beams has a higher impact bearing capacity; for external diaphragm-type joints, the combination of CFST columns and steel beams has a higher impact bearing capacity. Finally, it is found by comparing the two methods that the combination of bolt-type CFST columns and steel beams has a higher impact bearing capacity.

3.3. Displacement Ductility Analysis of Beam-Column Joints under Impact. For the joints connected by the external diaphragm-type, the measured displacement ductility of each combination is shown in Figure 9.

As shown in the figure, the ductility coefficients of the six models tested are all greater than 2, so they all meet the requirements of the steel structure and the difference is not large. After analysis, the following conclusions can be drawn. For bolt-type joints, the combination of concrete-filled steel tubular columns and steel-beam concrete has better displacement ductility; for external diaphragm-type joints, the combination of CFST columns and steel beams has better displacement ductility. Finally, comparison of the two methods reveals that the combination of the bolt-type CFST column and the steel-beam concrete has better displacement ductility.

3.4. The Bending Stiffness and Strength Degradation of Steel Beam-Column Joints. Under the action of the impact force, the performance degradation of the joint specimen is
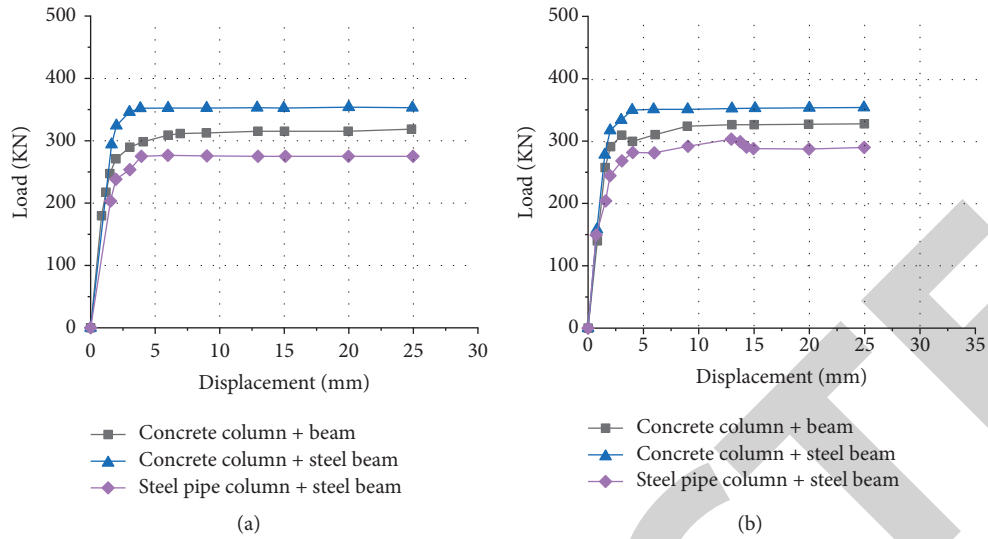
Figure 6: Impact curve: (a) bolt-type combination; (b) external diaphragm-type combination.
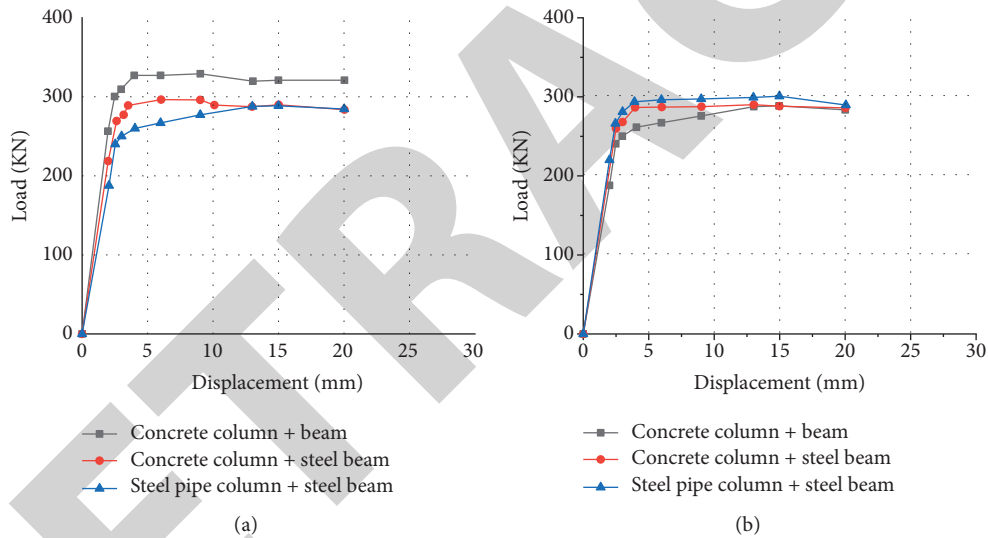
Figure 7: Simulation results of the ultimate bearing capacity of the steel beam joint: (a) bolt-type combination; (b) external diaphragm-type combination.

manifested in the degradation of the bending stiffness and bending strength. The degradation of the bending stiffness and bending strength is shown in Figure 10.

Under the action of the impact force, the performance degradation of the joint specimen is manifested in the degradation of the bending stiffness and bending strength. Figures 10(a) and 10(c) are the bolt-type, Figures 10(b) and 10(d) are the external diaphragm-type, Figures 10(a) and 10(b) are bending stiffness data, and Figures 10(c) and 10(d) are flexural strength data. The decrease in bending stiffness means that the joint's resistance to deformation is weakened when it resists the impact force, and the decrease in the bending strength means that the joint's bearing capacity when resisting the impact force is weakened. The overall analysis rule shows that both the bending stiffness and the

bending strength decrease significantly after the impact force pulse stage. However, when the impact force enters platform 1, 2, and subimpulse stages, the bending stiffness and strength decrease are more obvious. After analysis, the following conclusions can be drawn. For bolt-type joints, the combination of CFST columns and steel beams decreases slowly and the flexural strength decreases at a moderate rate; for joints connected by the external diaphragm-type, the combination of CFST columns and steel beams decreases slowly in the bending stiffness and the flexural strength. Finally, comparison of these two methods suggests that the combination of CFST columns and steel beams connected by external diaphragms has a slower decline in the bending stiffness and a slower decline in the flexural strength, so it is better.
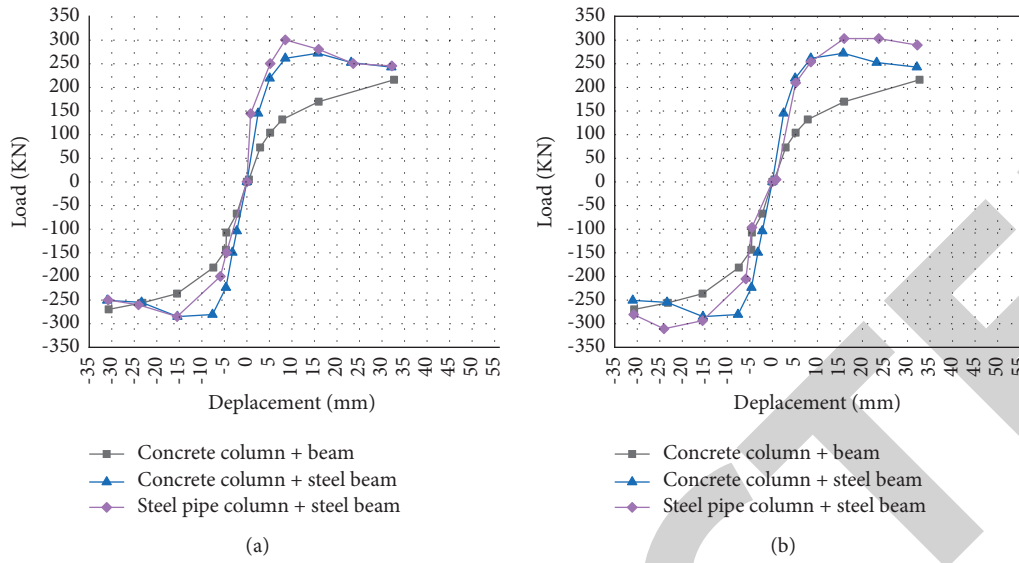
FIGURE 8: Simulation results of the ultimate bearing capacity of the steel beam joint: (a) bolt-type combination; (b) external diaphragm-type combination).
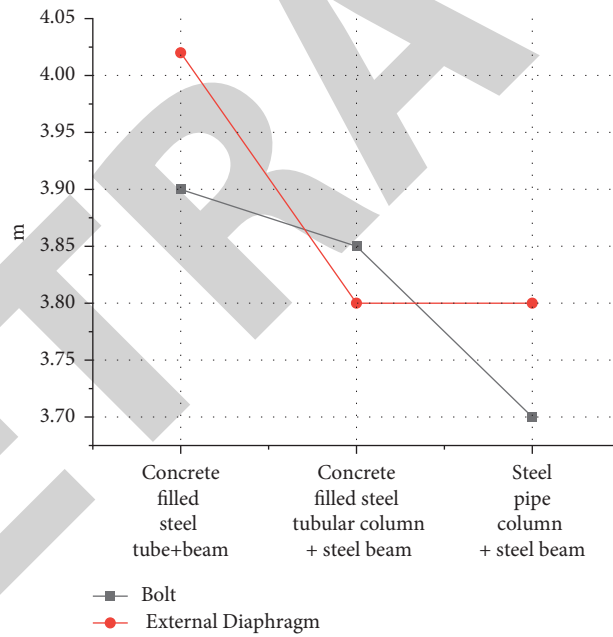
FIGURE 9: Displacement ductility data diagram of each specimen.

(a)

(b)

(c)

(d)
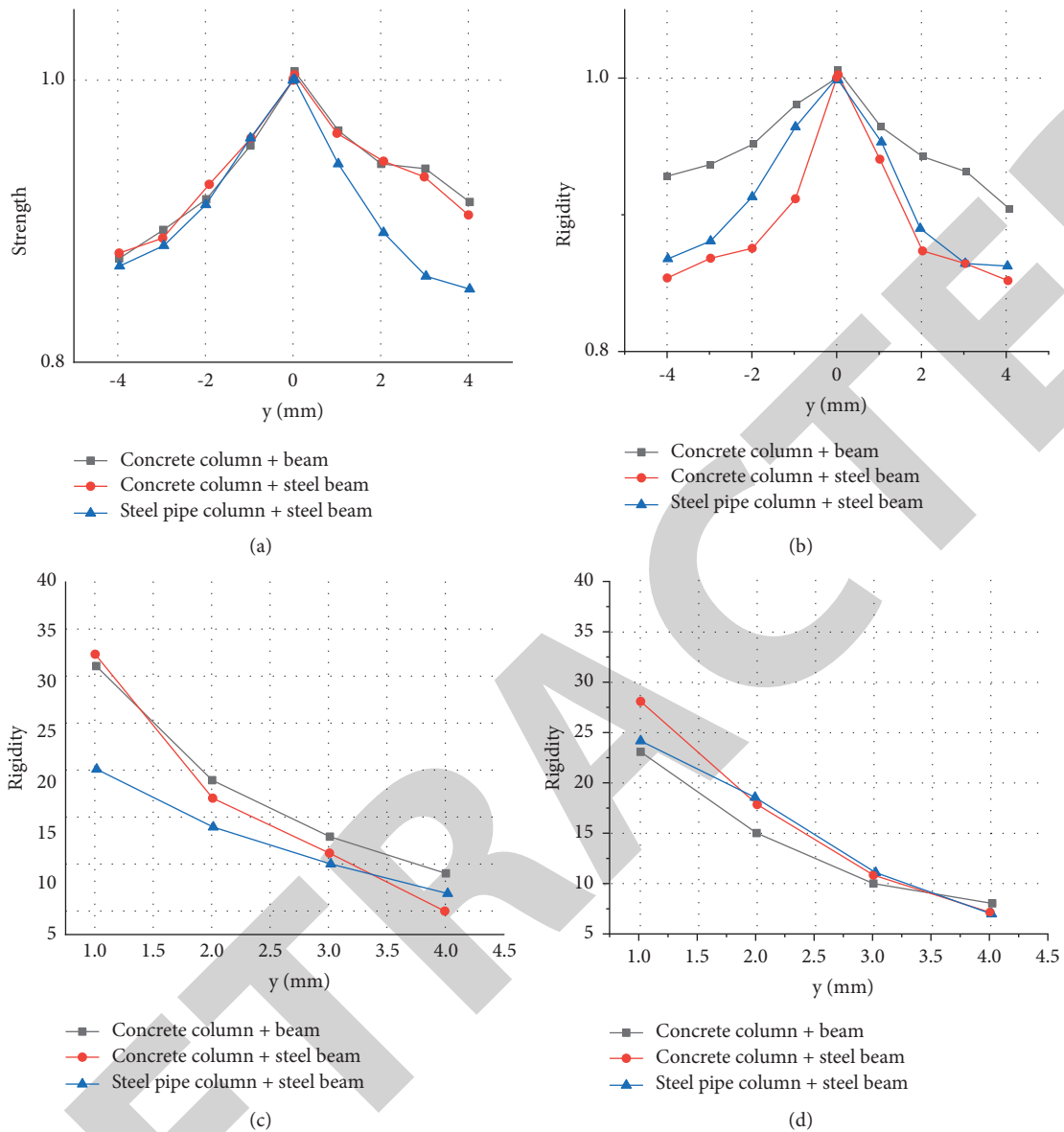
Figure 10: Bending stiffness and strength degradation curves: (a) bolt-type bending stiffness; (b) external diaphragm-type bending stiffness; (c) bolt-type bending stiffness; (d) external diaphragm-type bending stiffness).

4. Conclusion

It is no surprise that high-rise buildings have appeared in cities in recent years, and even low-rise buildings in developed cities are rare, so whether higher spans can still maintain stability and safety will be the biggest problem facing high-rise buildings. Many researchers have performed in-depth research in construction-related fields. Against the background of steel as the core of the basic quality of construction, seismic resistance has become the focus of extensive attention. The concrete analysis and description of the seismic performance is the bending resistance, the degree of deformation and displacement of the steel structure when resisting the impact force, and the degree of bearing capacity for the impact external force. In this work, the most

commonly used steel beam and the steel column joint are used as the research object and the applied data of the general impact force are sampled in the actual building to establish a simulated impact force and a finite element model of force. The changes in the performance of the joint under the action of the impact external force are deeply studied through simulation, and finally, the accuracy of the model is confirmed by the calculation. The experimental results comprehensively show that although the transmission mechanisms of the impact force of the six joints are different. Comprehensive analysis of the joint bending stiffness, strength, degree of deformation and displacement, and degree of bearing for impact external force is obtained through calculation and comparison, and a relatively complete conclusion is obtained. It means that the combined

Retraction

Retracted: Monitoring of Nitrogen Transport Data in Pear Leaves Based on Infrared Spectroscopy

Journal of Chemistry

This article has been retracted by Hindawi following an investigation undertaken by the publisher [1]. This investigation has uncovered evidence of one or more of the following indicators of systematic manipulation of the publication process:

(1) Discrepancies in scope

(2) Discrepancies in the description of the research reported

(3) Discrepancies between the availability of data and the research described

(4) Inappropriate citations

(5) Incoherent, meaningless and/or irrelevant content included in the article

(6) Peer-review manipulation

The presence of these indicators undermines our confidence in the integrity of the article's content and we cannot, therefore, vouch for its reliability. Please note that this notice is intended solely to alert readers that the content of this article is unreliable. We have not investigated whether authors were aware of or involved in the systematic manipulation of the publication process.

Wiley and Hindawi regrets that the usual quality checks did not identify these issues before publication and have since put additional measures in place to safeguard research integrity.

We wish to credit our own Research Integrity and Research Publishing teams and anonymous and named external researchers and research integrity experts for contributing to this investigation.

The corresponding author, as the representative of all authors, has been given the opportunity to register their agreement or disagreement to this retraction. We have kept a record of any response received.

References

[1] Z. Fan, D. Wang, and N. Zhang, "Monitoring of Nitrogen Transport Data in Pear Leaves Based on Infrared Spectroscopy," *Journal of Chemistry*, vol. 2022, Article ID 1547582, 9 pages, 2022.

Research Article

Monitoring of Nitrogen Transport Data in Pear Leaves Based on Infrared Spectroscopy

Zehua Fan [ID],[1] **Desheng Wang** [ID],[2] **and Nannan Zhang** [ID][1]

[1]*College of Information Engineering, Tarim University, Alar, Xinjiang 843300, China*
[2]*College of Plant Sciences, Tarim University, Alar, Xinjiang 843300, China*

Correspondence should be addressed to Zehua Fan; 2013071225@stu.zjhu.edu.cn

In order to better monitor the data of nitrogen transport in pear leaves, a method based on infrared spectroscopy was proposed. The near-infrared reflection spectrum imaging technology is used to collect the leaf scale spectral image of the target crop. Computer image analysis software is used to process the spectral digital image and extract the spectral data. After statistical analysis, the data are selected as variables. Combined with the chemical analysis test results, the crop nutrition detection model is established, and the conclusion is drawn. The experimental results show that the band gray data involved in the model are scaled and reorganized according to the coefficient proportion by using ENVI through the band calculation command. The final gray image, the original image, and the gray image in the process default to the three-channel analog image of the band (the wavelengths of the bands are 1446, 1373, and 1304 nm, respectively); 944 nm gray image; 1043 nm gray scale image; 1662 nm gray image; $(0.102R_{944} + 0.103R_{1\,043} + 0.206R_{1662})/(0.102 + 0.103 + 0.206)$ grayscale image with signal scaling according to the scale of model coefficient. It is proved that infrared spectroscopy can effectively monitor the data of nitrogen transport in pear leaves.

1. Introduction

Each substance has different absorption, reflection, and transmission of electromagnetic waves of different wavelengths (or frequencies). This response characteristic of substances to the spectra of different bands is called the spectral characteristic. Nondestructive monitoring of the crop nitrogen nutrition spectrum is based on the characteristic response of different nitrogen forms in crop leaves or other organs and tissues to different spectral bands. Using the remote sensing sensor to obtain the characteristic spectral information of crops without damaging the tissue structure of crops or far away from crops, and analyze and process these information, so as to judge the deficiency degree of nitrogen nutrition and quantitatively retrieve the status of nitrogen nutrition of crops [1]. The spectral monitoring principle of crop nitrogen nutrition is that the chemical bonds in the molecular structures of various protein nitrogen, amino acids, chloroplasts, and other nitrogen components in crop tissue vibrate under the irradiation of light energy at a certain radiation level (different frequencies or

wavelengths), resulting in differences in absorption and reflection of light at some wavelengths, forming different reflection, absorption, and transmission spectra. The changes of spectral reflectance in these bands are abnormally sensitive to the number of specific nitrogen components, which is called nitrogen band or sensitive spectrum [2]. The band range of the response of the main nitrogen forms in crops is concentrated in the visible and infrared regions. The former is the electron transition spectrum, and the latter is the molecular vibration spectrum. When these different energy lights irradiate crops with different nitrogen nutritional status, they produce characteristic nitrogen reflection and absorption spectrum. The realization of crop nitrogen nutrition spectrum monitoring is based on the quantitative relationship between the sensitive reflection spectrum or absorption spectrum of the crop nitrogen component and the content or concentration of the component [3].

The traditional methods of crop nitrogen diagnosis are qualitative and semiquantitative methods based on conventional indoor chemical quantitative analysis, seedling

fertilization, leaf color card, and so on. The former judges whether the crop is short of nitrogen by the nitrogen content of the crop plant (or leaf), starch content of the leaf sheath, nitrate nitrogen at the base of the stem, amino nitrogen content of the functional leaf or leaf sheath, and C/N ratio of the leaf [4]. Although this method is intuitive and reliable, it is difficult to be applied in time, generally, because of its destructive large number of samples, which leads to time-consuming, labor-consuming, and high-analysis cost. Although the latter is more intuitive and fast, it lacks quantitative diagnostic indicators, which are not conducive to accurately estimate the amount of nitrogen fertilizer. In recent years, the multispectral and hyperspectral remote sensing technology based on the spectral characteristics of ground objects has developed rapidly, which makes it possible to obtain the crop growth status and plant biochemical components in real time, fast, accurate, large-scale, and nondestructive means, thus providing a new technical means and method for the nondestructive monitoring of crop growth. This is because crop nitrogen deficiency will cause a series of changes in leaf color, thickness, and morphological structure, resulting in changes in spectral absorption, reflection, and transmission characteristics, which provides a theoretical basis for real-time monitoring and rapid diagnosis of crop nitrogen status based on spectral reflection characteristics [5].

The canopy color of crops is directly affected by the change of nutritional status. The leaf color of nitrogen deficient plants becomes lighter, and the canopy color is yellow and green. In this way, after the canopy image is obtained and processed by the computer program, the red light (R), green light (G), and blue light (B) reflected by plant canopy can be accurately quantified for nitrogen nutrition diagnosis. In recent years, more and more studies have been carried out to understand the nitrogen nutrition status of crops by judging the color depth of crop canopy or to recommend fertilization and predict yield [6]. Visible light color analysis technology has become a new research hot spot. In these studies, researchers mostly use the relative value of canopy image color or the ratio G/R of canopy green light reflection to red light reflection to diagnose nitrogen nutrition. Samadi and others predicted maize yield by analyzing the relative brightness of canopy on color photos. There was a very significant correlation between the red, green, and blue light and the maize yield [7]. Jani and others obtained the canopy image of winter wheat with a digital camera, analyzed the ratio of green light to red light in the canopy image, and considered that there was a very significant correlation between G/R and chlorophyll meter reading [8]. Fan showed that there was a good linear positive correlation between the relative green and blue depth values of canopy images from 6-leaf stage to 7-leaf stage and the optimal economic nitrogen application rate [9]. Au established the relationship model between canopy green depth and above ground plant total nitrogen at jointing stage and booting stage by using a digital camera. These research works lay a foundation for the application of color image processing technology based on digital camera and machine vision color recognition technology in crop growth monitoring. However, there is little research in this field, and there

is no consistent image acquisition and processing standard [10]. Therefore, the use of canopy color analysis for nitrogen nutrition diagnosis needs to be further studied. Wang Y. believes that changes in the contents of nitrogen, phosphorus, and potassium in crops will cause changes in the physiological and morphological structure of crop leaves and the spectral reflection characteristics of crops. This is the theoretical basis for obtaining crop nutrient information through spectral remote sensing, making it possible to diagnose the nutritional status in the field nondestructively, quickly, and simply [11]. Veeravu believes that the traditional remote sensing monitoring technology based on multispectral and broadband reflectance has made some progress. However, due to its few spectral bands and low resolution, it is easy to lead to the lack of some key spectral information [12]. Alwi believes that in recent years, the emergence and rise of hyperspectral remote sensing technology can subdivide the spectral band in a specific spectral region with its characteristics of high resolution, continuous band, and abundant data, which has injected new vitality into the nutrition diagnosis of crops [13]. Koroleva research on vegetation spectral repression monitoring has made some progress in the scales of dry powder, fresh leaf canopy, and aviation, which proves the feasibility of spectral remote sensing analysis technology for crop nitrogen nutrition diagnosis [14]. Using hyperspectral remote sensing technology, Estak I. can quickly and accurately obtain all kinds of information about crop growth status and environmental stress, so as to guide the corresponding management measures and the amount of input materials, so as to reduce waste, increase yield, and protect agricultural resources and environmental quality. It is an important means for the sustainable development of precision agriculture and agriculture in the future [15]. Andrade C. A. believes that hyperspectral remote sensing has the characteristics of high spectral resolution (band width <10 nm), strong band continuity (hundreds of bands in the range of 400~2500 mm), large amount of spectral information, and so on. It can simultaneously obtain continuous spectral images of ground objects with high spectral resolution in a specific spectral domain. The gray value of each pixel point in each channel on the spectral image can form a fine spectral line, which can form a unique ultra multidimensional spectral space, so that remote sensing applications focus on spatial information expansion in the spectral dimension to obtain more fine spectral information and provide parameters and basis for quantitative analysis of the physical and chemical change process of surface materials [16].

Based on the current research, a method based on infrared spectroscopy is proposed in this paper. The near-infrared reflectance spectral imaging technology is used to collect the leaf scale spectral image of the target crop, and the computer image analysis software is used to process the spectral digital image and extract the spectral data. The near-infrared reflectance hyperspectral imaging system is shown in Figure 1. After statistical analysis, the data are selected as variables, and the crop nutrition detection model is established in combination with the chemical analysis test results. The conclusion is drawn from the test model.
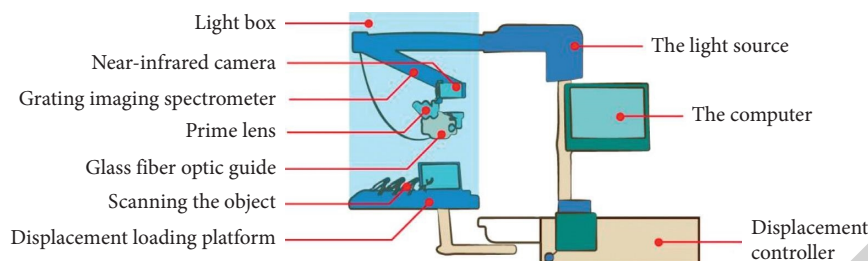
Figure 1: Hyperspectral image acquisition system.

2. Materials and Methods

2.1. Sample Selection and Collection. In the experiment, the leaves of the self-cultivated pear tree (the variety is pear tree: Hanyu seed industry, produced by the experimental field of the 6th regiment of the first division in southern Xinjiang) were selected as the test samples. In order to obtain the test samples with different levels of nutrient content, the nutrient supply in the process of crop cultivation adopts the uniform design of lack stress treatment. 9 groups A-I of the standard nutrient supply formula, 20%, 30%, 40%, 50%, 60%, 70%, 80%, 90%, and 100%, are taken as the actual nutrient supply level of the test samples. One group of control group O was arranged according to the standard nutrition supply formula. The number of sample plants in each experimental group and control group was 8. The other cultivation conditions except for nutrition supply were suitable, and the growth environment was the same.

After enough time of cultivation and nutrient stress treatment, the test samples were selected in the critical period of pear nutrition when most individuals have changed from vegetative growth stage to reproductive growth stage. Four plants in each group who have completed the excessive growth stage were randomly selected, and the 5th, 6th, and 7th true leaves were completely picked. The picked leaves were placed in fresh-keeping bags for temporary storage, and attention was paid to keeping them away from light. The time from leaf picking to the spectrum acquisition test shall not exceed 1 h [17].

2.2. Spectrum Acquisition Equipment and Test. In order to obtain all the near-infrared spectrum information on each crop leaf, the reflection hyperspectral scanning system (Inspector VIOE, Finland) is selected to collect the reflection spectrum information in the near-infrared region (900–1700 nm) of each leaf to be tested. The near-infrared reflection hyperspectral imaging system is shown in Figure 1.

The system is mainly composed of the near-infrared camera, grating imaging spectrometer, f/2.0 fixed focus lens, 150 W tungsten halogen lamp DC adjustable light source, glass fiber light guide, step displacement stage, step controller, and computer. The spatial resolution of the detection system is very high, and it can recognize the fine distance within 15 nm. The field resolution of its near-infrared camera is 320×256 (pixels). The spectral information collected by it contains the near-infrared reflection intensity of

872–1766 nm. This wide-range band is divided into 256 narrow-range bands: band 1-band 256, the spectral resolution is 5 nm, and the width of the illumination slit scanned by a single exposure is 30 μM. The distance between the spectrum detection camera and the stage is about 25 cm. Before hyperspectral data acquisition, turn on the light source to preheat the machine for more than 30 rain. The exposure time of the camera is set to 20 ms, and the speed of moving the stage is 1 mm/s [18]. After the preparation of black-and-white field calibration through equipment control software, near-infrared reflection hyperspectral imaging scanning was carried out one by one for three leaf samples of four individuals in each group, having a total of 120 samples, and the spectral information acquisition was completed.

2.3. Chemical Determination of Total Nitrogen Content in Sample Leaves. Complete the spectral data acquisition. The leaves of pear tree samples were treated immediately for subsequent chemical analysis. The total nitrogen content of the solution to be measured was measured after the leaves were treated with auto analyzer 3 (later abbreviated as aa3) continuous flow analyzer produced by German seal, such as killing, drying, grinding, screening, digestion, filtration, and constant volume. Each time the aa3 flow analyzer is used, it shall be noted that the process of starting up, preheating, running, and reading the baseline shall not be less than 1 h, so as to ensure that the machine is preheated completely, and the analysis is accurate. In order to obtain enough samples to complete the acquisition of the liquid to be tested, evenly mix the sample powder obtained after grinding and screening the three blades of four individuals in each group, weigh about 0.1 g for subsequent operation, that is, only one sample of the liquid to be tested in each group is obtained for chemical analysis and determination [19].

2.4. Remote Sensing Image Processing. Use formulas (1) and (2) to calculate the first-order guided etching of spectral reflectance, and determine the position, slope (amplitude), and area of blue edge, yellow edge, and red edge in the range of 490~530 nm, 550~582 nm, and 680~750 nm, respectively. The position of red edge is the wavelength corresponding to the maximum value of first-order derivative spectrum in the range of red light, the slope of red edge is the maximum value of first-order derivative spectrum of reflectance, and the area of red edge is the area surrounded by the spectral line of first-order derivative of reflectance. The yellow and

blue edge parameters have similar meanings to the red edge parameters. The above parameters can be combined through difference, ratio, and normalized difference processing. In addition, referring to the characteristics of trilateral parameters, the maximum value and corresponding wavelength of the first derivative of reflectance in the near-infrared range of 920–980 nm, 1000–1060 nm, and 1100 ~ 1180 nm are calculated [20].

$$R'(\lambda_i) = \frac{dR(\lambda_i)}{d\lambda} = \frac{R(\lambda_{i+1}) - R(\lambda_{i-1})}{2\Delta\lambda}, \tag{1}$$

$$R(\lambda_i) = \frac{dR(\lambda_i)}{d\lambda} = \frac{R(\lambda_{i+1}) - R(\lambda_{i-1})}{2\Delta\lambda}. \tag{2}$$

The red edge parameters can also be obtained by the anti-Gaussian red edge optical model (IG model). IG model suggests that the red edge (670–800 nm) reflection spectrum curve can be fitted with an inverse Gauss model (formula 3):

$$R(\lambda) = R_s - (R_s - R_0)\exp\left(\frac{-(\lambda_0 - \lambda)^2}{2\sigma^2}\right), \tag{3}$$

where R_s is the shoulder reflection value (maximum reflectivity) in the near-infrared region, R_0 is the minimum reflectivity in the red light region, λ_0 is the wavelength corresponding to R_0, σ is the standard deviation coefficient of Gaussian function, which is also the difference between the red edge spectral position of vegetation feature spectrum and the Red Valley spectral position, and corresponds to the width of the red edge absorption valley [21].

In this paper, the average value of spectral reflectance in the range of 670–675 nm is defined as R_0, and the average value of spectral reflectance in the range of 780–795 nm is defined as R_s. The reflectance in the range of 685–780 nm is selected as the object of inverse Gaussian model simulation. The reflectance spectrum at the red edge of wheat is logarithmically transformed using two parameters, R_0 and R_s, as shown in the following formula:

$$B(\lambda) = \left[-\ln\frac{R_s - R(\lambda)}{R_s - R_0}\right]^{1/2}, \tag{4}$$

where $B(\lambda)$ is the value after logarithmic transformation of wheat red edge reflectance spectrum. By linear fitting $B(\lambda)$ and λ, the slope a_1 and intercept a_0 can be obtained. Then, the Red Valley spectral position and absorption valley width λ_0 and σ are, respectively, as shown in the following formulas:

$$\lambda_0 = -\frac{a_0}{a_1}, \tag{5}$$

$$\sigma = \frac{1}{\sqrt{2a_1}}. \tag{6}$$

In this study, a new spectral index of nitrogen in the leaf layer of pear tree was constructed, and the algorithm with a large number of spectral parameters was synthesized and programmed in the MATLAB language environment. Comprehensive independent experiments were conducted to analyze the correlation between leaf layer nitrogen

nutrition and growth indexes, spectral reflectance, and characteristic spectral parameters in different growth stages, select the appropriate spectral index sensitive to agronomic indexes, establish the monitoring model, and further test, verify, and improve the model by using the experimental data of independent years [22].

At the same time, the relationship between the spectral ratio index (SR), normalization index (ND), and difference index (DI) combined by any two bands in the range of 350.2500 nm and leaf layer nitrogen status (equations (7)–(9)) was systematically studied in order to find the best band combination parameters for predicting pear leaf pigment content. MATLAB was used to display the equipotential diagram of the determination coefficient between the 2-band vegetation index and leaf nitrogen status.

$$SR(R_{\lambda 1}, R_{\lambda 2}) = \frac{R_{\lambda 1}}{R_{\lambda 2}}, \tag{7}$$

$$ND(R_{\lambda 1}, R_{\lambda 2}) = \frac{|R_{\lambda 1} - R_{\lambda 2}|}{R_{\lambda 1} + R_{\lambda 2}}, \tag{8}$$

$$DVI(R_{\lambda 1}, R_{\lambda 2}) = R_{\lambda 1} - R_{\lambda 2}. \tag{9}$$

The model is comprehensively evaluated by three general indexes: root mean square difference (RMSE), relative error (RE), and accuracy (R^2).

3. Experimental Results and Analysis

3.1. Data Analysis of Total Nitrogen Content in Sample Leaves.
The data obtained through aa3 chemical analysis are the three detection values of NH_4^+ concentration in the solution to be measured, which are averaged and expressed by AVE. According to formula (1), the percentage content of total nitrogen in the leaves of each group of pear tree samples can be obtained, as shown in the following formula:

$$N(\%) = \frac{AVE\left(M_N/M_{NH_4^+}\right)V}{m} \times 100\%, \tag{10}$$

where $N(\%)$ is the percentage of total nitrogen; AVE is the average value of three repetitions of machine measurement; M_N is the atomic weight of nitrogen; NH_4^+ is the relative mass of ammonium ion; V is the volume of liquid to be measured after digestion, filtration and constant volume; and M is the dry matter mass of the blade.

The calculation results are arranged from small to large, as shown in Figure 2.

Through the above analysis and the results obtained, it can be seen that with the above culture scheme, the nitrogen nutrition level of pear trees has indeed been properly opened, which is reflected in a certain gradient in the total nitrogen content of leaves [23].

3.2. Analysis of Reflection Spectrum Data of the Sample Blade.
The data collected by hyperspectral imaging scanning system is actually a four-dimensional data set containing two plane dimensions of spatial information, radiation wavelength
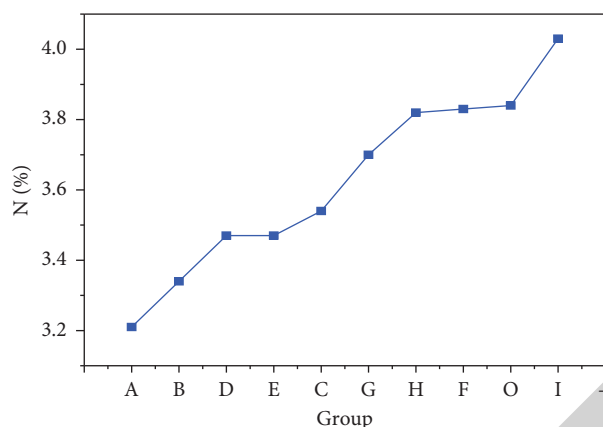
FIGURE 2: Percentage content of total nitrogen in leaves of 10 groups of samples.

information, and intensity information. In the study, ENVI 4.5 (Exelis visual information solutions, USA) was used to process and analyze the data set, and the special ROI (region of interest) selection command in software was used to quickly select all pixels constituting the leaf pattern of the target sample, so as to directly eliminate the information interference of the background pixels.

ENVI can quickly analyze the selected ROI, eliminate the spectral data that the computer considers to be abnormal points through statistical analysis, and directly establish the mean spectral curve with the screened data, and the spectral average reflectance curve of each group of 12 leaf samples can be simply drawn by using the spectral calculation command. The near-infrared reflectance mean spectral curve of 10 groups of leaf samples is shown in Figure 3, in which ε, λ are reflectance and wavelength, respectively [24].

The spectral reflection data of the near-infrared reflectance mean curve of 10 groups of leaf samples are derived by software. Each group of leaf samples has the gray value of 256 bands corresponding to the wavelength. Taking the gray $R_i (i = 1, 2, \ldots, 256)$ at each wavelength as the independent variable, the univariate linear regression is carried out for the dependent variable IV (%) one by one. There are 142 groups of regression determination coefficients $R^2 > 0.8$, and when retaining 3 decimal places, the minimum significance level of the original hypothesis is rejected in the model test, $P = 0.000$. This shows that the 142 band gray data is statistically significant to reflect the percentage of total nitrogen.

Figure 4 shows the univariate regression R^2 of gray level of each band to leaf nitrogen content. According to the variation trend of R^2 with wavelength in the figure, 142 bands with R^2 reaching 0.8 are divided into 6 regions and named according to the trend: B15-B21 (932~957 nm) is the "reliable near peak band;" B22-B46 (961–1054 am) is the "stable response band;" B47－B72 (1 058–1147 nm) is the "reliability fluctuation rising band;" B73-B103 (1 150~1 250 nm) is the "reliable peak band;" B104-B142 (1 253–1 373 AM) is the "reliability fluctuation decline band;" B219-B232 (1 626~1 673 nm) is the "reliable far peak band."

Due to the continuity of spectral data, in theory, there should be multiple collinearities between the gray levels of bands close to each other. Therefore, the collinearity diagnosis of spectral data in each region is carried out. The methods include correlation coefficient (r) analysis and the variance expansion factor (VIF) test. Taking the I region as an example, the test results are shown in Figures 5 and 6; R^2 in the table is the spectral reflectance at this i wavelength.

Figure 5 shows that the correlation coefficient r is higher than 0.9, the minimum is 0.968, and the maximum is 0.999, indicating that the correlation between gray levels in the first region of the band is very strong.

It can be seen from Figure 6 that the swelling of 7 variables is significantly higher than 10, so it can be considered that there is a serious multicollinearity between 6 gray levels in region 1. Using the above test method to test the collinearity of gray levels in other band regions, the results are similar, and the closer the band is, the more obvious the multicollinearity is [25].

In order to extract more useful information and avoid the influence of the multicollinearity between known spectral data in close bands as far as possible, the bands with the highest R2 regressed with total nitrogen content were selected from six regions, namely, B18 (944 nm), B43 (1043 nm), B72 (1147 nm), B87 (1198 nm), B104 (1253 nm), and B229 (1662 nm).

However, further research shows that when only R_{1043} and R_{1662}: 2 variables are retained, the estimated value of the ridge trace display coefficient will no longer tend to be stable with the increase of K, as shown in Figure 7.

When only R_{1043} and R_{1662} 2 variables are retained, the coefficient ridge estimation shows a rising trend as k increases, which does not tend to be stable, that is, there is a large deviation between the coefficient estimation and the real value. This shows that it is not appropriate to retain only two variables to establish the prediction model of nitrogen content in pear leaves.

The R^2 and F values are adjusted by the comprehensive determination coefficient, and the finally selected band gray levels are R_{994}, R_{1043}, and R_{1662}. The best prediction model of total nitrogen content in pear leaves is established by ridge regression, as shown in the following formula:
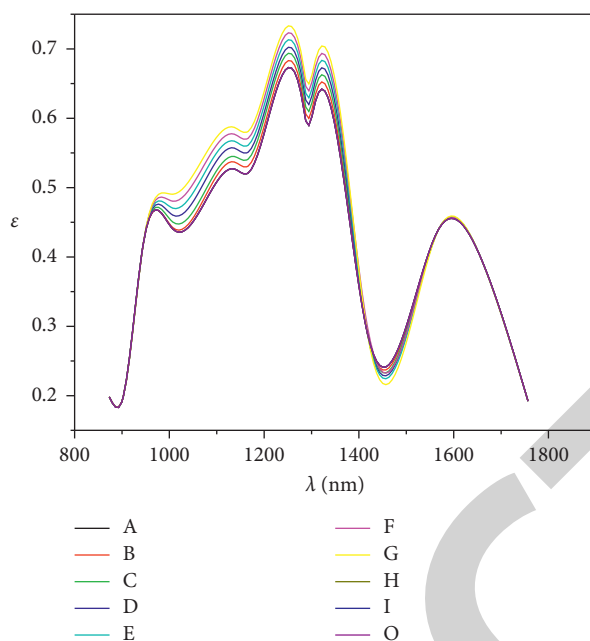
Figure 3: Near-infrared mean reflectance spectrum curve.
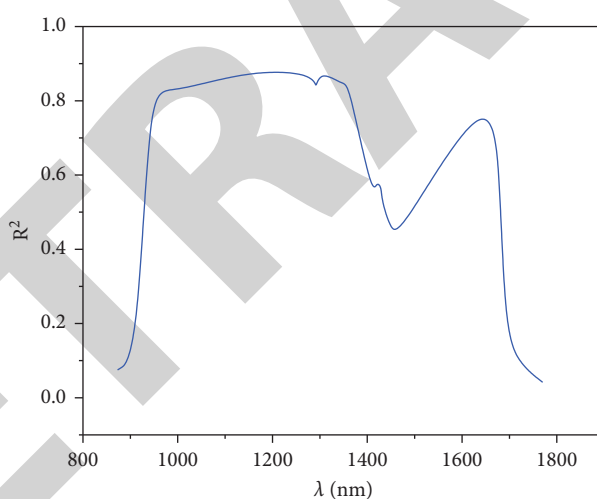
Figure 4: Univariate regression R^2 of gray level of each band on leaf nitrogen content.

$$N(\%) = -0.102R_{944} - 0.103R_{1043} - 0.206R_{1662} + 20.425. \tag{11}$$

The adjusted R^2 of the prediction model is 0.843, and the root mean square error RMSE is 0.105.

Use ENVI to scale and reorganize the band gray data involved in the model according to the coefficient proportion through the band calculation command. The final gray image, the original image, and the gray image in the process default to the 3-channel analog image of the band (the wavelengths of the bands are 1446, 1373, and 1304 nm, respectively); 944 nm gray image; 1043 nm grayscale image; 1662 nm gray image; and $(0.102R_{944} + 0.103R_{1\;043} + 0.206R_{1662})/(0.102 + 0.103 + 0.206)$ gray scale image are scaled by the model coefficient.
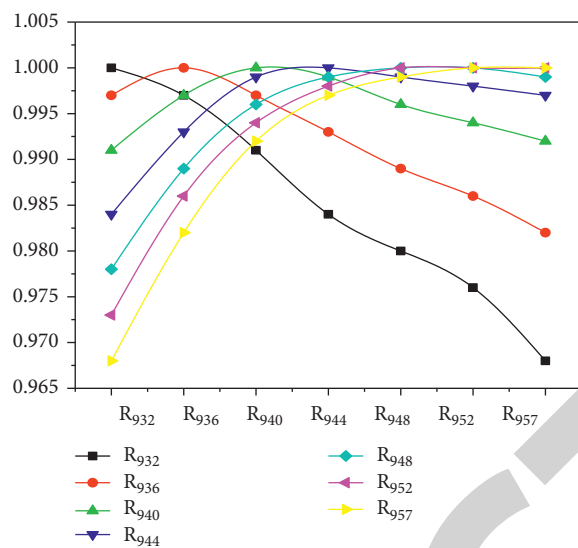
Figure 5: Correlation coefficient between gray values in the first region of the band.
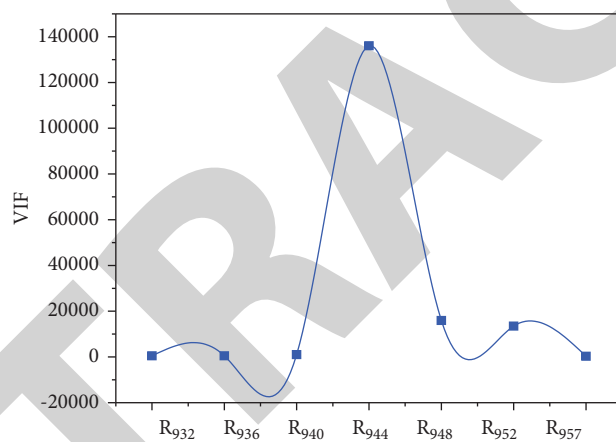
Figure 6: VIF test results of the gray value in the first region of band 4.
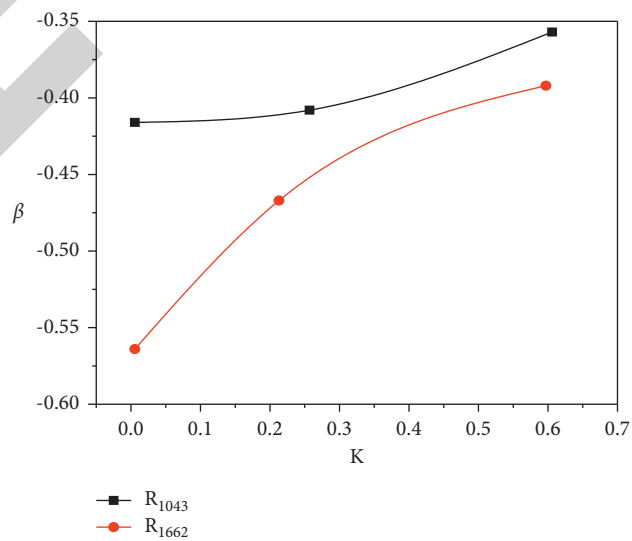
Figure 7: 2-variable ridge trace diagram.

4. Conclusion

Through the experimental operation and data analysis, based on the near-infrared reflection spectrum data and using ridge regression to screen the variables, a set of spectral detection model suitable for the total nitrogen content of pear leaves is finally obtained. The adjustment R^2 of the model is > 0.8, which shows that the fitting effect of the regression model is good, and the root mean square error RMSE is about 0.1, which shows that the model has high prediction accuracy. The model contains the spectral reflectance data of three near-infrared short wave characteristic bands, and the available information is more comprehensive.

Data Availability

The data used to support the findings of this study are available from the corresponding author upon request.

Conflicts of Interest

The authors declare that they have no conflicts of interest.

References

[1] J. Huang, M. Li, H. Zhang et al., "Using near infrared spectroscopy to quickly analyze different nitrogens during the shortcut biological removal of nitrogen from a polluted river," *Polish Journal of Environmental Studies*, vol. 28, no. 4, pp. 2623–2631, 2019.

[2] L. S. Wang, R. J. Wang, C. P. Lu, J. Wang, and L. T. Song, "Quantitative analysis of total nitrogen content in mono-ammonium phosphate fertilizer using visible-near infrared spectroscopy and least squares support vector machine," *Journal of Applied Spectroscopy*, vol. 86, no. 3, pp. 465–469, 2019.

[3] J. Liu, N. Li, F. Zhen, Y. Xu, W. Li, and Y. Sun, "Rapid detection of carbon-nitrogen ratio for anaerobic fermentation feedstocks using near-infrared spectroscopy combined with bipls and gsa," *Applied Optics*, vol. 58, no. 18, p. 5090, 2019.

[4] M. A. Hossen, P. K. Diwakar, and S. Ragi, "Total nitrogen estimation in agricultural soils via aerial multispectral imaging and libs," *Scientific Reports*, vol. 11, no. 1, Article ID 12693, 2021.

[5] L. Dan, Z. Huang, S. Men, and C. Wang, "Nitrogen and phosphorus adsorption in aqueous solutions by humic acids from weathered coal: isotherm, kinetics and thermodynamic analysis," *Water Science and Technology*, vol. 79, no. 11, pp. 2175–2184, 2019.

[6] H. Zhou, S. Gao, W. Zhang, Z. An, and D. Chen, "Dynamic adsorption of toluene on amino-functionalized sba-15 type spherical mesoporous silica," *RSC Advances*, vol. 9, no. 13, pp. 7196–7202, 2019.

[7] S. Wajizah and Z. Zulfahrizal, "Near infrared spectra features of cocoa pod husk used for feedstuff," *IOP Conference Series: Earth and Environmental Science*, vol. 922, no. 1, Article ID 012011, 2021.

[8] H. F. Ahmad Jani, R. Meder, H. A. Hamid, S. M. Razali, and K. H. M. Yusoff, "Near infrared spectroscopy of plantation forest soil nutrients in sabah, Malaysia, and the potential for microsite assessment," *Journal of Near Infrared Spectroscopy*, vol. 29, no. 3, pp. 148–157, 2021.

[9] Y. Fan, H. Wang, L. Deng et al., "Enhanced adsorption of pb(ii) by nitrogen and phosphorus co-doped biochar derived from camellia oleifera shells," *Environmental Research*, vol. 191, no. 26, Article ID 110030, 2020.

[10] J. Au, K. N. You Nge Ntob, W. J. Foley, B. D. Moore, T. Fea Rn, and J. Au, "Sample selection, calibration and validation of models developed from a large dataset of near infrared spectra of tree leaves," *Journal of Near Infrared Spectroscopy*, vol. 28, no. 4, pp. 186–203, 2020.

[11] Y. Wang, H. Huang, and X. Chen, "Predicting organic matter content, total nitrogen and ph value of lime concretion black soil based on visible and near infrared spectroscopy," *Eurasian Soil Science*, vol. 54, no. 11, pp. 1681–1688, 2021.

[12] H. P. Veeravu, S. Krishnapriya, G. Madhu, and D. K. Sahoo, "A statistical investigation into ammoniacal nitrogen adsorption on chitosan/bentonite nanocomposite films by response surface methodology," *Indian Journal of Environmental Protection*, vol. 39, no. 12, pp. 1106–1113, 2019.

[13] A. Alwi, R. Meder, Y. Japarudin, H. A. Hamid, R. Sanusi, and K. H. M. Yusoff, "Near infrared spectroscopy ofeucalyptus pellitafor foliar nutrients and the potential for real-time monitoring of trees in fertiliser trial plots," *Journal of Near Infrared Spectroscopy*, vol. 29, no. 3, pp. 158–167, 2021.

[14] A. O. Koroleva, T. A. Odintsova, M. Y. Tretyakov, O. Pirali, and A. Campargue, "The foreign-continuum absorption of water vapour in the far-infrared (50–500 cm1)," *Journal of Quantitative Spectroscopy and Radiative Transfer*, vol. 261, no. 5, Article ID 107486, 2021.

[15] I. Šestak, L. Mihaljevski Boltek, M. Mesić, Ž. Zgorelec, and A. Perčin, "Hyperspectral sensing of soil ph, total carbon and total nitrogen content based on linear and non-linear calibration methods," *Journal of Central European Agriculture*, vol. 20, no. 1, pp. 504–523, 2019.

[16] C. A. Andrade, L. A. Zambrano-Intriago, N. S. Oliveira, J. S. Vieira, L. S. Quiroz-Fernández, and J. M. Rodriguez-Diaz, "Adsorption behavior and mechanism of oxytetracycline on rice husk ash: kinetics, equilibrium, and thermodynamics of the process," *Water, Air, & Soil Pollution*, vol. 231, no. 3, p. 103, 2020.

[17] E. R. Thomson, M. P. Spiegel, I. H. J. Althuizen et al., "Multiscale mapping of plant functional groups and plant traits in the high arctic using field spectroscopy, uav imagery and sentinel-2a data," *Environmental Research Letters*, vol. 16, no. 5, Article ID 055006, 2021.

[18] X. Y. Li, P. P. Fan, Y. Liu, G. L. Hou, Q. Wang, and M. R. Lv, "Prediction results of different modeling methods in soil nutrient concentrations based on spectral technology," *Journal of Applied Spectroscopy*, vol. 86, no. 4, pp. 765–770, 2019.

[19] L. Zauska, S. Bova, E. Benova et al., "Thermosensitive drug delivery system sba-15-pei for controlled release of nonsteroidal anti-inflammatory drug diclofenac sodium salt: a comparative study," *Materials*, vol. 14, no. 8, p. 1880, 2021.

[20] X. Xu, L. Li, and A. Sharma, "Controlling messy errors in virtual reconstruction of random sports image capture points for complex systems," *International Journal of System Assurance Engineering and Management*, vol. 4, no. 3, 2021.

[21] M. Bradha, N. Balakrishnan, S. Suvi et al., "Experimental, computational analysis of Butein and Lanceoletin for natural dye-sensitized solar cells and stabilizing efficiency by IoT," *Environment, Development and Sustainability*, vol. 24, 2021.

[22] G. Vincenti, A. Bucciero, and C. Carvalho, "E-learning, E-education, and online training," *Lecture Notes of the*

Hindawi

Retraction

Retracted: Application of Computer-Aided Precious Metal Materials in Electrochemistry of Ceramic Jewelry Design

Journal of Chemistry

This article has been retracted by Hindawi following an investigation undertaken by the publisher [1]. This investigation has uncovered evidence of one or more of the following indicators of systematic manipulation of the publication process:

(1) Discrepancies in scope

(2) Discrepancies in the description of the research reported

(3) Discrepancies between the availability of data and the research described

(4) Inappropriate citations

(5) Incoherent, meaningless and/or irrelevant content included in the article

(6) Peer-review manipulation

The presence of these indicators undermines our confidence in the integrity of the article's content and we cannot, therefore, vouch for its reliability. Please note that this notice is intended solely to alert readers that the content of this article is unreliable. We have not investigated whether authors were aware of or involved in the systematic manipulation of the publication process.

Wiley and Hindawi regrets that the usual quality checks did not identify these issues before publication and have since put additional measures in place to safeguard research integrity.

We wish to credit our own Research Integrity and Research Publishing teams and anonymous and named external researchers and research integrity experts for contributing to this investigation.

The corresponding author, as the representative of all authors, has been given the opportunity to register their agreement or disagreement to this retraction. We have kept a record of any response received.

References

[1] J. Li, "Application of Computer-Aided Precious Metal Materials in Electrochemistry of Ceramic Jewelry Design," *Journal of Chemistry*, vol. 2022, Article ID 6990393, 8 pages, 2022.

Research Article

Application of Computer-Aided Precious Metal Materials in Electrochemistry of Ceramic Jewelry Design

Jing Li (ID)

Yangtze University, Jingzhou, Hubei 434023, China

Correspondence should be addressed to Jing Li; 2013062127@stu.zjhu.edu.cn

In order to solve the electrochemical application of precious metal materials in ceramic jewelry design, a computer-aided design method of precious metal materials in ceramic jewelry was proposed. First, the potential energy surface analyzed in this paper is composed of the sum of disomy and trisomy, with different proportions of disomy and trisomy. Therefore, in the fitting process, the above two relations can be used to measure the contribution of the two-body term and the three-body term, respectively; secondly, from the viewpoint of lattice dynamics, precious metals are of special significance, because they are simple fcc lattice and large and pure single crystals can be obtained. Therefore, their accurate phonon dispersion curves can be obtained experimentally; finally, the phonon dispersion curves along the highly symmetric vector direction are given, and the calculated results are in good agreement with the experimental data. This shows that the new analytical potential energy surface accurately reproduces the interactions inside these crystals. The new analytical potential energy surfaces of the three noble metals correctly reproduce the macroscopic properties of the system, including elastic modulus, cohesive energy, and phonon dispersion curve, as well as important surface features. For all three systems, the order of the surface energies of the unreconstituted surfaces is (110) > (100) > (111), which is also correct. At the same time, the new potential energy surface gives the correct relaxation behavior of the unreconstituted surface.

1. Introduction

The 20th century is an era of rapid development of science and technology, which not only promotes the improvement of industrial manufacturing technology but also promotes the development of the design industry with special significance. After entering the 1980s, the application of computer-aided design technology integrating science, economy, and art to the design industry has reflected its many advantages and brought new ideas and methods to the design industry. The ceramic industry is a traditional as well as modern industry, and the computer-aided design technology has injected new vitality into the series design process of ceramic products. However, due to the special properties of ceramic materials, such as shrinkage, easy deformation, and strong ductility, the design and manufacture of ceramic products has a unique process, which leads to an increase in the complexity of computer simulation. However, in the production stage of the model and the outer model, which is the most different, it is solved by the continuous development of virtual reality technology. Looking forward to the future, with the continuous development of computer software and hardware technology, the connection between them will also continue to increase [1]. The traditional design is mainly based on the appearance design of the product. Although it has played a very important role in the manufacture and consumption of the product in its development process, its design content is single and the means and methods are primitive. In today's rapid development of the modern society, it is far from meeting the needs of reality. The greatest charm of computer-aided design technology is that the traditional form of industrial ceramic production has been fully inherited and the special form of ceramic production has been brought into full play. Computer-aided design not only brings infinite imagination to today's industrial ceramics field but also brings us infinite possibilities.

As a means of industrial ceramic innovation, computer-aided design creates extraordinary visual effects and interactive chain effects that are unmatched by other media. It is imperative to develop ceramic art by means of computer-aided design (Figure 1).

2. Literature Review

With the development and popularization of computers, the status of computers in all walks of life is becoming more and more important and the ceramic industry is no exception. From ceramic formula design to control of ceramic production parameters and from ceramic modeling and decoration design to ceramics sales and enterprise management, we can use computers to control and adjust to improve efficiency and reduce labor intensity. The demand for technical ceramics is on the rise. With the development of the economy and the improvement of people's living standards, people's requirements for ceramic jewelry will become higher and higher and thus the pressure on the ceramic industry will also keep increasing. We have realized that the inevitable laws of market competition are not based on individual subjective will. In the development of ceramic jewelry, we should solve the problems of inheritance and innovation, pay attention to real life, absorb new ideas, new concepts and new technologies of modern high tech, and take the road of combining with modern technology.

To create a new situation in industrial ceramics, a breakthrough spirit and an avant-garde experimental spirit are also needed. Kang et al. used the numerical optimization technology based on genetic algorithm to optimize the isothermal CVI process parameters and optimized the ICVI process parameters of 2DC/C composites [2]. Moon et al. proposed a combination of genetic algorithm and finite element algorithm to optimize ceramic jewelry, and industrial applications show that this model is very efficient without the involvement of engineers [3]. Lu used multi-objective genetic algorithm to optimize the mechanical properties of ceramic mold materials [4]. Zhao established an artificial neural network model based on experimental data to predict the flexural strength and tensile strength of hot stamping die, and the prediction results were consistent with the experimental data [5]. Zheng established a neural network model of the relationship between the processing parameters and mechanical properties of magnesium oxide refractory metals. The simulation results show that the predicted flexural strength and Young's modulus are not significantly different from the experimental values, and the predicted values can replace the experimental values [6]. Hao applied artificial neural network to the study of austenitic stainless steel and established a neural network model of the effect of temperature and tensile force on the dynamic crystallization of D9 alloy. The simulation results show that the predicted results are consistent with the results in metallurgy [7]. Li puts forward the problems that should be paid attention to in the research of artificial neural network in materials science. There must be enough data when establishing the neural network model and explaining the use range of the neural network [8]. Liu established an
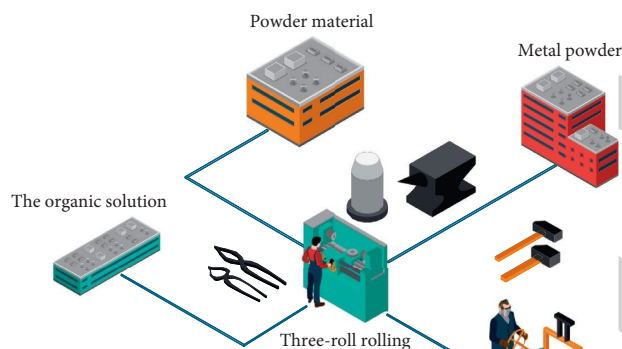
Figure 1: Computer-aided design.

artificial neural network model for predicting the parameters of gas-shielded arc welding. The composition of the gas mixture was used as the input of the network, and the mechanical properties of the welded metal were the output. The predicted results were consistent with the measured values [9]. Fan established a neural network model for predicting the conductivity and density of silver–nickel alloys, using the mass fraction of silver and nickel as the input, and the prediction results were satisfactory [10]. Li et al. proposed a genetic algorithm to optimize the weights of neural networks, gave the main optimization steps and operators, and realized the optimization of the weights by the genetic algorithm [11]. Hassan and Gholam used genetic algorithm to optimize the weights and thresholds of the BP network and used the optimized network to predict the mechanical properties such as hardness, flexural strength, and toughness of ceramic mold materials. The results show that the optimized network is stable and the efficiency has improved [12]. Nesterenko et al. established a neural network model for predicting the hole diameter of metal sheets based on air bending tests and optimized the weights of the neural network by genetic algorithm [13].

On the basis of current research, a computer-aided model for noble metal materials is proposed. The application of network technology enables industrial ceramics to enter a new information age, realizes human-computer interaction through the network, establishes a ceramic network sales and display platform, and provides convenience for industrial ceramic jewelry sales, design, and other aspects. It has also improved production efficiency and broadened the way of the sales of industrial ceramics.

3. Application of Computer-Aided Precious Metal Materials in Ceramic Jewelry Design

3.1. The Concept and Development of Ceramic Jewelry

3.1.1. The Concept of Ceramic Jewelry. Ceramic jewelry refers to the decorations that are mainly designed and made of clay materials and are used to decorate the human body, such as ceramic necklaces, ceramic bracelets, ceramic bracelets, and ceramic rings. The time when ceramic

materials were first used as jewelry-making materials has not yet been determined, but from what we know about the unearthed cultural relics, it can be traced back to the Song Dynasty. Song people have a soft spot for jade, but restricted by economic conditions and the feudal system, jade has always been the patent of princes and nobles. In addition, the Song Dynasty was also a period of great development of porcelain, especially the celadon of Ru kiln, and its smooth glaze was as lustrous as jade. Therefore, porcelain beads and porcelain cards appeared in the Song Dynasty, but due to the insufficient production technology, ceramic jewelry has not been further developed.

3.1.2. The Development of Ceramic Jewelry in Recent Years.
In recent decades, ceramic jewelry has witnessed great development, especially with the increasing improvement of people's living standards. People's demand for ceramics is no longer limited to being a practical tableware and tea set, but a work of art that decorates people's lives [14]. Ceramic jewelry came into being under the stimulation of the market. Ceramic jewelry was marketed on a large scale for the first time in Limoges, France. Once the novel design of ceramic jewelry came on the market, it was warmly sought after by people and gradually developed by other European countries. Many major brand ceramic companies have also started to deal in ceramic jewelry, and Asian countries have followed suit. Chinese ceramic jewelry started relatively late, and its production technology is relatively backward, but it is still sought after by many ceramic lovers due to its diverse shapes, rich glaze colors, unique personality, and strong decoration. However, it is also limited to the niche market in the field of ceramics and tourist souvenirs and has not been popularized in the mass consumer market.

3.2. Reasons for Using Precious Metal Materials in Ceramic Jewelry Design

3.2.1. Precious Metal Material Is a Classic Jewelry Material.
Since ancient times, jewelry has been processed from gold, silver, and precious stones, which are used to express wealth, status, and social class. Modern people mostly use it for decoration, expressing their own personality, collecting, or playing. Jewelry made of precious metal materials not only has ornamental value and decorative effect but also is durable and not easy to depreciate. Even in the modern and contemporary society, it is still a high-end durable jewelry material that is popular in the mass market.

3.2.2. The Need for Value-Added Ceramic Jewelry. Taking the ceramic jewelry industry in Jingdezhen as an example, the main body of ceramic jewelry is still high quality and low price, with small profits but quick turnover [15]. Its product design is mostly limited to the shape and color of ceramic materials. The production process is not sophisticated enough. Its shape design and decoration are very good, but it is easy to break and scratch the skin when wearing it. Because of its low price, no one will wear it often. It is often

underestimated and become only a decoration. Therefore, only by adding high-value materials and excellent design to enhance the value of ceramic jewelry itself, supplemented by exquisite production technology and taking the fine line, can ceramic jewelry achieve long-term development. It will gradually integrate into the mass market and achieve greater development space.

3.2.3. Ceramic Materials and Precious Metal Materials Complement Each Other. Ceramics means a lot to the Chinese people. In English, ceramics has the same name as China. It carries the culture and pride of the Chinese for thousands of years. Jewelry made of pure precious metal materials is tacky and cannot meet people's high-level spiritual and cultural needs. Therefore, the combination of ceramic materials and precious metals has become a trend and fashion [16]. In this way, it not only meets the pursuit of people's spiritual level but also meets the needs of people's aesthetics.

3.3. The Way and Current Situation of Precious Metal Materials Used in Ceramic Jewelry.
The combination of precious metal materials and ceramic jewelry belongs to the category of ceramic decoration, that is, to decorate and beautify the surface of ceramic utensils to achieve a perfect fit with the shape. At present, there are various ways to add precious metal materials to ceramic jewelry design. The following are two representative ways.

3.3.1. Precious Metal Material Is Covered on the Surface of Ceramic Jewelry in the Form of Patterns.
One of the methods of adding precious metal materials to ceramic jewelry is to use precious metal solution as a color-painting pigment to draw patterns on the surface of porcelain jewelry and then fire it at a temperature of about 800 to 1200 degrees Celsius. The precious metal is integrated with the porcelain surface, and the ceramic surface is covered with a golden coat. This method was first applied to ceramic tableware and ceramic art, and later, the French ceramic family business applied this method to ceramic jewelry. Generally, those fired at about 800 degrees Celsius are low-temperature on-glaze golden colors, and those fired at about 1200 degrees Celsius are high-temperature in-glaze golden colors [17]. With the advancement of science and technology and the improvement of production technology, precious metal materials can also be made into decals and then pasted on the ceramic jewelry made of porcelain, so that modern technology can rely on modern technology to mass-produce exquisite ceramic jewelry combining precious metals and ceramics.

3.3.2. Precious Metal Materials Are Assembled and Inlaid with Ceramic Materials in the Form of Accessories.
The second method of applying precious metal materials to ceramic jewelry is assembly and inlay. Assembling and inlaying is to combine precious metal materials and ceramic materials in the form of accessories according to the design intention to form a complete ceramic jewelry. Among them,

there are many inlays in the market. This method was first used to protect and decorate ancient porcelain. Later, designers applied this method in the design of ceramic jewelry. On the one hand, this method can overcome the shortcomings of the fragile ceramic ornaments and play a protective role. On the other hand, it can set off the shape, color, texture, and pattern to play a decorative role. The richness and sophistication of precious metal jewelry complements the simplicity and elegance of ceramic jewelry [18].

3.3.3. Domestic and Foreign Status of Precious Metal Materials Used in Ceramic Jewelry.

At present, most of the ceramic jewelry made of precious metal materials abroad have been industrialized with excellent production and exquisite craftsmanship. For example, France uses the ancient gold-plating technology to process gold leaf and platinum and other exquisite techniques and strict procedures to show the unique wrinkle effect between textures. Its products have a high degree of industrialization, but they cannot reflect the language of ceramics and the cultural connotation of ceramics and are not very different from jewelry made of other materials. Ceramic jewelry made of precious metal materials in China presents the opposite problem of insufficient "jewelry." Ceramic jewelry combined with precious metal materials is mostly inlaid with precious metal materials, which lacks the sense of design [19]. For example, the ceramic jewelry of the brand "Yi Qian Nian" is inlaid with ancient porcelain pieces from Jingdezhen and precious metal materials. Cultural marketing based on the unique history of ancient porcelain pieces has greatly enhanced the cultural value of ceramic jewelry; this is worthy of praise. However, we can still see that such ceramic jewelry is often too large in design, is not exquisite enough in workmanship, and relatively has less wearing comfort. There is still a certain distance from the ceramic jewelry of precious metal materials that is demanded by the mass market.

3.4. Feasibility of Introducing Computer-Aided Design into Industrial Ceramics.

In the acceptance chain passed down from generation to generation, the acceptance of a new thing is bound to undergo a process of continuous deepening, consolidation, development or revision, and overthrow. As long as human beings exist, this process will continue indefinitely and will never end. The acceptance of new information makes the judgment principles and standards constantly change and update in this process. The development process of art is always cumulative and progressive, and it is impossible to replace each other and die. The ever-changing high-tech forces re-integrate the nature, structure, and function of traditional ceramics and deconstruct them with new elements. However, integration or deconstruction does not mean extinction and will rely on the realization of multidirectional applications to promote the development of industrial ceramics. In the final analysis, it is with the help of new methods of computer-aided design that the space for continuous development has been obtained. There is no doubt that in the process of industrial ceramics going digital, the combination of industrial ceramics and computer-aided design is also imperative and even should be at the forefront. In addition, multidirectional application to solve various drawbacks of traditional crafts promotes the development of industrial ceramics. Computer-aided design technology builds a platform for "interaction" between designers and consumers. It is a great extension and synthesis of time and space, picture and sound, and vision and hearing, and it opens up the vision and realm of human knowledge and aesthetics [20].

With the development of computer-aided design technology, the formation and production of virtual digital images are no longer the results based on visual reality, and to a certain extent, there is no more connection with specific material reality. We can use computer-aided methods to obtain any form of images we need (i.e., virtual images of ceramic jewelry products). The "virtual reality" images produced by computer technology have the texture and effect of the objective world in the overall visual image, but in fact, such images do not exist in real life and are completely artificially synthesized [21]. Computer-aided design technology makes our ceramic virtual image production process more and more simplified, visualized, and real-time, while the effect of the picture is getting better and more vivid. We can see the results and effects of the picture before the product is produced and can also make complete changes in real time according to the creator's wishes, which not only saves production costs but also improves work efficiency. The virtual image is completely a mirror of the maker's personal heart. There is no need for a "real" connection between the image itself and the physical reality. All the images we see are real based on "hypothesis." The image form sense produced by computer technology will be very distinct, emphasizing the creation of visual effects, with the expression of personal style and taste, technology is completely the means of art. The technology is entirely a means of art. Digital thinking has become a part of our life, and computer-aided design technology is not only a means of production but also an efficient and creative process of artistic creation.

3.5. Application of Computer-Aided Design in Industrial Ceramics.

The invention of the computer has completely changed the entire development trend of human society, and at the same time, it has brought about substantial changes in almost all industries. It makes our work more efficient, easy, and convenient and also makes our life more comfortable, pleasant, and fulfilling. In short, it is reshaping human society in its own unique way. Various images and types of information, after editing and digital processing, can more completely express the communicator's thoughts, so digital images are significantly important. Compared to traditional "picture," "text," and "object," computer-aided design technology and virtual digital image have the nature of inheritance, expansion, perfection, and directional development. In the design of

Figure 2: Potential energy curve of Au.

Table 1: Coefficients of the new potential energy surface and calculated macroscopic parameters.

	Cu	Ag	Au
a_2	8	8	10
a_3	10	10	11
fsq	0.017	0.023	0.048
c_1	−0.11524	−0.24874	−0.24785
c_2	4.59623	6.25485	5.62156

surface and multibody expansion potential energy surface, respectively. Although these potential energy surfaces can give calculation results that are basically consistent with the experimental results, the existing potential energy surfaces lack universality and cannot give calculation results that are completely consistent with the experimental results, especially for Au metal [23]. For example, the SC potential greatly underestimates the surface energy, and the (1×2) reconstruction of the (110) plane is also incorrect. On the other hand, the MM potential can reproduce the (1×2) reconstruction of the (110) plane well but cannot give the correct order of the surface energy of the reconstructed and unreconstituted structures of the Au surface.

4.1. Potential Energy Surface. In this paper, the analytical potential energy surface is composed of the sum of two-body and three-body terms, which are defined as follows:

$$V_{(r)} = \sum_u \sum_{j>u} V_{uj} + \sum_u \sum_{j>u} \sum_{k>j} V_{ujk}. \tag{1}$$

The disomy and trisomy are

$$V_{uj} = -D\left(1 + a_2\rho_{uj}\right)\exp\left(-a_2\rho_{uj}\right), \tag{2}$$

$$V_{ujk} = DP\left(Q_1, Q_2, Q_3\right)T. \tag{3}$$

Here,

$$\rho_{uj} = \frac{\left(r_{uj} - r_e\right)}{r_e}. \tag{4}$$

Q_i is a symmetrical coordinate system consisting of triangles with sides ρ_i:

$$\begin{pmatrix} Q_1 \\ Q_2 \\ Q_3 \end{pmatrix} = \begin{pmatrix} \sqrt{\dfrac{1}{3}} & \sqrt{\dfrac{1}{3}} & \sqrt{\dfrac{1}{3}} \\ 0 & \sqrt{\dfrac{1}{2}} & -\sqrt{\dfrac{1}{2}} \\ \sqrt{\dfrac{2}{3}} & -\sqrt{\dfrac{1}{6}} & -\sqrt{\dfrac{1}{6}} \end{pmatrix} \begin{bmatrix} \rho_{uj} \\ \rho_{jk} \\ \rho_{uk} \end{bmatrix}. \tag{5}$$

D and re were chosen to correctly reproduce the nearest-neighboring interatomic distances for the lattice energy and equilibrium configuration of face-centered cubic (fcc) crystals. P is a polynomial in a symmetric coordinate system.

4. New Analytical Potential Energy Surface for Precious Metals and Its Application in Computer Simulation of Metal Surfaces

Surface computer simulation is one of the current active research areas, with intensive research on noble metal families both experimentally and theoretically over the years. It is well known that metal surfaces are often different from interiors. For example, the observed surface interlayer spacing and surface structure are quite different from those inside the metal, which is known as surface relaxation and reconstruction. For transition metals, the literature generally gives the compression of the outermost layer inward. For the Au solid, the (110) facet exhibits a (1×2) "Missing-row" reconstruction, corresponding to the facet that generates a small (111) facet. The experimental data indicate that the Cu and Ag surfaces do not exhibit "Missing-row" reconstruction but exhibit surface relaxation. Noble metal systems have been studied by using atomic intercalation potential energy

industrial ceramics, the computer can help the designer to undertake the work of calculation, information storage, and drawing. In the design, a large amount of calculation, analysis, and comparison of different schemes can be carried out by computer to determine the optimal scheme. All kinds of design information, whether digital, text, video, or graphics, can be stored in the computer's memory and can be retrieved quickly. Designers can use computers to design product sketches, and the heavy work of turning sketches into various complex product renderings can be done by computers [22]. The design results automatically generated by the computer can be quickly displayed in graphics, so that the designers can make judgments and modifications to the design in time. Computers can be used to process graphics data related to graphics editing, enlargement, reduction, translation, and rotation and can also display three-dimensional space.

TABLE 2: Cohesive energy and equilibrium bond length.

	Cu		Ag		Au	
	E_{eoh} (eV)	R_{eq} (nm)	E_{eoh} (eV)	R_{eq} (nm)	E_{eoh} (eV)	R_{eq} (nm)
fcc	3.462	0.264	2.998	0.284	3.785	0.287
bcc	3.488	0.254	2.978	0.287	3.875	0.248
sc	3.456	0.236	2.596	0.276	3.456	0.274
dia	2.755	0.239	1.674	0.267	2.789	0.276
hcp	3.598	0.247	2.835	0.245	3.359	0.265

Only the cubic term is used in this paper, which is defined as follows:

$$P(Q_1, Q_2, Q_3) = c_0 + c_1 Q_1 + c_2 Q_1^2 + c_3(Q_1^2 + Q_2^2) + c_4 Q_1^3$$
$$+ c_5 Q_1(Q_2^2 + Q_3^2) + c_6(Q_3^3 + 3Q_3 Q_2^2). \quad (6)$$

The coefficient c_i is determined by the elastic constant, macroscopic cohesion energy, hole formation energy, surface energy, and partial phonon frequency of the fitted fcc structure. T is a regional function, and there are 4 kinds of functions to choose from:

$$T = \exp(-a_3 Q_1);$$

$$T = \text{Tanh}(a_3 Q_1);$$

$$T = \exp(a_3 Q_1^2); \qquad (7)$$

$$T = \frac{1}{\cosh(a_3 Q_1)}.$$

The relationship between the Born–vonKarman force constant and the dynamics matrix elements and the phonon dispersion frequencies along the $[q, 0, 0]$, $[q, q, 0]$, and $[q, q, q]$ directions for any layer of the fcc lattice is given in the literature. The general formula for the elastic modulus of any layer of the fcc lattice is also given in the literature, and the energy required to generate a hole without considering lattice relaxation is

$$E_v = -\left(\frac{1}{2} \sum_i V_i + \frac{2}{3} \sum_i \sum_{j>i} V_{ij} \right). \qquad (8)$$

This energy is equal to the energy required to remove an atom from the lattice to infinity minus the cohesive energy. Noting the cohesive energy (atomic energy) as

$$E_{eoh} = -\left(\frac{1}{2} \sum_i V_i + \frac{1}{3} \sum_i \sum_{j>i} V_{ij} \right). \qquad (9)$$

There are different proportions of two-body and three-body items, so the above two relations can be used in the fitting process to measure the contributions of the two-body and three-body items, respectively [24]. In the process of deriving the potential energy surface, it is truncated at 2.9 times the nearest neighbor distance,
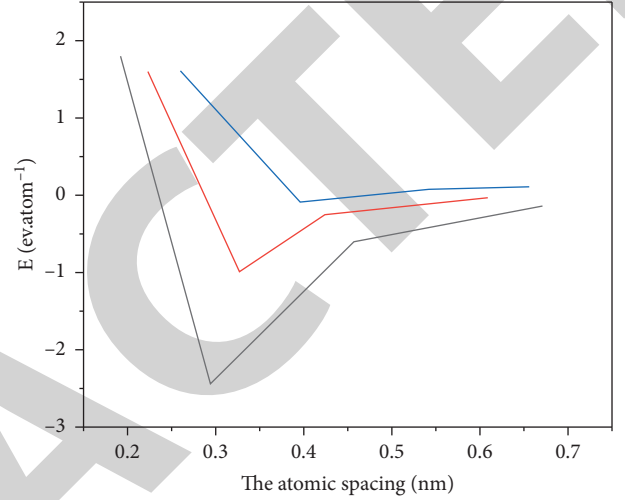
FIGURE 3: Potential energy curve of Ag.
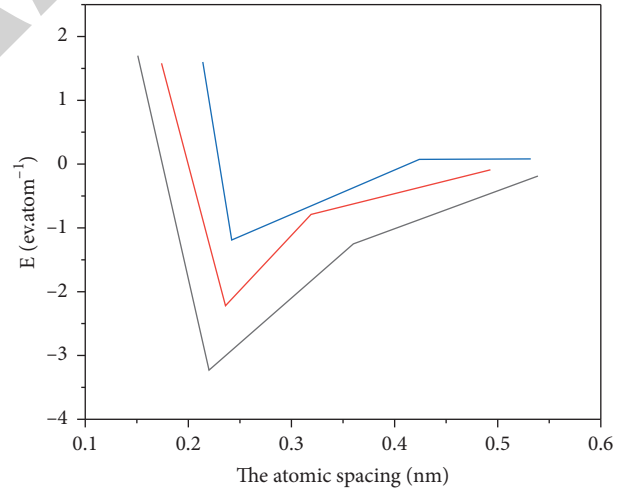
FIGURE 4: Potential energy curve of Cu.

which is equivalent to 8 layers of atoms being considered. A set of a_2 and a_3 values are selected between 5.0 and 10.0, and the coefficients in equation (9) are optimized. We found that for a given set of a_2 and a_3, the optimization process with different initial values can generally give basically the same potential function; sometimes, the coefficients are slightly different, indicating that the parameter space surface is relatively flat near the minimum point. For different combinations of a_2 and a_3, the coefficients are quite different. Now, we have the ability to
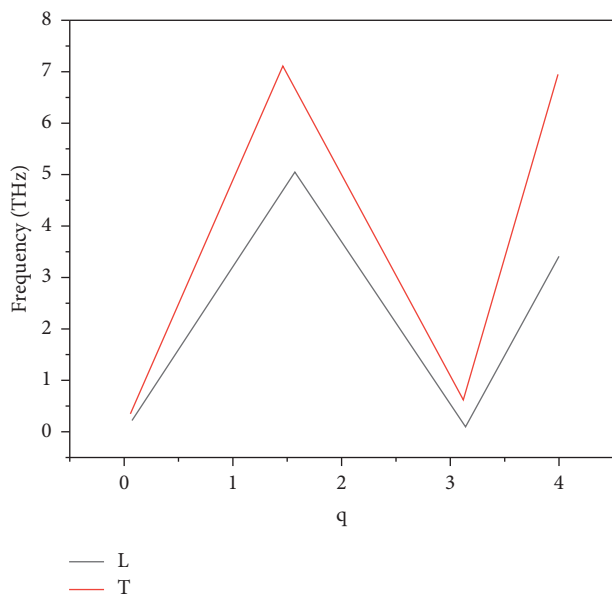
Figure 5: Phonon dispersion curve q of Cu crystal.
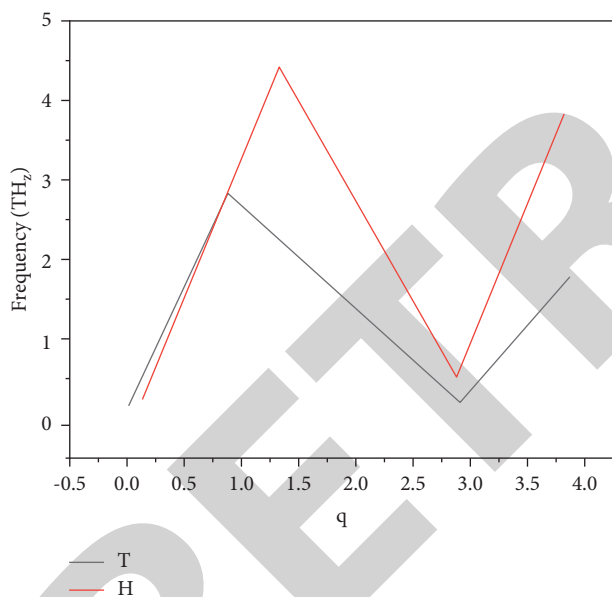
Figure 6: Phonon dispersion curve q of Au crystal.

use different area functions to calculate the grid of a_2 and a_3 to find the best combination of a_2 and a_3. For Au, we find that good fitting results are sometimes difficult to obtain, and sometimes some anomalous behaviors are found. For example, the first layer stretches outward, while the second layer compresses inward, especially when $a_2 < a_3$ or $a_2 = 5.0$ (Ag) and $a_3 < 5.5$ (Au), Au and Ag metals exhibit this anomalous phenomenon. For Cu, no such anomalous phenomenon was found. Among the four regional functions, we found that the sech function was the most suitable for the three systems studied. Table 1 shows the potential energy surface obtained by the final fitting and the calculated macroscopic parameters.

Table 2 lists the cohesive energies and equilibrium bond lengths of 12 three-dimensional structures and structures such as two-dimensional layers calculated using the obtained potential energy surfaces. The calculated hcp structure may be too stable. Although, in fact, the hcp of Cu is slightly more stable than the fcc, the 3rd significant figure is beyond the precision range [25]. Figures 1–3 show the potential energy curves of 15 different three-dimensional and two-dimensional structures for each of the three systems. It can be seen from the figure that the new potential energy surfaces of the three systems all give correct asymptotic trends.

Noble metals are of particular interest from the lattice dynamics point of view because they are simple fcc lattices of monovalent metals and large and pure single crystals can be obtained. Therefore, their precise phonon dispersion curves can be obtained experimentally. Figures 4–6 show the phonon dispersion curves along the highly symmetrical vector direction, and the calculated results agree very well with the experimental data, indicating that the new analytical potential energy surface accurately reproduces the interactions inside these crystals.

5. Conclusion

The calculation results indicate that the new analytical potential energy surfaces of the three noble metals correctly reproduce the macroscopic properties of the system, including elastic modulus, cohesive energy, and phonon dispersion curve as well as important surface features, such as the relative energy and the inward relaxation of the surface of the first layer. The surface energies calculated for the three precious metals are also generally acceptable, although the average surface energies are overestimated by 2.1% for Cu, 3.7% for Ag, and 6.6% for Au. Generally speaking, the unreconstituted surface relaxation problem is a great challenge for computer simulation. Glue potential as well as SC and MM potentials have been used to perform computer simulations for these three precious metals. In general, these potential energy surfaces can reproduce the surface energy relatively correctly and can give the correct order of the unreconstructed surface energy. SC and MM potentials can also characterize the inward compression of the (111) and (100) crystal planes. However, none of them can correctly give the reconstruction behavior of the Au (110) plane; for example, the reconstruction of the (1×2) "Missing-row" of the Au (110) plane is more efficient than the (110) unreconstituted structure. It is stable and tends to generate (111) facets. In addition, the motion of atoms on the (110) crystal plane reconstructed by the (1×2) "Missing-row" is also incorrect. Our new potential energy faces not only correctly reproduce the surface energy order of the unreconstituted crystal planes but also give reasonable surface reconstruction behaviors for the three noble metals. The calculation results are given: for Cu system, (110) > (110) (1×2); for Ag system, (110) > (110) (1×2); and for Au system, (110) (1×2) > (110) > (110) (1×3); this is in good agreement with the experimental

Retraction

Retracted: Application of Foam Glass-Ceramic Composite Thermal Insulation Material in Traditional Buildings

Journal of Chemistry

This article has been retracted by Hindawi following an investigation undertaken by the publisher [1]. This investigation has uncovered evidence of one or more of the following indicators of systematic manipulation of the publication process:

(1) Discrepancies in scope

(2) Discrepancies in the description of the research reported

(3) Discrepancies between the availability of data and the research described

(4) Inappropriate citations

(5) Incoherent, meaningless and/or irrelevant content included in the article

(6) Peer-review manipulation

The presence of these indicators undermines our confidence in the integrity of the article's content and we cannot, therefore, vouch for its reliability. Please note that this notice is intended solely to alert readers that the content of this article is unreliable. We have not investigated whether authors were aware of or involved in the systematic manipulation of the publication process.

Wiley and Hindawi regrets that the usual quality checks did not identify these issues before publication and have since put additional measures in place to safeguard research integrity.

We wish to credit our own Research Integrity and Research Publishing teams and anonymous and named external researchers and research integrity experts for contributing to this investigation.

The corresponding author, as the representative of all authors, has been given the opportunity to register their agreement or disagreement to this retraction. We have kept a record of any response received.

References

[1] Q. Yu, "Application of Foam Glass-Ceramic Composite Thermal Insulation Material in Traditional Buildings," *Journal of Chemistry*, vol. 2022, Article ID 9662805, 9 pages, 2022.

Hindawi

Research Article

Application of Foam Glass-Ceramic Composite Thermal Insulation Material in Traditional Buildings

Qi Yu [ID]

School of Architecture and Urban Planning, Jilin Jianzhu University, Changchun, Jilin 130000, China

Correspondence should be addressed to Qi Yu; 1432104225@post.usts.edu.cn

In order to solve the application of thermal insulation materials in traditional buildings, a foam glass-ceramic composite thermal insulation material was proposed for the application of traditional buildings. First, the preparation of the hydrated glass matrix was completed by using the colloidal chemical method with sodium water glass, boric acid, calcium bentonite, and fly ash as the main raw materials. Second, using the introduction of crystalline mineral powder fly ash and secondary heat treatment, a low-temperature foam glass-ceramic composite material with lightweight, high strength, good water resistance, and low cost is prepared. Finally, the process parameters such as dehydroxylation heat treatment temperature and holding time involved in the preparation process were explored and optimized. It is proved that the external content of fly ash is 20 wt.% and above, and the external content of boric acid is 1-2 wt.%. The mixed sol has a bulk density of 192–256 kg/m^2, a compressive strength of 0.44–0.63 MPa, a weight loss rate of 5.1–7.8 wt%, and a softening coefficient of 0.85–0.95, and thermal conductivity is 0.056–0.064 W/(m·K).

1. Introduction

In recent years, with the continuous introduction of new foam glass products by manufacturers of foam glass-ceramic composite thermal insulation materials in countries such as Germany and Japan, the market demand for foam glass has suddenly increased. In the early 1990s, the market demand for foam glass in China was only 6,000 m^3. In the mid-1990s, the market demand was about 8,000 m^3. By the end of the 1990s, the market demand for foam glass had risen to 20,000 m^3. Experts predicted that the annual demand for foam glass would reach 1.0×10^5 m^3 by 2010, and the demand for foam glass in the domestic market would show a rising trend of both production and sales. Foam glass manufacturers should use this favorable opportunity to vigorously develop, promote, and export high-quality foam glass products, so that the development and utilization of domestic wall building materials will produce qualitative changes, and high-quality, multivariety foam glass will enter the international market [1]. At present, there are small factories in China which use waste glass to produce foam

glass products. The annual production capacity of these small factories is only a few thousand cubic meters. The technical equipment is very backward, the product quality is unstable, the scrap rate is high, and the cost remains high, which hinders the promotion and use of the product. Despite this, the product is still in short supply.

Although there are many varieties of existing thermal insulation materials, they are very limited as building thermal insulation materials. Judging from the actual application of the existing building thermal insulation materials, there are certain defects. From the perspective of the performance of these materials, there are problems such as high water absorption, low strength, no fire resistance, and inconsistent expansion coefficients with concrete or brick wall materials. Judging from the actual situation after the thermal insulation construction, the cracks and hollowing of the wall surface are serious. Because most of the materials are organic, they are easy to age and have a short service life. These not only affect the overall appearance of the wall but also have extremely difficult maintenance and inconvenient issues, as shown in Figure 1. On the basis of the current

research, a foamed glass-ceramic composite thermal insulation material is proposed for use in traditional buildings. After a lot of exploration in the previous experiments, it was found that the water resistance of the low-temperature foamed glass-ceramic composite material was significantly improved when the high-temperature dehydroxylation heat treatment was completed at 525°C and higher.

2. Literature Review

With the rapid development of science and technology and the increasing improvement of people's living standards, foam glass-ceramic composite thermal insulation materials are widely used in housing construction and people's daily life and have become an indispensable material for scientific experiments and cutting-edge technologies. Therefore, a lot of waste glass is inevitably produced, and various waste glass occupies a certain proportion in glass factories and municipal waste. According to statistics, in some developed countries in Europe and in the United States, waste glass accounts for 4% to 8% of the total urban waste. About 3.2 million tons of waste glass are produced every year, accounting for 2% of the total municipal solid waste [2]. In the past, most of the waste glass was recycled by some Xiaoping glass factories, but the production process of Xiaoping glass is backward, the equipment is simple, the environmental pollution is serious, and the energy consumption is high. The flat glass produced has low light transmittance, and there are a lot of defects such as waves, bubbles, pitting, and scratches; and the glass is brittle and easily broken. In order to change this situation, these small flat glass production lines have been phased out within a time limit. Therefore, how to rationally reuse waste glass has important practical significance. The use of waste glass to produce foam glass is an effective way to solve this problem. Foam glass is mainly made of waste glass and various glass-containing substances. After crushing and grinding, adding foaming agents, modifiers, and other materials, and uniformly mixing to form batches, it is then placed in a specific mold to undergo melting, foaming, and annealing to form a porous glass material filled with uniform pores.

Sayan et al. used waste glass as the main raw material, borax as a flux, and carbon powder as a foaming agent and then added certain additives to prepare microcrystalline foam glass [3]. Melnikov et al. applied mathematical analysis methods to establish a relatively accurate mathematical relationship between the pore diameter and temperature of foam glass and improved its preparation research theory [4]. Shang prepared a foam glass material for military use to absorb radar waves, and the research on foam glass turned to the development of various new functions [5]. Lu and Shi used silica sand, soda ash, feldspar, and so forth as the basic raw materials, plus a small amount of foaming agent and crystal nucleating agent, sintered according to a certain system, and slowly cooled to prepare microcrystalline foam glass [6]. Liu et al. used hexachlorocyclotriphosphorus cyanide graft-modified expandable graphite as a flame retardant and added it to isocyanate and polyether, mixed and foamed to obtain a flame-retardant rigid polyurethane foam,

which improved the LOI and prolonged the ignition time; the performance is improved compared with pure rigid polyurethane foam [7]. Peng adopted the organic foam impregnation method and foamed gel process, externally doped with cerium phosphate and yttrium oxide for toughening to prepare siC-based foam ceramics, and optimized the slurry preparation and sintering system [8]. Chen et al. used fly ash, waste glass powder, and ceramic powder as the main raw materials, sulfate as foaming agent, and boric acid as foam stabilizer. A product with a bulk density of 645 kg/m^3 and a compressive strength of 8.01 MPa was produced. Although the product has high strength, its thermal insulation performance is poor [9]. Buriachok et al. used coal gangue and shale as the main raw materials and sintered them at 1200°C by powder sintering method to obtain a foam product with a thermal conductivity of 0.14 W/(m·K) [10]. Nguyen et al. used waste slope glass and water as the main raw materials to prepare foam slope glass by hydrothermal hot pressing-calcination method and finally obtained a foam slope glass product with a bulk density of 250 kg/m^3 and a compressive strength of 1.5–1.6 MPa [11]. Lu used the waste of foamed glass as the main raw material, mixed with part of fly ash, and used hydrogen peroxide as the foaming agent. The foam glass products with thermal conductivity of 0.043–0.061 w/(nvk) were obtained, and the production cycle was as long as 7 days [12].

On the basis of the current research, a foamed glass-ceramic composite thermal insulation material is proposed for use in traditional buildings. After a lot of exploration in the previous experiments, it was found that the water resistance of the low-temperature foamed glass-ceramic composite material was significantly improved when the high-temperature dehydroxylation heat treatment was completed at 525°C and higher. The series of mixed sols prepared by the optimized formula will complete the low-temperature foaming heat treatment at 400°C and then they will be directly placed at a dehydroxylation heat treatment temperature of 525°C for 30 min. It was found that the water resistance of the material was significantly improved, the weight loss rate was reduced to less than 5 wt.%, and the softening coefficient reached more than 0.9.

3. Application of Foam Glass-Ceramic Composite Thermal Insulation Material in Traditional Buildings

3.1. Foam Glass-Ceramic Composite Thermal Insulation Material

3.1.1. Introduction. Foam glass is made of glass as the base material, which is foamed and fired at high temperature by ball milling. It is divided into closed-cell foam glass and open-cell foam glass. The walls are insulated with closed-cell foam glass. Closed-cell foam glass is a lightweight, rigid material composed of millions of completely closed glass bubbles. Each airtight bubble can play a thermal insulation effect and is an inorganic environmental protection advanced thermal insulation material. Foam glass has excellent comprehensive properties, as well as strong weather

The wall at the grass-roots level

Bonding mortar

Heat preservation material

Patented air vent valve

The anchoring piece

Article bubble

screw

Decorative panel

Silicone sealant

Bearing parts
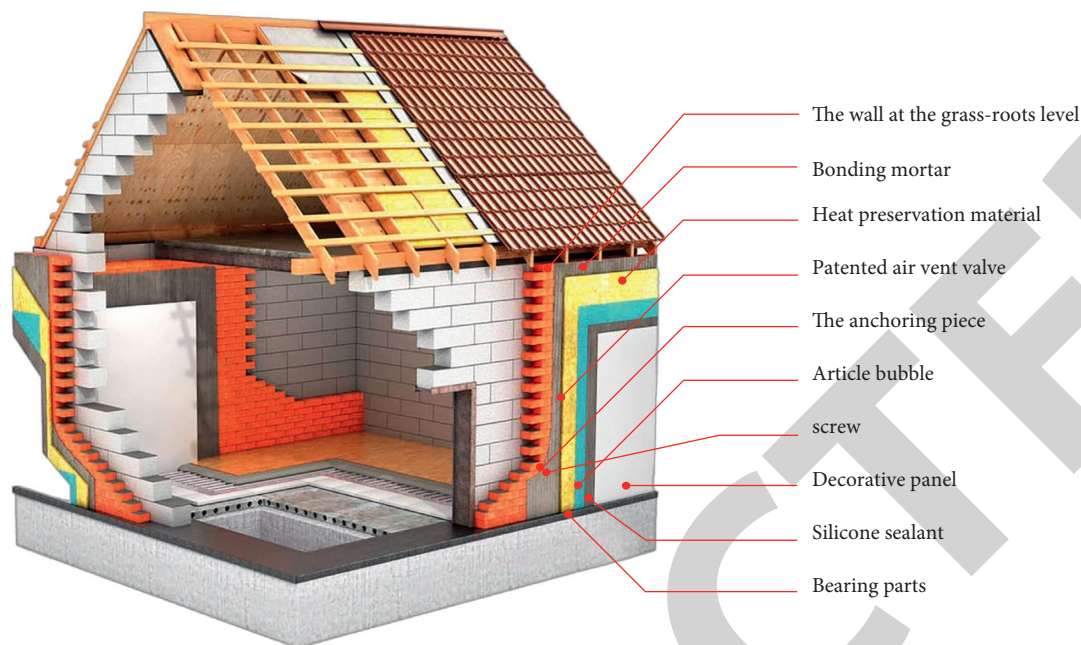
Figure 1: Composite thermal insulation material.

resistance and durability. It is an inorganic thermal insulation material. Its service life is synchronized with the building. The coefficient of linear expansion is basically the same as that of wall materials such as concrete. The surface is porous and the cement mortar is well bonded, and the construction is convenient. It has the characteristics of high strength, low thermal conductivity, and no water absorption. It has strong resistance to ultraviolet rays and wind and rain and has a permanent thermal insulation effect, which avoids the damage of the building structure due to changes in high and low temperatures [13].

3.1.2. Features. Foam glass thermal insulation material is an inorganic material and is firmly combined with other inorganic materials. It has good weather resistance, lightweight, high mechanical strength, good physical stability, and convenient transportation. It can be cut with common woodworking tools. It has good combination with ordinary cement mortar and is easy to paste on the wall. The construction of the material is simple and fast, and there is no need to set up a large area of reinforced mesh cloth and waterproof elastic putty, and the construction method is not limited by seasons. It can be pasted and installed by conventional methods. It is not only safe and reliable but also durable when used in harsh environments of low temperature and cryogenic temperature, underground engineering, flammation and explosion, humidity, and chemical erosion. It is known as "permanent thermal insulation material without replacement." Therefore, the foam glass wall insulation system is widely used in thermal insulation projects in civil and commercial housing construction, petroleum, chemical industry, underground engineering, shipbuilding, and defense and military industries.

3.1.3. Process Principle and Structure of Foam Glass Thermal Insulation Material. Foam glass has good dimensional stability. In actual use, there will be no cracks or deformation damage due to expansion and contraction. As long as a reasonable and matching protective layer and finishing layer are selected, the foam glass insulation system can have the same life as the building. When the foam glass is bonded to the base wall, the point-bonding method is used, and the coating area is required to be 40% to 70% of the area of the board. This not only effectively ensures the bonding strength of the foam glass plate and the wall but also forms a certain cavity, which is conducive to removing moisture. In the entire structural design of the foam glass exterior wall thermal insulation system, the compatibility of the materials in the system and the matching of the elastic modulus change indexes of the adjacent structural layers are fully considered. The special plastering mortar ensures a certain flexibility in order to release the deformation stress. Since the foam glass is a hard inorganic material, the mesh cloth is canceled in the ordinary structure, but the mesh cloth is added to disperse the deformation stress and prevent cracking when strengthening the structure or special parts such as door and window openings [14]. When making the paint finishing layer, the flexibility and deformation properties of the plastering mortar layer, putty layer, and paint layer are required to be gradually increased to prevent cracks in the finishing layer.

3.1.4. Comparison with Other Thermal Insulation Materials. At present, the applied building insulation materials mainly include rock wool boards, expanded perlite products, expanded vermiculite products, and foamed plastics. Although these thermal insulation materials have good thermal performance, they also have some disadvantages. For example,

rock wool has a high water absorption rate, and its thermal conductivity is small when it does not absorb water. Once it absorbs water, its thermal conductivity will increase sharply. Moreover, due to the internal water absorption of rock wool, it is not easy to evaporate for a long time, which has a negative effect on the thermal insulation and heat insulation of buildings. The water absorption rate of expanded perlite products and expanded vermiculite products is also very large. There are many varieties of foam plastic. Foamed plastics for building energy saving mainly include polystyrene board, polyurethane board, and polyethylene board. Generally, the thermal conductivity of foamed plastics is lower than that of foamed glass, but the water absorption rate is relatively high. The water absorption rate of polystyrene board is more than 6%, and the water absorption rate of polyurethane board is more than 4%. The expansion coefficient of foam is much larger than that of cement or steel, and its dimensional stability is relatively poor. Compared with foam glass, foam plastic has poor fire resistance and cannot be used in parts with high fire protection requirements (such as external wall insulation). As an organic material, foam plastic also has problems of aging and failure. Foam glass is used for roof insulation and can also play a second waterproof role [15]. Building thermal insulation materials generally requires low water absorption, high strength, low expansion coefficient, and low thermal conductivity. With its excellent performance, foam glass is not only suitable for thermal insulation of building exterior walls and basements but also more suitable for roof thermal insulation. The experience of using foam glass as a building insulation material in the United States has proved that foam glass is durable and has excellent performance and quality.

3.2. Application of Foam Glass in Building Energy Saving

3.2.1. Building Roof Insulation. There are three main types of foam glass used for building roof thermal insulation structure: upright flat roof, inverted flat roof, and sloping roof. Inverted roofs can be used for greening, planting flowers, or as roof sports fields and other roofing. Foam glass is easy to combine with other inorganic materials and easy to construct and has better waterproof, fireproof, and thermal insulation effects. The actual engineering applications include the office building of the State Planning Commission, the residential building of the Central National Song and Dance Troupe, and the No. 14 residential building in the second district of Fangguyuan, Beijing.

3.2.2. Building Exterior Insulation. As a wall thermal insulation material, foam glass can effectively reduce the thickness of the wall, reduce the quality of the building structure, and expand the usable area. The use of foam glass as external thermal insulation technology has been adopted in Changchun and other regions.

3.3. Problems Existing in Research and Production of Foam Glass.

Foam glass has not been widely used for building energy efficiency, mainly because of cost. In the early days, it was mainly used in the petrochemical industry and the price reached 2000–3000 yuan/m^3. For building insulation, if the price exceeds 1,500 yuan/m^3, it is difficult to be competitive with EPS sheets and polystyrene granular mortar. The reasons for the high production cost of foam glass are mainly as follows.

3.3.1. Production Scale. In the development process of the foam glass industry, due to the limited strength of the foam glass manufacturers and the lack of effective industry planning and guidance, the current production scale of foam glass is small and has not formed an industrial scale. For foam glass, the cost of fuel (energy consumption) is an important component, and the larger the production capacity of a single kiln, the lower the unit energy consumption [16]. If the annual kiln production capacity is increased from 300 m^3 to 10,000 m^3, the cost of blanks will correspondingly drop from 1,500 yuan/m^3 to about 400 yuan/m^3. However, the annual production capacity of most kilns is between 3000 and 5000 m^3, and less than 20 can maintain normal production.

3.3.2. Production Process. The current production of foam glass in China is the same as that in foreign countries. The glass, foaming agent, and additives are mixed together, ground into powder, and then heated and foamed in a kiln. According to the different preheating-foaming-stabilizing-annealing cooling firing processes, it can be divided into "two-step" process and "one-step firing" process. The characteristic of the two-step firing method is in the later stage of foaming and shaping. After the heat-resistant steel mold is removed outside the kiln, it is concentrated in the annealing kiln for annealing. The advantage of this process is that it can observe and judge the foaming quality in time, adjust the foaming temperature and time system in time, and separate the foaming kiln from the annealing kiln. The adjustable range of the front and rear process tables is large, and it can flexibly produce foam glass of different densities and varieties. At present, domestic manufacturers all adopt the "two-step method" production process. Whether it is the "one-step method" or the "two-step method" to produce foam glass, the powder is loaded into the mold and then sent to the foaming kiln. The mold and the powder are heated together and then cooled, which consumes a lot of energy [17]. In particular, the intermittent production unit consumes more energy. For example, the intermittent production of thermal insulation foam glass with an electric furnace accounts for more than 70% of the cost. At the same time, the foaming temperature of thermal insulation foam glass is above 800°C, and the mold is made of alloy steel, which is expensive and has a large loss after repeated high-temperature heating. Some enterprises use cast iron as molds. Although the price is low, it is oxidized, peeled off, and deformed after heating, and the loss is also serious. The energy consumption of the mold and the consumption of the mold itself are another important reason for the high cost of foam glass [18].

4. Research and Development of Low-Temperature Foam Glass-Ceramic Composite Building Insulation Material

4.1. Material Preparation Process. The preparation process of the low-temperature foam glass-ceramic composite insulation material is as follows: (1) preparation of multihydrated glass matrix, where a certain amount of glass matrix modifier (a kind of boric acid and calcium-based bentonite) is added to liquid sodium silicate by wet chemical method or shearing at a high speed for 10 min at a rotational speed of 4000 rpm/min to obtain Na_2O-B_2O_3-Al_2O_3-H_2O hydrated glass sol; (2) physically blending into crystalline phase mineral powder, where, introducing crystalline phase mineral powder fly ash into the Na_2O-B_2O_3-Al_2O_3-H_2O system hydrated glass sol, physical blending was carried out with a high-speed dispersing sand mill at 4000 rpm/min for 30 minutes, and a gray liquid mixed sol was obtained without gelling, and the viscosity was higher than that of liquid silicic acid; (3) low-temperature foaming heat treatment, where the mixed liquid sol was poured directly into a 100 mm × 100 mm × 50 mm alumina ceramic crucible mold, and it was moved to a program-controlled box-type resistance furnace; the heating rate is warmed up from room temperature to 400°C of insulation for 30 min and obtains the low-temperature foaming heat treatment sample where the residual hydroxyl content is about 5%; (4) high-temperature dehydroxylation heat treatment, where 400°C of low-temperature foaming heat treatments, demoulding, and cutting into several 40 mm × 40 mm × 30 mm cuboid test blocks is placed in an alumina porcelain boat and directly moved into an electric heating constant temperature blast drying oven that has been heated to 500°C for 60 min–240 min. After cooling in the furnace, the low-temperature foam glass-ceramic composite thermal insulation material was obtained [19].

4.2. Composition, Properties, Structure, and Formation Mechanism of Low-Temperature Foamed Glass Ceramics

4.2.1. Thermogravimetric Analysis. Sodium water glass, boric acid, and fly ash (particle size < 35 um) with a modulus of 2.33 and a solid content of 47.22 wt% are used as raw materials. The mixed sol was prepared according to the formula, and the thermogravimetric test was carried out after drying for 12 h to explore the weight loss during the heat treatment of the dried blank [20].

Boric acid was introduced into sodium water glass through high-speed shearing (4000 rpm/min for 30 min) to obtain Na_2O-B_2O_3-Al_2O_3-H_2O hydrated glass sol without gelation. Then, the fly ash is added to the sol and the physical blending is completed through high-speed dispersion to obtain a mixed sol. The mixed sol was dried in a blast drying oven at 100°C for 12 h to obtain a green body with a certain moisture content. At this time, the mixed sol mainly lost a part of free water. The thermogravimetric analysis was carried out, and the results obtained are shown in Figure 2.
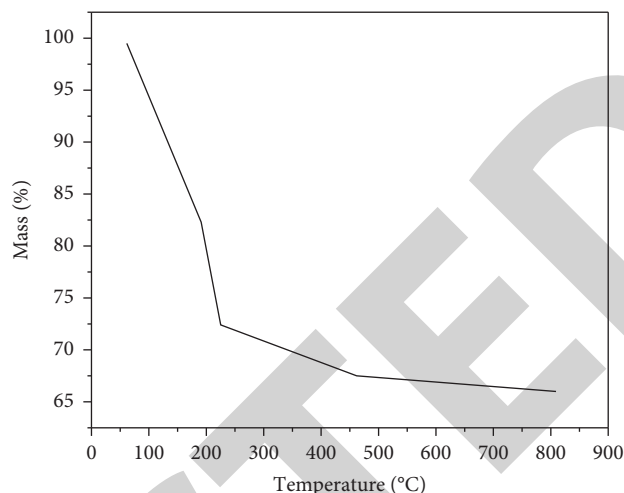
FIGURE 2: Thermogravimetric curve of the formulation.

From the thermogravimetric curve, it can be seen that the temperature range of severe weight loss of the dried green body is less than 400°C [9]. The water part contained in the hydrated glass material exists in the grid structure in the form of free water and can move back and forth in the gaps of the grid. Some are present in the form of silanol groups (Si-OH). Since there is no chemical change such as oxidative decomposition in the whole system, the whole heating process is the process of losing free water and hydroxyl groups in the system. Before 105°C, the green body first lost about 15 wt.% of free water. Within 105°C–150°C, the crystal water in the system is vigorously removed. Within 150°C–400°C, the weight loss rate of the green body is relatively severe. After 400°C, the weight loss of the dried green body becomes slow. Through multiple experiments, the foaming temperature was determined to be 400°C, the heating rate was 3°C/min, and the holding time was 30 min. At this time, the expansion ratio of the material is larger, the foaming is more uniform, and the obtained low-temperature foaming heat treatment sample is easier to demould, which is convenient for subsequent high-temperature dehydroxylation heat treatment [21].

4.2.2. Material Composition and Structural Analysis. Figure 3 shows Na_2O-B_2O_3-SiO_2 series low-temperature foam glass. Crystalline mineral powder raw material fly ash and formula is mixed sol with fly ash content of 20 wt.% and boric acid content of 2 wt.%. After the low-temperature foaming heat treatment was completed at 400°C for 30 min, the high-temperature dehydroxylation heat treatment was completed at 500°C for 3 h. The X-ray diffraction analysis of the obtained low-temperature foam glass-ceramic composite is shown in Figure 3 [22].

It can be seen that the low-temperature foam glass-ceramic composite is composed of two phases: crystalline phase and amorphous glass phase. The main crystal phase is quartz, and the Na_2O-B_2O_3-SiO_2 low-temperature foam glass is composed of glass phases. Crystalline mineral
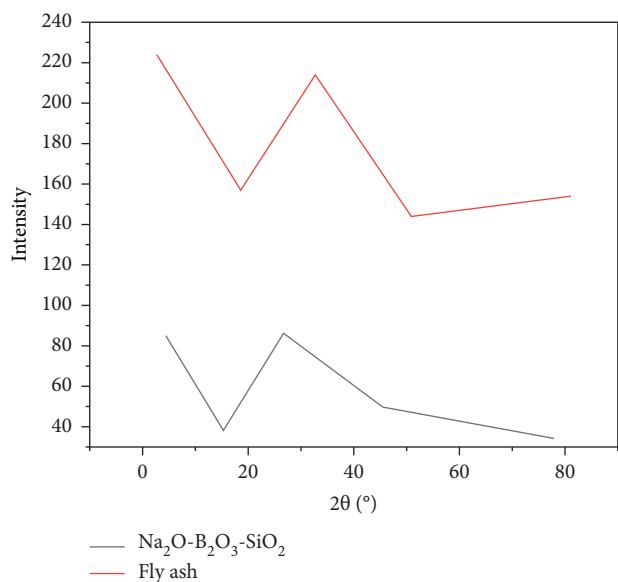
Figure 3: XRD phase analysis of low-temperature foam glass-ceramic composites.

Table 1: Experimental formulas of different boric acid content.

Formula number	Sodium water glass (g)	Boric acid (g)
1	100	2
2	100	3
3	100	4
4	100	5

Table 2: The effect of boric acid doping on the properties of low-temperature foam glass.

Performance	Bulk density	Weight loss rate	Softening factor
1	44	—	—
2	53	—	0.4
3	64	—	0.47

powder fly ash is mainly composed of quartz crystal phase and glass phase [23].

4.3. Exploration and Optimization of Various Process Parameters in Material Preparation

4.3.1. Determination of Glass Matrix Modifier Doping. A series of experiments were carried out using sodium water glass with a modulus of 2.33 and a solid content of 47.22 wt.% as the raw material and boric acid as the glass matrix modifier. The specific raw material composition in formulas 1–4 is shown in Table 1.

According to the ratio of each formula, the boric acid was introduced into sodium water glass by high-speed shearing (4000 rpm/min for 30 min) by colloidal chemical method. A series of hydrated glass sols with different amounts of boric acid were obtained without gelling. It is directly poured into the alumina ceramic crucible and is heated to 300°C. The furnace is according to the heating rate of 39°C/min under free foaming and kept for 30 min. After cooling to room temperature in the furnace, the mold is released to obtain low-temperature foam glass materials with different amounts of boric acid [24]. The influence of the amount of boric acid added on the foaming characteristics and water resistance of $Na_2O-B_2O_3-SiO_2-H_2O$ hydrated glass sol was mainly investigated. Therefore, this series of samples were demolded and cut into pieces for relevant performance tests. The results are shown in Table 2.

The "—"in the above table indicates that the low-temperature foam glass material with the external content of boric acid dissolves or becomes soft after being soaked in warm water at 70°C for 2 hours and loses the corresponding strength, so its weight loss rate and softening coefficient cannot be measured. It can be seen from the table that, with the increase of boric acid content, the bulk density of the

sample gradually increases, and the water resistance improves to a certain extent. This is because the $[BO_4]$ tetrahedron with negative potential is formed after the introduction of the acid into the water glass, and the $[BO_4]$ tetrahedron replaces part of the original $[SiO_4]$ tetrahedron. This further modifies the binary glass system, increasing the integrity of the glass network and improving the water resistance of the material. At the same time, the viscosity of the sol increases, so that the foaming ratio decreases and the bulk density gradually increases. The bulk density of the material does not change much when the external doping amount of succinic acid is 3 wt.% and above. Therefore, the material properties and raw material cost are considered comprehensively: ① When boric acid is introduced into the water glass system, with the increase of the external content of boric acid, the water glass is easier to gel, which will increase the shearing time and the complexity of the process. ② The introduction of boric acid greatly increases the raw material cost of the material. ③ Considering that the subsequent introduction of crystalline mineral powder will also improve the material properties to a certain extent, 2 wt.% boric acid is finally selected.

4.3.2. Effect of Glass Matrix Modifier Types on Material Performance. The experiments were carried out with sodium water glass (modulus of 2.33 and solid content of 47.22 wt.%), boric acid, calcium bentonite, and fly ash (particle size < 25 um). The experimental formulas are shown in Table 3. The effects of glass matrix modifier types on the properties of low-temperature foam glass-ceramic composites were investigated. In the previous section, boric acid was used as the modifier of the glass matrix, and the influence of different dosages of boric acid on the properties of the material was explored, and finally the dosage of 2 wt.% boric acid was optimized. This section explores the effects of different types of glass matrix modifiers and their ratios on material properties.

According to the formulas shown in the table and the experimental procedure shown in Figure 3, a series of mixed sols with different formulas were prepared. According to the heating rate of 3°C/min, with warming up to 400°C and incubation for 30 min, low-temperature foaming heat

TABLE 3: Experimental formula.

Formula number	Sodium water glass (g)	Fly ash (g)	Boric acid (g)	Calcium bentonite (g)
S1	100	15	0	0
S2	100	15	1	2
S3	100	15	2	1

treatment was carried out. After cooling to room temperature with the furnace, the mold was released, it was directly placed in a furnace at 500°C for 3 h for high temperature dehydroxylation heat treatment. After cooling, it was cut into regular shapes and characterized and tested. The results are as follows.

4.3.3. Bulk Density, Compressive Strength, and Thermal Conductivity.
The mixed sol of four groups of proportions completes the low-temperature foaming heat treatment through 400°C of insulation for 30 min and then at 500°C of insulation for 3 h. The bulk density, compressive strength, and thermal conductivity of the low-temperature foam glass-ceramic composite obtained after high-temperature dehydroxylation heat treatment are shown in Figure 4.

It can be seen from the variation law of bulk density that the addition of boric acid reduces the bulk density of the composite material; that is, the foaming performance of the mixed sol is better. After the addition of boric acid, B element captures free oxygen to form a negatively charged $[BO_4]$ tetrahedron, which firmly attracts Na^+ and H^+ in the system, making the original $Na_2O\text{-}SiO_2$ binary system structure tend to be dense, and the viscosity of the mixed sol increases. In the process of low-temperature foaming heat treatment, the uniformity of foaming is improved. However, according to the experimental results, at this stage, the bulk density of the low-temperature foaming heat-treated samples obtained from the two formulations is not much different. The difference occurs in the high-temperature dehydroxylation heat treatment stage. After 3 h of heat preservation at a high temperature of 500°C, the low-temperature foaming sample obtained by the formula has uneven distribution of pores and weak skeleton strength, so volume shrinkage occurs, resulting in an increase in bulk density. The addition of calcium-based bentonite affects the foaming performance of the mixed sol during the low-temperature foaming heat treatment process; that is, the expansion ratio is reduced, resulting in a larger bulk density of the material. The compound modification of boric acid and calcium-based bentonite balances the advantages and disadvantages of both. On the one hand, the low-temperature foaming characteristics are guaranteed. On the other hand, the cost of raw materials is further reduced.

The following can be seen from the variation law of thermal conductivity: after four proportions of samples are processed, the obtained foam glass-ceramic composite thermal insulation material has good thermal insulation performance, and the thermal conductivity is about 0.06 W/(m·K). When boric acid is added, the foaming performance of the material is improved, the pore distribution is uniform,
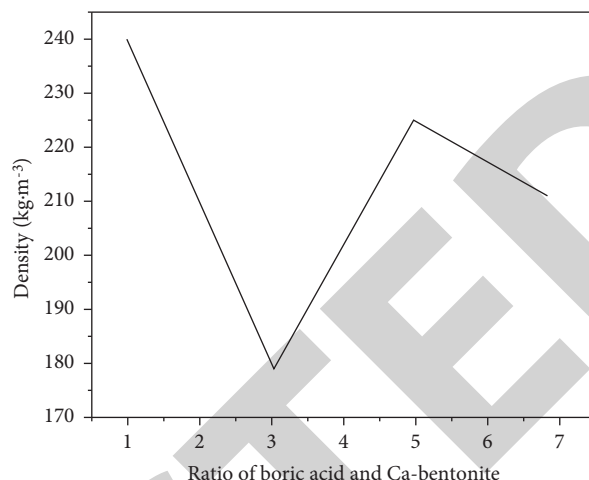
FIGURE 4: Variation diagram of low-temperature foam glass-ceramic composites obtained with different ratios of boric acid and Ca-bentonite.
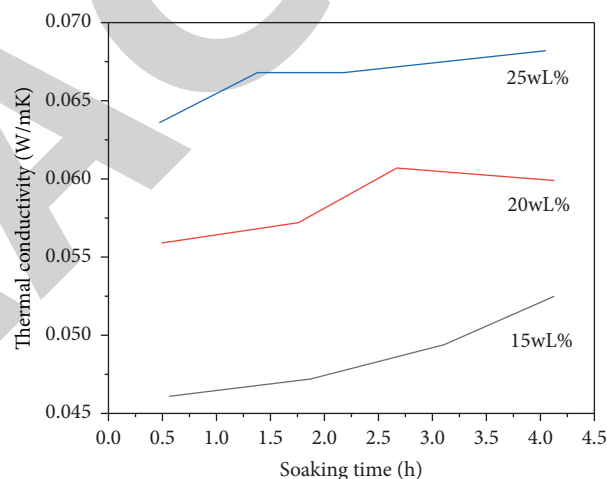
FIGURE 5: Effect of different soaking time on thermal conductivity of low-temperature foam glass-ceramic composites obtained by different formulations.

and the thermal conductivity is the lowest among the four formulations, only 0.055 W/(m·K). It can be seen that although the addition of calcium bentonite improves the mechanical properties and water resistance of the material, it still affects the expansion ratio of the material, which increases the bulk density and reduces the thermal insulation performance.

4.3.4. Thermal Conductivity.
The thermal conductivity test results of the formulations are shown in Figure 5.

With the extension of heat treatment time, the volume shrinkage rate of the material gradually increases, and the internal pores collapse or disappear after being squeezed, the porosity of the material was reduced to a certain extent, and the thermal conductivity increased continuously. It can be seen that, within 2 h of heat treatment, the thermal conductivity of the material did not change much, and the

thermal conductivity of each formulation was below 0.06 W/(m·K). When the heat treatment time was 3-4 h, the thermal conductivity of the material increased significantly; in particular, the thermal conductivity of the samples with high fly ash content exceeded 0.06 W/(m·K) and even approached 0.07 W/(m·K). Therefore, it is best to heat the board for about 2 h.

5. Conclusion

In this paper, the preparation of hydrated glass matrix, the introduction of crystalline mineral powder fly ash, and the secondary heat treatment were completed by using colloidal chemical method and using sodium water glass, boric acid, calcium bentonite, and fly ash as the main raw materials. Thus, a low-temperature foam glass-ceramic composite material with lightweight, high strength, good water resistance, and low cost is prepared. At the same time, the process parameters such as dehydroxylation heat treatment temperature and holding time involved in the preparation process were explored and optimized. The conclusions are as follows:

(1) By using the colloidal chemical method, the Na_2O-B_2O_3-Al_2O_3-SiO_2-H_2O system hydrated glass sol is used as the matrix, and the crystalline phase mineral powder fly ash is externally mixed. A low-temperature foam glass-ceramic composite material was prepared through low-temperature foaming heat treatment and high-temperature dehydroxylation heat treatment.

(2) The modification mechanism of crystalline mineral powder fly ash was explored. First, fly ash mainly contains two parts: crystalline phase and amorphous phase. After the fly ash was added, an alkali-aggregate reaction occurred with the water glass. The amorphous component and the glass matrix were dissolved in one phase, and the crystal grains were also reduced in size due to the reaction of alkali aggregates and were evenly distributed in the pore walls. By overlapping each other, they played a certain role of skeleton support, which reduced the problems of hydroxyl content reduction and volume shrinkage during the high-temperature dehydroxylation heat treatment of the material to a certain extent. At the same time, many microcracks were formed on the interface between these grains and the glass phase, which buffered the deformation caused by external force and increased the mechanical strength of the material. Second, after the fly ash was added, the alkali aggregate reacted to form $[AlO_4]$ tetrahedron and $[SiO_4]$ tetrahedron. These tetrahedrons formed long silicate chains through bonding, which improved the integrity and tightness of the glass system and improved the water resistance of the material. Third, after the addition of fly ash, the viscosity of the mixed sol was increased, which affected the foaming of the mixed sol and changed the performance parameters such as the bulk density of

the material. With the increase of fly ash content, the modification effect was stronger.

(3) The microstructure of the prepared material was characterized, and a schematic diagram of the structure of the low-temperature foam glass-ceramic composite material was obtained. From the XRD and TEM test results of the composite material, it can be seen that the material is composed of glass phase and crystal phase. The main crystal phase is the quartz crystal phase, wherein the crystal grains of 5–10 nm are uniformly dispersed in the glass matrix.

(4) The exploration and optimization of process parameters were completed, and the optimal raw material ratio and heat treatment system were obtained. For the effects of glass matrix modifier, the content and proportion of boric acid and calcium bentonite, the time of high-temperature dehydroxylation heat treatment, and the content of fly ash on the microstructure and physical and chemical properties of the material were explored. With the prolongation of the holding time of high-temperature dehydroxylation heat treatment, the content of hydroxyl group in the system is continuously reduced, and the water resistance of the material is continuously improved. At the same time, the softening degree of the green body is intensified, the volume shrinkage is gradually increased, the bulk density and thermal conductivity of the material are increased, and the mechanical strength is increased. Finally, when the external content of fly ash is 20 wt.% or more, the external content of boric acid is 1-2 wt.%, and the calcium-based bentonite is 1 wt.%, the mixed sol is subjected to low-temperature foaming heat treatment at 400°C for 30 min and then 500°C high-temperature dehydroxylation heat treatment for 2 hours or more, the bulk density of the obtained low-temperature foam glass-ceramic composite material is 192–256 kg/m^2, the compressive strength is 0.44–0.63 MPa, the weight loss rate is 5.1–7.8 wt.%, the softening coefficient is 0.85–0.95, and the thermal conductivity is 0.056–0.064 W/(m·K).

Data Availability

The data used to support the findings of this study are available from the corresponding author upon request.

Conflicts of Interest

The author declares that there are no conflicts of interest.

Acknowledgments

Retraction

Retracted: Numerical Simulation of Hot Stamping Forming of AZ Series Magnesium Alloys and Optimization of Die Process

Journal of Chemistry

This article has been retracted by Hindawi following an investigation undertaken by the publisher [1]. This investigation has uncovered evidence of one or more of the following indicators of systematic manipulation of the publication process:

(1) Discrepancies in scope

(2) Discrepancies in the description of the research reported

(3) Discrepancies between the availability of data and the research described

(4) Inappropriate citations

(5) Incoherent, meaningless and/or irrelevant content included in the article

(6) Peer-review manipulation

The presence of these indicators undermines our confidence in the integrity of the article's content and we cannot, therefore, vouch for its reliability. Please note that this notice is intended solely to alert readers that the content of this article is unreliable. We have not investigated whether authors were aware of or involved in the systematic manipulation of the publication process.

Wiley and Hindawi regrets that the usual quality checks did not identify these issues before publication and have since put additional measures in place to safeguard research integrity.

We wish to credit our own Research Integrity and Research Publishing teams and anonymous and named external researchers and research integrity experts for contributing to this investigation.

The corresponding author, as the representative of all authors, has been given the opportunity to register their agreement or disagreement to this retraction. We have kept a record of any response received.

References

[1] F. Qian, "Numerical Simulation of Hot Stamping Forming of AZ Series Magnesium Alloys and Optimization of Die Process," *Journal of Chemistry*, vol. 2022, Article ID 6484242, 7 pages, 2022.

Research Article

Numerical Simulation of Hot Stamping Forming of AZ Series Magnesium Alloys and Optimization of Die Process

Fang Qian (iD)

College of Engineering, Inner Mongolia Minzu University, Tongliao, Inner Mongolia 28000, China

Correspondence should be addressed to Fang Qian; 1432104107@post.usts.edu.cn

In order to deal with the bottleneck of poor plasticity and low formability of magnesium alloys at room temperature, a numerical simulation and a die process optimization method based on hot stamping of AZ series magnesium alloys were proposed. Firstly, based on the PAM-STAMP finite element analysis platform, the thermomechanical coupling numerical simulation is carried out for the cross cup-shaped deep drawing, and the changes in the stress and temperature field during the forming process are analyzed. Aiming at the influence of various process parameters on the plastic formability of magnesium alloys, the effects of sheet metal shape, die fillet size, friction factor, and blank holder force on the forming quality were analyzed through experiments. The experimental results show that under the same conditions such as temperature and blank holder force, the numerical simulation method and the mold process optimized in this paper can be used to form parts that are 25% deeper than the traditional process, and the sheet material can be thinned to the maximum at this time. The amount is 0.152 mm, which verifies the correctness and superiority of the method and process in this paper.

1. Introduction

With the development of the automobile and electronic industries, the demand for magnesium alloy products is increasing, especially the demand for magnesium alloy sheets is increasing significantly. The parts produced by the magnesium alloy sheet have good mechanical properties and microstructure properties, and the cost is low. However, because the commonly used magnesium alloys have a hexagonal close-packed crystal structure [1], it has always been considered that magnesium alloys have a very low forming limit value at room temperature and poor stamping performance, making it difficult to draw parts with complex shapes. Therefore, the main processing method is die casting, which is not conducive to protecting the environment.

In recent years, a large number of scholars' studies have shown that when the magnesium alloy sheet is heated to above 200°C, the first-order conical surface of the crystal structure and {1011}, {1021} slip systems are activated, and the plastic deformation capacity begins and improves.

When the temperature is heated to 225°C, the {1122} slip system of the second-stage cone surface is activated, and the plasticity of the magnesium alloy will be further improved [2]. Since temperature is a major factor affecting the plastic deformation of magnesium alloys, many scholars have done a lot of research on hot stamping and finite element simulation of magnesium alloys. However, the research on hot stamping of magnesium alloys is almost limited to cylindrical parts, above models such as square cups and conical cups.

This paper takes AZ31B magnesium alloy as the research object, based on the PAM-STAMP finite element analysis platform, conducts thermomechanical coupling numerical simulation for cross cup-shaped parts, analyzes the stress change and temperature field change in the forming process, and summarizes various processes. The influence of parameters on the plastic formability of magnesium alloys was discussed. The influence of the size and shape of the sheet, the fillet of the die, the friction factor, and the blank holder force on the forming quality was discussed, and a better solution was obtained. The use of numerical simulation
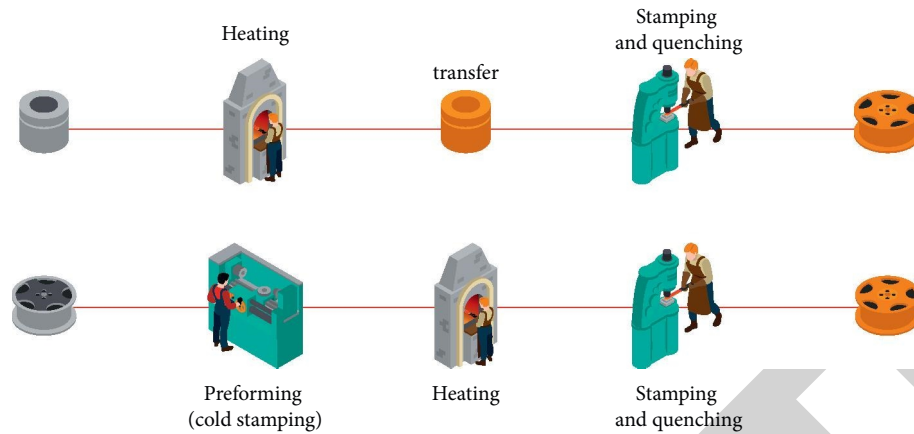
FIGURE 1: The process of stamping and forming AZ series magnesium alloys by different processes.

methods can effectively simulate the forming law of AZ31B magnesium alloy sheet hot drawing, which is of great significance for the design of magnesium alloy hot drawing process parameters and die structure design. Using simulation methods to conduct repetitive experiments can save a lot of time and financial resources. Figure 1 shows the basic process of stamping and forming AZ series magnesium alloys by direct and indirect processes.

2. Literature Review

Tozuka et al. proposed that the thermal incremental forming technology of sheet metal is a flexible forming technology. It heats the sheet to soften the sheet and adopts the idea of layered manufacturing to form a three-dimensional shape along the high line which is divided into a series of two-dimensional layers, and the final shape is obtained after the local deformation of the sheet material layer by layer [3]. Chen et al. pointed out that this method does not need to make molds. For single-piece and small batch production, it is more convenient and faster, and the cost is greatly reduced. It is widely used in product trial production and personalized customized production. It is an important part of advanced manufacturing technology [4].

Chen et al. designed a hot air heating device to heat the sheet material. In order to maintain the consistent temperature of the sheet during the test, a noncontact temperature measurement device was used to continuously monitor the sheet. The forming limits of the material at 20°C, 100°C, 150°C, 200°C, and 250°C were obtained by plane strain tensile and axisymmetric tensile experiments, respectively. Based on these forming limits, truncated cones with different inclination angles were designed and successfully completed at different temperatures. To understand the deformation characteristics in the experiments, a finite element analysis of the forming process was performed. And using the obtained results, a high-inclination round cup was successfully formed using the hot incremental forming method when the forming limit was exceeded [5]. Yang et al.'s team found in their research that the formability of the AZ31 sheet began to sharply improve at 150°C, achieving the effect of forming. At the same time, taking the egg surface

as an example of a free surface, according to the law of thermal incremental forming, the optimal tool path mainly composed of conical and helical shapes was successfully planned, and the egg surface was successfully processed using AZ31 material [6].

Wang et al. used the heat generated by the friction between the tool head and the sheet to heat the magnesium alloy sheet and successfully formed the magnesium alloy inverted pyramid frustum. And the forming performance, hardness, and tensile strength of the formed parts under different tool rotation speeds, feed speeds, and forming angles were measured. The experimental results show that the sheet metal with a forming angle of 25° and a thickness of 0.5 mm is gradually heated by the friction of the tool head. The tensile strength of the formed inverted-square frustum formed part is about 10% higher than that of the general hot incremental formed part [7]. Demler et al. formed AZ31, AZ61, and AZ80 magnesium alloy sheet square cone box-shaped parts by adjusting the spindle speed and feed speed, and the minimum half cone angles could reach 25°, 30°, and 40°, respectively. The AZ31 sheet was thermally incrementally formed by using a six-axis manipulator and a temperature-adjusting heating device. The influence of different heat treatment methods on the formed parts was studied, and the shape and mechanical properties of the formed parts were simultaneously controlled [8].

Li et al. also adopted the method of heating the sheet metal by friction heat with tool head rotation and studied the rotational incremental sheet forming (RISF) method of magnesium alloy sheet at room temperature through experiments. Heat can promote plastic deformation. The team formed square cups with a width of 80 mm, a length of 80 mm, and a length of 25 mm at room temperature, obtained the forming limit curve of RISF considering factors such as tool head radius, and effectively predicted the RISF of magnesium alloy sheets forming limit [9]. The team of Hajbarati et al. developed a set of equipment for performing incremental forming experiments at different temperatures and carried out an appropriate experimental design [10]. Peng et al. specially designed heating and insulation systems for efficient heating control. The device places the heater belt on the outer surface of the mold, and the PID controller

controls three thermocouples placed on different radii, and the heater is controlled by the signal returned by the thermocouple. Insulation systems are placed under the unit to reduce the effect of temperature on the processing equipment. Throughout the test, the temperature of the sheet is relatively uniform, and the temperature difference is less than 5°C [11]. Ubeda et al. studied the influence of main process parameters on the formability of materials through a large number of experiments and strict statistical analysis and concluded that the temperature and the depth of the cutting tool have a great influence on the formability, and the diameter of the tool has a great influence on the formability. The influence of formability is not great. When the temperature is 250°C, the formability is the best. In another paper, the team also proposed a method of using uniaxial tensile experiments to analyze the specimens at the fracture during hot incremental forming at different temperatures to determine the forming limit of the material and carry out experiments for validation [12].

3. Research Method

3.1. Numerical Simulation of Cross-Cup Hot Stamping. The AZ31B magnesium alloy cross cup workpiece, blank and mold model are symmetrical models. From the perspective of improving the calculation speed, the symmetrical model structure is usually adopted, and the 1/4 model is calculated by setting boundary conditions. Based on the pro/E 3D design platform 1/4 model is created and imported into PAM-STRAMP to create a finite element model. Thermal model-related parameters are set at the same time and adaptive meshing in the simulation is used. The deep drawing depth is 40 mm, the temperature of the blank holder, die, and sheet metal is 250°C, the temperature of the punch is 100°C, the blank holder force is 800 kN, the stamping speed is 10 mm/sec, and the model factor is 0.12. The equivalent stress is obtained by the following formula [13]:

$$\overline{\sigma} = \sqrt{\frac{1}{2}\left[\left(\sigma_x - \sigma_y\right)^2 + \left(\sigma_y - \sigma_z\right)^2 + \left(\sigma_z - \sigma_x\right)^2\right]}. \quad (1)$$

Then, its dimensionless form can be obtained as

$$\frac{\sigma_z}{\tau} = (\tan \alpha + \cot \alpha) - \frac{\sigma_f}{\tau} \cot \alpha, \quad (2)$$

where τ is the shear stress of the tool head on the sheet.

During the deep drawing process, with the increase of the deep drawing depth, the sheet metal is continuously divided into finer meshes, which is beneficial to the forming of the sheet metal. In this experiment, when the depth of drawing is 8 mm, the grid of the sidewall has been distorted, and when the depth of drawing reaches 12 mm, the grid of the sidewall is distorted to a large extent, indicating that the amount of deformation here is large. In the initial stage of deep drawing, the deformation of the punch fillet is the most severe, which makes the maximum strain value here. In the latter stage of the deep drawing process, the deformation of the sheet material begins to transfer to the side wall and the die fillet, so that the maximum strain occurs at the side wall
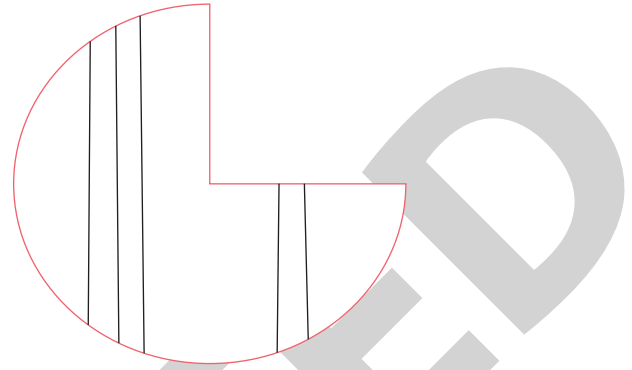
Figure 2: Sheet model in Scheme 4.

or the die fillet. Therefore, at this stage, the die fillet and the cylinder wall are the parts where the thinning of the sheet in the postdrawing stage is the largest [14].

3.2. Hot Drawing Process Scheme of Cross-Cup. According to the thermal deep drawing simulation in the previous section, the following process plan is formulated:

Scheme 1: AZ31B magnesium alloy cross cup-shaped 1/4 model, the drawing depth is 40 mm. The temperature of the blank holder ring, the die, and the sheet metal is 250°C, and the temperature of the punch is 100°C; the blank holder force is 800 kN; the punching speed is 10 mm/sec; the model factor is 0.12.

Scheme 2: On the basis of the experiment of Scheme 1, the fillet radius at the flange of the die is changed from 0.5 mm to 1.5 mm, and other conditions remain unchanged. The finite element simulation results show that changing the mold structure; that is, changing the fillet radius of the die flange from 0.5 mm to 1.5 mm, can greatly improve the elongation of the sheet and can form parts with a depth of 25 mm, but it cannot be formed yet. A cross-cup-shaped part with a depth of 40 mm is formed. The reasons for these two situations are analyzed as follows: first, the size of the sheet itself is not enough or the shape needs to be improved; second, the blank holder force is small; third, the model factor is too large [15].

Scheme 3: On the basis of the experiment of scheme 2, the blank holder force was increased from 800 kN to 1000 kN, and other conditions remained unchanged. After the blank holder force is increased, the increase in sheet thickness is obviously controlled. In scheme 2, due to the increase in sheet thickness, the maximum thickness of the sheet is 1.75 mm. After the blank holder force is increased, the maximum sheet thickness is 1.24 mm. The forming performance has also been improved to a certain extent, and the forming depth has been increased from 25 mm to 32 mm. Although the forming quality has been greatly improved after increasing the blank holder force, it is still impossible to draw a cross-cup-shaped part with a depth of 40 mm [16]. The reasons are as follows: first, the size of the

TABLE 1: Optimized hot drawing process plan.

Name	Temperature (°C)	Model factor	Blank holder force (kN)	Die fillet (mm)	Sheet shape and size
Sheet	250	—	—	—	148 mm round sheet
Die	250	0.02	—	1.5	—
Punch	100	0.02	—	—	—
Hemming ring	250	0.02	1000	—	—

sheet is not enough or the shape of the sheet itself is unreasonable; second, it may be that the model factor is too large, resulting in a relatively large amount of sheet metal thinning.

Scheme 4: On the basis of Scheme 3, change the shape of the sheet to a circular sheet with a diameter of 148 mm, as shown in Figure 2. After increasing the size of the sheet, it is possible to form a cross-cup-shaped part with a deep drawing depth of 40 mm, but some sheets are severely thinned, and the results of the finite element simulation of Scheme 4 show that a qualified product cannot be obtained. The reasons for the serious thinning of the sheet may be: first, the model shape of the mold itself; second, the restriction of the shape of the sheet as the shape of the sheet itself affects the flow of the material during plastic deformation; third, the model factor is too big.

Scheme 5: On the basis of the experiment of Scheme 4, the model factor is changed to be smaller, and 0.12 is changed to 0.05. Compared with scheme 4, although the area with severe sheet metal thinning is significantly reduced this time, there is still a thinning area, indicating that changing the model factor to 0.05 still cannot solve the problem of scheme 4. The reasons may be as follows: first, the model shape of the mold itself. The side wall where this area is located is more difficult to flow than other places; secondly, the shape of the sheet is restricted. The shape of the sheet itself affects the flow of material during plastic deformation [17].

Scheme 6: Based on the results of the above experiments, adjust the experimental scheme again and change the model factor to 0.02 on the basis of scheme 5. It can be clearly seen that the phenomenon of sheet metal thickening is basically reduced to a minimum, and the elongation of sheet metal is also greatly improved. When the depth of drawing is 40 mm, the minimum thickness of sheet metal is 0.847342 mm. After analyzing the above sheet material adaptation from the results of grid division, it can be seen that there is no distortion in the grid, which proves that the results of this experiment are reasonable. Through the continuous optimization of the above schemes, the best forming scheme obtained is shown in Table 1 [18].

4. Result Analysis

4.1. Principal Strain Distribution Cloud Map Analysis.
Figure 3 is the principal strain change curve made by taking 7 different points on the part when the drawing depth is 12 mm. From the curve, it is known that the maximum
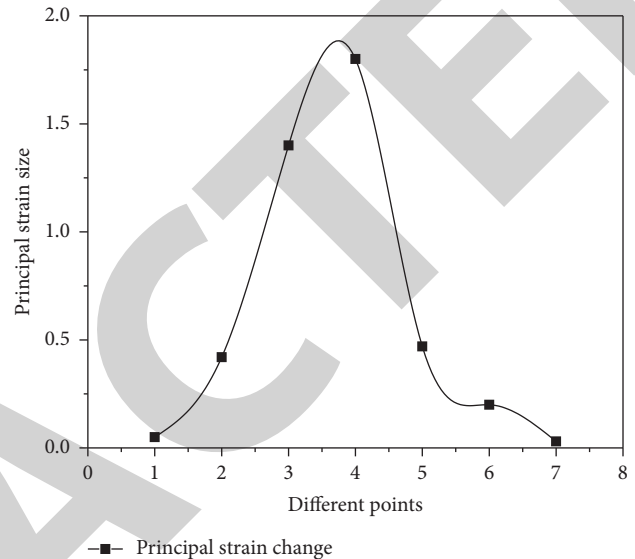
FIGURE 3: Cloud map of principal strain distribution at different drawing moments.

principal strain on the sidewall of the cross cup reaches 1.86. At this time, the thinning of the sheet is very serious, and if the drawing is continued, cracking will occur [19].

4.2. Sheet Temperature Distribution.
In this experiment, the temperature of the die, sheet metal, and blank holder were all set to 250°C, the temperature of the punch was 100°C, and the drawing speed was 10 mm/sec. Figure 4 shows the temperature of different points on the part when the drawing depth is 12 mm. The curve indicates that the temperature of the sheet decreases from the center of the sheet to the edge of the sheet [20]. This is because in the process of deep drawing, the sheet at 250°C contacts the punch at 100°C, and a lot of heat is generated caused by losses.

4.3. Sheet Thickness Distribution Cloud Map.
In the process of sheet metal deep drawing, the degree of deformation of each part is not uniform. In the initial stage of deep drawing, the rounded part of the punch first deforms. The corner portions are shifted towards the side walls of the cross cup. Combined with the results of the simulation analysis, it can be seen that the thinning trend in this test is particularly large. Figure 5 is a curve drawn by taking 8 points on the part when the drawing depth is 12 mm [21]. The minimum thickness of some sheets is 0.16952 mm, which means that in this case, the parts we need cannot be drawn [22]. This hot stamping simulation experiment has a large amount of sheet
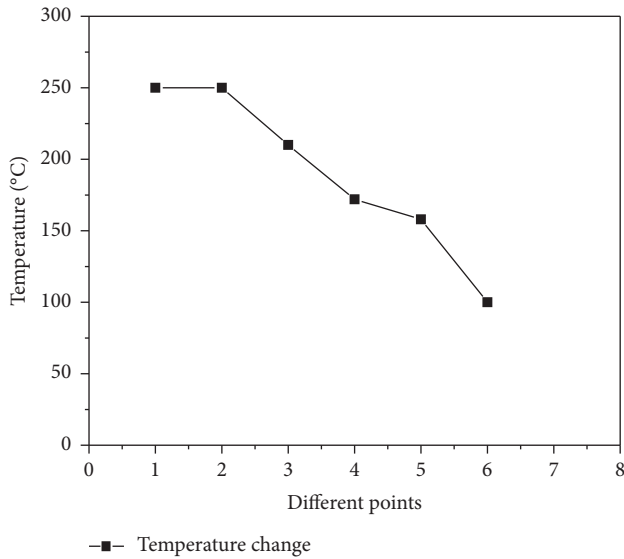
FIGURE 4: Distribution map of sheet metal temperature at different times of deep drawing.
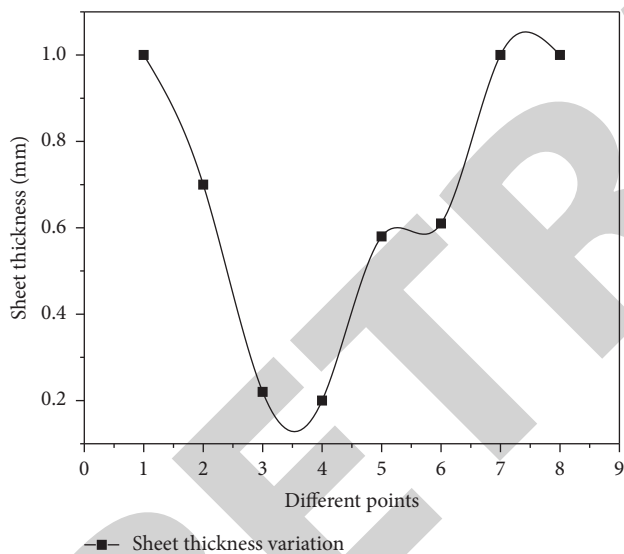
FIGURE 5: Thickness distribution results of sheet metal at different times of deep drawing.

metal thinning, which may be due to the following reasons: too large blank holder force, too large model factor, too small rounded corners of the flange part of the die, and the shape and size of the sheet itself affect its stamping, etc.

By analyzing the distribution cloud map of different properties of the sheet during the above hot stamping process, the following conclusions can be drawn:

(1) The deep drawing simulation results show that the punch fillet and the concave die fillet are areas with large stress and large deformation. The deep drawing deformation first occurred in the punch fillet and then transferred to the cylinder wall. The rounded part of the punch is the easy-to-crack area in deep

drawing, and the cracking tendency of the cylinder wall is smaller than that of the rounded part of the punch [23]. (2) The finite element simulation results show that with the increase of the model factor, the thinning of the sheet metal is greater. It is once again verified that the larger the model factor, the less conducive it is to the hot drawing of AZ31B magnesium alloy [24]. (3) The simulation results show that the blank holder force is also an important factor. With the change of the blank holder force, the quality of magnesium alloy deep drawing also changes [25]. (4) The simulation results show that the influence of the shape of the blank on the forming performance of the thin plate is very obvious. A reasonable shape of the blank can help to improve the stress and strain distribution of the workpiece during the drawing process, increase the drawing limit, and make the thickness change of the workpiece more comparable, uniform, and of high forming quality. When the shape of the blank is a square trimmed sheet, it can be formed under the process parameters that the temperature of the die, sheet, and blank holder is 250°C, the temperature of the punch is 100°C, the friction factor is 0.12, and the blank holder force is 1000 KN. When the drawing depth is 32 mm, the maximum thinning of the sheet is 0.167 mm. When the shape of the blank is a circular sheet, the temperature of the die, sheet, and blank holder is 250°C, and the temperature of the punch is 250°C. Under the process parameters of 100°C, a friction factor of 0.02, and a blank holder force of 1000 KN, a part with a drawing depth of 40 mm can be formed. At this time, the maximum thinning of the sheet is 0.152 mm. Therefore, it is more appropriate to use circular blanks for this part.

5. Conclusion

In this paper, taking AZ31B magnesium alloy as the research object, based on the PAM-STAMP finite element analysis platform, the thermomechanical coupling numerical simulation is carried out for the cross cup-shaped deep drawing, the stress changes and temperature field changes in the forming process are analyzed, and various processes are summarized. The influence of parameters on the plastic formability of magnesium alloys was discussed. The influence of the shape of the sheet metal, the size of the die fillet, the friction factor, and the blank holder force on the forming quality was discussed, and a better solution was obtained. Using sheet metal hot incremental forming technology to form magnesium alloy sheet, no molds are required to be made, a lot of time and money is saved, and it is very suitable for the design, development, and verification of new products, as well as customized, small batch, multivariety products. It has a very broad application prospect in aviation, aerospace, navigation, automotive engineering, and other fields.

However, at present, this technology has not been widely promoted and applied, and it is in the stage of laboratory

theoretical research. Research can be carried out from the following aspects: (1) In the study of the mechanism of the liquid medium support heating incremental forming process, in order to simplify the calculation, some assumptions are made, which make the actual situation and the calculation results to have a certain deviation. Although they can reflect a certain law change, there is still a certain gap with the actual processing process. In the actual processing process, the influencing factors are very complex, so to achieve industrial application, more detailed research on the mechanism is needed. (2) The final size of the part is generated by the coupling of multiple factors such as springback, material thinning, insufficient forming, and forming path design. Therefore, in-depth research is needed on other factors that affect the accuracy of formed parts. In addition, in order to further reduce the accuracy error, further research can be carried out on the establishment of the accuracy prediction model, the accuracy compensation, and the automatic programming of the machining path. (3) In addition to the factors that affect product quality listed in this paper, there are other factors such as wrinkling, instability, forming microcracks, indentation, metal accumulation, and more in-depth research will be carried out in the future.

Data Availability

The data used to support the findings of this study are available from the author upon request.

Conflicts of Interest

The author declares that there are no conflicts of interest.

References

[1] X. Y. Chang, Q. Shen, W. X. Fan, and H. Hao, "Optimization of magnesium alloy casting process: an integrated computational materials engineering (icme) approach," *Materials Science Forum*, vol. 1035, no. 1, pp. 808–812, 2021.

[2] S. Taylor, G. D. West, E. Mogire, F. Tang, and H. R. Kotadia, "Superplastic forming characteristics of az41 magnesium alloy," *Transactions of Nonferrous Metals Society of China*, vol. 31, no. 3, pp. 648–654, 2021.

[3] H. Tozuka, K. Seki, H. Watari, and T. Haga, "Casting of high aluminum content am series magnesium alloys by using a horizontal twin roll caster," *Key Engineering Materials*, vol. 841, no. 2, pp. 340–345, 2020.

[4] Y. Chen, H. Yan, K. Ji et al., "Effect of ultrasonic treatment during solidification on corrosion behavior of mg-3al-1zn and mg-4zn magnesium alloys," *Journal of the Electrochemical Society*, vol. 167, no. 16, Article ID 161505, 2020.

[5] J. Chen, W. Wu, R. Cheng, Y. Jin, and Z. Liu, "Optimization of hot air drying process of corn using genetic algorithm and response surface methodology," *International Journal of Food Properties*, vol. 23, no. 1, pp. 753–764, 2020.

[6] X. Yang, B. Wang, and J. Zhou, "Numerical and experimental study on formability of tc4 alloy in a novel multi-layer sheet hot stamping process," *International Journal of Advanced Manufacturing Technology*, vol. 110, no. 5-6, pp. 1233–1247, 2020.

[7] D. D. Gu, J. W. Wang, Y. B. Chen, and J. Peng, "Effect of mn addition and refining process on fe reduction of mgmn alloys made from magnesium scrap," *Transactions of Nonferrous Metals Society of China*, vol. 30, no. 11, pp. 2941–2951, 2020.

[8] E. Demler, A. Diedrich, A. Dalinger, G. Gerstein, S. Herbst, and S. Zaefferer, "Changes in mechanical and microstructural properties of magnesium alloys resulting from superimposed high current density pulses," *Materials Science Forum*, vol. 1016, no. 6, pp. 385–391, 2021.

[9] Y. Li, Y. Zhang, and S. Li, "Viscoplastic constitutive modeling of boron steel under large strain conditions and its application in hot semi-cutting," *Journal of Manufacturing Processes*, vol. 66, no. 1, pp. 532–548, 2021.

[10] H. Hajbarati and A. Zajkani, "A novel finite element simulation of hot stamping process of dp780 steel based on the chaboche thermomechanically hardening model," *International Journal of Advanced Manufacturing Technology*, vol. 111, no. 9-10, pp. 2705–2718, 2020.

[11] S. Peng, J. Zhou, M. Zhang, K. Zhang, and J. Liu, "Fundamental research and numerical simulation of new hot stamping tool manufactured by surfacing technology," *International Journal of Advanced Manufacturing Technology*, vol. 107, no. 7-8, pp. 3527–3541, 2020.

[12] C. Ubeda, G. Garces, P. Adeva, I. Llorente, and G. Frankel, "The role of the beta-mg17al12 phase on the anomalous hydrogen evolution and anodic dissolution of az magnesium alloys," *Corrosion Science*, vol. 165, no. 3, Article ID 108384, 2020.

[13] G. Sutton, S. Korniliou, A. Andreu, and D. Wilson, "Imaging luminescence thermometry to 750°C for the heat treatment of common engineering alloys and comparison with thermal imaging," *International Journal of Thermophysics*, vol. 43, no. 3, pp. 36–26, 2022.

[14] G. Zhang, Q. Shuyang, L. Yan, and X. Zhang, "Simultaneous improvement of electromagnetic shielding effectiveness and corrosion resistance in magnesium alloys by electropulsing," *Materials Characterization*, vol. 174, no. 6, Article ID 111042, 2021.

[15] D. V. Prashant, S. K. Agnihotri, and D. P. Samajdar, "Geometric optimization and performance enhancement of pedot: pss/gaas np array based heterojunction solar cells," *Optical Materials*, vol. 117, no. 3, Article ID 111080, 2021.

[16] C. Tong, G. Zhu, Q. Rong et al., "Investigation of austenitising behaviour of medium-mn steel in the hot-stamping heating process," *Journal of Materials Processing Technology*, vol. 297, no. 4, Article ID 117269, 2021.

[17] J. Wu, Y. Yuan, X. Yu et al., "The high-temperature oxidation resistance properties of magnesium alloys alloyed with gd and ca," *Journal of Materials Science*, vol. 56, no. 14, pp. 8745–8761, 2021.

[18] P. Zhu, G. Zhang, J. Du, L. Jiang, and Y. Cui, "Removal mechanism of magnetic abrasive finishing on aluminum and magnesium alloys," *International Journal of Advanced Manufacturing Technology*, vol. 114, no. 5-6, pp. 1717–1729, 2021.

[19] T. Vo, T. N. Nguyen, T. H. Nguyen, and S. Antonov, "A research of optimization of the forming parameters to the minimum radial dimension error when forming sheet by hotspif technology," *Key Engineering Materials*, vol. 863, no. 7, pp. 13–17, 2020.

[20] K. Zheng, C. Tong, Y. Li, J. Lin, and Z. C. Kolozsvari, "An experimental and numerical study of feasibility of a novel technology to manufacture hot stamping dies with preconstructed tube network," *International Journal of Advanced*

Retraction

Retracted: Electrochemical-Based Extraction, Separation, and Purification of Coumarin Compounds from *Trifolium chinensis*

Journal of Chemistry

This article has been retracted by Hindawi following an investigation undertaken by the publisher [1]. This investigation has uncovered evidence of one or more of the following indicators of systematic manipulation of the publication process:

(1) Discrepancies in scope

(2) Discrepancies in the description of the research reported

(3) Discrepancies between the availability of data and the research described

(4) Inappropriate citations

(5) Incoherent, meaningless and/or irrelevant content included in the article

(6) Peer-review manipulation

The presence of these indicators undermines our confidence in the integrity of the article's content and we cannot, therefore, vouch for its reliability. Please note that this notice is intended solely to alert readers that the content of this article is unreliable. We have not investigated whether authors were aware of or involved in the systematic manipulation of the publication process.

Wiley and Hindawi regrets that the usual quality checks did not identify these issues before publication and have since put additional measures in place to safeguard research integrity.

We wish to credit our own Research Integrity and Research Publishing teams and anonymous and named external researchers and research integrity experts for contributing to this investigation.

The corresponding author, as the representative of all authors, has been given the opportunity to register their agreement or disagreement to this retraction. We have kept a record of any response received.

References

[1] Y. Zhu, W. Wang, R. Ruan, and J. Chen, "Electrochemical-Based Extraction, Separation, and Purification of Coumarin Compounds from *Trifolium chinensis*," *Journal of Chemistry*, vol. 2022, Article ID 6466271, 6 pages, 2022.

Research Article

Electrochemical-Based Extraction, Separation, and Purification of Coumarin Compounds from *Trifolium chinensis*

Yujie Zhu ⓘ**, Wenle Wang** ⓘ**, Renyu Ruan** ⓘ**, and Jinquan Chen** ⓘ

Pharmacy Department, Jiangsu Food and Pharmaceutical Science College, Huaian, Jiangsu 223003, China

Correspondence should be addressed to Wenle Wang; 2020150061@stu.cpu.edu.cn

In order to deal with the problems of the unstable transformation process and volatile palatability of coumarin compounds in *C. chinensis*, a method for the extraction, separation, and purification of coumarins in Chinese medicinal materials based on electrochemistry was prepared. First, an electrochemical distance-independent localization mechanism is used to determine node locations and routing mechanisms, and an extraction method is designed to achieve automatic and accurate real-time collection, aggregation, and transmission of ever-growing data. Environmental information for *C. chinensis* is collected. On the basis of this method, according to the chemical properties of coumarin and the extraction rate of coumarin as an index, the two-phase solvent extraction method and macroporous adsorption resin method were used to separate and purify it, and the best separation was determined. The purification process achieves efficient purification of coumarin. The experimental results show that the retention rate of coumarin by ethyl acetate is 34.5–56.8% higher than that of the other three extractants. When the optimal process determined in this study is adopted, the coumarin adsorption rate is greater than 98% and the recovery rate is greater than 85%. The purity of samples with 50% coumarin content can be increased to more than 97%, which verifies the correctness and advancement of the separation and purification process in this study.

1. Introduction

The Internet of Things (IOT) combines electronic devices, computer peripherals, information-sharing technologies, modern networks, and wireless communications, among others. It can collaboratively monitor and record real-time experimental data of various devices through various integrated microsensors. Data are transmitted wirelessly in an ad hoc multihop network and sent to user terminals, identifying the global connections of global bodies, global computers, and human life [1]. With the continuous development and maturity of the Internet of Things technology, it will effectively solve the way that people obtain important ingredients in medicinal materials through manual grinding in the traditional pharmaceutical industry. In various control systems, the temperature sensor, humidity sensor, pH sensor, light sensor, ion sensor, biosensor, CO_2 sensor, and other equipment of the IoT system can detect physical properties such as temperature, relative humidity, pH value, light utilization rate, and soil. Deficient nutrients and CO_2

concentrations are automatically controlled when released by various devices or as automatic controls, so as to ensure a good and suitable separation and purification environment when extracting components of medicines [2].

Melilotus is an annual or biennial herb of the family Leguminosae. The root system is developed; the stem is erect and has many branches. There are three-leaf compound leaves; the leaflets are elliptic, and the margins are sparsely toothed. It has racemes axillary and butterfly shaped corolla. The pods are oval, with obvious reticulation. The seeds are kidney-shaped, yellow-green, and multiply. The development and utilization of *C. chinensis* have a wide range of development and utilization, and it is called "baby grass." The main development and utilization aspects include forage feed, soil improvement/fertilization, nectar plants, windbreak and sand fixation, water and soil conservation, spices, and medicinal purposes. Among them, the main medicinal ingredient is coumarin. How to determine the content of coumarin in *C. chinensis* and its separation and purification is becoming a hot topic in the world today.

In this study, an IoT-based coumarin extraction method was developed. By placing sensors with different functions in the area to be measured, it can monitor small climate changes, including temperature, humidity, moisture, and other growing environment information of *C. chinensis*. Accordingly, the growth of *C. chinensis* requires corresponding changes to the environment in a timely manner. The method can reduce the error of manual operation and manual measurement in the actual production process, reduce the cost of extraction, separation, and purification of *C. chinensis*, can realize the automatic and accurate real-time collection, aggregation, and transmission of *C. chinensis* growth environment information to the greatest extent, and design the structure, as shown in Figure 1. On the basis of this extraction method, according to the actual characteristics of coumarin in *C. chinensis*, it was separated and purified by the two-phase solvent extraction method and macroporous adsorption resin method, and finally, the efficient purification of coumarin was realized.

1.1. Literature Review. According to the research of Lu S. et al., coumarins, scientific name: 1,2-benzo α-pyrone, molecular weight 146.15, melting point 68–70°C, boiling point 303°C, volatile, composed of molten benzene. It is composed of α-pyridone ring and is a white solid, which is easily soluble in organic solvents such as ethanol and chloroform [3]. Coumarin has been shown to be important in plant metabolites and is found in essential oils such as cinnamon bark oil, cinnamon leaf oil, and lavender oil. Coumarin is also found in fruits (such as bilberries and cloudberries), green tea, and other foods such as chicory. Coumarin mainly comes from Rutaceae, Umbelliferae, Compositae, and Leguminosae, and some of them come from microorganisms [4]. Yusof et al. found that in plants, coumarin compounds exist in the form of free or glycosides and are mainly distributed in leaves, flowers, stems, and fruits [5]. The research of Sperotto et al. pointed out that the determination of coumarin content generally adopts the process of first separation and then quantification according to different concentrations of standard products. The principle of determination is mainly based on the UV absorbance of coumarin at a specific wavelength. Commonly used diagnostic procedures include thin layer chromatography scans, high performance liquid chromatography-mass spectrometry (HPLC-MS), supercritical fluid chromatography (SFC), and gas chromatography (GC) [6].

Thin layer chromatography was first proposed by Mishra et al., which is an adsorption chromatography that separates by successive adsorption, desorption, resorption, and redesorption. The thin layer scanning method mainly determines the content according to the absorption intensity of ultraviolet fluorescence [7]. Louisa et al. used thin layer chromatography to extract and isolate dicoumarin and determined its content by UV spectrophotometry. Thin layer chromatography is simple and low cost. However, the number of theoretical plates is relatively low, which will result in a certain quantitative deviation [8]. A liquid chromatography-mass spectrometry (LC-MS) method was prepared, which has the characteristics of small injection volume, high sensitivity, and fast analysis speed. It has long been the most common mainstream method, analytical method. LC-MS plays an irreversible role in the evaluation of coumarin quality and value. Fast and efficient analysis of complex in-process systems is without complete chromatographic separation. In recent years, this method has been widely used in biological, plant, food, and environmental samples [9]. Selivanova et al. used high performance liquid chromatography on the water extract of red sandalwood, quantitatively determined the content of coumarin using a photodiode array detector, and determined the active components of licorice in different traditional Chinese medicines by the HPLC-MC method, which mainly included Coumarin compounds [10]. Nguyen et al. compared classifications at different levels of the separation effect. In addition, in order to improve the resolution of the target compounds, a three-phase mobile phase gradient method (such as water: methanol: acetonitrile) was also used. The three-phase mobile phase gradient method (0.01 % phosphoric acid/water, acetonitrile, and methanol) was used to separate coumarin, furocoumarin, and methoxyflavonoids. There are separate isolated bases for each use [11]. With the development of analytical equipment, high performance liquid chromatography (UHPLC) is increasingly used for the separation of coumarins, as these techniques can improve synthesis, separation, and shorten detection time. For example, Dukare et al. separated and determined 22 coumarin derivatives in cosmetics using a UPLCBEHC18 column (2.1×100 mm, 1.7 mm). A total of 22 coumarin derivatives were separated in 5 minutes, saving time [12].

2. Research Method

2.1. Environmental Information Collection for Extraction of Coumarin Compounds from C. chinensis. The sensor nodes in the environmental information collection method for coumarin extraction are deployed in the monitoring area and constitute the basic unit of the Internet of Things. Sensor nodes can communicate with each other and form a node network through self-organization. Adjacent nodes in the network form clusters, and the cluster head node collects the data collected by each node in the cluster and then sends the compressed data to the sink node after data fusion. The sink node is responsible for the task of communication between the task management node and the sensor node and is generally served by a sensor node with strong energy or a router with wireless gateway capability [13].

The task management node is the data and instruction management center of the wireless sensor network (WSN), which generally consists of several servers [14]. The user configures and manages the sensor network through the task management node, publishes monitoring tasks, and collects monitoring data. The task management node can analyze and store the collected information and can issue instructions to the sensor node in real time. The position of each sensor node in the monitoring area can be obtained through GPS positioning or the node's own positioning algorithm. They collect information according to the instructions sent
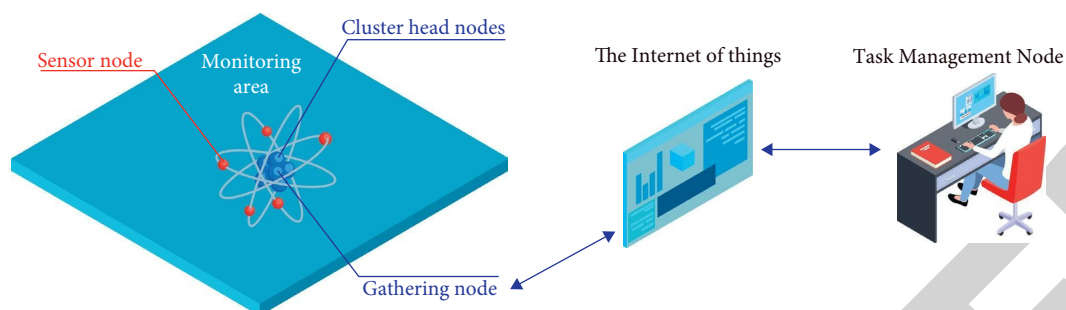
Figure 1: Environmental information collection, separation, and purification method framework for the extraction of coumarin compounds from *Trifolium chinensis*.
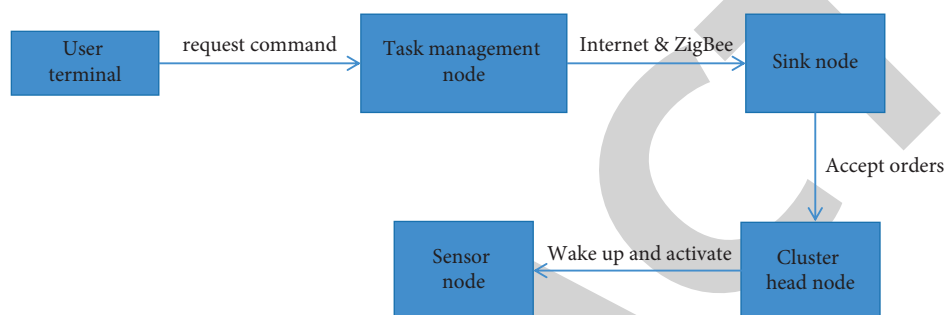

Figure 2: Workflow of the environmental information collection method for coumarin extraction.

by the task management node and send the collected information to the cluster head node. The cluster head node fuses the data and then sends it to the corresponding sink node. The data received by the sink node will be screened and sorted and then sent to the task management node through the Internet or communication satellites [15]. The working process of the environmental information collection method for coumarin extraction is shown in Figure 2.

The specific process is as follows. (1) The user sends a request command to query various indicators of the coumarin extraction environmental information through the task management node and transmits it to the sink node through the Internet and ZigBee network. (2) The sink node selects the cluster to be queried according to the specific requirements of the request command. After receiving the command, the cluster head wakes up and activates all nodes in the cluster to collect, store, and communicate data. The node collects data in time according to the command requirements and sends it to the corresponding cluster head node after digital-to-analog conversion. The cluster head fuses all the incoming data and sends the fused data back to the sink node. (3) The gathering node will screen and sort the obtained data and send it to the task management node through the external network. The task management node will feedback the collected data to the user and will store it in the coumarin extraction environment information database to provide a basis for future analysis and decision-making [16].

2.2. Separation and Purification of Coumarin. The components in the solid substance are dissolved in the solvent by the extraction method, and after solid-liquid separation, a liquid mixture containing multiple components is obtained, which is called the extraction solution, and then, various separation methods are used to separate the chemical components in the extraction solution. In this study, the two-phase solvent extraction method is mainly used for separation, and the macroporous adsorption resin method is used for purification [17]. According to the properties of coumarin and applicability of various separation and purification methods to coumarin, a separation and purification process route was drawn up for the ethanolic extract of coumarin, as shown in Figure 3.

The extract concentrate (extraction stock solution) of *C. chinensis* has been concentrated under reduced pressure to a certain concentration, add the extractant in a certain proportion, shake and stand for 30 minutes, take the organic phase, and repeat for several times. The organic phases were combined, concentrated under reduced pressure, and dried under vacuum at 50°C. The extracted product was weighed, and the coumarin content was measured by HPLC to calculate the coumarin content and coumarin retention rate in the extracted product. The extraction effect was evaluated by the coumarin content and coumarin retention rate in the extracted product. The definition formula is shown in the following formula [18]:
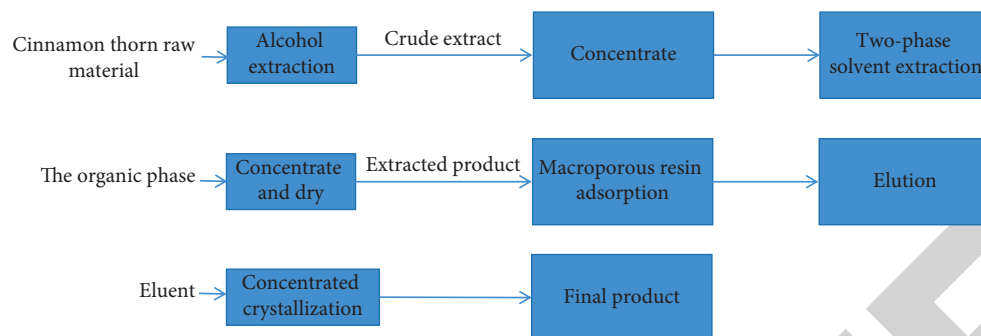
FIGURE 3: Extraction, separation, and purification process route of coumarin compounds in *C. chinensis*.

$$\text{The content of coumarin in the extract}\,(\%) = \frac{\text{Coumarin quality}}{\text{Extracted product quality}} \times 100. \tag{1}$$

$$\text{Coumarin retention rate}\,(\%) = \frac{\text{Coumarin quality} - \text{coumarin content} \times \text{extracted product quality}}{\text{The quality of coumarin in the extraction solution}} \times 100. \tag{2}$$

For the extraction effect, the highest content of coumarin in the extraction product and the high retention rate of coumarin are the best results, and these two indicators should be considered comprehensively in the evaluation [19].

The macroporous adsorption resin experiment is divided into the following steps. (1) Pretreatment: soak the unused resin in 95% ethanol for 24 hours, wash it with distilled water until there is no alcohol smell, and then use 5% hydrochloric acid and 5% hydrogen peroxide, respectively. Soak in sodium solution for 3 hours, wash with distilled water to neutral pH, and take part of the wet resin for use; the remaining resin is vacuum-dried at 333 K to constant weight for use. (2) Regeneration: the used resin is dynamically washed with 95% ethanol on a chromatography column. (3) Static adsorption and desorption: precisely weigh 0.5 g (dry weight) of the pretreated macroporous adsorption resin and add 50 ml of the extracted product to prepare an aqueous solution, Cinnamon officinalis sample solution, shake for 24 h at a shaking speed of 130 r/min in a shaker, measure the coumarin concentration in the supernatant, and calculate the resin adsorption capacity and adsorption rate. Discard the supernatant, wash the resin with water and dry it naturally, add 50 ml of 95% ethanol, desorb under the same conditions, measure the coumarin concentration in the desorption solution, and calculate the resin desorption rate. (4) Dynamic adsorption and desorption of resin: weigh 20 ml of pretreated wet screening macroporous adsorption resin and put it into a glass column (15×450 mm), use HPD300 resin to absorb coumarin, accurately weigh 0.5 g of HPD300 resin, and add 50 ml. The coumarin concentration was 2.0447 mg/ml in the sample solution, which was shaken in a shaker (298 K, 130 r/min), and the coumarin concentration in the supernatant was regularly detected [20].

3. Result Analysis

The equipment used in the experiment is given in Table 1.

Depressurize the *C. chinensis* extract to an extraction stock solution of 0.2 g/ml (raw material quality/volume of solution) and add different extractants at a ratio of 1 : 3 (volume of extract: volume of stock solution): chloroform, ethyl acetate ester, petroleum ether, and n-butanol, shake, after standing for 30 min, take the organic phase, and repeat 3 times. The organic phases were combined, compressed under reduced pressure, and dried under vacuum at 50°C. The coumarin content in the extracted product was determined by HPLC, and the coumarin retention rate was calculated [21]. The results are shown in Figure 4.

As can be seen from Figure 4, chloroform, ethyl acetate, and petroleum ether are used as extractants to extract coumarin, and the content of coumarin in the extraction product is similar, 34.5–56.8%, and serious emulsification will occur when the other three extractants are used as extractants. Ethyl acetate is recognized as a good extractant, with low cost, good biodegradability, and high extraction rate of lactones. Therefore, combined with the method of collecting environmental information for the extraction of coumarin compounds from *Trifolium chinensis* based on the Internet of Things [22], this study comprehensively considers the factors such as the good extraction effect, low toxicity, and good economy when ethyl acetate is used as the extraction agent, and ethyl acetate should be selected. Esters were used as extractants to separate and purify coumarin compounds in *C. chinensis*, and the dynamic breakthrough curve of HPD300 adsorption of coumarin obtained at the same time is shown in Figure 5.

It can be seen from the figure that 20 ml of wet HPD300 resin can handle 30 BV of sample solution without leakage under the optimized sample concentration (3.0 mg/ml) and flow rate (3.0 BV/h). When the effluent volume exceeds 30 BV, it begins to leak slowly. When the effluent volume is 33 BV, the coumarin concentration in the effluent reaches 1/10 of the sample concentration, which is called the breakthrough point [23]. When the effluent volume exceeds 33 BV, the leakage rate begins to increase sharply. When the

TABLE 1: Laboratory equipment table.

| Name	Specification	Origin
Chinese herbal medicine grinder	FW135	Tianjin
Rotary evaporator	RE-52AA	Shanghai
Circulating water type multipurpose vacuum pump	SHB-B	Zhengzhou
Ultrasonic cleaner	KQ3200	Kunshan
Instant thermostatic heating magnetic stirrer	DF-101S	Shanghai
Shelf balance	JPT-10C	Shanghai
Electronic balance	BP211D	Shimadzu
Low speed centrifuge	LDA-2	Beijing
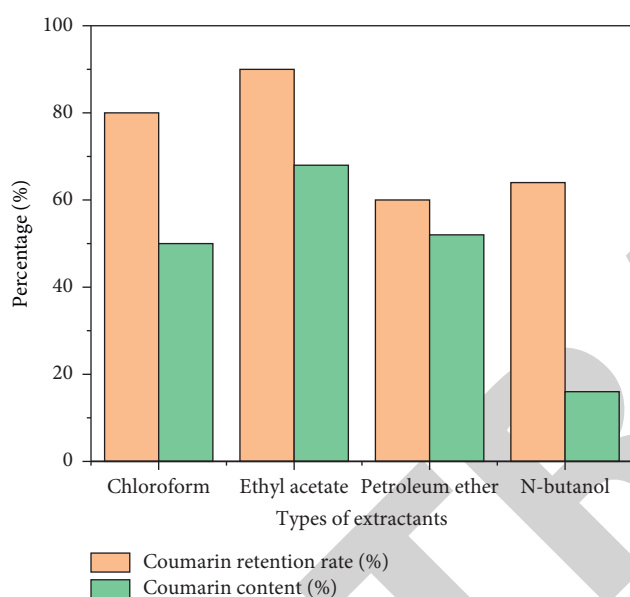
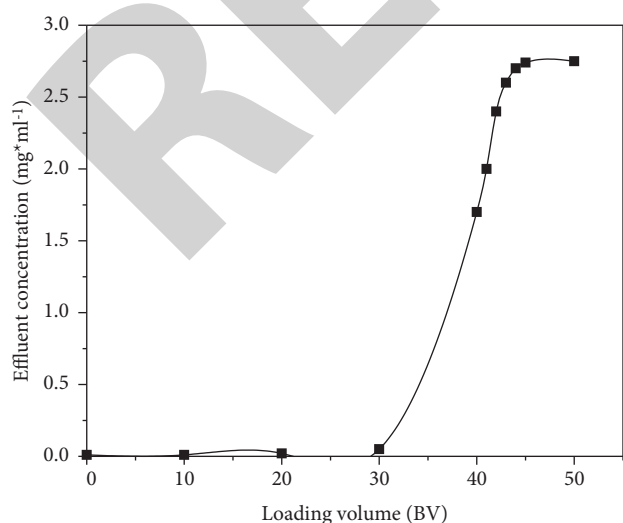FIGURE 4: Effects of different extraction solvents on liquid-liquid extraction.

FIGURE 5: Dynamic breakthrough curve of coumarin adsorption by HPD300 resin.

effluent liquid agent reaches 42 BV, the effluent concentration is basically the same as that of the sample solution, and the resin reaches adsorption saturation, which is the saturation point of the resin [24, 25]. The experimental results show that under this process condition, 20 ml wet HPD300 resin can process 33 BV sample solution, its working adsorption capacity is 95.82 mg/ml wet resin, the coumarin adsorption rate is greater than 98%, and the recovery rate is greater than 85%. The purity of the samples with bean content of 50% increased to more than 97%, which verifies the correctness and advancement of the separation and purification process in this study.

4. Conclusion

As an important part of the new generation of information technology, the Internet of Things is used in many aspects such as data collection, transmission, processing, and business management, providing people with a new way to obtain and process information. Aiming at the characteristics of large amount of data collection in the collection method of coumarin extraction environmental information, combined with the advantages of Internet of Things technology, this study designed a coumarin extraction environmental information collection method and a coumarin separation and purification method based on the Internet of Things. The GEAR routing mechanism and the distance-independent positioning algorithm are adopted, thereby avoiding the energy consumed by nodes due to self-organizing network calculations. Meanwhile, the application of geographic location routing can more accurately locate the position of crops, which can effectively prolong the service life of the method. The macroporous adsorption resin method for the separation and purification of coumadin was determined. The experimental results show that 20ml wet HPD300 resin can treat 33BV sample solution under this process condition, and its working adsorption capacity reaches 95.82 mg/ml wet resin. The adsorption rate of coumarin was more than 98% and the recovery was more than 85%. The purity of the sample with 50% coumarin content can be increased to more than 97%, which verifies the correctness and advancement of the separation and purification technology in this paper.

There are still deficiencies in the research in this study. For the areas not covered, I would like to propose the following suggestions. (1) The pharmacological effects of the extracted and isolated high-purity coumarin products can be studied, and the anti-inflammatory and analgesic properties of the products can be studied. The pharmacological effects of detumescence and other aspects provide a basis for its development into a new drug. (2) Industrial scale-up experiments can be carried out on the extraction and separation of coumarin, so as to realize industrialization and bring economic effects as soon as possible and social benefits.

Data Availability

The data used to support the findings of this study are available from the corresponding author upon request.

Retraction

Retracted: Surface Damage Coupling Mechanism of Plain Weave Art Ceramic Matrix Composites

Journal of Chemistry

This article has been retracted by Hindawi following an investigation undertaken by the publisher [1]. This investigation has uncovered evidence of one or more of the following indicators of systematic manipulation of the publication process:

(1) Discrepancies in scope

(2) Discrepancies in the description of the research reported

(3) Discrepancies between the availability of data and the research described

(4) Inappropriate citations

(5) Incoherent, meaningless and/or irrelevant content included in the article

(6) Peer-review manipulation

The presence of these indicators undermines our confidence in the integrity of the article's content and we cannot, therefore, vouch for its reliability. Please note that this notice is intended solely to alert readers that the content of this article is unreliable. We have not investigated whether authors were aware of or involved in the systematic manipulation of the publication process.

Wiley and Hindawi regrets that the usual quality checks did not identify these issues before publication and have since put additional measures in place to safeguard research integrity.

We wish to credit our own Research Integrity and Research Publishing teams and anonymous and named external researchers and research integrity experts for contributing to this investigation.

The corresponding author, as the representative of all authors, has been given the opportunity to register their agreement or disagreement to this retraction. We have kept a record of any response received.

References

[1] G. Li, "Surface Damage Coupling Mechanism of Plain Weave Art Ceramic Matrix Composites," *Journal of Chemistry*, vol. 2022, Article ID 3519967, 7 pages, 2022.

Research Article

Surface Damage Coupling Mechanism of Plain Weave Art Ceramic Matrix Composites

Guangsong Li 🔟

Hunan University of Arts and Science, Changde, Hunan 415000, China

Correspondence should be addressed to Guangsong Li; 2013052129@stu.zjhu.edu.cn

In order to solve the problem of the surface damage coupling mechanism of ceramic matrix composites, a method oriented to the damage coupling mechanism of the plain weave art ceramic matrix is proposed by the author. First, the author uses the composite material prepared by a chemical vapor infiltration process as the research object, and the damage mechanical behavior of materials under simple and complex plane stress states is studied. Second, the calculation of the mechanical property parameters of the material components and the research on the mechanical behavior of the material in-plane shear mesodamage are studied; Finally, the research on the damage coupling effect of materials under complex stress state is conducted, as well as the decoupling test research of the damage coupling effect. It is demonstrated that based on 0 and $45°$ off-axis tensile stress-strain behavior, a prediction model of off-axis tensile stress-strain behavior of the material was established, and the prediction results were in good agreement with the experimental results.

1. Introduction

As a new type of high temperature-resistant structural material, plain weave ceramic matrix composite, hot-end components have requirements on structural weight reduction and operating temperature [1]. To understand and master the damage mechanism of materials under different stress states and mechanical behavior is to optimize the material preparation process and promote the important theoretical basis for its engineering practical application. During the service process, the composite material of the component is usually in a complex stress state; at present, the damage mechanical behavior of materials under a single axial stress state is studied, and it can no longer meet the needs of engineering design. At the same time, under the complex stress state, during the evolution process of material damage caused by different stress components, there are significant coupling effects. The existence of the damage coupling effect will significantly accelerate the damage process of the material, change the failure mode of the material, and reduce the mechanical properties of the material; thus, it seriously affects the structural strength and service life of composite components, and it must be studied in a targeted manner, as shown in Figure 1.

2. Literature Review

Although a great deal of research has been done on the mechanical behavior of ceramic matrix composites, it is mostly about its elastic properties. Its nonlinear properties are rarely studied. Due to the complex process of production and preparation, there are a lot of defects in the material, and the damage gradually accumulates under the load, causing the material stiffness to degrade. This makes it difficult to accurately predict the nonlinear mechanical response. Further research is still needed to reveal its destruction mechanism. Based on the previous research results, the author adopts the method of combining experiment and finite element calculation, and the tensile damage failure mechanism of ceramic matrix composites was revealed. The macromechanical constitutive of the material is established, and the strength envelope and proportional limit envelope under in-plane loads are obtained.
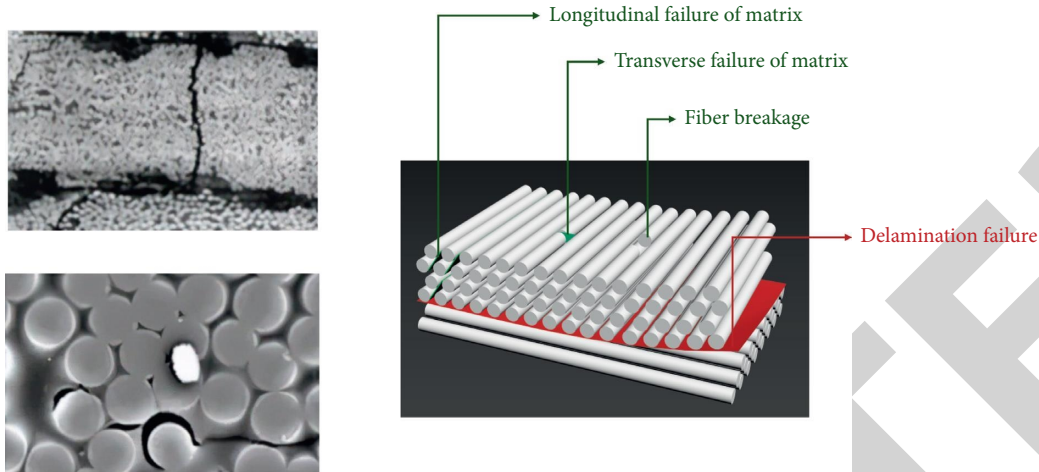
Figure 1: Damage coupling mechanism.

The study by Prasad, N. E et al. showed that matrix cracking is a significant shear nonlinear stress-strain behavior of ceramic matrix composites and is the main cause of large shear plastic deformation [2]. Reynaud, P. et al. and Rouby, D. et al. argue that the rigid body displacement of the longitudinal matrix fragments caused by a damage inside the material is the reason for the large irrecoverable strain of the material, and that it is controlled by the interfacial properties between the fiber and the matrix [3]. Ma, J. et al. found that under shear load, 2D-C/SiC composites, the included angles between the matrix crack and the fiber axis are basically 0°, 90°, and 45°; the 45° direction crack is the main reason for the final shear failure of the material [4]. Murthy, P. et al. established a multiscale finite element model, where the damage initiation, propagation process, and stiffness degradation law of laminate structural composites under a complex stress state are studied [5]. By the finite element method, suggested by Wang, Z. G. et al., the damage mechanical behavior of ceramic matrix composites under a complex stress state was studied, and the in-situ mechanical properties of the material components in the model were obtained by a 45° off-axis tensile test [1]. Prasad, N. E. et al. through cyclic off-axis loading and unloading experiments with different angles studied the damage initiation and propagation laws of resin matrix composites under a complex stress state [2]. Reynaud, P. et al. combined tension-torsion and tension-internal pressure loading on SiC/SiC composite circular tubes, and the damage and failure behavior of materials under complex stress states was studied [3]. Ma, J. et al. based on the biaxial tensile stress-strain behavior of ceramic matrix composites in the axial and 45° directions established a phenomenological constitutive model of the material under the plane stress state [4]. Prasad, N. E. performed off-axis tensile tests on 2D-C/SiC and 2D-SiC/SiC composites, respectively, using the obtained experimental data; the continuous damage constitutive model of the material was established and verified[6].

Based on the current research, a method for the damage coupling mechanism of plain weave art ceramic substrates is proposed. The axial tensile hysteresis model of plain weave

ceramic matrix composites was established, the influence of the long and short fragments of the matrix on the hysteresis behavior of the material is analyzed. Four parameters to characterize the mechanical properties of the material components were obtained by calculation: Matrix cracking stress, thermal residual stress, interfacial debonding energy, and interfacial slip force [7]. Based on the off-axis tensile stress-strain behavior of 0 and 45°, a prediction model of off-axis tensile stress-strain behavior of the material was established, and the predicted results were in good agreement with the experimental results.

3. Study on the Surface Damage Coupling Mechanism of Plain Weave Art Ceramic Matrix Composites

3.1. Overview of Plain Weave Ceramic Matrix Composites

3.1.1. Material Overview. The reinforcing phase fibers of plain weave ceramic matrix composites are mainly C fibers and SiC fibers. The C fiber is one of the most successfully developed fibers with the best performance so far and has been widely used as a reinforcing phase material for composite materials. In an inert gas environment, its strength does not decrease at a high temperature of 2000°C, and it is the most stable type of fiber with high temperature performance among the current reinforcement fibers [8]. However, the poor oxidation resistance at high temperature is the biggest weakness of C fibers. By coating and modifying the surface of the fiber, it can effectively avoid its high temperature oxidation damage. As another important reinforcing phase of composite materials, SiC fiber has similar mechanical properties to C fiber at room temperature. Since the SiC fiber and the SiC matrix have similar thermal expansion coefficients, the thermal deformation mismatch problem during the process from the as-prepared state to the room temperature can be greatly alleviated, and the initial damage problem of the material can be improved. However, SiC fibers contain oxygen and free carbon impurities to varying degrees, which seriously affects their

TABLE 1: Main properties of plain weave ceramic matrix composite components.

	Strength/Mpa	Modulus/Gpa	Density (g/cm^3)	Tce/(10^{-6}K^{-1})
Sic matrix	602	460	3.26	4.1
T-300 fiber	3101	230	1.77	0.1~0.6
Hi-Nicalon fiber	2801	270	2.75	3.6

high-temperature mechanical properties [9]. At present, the low oxygen content SiC fiber (Hi-Nicalon) produced by the Nippon Carbon Corporation has good high temperature stability, and its strength can be guaranteed to change little at 1500~1600°C.

The matrix phase materials of plain weave ceramic matrix composites are mainly non-oxide matrix, mainly referring to SiC ceramics and Si: N ceramics. Compared with other inorganic nonmetallic materials, non-oxide ceramics have higher hardness and strength, excellent wear resistance, and high temperature resistance; in particular, it has good high temperature strength and thermal shock resistance, and the SiC ceramic matrix is the earliest and most successful example of research. In addition to the fiber reinforcement phase and the ceramic matrix phase, the material composition also includes an interface phase material, generally a flexible pyrolytic carbon (PyC) material. The interface is the key to improve the brittleness of the material, and it is an important factor to control the load transfer mechanism and damage failure mode between the fiber and the matrix inside the material [10]. Table 1 gives some basic properties of the C fiber, SiC fiber, and SiC matrix in the form of a single substance. After the composite material is formed as a whole, due to the influence of factors such as preparation damage and thermal residual stress, the mechanical properties of the above components will decrease to varying degrees, so the mechanical properties listed in Table 1 cannot be directly used for the prediction and calculation of the overall mechanical properties of the material.

3.1.2. Application Status.

Ceramic matrix composites are widely used in aviation (including aeroengine) aerospace field. In addition, it also has good application prospects in the fields of nuclear energy applications and hypersonic aircraft thermal protection systems [11]. Since the 1950s, western countries have begun to try to apply SiC/SiC ceramic matrix composites to high-temperature parts of aeroengines. Among them, SNECMA of France and General Electric of the United States have carried out initial research studies in this field, and the technology is relatively mature and has high industrialized water. In the early eighties, the SiC/SiC ceramic matrix composite material was developed by the French SNECMA company, and it was applied to the engine nozzle adjustment sheet. In the mid-1990s, SNECMA and PW jointly conducted exploration and research on the engineering application of SiC/SiC ceramic matrix composites: The nozzle seal adjustment piece made of SiC/SiC ceramic matrix composite material passed the ground acceleration task test [12]. Since the late 1980s, the preparation and industrial application of SiC/SiC ceramic matrix composites have been explored. With the support of projects

TABLE 2: Application of composite materials in the aeroengine.

Engine model	Applied parts
M88-2E4 development type	Inner nozzle adjustment plate
F100-pw-229ˏF100-pw-220	Nozzle seal adjuster
CFM56	Mixer
XTC76/3	Combustion chamber fire chimney

such as IHPTET, EPM (Enabling Propulsion Materials), UEET (Ultra Efficient Engine Technology Program), and NGLT (Next Generation Launch Technology), the preparation process of SiC/SiC ceramic matrix composites tends to be mature, and the company has conducted a large number of experiments and engineering verifications on the hot end components of aeroengines using SiC/SiC ceramic matrix composites. In addition, many companies in the United Kingdom and Japan have also designed and tested SiC/SiC composite combustion chamber linings, heat shields, turbine blades, turbine rotors, and other hot-end components. The application of foreign SiC/SiC composite materials in aeroengines is shown in Table 2.

The development of SiC/SiC composite components began in the 1980s, and the main development units include AVIC Composite Center, Aerospace Materials and Technology Research Institute, Northwestern Polytechnical University, National Defense Science and Technology University and other units. Among them, the combustion chamber floating wall simulation and the tail nozzle adjustment piece were developed by Northwestern Polytechnical University, and they have passed the preliminary verification and short-term assessment of the aeroengine environment, and the regulator developed by the National University of Defense Technology has also passed the relevant test runs [13]. In short, it has the capability of component development and small batch production, but there is still a clear gap with the western developed countries in terms of engineering industrialization.

3.2. Damage Behavior of Ceramic Matrix Composites

3.2.1. Damage Mechanics of Composite Materials.

The damage of solid materials under the action of an external load is generally a process of accumulation of damage, and physically, it is a process of accumulation of microstructure changes; mechanics is the cumulative process of the generation and development of macroscopic defects. Under a certain load environment, the microstructural change that causes the deterioration of material properties is called damage. Damage mechanics is the study of the mechanical laws of materials under various loading conditions, in which damage evolves with deformation and eventually leads to the

failure process. Initial defects and damage activity in composites accompany the material throughout its use stage; in order to optimize the design of materials and correctly evaluate the performance of composite materials, it is necessary to deeply study the damage and failure mechanism of composite materials; furthermore, the damage evolution law of composite materials is revealed, and the influence of the existence of damage on the macroscopic properties such as stiffness and strength of composite materials is predicted [14].

Compared with other kinds of materials, the reason why composite materials can have a comprehensive and excellent mechanical behavior is because the material is composed of component materials with different mechanical properties, and the advantages of each component material are coupled at the same time [15]. Under the action of external load, the mesoscopic damage failure mechanism of component materials is the internal determinant of the overall macroscopic mechanical behavior and properties of the material. The research on the mechanical behavior of composite materials has become one of the most active and important fields of meso-mechanics; the purpose of micromechanics is to develop fundamental principles and methods based on the relationship between the microstructure of materials and their macroscopic physical properties. These principles and methods can not only guide people to synthesize composite materials with desired mesostructures in a targeted manner but also predict the mesoscopic and macroscopic mechanical behaviors of these composites in use [16].

Combining the above two research ideas, the purpose of the mesodamage mechanics research of composite materials is to establish the corresponding relationship between the macroscopic properties of the composite material and its component material properties and microstructure, reveal the intrinsic mechanism of different macroscopic properties of different material combinations, and to elucidate the mesoscopic mechanism of action that endows composites with high strength, high modulus, and good fracture toughness. Conversely, based on the study of mesodamage mechanism, it can also provide direct feedback suggestions for the selection of composite material components, the selection of preparation process, and the optimization of process parameters and help design composite material systems with optimal mechanical properties [17]. Therefore, there is a clear engineering application background to study the mesodamage mechanical behavior of composite materials, which is an important theoretical basis for the development of composite materials.

3.2.2. Research Status of Material Damage Mechanical Behavior. Ceramic matrix composites are typical brittle matrix materials; usually, the fracture strain (1%~1.5%) of the fiber is greater than the fracture strain (0.1%~0.2%) of the matrix. At the same time, the thermal expansion coefficient of the matrix is generally greater than that of the fibers. When the temperature of the material is lowered from the prepared state to room temperature, the thermal residual stress inside the material appears as tensile stress inside the

matrix, and as axial and radial compressive stress inside the fiber, this in turn leads to an initial damage to the material such as matrix cracking and interfacial debonding. Under the action of an external load, matrix cracking is the initial mesoscopic damage mode of the material. With the increase of the load, the microcracks in the matrix will continue to initiate and expand. When a matrix crack propagates to the interface layer between the fiber and the matrix, its propagation path depends on the relative strength of the interface and the fiber. When the interface is strong, the crack penetrates the interface layer into the fiber and causes the fiber to fracture, and the composite exhibits brittle fracture similar to pure ceramic. When the interface is weak, the cracks deflect and propagate along the interface, the fibers do not break, and interface debonding and slip damage occur, resulting in the material exhibiting ductile failure behavior [18, 19]. As the load continues to increase, the proportion of bridging fibers between adjacent matrix crack surfaces to the overall fiber continues to increase, and the proportion of the load borne by them also increases, causing the fibers to begin to break. When the broken fiber reaches a certain proportion, the material loses its continuous bearing capacity and the overall failure occurs.

For the mesodamage mechanical behavior of plain weave ceramic matrix composites, the research on axial tensile damage is the most thorough, the theoretical model is the most complete, and the research results are very remarkable: The research work is mainly based on the shear lag model (ACK theory), combined with the random cracking of the matrix and the random fracture of the fibers, the axial tensile stress-strain behavior of the material can be completely predicted [20]. Among them, by studying the stress-strain behavior of axial tensile cyclic loading and unloading, the relationship between the macroscopic tensile mechanical behavior of the material and the mechanical properties of the components can be directly established, which lays a necessary foundation for the quantitative study of the damage mechanical behavior of the material.

4. Experiments and Analysis

4.1. Monotonic Loading and Damage Distribution. The stress-strain behavior and damage distribution of a uniform section of the specimen under a single axial load were obtained through monotonic axial tensile, axial compression, and in-plane shear tests, respectively, where typical monotonic axial tensile and compressive stress-strain curves measured are given in Figure 2; the longitudinal axis is the average tensile and compressive stress of the uniform section of the specimen [21]. As can be seen from Figure 2, under the same tensile stress level, the tensile strain measured by the strain gauge closer to the edge of the specimen is larger; this shows that there is obvious strain concentration phenomenon in the middle section of the specimen during the tensile process. Under the action of axial compressive load, the stress-strain curves corresponding to different strain gauges all behave as approximate linear elasticity. During the compression process, there is still a certain strain concentration phenomenon in the middle section of the specimen,
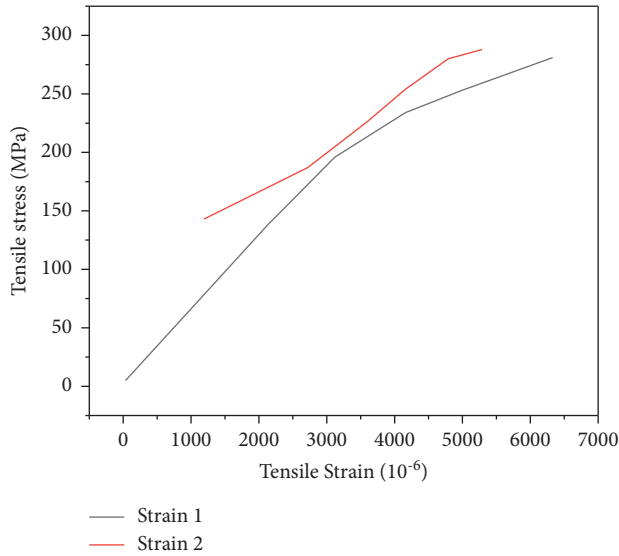
Figure 2: Monotonic axial tensile and compressive stress-strain curves.

but the concentration degree is significantly smaller than that in the axial tension state.

Under axial tension and compression loading, the strain concentration phenomenon on the middle section of the specimen shows that the axial tensile and axial compression damage distributions of the uniform section of the specimen are nonuniform, and this will bring errors and inconveniences to the quantitative decoupling analysis of the subsequent tensile-shear and compression-shear damage coupling effects, as well as the calculation of the damage coupling components D16 and Do1. In order to minimize the error, in the subsequent analysis, the average strain of the loaded section will be used, the real-time elastic modulus of axial tension and compression of the entire uniform segment material is fitted and calculated, that is, the damage degree is characterized. At the same time, in order to be consistent with the subsequent strain measurement scheme, it is also necessary to establish the overall average strain of the material in the uniform section of the test, the corresponding relationship with the strain data at the center position, and the degree of damage. To this end, the typical variation curves of the calculated ratio of E_ε to e, with the applied tensile and compressive stress are shown in Figures 3 and 4. The calculation steps are as follows in formula (1):

$$R\left(\varepsilon_{Aw}, \varepsilon_{1m}\right) = \frac{\varepsilon_{AW}}{\varepsilon_{1W}} = \frac{1}{7} \sum_{lm1}^{7} \frac{\varepsilon_1}{\varepsilon_{1w}}. \tag{1}$$

As shown in Figure 3, during the monotonic axial tensile loading process, the value of R(εxe, E) slightly increases with the increase of tensile stress, which is mainly due to the high stress level. Due to the influence of stress concentration, the tensile damage of the local material at the edge of the loaded section in the middle of the specimen develops rapidly, and the corresponding strain value increases rapidly. On the whole, the abovementioned ratios did not change much and remained at around 1.38. In order to simplify the subsequent
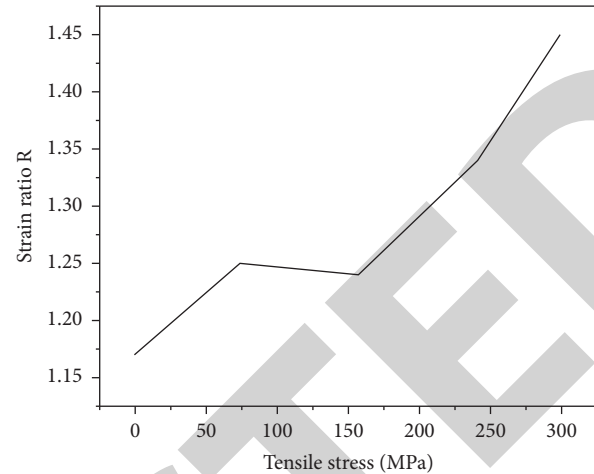
Figure 3: Variation curve of monotonic axial tensile strain to cross ratio.
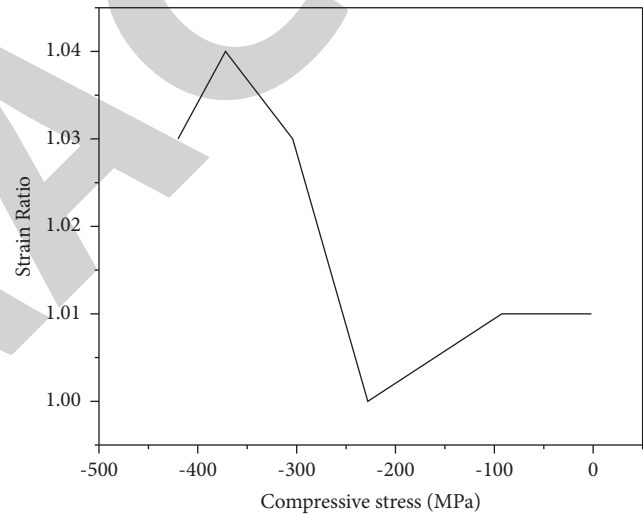
Figure 4: Variation curve of monotonic axial compression strain ratio.

calculation and analysis process, in the following, ε of 1.38 times will be used as the average axial tensile strain of the loaded section, and the fitting calculation of the axial tensile elastic modulus of the material will be performed, as well as the characterization of the degree of tensile damage. During the axial compression process, the value of R (e., e) basically remains around 1.05. Similarly, in the subsequent calculation analysis, 1.05 times ε will be used as the average axial compressive strain of the loaded section, in order to characterize the degree of compression damage of the test uniform section material, and the fitting calculation of compressive elastic modulus.

Typical shear stress-strain curves obtained under monotonic in-plane shear loads are shown in Figure 5. The corresponding curves of the strain gauges basically overlap, but the strain values measured by the strain gauges under the same stress level are significantly smaller than the first three. The above differences show that on the sheared cross section

Figure 5: Monotonic in-plane shear stress-strain curve.

Figure 6: Variation curve of shear strain ratio in the monotonic plane.

of the specimen, there is also an obvious uneven distribution of shear strain, that is, uneven distribution of the shear damage.

Similarly, in order to reduce the analysis error, the average shear strain of the section will be used to indicate the degree of shear damage of the material in the uniform section of the test. At the same time, the shear strain 7 measur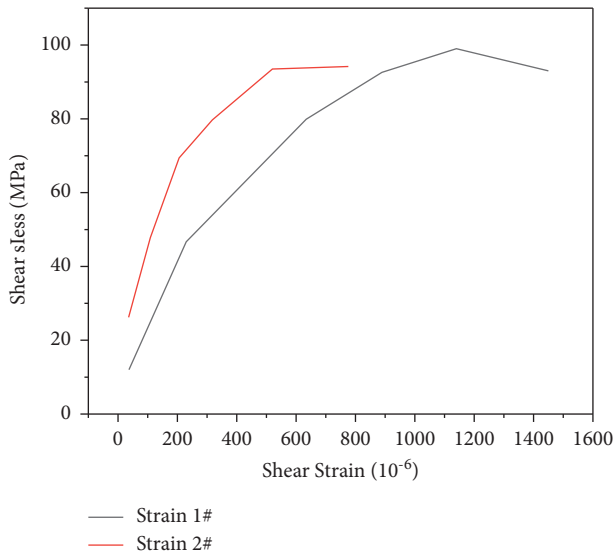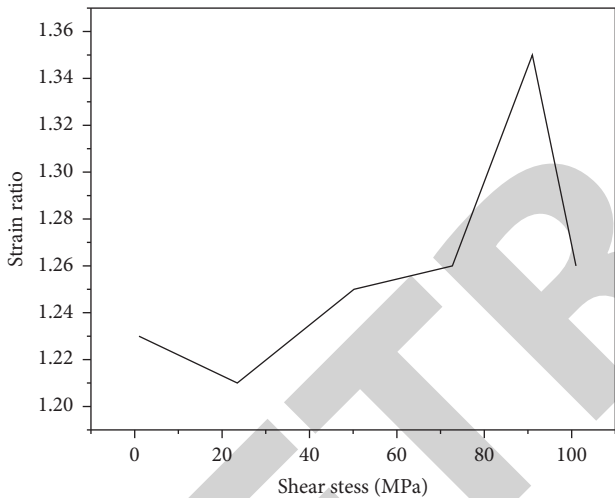ed by the strain gauge is obtained. The typical change curve of the ratio R(y,7) to the average shear strain γ ne of the section changes with the application of shear stress, as shown in Figure 6, and the calculation steps are as follows in formula (2):

$$R\left(y_{1w}, y_{Ave}\right) = \frac{y_{1m}}{y_{Ave}} = \frac{5y_{1w}}{\sum_{i-1}^{5} y_3}. \tag{2}$$

It can be seen that in the whole shear loading process, the above ratio is basically constant at about 1.36. In the

subsequent calculation and analysis, y/1.36 will be used as the average shear strain of the loaded section to characterize the degree of the shear damage of the material in the test uniform section and to perform the fitting calculation of the shear modulus.

5. Conclusion

The author first discusses the composition, mechanical properties, preparation process, application status, and prospects of plain weave ceramic matrix composites in aerospace high-temperature thermal structures; additionally, the main problems that need to be solved in terms of the mesoscopic damage mechanical behavior of materials and their research status are introduced. The main research subjects are 2D-C/SiC and 2D-SiC/SiC composites prepared by a chemical vapor infiltration (CVI) process, and the damage mechanical behavior of materials under simple and complex plane stress states is studied systematically. The focus is on the calculation of the mechanical property parameters of the material components, the research on the mechanical behavior of the material in-plane shear mesoscopic damage, research on material damage coupling effect under complex stress state, and decoupling test research on damage coupling effects. The specific research work and conclusions are as follows:

(1) By conducting axial tensile, compression, and in-plane shear tests on 2D-C/SiC and 2D-SiC/SiC composites under various loading forms, the basic stress-strain behavior and mechanical properties parameters of the material are obtained. Based on this, the damage mechanical behaviors of the two materials were compared and analyzed. During this period, the effects of different loading histories on the damage failure process and mechanical properties of materials were mainly studied.

(2) Based on off-axis tensile and off-axis compression tests, the effects of off-axis angle on the stress-strain behavior, damage process, failure mode, and mechanical properties of 2D-C/SiC composites were compared and analyzed. Based on the off-axis tensile stress-strain behavior of 0 and 45°, a prediction model of off-axis tensile stress-strain behavior of the material was established, and the predicted results were in good agreement with the experimental results.

(3) Based on the shear lag theory, the axial tensile hysteresis model of plain weave ceramic matrix composites was established, the influence of the long and short fragments of the matrix on the hysteresis behavior of the material is analyzed. To characterize the mechanical properties of the material components, four parameters are obtained by calculation: Matrix cracking stress, thermal residual stress, interfacial debonding energy, and interfacial slip force. According to the calculation results, the effects of fiber properties and interfacial layer thickness on the above parameters were compared and analyzed.

Hindawi

Retraction

Retracted: Art Decoration Design of Electrochemical Silicon Oxide Ceramic Sculpture Based on 3D Printing Technology

Journal of Chemistry

This article has been retracted by Hindawi following an investigation undertaken by the publisher [1]. This investigation has uncovered evidence of one or more of the following indicators of systematic manipulation of the publication process:

(1) Discrepancies in scope

(2) Discrepancies in the description of the research reported

(3) Discrepancies between the availability of data and the research described

(4) Inappropriate citations

(5) Incoherent, meaningless and/or irrelevant content included in the article

(6) Peer-review manipulation

The presence of these indicators undermines our confidence in the integrity of the article's content and we cannot, therefore, vouch for its reliability. Please note that this notice is intended solely to alert readers that the content of this article is unreliable. We have not investigated whether authors were aware of or involved in the systematic manipulation of the publication process.

Wiley and Hindawi regrets that the usual quality checks did not identify these issues before publication and have since put additional measures in place to safeguard research integrity.

We wish to credit our own Research Integrity and Research Publishing teams and anonymous and named external researchers and research integrity experts for contributing to this investigation.

The corresponding author, as the representative of all authors, has been given the opportunity to register their agreement or disagreement to this retraction. We have kept a record of any response received.

References

[1] J. Guo, "Art Decoration Design of Electrochemical Silicon Oxide Ceramic Sculpture Based on 3D Printing Technology," *Journal of Chemistry*, vol. 2022, Article ID 9728402, 9 pages, 2022.

Research Article

Art Decoration Design of Electrochemical Silicon Oxide Ceramic Sculpture Based on 3D Printing Technology

Jifeng Guo [1,2]

^{1}*Xi'an Academy of Fine Arts, Xi'an, Shaanxi 710065, China*
^{2}*The Youth Innovation Team of Shaanxi Universities, Xi'an, Shaanxi 710065, China*

Correspondence should be addressed to Jifeng Guo; 20152911106@stu.qhnu.edu.cn

In order to solve the art decoration design of silicon oxide ceramic sculpture, a method for silicon oxide ceramic sculpture based on 3D printing technology is proposed. Firstly, the density of photosensitive resin premix before curing was measured by pycnometer method; the photosensitive resin was coated on tinplate and then put into a self-made UV curing box for curing. Secondly, the critical exposure and critical transmission depth of photosensitive resin without formula are calculated. Finally, the viscosity of ceramic slurry was measured by mixing S2 photosensitive resin formula with ceramic powder with different nano silica content. It is proved that the addition of nano silica powder can promote the decomposition of quartz glass and increase the sintering degree of the ceramic core. The primary sintering shrinkage of ceramic core gradually increases with the increase of nano silica content. In the length direction, the shrinkage increases from 3.33% to 5.61%; in the width direction, the shrinkage increases from 2.98% to 4.74%; and in the height direction, the shrinkage increases from 3.18% to 5.00%.

1. Introduction

Ceramic sculpture is one of the cultural elements with a long history in China. Ceramic products not only have ornamental value but also have a strong practicability. Therefore, ceramic sculpture products are widely used in all walks of life. The production process of traditional ceramic sculpture is relatively complex, and there are many processes, but modern ceramic sculpture production uses 3D printing technology to simplify the manufacturing process and shorten the production time, which makes the traditional ceramic culture and technology sublimate and develop while inheriting. Relevant researchers and technicians use modern advanced technical means for design and 3D printing technology for manufacturing and processing, which can produce ceramic products with rich colors, unique shapes, and strong functionality to meet the needs of various industries and different audiences for ceramic products.

3D printing technology is a kind of rapid prototyping technology. It is based on 3D digital model software and uses curable molding materials such as powder metal or plastic to realize a 3D digital model as a space object by printing layer by layer, as shown in Figure 1 [1]. This technology appeared in the mid-1990s, and its working principle is basically the same as that of ordinary printing. The 3D printer is equipped with curable "printing materials" such as liquid or powder. After connecting with the computer, the "printing materials" are superimposed layer by layer through computer control, and finally, the three-dimensional digital model on the computer is turned into a real object.

2. Literature Review

With the rapid development of rapid prototyping technology, 3D printing technology can be involved in more and more fields, from printing simple model parts to pistols that can fire bullets to houses for people to live in, from industrial processing to architectural design to medical and health care. We found that 3D printing technology and sculpture art have natural commonalities. They are all involved in space modeling, and they are using some material medium to express their demands on space form. Three-dimensional
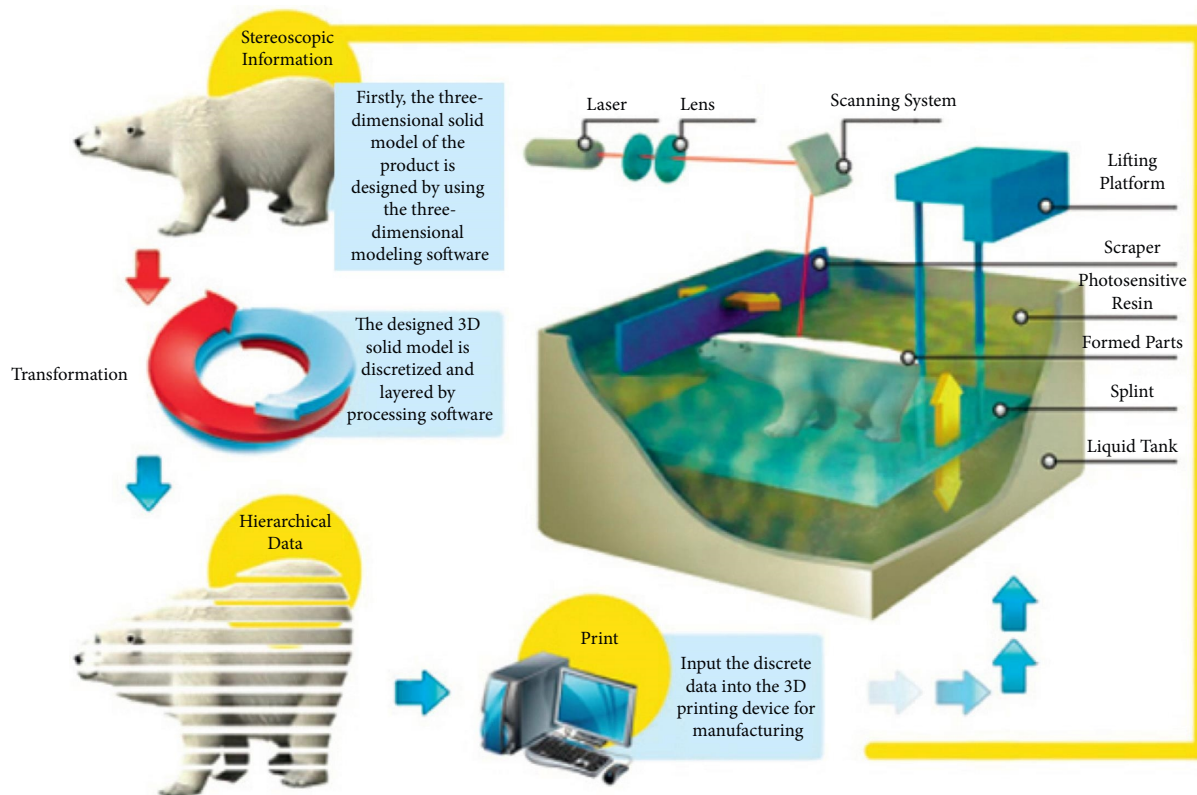
Figure 1: 3D printing technology.

printing technology will have a far-reaching impact on the development of sculpture art.

Some progress has been made in the research of 3D printing SiO_2 ceramics at home and abroad. Yao and others directly formed ceramic blank by light-curing technology and studied the relationship between powder volume fraction and slurry viscosity and curing thickness [2]. Qiu and others studied the effect of shear rate on the viscosity of SiO_2 ceramic slurry. When the shear rate reached 100s-1, the slurry viscosity was lower than that when the shear rate was 0 [3]. Torda and others studied the effect of dispersant on the viscosity of water-based SiO_2 ceramic slurry and considered that when the content of sodium polyacrylate dispersant reached 0.3 wt.%, low viscosity silica ceramic slurry could be prepared [4]. Hegyi et al. used Cao powder as precursor material and nano zirconia absolute ethanol as a binder to prepare printing slurry; the sintered ceramic core has high bending strength, low shrinkage, and high hydration resistance [5]. Mei et al. used DLP printing technology to manufacture porous zROC ceramics with an octagonal truss structure. After sintering, the porosity of ceramic samples reached 55.49%, which promoted the application of ultralight and porous ceramics [6]. Belaid by using polyvinyl alcohol (PVA) as the organic binder in the slurry, the method of heat treatment and impregnation of the inorganic precursor is adopted to improve the strength of the core after sintering and reduce the shrinkage of the printed ceramic core after sintering [7]. Khanna invented the stereolithography technology of stacking high molecular polymers cured by UV laser layer by layer [8]. McDonough invented

two methods of manufacturing three-dimensional plastic models using additives of light-curing polymers, and its ultraviolet irradiation area is controlled by a mask pattern or scanning optical fiber transmitter [9]. Arnay first successfully proposed the organic combination of light-curing molding technology and ceramic material preparation molding technology [10]. Zheng studied the effect of particle size on ceramic slurry. The results showed that adding powder with a larger particle size into the powder could improve the fluidity of ceramic slurry [11].

Based on the current research, a 3D printing technology is proposed for silicon oxide ceramic sculpture. By adding nano silicon oxide, the viscosity of ceramic slurry can be appropriately reduced. However, when the content of nano silicon dioxide is too high, the viscosity of the slurry will increase due to the agglomeration of nano powder. When the content of nano silicon dioxide is 0.5 wt.%, the lowest viscosity of the ceramic slurry is 2010. When the content of nano silica is 2.5 wt.%, the highest viscosity of the ceramic slurry is 2,900.

3. Art Decoration Design of Silicon Oxide Ceramic Sculpture Based on 3D Printing Technology

3.1. Ceramic 3D Printing Technology

3.1.1. General. Ceramic 3D printing technology belongs to the detailed classification of 3D printing technology, which is essentially the same as the principle of 3D printing

technology. The raw materials of ceramic 3D printing technology generally choose ceramic slurry or ceramic powder, which is based on digital model files, and then build designed ceramic products in the form of repeated printing layer by layer, which is a new ceramic manufacturing technology that can meet modern needs [12]. Compared with the traditional ceramic manufacturing process, modern ceramic 3D printing technology can effectively reduce the manufacturing cost of ceramic products, simplify the process flow of ceramic manufacturing, and break the confinement of the manufacturing process on ceramic design. In this way, the ceramic products with unique and novel shapes cannot only appear on the drawings but can be manufactured in kind.

3.1.2. Classification.

At present, ceramic 3D printing technology is mainly divided into layer-by-layer bonding method and direct molding method. The layer-by-layer bonding method refers to that firstly, the ceramic powder is paved, and then the nozzle sprays adhesive to the ceramic powder according to the specified path. After spraying one layer, another layer of powder is laid. This is repeated until the excess ceramic powder on the model is removed after full molding to obtain a three-dimensional object [13]. The direct molding method is to prepare ceramic slurry from ceramic powder and adhesive and squeeze out the slurry through the nozzle. Because the slurry has certain adhesion, it will be bonded with the previous layer of slurry immediately after extrusion. Then repeat the above steps until fully formed. In principle, this process is similar to the traditional clay bar dish building process, but the works are more fine and orderly due to the control of the computer.

3.1.3. Workflow in Ceramic Design

(1) 3D Model Making. The manufacture of a three-dimensional model is the basis of ceramic product design. Only when the three-dimensional model is determined can the manufacture of ceramic products be carried out. The digital model can more intuitively reflect the designer's ideas on the computer and can also provide technical support to clarify the design scheme and make it more convenient for later production. For example, in the process of polyhedron design, designers need to use software to establish models. These designs can be quickly converted into STL format and sent to 3D printers. The three-dimensional model provides technical support for the production of ceramic products and can design ceramic products with more complex shapes [14]. In order to ensure the beautiful appearance of ceramic products, curves need to be applied, and the smoothness of ceramics needs to be improved in this process. Therefore, 3D technology is needed to design the shape and print it to see the effect. Designers can constantly adjust the data in this process, so as to activate the complex surface flexibly.

(2) 3D Printer Reduces Dimension. The three-dimensional object is processed into a two-dimensional model for printing, and rectangular coordinate points are generated to form a three-dimensional shape. The application of 3D technology in the design of ceramic products usually uses wet clay as the printing material, but the wet clay has some defects, which are difficult to form, not strong enough, and easy to deform in the printing process. Therefore, hard clay can be used to avoid this problem. The printing layer of 3D printing technology is 10 mm, which cannot better ensure the printing quality and printing speed. Therefore, the thickness can be reduced to improve the printing accuracy. After air-drying, the surface can be polished to ensure its smoothness.

(3) Ceramic Embryo Surface Treatment. The 3D printing technology is not perfect, so the printed surface is not very smooth, and there will be a surplus or lack of materials. During the printing process, the clay will also be brushed and left on the surface. Therefore, it should be further improved and polished after making, so as to form a smooth and useable model, and take out the floating ash on the surface and glaze it. Otherwise, the ideal effect will not be achieved. After glazing, it will be put into the kiln for firing. The traditional production process relies more on manual work, which increases human and material resources. Moreover, the production of the template is very complex and needs to be modified continuously, which increases the workload [15]. Three-dimensional printing technology is a common product model design at present. It makes three-dimensional models by the computer. In this process, the designer's thinking can be accurately reflected by computer, and then the three-dimensional model can be converted into two-dimensional images by software. Finally, the texture can be accumulated through layer-by-layer printing by a 3D printer. If you want a smooth surface, you can polish it. This not only saves time but also reduces costs and saves human and material resources.

3.2. Adaptability of 3D Printing Technology to Sculpture Language.

3D printing technology has basically formed a set of systems, and the applicable industries have gradually expanded, involving many fields such as product design, mold design and manufacturing, material engineering, medical research, culture and art, construction engineering, and so on. Sculpture art, like other art categories, has its own language to express creative ideas. The three-dimensional possession of space, the mass feeling, or the sense of space and volume are the most basic language features of sculpture art. The most basic essence of 3D printing technology is rapid prototyping. At this point, it meets the needs of sculpture art language expression, can quickly realize the spatial materialization of digital-physical state and meets the basic requirements of sculpture art creation for language materials. The advantages of 3D printing technology are: first, save materials, improve material utilization, and reduce costs by abandoning production processes; second, it can achieve high precision and complexity; third, without any traditional mold, we can directly generate any shape state from computer graphics data; fourth, it can automatically, quickly, directly, and accurately convert the design in the computer into a model, so as to effectively shorten the product R & D cycle; and fifth, it can be formed in a few

hours, which makes the artist realize the leap from plan to entity [16]. It can be seen that 3D printing technology can quickly express the artist's artistic purpose in the form of blocks and volumes in the sense of sculpture language in space, realize the artist's creative purpose, and meet the expression needs of sculpture language.

3.3. Impact of 3D Printing Technology on Sculpture Art Creation.
Technological innovation can always bring convenience to practical activities and improve the efficiency and success rate of the practice. The impact of 3D printing technology on sculpture art creation mainly includes the following points.

3.3.1. It Enhances the Predictability of Artistic Creation Effect.
Sculpture art creation and painting art creation have certain similarities in steps. In the early stage of his creation, the forms of expression are mostly sketches on paper. On this basis, what painting creation needs to do is still the effect treatment on the plane, while sculpture is further deliberation on the physical space. Three-dimensional printing technology can realize the spatial state of sculpture creation from the paper state and shorten the process of sculpture art creation through digital creation intention and rapid prototyping printing. It can also study and judge the spatial state of sculpture in advance by regulating the digital sculpture data to enlarge or reduce the sculpture or adjusting the shape and proportion of sculpture in space. In addition, the possibility of forming material effect of sculpture can be speculated through the selection of printing material [17]. The application of 3D printing technology in sculpture art creation shortens the process from plane to space, increases the prediction of space art effect in the process of sculpture art creation, and saves the time and cost of art creation.

3.3.2. Changed the Single means of Sculpture Art Creation.
Manual work has always been the main means of sculpture art creation. The clay sculpture is made by kneading, reducing, and molding the clay by hand. The clay sculpture completed by molding is turned over and then injected into other molding media, For example, what is made with gypsum as the forming medium is called gypsum statue, and what is made with resin is commonly known as FRP. It is also called cast copper, cast iron, and cast bronze due to its different materials. Cutting and chiseling wood or stone is called wood carving or stone carving. These sculpture categories are inseparable from a single manual work, which also increases the amount of labor of artists, increases unpredictable variables for the release of sculpture works of art, and reduces the efficiency of transforming sculpture artists' artistic ideas into sculpture works of art. Three-dimensional printing changed the sculptor's helplessness to heavy physical labor, made the sculptor's creation complete in the design stage of sculpture, and handed over the heavy realization process to the machine that can fully realize the sculptor's intention. Sculptors only need to sit in front of the computer and express their design intention or creative intention into digital 3D images through 3D software, deliberate and modify them on the computer until the digital 3D images can fully reflect their artistic ideas, and then select appropriate expression materials and supporting structures. The next step is to let the 3D printer easily and quickly realize the physical form of their design ideas [18]. Such examples are numerous.

3.3.3. It Enriches the Form of Sculpture Works of Art.
How much material you master always affects the creativity of a sculptor. After mastering the technology of copper casting, the sculptor created copper casting sculpture. After mastering the characteristics of resin materials, sculptors began to use resin to realize their own sculpture works. Knowing the corrosion-resistant characteristics of stainless steel, you can see the "stainless steel monsters" standing in the street squares of various cities [19]. The continuous enrichment of 3D printing materials is also broadening the creative ideas of sculpture artists and enriching the types of sculpture works of art, making artists break the traditional understanding that products in the industrial field only have use value and lack artistic thought [20].

4. Experimental Method

4.1. Experimental Materials and Equipment.
The experimental raw materials used in this paper are mainly divided into photosensitive resin system and ceramic core system, as shown in Table 1.

4.2. Experimental Method.
This experiment is divided into three parts: the design and preparation of photosensitive resin, nano-silica-modified silicon-based ceramic core, and nano-alumina-modified silicon-based ceramic core. The process diagram is shown in Figure 2.

4.2.1. Design and Preparation of Photosensitive Resin.
Ceramic light-curing slurry is made of a certain proportion of photosensitive resin and ceramic powder. The photosensitive resin is made of a series of oligomers, monomers, photoinitiators, and other additives. The parameters such as viscosity, volume shrinkage, curing rate, and double bond conversion shall meet the requirements of 3D printing [21]. In this paper, polyurethane acrylate (PUA) as oligomer, dipropylene glycol diacrylate (DPGDA), 16 hexanediol diacrylate (HDDA), trimethylolpropane triacrylate (TMPTA) as active diluent, 2,4,6-trimethylbenzoyl ethoxy phenylphosphine oxide (TPO) as photoinitiator, and a small amount of defoamer were added to form photosensitive resin premix. The specific research contents are as follows:

(1) Mix the oligomer PUA: monomer (HDDA, dpgda, TMPTA) = 1:1, then add 4 wt.% (monomer + oligomer) photoinitiator (TPO), stir with a mechanical stirrer at the stirring speed of 600 rpn/min for 60 min, and then let it stand until the bubbles

TABLE 1: Raw materials used in the experiment.

Serial number	Category	Component	Purity	Place of origin
1	Quartz glass powder	Silicon dioxide	>99.95%	City A
2	Mineralizer	Corundum	99.9%	City B
3	Mineralizer	Nano silica	99.9%	City C
4	Mineralizer	Nano alumina	99.9%	City D
5	Oligomer	Polyurethane acrylic resin	Analytical purity	City E

The equipment used in this experiment is shown in Table 2.

TABLE 2: Equipment used in the experiment.

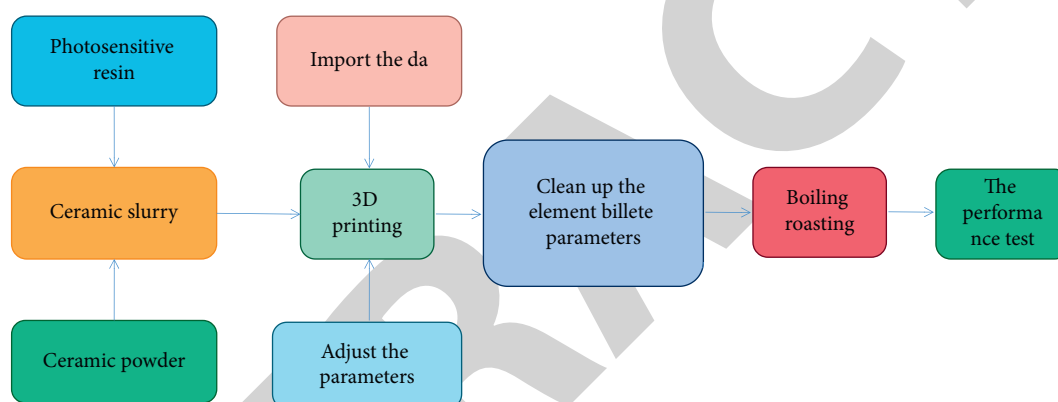| Serial number	Equipment name	Model	Manufacturer
1	Three-dimensional motion mixer	SYH-100	Company A
2	Vertical planetary ball mill	DECO-PBM-V4L	Company B
3	Box roaster	DC-B 460/13	Company C
4	Ceramic additive manufacturing equipment	Autoceramics	Company D
5	Digital rotary viscometer	3D printer	Company E

FIGURE 2: Process diagram of 3D printing ceramic core.

disappear completely. So far, the light-sensitive resin premix containing different monomers is obtained; then the effects of different monomers on the properties of light-cured resin were compared by testing its viscosity, volume shrinkage, critical light transmission depth, and critical exposure [22].

(2) HDDA, DPGDA, and TMPTA are mixed in the ratio of 1:1:1; then the monomer and oligomer are mixed in different proportions (monomer:oligomer = 4:6, 5: 5, 6:4, 73, 8:2, 9:1); then 4 wt.% (monomer- + oligomer) photoinitiator (TPO) is added, stirred with a mechanical stirrer at the stirring speed of 600 rpn/min for 60 min, and then stood until the bubbles disappear completely. So far, photosensitive resins with different oligomer contents are obtained, and then the proportion of oligomer monomers with the best performance is selected for further research by testing its viscosity, volume shrinkage, critical light transmission depth, and critical exposure [23].

4.2.2. Nano Silica Modification Experiment. 85 wt% quartz glass powder (D50 = 6) as the base powder,10 wt.% 320 mesh white corundum (D50 = 17.9), and 5 wt.% silicate drill (D50=20.51) as the mineralizer are taken. Nano silica powder (50 – 100 nm) content is 0 wt. %, 0.5 wt. %, 1.0 wt. %, 1.5 wt. %, 2.0 wt. %, 2.5 wt. The ceramic powder was mixed evenly in a three-dimensional motion mixer for 1 h. The prepared photosensitive resin premix and ceramic powder were loaded into a vertical planetary ball mill with a solid content of 56 vol% for ball milling for 6 h to obtain the photocurable ceramic slurry, and its viscosity was tested immediately. Adjust the parameters of the photocuring printer to the appropriate parameters, and import the digital model of the test bar into the 3D printer in advance, then pour into the ceramic paste with uniform mixture to start printing. After printing, put the test bar into the ultrasonic cleaning machine to clean the excess slurry on the surface. After natural drying, measure the length, width, and height of the blank test bar and then bury it into a bowl filled with aluminum oxide powder for degreasing roasting. The final firing temperature of the initial roasting is 1,200°C and kept warm for 6 h [24]. The electronic universal testing machine is used to test the bending strength of the ceramic core after the initial sintering; the vernier caliper is used to test the primary sintering shrinkage; the electronic balance and constant temperature bath pot are used to test the porosity, water absorption, and bulk density, and the pore size distribution

instrument; and X-ray calorimeter and thermal expansion instrument are used to test the physical and chemical properties of the ceramic core. The morphology was analyzed by scanning electron microscope and laser confocal microscope. In order to simulate the performance of the ceramic core in the casting process, the ceramic core test bar after initial sintering was put into the sintering furnace to raise the temperature to 1,540°C, and its performance was tested again after coming out of the furnace.

4.3. Performance Test

4.3.1. Slurry Viscosity. A company's digital rotary viscometer is used to measure the viscosity of photosensitive resin premix and ceramic slurry with different formulations. The measurement accuracy is ± 2%, and the measurement range is $1 \sim 2 \times 10^6 \, MPa \cdot s$.

4.3.2. Volume Shrinkage of Photosensitive Resin. Use the pycnometer method to test the density $\rho 1$ of the photosensitive resin premix before curing, smear the photosensitive resin on the tinplate, and then put it into a self-made UV curing box (10 cm away from the UV light source) for curing. The curing time is 5 s. After curing, use an electronic balance to test the density $\rho 2$ of the photosensitive resin after curing and then calculate the volume shrinkage η, as in the following formulas:

$$\rho = \frac{m_2}{m_1}, \tag{1}$$

$$\eta = 1 - \frac{\rho_1}{\rho_2}, \tag{2}$$

where m is the mass of the pycnometer filled with distilled water and m_2 is the mass of the pycnometer filled with resin.

4.3.3. Critical Exposure and Critical Transmission Depth of Photosensitive Resin. Beer–Lambert theorem is applicable to the classical theoretical basis of light-curing molding, which reveals the absorption and attenuation characteristics of light propagation in the medium. Its expression is as follows:

$$C_p = D_p In\left(\frac{E_i}{E_c}\right), \tag{3}$$

where C_p represents the curing thickness of light-curing molding, that is, the thickness measured by curing the photosensitive resin after UV irradiation with a certain intensity; D_p is the penetration depth of the incident light, specifically defined as the depth at which the exposure intensity is reduced to $1/E$ of the incident intensity; and E_c is the critical exposure energy of the photosensitive resin. When the input energy is less than the critical exposure light intensity, the slurry cannot be cured. D_p and E_c are determined by the properties of the light-curing resin itself; E_i is the energy input by the incident light to the resin surface, which is determined by the exposure parameters of the light-

curing equipment, The value is equal to the exposure light intensity W (unit: MW/cm2) and exposure duration t (unit: s); it can be expressed as follows:

$$E_i = W_i \times t. \tag{4}$$

The maximum input power of the 3D printer used is 30MW/cm2, and the exposure power increases every 10% from 20% to 100% of the maximum power. In order to be closer to the subsequent printing parameters, set the exposure time of the resin to 5 S. By testing the curing thickness C_p (mm) of photosensitive resins of three different monomers under different exposure power, after fitting the curve, the slope is the curing depth D_p and intercept $= -D_p In E$. Finally, the critical exposure and critical transmission depth of photosensitive resin without formula are calculated [25].

4.4. Nano-Silica-Modified Light-Curing 3D Printing Silica-Based Ceramic Core

4.4.1. Degreasing and Sintering System. Figure 3 shows the TG-DTG (thermal weight loss-thermal weight loss rate) diagram of the ceramic core blank. It can be seen that the wet core has mass loss at 262°C, 365°C, and 505°C, and the DTG curve tends to be stable after 600°C, indicating that the thermal decomposition process of the whole resin is completed. After the degreasing process is completed, the mass loss of the core blank is about 25 wt.%. Therefore, the determination of the sintering system should be properly insulated at 262°C, 365°C, and 505°C so that the resin can be fully eliminated.

The adjusted sintering system is shown in Figure 4. During the degreasing process, keep the temperature at 262°C, 365°C, and 505°C for 1 hour. After the degreasing is completed, accelerate the sintering rate to fully sinter the ceramic core.

4.4.2. Influence of Sintered Core Performance. The viscosity of ceramic slurry measured after mixing S2 photosensitive resin formula and ceramic powder with different nano silica content is shown in Figure 5 (black). The viscosity of slurry decreases first and then increases with the increase of nano silica particles. When 0.5 wt.% nano silica was added, the viscosity of the slurry decreased from 2,200 to 2,010. Because the content of nano silica particles is very low, it can be evenly distributed in the gap between ceramic particles, which increases the stacking rate of ceramic particles and forms better particle fluidity (also known as self-lubrication). In addition, nano silica particles with very fine particle sizes are easier to be wrapped by photosensitive resin, which reduces the friction and collision between ceramic particles and further reduces the viscosity of the slurry. However, once the nano silica content exceeds 1.0 wt.%, the viscosity of the slurry increases, and when the nano silica content is 2.5 wt.%, the viscosity of the slurry reaches the maximum value of 2,900 $MPa \cdot s$. If the content of nano silica is very high (more than 10 wt.%), these nanoparticles are easy to agglomerate, resulting in a higher
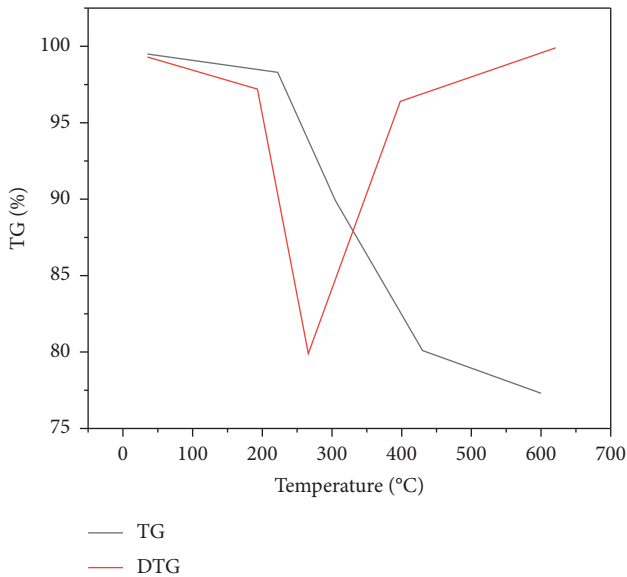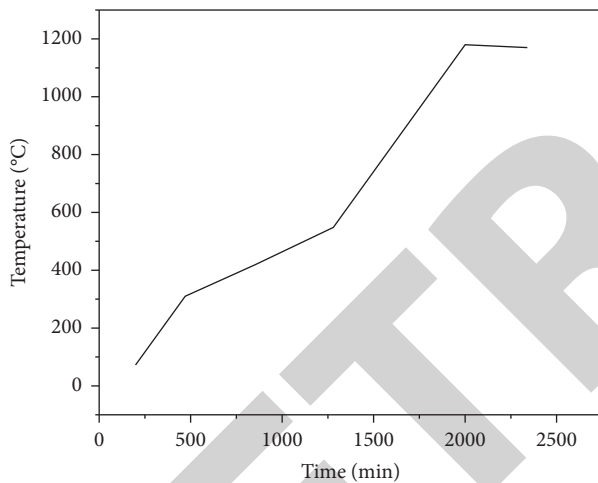
FIGURE 3: TG-DTG diagram of ceramic core blank.

FIGURE 5: Slurry viscosity and surface roughness after core sintering.

FIGURE 4: Sintering system of core sintering.
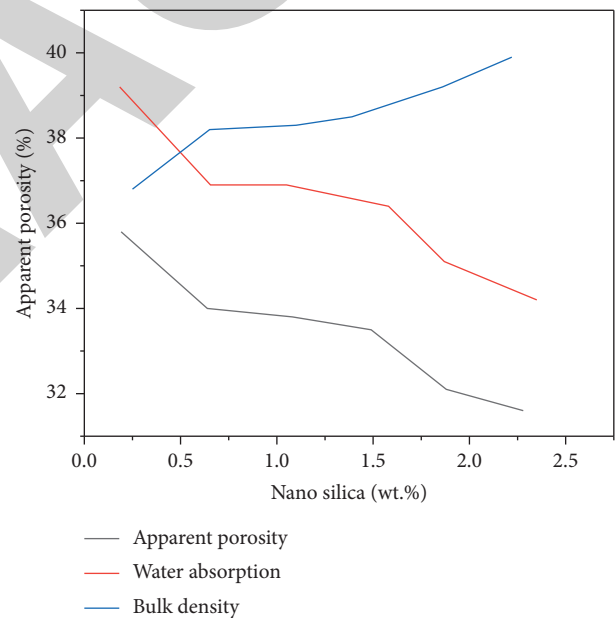
FIGURE 6: Porosity, water absorption, and bulk density of the ceramic core.

viscosity of the slurry, which is extremely unfavorable for paving and printing. The experimental results show that when the viscosity of the slurry is less than 3,000 $MPa \cdot s$, the ceramic slurry can meet the requirements of the laying and light-curing process. Figure 5 also shows the surface roughness of the ceramic core after one-time sintering. When the content of nano silica increases from 0 wt.% to 2.5 wt.%, the surface roughness of the ceramic core decreases from 1.85 μm to 1.65 μm. This is mainly due to the high surface energy of nano silicon oxide. In the sintering process, nano silicon oxide is easy to form liquid phase, which promotes the sintering of ceramic particles, enhances the adhesion between printing layers, and gradually reduces the aging of interlayer cracks. Therefore, with the increase of nano silicon oxide content, the surface roughness of the core tends to decrease, and the lower surface roughness will make the inner cavity of the subsequent alloy blade have better surface quality.

Figure 6 shows the porosity, water absorption, and bulk density of ceramic cores containing different nano silica after initial sintering. With the increase of nano silica content, the porosity and water absorption of the core gradually decreased, and the bulk density gradually increased. The porosity of the core sample without nano silica powder is 35.83%; the water absorption is 23.83%; and the bulk density is 1.50 g/cm^3. When the content of nano silica powder is 25 wt.%, the porosity of the ceramic core is the lowest, 31.56%; the water absorption is the lowest, 19.6%; and the bulk density is the highest, 1.61 g/cm^3.

5. Conclusion

Through thermogravimetric analysis, the sintering system of the ceramic core is determined: the viscosity of ceramic slurry can be appropriately reduced by adding nano silica, but when the content of nano silica is too high, the viscosity of slurry will increase due to the agglomeration of nano powder. When the content of nano silica is 0.5 wt.%, the lowest viscosity of ceramic slurry is $2,010\,MPa \cdot s$: when the content of nano silica is 2.5 wt.%, the highest viscosity of ceramic slurry is $2,900\,MPa \cdot s$. After the initial sintering, with the increase of nano silica powder content, the apparent porosity and pore diameter of the ceramic core gradually decrease, and the bulk density increases. When the nano silica content is 2.5 wt.%, the ceramic core reaches the lowest porosity of 31.56%, the lowest water absorption of 19.6%, and the highest bulk density of 1.61 g/cm^3. At the same time, the printing layer spacing is significantly reduced, the surface roughness is reduced, and the bending strength is improved. When the nano silica content is 2.5 wt.%, the surface roughness of the ceramic core is $1.65\,\mu m$, and the bending strength is 13.8 MPa. It is found that the addition of nano silica powder can promote the decomposition of quartz glass and increase the sintering degree of the ceramic core. The primary sintering shrinkage of ceramic core gradually increases with the increase of nano silica content. In the length direction, the shrinkage increases from 3.33% to 5.61%; in the width direction, the shrinkage increases from 298% to 4.74%; and in the height direction, the shrinkage increases from 3.18% to 5.00%.

Data Availability

The data used to support the findings of this study are available from the corresponding author upon request.

Conflicts of Interest

The author declares that there are no conflicts of interest.

References

[1] V. A. Gritsenko, "Hot electrons in silicon oxide," *Physics-Uspekhi*, vol. 60, no. 9, pp. 902–910, 2017.

[2] G. Yao, H. Ma, S. Sambandan, J. Robertson, and A. Nathan, "Indium silicon oxide tft fully photolithographically processed for circuit integration," *IEEE Journal of the Electron Devices Society*, vol. 8, no. 99, pp. 1162–1167, 2020.

[3] D. F. Qiu, X. Ma, J. D. Zhang, Z. X. Lin, and B. Zhao, "Mesoporous silicon microspheres produced from in situ magnesiothermic reduction of silicon oxide for high-performance anode material in sodium-ion batteries," *Nanoscale Research Letters*, vol. 13, no. 1, p. 275, 2018.

[4] B. Torda, L. Rachdi, A. Mohamed Okasha Mohamed Okasha, P. Saint-Cast, and M. Hofmann, "The effects of carbon incorporation on the refractive index of pecvd silicon oxide layers," *AIP Advances*, vol. 10, no. 4, Article ID 045331, 2020.

[5] B. Hegyi, R. Shimkunas, Z. Jian, L. T. Izu, and D. M. Bers, "Mechanoelectric coupling and arrhythmogenesis in cardiomyocytes contracting under mechanical afterload in a 3d viscoelastic hydrogel," *Proceedings of the National Academy of Sciences*, vol. 118, no. 31, Article ID e2108484118, 2021.

[6] H. Mei, W. Huang, H. Liu, L. Pan, and L. Cheng, "3d printed carbon-ceramic structures for enhancing photocatalytic properties," *Ceramics International*, vol. 45, no. 12, pp. 15223–15229, 2019.

[7] H. Belaid, S. Nagarajan, C. Teyssier et al., "Development of new biocompatible 3d printed graphene oxide-based scaffolds," *Materials Science and Engineering: C*, vol. 110, no. 1–22, Article ID 110595, 2020.

[8] A. Khanna, K. U. Ritzau, M. Kamp et al., "Screen-printed masking of transparent conductive oxide layers for copper plating of silicon heterojunction cells," *Applied Surface Science*, vol. 349, no. sep.15, pp. 880–886, 2015.

[9] C. Mcdonough, D. La Tulipe, D. Pascual et al., "Heterogeneous integration of a 300 mm silicon photonics-cmos wafer stack by direct oxide bonding and via-last 3d interconnection," *International Symposium on Microelectronics*, vol. 2015, no. 1, pp. 000621–000626, 2015.

[10] I. Arnay, J. López-Sánchez, E. Salas-Colera, F. Mompeán, A. del Campo, and G. R. Castro, "The role of silicon oxide in the stabilization and magnetoresistance switching of fe3o4/sio2/si heterostructures," *Materials Science and Engineering B*, vol. 271, no. 7, Article ID 115248, 2021.

[11] Z. H. Lim, M. Chrysler, A. Kumar et al., "Suspended single-crystalline oxide structures on silicon through wet-etch techniques: effects of oxygen vacancies and dislocations on etch rates," *Journal of Vacuum Science and Technology*, vol. 38, no. 1, Article ID 013406, 2020.

[12] J. Kim, H. J. Chung, and S. W. Lee, "Multi-level memory comprising low-temperature poly-silicon and oxide tfts," *IEEE Electron Device Letters*, vol. 42, 2020.

[13] Y. Z. Wan, M. Gao, Y. Li et al., "Potentiality of delocalized states in indium-involved amorphous silicon oxide," *Applied Physics Letters*, vol. 110, no. 21, Article ID 213902, 2017.

[14] O. Soloviova, "3d printing technology," *Applied Geometry and Engineering Graphics*, vol. 0, no. 97, pp. 136–148, 2020.

[15] Y. Melnikov, S. Zholudev, E. Vladimirova, and D. Zaikin, "Precision of production crown manufacturing using 3d-printing technology. immediate temporary restoration after dental implantation," *Actual problems in dentistry*, vol. 16, no. 4, pp. 109–114, 2021.

[16] S. L. Ng, S. Das, Y. P. Ting, R. C. W. Wong, and N. Chanchareonsook, "Benefits and biosafety of use of 3d-printing technology for titanium biomedical implants: a pilot study in the rabbit model," *International Journal of Molecular Sciences*, vol. 22, no. 16, p. 8480, 2021.

[17] A. Posmyk and P. Marzec, "Influence of 3d printing technology of automotive parts made of plastics on their tribological properties," *Tribologia*, vol. 294, no. 6, pp. 65–70, 2021.

[18] D. Zhang and X. Zhang, "Rehabilitation brace based on the internet of things 3d printing technology in the treatment and repair of joint trauma," *Journal of Healthcare Engineering*, vol. 2021, no. 9, pp. 1–11, 2021.

[19] X. Wang, C. Li, T. Q. He et al., "Repair of mandibular defects with free iliac musculocutaneous flap assisted by digital and 3d printing technology: a case report," *Zhonghua er bi yan hou tou jing wai ke za zhi = Chinese journal of otorhinolaryngology head and neck surgery*, vol. 56, no. 1, pp. 89–92, 2021.

[20] V. V. Batrakov, A. I. Krylov, V. N. Saev, B. N. Nefyodov, and V. Novichkov, "Upgrade and repair of the instrumentation equipment on the iss rs simulators using fdm 3d printing technology," *Manned Spaceflight*, vol. 2, no. 39, pp. 97–110, 2021.

Retraction

Retracted: Quantitative Detection of Amino Acids and Carnitine in Human Blood and Quality Control of Peptide Drugs

Journal of Chemistry

This article has been retracted by Hindawi following an investigation undertaken by the publisher [1]. This investigation has uncovered evidence of one or more of the following indicators of systematic manipulation of the publication process:

(1) Discrepancies in scope

(2) Discrepancies in the description of the research reported

(3) Discrepancies between the availability of data and the research described

(4) Inappropriate citations

(5) Incoherent, meaningless and/or irrelevant content included in the article

(6) Peer-review manipulation

The presence of these indicators undermines our confidence in the integrity of the article's content and we cannot, therefore, vouch for its reliability. Please note that this notice is intended solely to alert readers that the content of this article is unreliable. We have not investigated whether authors were aware of or involved in the systematic manipulation of the publication process.

In addition, our investigation has also shown that one or more of the following human-subject reporting requirements has not been met in this article: ethical approval by an Institutional Review Board (IRB) committee or equivalent, patient/participant consent to participate, and/or agreement to publish patient/participant details (where relevant).

Wiley and Hindawi regrets that the usual quality checks did not identify these issues before publication and have since put additional measures in place to safeguard research integrity.

We wish to credit our own Research Integrity and Research Publishing teams and anonymous and named external researchers and research integrity experts for contributing to this investigation.

The corresponding author, as the representative of all authors, has been given the opportunity to register their agreement or disagreement to this retraction. We have kept a record of any response received.

References

[1] Y. Ma, Y. Zhu, Z. Lu et al., "Quantitative Detection of Amino Acids and Carnitine in Human Blood and Quality Control of Peptide Drugs," *Journal of Chemistry*, vol. 2022, Article ID 1652592, 6 pages, 2022.

Research Article

Quantitative Detection of Amino Acids and Carnitine in Human Blood and Quality Control of Peptide Drugs

Yuchun Ma [ID]**, Yujie Zhu** [ID]**, Zhengqing Lu** [ID]**, Huiqing Hu** [ID]**, Jinmei Li** [ID]**,
Shangqing Yang** [ID]**, and Jiaru Han** [ID]

Pharmacy Department, Jiangsu Food &Pharmaceutical Science College, Huaian, Jiangsu 223003, China

Correspondence should be addressed to Yuchun Ma; 201812214003020@zcmu.edu.cn

In order to deal with the biochemical metabolic disorder and the lack of end metabolites caused by hereditary metabolic diseases, a quantitative detection method of amino acids and carnitine in human blood and the quality control method of polypeptide drugs were proposed. First, a method for the detection of 10 amino acids and 32 acylcarnitine metabolites in human blood was established and analyzed by liquid chromatography tandem mass spectrometry. Through the experimental research on typical peptide drugs, combined with the classical synthesis process and the PLS-DA model of human body in different regions, the relevant detection methods for the quality control of peptide drugs were established, which provided a reference for the formulation of peptide drug quality standards. The experimental results show that the quantitative detection method proposed in this paper can effectively detect the content of most amino acids and acylcarnitine. The classical detection method achieved a loss of 16.74% smaller mass-to-charge ratio, and based on this, the quantitative standard for polypeptide drug delivery was determined, which verifies the correctness and superiority of the detection method in this paper.

1. Introduction

In recent years, the quantitative detection of amino acids and carnitine in human blood has become a hot research topic worldwide. In the related background, inherited metabolic diseases (IMD), also known as inborn errors of metabolism, refer to the function of certain enzymes, transport proteins, membranes, or receptors that maintain normal metabolism in the body due to gene mutation. A type of disease that causes changes in the body's biochemical metabolism, resulting in accumulation of intermediate or bypass metabolites or lack of terminal metabolites, and a series of clinical symptoms [1]. At present, more than 500 hereditary metabolic diseases have been found, most of which are autosomal recessive inheritance, mainly including amino acids, organic acids, fatty acids, lysosomes, mitochondria, peroxidase, purines, metals, urea cycle, carbohydrate compounds and porphyrin, bilirubin, red blood cells, and other abnormal substance metabolic diseases [2].

The quality control of peptide drugs associated with it has also attracted widespread attention from scholars. Taking the typical peptide drug exenatide as an example, exenatide is a polypeptide diabetes treatment drug containing 39 amino acids. Glucagon-like peptide-1 (GLP-1) analogs have a good effect on patients with type 2 diabetes who cannot control blood sugar with oral metformin or sulfonylureas and can promote pancreatic β-cell proliferation and insulin secretion, inhibit glucagon release and slow gastric emptying, and inhibit food intake. It is the first new drug for the treatment of type 2 diabetes approved worldwide in recent years. The technical means of quality control of peptide drugs include chromatography, mass spectrometry, nuclear magnetic resonance, electrophoresis, and other methods, of which it is worth mentioning the full-column imaging capillary isoelectric focusing electrophoresis method. Capillary isoelectric focusing-whole column imaging detection (CIEF-WCID) is a new type of electrophoresis system that combines capillary isoelectric focusing and whole-column imaging technology [3, 4]. Figure 1 is a
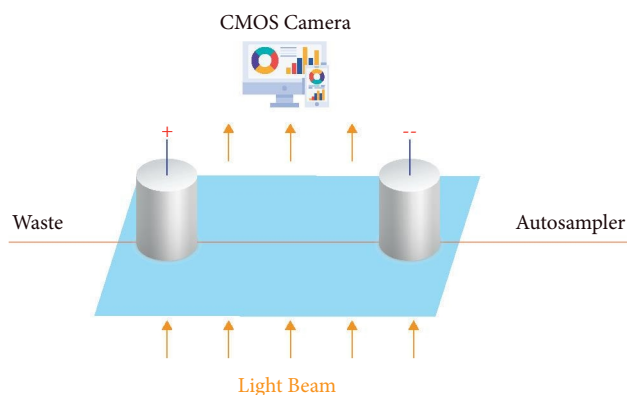
FIGURE 1: Schematic diagram of full-column imaging capillary isoelectric focusing electrophoresis apparatus.

schematic diagram of a full-column imaging capillary iso-electric focusing electrophoresis apparatus, in which one end of the capillary column is connected to an automatic sampler, and the other end is connected to a waste liquid bottle. When high-voltage direct current is applied to both ends of the cathode and the anolyte, the carrier ampholyte forms a pH gradient in the capillary column, and the sample moves to the anode or cathode according to the charged property in the 50 mm-long separation channel. When the sample moves to its isoelectric point at the same pH value, the net charge of the sample is zero, that is, isoelectric focusing separation is completed. During the entire focusing process, complementary metal oxide semiconductor (CMOS) is used as an imaging detection technology to perform dynamic imaging detection throughout the focusing process of the entire focusing separation channel.

2. Literature Review

Ashrafuzzaman et al. pointed out that one of the main characteristics of IMD is age dependence, the earlier symptoms appear, the more severe the disease, and the higher the mortality rate. In the neonatal period, abnormal symptoms of the nervous system first appear in IMD, which are mainly manifested as difficulty in sucking and feeding, abnormal breathing, slow heart rate, hiccups, and even coma. Digestive symptoms such as refusal to eat, vomiting, and diarrhea also occur shortly after eating [5, 6]. Zhang et al. found after investigation that some patients will not develop disease until months or even years after birth. The cause of the disease may be infection or eating a lot of protein-containing food, common hypoglycemia, hyper-lactatemia, metabolic symptoms such as sexual acidosis, cyclic ataxia, and coma are often misdiagnosed because they are similar to the symptoms of hypoxia, severe dehydration, infection, diabetes, and endocrine disorders. In the early stage, some diseases can be controlled, and patients can recover partially or completely through treatment methods such as drug therapy, diet control, hormone replacement therapy, gene therapy, enzyme replacement therapy, and stem cell transplantation [7]. Prof. Gao et al. successfully established a diagnostic method for phenylketonuria by the

bacterial inhibition method, started the screening of he-reditary metabolic diseases, and applied enzymatic analysis to screen galactosemia [8]. Zhang et al. carried out screening for metabolic diseases such as phenylketonuria, maple syrup, and homocystinemia [9]. The results of Song et al. showed that, in China, the screening of genetic metabolic diseases took the lead in screening newborns for phenylketonuria, congenital hypothyroidism, and galactosemia [10]. Li et al. discovered the first case of isovaleric acidemia using gas chromatography-tandem mass spectrometry. Since then, gas chromatography-tandem mass spectrometry has been widely used in the screening of genetic metabolic diseases, especially organic aciduria. However, this method has the problems of long detection time and high analysis cost [11]. Liu et al. and other researchers found that electrospray tandem mass spectrometry can rapidly detect acylcarnitines in blood samples and introduced tandem mass spectrometry technology to the screening of inherited metabolic diseases for the first time. This method requires a small amount of samples, and the analysis time is only 2-3 minutes to screen for a variety of diseases. Studies have shown that the de-tection rate of tandem mass spectrometry is twice that of traditional screening methods [12].

Bf et al. were among the first scholars to enable tandem mass spectrometry for newborn screening for inborn errors of metabolism. They screened 944,078 infants over an 8-year period, of whom 219 had disorders of amino acid or acyl-carnitine metabolism, an overall incidence rate of 1 in 4300 [13]. Louge et al. pointed out that the application of tandem mass spectrometry for the screening of inherited metabolic diseases has been gradually carried out in many economi-cally developed regions of China. Among 748 high-risk children with clinically suspected genetic metabolic diseases in a certain province, amino acid and acylcarnitine were detected, and a total of 95 cases were abnormal, with a detection rate of 12.7%, including 54 cases of amino acid metabolism diseases and 19 cases of organic acidemia and 22 cases of fatty acid oxidation deficiency disease. Researchers in another province screened 116,000 newborns, and the results showed that the incidence of amino acid and acyl-carnitine-based metabolic diseases in this region was about 1/5,800. With the gradual development of this method in China, more and more regions have successively used tandem mass spectrometry to screen various genetic and metabolic diseases [14]. Deng et al believe that the screening of inherited metabolic diseases by tandem mass spectrom-etry was first applied to detect abnormal metabolic diseases related to amino acids and acylcarnitines. For example, amino acid diseases such as phenylketonuria, maple syrup, citrulline, and argininemia; propionic acidemia, glutaric acidemia, 2-methylcrotonyl-CoA carboxylase deficiency, and other organic acid diseases; and medium and long-chain acyl-CoA dehydrogenase deficiency, trifunctional protein deficiency, and other fatty acid metabolism diseases. To enhance detection sensitivity, pre- or postcolumn deriva-tization is usually employed. Routine mass spectrometry screening for some diseases produces false-positive or false-negative results, and researchers are working to improve detection methods for these diseases. L-isoleucine is a

specific marker for diagnosing maple syrup, but because it has the same molecular weight as leucine and isoleucine, it is directly injected without chromatographic separation and mass spectrometry cannot distinguish these substances [15]. Wang et al. successfully separated leucine, isoleucine, and alloisoleucine by chromatographic separation and quantified it from valine and hydroxyproline. The results show that alloisoleucine can only be detected in patients with maple syrup diabetes mellitus. Some researchers have also explored the use of nonderivatized methods to quantify amino acids and acylcarnitines, using high-performance liquid chromatography electrospray tandem mass spectrometry for simple and rapid quantification of 20 amino acids. To obtain good chromatographic separation, perfluoroheptanoic acid was added to the mobile phase as an ion-pairing reagent [16].

On this basis, a method for the determination and control of amino acids and carnitine in human blood was established. First, the quantitative detection method of 42 amino acids and acylcarnitine in human blood was established. 37 genetic metabolic diseases of amino acid, organic acid, and fatty acid were screened by liquid chromatography and tandem mass spectrometry at 2 min simultaneously, expanding the type of disease screening. Screening of genetic metabolic diseases in 205 samples. Then, the data of 205 cases were analyzed and found a different amino acid and acylcarnitine content in different age groups, providing a guiding role in further improving the screening of genetic metabolic diseases.

3. Research Method

In this paper, a method for quantitative detection of 42 endogenous metabolites of amino acids and acylcarnitines in human blood was established mainly by liquid chromatography tandem mass spectrometry, which can simultaneously diagnose 37 kinds of amino acid, organic acid, and fatty acid metabolic diseases. The multivariate statistical analysis of the results was carried out by means of target metabolomics to study the influence of age and geographical factors on the content of amino acids and acylcarnitines, so as to control the delivery quality of peptide drugs and find possible differential metabolites [17].

3.1. Sample Collection. For newborns, blood collection should be carried out at 72 hours after birth and after 6 times of breastfeeding, and 1–1.5 hours after breastfeeding is the best time for blood collection. Sterilize the baby's heel with 75% alcohol, pierce the triangular needle or vertebral needle obliquely into the inner 0.5–0.8 cm, 2.5–3.0 mm deep from the outer edge of the heel, 1–2 cm away from the heel, discard the first drop of blood, when the blood drips naturally, touch the blood drop with 903 filter paper, so that the blood can be sucked in and penetrate the filter paper by itself, and three blood spots are collected at a time [18]. For adults, sample blood from the fingertip. After the blood samples were collected, they were naturally dried at room temperature for at least 5 hours, sealed in plastic bags, and stored in a refrigerator at 4°C.

3.2. Configuration of Working Fluid. The internal standard of amino acid and acylcarnitine isotope was dissolved in 1 mL of methanol extractant, and after shaking for 2 h, it was used as a stock solution and stored in a −20°C refrigerator. When using, the stock solution was diluted 200 times with methanol extractant as the working solution, and the working solution should be prepared on the same day [19].

3.3. Sample Preparation Method. The dry filter paper blood slices of the quality control and samples were punched into circular slices with a diameter of 3 mm with a hole punch and placed in a flat-bottom 96-well plate, and 90 μL of methanol working solution containing amino acids and acylcarnitine internal standard was added to each well to cover the viscosity. The membrane was incubated at 700 r/min at a speed of 700 r/min and shaken for 30 min at a temperature of 30°C to extract amino acids and acylcarnitines from the blood slices. Add 50 μL of 3.0 mol/L n-butanol hydrochloride derivatization reagent to each well of a 96-well plate with a pointed bottom, cover with a heat-sealing film, heat-seal at 175°C for 8 s, and then incubate at 60°C for 30 min to make amino acids and acylcarnitines after being fully derivatized [20]. The heat-sealing film was lifted off, dried with nitrogen at 50°C, 75 μL of acetonitrile reconstituted solution was added, covered with aluminum foil, the speed was 600 r/min, and the sample was reconstituted at 27°C for 10 min, and then the sample was injected with an autosampler.

3.4. Liquid Phase Method. 90% acetonitrile was used as the mobile phase, the injection volume was 10 μL, and the flow rate was set to 0–0.16 min 0.15 mL/min, 0.16–1.20 min 0.01 mL/min, and 1.20–1.40 min 0.6 mL/min [21].

3.5. Mass Spectrometry. Electrospray positive ion detection mode was used, Ala, Leu, Met, Phe, Tyr, Val, and corresponding isotope internal standards were scanned by neutral loss; the mass-to-charge ratio of neutral loss group was 102.1 Da, cone voltage: 22 V, collision energy: 13 V. C4, C4-OH, C5, C5-OH, C5: 1, C6, C8, C8: 1, C10, C10: 1, C10: 2, C12, C12: 1, C14, C14-OH, C14: 1, C14:2, C16, C16-OH, C18, C18-OH, and C18:2; and the corresponding isotope internal standard was scanned by parent ion, product ion was 85 Da, cone voltage: 30 V, collision energy: 27 V. Gly, Orn, Arg, Cit, C0, C2, and the corresponding isotope internal standards were scanned by multiple reaction monitoring. The mass spectrometry parameters are shown in Table 1 [22].

3.6. Data Processing and Statistical Analysis. MassLynx software was used for data processing, and the contents of amino acids and acylcarnitine metabolites were calculated. The calculation formula is

$$C = \frac{m_1}{m_2} + \mathrm{IS} + \mathrm{RRF} + X, \tag{1}$$

Table 1: Multiple reaction monitoring scan mode mass spectrometry parameters.

	Parent (m/z)	Daughter (m/z)	Dwell (s)	Cone (V)	Collision (V)
Gly	132.1	76	0.05	20	8
Orn	189.2	70.1	0.05	21	16
Arg	231.2	70.1	0.05	24	20
Cit	232.2	113.1	0.05	22	19
C0	218.3	103	0.05	26	17
C2	260.3	85	0.05	28	21

where m_1 is the peak area of the detected component, m_2 is the peak area of the internal standard, IS is the concentration of the internal standard, RRF is the relative response factor, and X is a custom factor. Using SIMCA-P+ (version12.0, Umetrics, Umea, Sweden) statistical analysis software, multivariate statistical analysis was carried out on the content of amino acids and acylcarnitine metabolites. The pattern recognition method included principal component analysis (PCA) and partial least squares-discriminate analysis (PLS-DA). The differential variables were screened by the VIP value (variable importance on projection) of the PLS-DA model variables, and the variables with VIP >1 were selected as differential metabolites, which were further screened by combining the T test. When $P < 0.05$, there was a significant difference [23].

4. Result Analysis

When using tandem mass spectrometry to detect amino acids and acylcarnitines in blood slices, the samples are not separated by a chromatographic column, but a lower flow rate is selected to allow the samples to enter the mass spectrometer directly and slowly, using electrospray ionization. Select the appropriate liquid phase conditions to obtain the ideal mass spectral response [24]. Figure 2 shows the total ion current chromatogram of metabolites in normal human body, and the total running time of each sample does not exceed 2 min.

Most α-amino acids react with the derivatizing reagent n-butanol to generate the corresponding butyl esterification products, and the neutral fragments with a molecular weight of 102.1 Da are lost under the action of collision-induced cleavage. Therefore, the neutral loss scanning method is adopted. The scanning range is the same. The butyl esterification product formed by the reaction of acylcarnitine with n-butanol undergoes 1,4 rearrangement and α-cleavage under the action of collision-induced cleavage to lose 1-butene, fatty acid, and trimethylamine, resulting in a molecular weight of 85 Da. The fragment ion is suitable for the method of parent ion scanning, and Q3 only allows ions with a molecular weight of 85 Da to pass and detect. A small number of amino acids and acylcarnitines are more sensitive in the scanning mode of multiple reaction monitoring [25]. Therefore, in the experiment, we used a combination of neutral loss scanning, parent ion scanning, and multiple reaction monitoring scanning to detect amino acids and acylcarnitines. The experimental results showed that the detection method proposed in this paper achieved a 16.74%
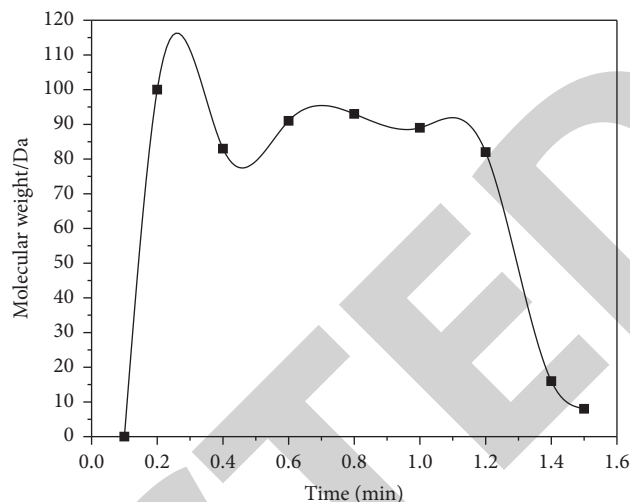

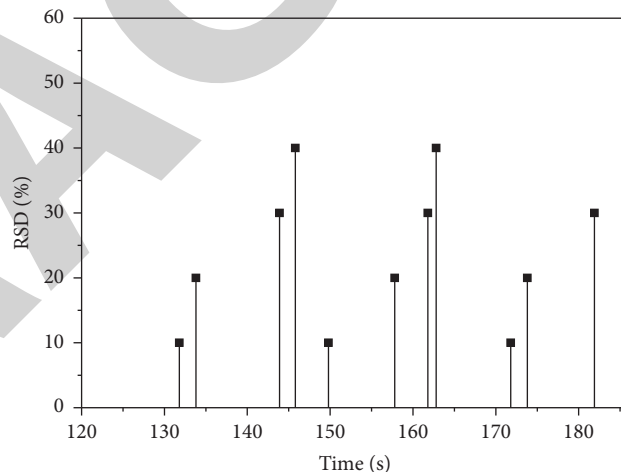Figure 2: Total ion chromatogram of metabolites in normal humans.

Figure 3: α amino acid neutral loss scan mass spectrum.

of the missing mass-to-charge ratio. Figure 3 is a mass spectrogram of metabolites in a normal human body.

In this experiment, the intraday and interday precision of the method was also investigated, and the RSDs of amino acids and acylcarnitines in the low- and high-concentration quality controls were calculated, respectively. The experimental results are shown in Table 2. The intraday and interday RSDs of the low-concentration quality control were 2.55%–20.58% and 7.42%–23.68%, respectively, and the intraday and interday RSDs of the high-concentration quality control were 1.31%–17.15% and 7.35%–22.01, respectively (%). This method can fully meet the experimental needs in which the slightly higher RSD may be due to the different sampling locations of the quality control blood slices each time or because of the longer time interval between repeated measurements during the day.

According to different regions, people aged 22–35 can be divided into high-altitude group and nonaltitude group, and a PLS-DA model was established to determine the delivery

TABLE 2: Within-day ($n = 3$) and between-day precision ($n = 18$) of metabolites in quality control.

Metabolites	Intraday RSD (%)		Daytime RSD (%)	
	Low concentration quality control	High concentration quality control	Low concentration quality control	High concentration quality control
Gly	4.15	4.88	7.42	7.35
Cit	5.26	1.31	8.31	7.82
Ala	6.52	17.15	14.50	17.19
Val	10.98	14.24	14.09	22.01
Leu	5.58	3.88	11.80	8.48
Met	7.38	4.90	9.23	10.20
Phe	3.76	4.06	9.49	8.47
Tyr	8.97	7.72	10.83	10.57
C0	19.53	14.64	19.74	19.14
C2	11.70	6.66	13.22	12.62

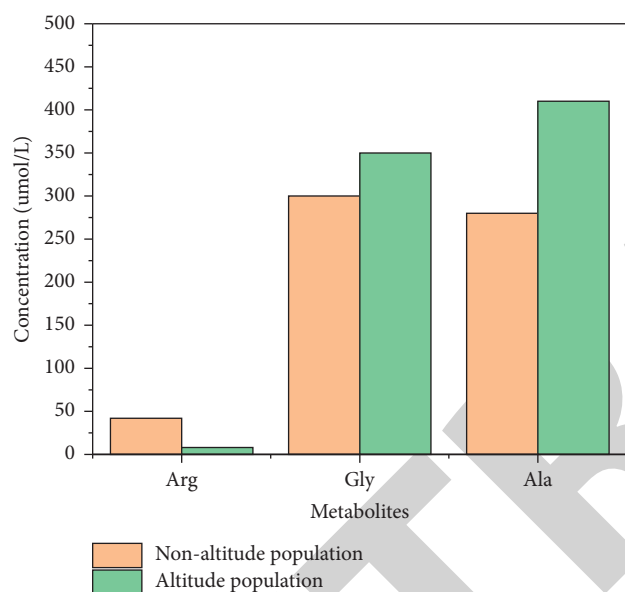FIGURE 4: Reference amount of human peptide drug quality delivery in different regions.

quality of peptide drugs. The model R2X = 0.758, R2Y = 0.893, and Q2 = 0.717. There is a separation trend between the endogenous metabolite PLS-DA group in the 20–35-year-old high-altitude population and the non-altitude population, indicating that there are differences in the metabolite content in the blood of the two populations. Ala, Arg, Gly, Leu, Tyr, Orn, Val, and Phe are the main differential metabolites. Among them, Ala, Gly, Orn, Leu, and Val are higher in the plateau population, while Arg, Tyr, and Phe are in the nonaltitude population. In order to further verify the significant difference of the differential metabolites, combined with T test, the differential metabolites Arg, Ala, and Gly were found ($P < 0.05$). Figure 4 shows the reference amount of peptide drug quality delivery in different geographical populations based on the experimental results. The average Arg value detected in 9 high-altitude samples was 9.12 μmol/L, and the average Arg value in 10 nonaltitude samples was 46.09 μmol/L; in the corresponding two groups, the mean values of data Ala were

432.26 μmol/L and 291.74 μmol/L and Gly contents were 365.39 μmol/L and 306.18 μmol/L, respectively. The obvious decrease of Arg content in the population in the plateau area may be due to the increase in the utilization of Arg. Arg can not only be used for protein synthesis but also a substrate for NO synthase and Arg enzymes. The enhanced utilization of Arg leads to an increase in NO synthesis and a significant expansion of NO. Vascular effect and some studies have also shown that the exhaled NO level in the plateau population is higher than that in the nonaltitude population. The Arg enzyme converts Arg to Orn, which is consistent with the increase in Orn. The different contents of amino acids in different regions may be related to plateau hypoxia and dietary habits, which may provide some guidance for the evaluation of nutritional health status of plateau population.

5. Conclusion

This paper is mainly divided into two parts, the first part is the quantitative detection of amino acids and carnitine in human blood, and the second part is the quality control research of polypeptide drugs. First, a quantitative detection method for 42 amino acids and acylcarnitines in human blood was established, and 37 amino acids, organic acids, and fatty acids were screened simultaneously by liquid chromatography tandem mass spectrometry in 2 minutes, and the disease screening was expanded. Type: cthe screening of 205 samples of hereditary metabolic diseases was completed. Then, the data of 205 samples were analyzed and counted, and it was found that the contents of amino acids and acylcarnitines in the blood of different age groups were different, which provided guidance for further improving the screening of inherited metabolic diseases. The contents of some amino acids in different regions are also different, which will provide a basis for the quality of peptide drug delivery required by different regions. The method of electrofocused electrophoresis is rapid, accurate, and reproducible. By optimizing the experimental conditions, the detection method of related substances of exena skin is established, proving the feasibility of the method and checking the related substances of exena skin samples, to provide a new technical means for the determination of electric points and the inspection of related substances.